SYNTHETIC, SPECTRAL AND SUPRAMOLECULAR EXPLORATION OF SOME METAL COMPLEXES WITH NITROGEN-BASED HETEROCYCLES

THESIS SUBMITTED FOR THE DEGREE OF

DOCTOR OF PHILOSOPHY (SCIENCE)

OF

JADAVPUR UNIVERSITY

SAMIT PRAMANIK, M. Sc

DEPARTMENT OF CHEMISTRY

JADAVPUR UNIVERSITY

KOLKATA 700 032

INDIA

2023

CERTIFICATE FROM THE SUPERVISORS

This is to certify that the thesis entitled **"Synthetic, spectral and supramolecular exploration of some metal complexes with nitrogen-based heterocycles"** submitted by Sri Samit Pramanik who got his name registered on 28. 08. 2019 for the award of Ph. D. (Science) degree of Jadavpur University, is absolutely based upon his own work under the supervision of Dr. Subrata Mukhopadhyay, Professor, Department of Chemistry, Jadavpur University, Kolkata 700032 and co-supervision of Dr. Sudipta Pathak, Assistant Professor, Department of Chemistry, Haldia Government College, Debhog, Purba Medinipur 721657. It is also mentioning that neither this thesis nor any part of it has been submitted for any degree / diploma or any other academic award anywhere before.

Subrata Mukhopadhyay 6/2/2023

Dr. Subrata Mukhopadhyay (Supervisor)

Professor
Department of Chemistry
Jadavpur University

Dr. Subrata Mukhopadhyay
Professor of Chemistry
Jadavpur University
Kolkata – 700032

Sudipta Pathak 6/2/2023

Dr. Sudipta Pathak (Co-supervisor)

Assistant Professor
Department of Chemistry
Haldia Government College

Dr. Sudipta Pathak
Assistant Professor (W.B.E.S)
Department of Chemistry
Haldia Government College
Debhog, Purba Medinipur

Signature of the Supervisors and date with official seal

Dedicated to
My
Beloved Parents

Acknowledgements

This is one of the finest moments in my academic career when I get the opportunity to express my indebtedness to all, who have been attached to my academic career and all of my near and dear ones.

First of all, I would like to express my deep sense of gratitude and indebtedness to my esteemed supervisor, Prof. Subrata Mukhopadhyay, Department of Chemistry, Jadavpur University, Kolkata 700032 and the co-supervisor, Dr. Sudipta Pathak, Assistant Professor, Department of Chemistry, Haldia Government College, Debhog, Purba Medinipur for introducing me into the field of research work. Their active guidance, advice and constant encouragement throughout the duration made the completion of the thesis possible.

Apart from the invaluable guidance, helpful suggestions, informative discussions, their endless tolerance in organizing and representing scientific results with ultimate precision deserve special mention.

I cordially convey my gratitude to the Indian and foreign collaborators, Prof. Antonio Frontera and Prof. Joaquin Ortega-Castro of the Universitat de les IllesBalears, Spain for DFT calculations and Dr. Parimal Karmakar, Department of Life Science and Biotechnology, Jadavpur University, Kolkata 700032, for biological study of a few samples.

I gratefully acknowledge Dr. Sumanta Jana, Micro Analyst, Department of Chemistry, Jadavpur University, Kolkata 700032, for photoconductive property analysis as well as for his constant support throughout my Ph.D. work.

I have hardly any words to express my sincere gratitude to Dr. Kinsuk Das, Assistant Professor, Department of Chemistry, Chandernagore College for his tremendous support and constant encouragement during the progress of my work. I will always memorize his fruitful association during my Ph.D. work.

I wish to thank my seniors Dr. Abdullah Al Masum, Dr. Sanchita Mandal, Dr. Anowar Hossain, Dr. Tripti Mandal, Dr. Nurunnesa Siddiqui, Dr. Pampi Paul, Dr. Joydeb Goura for their valuable suggestions and kind co-operation whenever I needed them. I especially wish to thank my lab mates Arjina Khatun, Subhajit Saha, Nirvik Ghosh, Pue Dutta, Ersad Hossain, Tanmay Mondal and Biplab Biswas not only for their cooperation during my Ph.D. research work but also for making the entire journey so

memorable. It has been my pleasure to work in this team that has become an extended family for me.

Dated: 06/02/2023

Department of Chemistry

Jadavpur University

Kolkata 700 032

INDIA

SAMIT PRAMANIK

CONTENTS

Foreword

Supramolecular chemistry is described as "chemistry beyond the molecule" and mainly business with weak and reversible intermolecular interactions. This extensive field of chemistry deals with the chemical systems made up of a discrete number of assembled molecular subunits or components and focuses on the non-covalent interactions, such as hydrogen bonding, hydrophobic forces, electrostatic effects, van der Waals forces, $\pi\bullet\bullet\bullet\pi$, lone pair$\bullet\bullet\bullet\pi$, anion$\bullet\bullet\bullet\pi$, C─H$\bullet\bullet\bullet\pi$ interactions that govern the structures, properties and transformations of molecular species. The advancement of this field is now applied for the drug delivery system, nanotechnology, medical applications, environmental, energy technologies through the specific interactions between related molecules. It thus establishes the emergence of supramolecular science and technology as an expansive interdisciplinary and multidisciplinary domain that creates a vast productive field from all origins of science.

Nitrogen-based heterocycles resemble one of the large classical divisions of chemistry and an enormous amount of research work is carried out in this area. Nitrogen based heterocycles have applications in a wide variety of drugs, biologically active compounds, and sensing. These compounds are capable of forming metal complexes, besides they have applications in supramolecular chemistry and polymer chemistry.

In recent years, crystal engineering has developed as one of the most appealing areas of chemical research. The huge attraction in this field is mainly due to fundamental and applied reasons. Due to its uncanny nature it is hard to predict what network will be formed for a given ligand–metal combination and how these networks will interact with one another in the crystal. Understanding the relationships between molecular and supramolecular chemistry is one of the major challenges in this area.

In this dissertation, some nitrogen-based heterocycles and their metal complexes were synthesized and crystallographically characterized. A detailed investigation and exploration of various non-covalent interactions those play a significant role in forming the supramolecular architectures of those newly synthesized metal complexes have been described. Advanced level theoretical studies have been used to analyze the different non-covalent interactions present in the solid state of the newly synthesized complexes. Finally, some of these metal complexes have been used to study photo-physical and biological properties.

Chapter 1

This chapter illustrates the background for the work presented in this thesis. This chapter briefly describes salient features of supramolecular chemistry, crystal engineering, supramolecular synthon, molecular recognition, host-guest chemistry, non-covalent interactions and theoretical (DFT) studies. It also includes various nitrogen-based heterocycles and their application in coordination chemistry, metal ion sensing, photophysical and biological studies.

Chapter 2

This chapter describes the preparation of two copper (II) complexes from a newly synthesized ligand, N**L** [4-(1-methylimidazole)-2,6-di(pyrazinyl)pyridine] and their characterization by spectroscopic as well as by single crystal X-ray diffraction method. Mainly, lone pair•••π(chelate ring) and π•••π(chelate ring) interactions are well investigated in governing the solid state architecture of the complexes. Besides, the other non-covalent interactions like π•••π stacking, sulphur•••π and hydrogen bonding interactions play crucial role in the crystal packing for both the complexes. Theoretical (DFT) calculations including QTAIM and NCI Plot index have been carried out to analyze the non-covalent interactions in the solid state for both the complexes.

Chapter 3

This chapter includes synthesis, X-ray structural determination, Hirshfeld surface analyses and DFT studies of two Cu (II) complexes derived from 4-(1-methylimidazole)-2,6-di(pyrazinyl)pyridine moiety. The structural insights reveal that non-classical hydrogen bonding (C–H•••Cl, C–H•••O, C–H•••N) and π•••π stacking interactions play a crucial role in stabilizing various supramolecular architectures of the title complexes in the solid state. All the non-classical hydrogen bonding interactions have been quantified through the infographic 2D fingerprint plots. Additionally, theoretical calculations (density functional theory) have been carried out for both complexes to analyze these non-covalent interactions in the solid state including their characterization using Bader's theory of atoms in molecules and the non-covalent interaction (NCI) plot index.

Chapter 4

This chapter presents the synthesis of nickel(II) complexes where both 2,4,6-tri(pyridin-2-yl)-1,3,5-s-triazine and di-picolinic acid act as tridentate ligands for complex **1** and only 2,4,6-tri(pyridin-2-yl)-1,3,5-s-triazine is employed as tridentate ligand for complex **2**. The non-covalent interactions witnessed in the crystal packing of both complexes have been well-defined focusing on $\pi\bullet\bullet\bullet\pi$, $\pi\bullet\bullet\bullet\pi^+$, lone pair$\bullet\bullet\bullet\pi$ (complex **1**) and $\pi\bullet\bullet\bullet\pi$, anion$\bullet\bullet\bullet\pi$, C—H$\bullet\bullet\bullet\pi$, $\pi^+\bullet\bullet\bullet\pi^+$, anion$\bullet\bullet\bullet\pi^+$ (complex **2**) along with hydrogen bonding interactions, which have been analysed using DFT calculations. Change in the auxiliary ligand exhibits variation on substantial structures, band gaps and photo-response properties in the present complexes.

Chapter 5

This chapter deals with the design and synthesis of a simple pyridine-dicarbohydrazide based chemosensor (**L**) for Al^{3+} ions sensing in organo aqueous solution. In presence of Al^{3+} ions, probe **L** exhibits visible color changes and fluorescence enhancement (20-fold) due to Al^{3+} induced chelation-enhanced fluorescence (CHEF) effects. The chemosensor **L** reveals high selectivity toward Al^{3+} ions by "turn-on" fluorescence among the other competitive metal ions examined with a detection limit of 0.8 µM. The probe **L** has been found to bind with Al^{3+} ions in a 1: 2 (probe: metal) stoichiometric fashion, with the association constant (K_a) of 4.26×10^4 M^{-2}. In addition, DFT and TDDFT calculations have been carried out to recognize the binding nature and electronic properties of the probe **L** and its Al-complex. Furthermore, *in situ* prepared [**L**-Al] complex is able to detect HF_2^- anions via a metal displacement strategy. The bioimaging application of Al^{3+} and HF_2^- have been implemented in the living human liver cancer cells (Hep G2).

Chapter 6

This chapter covers the preparation of two Zn(II) complexes using newly synthesized [(1-methylimidazol-2-yl)methylene]isonicotinohydrazide [H**L**] moiety as the backbone ligand with two different metal salts. Single crystal X-ray diffraction structures of both the complexes have been established. The non-covalent interactions and supramolecular assemblies observed in the crystal packing of both complexes have been described focusing on $\pi\bullet\bullet\bullet\pi$ (complex **1**) and O$\bullet\bullet\bullet\pi$-hole (complex **2**) interactions along

with various hydrogen bonding interactions. A DFT study has been carried out to analyze the non-covalent interactions with their rationalization using molecular electrostatic potential (MEP) surfaces and the combined QTAIM/NCI plot computational tools. In addition, the *in vitro* biological activities of the synthesized ligand (H**L**) and the water soluble complex **2** have been evaluated against *Escherichia coli* and *Staphylococcus aureus*.

Chapter 7

This chapter involves the synthesis and crystallographic characterization of a series of tetrachlorometallates including Zn (II) (complex **1**), Cd (II) (complex **2**) and Hg (II) (complex **3**) with the help of a triply protonated tptz (H$_3$tptz^{3+}) ligand. The crystallographic analysis reveals that the anion•••π, anion•••π$^+$ and several hydrogen boding interactions play a fundamental role in the stabilization of the self-assembled architectures that in turn helps to enhance the dimensionality of all the complexes. In addition, Hirshfeld surfaces and fingerprint plots have been deployed here to visualize the similarities and differences of hydrogen bonding interactions in **1−3**, which are crucial in building supramolecular architectures. A DFT study has been used to analyze the non-covalent interactions with their rationalization using molecular electrostatic potential (MEP) surfaces and the combined QTAIM/NCI plot computational tools. Then, the device parameters for complexes **1** to **3** have been thoroughly investigated by fabricating SBD on ITO substrate. It has been observed that the device made from complex **2** is superior to complexes **1** and **3**. Finally, theoretical calculations have been carried out to rationalize the experimental differences in band gap and conductivity observed for all the complexes.

CHAPTER 1

A brief introduction of supramolecular chemistry and crystal engineering: emphasis on nitrogen-based heterocycles and their coordination complexes

Host-guest Chemistry

H-bonding   π···π   C–H···π

cation···π   anion···π   lone pair···π

Non-covalent Interactions

Supramolecular Chemistry

Molecular Recognition

Self-Assembly and Self-Organization

Supramolecular Synthon
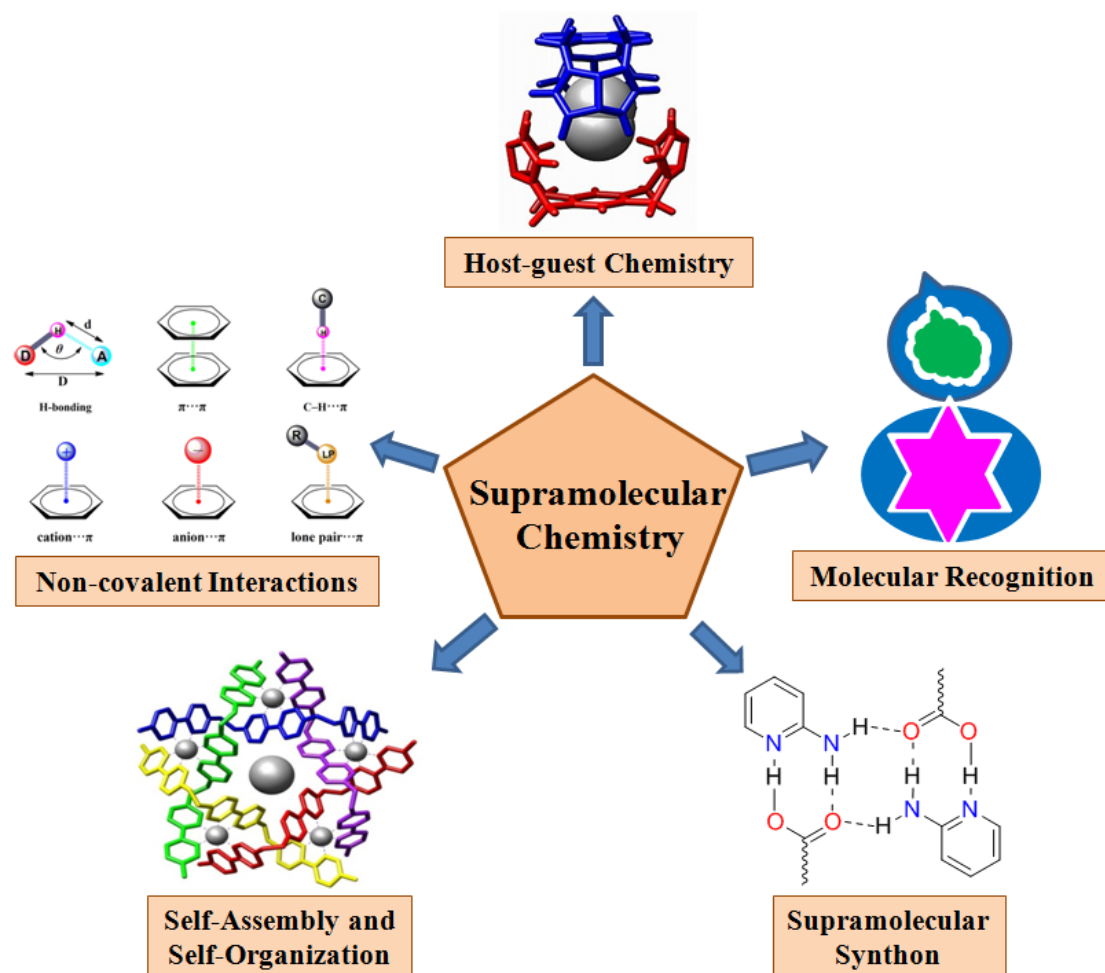
1.1. GENERAL INTRODUCTION

After the excellent proposal of Alfred Werner [1866–1919: The Swiss Chemist, received the Nobel prize in 1913] concerning bonding and structural features of coordination compounds, chemists gained enormous interest in synthesizing variety of complexes worldwide. In this synthetic journey, the judicious choice of metal ion, primary ligand, ancillary ligand, counter ions, solvent, temperature, pH *etc.*, play a crucial role in synthesizing the complex. In the last few decades, there has been a tremendous growth in 'coordination chemistry' due to their broad multidisciplinary applications, *e.g.*, pure, applied, analytical and in particular material and biological fields.

The chemistry of heterocyclic bases with at least one heteroatom like nitrogen, oxygen, sulfur *etc.*, arrest significant attention not only for their potent role as ligands for complex formation with several transition metal ions but also for their physiological and medicinal importance. In all the complexes of heterocycle ligands, the lone pair of electrons on the heteroatoms takes part in forming metal-ligand bonds effectively.

Among other heterocyclic ligands, the appearance of multidentate chelate ligands has brought huge improvements in the field of coordination chemistry. It is extensively acknowledged that the ligand design is vital for the synthesis of coordination complexes with desired properties. In this context, multidentate ligands may support several transition metal centers having different electronic states through the chelate coordination approach. However, they may be specifically planned by their organized structural modulations that set up the unique balance of stability *vs* reactivity of the synthesized complexes.

Generally, the ligands are synthesized directly from desired chemical constituents and then characterized using CHN (carbon, hydrogen, nitrogen) analysis, ^{1}H NMR spectroscopy, ^{13}C NMR spectroscopy, IR spectroscopy, mass spectrometry, *etc*. Then, it was utilized for complex formation by selecting appropriate metal salts. In this synthetic journey, scientists exposed that the transition metal ions are the most effective candidates for complex formation.

The level of synthetic chemistry has reached at its supreme through a dramatic transformation from covalent synthesis and formulation of molecular compounds to the programmed design of more elaborate either nanoscaled, mesoscaled, or macroscaled supramolecular materials sustained by a combination of covalent, coordinative and noncovalent forces. These supramolecular materials are capable of generating effectively well organized supramolecular hierarchical architectures, by self-assembly from their components, and new forms of matter with unique properties that are not found in the

individual building blocks. Hence supramolecular chemistry is a highly interdisciplinary field that has rapidly expanded at the frontiers of chemical science with physical and biological phenomena.

In recent years the world of non-covalent interactions is growing fast. Particularly, those related with aromatic rings, have attracted interest among physicists, chemists, theoreticians and material scientists, mostly due to their abundances in chemical as well as in biochemical processes. The remarkable progress achieved in the history of supramolecular chemistry is supported by mounting theoretical studies of solid-state structures.

Before going into the discussion in detail on the subject matter of the present thesis entitled "*SYNTHETIC, SPECTRAL AND SUPRAMOLECULAR EXPLORATION OF SOME METAL COMPLEXES WITH NITROGEN-BASED HETEROCYCLES*" it is a convention to depict a brief review of the work done so far on the synthetic and structural elucidation of coordination compounds from supramolecular point of view.

1.2. A BRIEF DISCUSSION OF NITROGEN BASED HETEROCYCLIC LIGANDS USED IN COORDINATION CHEMISTRY

Heterocyclic compounds are the group of cyclic compounds that contain at least one heteroatom (different from carbon and hydrogen) as a member of their cyclic ring(s) [1–3]. The field of heterocyclic chemistry mainly deals on stable ring structure which does not go on hydrolyses easily. However, heterocyclic compounds can comprise more than one heteroatom (*e.g.*, pyrimidine, pyridazine, pyrazine, imidazole, triazine, *etc.*) in their cyclic structure. It is noteworthy to mention that heterocycles with one heteroatom are generally stable whereas heterocycles with two heteroatoms are likely to be more reactive owing to the ring strain.

Nitrogen-containing aromatic heterocyclic compounds are one of the largest classical divisions of heterocyclic chemistry (Fig.1.1). With inherent lone pair electrons, nitrogen can coordinate with various transition metal cations. These heterocycles are well known for having various pharmacological properties as well as they are the major structural ingredients of several bioactive natural products including vitamins, antibiotics, glycosides, hormones, alkaloids, *etc*. [4–6]. Thus, the synthesis of these heterocycles has immersed widespread attention for their ever-growing applications in industrial, agricultural, food flavoring, dyes and adhesive sectors.

Pyridine is the supreme prevalent among nitrogen-containing heterocycles, which has been selected as a unique ligand towards metal ions for many years and now the coordination

chemistry of pyridine and substituted pyridines are well established. Pyridine ring containing compounds also cover a broad bio-spectrum with several pharmacological properties such as anti-inflammatory, antimicrobial, anti-convulsant, anticancer, and antibacterial activities [7–10]. Since five membered hetero cycles are π-excessive, they act as better π donor (hard donor centre) compared to six membered heterocycles.
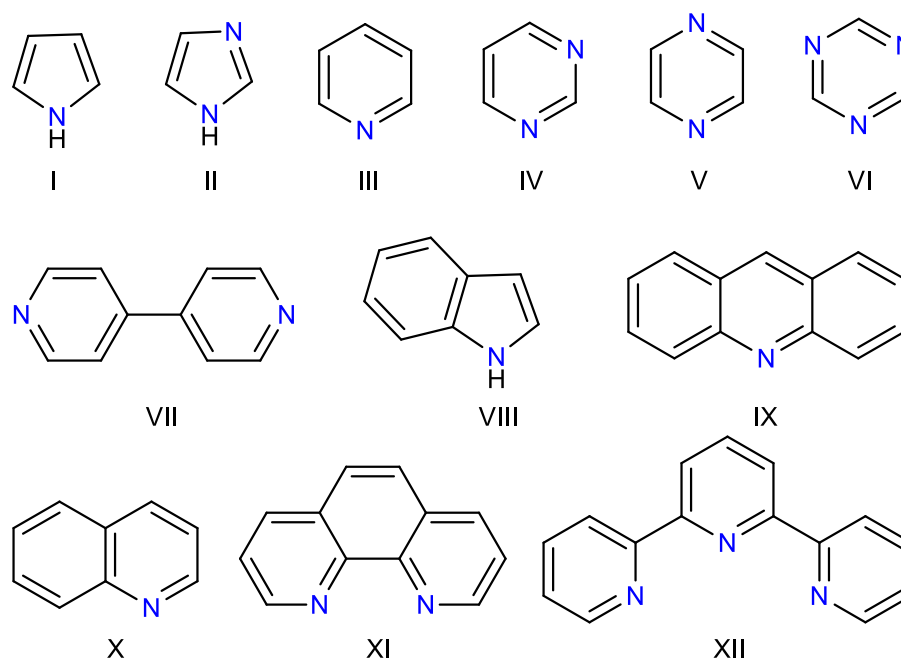
Fig. 1.1. Structures of some nitrogen-based heterocyclic compounds, (I) pyrrole, (II) imidazole, (III) pyridine, (IV) pyrimidine, (V) pyrazine, (VI) 1,3,5-triazine, (VII) 4,4′-bipyridine, (VIII) indole, (IX) acridine, (X) quinoline, (XI) 1,10-phenanthroline, (XII) 2,2′:6′,2″-terpyridine.

Among nitrogen-based heterocyclic structures, 2,2′:6′,2″-terpyridine (terpy) is has gained substantial interest in recent years [11,12]. In 1932, this was first synthesized by heating pyridine with anhydrous iron(III) chloride at a temperature of 340 °C in an autoclave for 36 hours [13]. From that time, a variety of terpyridine ligands functionalized at different positions, have been prepared and numerous review articles have been published on this topic. As an *NNN*-tridentate ligand, terpyridine plays an important role in coordination chemistry due to its outstanding chelating ability (*cis*, *cis* arrangement of the three nitrogen atoms) towards various metal ions as well as dπ−pπ* back bonding of the metal to pyridine rings. Besides, it always prefers to adopt a planar geometry to attain maximum conjugation in the metal complexes.

From the view of supramolecular chemistry, terpyridine or their analogs have found as building blocks for the creation of highly sophisticated architectures, such as racks, ladders, grids, helicates, catenanes, knots and dendrimers [14,15]. The effortless functionalization of terpyridine at the 4′-position with various organic or inorganic moieties and its capability to produce stable complexes with several transition metal ions tunes several photo-physical and electrochemical properties [16–18]. Some 4′-substituted 2,2′:6′,2″-terpyridines which have been found imperative as molecular building blocks in both organic and inorganic supramolecular chemistry (Fig. 1.2).
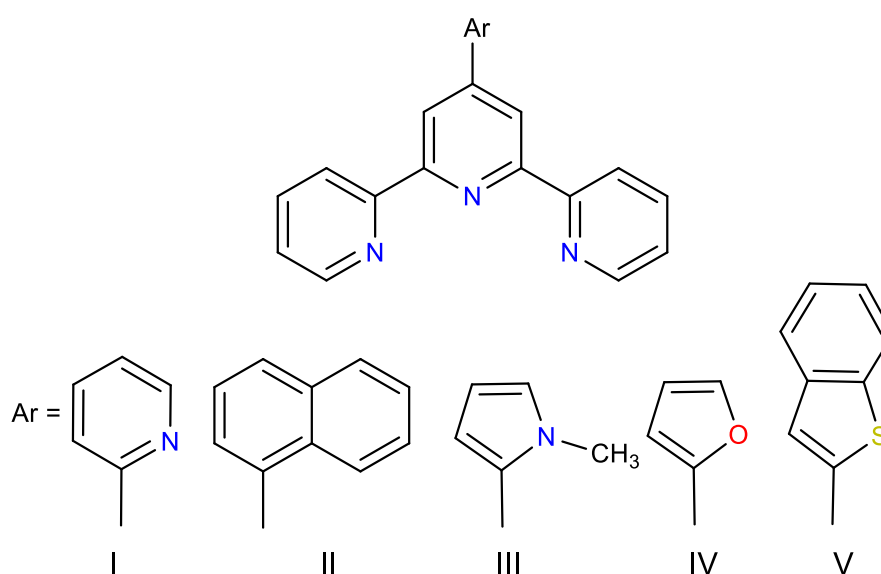
Fig. 1.2. Structures of some 4′-substituted 2,2′:6′,2″-terpyridines employed as molecular building blocks in supramolecular chemistry, (I) – 2-pyridyl, (II) – naphthalen-1-yl, (III) – 1-methyl-1*H*-pyrrol-2-yl, (IV) –furan-2-yl, (V) – benzothiophen-2-yl.

2,4,6-tris(2-pyridyl)-1,3,5-triazine (tptz) or its structural analogues have been well recognized metal binding sites which can generate an enormous curiosity in the field of modern supramolecular chemistry [19,20]. As a flexidentate coordinating ligand it exhibits different coordination modes with the metal centres (Fig. 1.3). The major coordination mode of 'tptz' is tri-dentate terpyridine like (Fig. 1.3a).

Furthermore, it is capable to coordinate two metal centres in one terpyridine and one bipyridine like coordination modes (Fig. 1.3b) and to bind three metal centres via all bipyridine-like coordination, though this binding mode is quite infrequent (Fig. 1.3c).
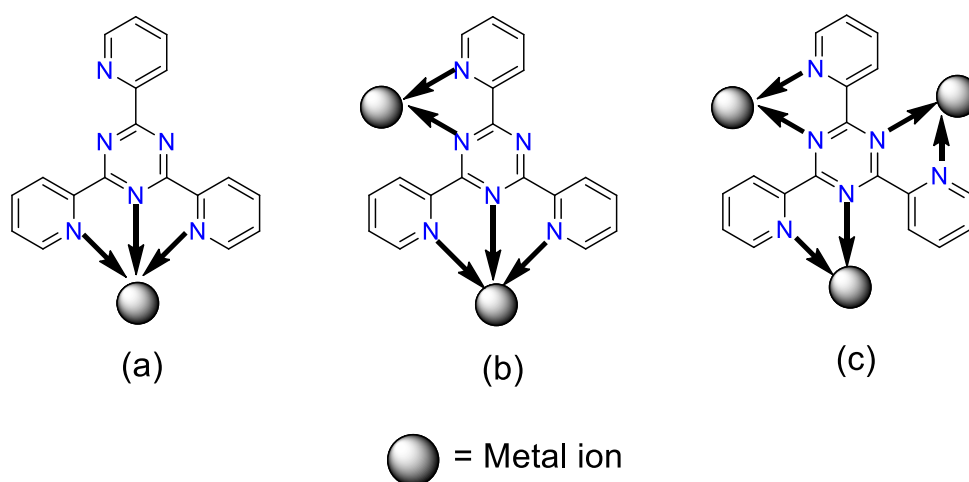
Fig. 1.3. Schematic representation of the possible coordination modes of the ligand '**tptz**'

From crystal engineering point of view nitrogen-based heterocycles have been preferred due to their ability to build $\pi\bullet\bullet\bullet\pi$, cation$\bullet\bullet\bullet\pi$, anion$\bullet\bullet\bullet\pi$, lone pair$\bullet\bullet\bullet\pi$, C–H$\bullet\bullet\pi$ interactions. The potentiality of such interactions is based on interaction between electron deficient and electron rich moieties that in turn forms the self-assembly of small molecules into supramolecular architecture. These interactions are also responsible to enhance both dimensionality and directionality in the solid state of transition metal complexes.

Here, strategically π-rich aromatic ligand systems have been selected for metal coordination. The role of auxiliary ligands and counter ions has been explored from crystal engineering point of view. The metal salts of nickel, copper and zinc have been chosen due to their capability in forming various coordination geometries.

The complexes produced after the careful selection of transition metal and heterocyclic ligands have revealed potential applications as functional materials due to their interesting structural aspects as well as supramolecular activities. Although the electrical properties of these complexes are not much prominent due to the presence of a large number of insulating carbon atoms in the structural assembly, but; the judicious choice of nitrogen-based heterocycles as primary ligands can stimulate the charge transport phenomenon of the complexes [21−23]. Besides, the polymeric nature of the complex may influences the electrical property at specified photon absorption energy. The electron-transfer mechanism is assisted by the regular periodicity of the conjugated π system in heterocycle-based coordination polymer, leading to the improvement in device performances than the discrete complexes that is stabilized by non-covalent interactions like hydrogen-bonding and π–π stacking interaction.

In addition, the extended conjugation of the directly linked aromatic ring via π-electrons enhances the photosensitization and light-harvesting ability of the terpyridine ligand. Particular research has been devoted on the outstanding photo-physical and redox properties of terpyridine-metal complexes, which have arrested noticeable attention in the field of organic light-emitting devices including molecular electronics, catalysis, solar energy, photo-sensitizers and electroluminescent dyes [24]. Hence, there is a requirement for developing novel metal-terpyridine complex with better optoelectronic features and related theoretical studies to enhance our knowledge of the interplay between the structure and photo-physical properties.

1.3. FLUORESCENCE SPECTRAL PROPERTIES OF NITROGEN-BASED HETEROCYCLES

The term 'sensor' can be defined as the system which on stimulation by any form of energy undergoes a change in its state and this change also affects one or more of its characteristics that can be measured both qualitatively as well as quantitatively [25]. A chemosensor is a compound which provides a detectable change in electrical, optical, or magnetic signal when it binds to a specific guest counterpart. These receptor molecules can selectively response to specific ions or neutral species. According to Cambridge definition [26], *"chemical sensors are miniaturized devices that can deliver real time and on-line information on the presence of specific compounds or ions in even complex samples"*. Chemosensing (application of chemosensors) is a special type of molecular recognition. The application of fluorescence devices for the sensing of chemical species has achieved momentous significance presently in the field of chemical, biological and environmental science.

The main objective for the improvement of fluorescent chemosensors is to study the physiological processes of the target analyte in their original environment. Although the employment of fluorescent chemosensors has been started over 150 years we have observed the massive growth of this field over the past few years. Fluorescent chemosensors are those compounds which have a binding site (fluorophore) and a mechanism for communication between the two sites [27]. Again, ion-selective sensors can be employed to examine metal ion concentrations in solutions, waste sewage watercourses as well as in drinking water. The design and synthesis of chemosensors as a tool for the selective and sensitive detection of transition as well as heavy metal ions has gained explosive curiosity not only due to their vital functions in a living organism but also their enormous toxic impact on the environment

[28–31]. Additionally, some metal ions like Zn^{2+} and Cd^{2+} are magnetically as well as spectroscopically silent due to their $3d^{10}4S^0$ and $4d^{10}5S^0$ electronic configurations, respectively. Besides, Al^{3+} detection is also often hampered due to its low coordination capability, high hydrationaptitude as well as lack of spectroscopic features.

Henceforth, the development of either turn on or turn off (Fig. 1.4) fluorescent chemosensors have become the most authentic tool for its ease of measurement, high sensitivity for the elemental research of those metal ions as well as for detection of these metal ions in the environment.
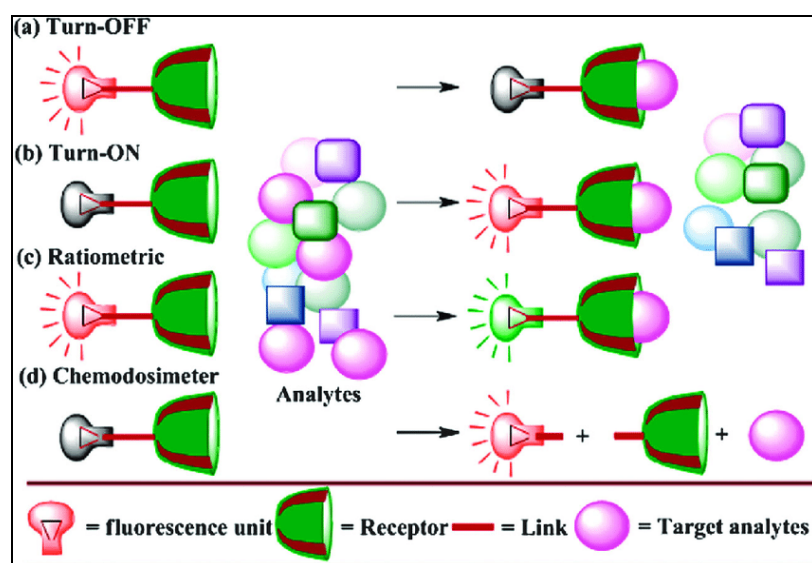
Fig. 1.4. Schematic representation of various types of fluorescent sensors [32]

In the field of fluorescence chemosensor, nitrogen-based compounds are the "hotspot" research area, for their crucial function in charge transfer procedure and brilliant photophysical applications [33]. Nitrogen-containing ligands bound metal complexes represent a special class of sensor molecules in which the binding event takes place through significant changes in absorption but very modest changes in emission [34] as a result of the release or decoordination of the metal ion upon electronic excitation [35,36]. The main criterion of a proficient chemosensor is, it should bind rapidly with the species which is responsible for signaling with sufficient selectivity and sensitivity.

The design of fluorogenic chemosensors for detection of metal ions was based on fluorophore-spacer-ionophore skeleton. Usually hetero atoms like O, N or S containing ionophores merge with the fluorophores, where, the electron-dense hetero atoms acts as donor and eagerly bind with several metal ions *via* chelation. The receptor moiety is often engaged to a metal ion through various non covalent forces, including electrostatic force, van

der Waals force, hydrophilic, hydrophobic, hydrogen bonding and π-π stacking [37]. During the interaction with a receptor moiety, a change in absorption or emission intensity could be detected based on different energy or electron or proton transfer. Such a change results a deviation in absorbance and/or fluorescence measurements, which recognizes metal ion binding.

During this current scenario, the scientific community needs to prepare the analyte-specific receptors, to detect multiple ions selectively in bio-imaging studies is urgently necessary to make cleaner as well as healthier environment.

1.4. A BRIEF INTRODUCTION OF SUPRAMOLECULAR CHEMISTRY AND CRYSTAL ENGINEERING

The term "supramolecular chemistry", also known as "chemistry beyond the molecule", was coined by Jean-Marie Lehn in 1978 to emphasize on the study of molecular recognition and higher-order assemblies formed by non-covalent interactions. Later (1987), the Nobel Prize in Chemistry was shared equally by Donald J. Cram, Jean-Marie Lehn, and Charles J. Pedersen "*for their development and use of molecules with structure-specific interactions of high selectivity*". Jean-Marie Lehn defined the supramolecular chemistry as ''*chemistry beyond the molecule, bearing on the organized entities of higher complexity that results from the association of two or more chemical species held together by intermolecular forces*''(Fig. 1.5). The review [38] is focused on some specific examples of host–guest complexes determined through single crystal X-ray crystallography. This established supramolecular chemistry deals with the chemical systems made up of a discrete number of assembled molecular components that are linked together by non-covalent forces, including metal coordination, hydrogen bonding, hydrophobic forces, hydrophilic forces, van der Waals forces [39–44]. The self-assembling ability of the systems generally plays a vital role from the point of view of reversibility and molecular designing, as it leads the system to build highly complex structures which are usually complicated to prepare by traditional covalent synthetic procedures. An additional benefit of self-organization is that the comparatively weak interactions associated with these assembling systems, which can afford flexibility to execute dynamic processes like catalytic properties and allosteric conformational changes [45]. After 50 years of the modesty, the field of supramolecular chemistry has put its signature in diverse multidisciplinary applications like: molecular sensors, gas absorption, nano-reactors, drug delivery and chemical catalysis [46–50]. Supramolecular chemistry, thus,

is an intersection topic of chemical science, physical science, materials science, biologicalscience, and so on.
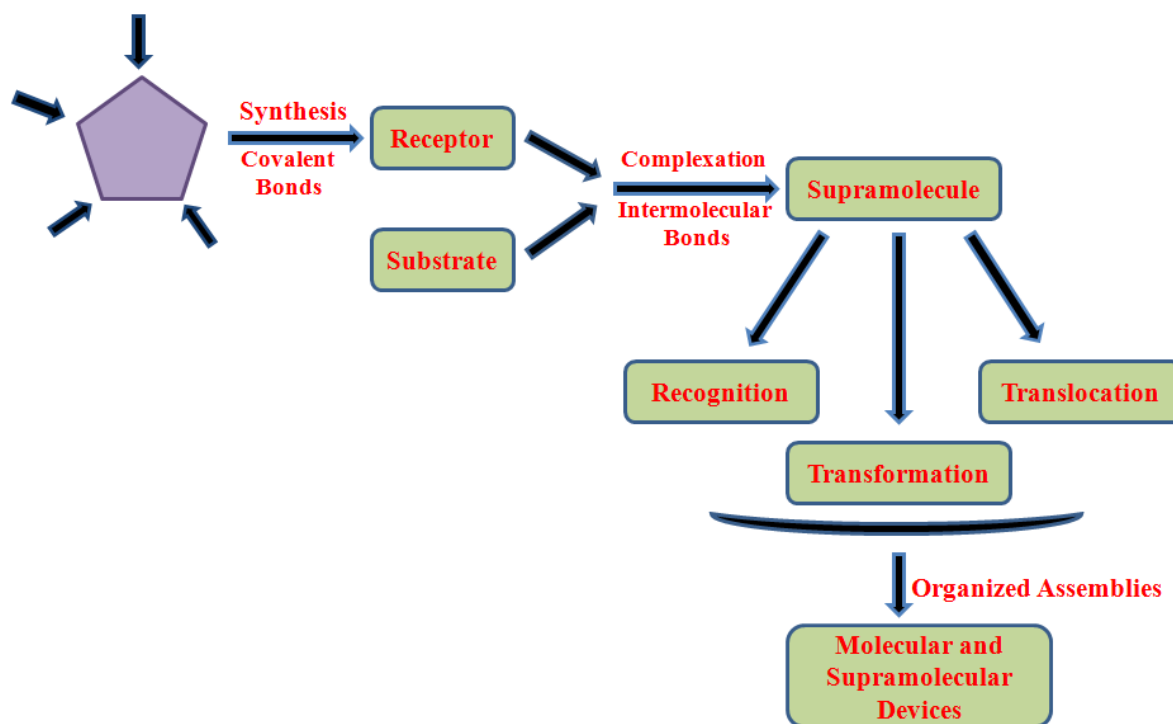
Fig. 1.5. From molecular to supramolecular chemistry, according to Lehn [51]

Single crystal X-ray crystallography is the most authentic tool for the structural analysis in detail involving intermolecular interactions in crystalline complexes. A crystal is nothing but a supramolecular entity where the constituent molecules interact implicitly among themselves during crystallization. Sometimes to make sure the existence of such weak interactions in the solid state of the complex can be supported with powder X-ray crystallography (as it is a bulk property compared to a single crystal X-ray crystallography). The improvement of the concept of non-covalent interactions in crystals has been combined in the 1980's and 1990's by famous crystallographers like G. R. Desiraju and M. Zaworotko to a new research area called crystal engineering [52–55]. The term ''Crystal Engineering'' comes up first in the proceedings of the American Physical Society Meeting (as abstract) in 1955 [56]. After the using the term by G. M. J. Schmidt in 1971, it became usually accepted.

Crystal engineering is imprinted as rational design functional molecular solids. This field has grown and developed enough over the last few decades as a natural outcome of the interplay between crystallography and chemistry. Crystal engineering is basically the understanding of intermolecular interactions in the light of crystal packing. The exploitation of such understanding is utilized in designing new crystalline solids with preferred physical

as well as chemical properties [57,58]. Chemistry deals with molecules where as crystallography is concerned with crystals which are extended, ordered assemblies of molecules. Crystal engineering has connections to theoretical chemistry as well as to the properties arising from newly designed functional materials. The crystal properties are the resultant of their molecular components and the manners in which these components are linked or aligned in the crystalline state. Thus the design of ordered structures with an intended supramolecular organization which fabricates the certain properties of synthesized materials attainable is the key proposal of "crystal engineering".

Crystal engineering constitutes three distinct and consequent activities which are: (1) the exploration of non-covalent interactions; (2) the study of crystal packing modes and utilization of those interactions in designing approach; and finally, (3) the study of the properties of crystal and their modifications with aim of variations in the packing. These three activities collectively symbolize the "what", "how", and "why" of crystal engineering [59].

Crystal engineering has wide applicationsin the domain of material science, molecular biology and pharmaceutical science [60,61].Organization of molecules in solids mainly depends on the directional interactions resulting from the multiple hydrogen bonds with the neighbors. Besides hydrogen bonding interactions, C–H•••π, π•••π, anion•••π, cation•••π andlone pair•••π interactions are also the important forces whose nature is still a subject of discussion [62–65].Presently, these types of non-covalent interactions are considered as backbones of supramolecular chemistry, material science, and even biochemistry.

1.4.1. Self-assembly and self-organization

Molecular self-assembly is a basic feature of supramolecular chemistry and it is the way where molecules achieve a definite arrangement without the help of any external guidance or management [66]. It is a process in which comparatively small molecules go through spontaneous association to give large, stable and structurally well-defined aggregates under equilibrium conditions. The main concept of self-assembly is the design of molecular building blocks that take part in spontaneous and stepwise interactions involving various weak interactions (Fig. 1.6) [67,68].Synthesis creates molecules whereas self-assembly provides ordered and assembled macromolecules [69]. The self-assembled structure has been applied vastly for the demand of many purposes in science and technology, including sensors, electronics, and various electromechanical devices [70–72].
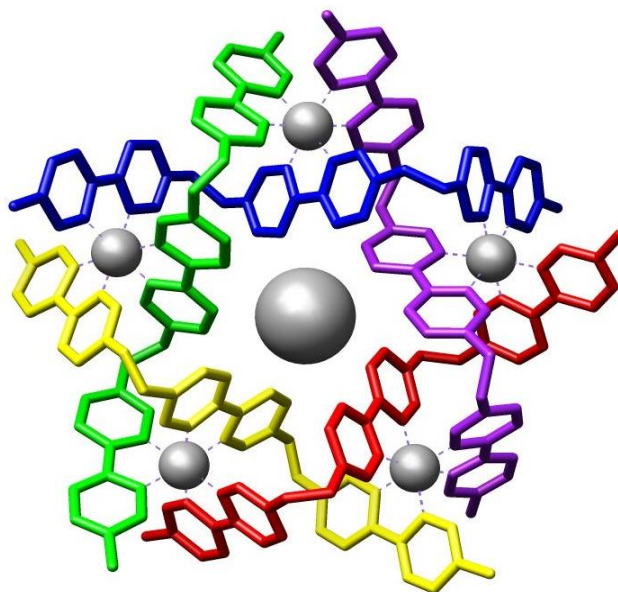
Fig. 1.6. Representative example of supramolecular assembly [73]

In the process of self-organization, some form of orderliness arises from local interactions among parts of a primarily disordered system. When sufficient energy is available, the process is spontaneous and there is no need to control by any external agent. It is considered to involve three major steps. Firstly, the molecular recognition occurs for the selective binding of the basic constituents. Secondly, the growth involving chronological and hierarchical binding of multiple constituents occurs in the proper comparative disposition. Finally, in the termination of the process, a stop signal specifies and verifies the end point of the process.

In contemporary research, self-assembly and self-organization are growing interest as a "bottom-up" approach in chemistry, life science as well as in material science. Therefore, formulating and fabricating living and natural systems from nonliving and artificial systems, a wide range of micrometer or nanometer-scale structural assemblies has been produced, including films, micelles, fibers, and many more [74–77]. The dynamic behaviour of supramolecular self-assembly arises from the reversibility of intermolecular interactions, motivating supramolecular chemists to explore the creation of multi-component self-assemblies with increasing complexity, functionality and diversity. It rests on the progressive build-up of more complex entities following a conditional pathway by multiple, sequential and hierarchical self-organization steps. Recently, more powerful self-assembly strategies have been developed for the controlled access to a diversity of nano-sized objects particularly

of metallo-supramolecular types, including rods, squares, cages, circles, focusing mainly on structural features like size, symmetry as well as chirality of the compounds [78–80].

1.4.2. Supramolecular synthon

The term 'supramolecular synthon' has been defined by Desiraju as "*supramolecular synthons are structural units within supermolecules which can be formed and/ or assembled by known or conceivable synthetic operations involving intermolecular interactions*" [81]. These are the smallest structural unit in which the total information regarding the mutual recognition of molecules to produce solid-state supramolecules is encoded. The concept of supramolecular synthons is an immensely significant step for the easy understanding of the association of molecular crystals.

The organization of molecules with one or more functional groups to generate only one type of relatively strong intermolecular interaction is the main objective of the supramolecular synthon approach. Identification of supramolecular synthons depends on the determination of particular intermolecular interactions such as hydrogen bonds, stacking interactions, *etc*. (Fig. 1.7). The spatial arrangements of non-covalent interactions within the supramolecular synthon imply the formation of supramolecular functional materials [82–84]. Thus, supramolecular synthons permit structural chemists to develop the new concepts of the supramolecular approach, target identification and synthetic methodology as a part of fruitful crystal engineering.

Crystal structure that comprises only one kind of supramolecular synthon, giving the key contribution in binding crystal structure, depends on the mutual arrangement of these synthons. The formation of supramolecular synthons which is a retro synthetic pathway to supramolecular chemistry where one can fragment the crystal structures into supramolecular synthons. Based on their abundance available in the structural database, new synthetic approaches can be designed. When one initiates with a crystal structure and deconstructs it into its synthon, both chemical and geometrical factors get deconstructed. Thus, the synthon scores over individual molecules in respect of consistency and robustness [85]. This generated an opportunity for the synthesis of new complexes with desired prototypes of binding between moieties which are analogous to the synthesis of organic moieties using synthons [86]. By these concepts of synthons and their stabilizing motif one can utilize them in crystal engineering and may create a plan to form new synthons.
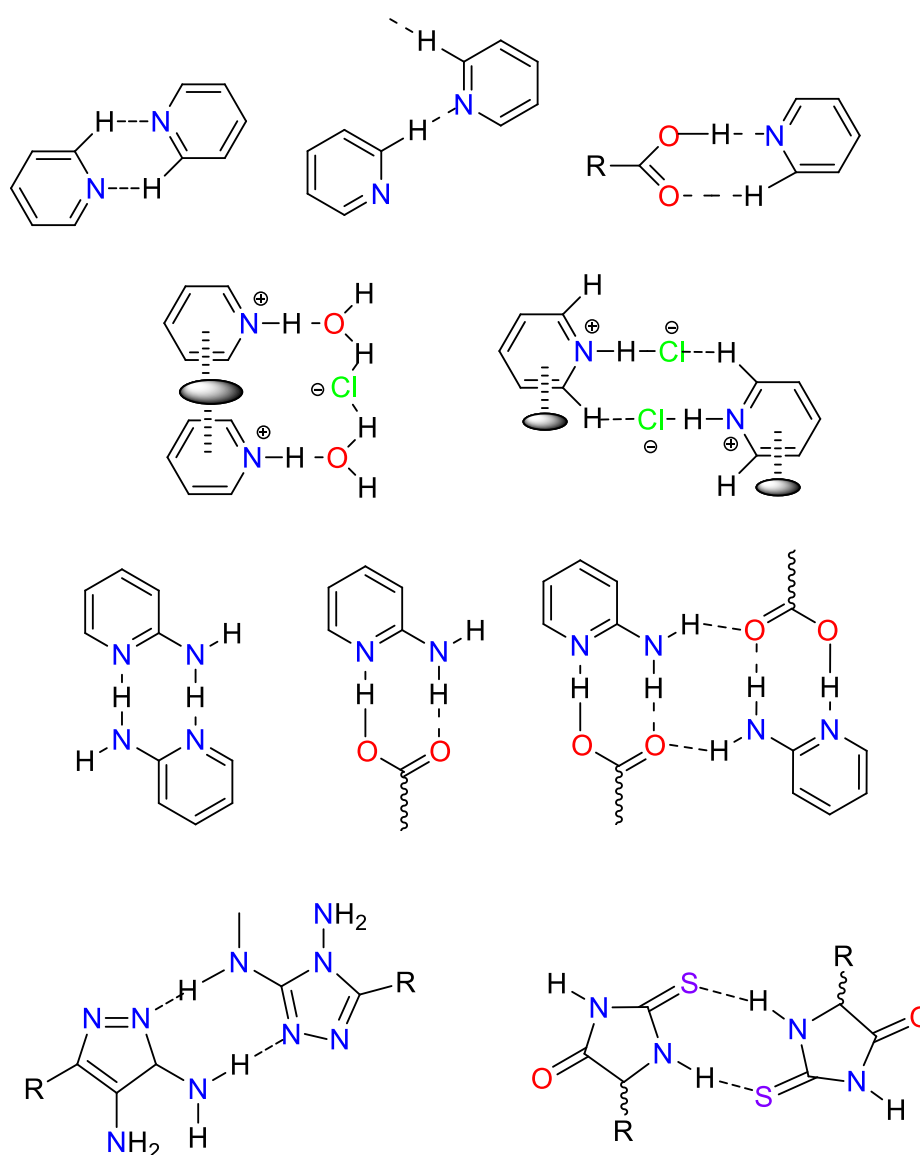
Fig. 1.7. Some representative supramolecular synthons

1.4.3. Host-guest chemistry

Host-guest chemistry is a special branch of supramolecular chemistry that is related with the generation of structural aggregates with the help of forces including: ion-ion, ion-dipole, π•••π, van der Waals, hydrogen bonding and hydrophobic interactions [87]. In this context generally, a molecule (a 'host') is considered to bind another molecule (a 'guest') to generate a 'host-guest' complex. Guests may be ionic or neutral, and can comprise metal ions, carboxylic acids, ammonium ions, amino acid derivatives and many more. The definition of hosts and guests was given by D. Cram, who said "*The host component is defined as an organic molecule or ion whose binding sites converge in the complex. The guest component is any molecule or ion whose binding sites diverge in the complex*" [88]. The differentiation

between these 'host' and 'guest' is commonly done in terms of size and shape. Typically the larger molecule is termed as 'host' and the smaller one is its 'guest'. The 'host' can wrap around the 'guest' and operate as an envelope around the 'guest'. Possibly the earliest and most familiar example of "host-guest" chemistry is enzyme-substrate complex where the substrate fits itself into the enzyme's active site having whole specificity (Figs. 1.8 and 1.9).
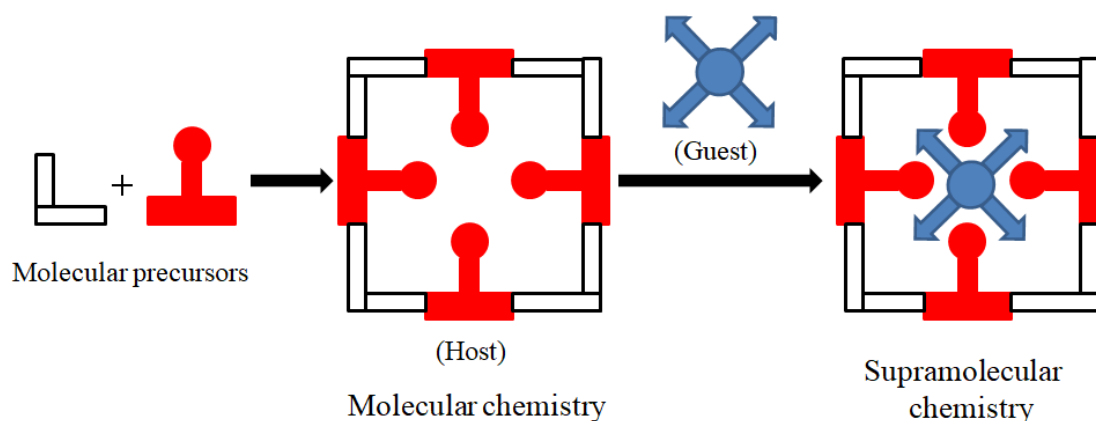
Fig. 1.8. Schematic representation of host-guest complex and comparison between molecular and supramolecular chemistry

In 1967, the discovery of crown ethers directs to the exceptional growth of this field and new type of molecules such as cavitands, calixarenes, carcerands, spherands, cryptands, crypta-spherands *etc.*, have been synthesized [89–93].

Over the past decade synthesis of inorganic macrocycles has become an emerging research area, which has shown particular promise in host-guest chemistry [94]. Metal–ligand complexes, discussed in coordination chemistry can also be understood as host-guest type, where the large, *i.e.*, macrocyclic ligands perform as hosts for guest metal cations. The rational synthesis of polyoxometalates containing coordination polymers is still mainly driven via host-guest interactions of each component [95].

In porous metal-organic coordination polymers, the nature of multiple host-guest interactions is also responsible for the stereoselective recognition and it can be explained by and theoretical calculations as well [96]. Host-guest chemistry involving intermolecular and intramolecular hydrogen bonding interactions performs a crucial function in controlling the structure as well as the function of biological systems. This extensive field of chemistry has also influence in the systems such as enzymes and their substrates, with enzymes being the host and the substrates the guest, biomolecular structure, information storage and transfer, replication and catalysis in living organisms [97].
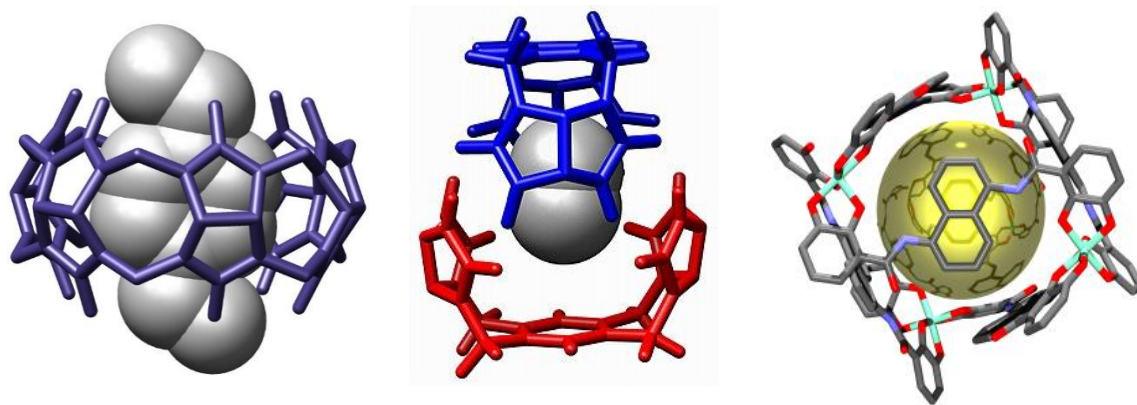
Fig. 1.9. Some representative molecular view of host-guest complexes [98,99]

Host–guest complexes have examples to act as selective binding and sensing agents. Sensing systems based on host-guest systems (such as hosts having positively-charged organic and organometallic ligands) have been designed for anion recognition [100].

1.4.4. Molecular recognition

The knowledge of molecular recognition is a comparatively new field dating to 1967, when C. J. Pedersen discovered crown ether, which were found to bind alkali metal ions to form highly structured complexes [101,102]. Subsequently, Cram, Lehn and others synthesized a large variety of macrocyclic polyethers and studied their complex-forming ability.Molecular recognition chemistry is referred to as 'host-guest' chemistry by Cram, while Lehn (1988) calls it supramolecular chemistry [103]. The concept of molecularrecognition intends to design self-assembled supramolecular structures for their utilization in both types of organic as well as hybrid organic-inorganic functional materials [104,105].

Molecular recognition is now appreciated as a special recognition at molecular level in living and chemical systems. Extensive research work in this field has evaluated the involvement of weak intermolecular forces when two molecules come across each other. Molecular recognition plays a vital role in various areas of science and technology, such as host-guest systems, catalysis, nano-scale assembly, design of sensor materials, surface patterning, and so on [106–109].

Molecular recognition can be divided in two branches, static molecular recognition and dynamic molecular recognition. Static recognition occurs between a guest and a host (1:1 type complexation reaction) whereas, in dynamic recognition, binding the first guest at the first binding site stimulates a conformation transformation that influences to associate the second guest at the second binding site (Fig. 1.10).
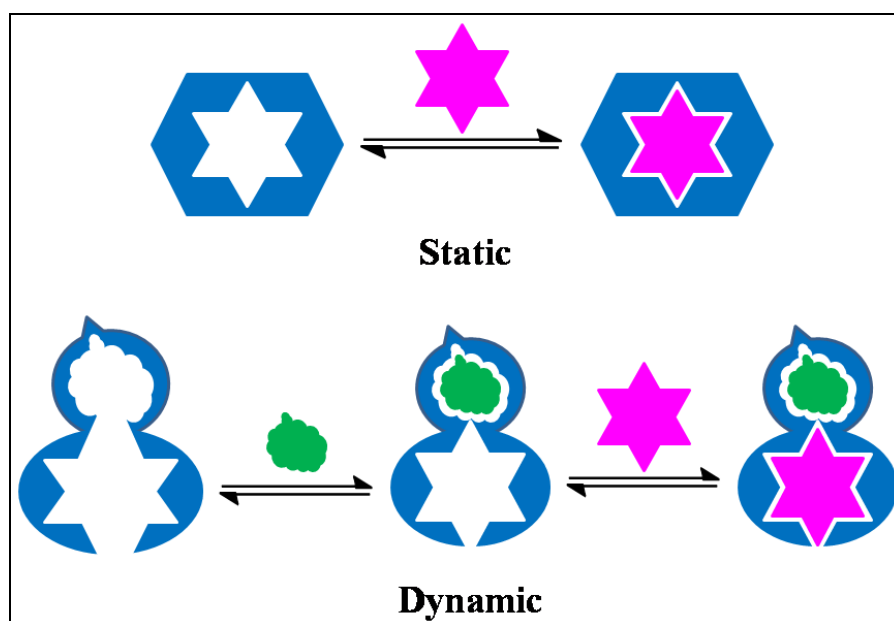
Fig. 1.10. Schematic representation of static and dynamic molecular recognition

Supramolecular chemistry is deeply connected to molecular recognition which explores how host molecules distinguish guests and how they get associated with one another. The main concept affiliated with molecular recognition is the "lock and key" concept proposed by Emil Fisher where enzymes identify substrates by a "lock and key" strategy [110]. Therefore, structural fit between the identifying molecule and the identified molecule is very important in this mechanism. In molecular recognition, a molecule selectively recognizes its partner molecule through various molecular interactions which are mainly non-covalent in nature (hydrogen bonding, π•••π, C–H•••π, *etc.*) [111].

In general, it is presumed that indistinguishable recognition patterns exist in solution as well as in the solid state. Moreover, in most of cases, this has been unambiguously established. The rational design of preferred supramolecular materials has arrived to a state of the art where anyone can anticipate the most common recognition pattern among a set of molecular building blocks [112]. However, several unexpected factors such as, the pH of the solution or the participation of solvent molecules, play a significant role in the self-assembly process [113]. The molecular recognition process plays an imperative role in nature where the best-recognized example is the complementarity present in the pairs of nucleobases in DNA [114]. Moreover, enzymes,having a redox-active organic part (*i.e.*, quinones, flavins, nicotinamides) also engage molecular recognition to direct the redox process where the enzymes are usually treated as proficient and complex molecular devices [115].

1.5. A BRIEF INTRODUCTION OF NON-COVALENT INTERACTIONS

The main disunity between non-covalent bonds with the covalent bond is in terms of bonding connectivity. Molecular chemistry describes the covalent bonds whereas the supramolecular chemistry dealswiththe chemistry of molecular componentsthat held together through non-covalent interactions. The field of supramolecular chemistry has introduced new verities of non-covalent forces includingion-ion, ion-dipole, dipole-dipole, London dispersion and hydrogen bonding interactions [116–118]. In contemporary chemistry, a new class of non-covalent interactions involving aromatic rings of type π•••π, C–H•••π,cation•••π, anion•••π and lone pair•••π, have attained significant consideration as aromatic rings are ubiquitous in biological systems [119–121] (Fig.1.11). Recently supramolecular forces come forward asπ$^+$•••π,π$^+$•••π$^+$, π•••π(chelate ring), C–H•••π (chelate ring), lone pair•••π (chelate ring) interactions which also becomes a matter of discussion [122–126].
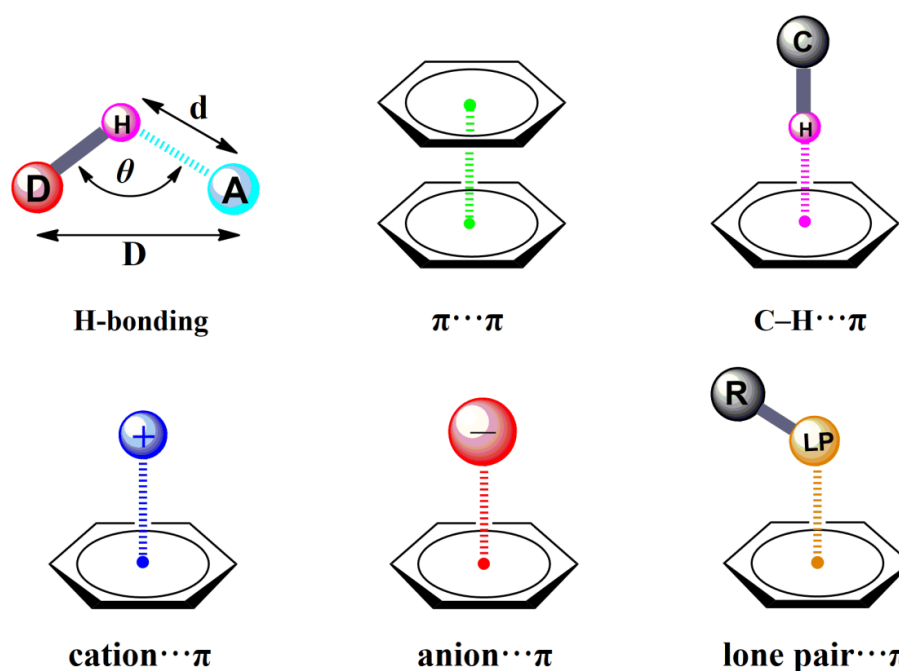
Fig. 1.11. Some representative non-covalent interactions.

These types of non-covalent interactions play a vital role in modern chemical research and considered as framework of supramolecular chemistry, biochemistry and even materials science. However, such interactions have concerned in crystal packing and producing multi-dimensionality of coordination complexes, macro molecules like nucleic acids and proteins. There are several examples of non-covalent bonds which are responsible for holding the two strands of DNA together in its double helix form, folding polypeptides into secondary structures, assist enzymes to bind to their substrate and allow antibodies to bind to their

antigen [127,128].Approximate supramolecular interaction energies have been included in Table 1 [129].

Table 1.1. Approximate chemical interaction energeias (in kJ mol^{-1})

Interaction type	Directionality	Bond Energy (kJ mol^{-1})	Example
Ion – ion	Omnidirectional	200 – 300	Tetrabutylammonium chloride
Coordination bonds	Directional	100 – 300	Metal - pyridine
Ion – dipole	Nondirectional	50 – 200	[Na (15-crown 5)]$^+$
Closed-shell metal – metal bond	Nondirectional	5 – 60	Argentophilic (Ag•••Ag) Aurophilic (Au•••Au)
Hydrogen bonds	Directional	4 – 120	Carboxylic acid dimer
Halogen bonds	Directional	10 – 50	Sulphur – iodine complex
cation•••π/ anion•••π	Directional	5 – 80	K$^+$•••benzine
π•••π interactions	Directional	2 – 50	Benzene dimer
Dipole – induced dipole interaction	Directional	2 – 10	HCl•••Cl_2
van der Waals	Directional	<5	Argon

1.5.1. Hydrogen bonding interaction

Hydrogen bonding is nothing but an electrostatic interaction where a hydrogen atom that is already bonded to an atom (H-bond donor) of a molecule, forms a second bond with a different atom (H-bond acceptor), either in the same molecule or in a different one [Fig. 1.12]. In the periodic table, generally the atoms having higher electronegativity than that of H atom (*i.e.*, C, N, O, F, P, S, Cl, Br, and I) can take part in the hydrogen bonding interaction. There is also evidence of hydrogen bonding with atom of lower electronegativity (e.g., B–H–B banana bond in the diborane) [130]. The conception of the hydrogen bond as an electrostatic interaction was entitled by Pauling.
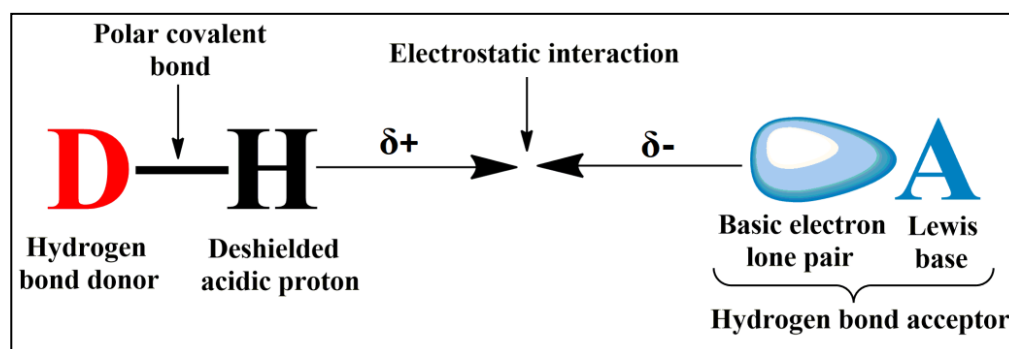
Fig. 1.12. Schematic representation of hydrogen bonding.

He assumed that only if the atoms D(H-bond donor) and A (H-bond acceptor) are more electronegative (N, O, F, Cl, Br), they would incite the deshielding of the H atom and hence the electrostatic attraction between the H atom and accepter atom will become sufficiently high to consider the interaction as a bond [131].

Besides the traditional hydrogen bonds (D─H•••A, D =A = F, O, N), non-traditional hydrogen bonds has arrested remarkable attention from several points of view [132,133]. Non-traditional hydrogen bond concerns less polar C─H donors in presence of lone-pair bearing atoms [*i.e.*, N, O, X (halogen)]. Basically, the strength of the H•••N/O/X interaction depends on the polar character of the C─H bond and the charge of the acceptor atom.

The strength of hydrogen bonds can differ from very weak (1 to 2 kJmol^{-1}) to extremely strong (161.5 kJmol^{-1}in the bifluoride ion) [134,135]. According to the research, O–H•••O is the strongest among all types of hydrogen bonds and C–H•••O is considered as a model as well as the oldest weak hydrogen bonding interaction. Based on donor-acceptor distances of hydrogen bond, Jeffrey categorized into three ranges: donor-acceptor distance 2.2–2.5 Å (strong, mainly covalent), 2.5–3.2 Å (modest, mainly electrostatic) and 3.2–4.0 Å (weak, electrostatic) [136]. Table 1.2 contains a brief collection of some typical values of distance and energies.

Table 1.2. Approximate interaction energies and distances of various H-bonding interactions

Interaction	Energy (kcal mol^{-1})	H•••A (Å)	D – A (Å)
O–H•••O	3.8	1.51	2.78
O–H•••C	1.79	2.66	3.30
O–H•••S	4.0	2.49	3.25
N–H•••O	6.0	1.80	2.81
N–H•••C	3.0	2.61	3.30
N–H•••N	6.0	1.92	2.83
N–H•••S	3.0	2.60	3.12
C–H•••O	2.0	2.6	3.50
C–H•••N	2.0	2.51	3.41
C–H•••S	1.5	2.7	3.66
C–H•••C	0.33	2.74	3.59

1.5.1.1. Types of hydrogen bonding

Based on the geometry, hydrogen bonds can be classified in different categories as depicted in Fig.1.13. The simplest and prototype arrangement of a hydrogen bond is D–H•••A model, where the angle is ~180°, (Fig. 1.13a). In the 2nd type the angle shows a deviation from 180°

in D–H•••A model (Fig. 1.13b). Fig. 1.13c shows that one hydrogen atom interacts with two acceptor atoms generating a centre of three atoms known as bifurcated arrangement. Similarly, Fig. 1.13d provides a multi-furcated hydrogen bond, where a donor creates hydrogen bonds with more than two acceptors simultaneously. Multi-furcated hydrogen bonding needs a large concentration of acceptors, at least locally [137]. Multi-furcated hydrogen bonds are present in protein molecules in large numbers. However, bond directions have been shown by rigorous theoretical calculation for both components for a number of bifurcated bonds [138].
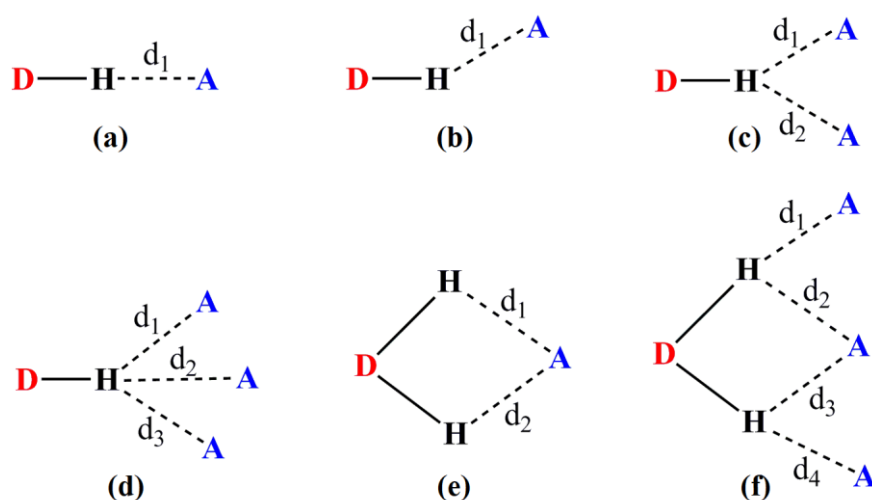
Fig. 1.13. Different kinds of hydrogen bonding geometries: (a) linear; (b) bent; (c) donating bifurcated; (d) trifurcated; (e) accepting bifurcated; (f) three-centre bifurcated.

1.5.1.2. Role of hydrogen bonding in bio-chemical system

Hydrogen bonds formation is highly important in biological systems as they stabilize the structure and shape of various large macromolecules, mainly, nucleic acids and proteins. This type of bonding interactions occurs in biologically important structures, like DNA and RNA. This is the force that acts among water molecules to hold them together. Water is the most important solvent for many chemical and biological reactions which are occurring naturally. Thus, rationalization of the various chemical and physical characteristics of water is the ancient target of science.

The hydrogen bond formation between the water molecules (both as a liquid and as solid ice) occurs due to the electrostatic attraction that holds the molecules together. Intermolecular hydrogen bonds are responsible for the high boiling point (B.P.) of water as it enhances the amount of energy that is necessary to break the bonds just before boiling of water can initiate. During the freezing of water, the hydrogen bond forces water molecules to shape crystals. The positive and negative ends of the water molecules arrange

themselves in an order that enables the positive ends to attract the negative ends of the molecules. The framework of the ice isn't as firmly meshed as the liquid state that permits ice to float in water (Fig. 1.14).
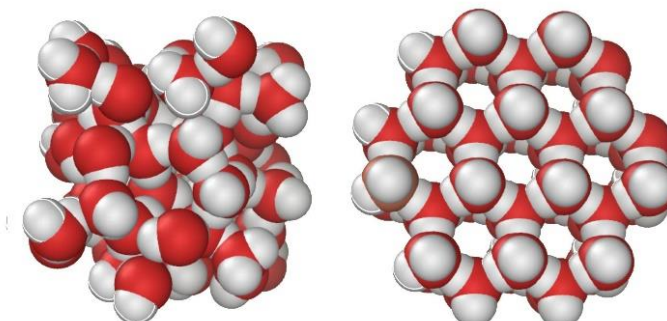
Fig. 1.14. Hydrogen bonding in water and ice (space fill model).

The 3-D structure of proteins is very significant in biological reactions such as those involving enzymes where the shape of one or more proteins should fit into openings in enzymes much as a lock and key mechanism (Fig. 1.15a). Hydrogen bonding allows these proteins to bend, fold and fit into various shapes as essential which describes the protein's biological activity.
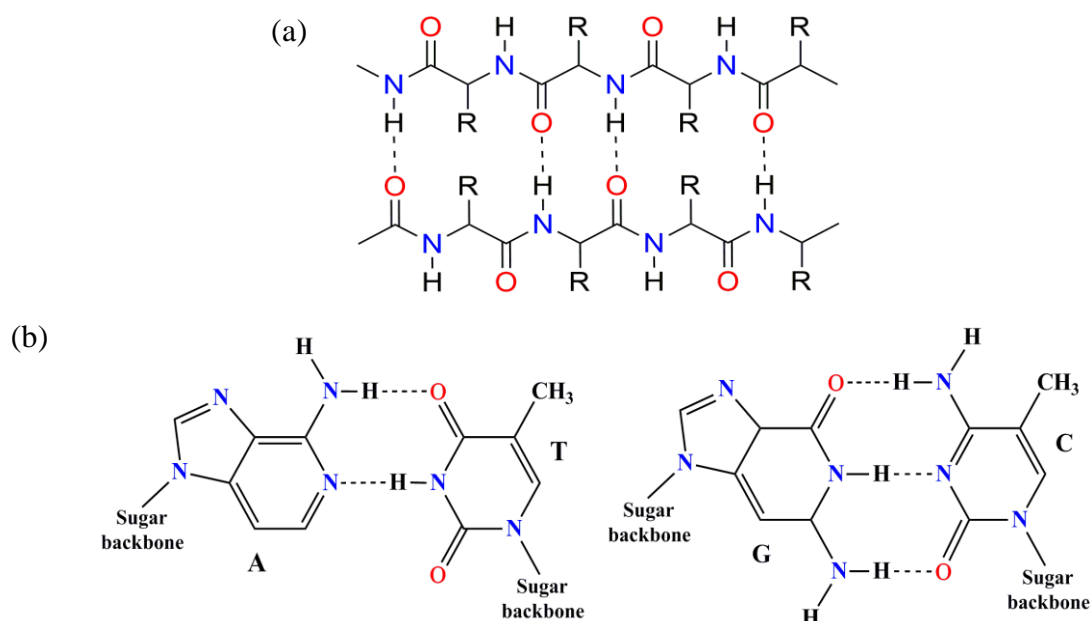
Fig. 1.15. Hydrogen bonding in (a) protein chain and (b) DNA.

This is much significant in DNA as the formation of various hydrogen bonds enables the molecule to accept its double helix framework. The double helix of DNA is

created by complementary hydrogen bonding between cytosine (C) and guanine (G), and adenine (A) and thymine (T) base pairs (Fig. 1.15b), which connect one complementary strand to the other and facilitates DNA replication.

It is noteworthy to mention that the individual hydrogen bonds are weak, but a couple of hydrogen bonds are very strong enough. When one ligand binds through two or more sites with metal ion or ions, a ring structure (chelate) is generated (Fig. 1.16). Chelating complexes are very helpful for removing or mobilizing molecules and metal ions.
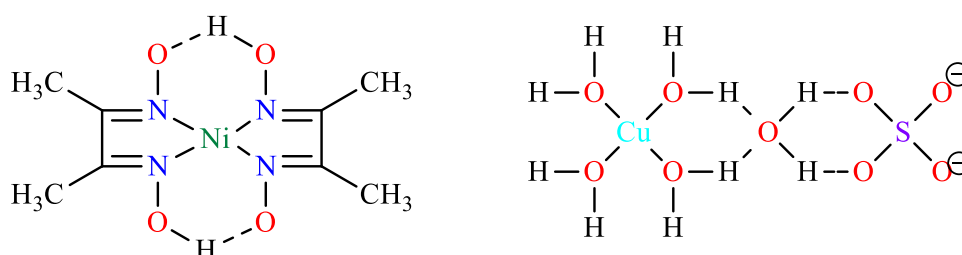
Fig. 1.16. Hydrogen bonding in some metal complexes.

1.5.2. π•••π stacking interaction

The arene-arene or π•••π interaction is the most fundamental non-covalent interaction which is commonly discussed in supramolecular chemistry. Interactions concerning aromatic rings are abundant in chemical and biological systems, however, they can extent from molecular recognition to self-assembly and catalysis [139–144]. As a consequence, a broad scientific community has focused on exploring the π-stacking behaviour of aromatic rings. The most common arene-arene interaction is the benzene dimer which is generally studied as a representative π•••π interactions. Three geometries of the benzene dimer have been modeled (Fig. 1.17) after high level of theoretical calculation, which are (1) eclipsed face-to-face (2) parallel-displaced and (3) edge-to-face or T-shaped [145–147]. In the face-to-face arrangement, the benzene rings are approximately parallel to each other having an interplanar spacing of about 3.3−3.8 Å. A displacement of benzene rings from parallel orientation results a slipped or offset arrangement. The 'T'-shaped or point-to-face arrangement is nothing but a C─H•••π type of interaction [148]. For the benzene dimer, the parallel-dispalced and 'T'-shaped geometries have been calculated to be nearly equal in stability (~ −2.5 kcal/ mol) whereas the face-to-face geometry is comparatively less stable (−1.6 kcal/mol) [149]. There are limited examples of both 'T'-shaped and face-to-face arrangements in aromatic

interactions whereas parallel-displaced or slipped arrangement is most common. An extensive investigation ranging from initial gas-phase studies to modern computational studies is going on, which assists us to explore several useful basic properties of $\pi\cdots\pi$ interactions.

Three main factors are responsible to stabilize the $\pi\cdots\pi$ interaction, namely, (a) Dipole−dipole interactions, (b) Induced dipole−dipole interactions, and (c) Induced dipole–induced dipole (London) dispersion interaction.
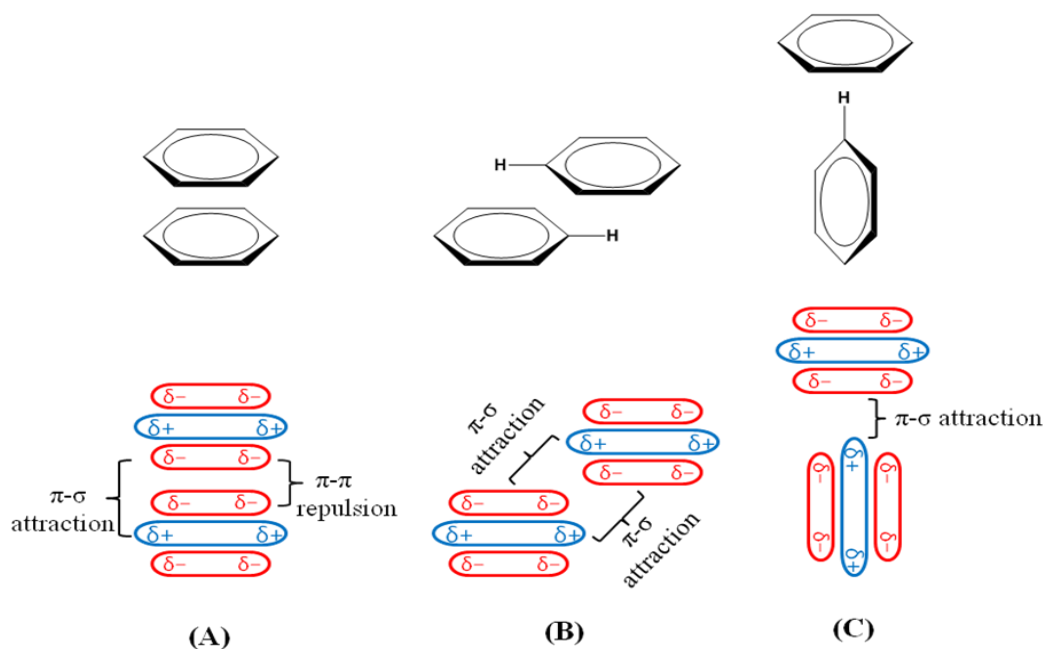
Fig. 1.17. Principal orientations of aromatic-aromatic interactions and schematic representations of their electrostatic view [150].

To analyze interactions between two aromatic systems qualitatively, Hunter and Sanders provided a set of rules depending on a basic model of the charge delocalization in a π electron system. They differentiated the σ framework as well as the π frameworks and took into account that, the $\pi\cdots\pi$ interactions as the outcome of $\pi\cdots\sigma$ attractions that can score over $\pi\cdots\pi$ repulsions [150]. These "Hunter-Sanders" rules for the non-polarized π-systems are:

- Rule 1: *"$\pi\cdots\pi$ repulsion dominates in a face-to-face π-stacked geometry"*.
- Rule 2: *"$\pi\cdots\sigma$ attraction dominates in an edge on or T-shaped geometry"*.
- Rule 3: *"$\pi\cdots\sigma$ attraction dominates in an offset π-stacked geometry"*.

For polarized π systems, there are additional three rules, which are given here to understand favorable (face-to-face) π-stacking interactions.

- Rule 4: *"For interaction between highly charged atoms, charge-charge interaction dominates"*.

- ◆ Rule 5: *"A favorable (face-to-face) interaction with a neutral or weakly polarized site requires as a π–polarization a π-deficient atom (in the aromatic ring)".*

- ◆ Rule 6: *"A favorable (face-to-face) interaction with a neutral or weakly polarized site requires a σ polarization or positively charged atom (in the aromatic ring)".*

Experimental analysis reveals that electron-withdrawing substituent and/or heteroatom (attached with the aromatic ring) enhance the strength of π•••π interaction. The electron-withdrawing substituent or heteroatom decrease the π-cloud density in the aromatic rings, thus minimizing the π•••π repulsion [151–153]. The stability of π•••π (face-to-face) stacking between aromatic moieties increases when both rings are electron-poor, whereas electron-donating substituents disfavor the π•••π interaction. Thus, the stability order in the interactions between two π systems is π-deficient–π-deficient > π-deficient–π-rich > π-rich–π-rich system.

In nitrogen-containing aromatic ligands, the π•••π stacking interaction played a crucial role in the formation of several metal complexes [154]. In the case of pyridine moiety, the centroid–centroid separation distance between two pyridine rings is in the range of 3.4 Å – 3.8 Å. In major cases, the intermolecular planes are nearly side by side to each other, *i.e.*, the inter-planar angle tends to zero. So far, the two pyridine rings can demonstrate parallel displacement in regards to each other with the shifted angles range from 16º to 40º. For centroid–centroid distance at 3.8 Å, the shifted angle becomes around 20º where the corresponding horizontal displacement is 1.30 Å (Fig. 1.18).
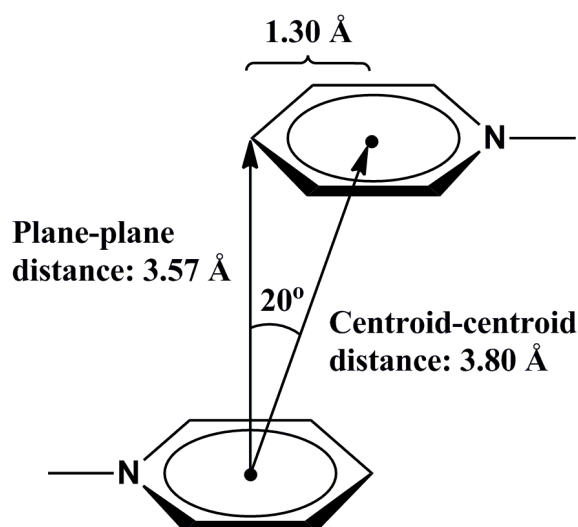
Fig. 1.18. Graphical presentation of usual offset or slipped π•••π interaction in pyridine moiety.

This transfigures to a slipped or offset $\pi\cdots\pi$ stacking interaction which is quite often observed between heterocyclic π-systems. In this type of arrangement, the ring planes are oriented in such a fashion where a ring atom reclines almost over the center of the other ring and its hydrogen atom lies nearly on top of a carbon atom.

1.5.3. $\pi^+\cdots\pi$ interaction

The introduction of $\pi^+\cdots\pi$ interaction is one of the contemporary progression of supramolecular chemistry. The interaction is observed between two aromatic rings where one of the rings is protonated (Fig. 1.19). Experimental analysis shows that the $\pi^+\cdots\pi$ interaction have greater stability than $\pi\cdots\pi$ interactions but it is quite different from conventional non-aromatic cation$\cdots\pi$ interaction as the strong dispersion interactions act in $\pi^+\cdots\pi$ interaction between the well-stacked aromatic ring systems [155]. The positively charged aromatic π systems involve anionic moieties for stabilization and they can be used in anion receptor, molecular recognition, and rational material design with desirable physical properties. Besides, the attractive nature between positively charged π systems and anionic species is mostly fruitfulto design solid state assembly of host-guest complexes for anion-induced molecular devices [156].

Mainly there are two different types of $\pi^+\cdots\pi$ interactions, namely, displaced-stacked (D) and T-shaped structure (T) arrangements. Kim and his co-workers have calculated the binding energies for various orientation of $\pi^+\cdots\pi$ interactions which are stabilized mainly by both dispersion and electrostatic energies. The binding energies of the $\pi^+\cdots\pi$ (D) arrangements (~8–11 kcal mol^{-1}) and the $\pi^+\cdots\pi$ (T) arrangements (~9–14 kcal mol^{-1}) are quite higher in comparison to the typical hydrogen-bonding energy (~5 kcal mol^{-1} for the water dimer) [157], C–H$\cdots\pi$ (~1.5–3 kcal mol^{-1}) and H$\cdots\pi$ binding energy (~2–4 kcal mol^{-1}), but lesser than the characteristic cation$\cdots\pi$ (M$^+\cdots\pi$ and H$^+\cdots\pi$) binding energy (~9–23 kcal mol^{-1}) [158]. Besides, they also established that the $\pi^+\cdots\pi$ (D) orientations are stabilized mainly by dispersion energy (~44%) while electrostatic energy is the major component (~43%) for the $\pi^+\cdots\pi$ (T) orientations.

Interactions between positively charged π-systems and neutral π-systems play a crucial role in controlling conformations in stereo- and regio-selective organic synthesis, protein-drug complex formation, assisting catalytic activities, stabilizing protein-DNA complexes and many more [159–165].
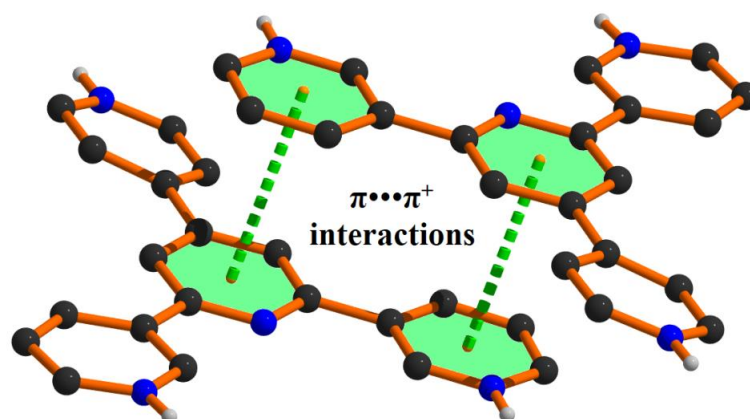
Fig. 1.19. Formation of a dimer through $\pi^+ \cdots \pi$ interactions

Recently, Xiao and Pignatello [166] have recognized some hetero aromatic amine cations which can perform as the π-acceptors for producing $\pi^+ \cdots \pi$ electron donor-acceptor (EDA) interactions with the π electron-rich polyaromatic surface of pyrogenic carbonaceous materials (*i.e.*, grapheme, black carbon and biochar).The $\pi^+ \cdots \pi$ (EDA) interaction is the combination of cation$\cdots\pi$ and $\pi\cdots\pi$ (EDA) forces resulting from charge polarization of the ring's quadrupole.

Besides, $\pi^+ \cdots \pi^+$ interaction is another important non-covalent force in the field of supramolecular chemistry. Though the $\pi^+ \cdots \pi^+$ interaction is an anti-electrostatic interaction, sometimes it has been proven to have significant contribution towards supramolecular systems than conventional $\pi\cdots\pi$ interactions. Monojit Mitra *et. al* showed the parallel and anti-parallel $\pi^+ \cdots \pi^+$ stacking between protonated melamines and rationalized energetically [167]. Prankrisna Manna *et. al* also analyzed the energetic features of the repulsive $\pi^+ \cdots \pi^+$ interaction, which is compensated by counter anions [168].

1.5.4. C–H$\cdots\pi$ interaction

The C–H$\cdots\pi$ interactions have been recognized to be the weakest non-classical hydrogen bond contributing appreciably in diverse fields of chemistry like self-assembly, chiral recognition, stabilization of structures of proteins and nucleic acids and many more [169–172]. The C–H$\cdots\pi$ interaction has been identified as the attractive interaction operating between a non-polar or feebly polar C–H bond and an aromatic π-system [173]. In spite of the recognition in various fields of chemistry, the nature of the C–H$\cdots\pi$ interaction is still controversial. C–H$\cdots\pi$ interaction has different characteristic from classical hydrogen bond as electrostatic interactions are mainly responsible for the attraction in classical hydrogen

bonds whereas, C–H•••π interactions have similar character with the trivial van der Waals attractive force. Furthermore, the hydrogen bonding interactions usually have strong directionality whereas, the C–H•••π interactions mainly take place between soft acids and bases comprise dispersion energy or electron correlation energy through the electrostatic interactions can have a little contribution in few cases [174]. Therefore, it is appreciated as the weakest non-classical hydrogen bonding interactions [175].

M. Tamres first predicted the attractive nature of CHs and π-systems through his thermo-chemical observations [176]. Afterward, it was supported by spectroscopic evidence and theoretical calculations [177,178]. Andreetti and his co-workers first disclosed the importance of C–H•••π interaction in the field of supramolecular chemistry based on crystallographic data of a range of calix-[4]-arene complexes with toluene [179,180].Various evidences for the C–H•••π interactions (Fig. 1.20) was found afterward from the analysis of different crystal structures and supramolecular systems [181,182].
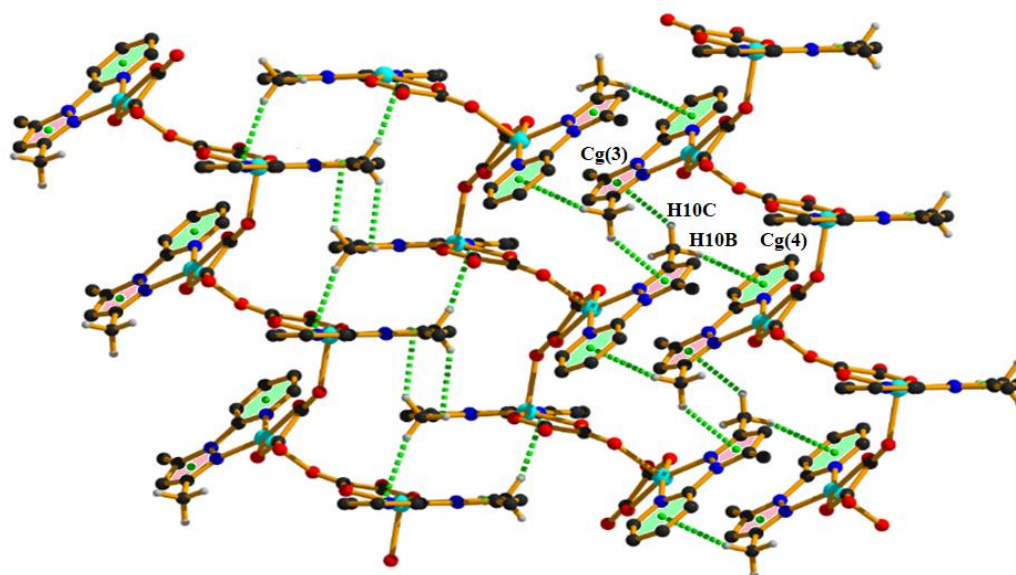
Fig. 1.20. Representation of the C–H•••π interactions in molecular crystal [181]

The T-form conformation of benzene dimer is nothing but a C–H•••π interaction. Theoretical calculations reveal that the stabilization of the C–H•••π bond basically emerges from the dispersion force. The nature of C–H•••π interactions was established by AIM (atoms in molecule) analyses and by relative MO studies of intramolecular systems [183,184]. The significance of interaction between the C–H dipole and the quadrupole of aromatic moieties was reported by Nakagawa and Nikki [185]. The stronger is the protonic character of the CH, the stronger is the stabilizing effect and thus the array for C–H•••π interaction become as *sp-*

CH•••π>sp^2-CH•••π >sp^3-CH•••π. Interactions involving aromatic CHs are stronger than the aliphatic ones. Recently, a theoretical study proposed that C–H•••π interactions between monomeric units can also be used for consenting novel single-chain magnets [186].

Besides CH donor, π systems have been noticed to act as acceptor for OH and NH donor also. These interactions also play significant roles in protein biochemistry and supramolecular chemistry [187]. The NH•••π interaction has been observed in several proteins and in hemoglobin-drug complexes [188]. NH•••π interaction has been found to play significant role in Spin-Crossover phenomenon in some Fe(II) complexes [189]. For uncharged systems the energy range of O/N–H•••π interactions is about 2–4 kcal mol^{-1} (half the strength of a normal hydrogen bond). From the energy value they are more significant than typical C–H•••O interactions [190].

1.5.5. Cation•••π interaction

Cation•••π interaction is an attractive non-covalent force acting between a positively charged ion (cation) and negatively charged (π cloud density of an aromatic system) species (Fig.1.21) [191]. Generally, staking interactions are weaker than hydrogen bonding interactions though cation•••π interactions tend to be stronger [192]. Such interactions are of foremost importance in numerous fields of modern research, including biology, chemistry, material science, nanotechnology and related fields [193–195]. An interaction between a neutral molecule and an ion tends to be favorable electrostatically and the interaction energy becomes greater than that between two neutral molecules, in particular when the neutral molecule is easily polarizable. A non-covalent cation•••π interaction is occurred when a closed shell cation gets nearer and interacts with a neutral π-system.
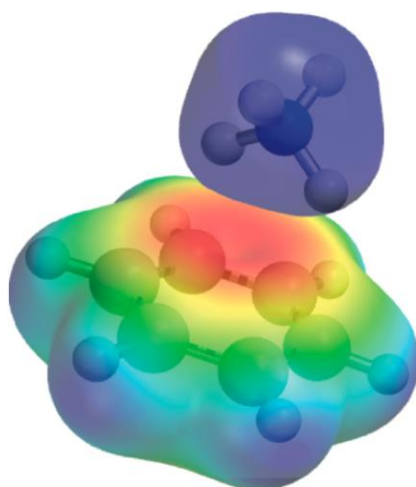
Fig. 1.21. Cation•••π interaction [191]

Thus, the modern scientific interest have been focused on understanding of the nature, range and significance of the cation•••π interaction which is of great importance in designing molecules and materials.

Since its discovery in the 1980s [195], a detail synthetic, experimental and computational investigation have been carried out to quantify and further understanding the extent of this interaction in both gas and condensed phases [196,197]. Usually, in solution phase the strength of cation•••π interactions are weaker compare to that in the gas phase although their strength is almost comparable to other strong non-covalent interactions, involving ion pairs and hydrogen bonds.

Additionally, the cation•••π interaction shows a high degree of directionality, where the cation has a prominent energetic tendency for placing themselves just over the centroid of the π-system. A detail analysis regarding the geometrical orientation of the cation with respect to the π-system was also carried out to study the alternation of cation•••π interaction energy. The strength of cation•••π interaction is portrayed by considering the factors: R, ϕ and θ (Fig. 1.22). The cation•••π interaction is best when the cation is positioned perpendicular to the centroid of the aromatic system and the interaction energy decreases on shifting the cation from centroid [198]. Besides, environment and solvation effects have an important role towards the stability of cation•••π complexes due to the charged nature of the cation [199].
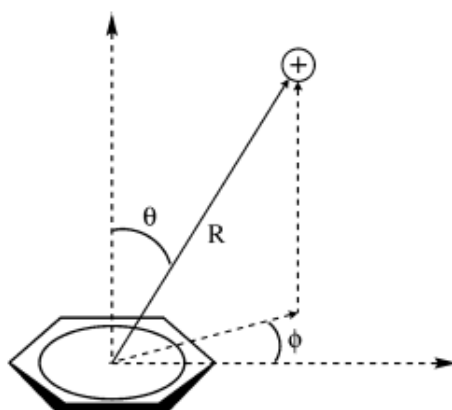
Fig. 1.22. Geometries for cation•••π systems

Cation•••π interaction was first experimentally confirmed by Kebarle and co-workers [200]. They calculated the interaction enthalpy between benzene and K^+ ion, which wasfound to be momentous and comparable to the interaction of K^+ with either water or methanol. Latter, similar interactions with Na^+ using mass spectrometry, was studied by Castleman *et al.* [201]. It was observed that the interaction enthalpy between Na^+ and benzene is greater than that for K^+ and benzene as K^+ has less charge density than Na^+. In addition, Lisy *et al.* reported

computational and mass spectrometric evidences on alkali metal-arene cation•••π interactions [202,203].In studying molecular recognition, host guest complexes having synthetic receptors and guest molecules arbitrated by cation•••π interactions, are exceptionally useful [204–207].

Dougherty *et al.* established in their pioneer investigation regarding the design, synthesis and characterization of a huge number of derivatives of cyclophane hosts that give insights into host-guest binding both in aqueous and in organic solvents [208–211]. Various cage-like structures have been reported, which were able to hold cations in their cavities or clefts [212,213]. Tran *et al.* described the synthesis of zorbarene and demonstrated that the tetramethylammonium cation has moderately strong binding constants which suggest better cation•••π interactions with the hosts [214]. Rathore *et al.* reported the design and synthesis of a hexaaryl benzene-based receptor which comprises a bipolar receptor site, that permits proficient association of a single K^+ ion by way of a symbiotic interaction having a polar ethereal fence as well as with the central benzene ring by a cation•••π interaction [215,216]. The primary studies on the thermodynamics of the interaction and its emergent importance in biology, have been framed for its application as a design element in synthetic chemistry [217].

Furthermore, directionality and complementary nature of cation•••π interaction can drive the organization of small molecule into controlled assemblies. As a result, this interaction is extremely significant for molecular recognition [218,219], crystal engineering [220] (Fig. 1.23), and materials design [221]. The cation•••π interactions have also found imperative applications in the rising area of supramolecular chemistry. Supramolecular associations such as catenanes [222], rotaxanes [223], dendrimers [224] have been connected through the participation of cation•••π interactions [225–228].
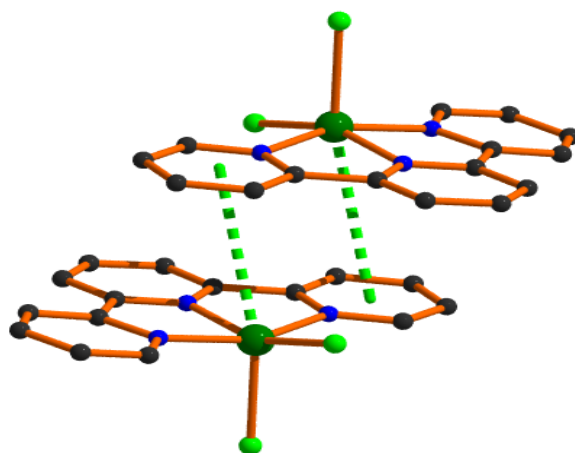
Fig. 1.23. Cation•••π interactions in a copper complex [229].

1.5.6. Anion•••π interactions

The anion•••π interaction is very important insight of supramolecular chemistry [230–233]. Typically, the anion•••π interaction is termed as favorable non-covalent interaction between an anion and the partially positive electrostatic potential on the ring edge of an aromatic ring which is electronically deficient (Fig. 1.24) [234]. Currently, the research on anion•••π interaction is highly noteworthy in the scientific community and as a result considerable amount of chemical literatures are available. The significance of anion•••π interaction was further fueled by the importance of anions in several chemical as well as biological processes like involvement of π-rings in host−guest chemistry, molecular anion recognition, ion transport, stabilization of reactive anionic species and catalysis [235–239]. Additionally, Matile *et al*. illustrated the interactions of anions and cations with naphthalenediimide (NDI) derivatives coincidently that generate a novel route in ion pair sensing as well as catalysis employing anion•••π interactions [240,241].
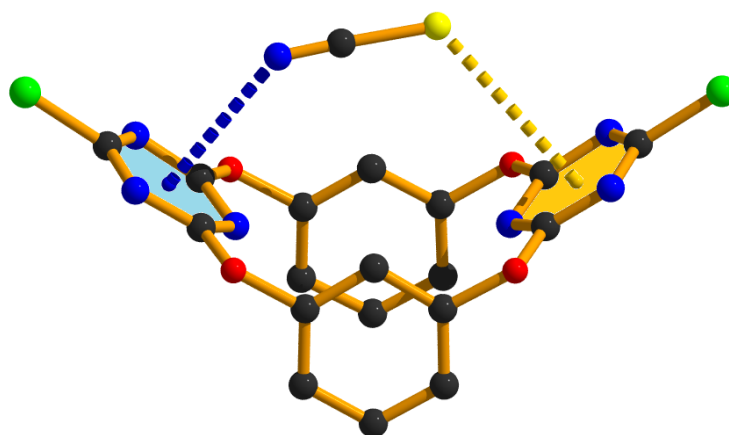
Fig. 1.24. Anion•••π interactions between a [SCN]⁻ anion and electron-deficient aromatic ring [234].

In 1968, Park and Simmons stated in their pioneering report that macrobicyclic ammonium host molecules interact through energetically favourable electrostatic interactions and hydrogen bonds with chloride anions [242]. In the year 1987, Hiraoka*et al.* reported a great work stating that the interactions between hexafluorobenzene and halide ions (C_6F_6•••X^-; where, X= F, Cl, Br, I) are mostly electrostatic but not covalent [243]. Schneider *et al.* in 1993 reported weak but distinct attractive interactions between polarisable aryl parts of host and negatively charges guest [244]. Thereafter, in 2002 three theoretical research groups (Alkorta *et al.*, Deya` *et al.*, and Mascal *et al.*) independently proposed and theoretically established that anion•••π interactions are the imperative interactions between negatively charged anions and electronically deficient aromatic rings [245–247]. The X-ray

crystal structures were reported by Meyer *et. al* [248] and Reedijik *et. al*, [249] where recognized and unambiguous anion•••π interactions were exploited using hexakis-(pyridine-2-yl)-[1,3,5]-triazine-2,4,6-triamine moiety. In their report the anion•••π distance is 3.11Å and the angle of contact is 88° both of which are correlating with theoretical data as predicted by Deya [246] and Mascal [247]. Both crystallographic database and theoretical elucidation proved that the strength of this anion•••π interaction is dependent on anion•••π non-covalent interaction distance and as well as on the angle (θ). The said angle represents the angle of the line connecting the ring centroid with a ring atom and [X]⁻•••aryl centroid axis.

Frontera and his collaborators has carried out imperative research on the directionality of anion•••π interactions by DFT studies [248–250]. Furthermore, they combined the experimental and theoretical studies for anion•••π interactions of Zn(II) complexes with *N*-imidazolyl and *N*-pyrazolylpyrimidine donor ligands [251,252]. The anion•••π interactions mostly depend on electrostatic interactions and anion induced polarization effects, which is established by computational studies. The electrostatic component of the aromatic ring sharply connects with the magnitude of the ring having permanent quadrupole moment, that is actually the charge separation both sides of the aromatic plane (Fig. 1.25) [253].
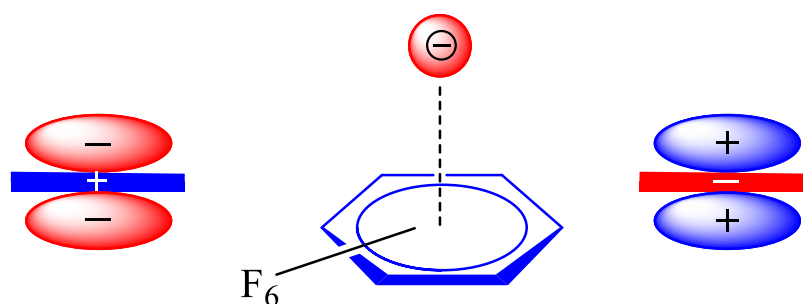
Fig. 1.25. Representations of the quadrupole moments of benzene (left) and hexafluorobenzene (right) and the anion•••π interaction (middle) [253].

The anion•••π interactions are well understood from the theoretical/computational point of view (Fig. 1.26). The additivity of anion•••π interactions (Fig. 1.26a) along with interrelationship with other competitive interactions like π•••π stacking (Fig. 1.26c), cation•••π (Fig. 1.26b), halogen bonding (Fig. 1.26d), steric hindrance and electronic interfering effects (Fig. 1.26e) can be justified by computational studies [254]. Besides, the complex structure and interplay of additional weak non-covalent interactions make the structural prediction of anion•••π acceptor complexes very much difficult.
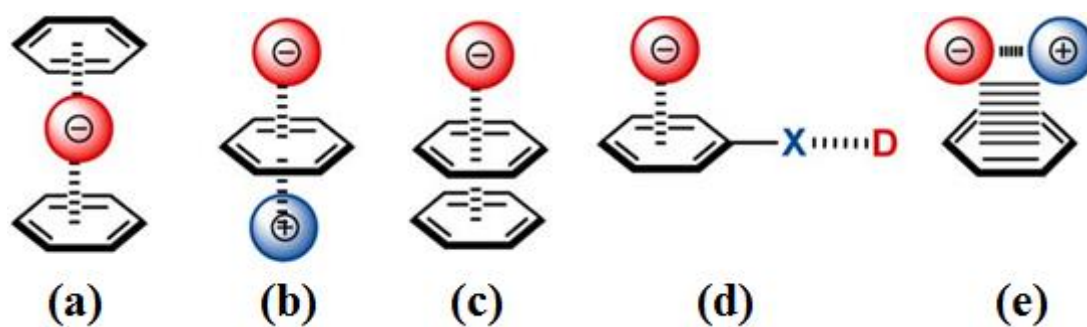
Fig. 1.26. Schematic representation of additivity as well as completive and cooperative intermolecular forces influencing the strength of anion•••π interaction [254].

It was clear from crystallographic database that the interplay between anion•••π and hydrogen bonding or anion•••π and π•••π interactions acts as an important role in a synergistic manner to establish the crystal packing in solid state. But the challenging job is to prepare systems where both anion•••π and π•••π interactions interact simultaneously. Here former electron deficient π system and the later electron rich π systems are necessary. When an aromatic heterocyclic ring is coordinated to a metal ion, the aromatic ring became electronically deficient. But this electron deficiency is not to such extent so that it can be used to ensure a strong anion•••π interaction. This interaction became a crucial one if the heterocyclic aromatic ring is protonated [246].

1.5.7. Lone pair•••π interaction

Lone pair•••π interaction is one of the weak yet significant supramolecular interaction recognized by the scientific society.The lone pair•••π (lp•••π) bonding is a stabilizing interaction occurs between a lone pair of electrons and π-system (Fig. 1.27). Generally, the interaction between lone pair and π-cloud is assumed to be electrostatically unfavourable but, various computational studies have confirmed that the lone pair•••π bonding interaction is energetically favorable [255,256]. From the crystalline structures, two similar but unusual type of interactions have been appeared, namely anion•••π and lp•••π interactions. In both cases, electron rich atoms are found to place themselves just over the aromatic system.

In 1995, Elgi and co-workers reported a paper where they stated the presence of lp•••π interaction in biological macromolecule Z-DNA [258,259]. They explained the unusual stability of the left handed Z-DNA arising due to the interaction between lone pair of an oxygen atom of cytidine-2′-deoxyribose fragment and guanidinium part of guanosine (Fig. 1.28). After few years of this report, they published another report demonstrating H_2O•••π interactions within a ribosomal frame-shifting RNA pseudoknot. Indeed, the RNA pseudo

knot has a crystal structure that exposed lone pair•••nucleobase interaction where the separation distance between carbon atom of cytosine moiety and the water oxygen atom was 2.93 Å [260].
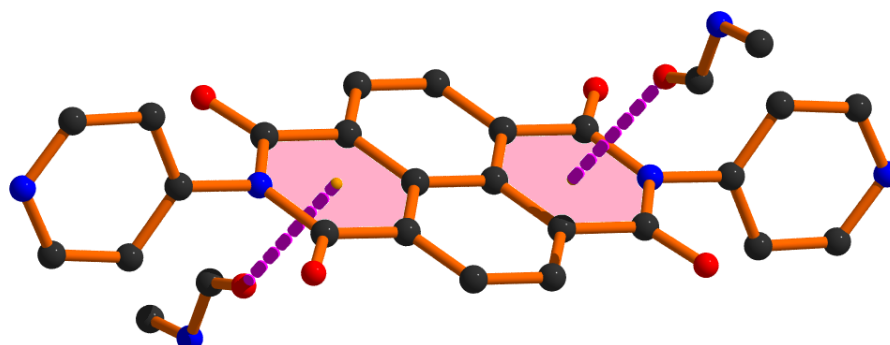
Fig. 1.27. Representation of the Lone pair•••π interactions in molecular crystal [257]

Recently, in a comprehensive review [261], such type of lp•••π interactions was designated as a new supramolecular bond by Gamez*et al.* and an exhaustive scrutiny of the Cambridge Structure Database (CSD) exhibited that such interactions are not uncommon in organic/inorganic compounds. This rigorous investigation of the CSD clearly exhibits that lp•••π interactions are abundant in solid state structures.
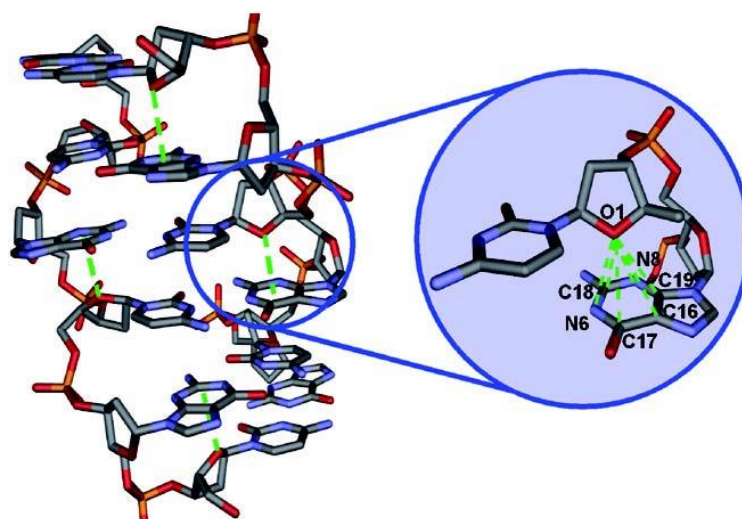
Fig. 1.28. Lone pair•••π interactions (green dashed lines) stabilizing the left-handed supramolecular structure of Z-DNA [262].

Luisi*et al.* investigated the protein data bank for water-tryptophan and water-histidine contacts and found many cases where a water molecule is in contacts with the centroid of an imidazole or an indole residue through an endocyclic nitrogen atom [263]. For instance, lp•••π interactions in water-tryptophan contact was stabilized the engrailed homeodomain and

help in the recognition of its cognate DNA [264].Also in 2004, Kochi et al. reported crystal structure of tetraalkylammonium halides-tetracyanopiperazine (*e.g.* $NEt_4Br \cdot \cdot \cdot TCP$) adducts, featuring spectacular halide–TCP contacts [264].

A detail investigation of protein database was made for carbonyl (lp)•••π interactions in bio-macromolecules by Sankararamakrishnan and co-workers [265]. From the investigation 250 protein structures were observed where oxygen atoms of carbonyl groups are within 3.5 Å from the centroid of aromatic rings. In recent times, lp•••π interactions have been detected in small molecular host-guest system and the fact was well demonstrated by means of computational studies [266−268]. In a very recent article, it has been shown that supramolecular architectures based on lp•••π interactions provide stability to crystal structure [269].

1.6. DENSITY FUNCTIONAL THEORY (DFT)

Density Functional Theory (DFT) is a computational tool commonly used in physical science, chemical science and material science to determine the electronic structure of several body systems (*i.e.*, atoms, molecules and clusters) [270–272]. DFT has found significance in solid state physics since 1970's. Still, it was not appreciated as an important tool till 1990's as DFT was not taken into account correct enough for calculations in quantum chemistry. But, after 1990's the approximations utilize in the theoretical calculation were refined several times to get better model for the correlation interaction. Electronic structure calculation not only help us to determine physical as well as chemical properties of compounds accurately, but also give data for the modification of parameters in greater scale methods like, molecular dynamics, cluster dynamics, *etc*. As most of the properties of a compound rely on the behavior of its electrons, thus it is necessary to have an accurate method to compute the electronic structure in order to model or predict them.

DFT is basically depend on quantum theory and does not use any empirical parameter. Only the atomic number of the component atoms and some initial fundamental structural information has to input here. This theory has been applied fruitfully to the elucidation of structural and dynamical properties (charge density, lattice structure, magnetization, *etc*.) of a large variety of solids [273–278]. The proficiency and enormous prospect of this computational method was acknowledged by Noble committee in 1998 and the prize was shared equally to Walter Kohn (for his development of the DFT) for their significant contributions in chemistry.

In this DFT, several models have been preferred (almost comparable to the molecular structure which is observed in single crystal X-ray crystallography) to fit them using different softwires and the interaction energy values are calculated. For better understanding and visualization of inherent electronic structure of molecules in the solid state, Molecular Electrostatic Potential (MEP), Atoms in Molecule (AIM), Non-covalent Interactions Plot (NCI plot) with specific isosurfaces have been introduced.

1.6.1. Molecular Electrostatic Potential (MEP)

Electrostatic potential ties in with electronegativity, dipole moment as well as partial charges. It gives an easy visualization method to know the comparative polarity of a molecule [279–282]. The molecular electrostatic potential (MEP) is the potential energy of a proton at a definite position close to a molecule. Generally, the MEP surface represents the charge separations in the molecules three dimensionally and these surface analyses allow us to interpret as a map of area of electron excess and electron deficiency in the molecules. The partial charges illustrated as spheres (red color is positive, yellow color is negative) which exhibit how the molecule would interact with incoming protons or positive charges. When a proton faces a positive region of the molecule, the repulsive interaction occurs, thus resulting in an increasing positive potential (+ve) energy (shown in blue color). Similarly, when a proton faces a negative region of the molecule, an attractive interaction results, thus producing in increasing negative potential (−ve) energy (shown in red color). Positive electrostatic potential indicates a repulsion of the proton by the atomic nuclei (low electron density) whereas negative electrostatic potential indicates an attraction of the proton by the concentrated electron density (from lone pairs, negative charges, pi-bonds, *etc*.) in the molecules. The electron density isosurfaces is a surface that encompasses a particular portion of the molecule's electron probability density.

The electrostatic potential at various points on the electron density isosurface is displayed by coloring the isosurface with contours (Fig.1.29). The greater red/blue differences signify more polar is the molecule. If the surface is white or lighter color shades, the molecule is mostly non-polar. The MEP surface analysis plays an important role in the linear/bipodal receptor designing [283]. Besides, from these surface analyses, one can explain the selectivity and nature of interactions present in host-guest complexes [284,285].
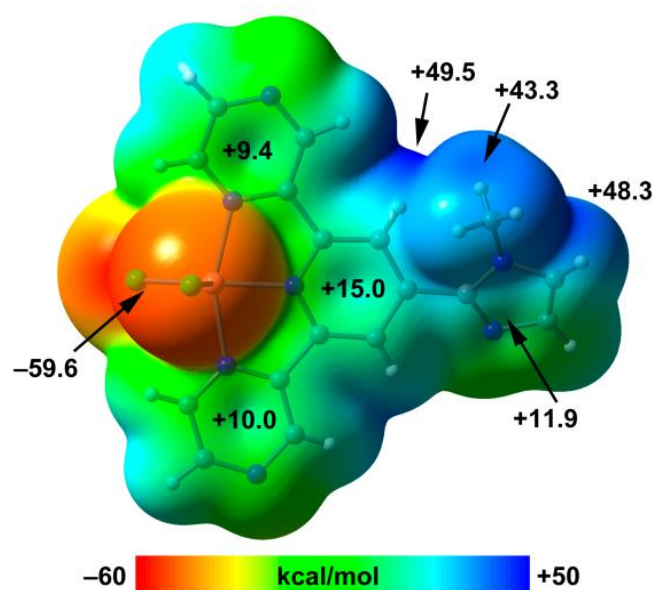
Fig. 1.29. Perspective view of Molecular Electrostatic Potential (MEP).

1.6.2. Atoms in Molecule (AIM)

The theory of 'Atoms in Molecule' (AIM) is an interpretative theory which reveals the wealth of information hidden in the electron density and its derived functions. The extended theory of atoms in molecule has been clearly described in the Bader's Book [286]. To give a deeper insight into the intermolecular interactions between the molecules, Bader's Quantum Theory of Atoms in Molecules (QTAIM) is used. In the QTAIM, the bond critical points (BCPs) between the two attractors (two atoms interacting or bonded) are calculated (Fig. 1.30). This theory has been extensively applied to explore atom-atom interactions (covalent and non-covalent interactions) in molecules, small molecular crystals, molecular clusters, proteins and DNA base pairing [287–291].

Bader's group has also investigated various formative contributions to the improvement of the QTAIM and its uses in chemical bonding [292,293]. Popelier and his co-workers have applied the QTAIM to solve numerous problems in chemistry [294]. In particular, they have established the possibility of improving structure-activity-relationship to forecast several physical and chemical properties [295]. Various groups have employed the QTAIM for exploring the non-covalent interactions, including van der Waals, C─H••π, π•••π, cation•••π, anion•••π, hydrogen bonding interactions, *etc.* and their uses in several fields of chemistry [296–298]. All these interactions have been successfully characterized with the help of theory of QTAIM [299–302].
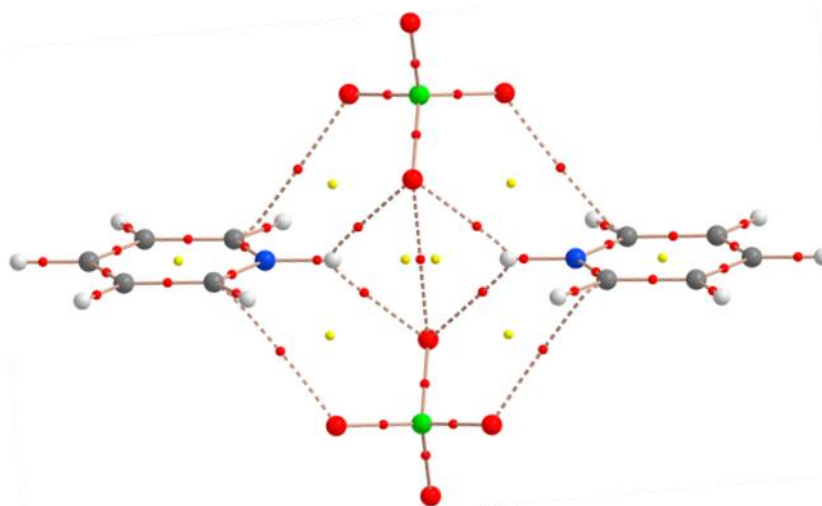
Fig. 1.30. Perspective view of Atoms in Molecules [303].

1.6.3. Non-covalent Interaction plot (NCI Plot)

The non-covalent interaction plot (NCI plot) is very useful visualization index that efficiently provides information about characterization of non-covalent interactions [304-306]. The information generated from NCI plot is mostly qualitative *i.e*. it clearly shows molecular regions which are interacting. The non-covalent interactions are presented using isosurfaces rather than critical points. It also enables clear visualization and identification of non-covalent interaction. The isosurfaces are dealing with either favorable or unfavorable interactions, which are distinguished by the signs of second density Hessain eigen value. This is described by the isosurface color. A color scheme (red-blue-green-blue) is chosen to highlight the strength of interactions, where red is used for repulsive interaction and blue color is for attractive interactions (Fig. 1.31). Green and yellow surfaces represents to weak attractive and weak repulsive interactions, respectively. The intensities of these colors (*i.e.*, deepness of the color) are associated with a higher local density that leads to a stronger interaction. Non-covalent interactions often help us to understand many chemical and biological problems. Illustrating these non-covalent interactions precisely, together with their relative positions in real space, one has to assign an initial step in the procedure of decoupling the complex balance of forces that characterize non-covalent interactions. Due to the size of the macromolecules, the most conventional approach has been used to identify van der Waals forces, steric clashes and hydrogen bonding interactions depending on pair wise distances between the interacting atoms in accordance with their der Waal radii. Recently, an alternative aspect obtained from the electron density, the non-covalent interactions (NCI)

index that has the double benefits of being usually transferable to various chemical applications and being prompt to calculate as it can be measured from promolecular densities.
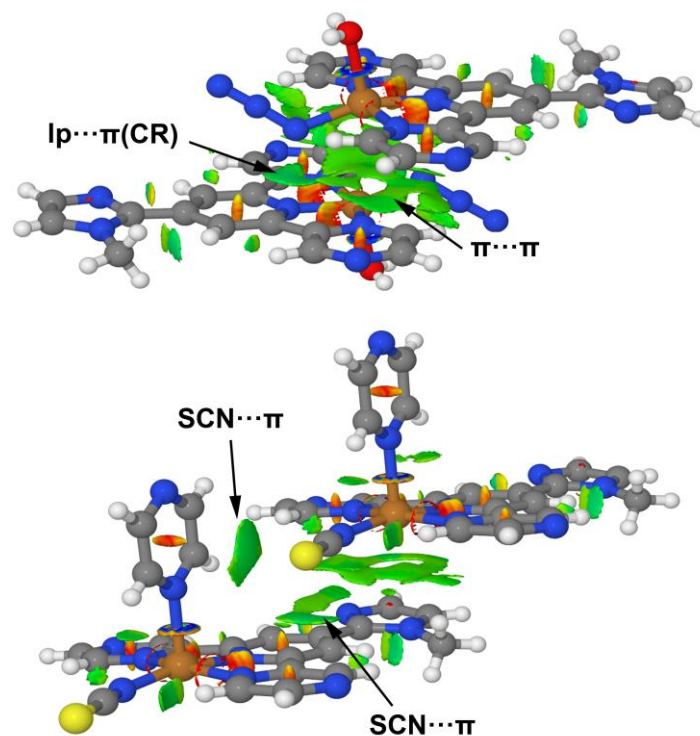
Fig. 1.31. Representative figures for NCI isosurfaces to visualize the non-covalent interactions.

Hence, NCI analysis is applicable to large systems, such as DNA and proteins, where study of non-covalent interactions is of enormous potential value. Thus, NCI computation algorithm has been used to analyze and visualize the non-covalent interactions using both self-consistent fully quantum mechanical as well as promolecular densities [307,308].

REFERENCES

1. J. Alvárez-Builla and J. Barluenga, *Mod. Heterocycl. Chem.*, 2011, **1**, 1.

2. E. Campaigne, *J. Chem. Educ.*, 1986, **63**, 860.

3. R. H. Wiley and L. C. Behr, *Pyrazoles, pyrazolines, pyrazolidines, indazoles and condensed rings*, John Wiley & Sons Ltd, 1967.

4. A. T. Balaban, D. C. Oniciu and A. R. Katritzky, *Chem. Rev.*, 2004, **104**, 2777.

5. G. Bacolini, *Top. Heterocycl. Syst.: Synth., React. Prop.*, 1996, **1**, 103.

6. M. Brichacek and J. T. Njardarson, *Org. Biomol. Chem.*, 2009, **7**, 1761–1770.

7. H. Liu, Y. Li, X. Y. Wang, B. Wang, H. Y. He, J. Y. Liu, M. L. Xiang, J. He, X. H. Wu, L. Yang, *Bioorg. Med. Chem. Lett.*, 2013, **23**, 2349–2352.

8. Y. Kaddouri, F. Abrigach, E. B. Yousfi, M. El. Kodadi and R. Touzani, *Heliyon*, 2020, **6**, e03185.

9. A. H. Abadi, T. M. Ibrahim, K. M. Abouzid, J. Lehmann, H. N. Tinsley, B. D. Gary and G. A. Piazza, *Bioorg. Med. Chem.*, 2009, **17**, 5974.

10. Y. Zhou, X. Zhu, L. Zhang, C. Tang, B. Feng, *Chem. Biol. Drug Des.*, 2019, **93**, 67–74.

11. A. F. Henwood, I. N. Hegarty, E. P. McCarney, J. I. Lovitt, S. Donohoe and T. Gunnlaugsson, *Coord. Chem. Rev.*, 2021, **449**, 214206–214252.

12. R. R. Panicker, and A. Sivaramakrishna, *Coord. Chem. Rev.*, 2022. **459**, 214426.

13. H. Hofmeier and U. S. Schubert, *Chem. Soc. Rev.*, 2004, **33**, 373–399.

14. G. Wang, C. T. He, R. Huang, J. Mao, D. Wang and Y. Li, *J. Am. Chem. Soc.*, 2020, **142**, 19339–19345.

15. G. Wu, L. Chen, L. Xu, X. Zhao and H. Yang, *Coord. Chem. Rev.*, 2018, **369**, 39–75.

16. A. M. Mansour, *J. Mol. Struct.*, 2021, **1242**, 130737.

17. A. Szlapa-Kula, M. Małecka and B. Machura, *Dyes Pigm.*, 2020, **180**, 108480.

18. A. Maroń, A. Szlapa, T. Klemens, S. Kula, B. Machura, S. Krompiec, J. G. Małecki, A. Świtlicka-Olszewska, K. Erfurt and A. Chrobok, *Org. Biomol. Chem.*, 2016, **14**, 3793–3808.

19. M. G. Alexandru, D. Visinescu, B. B. Cula, F. Lloret, M. Julve, *Eur. J. Inorg. Chem.*, 2018, **3-4**, 349–359.

20. H. Hadadzadeh, M. Maghami, J. Simpson, A. D. Khalaji, K. Abdi, *J. Chem. Crystallogr.*, 2012, **42**, 656–667.

21. S. Islam, J. Datta, F. Ahmed, B. Dutta, S. Naaz, P. P. Ray and M. H. Mir, *New J. Chem.*, 2018, **42**, 13971–13977.

22. A. Hossain, A. Dey, S. K. Seth, P. P. Ray, P. Ballester, R. G. Pritchard, J. Ortega-Castro, A. Frontera and S. Mukhopadhyay, *ACS Omega*, 2018, **3**, 9160–9171.

23. S. Konar, A. Dey, S. R. Choudhury, K. Das, S. Chatterjee, P. P. Ray, J. O. Castro, A. Frontera and S. Mukhopadhyay, *J. Phys. Chem. C*, 2018, **122**, 8724–8734.

24. S. M. Elahi, M. Raizada, P. K. Sahu and S. Konar, *Chem. – Eur. J.*, 2021, **27**, 5858–5870.

25. L. Prodi, *New J. Chem.*, 2005, **29**, 20–31.

26. G. Orellana and M. C. Moreno-Bondi, *Frontiers in Chemical Sensors: Novel Principles and Techniques*, Springer, New York, 2005.

27. A. W. Czarnik, *Acc. Chem. Res.*, 1994, **27**, 302–308.

28. A. P. De Silva, D. B. Fox, A. J. M. Huxley and T. S. Moody, *Coord. Chem. Rev.*, 2000, **205**, 41–47.

29. A. P. de Silva, H. Q. N. Gunaratne, T. Gunnlaugsson, A. J. M. Huxley, C. P. McCoy, J. T. Rademacher and T. E. Rice, *Chem. Rev.*, 1997, **97**, 1515–1566.

30. Q. He, E. W. Miller, A. P. Wong, C. J. Chang, *J. Am. Chem. Soc.*, 2006, **128**, 9316–9317.

31. M. Zhu, M. Yuan, X. Liu, J. Xu, J. Lv, C. Huang, H. Liu, Y. Li, S. Wang and D. Zhu, *Org. Lett.*, 2008, **10**, 1481–1484.

32. S. K. Sahoo, D. Sharma, R. K. Bera, G. Crisponi, J. F. Callan, *Chem. Soc. Rev.*, 2012, **41**, 7195–7227.

33. B. Varghese, S. N. Al-Busafi, F. O. Suliman and S. M. Z. Al-Kindy, *RSC Adv.*, 2017, **7**, 46999–47016.

34. R. Rudolf, M. Mongillo, R. Rizzato, T. Pozzan, *Nat. Rev.*, 2003, **4**, 579–586.

35. P. Plaza, I. Leray, P. Changenet-Barret, M. M. Martin and B. Valeur, *ChemPhysChem*, 2002, **3**, 668–674.

36. Y.-Q. Li, J. L. Bricks, U. Resch-Genger, M. Spieles and W. Rettig, *J. Phys. Chem. A*, 2006, **110**, 10972–10984.

37. R. Nagarajan, C. Varadaraju, K. H. Lee, *Dyes Pigm.*, 2021, **191**, 109331–109358.

38. G. A. Jeffrey and W. Saenger, *Hydrogen bonding in biological structures*. Springer-Verlag, Berlin, 1991.

39. T. Steiner, *Angew. Chem., Int. Ed.*, 2002, **41**, 48–76.

40. R. K. Raju, H. Hillier, N. A. Burton, M. A. Vincent, S. Doudou and R. A. Bryce, *Phys. Chem. Chem. Phys.*, 2010, **12**, 7959–7967.

41. P. Politzer, J. S. Murray and T. Clark, *Phys. Chem. Chem. Phys.*, 2010, **12**, 7748–7757.

42. C. Murcia-García, A. Bauzá, G. Schnakenburg, A. Frontera and R. Streubel, *CrystEngComm*, 2015, **17**, 1769–1772.

43. G. Gil-Ramirez, E. C. Escudero-Adan, J. Benet-Buchholz and P. Ballester, *Angew. Chem., Int. Ed.*, 2008, **47**, 4114–4118.

44. A. Caballero, F. Zapata, L. Gonzalez, P. Molina, I. Alkorta and J. Elguero, *Chem. Commun.*, 2014, **50**, 4680–4682.

45. Y. Kuroda, A. Kawashima, Y. Hayashi and H. Ogoshi, *J. Am. Chem. Soc.*, 1997, **119**, 4929–4933.

46. N. Saleh, A. L. Koner and W. M. Nau, *Angew. Chem., Int. Ed.*, 2008, **47**, 5398–5401.

47. M.-C. Daniel and D. Astruc, *Chem. Rev.*, 2003, **104**, 293–346.

48. C. Y. Wei, Y. He, X. D. Shi and Z. G. Song, *Coord. Chem. Rev.*, 2019, **385**, 1–19.

49. W. Knoll, F. Yu, T. Neumann, S. Schiller and R. Naumann, *Phys. Chem. Chem. Phys.*, 2003, **5**, 5169–5175.

50. G. A. Hudalla, J. A. Modica, Y. F. Tian, J. S. Rudra, A. S. Chong, T. Sun, M. Mrksich and J. H. Collier, *Adv. Healthcare Mater.*, 2013, **2**, 1114–1119.

51. J. Lehn, *Concept and perspectives*, VCH: Weinheim, Germany, 1995.

52. E. R. T. Tiekink, J. Vittal and M. Zaworotko, *Organic Crystal Engineering: Frontiers in Crystal Engineering*, Wiley, 2010.

53. E. R. T. Tiekink and J. Zukerman-Schpector, *The Importance of Pi-Interactions in Crystal Engineering*, John Wiley & Sons, Chichester, UK, 2012.

54. G. R. Desiraju, J. J. Vittal and A. Ramanan, *Crystal engineering: a textbook*, World Scientific, 2011.

55. G. R. Desiraju, *J. Am. Chem. Soc.*, 2013, **135**, 9952–9967.

56. G. M. J. Schmidt, *Pure Appl. Chem.*, 1971, **27**(4), 647–678.

57. A. I. Cooper, *Angew. Chem., Int. Ed.*, 2012, **51**, 7892–7894.

58. L. Brammer, *Chem. Soc. Rev.*, 2004, **33**, 476–489.

59. G. R. Desiraju, *Angew. Chem., Int. Ed.*, 2007, **46**(44), 8342–8356.

60. A. Nangia, *Curr. Opin. Solid State Mater. Sci.*, 2001, **5**, 115–122.

61. L. Addadi and M. Geva, *CrystEngComm*, 2003, **5**, 140–146.

62. R. K. Raju, H. Hillier, N. A. Burton, M. A. Vincent, S. Doudou and R. A. Bryce, *Phys. Chem. Chem. Phys.*, 2010, **12**, 7959–7967.

63. P. Politzer, J. S. Murray and T. Clark, *Phys. Chem. Chem. Phys.*, 2010, **12**, 7748–7757.

64. A. Caballero, F. Zapata, L. Gonzalez, P. Molina, I. Alkorta and J. Elguero, *Chem. Commun.*, 2014, **50**, 4680–4682.

65. M. Savastano, C. García-Gallarín, M. D. López de la Torre, C. Bazzicalupi, A. Bianchi and M. Melguizo, *Coord. Chem. Rev.*, 2019, **397**, 112–137.

66. Q. Song, Z. Cheng, M. Kariuki, S. C. L. Hall, S. K. Hill, J. Y. Rho and S. Perrier, *Chem. Rev.*, 2021, **121**, 13936–13995.

67. G. Mahmoudi, S. K. Seth, F. I. Zubkov, E. López-Torres, A. Bacchi, V. Stilinović and A. Frontera, *Crystals*, 2019, **9**, 323.

68. J. M. Zayed, N. Nouvel, U. Rauwald and O. A. Scherman, *Chem. Soc. Rev.*, 2010, **39**, 2806–2816.

69. J. T. Davis and G. P. Spada, *Chem. Soc. Rev.*, 2007, **36**, 296–313.

70. S. Park, J. H. Lim, S. W. Chung and C. A. Mirkin, *Science*, 2004, **303**, 348–351.

71. D. M. Vriezema, M. C. Aragones, J. A. A. W. Elemans, J. J. L. M. Cornelissen, A. E. Rowan and R. J. M. Nolte, *Chem. Rev.*, 2005, **105**, 1445–1490.

72. C. Du, G. Falini, S. Fermani, C. Abbott and J. Moradian-Oldak, *Science*, 2005, **307**, 1450–1454.

73. https://en.wikipedia.org/wiki/Supramolecular_assembly.

74. L. Zhang, K. Yu and A. Eisenberg, *Science*, 1996, **272**, 1777–1779.

75. S. I. Stupp, V. LeBonheur, K. Walker, L. S. Li, K. E. Huggins, M. Keser and A. Amstutz, *Science*, 1997, **276**, 384–389.

76. J. D. Hartgerink, E. Beniash and S. I. Stupp, *Science*, 2001, **294**, 1684–1688.

77. M. E. Kosal, J. H. Chou, S. R. Wilson and K. S. Suslick, *Nat. Mater.*, 2002, **1**, 118–121.

78. C. J. Kuehl, T. Yamamoto, S. R. Seidel and P. J. Stang, *Org. Lett.*, 2002, **4**, 913–915.

79. B. J. Holliday and C. A. Mirkin, *Angew. Chem.*, 2001, **113**, 2076–2097.

80. S. Leininger, B. Olenyuk and P. Stang, *Chem. Rev.*, 2000, **100**, 853–908.

81. G. R. Desiraju, *Chem. Commun.*, 1997, 1475–1482.

82. C. B. Aakeroy, B. M. T. Scott, M. M. Smith, J. F. Urbina and J. Desper, *Inorg. Chem.*, 2009, **48**, 4052–4061.

83. L. S. Reddy, N. J. Babu and A. Nangia, *Chem. Commun.*, 2006, 1369–1371.

84. S. Kohmoto, Y. Kuroda, Y. Someya, K. Kishikawa, H. Masu, K. Yamaguchi and I. Azumaya, *Cryst. Growth Des.*, 2009, **9**, 3457–3462.

85. A. Mukherjee, *Cryst. Growth Des.*, 2015, **15**, 3076–3085.

86. O. V. Shishkin, R. I. Zubatyuk, S. V. Shishkina, V. V. Dyakonenko and V. V. Medviediev, *Phys. Chem. Chem. Phys.*, 2014, **16**, 6773–6786.

87. G. Pérez-Mitta, A. G. Albesa, W. Knoll, C. Trautmann, M. E. Toimil-Molares and O. Azzaroni, *Nanoscale*, 2015, **7**, 15594–15598.

88. D. J. Cram, *Angew. Chem., Int. Ed. Engl.*, 1986, **25**, 1039–1057.

89. C. J. Pedersen, *J. Am. Chem. Soc.*, 1967, **89**, 2495–2496.

90. D. J. Cram and J. M. Cram, Container Molecules and Their Guests; Royal Society of Chemistry, London, 1994.

91. Y. H. Luo, S. W. Ge, W. T. Song and B. W. Sun, *New J. Chem.*, 2014, **38**, 723–729.

92. F. N. Diedrich, Cyclophanes; Royal Society of Chemistry, London, 1991.

93. J. R. Moran, S. Karbach and D. J. Cram, *J. Am. Chem. Soc.*, 1982, **104**, 5826–5828.

94. D. Fiedler, R. G. Bergman and K. N. Raymond, *Angew. Chem., Int. Ed.*, 2004, **43**, 6748– 6751.

95. R. Yu, X.-F. Kuang, X.-Y. Wu, C.-Z. Lu and J. P. Donahue, *Coord. Chem. Rev.*, 2009, **253**, 2872–2890.

96. D. N. Dybtsev, M. P. Yutkin, D. G. Samsonenko, V. P. Fedin, A. L. Nuzhdin, A. A. Bezrukov, K. P. Bryliakov, E. P. Talsi, R. V. Belosludov, H. Mizuseki, Y. Kawazoe, O. S. Subbotin and V. R. Belosludov, *Chem. – Eur. J.*, 2010, **16**, 10348–10356.

97. G. Cooke and V. M. Rotello, *Chem. Soc. Rev.*, 2002, **31**, 275–286.

98. C. Valdes, L. M. Toledo, U. Spitz and J. Rebek Jr., *Chem.–Eur. J.*, 1996, **2**, 989–991.

99. W. A. Freeman, *Acta Crystallogr., Sect. B: Struct. Sci.*, 1984, **40**, 382–387.

100. S. Valimaki, N. K. Beyeh, V. Linko, R. H. A. Ras and M. A. Kostiainen, *Nanoscale*, 2018, **10**, 14022–14030.

101. G. W. Gokel, W. M. Leevy and M. E. Weber, *Chem. Rev.*, 2004, **104**(5), 2723–2750.

102. Z. Liu, S. K. M. Nalluri and J. F. Stoddart, *Chem. Soc. Rev.*, 2017, **46**(9), 2459–2478.

103. J. M. Lehn, *Angew. Chem. Int. Ed.*, 1988, **27**(1), 89–112.

104. A. B. Descalzo, R. Martínez-Máñez, F. Sancenon, K. Hoffmann and K. Rurack, *Angew. Chem. Int. Ed.*, 2006, **45**(36), 5924–5948.

105. B. Escuder, M. LLusar and J. F. Miravet, *J. Org. Chem.*, 2006, **71**(20), 7747–7752.

106. K. Ariga, H. Ito, J. P. Hill and H. Tsukube, *Chem. Soc. Rev.*, 2012, **41**(17), 5800–5835.

107. H. J. Kim, M. H. Lee, L. Mutihac, J. Vicens and J. S. Kim, *Chem. Soc. Rev.*, 2012, **41**(3), 1173–1190.

108. G. Yu, K. Jie and F. Huang, *Chem. Rev.*, 2015, **115**(15), 7240–7303.

109. K. S. Mali, J. Adisoejoso, E. Ghijsens, I. De Cat and S. De Feyter, *Acc. Chem. Res.*, 2012, **45**(8), 1309–1320.

110. K. Ariga and T. Kunitake, The Chemistry of Molecular Recognition—Host Molecules and Guest Molecules. *In Supramolecular Chemistry—Fundamentals and Applications*; Springer: Berlin, Germany, 2006.

111. Y. Zhang, M. Z. Yang, F. Yuan, H. W. Gu, P. Gao, B. Xu, *J. Am. Chem. Soc.*, 2004, **126**, 15028–15029.

112. R. A. Potyrailo, *Angew. Chem., Int. Ed.*, 2006, **45**, 702–723.

113. S. R. Choudhury, B. Dey, S. Das, A. Robertazzi, A. D. Jana, C.-Y. Chen, H. M. Lee, P. Gamez and S. Mukhopadhyay, *Dalton Trans.*, 2009, **37**, 7617–7624.

114. E. Persch, O. Dumele and F. Diederich, *Angew. Chem., Int. Ed.*, 2015, **54**, 3290–3327.

115. D. E. Torres Pazmiño, M. Winkler, A. Glieder and M. W. Fraaije, *J. Biotechnol.*, 2010, **146**, 9–24.

116. Y. Song, Y. Liu, T. Qi and G. L. Li, *Angew. Chem., Int. Ed.*, 2018, **57**, 13838–13842.

117. W. D. Newman, C. L. Cortes, A. Afshar, K. Cadien, A. Meldrum, R. Fedosejevs and Z. Jacob, *Sci. Adv.*, 2018, **4**, eaar5278.

118. D. J. Liptrot and P. P. Power, *Nat. Rev. Chem.*, 2017, **1**, 0004.

119. P. A. Kollman, *Acc. Chem. Res.*, 1977, **10**, 365–371.

120. T. J. Mooibroek, C. A. Black, P. Gamez and J. Reedijk, *Cryst. Growth Des.*, 2008, **8**, 1082–1093.

121. M. Albrecht, C. Wessel, M. de Groot, K. Rissanen and A. Lüchow, *J. Am. Chem. Soc.*, 2008, **130**, 4600–4601.

122. P. Manna, S. K. Seth, M. Mitra, A. Das, N. J. Singh, S. R. Choudhury, T. Kar and S. Mukhopadhyay, *CrystEngComm*, 2013, **15**, 7879–7886.

123. A. Hossain, A. Dey, S. K. Seth, P. P. Ray, J. Ortega-Castro, A. Frontera and S. Mukhopadhyay, *CrystEngComm*, 2021, **23**, 3569–3581.

124. E. R. T. Tiekink, *CrystEngComm*, 2020, **22**, 7308–7333.

125. S. Mirdya, S. Roy, S. Chatterjee, A. Bauzá, A. Frontera and S. Chattopadhyay, *Cryst. Growth Des.*, 2019, **19**, 5869–5881.

126. S. L. Tan, S. M. Lee, K. M. Lo, A. Otero-de-la-Roza and E. R. T. Tiekink, *CrystEngComm*, 2021, **23**, 119–130.

127. A. D. Bond, *Chem. Commun.*, 2002, **16**, 1664–1665.

128. A. J. Neel, M. J. Hilton, M. S. Sigman and F. D. Toste, *Nature*, 2017, **543**, 637.

129. J. W. Steed, D. R. Turner and K. Wallace, *Core Concepts in Supramolecular Chemistry and Nanochemistry*, Wiley, 1st edn, 2007.

130. P. A. Kollman and L. C. Allen, *Chem. Rev.*, 1972, **72**, 283–303.

131. L. Pauling, *The Nature of the Chemical Bond*, Cornell University Press, Ithaca, New York, 1960.

132. L. M. Eytel, H. A. Fargher, M. M. Haley and D. W. Johnson, *Chem. Commun.*, 2019, **55**, 5195–5206.

133. Y. Liu, W. Zhao, C.-H. Chen and A. H. Flood, *Science*, 2019, **365**, 159–161.

134. J. W. Larson and T. B. McMahon, *Inorg. Chem.*, 1984, **23**, 2029–2033.

135. J. Emsley, *Chem. Soc. Rev.*, 1980, **9**, 91–124.

136. G. A. Jeffrey, *An Introduction to Hydrogen Bonding*, Oxford University Press, 1997.

137. R. C. Johnston and P. H. Y. Cheong, *Org. Biomol. Chem.*, 2013, **11**, 5057–5064.

138. I. Rozas, I. Alkorta and J. Elguero, *J. Phys. Chem. A*, 1998, **102**, 9925–9932.

139. V. R. Talladi, S. Brasselet, H. -C. Weiss, D. Blaser, A. K. Katz, H. L. Carrell, R. Boese, J. Zyss, A. Nangia and G. R. Desiraju, *J. Am. Chem. Soc.*, 1998, **120**, 2563–2577.

140. A. J. Stone and S. Tsuzuki, *J. Phys. Chem. A*, 1997, **101**, 10178–10183.

141. R. Vallee, P. Damman, M. Dosiere, E. Toussaere and J. Zyss, *J. Am. Chem. Soc.*, 2000, **122**, 6701–6709.

142. C. A. Hunter, M. N. Meah and J. K. Sanders, *J. Am. Chem. Soc.*, 1990, **112**, 5773–5780.

143. F. M. Raymo, K. N. Houk and J. F. Stoddart, *J. Org. Chem.*, 1998, **63**, 6523–6528.

144. S. Tsuzuki, K. Honda, T. Uchimaru, M. Mikami and K. Tanabe, *J. Am. Chem. Soc.*, 2002, **124**, 104–112.

145. K. M. Guckian, B. A. Schweitzer, R. X. F. Ren, C. J. Sheils, D. C. Tahmassebi and E. T. Kool, *J. Am. Chem. Soc.*, 2000, **122**, 2213–2222.

146. S. Burattini, B. W. Greenland, D. H. Merino, W. Weng, J. Seppala, H. M. Colquhoun, W. Hayes, M. E. Mackay, I. W. Hamley and S. J. Rowan, *J. Am. Chem. Soc.*, 2010, **132**, 12051–12058.

147. Z. Zhang, H. Huang, X. Yang and L. Zang, *J. Phys. Chem. Lett.*, 2011, **2**, 2897–2905.

148. C. Janiak, S. Temizdemir and S. Dechert, *Inorg. Chem. Commun.*, 2000, **3**, 271–275.

149. C. A. Hunter, *Chem. Soc. Rev.*, 1994, **23**, 101–109.

150. C. Janiak, *J. Chem. Soc., Dalton Trans.*, 2000, **21**, 3885–3896.

151. C. A. Hunter, *Angew. Chem. Int. Ed.*, 1993, **32**, 1584–1586.

152. F. Cozzi and J. S. Siegel, *Pure Appl. Chem.*, 1995, **67**, 683–689.

153. F. Cozzi, M. Cinquini, R. Annuziata and J. S. Siegel, *J. Am. Chem. Soc.*, 1993, **115**, 5330–5331.

154. M. A. Bernardo, F. Pina, B. Escuder, E. García-España, M. L. Godino-Salido, J. Latorre, S. V. Luis, J. A. Ramírez and C.Soriano, *J. Chem. Soc., Dalton Trans.*, 1999, **6**, 915–922.

155. I. Geronimo, N. J. Singh and K. S. Kim, *Phys. Chem. Chem. Phys.*, 2011, **13**, 11841–11845.

156. A. Das, A. D. Jana, S. K. Seth, B. Dey, S. R. Choudhury, T. Kar, S. Mukhopadhyay, N. J.　Singh, I.-C. Hwang and K. S. Kim, *J. Phys. Chem. B*, 2010, **114**, 4166–4170.

157. H. M. Lee, S. B. Suh, J. Y. Lee, P. Tarakeshwar and K. S. Kim, *J. Chem. Phys.*, 2000, **112**, 9759–9772.

158. N. J. Singh, S. K. Min, D. Y. Kim and K. S. Kim, *J. Chem. Theory Comput.*, 2009, **5**, 515–529.

159. D. S. Murray, M. A. Schumacher and R. G. Brennan, *J. Biol. Chem.*, 2004, **279**, 14365–14371.

160. P. Ghosh, C. Park, M. S. Peterson, P. B. Bitterman, V. A. Polunovsky and C. R. Wagner, *Bioorg. Med. Chem. Lett.*, 2005, **15**, 2177–2180.

161. P. B. Crowley and A. Golovin, *Proteins: Struct., Funct., Bioinf.*, 2005, **59**, 231–239.

162. H. L. Li, A. Galue, L. Meadows, D. S. Ragsdale, *Mol. Pharmacol.*, 1999, **55**, 134–141.

163. C. Biot, R. Wintjens and M. Rooman, *J. Am. Chem. Soc.*, 2004, **126**, 6220–6221.

164. S. Yamada and C. Morita, *J. Am. Chem. Soc.*, 2002, **124**, 8184–8185.

165. V. B. Birman, E. W. Uffman, J. Hui, X. M. Li and C. J. Kilbane, *J. Am. Chem. Soc.*, 2004, **126**, 12226–12227.

166. F. Xiao and J. J. Pignatello, *Environ. Sci. Technol.*, 2015, **49**, 906–914.

167. M. Mitra, A. Hossain, P. Manna, S. R. Choudhury, S. Kaenket, M. Helliwell, A. Bauzá, A. Frontera and S. Mukhopadhyay, *J. Coord. Chem.*, 2017, **70**, 463–474.

168. P. Manna, S. K. Seth, M. Mitra, A. Das, N. J. Singh, S. R. Choudhury, T. Kar and S. Mukhopadhyay, *CrystEngComm*, 2013, **15**, 7879–7886.

169. M. Akazome, Y. Ueno, H. Ooiso and K. Ogura, *J. Org. Chem.*, 2000, **65**, 68–76.

170. Y. Umezawa and M. Nishio, *Bioorg. Med. Chem.*, 2000, **8,** 2643–2650.

171. A. Arduini, G. Giorgi, A. Pochini, A. Secchi and F. Ugozzoli, *Tetrahedron*, 2001, **57**, 2411–2417.

172. M. Muraki, K. Harata, N. Sugita and K. I. Sato, *Biochemistry*, 2000, **39**, 292–299.

173. M. Nishio, M. Hirota and Y. Umezawa, *The CH/π Interaction. Evidence, Nature, and Consequences*, Wiley-VCH, New York, 1998, ch. 2.

174. H. Suezawa, T. Yoshida, Y. Umezawa, S. Tsuboyama and M. Nishio, *Eur. J. Inorg. Chem.*, 2002, **2002**, 3148–3155.

175. D. Sadhukhan, M. Maiti, G. Pilet, A. Bauzá, A. Frontera and S. Mitra, *Eur. J. Inorg. Chem.*, 2015, **11**, 1958–1972.

176. M. Tamres, *J. Am. Chem. Soc.*, 1952, **74**, 3375–3378.

177. T. Aoyama, O. Matsuoka and N. Nakagawa, *Chem. Phys. Lett.*, 1979, **67**, 508–510.

178. T. Takagi, A. Tanaka, S. Matsuo, H. Maezaki, M. Tani, H. Fujiwara and Y. Sasaki, *J. Chem. Soc., Perkin Trans.*, 1987, **2**, 1015–1018.

179. G. D. Andreetti, A. Pochini and R. Ungaro, *J. Chem. Soc., Perkin Trans.*, 1983, **2**, 1773–1779.

180. R. Ungaro, A. Pochini, G. D. Andreetti and V. Sangermano, *J. Chem. Soc. Perkin Trans.*, 1984, **2**, 1979–1985.

181. Z. Lu, P. Gamez, I. Mutikainen, U. Turpeinen and J. Reedijk, *Cryst. Growth Des.*, 2007, **7**, 1669–1671.

182. S. K. Singh and A. Das, *Phys. Chem. Chem. Phys.*, 2015, **17**, 9596–9612.

183. O. Takahashi, Y. Kohno and K. Saito, *Chem. Phys. Lett.*, 2003, **378**, 509–515.

184. M. Hirota, K. Sakakibara, H. Suezawa, T. Yuzuri, E. Ankai and M. Nishio, *J. Phys. Org. Chem.*, 2000, **13**, 620–623.

185. N. Nakagawa, K. Nikki, Y. Takeuchi and I. Kumagai, *Chem. Lett.*, 1972, **1**, 1239–1242.

186. M. K. Singh and G. Rajaraman, *Chem.: Eur. J.*, 2015, **21**, 980–983.

187. D. A. Rodham, S. Suzuki, R. D. Suenram, F. J. Lovas, S. Dasgupta, W. A. Goddard III and G. A. Blake, *Nature*, 1993, **362**, 735.

188. T. M. Fong, M. A. Cascieri, H. Yu, A. Bansal, C. Swain and C. D. Strader, *Nature*, 1993, **362**(6418), 350–353.

189. S. Arata, H. Torigoe, T. Iihoshi, N. Matsumoto, F. Dahan and J.-P. Tuchagues, *Inorg. Chem.*, 2005, **44**, 9288–9292.

190. S. Tsuzuki, K. Honda, T. Uchimaru, M. Mikami and K. Tanabe, *J. Am. Chem. Soc.*, 2000, **122**, 3746–3753.

191. D. A. Dougherty, *Acc. Chem. Res.*, 2013, **46**, 885–893.

192. M. O. Sinnokrot, E. F. Valeev and C. D. Sherrill, *J. Am. Chem. Soc.*, 2002, **124**, 10887–10893.

193. K. Morokuma, *Acc. Chem. Res.*, 1977, **10**, 294–300.

194. R. D. Bowen, *Acc. Chem. Res.*, 1991, **24**, 364–371.

195. M. Meot-Ner and C. A. Deakyne, *J. Am. Chem. Soc.*, 1985, **107**, 474–479.

196. R. K. Raju, J. W. G. Bloom, Y. An and S. E. Wheeler, *Chem. Phys. Chem.*, 2011, **12**, 3116–3130.

197. S. L. Cockroft and C. A. Hunter, *Chem. Soc. Rev.*, 2007, **36**, 172–188.

198. M. S. Marshall, R. P. Steele, K. S. Thanthiriwatte and C. D. Sherrill, *J. Phys. Chem. A*, 2009, **113**, 13628–13632.

199. B. U. Emenike, S. N. Bey, R. A. Spinelle, J. T. Jones, B. Yoo and M. Zeller, *Phys. Chem. Chem. Phys.*, 2016, **18**, 30940–30945.

200. J. Sunner, K. Nishizawa and P. Kebarle, *J. Phys. Chem.*, 1981, **85**, 1814–1820.

201. B. C. Guo, J. W. Purnell and A. W. Castleman, *Chem. Phys. Lett.*, 1990, **168**, 155–160.

202. O. M. Cabarcos, C. J. Weinheimer and J. M. Lisy, *J. Chem. Phys.*, 1999, **110**, 8429–8435.

203. O. M. Cabarcos, C. J. Weinheimer and J. M. Lisy, *J. Chem. Phys.*, 1998, **108**, 5151–5154.

204. R. Faraoni, R. K. Castellano, V. Gramlich and F. Diederich, *Chem. Commun.*, 2004, 370–371.

205. V. Dvornikovs and D. V. Smithrud, *J. Org. Chem.*, 2002, **67**, 2160–2167.

206. M. O. Vysotsky, A. Pop, F. Broda, I. Thondorf and V. Böhmer, *Chem. Eur. J.*, 2001, **7**, 4403–4410.

207. A. L. Whiting and F. Hof, *Org. Biomol. Chem.*, 2012, **10**, 6885–6892.

208. T. J. Shepodd, M. A. Petti and D. A. Dougherty, *J. Am. Chem. Soc.*, 1988, **110**, 1983–1985.

209. P. C. Kearney, L. S. Mizoue, R. A. Kumpf, J. E. Forman, A. McCurdy and D. A. Dougherty, *J. Am. Chem. Soc.*, 1993, **115**, 9907–9919.

210. J. E. Forman, Jr. R. E. Barrans and D. A. Dougherty, *J. Am. Chem. Soc.*, 1995, **117**, 9213–9228.

211. M. A. Petti, T. J. Shepodd, R. E. Barrans and D. A. Dougherty, *J. Am. Chem. Soc.*, 1988, **110**, 6825–6840.

212. J. Kim, Y. K. Kim, N. Park, J. H. Hahn and K. H. Ahn, *J. Org. Chem.*, 2005, **70**, 7087–7092.

213. P. Cheng, P.Huang, W. Li, S. Ueng, W. Hung, Y. Liu, C. Lai, Y. Wang, S. Peng, I. Chao and S. Chiu, *J. Org. Chem.*, 2006, **71**, 2373–2383.

214. A. H. Tran, D. O. Miller and P. E. Georghiou, *J. Org. Chem.*, 2005, **70**, 1115–1121.

215. R. Shukla, S. V. Lindeman and R. Rathore, *J. Am. Chem. Soc.*, 2006, **128**, 5328–5329.

216. R. Shukla, S. V. Lindeman and R. Rathore, *Chem. Commun.*, 2009, 5600–5602.

217. L. M. Salonen, M. Ellermann and F. Diederich, *Angew. Chem., Int. Ed.*, 2011, **50**, 4808–4842.

218. J. M. Lehn, R. Meric, J. -P. Vigneron, M. Cesario, J. Guilhem, C. Pascard, Z. Asfari and J. Vicens, *J. Supramol. Chem.*, 1995, **5**, 97–103.

219. R. A. Bissell, E. Cordova, A. E. Kaifer and J. F. Stoddart, *Nature*, 1994, **369**, 133–137.

220. E. R. T. Tiekink and J. Zukerman-Schpector, *The Importance of Pi-Interactions in Crystal Engineering*, John Wiley & Sons, Chichester, UK, 2012.

221. B. H. Hong, S. C. Bae, C. W. Lee, S. Jeong and K. S. Kim, *Science*, 2001, **294**, 348–351.

222. J. Frey, T. Kraus, V. Heitz and J. P. Sauvage, *Chem. Commun.*, 2005, 5310–5312.

223. F. G. Gatti, D. A. Leigh, S. A. Nepogodiev, A. M. Z. Slawin, S. J. Teat and J. K. Y. Wong, *J. Am. Chem. Soc.*, 2001, **123**, 5983–5989.

224. R. E. Bauer, V. Enkelmann, U. M. Wiesler, A. J. Berresheim and K. Müllen, *Chem. Eur. J.*, 2002, **8**, 3858–3864.

225. H. Masu, M. Sakai, K. Kishikawa, M. Yamamoto, K. Yama-guchi and S. Kohmoto, *J. Org. Chem.*, 2005, **70**, 1423–1431.

226. X. Bao, I. Isaacsohn, A. F. Drew and D. B. Smithrud, *J. Org. Chem.*, 2007, **72**, 3988–4000.

227. J. M. Heemstra and J. S. Moore, Chem. Commun., 2004, 1480–1481.

228. R. Ruloff, U. P. Seelbach, A. E. Merbach and F. G. Klarner, *J. Phys. Org. Chem.*, 2002, **15**, 189–196.

229. P. Pal, K. Das, A. Hossain, A. Frontera and S. Mukhopadhyay, *New J. Chem.*, 2020, **44**(18), 7310–7318.

230. D.-X. Wang and M.-X. Wang, *Acc. Chem. Res.*, 2020, **53**, 1364–1380.

231. I. A. Rather, S. A. Wagay and R. Ali, *Coord. Chem. Rev.*, 2020, **415**, 213327–213387.

232. P. A. Gale and C. Caltagirone, *Chem. Soc. Rev.*, 2015, **44**, 4212–4227.

233. E. S. Funck, *Investigation of Anion-pi Interactions in Inorganic, Organic and Biological Systems*; Texas A&M University, College Station, 2011.

234. D. -X. Wang and M. -X. Wang, *J. Am. Chem. Soc.*, 2013, **135**, 892–897.

235. M. Giese, M. Albrecht and K. Rissanen, *Chem. Commun.*, 2016, **52**, 1778–1795.

236. Y. Zhao, Y. Domoto, E. Orentas, C. Beuchat, D. Emery, J. Mareda, N. Sakai and S. Matile, *Angew. Chem., Int. Ed.*, 2013, **52**, 9940–9943.

237. A. Berkessel, S. Das, D. Pekel and J. M. Neudörfl, *Angew. Chem., Int. Ed.*, 2014, **53**, 11660–11664.

238. S. Guha and S. Saha, *J. Am. Chem. Soc.*, 2010, **132**, 17674–17677.

239. M. Cametti and K. Rissanen, *Chem. Soc. Rev.*, 2013, **42**, 2016–2038.

240. K. Fujisawa, C. Beuchat, M. Humbert-Droz, A. Wilson, T. A. Wesolowski, J. Mareda, N. Sakai and S. Matile, *Angew. Chem., Int. Ed.*, 2014, **53**, 11266.

241. X. Zhang, X. Hao, L. Liu, A.-T. Pham, J. López-Andarias, A. Frontera, N. Sakai and S. Matile, *J. Am. Chem. Soc.*, 2018, **140**, 17867–17871.

242. C. H. Park and H. E. Simmons, *J. Am. Chem. Soc.*, 1968, **90**, 2431–2432.

243. K. Hiraoka, S. Mizuse and S. Yamabe, *J. Phys. Chem.*, 1987, **91**, 5294–5297.

244. H. -J. Schnieder, F. Werner and T. Blatter, *J. Phys. Org. Chem.*, 1993, **6**, 590–594.

245. I. Alkorta, I. Rozas, J. Elguero, *J. Am. Chem. Soc.*, 2002, **124**, 8593–8598.

246. D. Quinonero, C. Garau, C. Rotger, A. Frontera, P. Ballester, A. Costa, P. M. Deya, *Angew. Chem. Int. Ed.*, 2002, **41**, 3389–3392.

247. M. Mascal, A. Armstrong, M. D. Bartberger, *J. Am. Chem. Soc.*, 2002, **124**, 6274–6276.

248. S. Demeshko, S. Dechert, F. Meyer, *J. Am. Chem. Soc.*, 2004, **126**, 4508–4509.

249. P. de Hoog, P. Gamez, I. Mutikainen, U. Turpeinen, J. Reedijik, *Angew. Chem. Int. Ed.*, 2004, **43**, 5815–5817.

250. A. Frontera, P. Gamez, M. Mascal, T. J. Mooibroek and J. Reedijk, *Angew. Chem., Int. Ed.*, 2011, **50**, 9564–9583.

251. C. Garau, A. Frontera, D. Quiñonero, P. Ballester, A. Costa and P. M. Deyà, *ChemPhysChem*, 2003, **4**, 1344–1348.

252. A. Bauzá, T. J. Mooibroek and A. Frontera, *CrystEngComm*, 2016, **18**, 10–23.

253. A. García-Raso, F. M. Albertí, J. J. Fiol, A. Tasada, M. Barceló-Oliver, E. Molins, D. Escudero, A. Frontera, D. Quiñonero and P. M. Deyà, *Eur. J. Org. Chem.*, 2007, 5821–5825.

254. A. Garcia-Raso, F. M. Albertí, J. J. Fiol, Y. Lagos, M. Torres, E. Molins, I. Mata, C. Estarellas, A. Frontera, D. Quiñonero and P. M. Deyà, *Eur. J. Org. Chem.*, 2010, 5171–5180.

255. B. W. Gung, Y. Zou, Z. G. Xu, J. C. Amicangelo, D. G. Irwin, S. Q. Ma and H. C. Zhou, *J. Org. Chem.*, 2008, **73**, 689–693.

256. J. C. Amicangelo, B. W. Gung, D. G. Irwin and N. C. Romano, *Phys. Chem. Chem. Phys.*, 2008, **10**, 2695–2705.

257. X. Fang, X. Yuan, Y.-B. Song, J.-D. Wang and M.-J. Lin, *CrystEngComm*, 2014, **16**, 9090–9095.

258. M. Egli and R. V. Gessner, *Proc. Natl. Acad. Sci. U. S. A.*, 1995, **92**, 180–184.

259. D. Bancroft, L. D. Williams, A. Rich and M. Egli, *Biochemistry*, 1994, **33**, 1073–1086.

260. S. Sarkhel, A. Rich and M. Egli, *J. Am. Chem. Soc.*, 2003, **125**, 8998–8999.

261. T. J. Mooibroek, P. Gamez and J. Reedijk, *CrystEngComm*, 2008, **10**, 1501–1515.

262. E. J. Stollar, J. L. Gelpi, S. Velankar, A. Golovin, M. Orozco and B. F. Luisi, *Proteins*, 2004, **57**, 1–8.

263. E. Fraenkel, M. A. Rould, K. A. Chambers and C. A. Pabo, *J. Mol. Biol.*, 1998, **284**, 351–361.

264. Y. S. Rosokha, S. V. Lindeman, S. V. Rosokha and J. K. Kochi, *Angew. Chem., Int. Ed.*, 2004, **43**, 4650–4652.

265. A. Jain, C. S. Purohit, S. Verma and R. Sankararamakrishnan, *J. Phys. Chem. B*, 2007, **111**, 8680–8683.

266. C. Q. Wan, X. D. Chen and T. C. W. Mak, *CrystEngComm*, 2008, **10**, 475–478.

267. P. J. Kitson, Y. F. Song, P. Gamez, P. de Hoog, D. L. Long, A. D. C. Parenty, J. Reedijk and L. Cronin, *Inorg. Chem.*, 2008, **47**, 1883–1885.

268. Z. Lu, P. Gamez, I. Mutikainen, U. Turpeinen and J. Reedijk, *Cryst. Growth Des.*, 2007, **7**, 1669–1671.

269. J. Zukerman-Schpector, A. Otero-de-la Roza, V. Luaña and E. R. T. Tiekink, *Chem. Commun.*, 2011, **47**, 7608–7610.

270. W. Kohn, A. D. Becke and R. G. Parr, *J. Phys. Chem.*, 1996, **100**, 12974–12980.

271. J. Hafner, *J. Comput. Chem.*, 2008, **29**, 2044–2078.

272. C. J. Cramer and D. G. Truhlar, *Phys. Chem. Chem. Phys.*, 2009, **11**, 10757–10816.

273. W. Kohn and L. J. Sham, *Phys. Rev.*, 1965, **140**, A1133.

274. L. Petit, A. Svane, Z. Szotek, W. M. Temmerman and G. M. Stocks, *Phys. Rev. B*, 2009, **80**, 045124.

275. B. Dorado, G. Jomrad, M. Freyss and M. Bertolus, *Phys. Rev. B*, 2010, **82**, 035114.

276. L. Petit, A. Svane, Z. Szotek, W. M. Temmerman and G. M. Stocks, *Phys. Rev. B*, 2010, **81**, 045108.

277. J. P. Crocombette, D. Torumba and A. Chartier, *Phys. Rev. B*, 2011, **83**, 184107.

278. X. Ren, P. Rinke, C. Joas and M. Scheffler, *J. Mater. Sci.*, 2012, **47**, 7447–7471.

279. E. E. Hodgkin and W. G. Richards, *Int. J. Quantum Chem.*, 1987, **32**, 105–110.

280. G. G. Hall and K. Tsujinaga, *Theor. Chim. Acta*, 1986, **69**, 425–436.

281. D. L. Wang, H. T. Shen, H. M. Gu and Y. C. Zhai, *J. Mol. Struct: Theochem*, 2006, **776**, 47–51.

282. R. Rahmani, N. Boukabcha, A. Chouaih, F. Hamzaoui and S. Goumri-Said, *J. Mol. Struct.*, 2018, **1155**, 484–495.

283. J. L. Mancuso, A. M. Mroz, K. N. Le and C. H. Hendon, *Chem. Rev.*, 2020, **120**, 8641–8715.

284. O. V. Kharissova, B. I. Kharisov and L. T. González, *J. Mater. Res.*, 2020, **35**, 1424–1438.

285. J. S. Murray and K. Sen, *Molecular electrostatic potentials: concepts and applications*, Elsevier, 1996.

286. F. Richard and R. Bader, *Atoms in molecules: a quantum theory*, Oxford University Press, Oxford, 1990.

287. S. J. Grabowski, *Chem. Rev.*, 2011, **111**, 2597–2625.

288. R. Parthasarthi, V. Subramanian and N. Sathyamurthy, *J. Phys. Chem. A*, 2005, **109**, 843–850.

289. M. S. Pavan, R. Pal, K. Nagarajan and T. N. G. Row, *Cryst. Growth Des.*, 2014, **14**, 5477–5485.

290. Y. Hirano, K. Takeda and K. Miki, *Nature*, 2016, **534**, 281–284.

291. R. Parthasarthi and V. Subramanian, *Struct. Chem.*, 2005, **16**, 243–255.

292. E. C. Brown, R. F. W. Bader and N. H. Werstiuk, *J. Phys. Chem. A*, 2009, **113**, 3254–3265.

293. R. F. W. Bader and P. J. MacDougall, *J. Am. Chem. Soc.*, 1985, **107**, 6788–6795.

294. U. A. Chaudry and P. L. A. Popelier, *J. Org. Chem.*, 2004, **69**, 233–241.

295. M. Z. Griffiths and P. L. A. Popelier, *J. Chem. Inf. Model.*, 2013, **53**, 1714–1725.

296. K. T. Mahmudov, M. N. Kopylovich, M. F. C. Guedes da Silva and A. J. L. Pombeiro, *Coord. Chem. Rev.*, 2017, **354**, 54–72.

297. R. M. Kumar, M. Elango and V. Subramanian, *J. Phys. Chem. A*, 2010, **114**, 4313–4324.

298. S. J. Grabowski, *J. Phys. Chem. A*, 2011, **115**, 12340–12347.

299. F. C. Guzman and R. F. W. Bader, *Coord. Chem. Rev.*, 2005, **249**, 633–662.

300. C. F. Nejad, S. Shahbazian and R. Marek, *Chem. Eur. J*, 2014, **20**, 10140–10152.

301. C. R. Wick and T. Clark, *J. Mol. Model.*, 2018, **24**, 142.

302. L. Reuter and A. Luchow, *Phys. Chem. Chem. Phys.*, 2020, **22**, 25892–25903.

303. P. Manna, S. K. Seth, M. Mitra, S. R. Choudhury, A. Bauzá, A. Frontera and S. Mukhopadhyay, *Cryst. Growth Des.*, 2014, **14**, 5812–5821.

304. E. R. Johnson, S. Keinan, P. Mori-Sanchez, J. Contreras-Garcia, A. J. Cohen and W. Yang, *J. Am. Chem. Soc.*, 2010, **132**, 6498–6506.

305. J. Contreras-García, E. R. Johnson, S. Keinan, R. Chaudret, J.-P. Piquemal, D. N. Beratan and W. Yang, *J. Chem. Theory Comput.*, 2011, **7**, 625–632.

306. A. Otero-de-la Roza, E. R. Johnson and J. Contreras-García, *Phys. Chem. Chem. Phys.*, 2012, **14**, 12165–12172.

307. J. C. Garcia, E. R. Johnson and W. Yang, *J. Phys. Chem. A*, 2011, **115**, 12983–12990.

308. E. R. Johnson and A. O. Roza, *J. Chem. Theo. Comput.*, 2012, **8**, 5124–5131.

CHAPTER 2

Syntheses, crystal structures and supramolecular assemblies of two Cu(II) complexes based on a new heterocyclic ligand

1 (Monomer)

2 (Polymer)
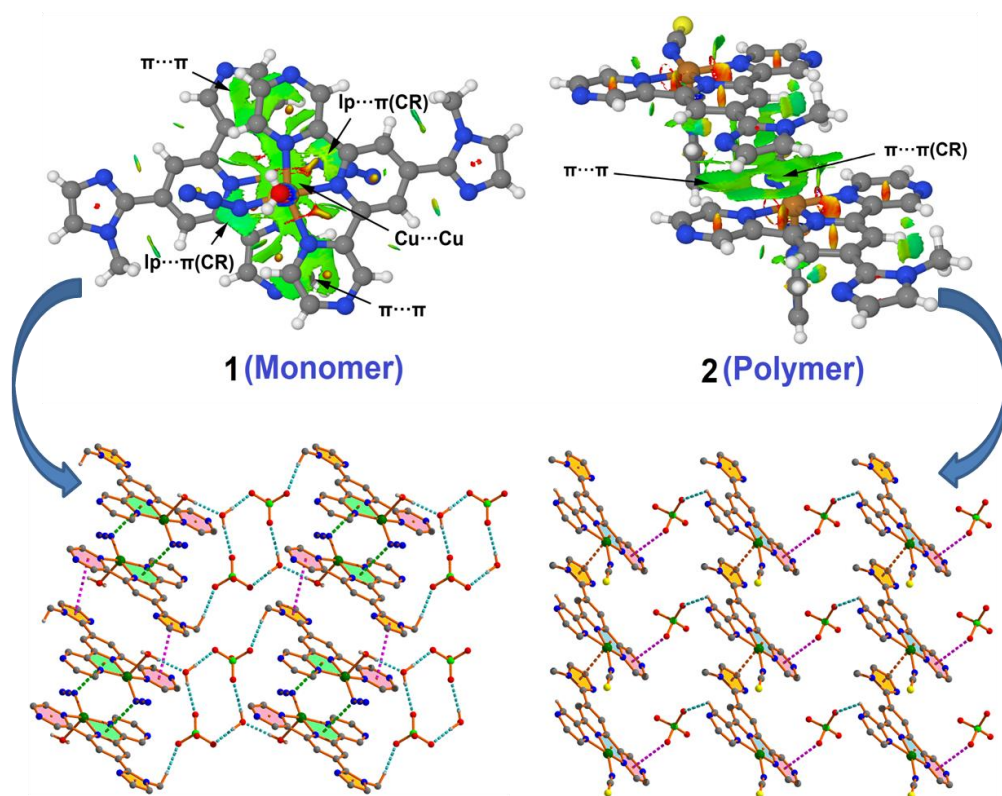
2.1. INTRODUCTION

Supramolecular chemistry comprises the design, synthesis and self-assembly of well-defined molecular components into tailor-made architectures by means of intermolecular interactions [1–3]. Crystal engineers often help to study various intermolecular interactions in the journey from molecule to crystal in the solid state [4–7]. Over the past 50 years, the field of crystal engineering has developed enough and interplayed between structure and properties of molecules in a programmed way [8–10]. However, finding of new interactions by creative and intellectual way in scheming and building crystal architecture is one keen interest in crystal engineering.

Hydrogen bonding has been extensively well studied as it universally exists in both natural and artificial substances [11,12]. Not only hydrogen bonds but also other dispersive interactions like π•••π stacking, anion•••π and lone pair•••π interactions play a decisive role in nucleation and growth of molecular crystals in recent years [13–21]. Among those, lone pair•••π interaction is a significant binding mode which plays a key role in stabilizing the structures of nucleic acids and modulating the recognition of protein DNA and enzyme substrates [22–24].

Recently, the attention has shifted toward more unconventional interactions such as π(arene)•••π(chelate ring), π(chelate ring)•••π(chelate ring), lone pair•••π(chelate ring), C−H•••π(chelate ring), *etc*. interactions which have been proven to have equal or even dominating contributions to molecular crystal formation [25–34]. Chelate rings are recognized to exhibit metallo-aromatic behavior and undoubtedly they can take part in similar interactions to their organic counterparts [35,36]. In the context of supramolecular architecture of coordination complexs, contribution of chelate ring (formed by metal coordination using heterocyclic π-systems) assisted interactions have arrested recent interest of researchers.

As an NNN-tridentate ligand, terpyridine plays an important role in supramolecular chemistry as well as in coordination chemistry due to its π stacking ability among themselves and excellent chelating capability with various metal cations [37]. Terpyridine or their structural analogs show very high binding potentiality towards transition metal ions due to *cis*, *cis* arrangement of the three nitrogen atoms and dπ−pπ* back bonding of the metal to pyridine rings [38]. However, they always prefer to adopt a planar geometry to achieve maximum conjugation in the complexes [39]. Terpyridine metal complexes have been synthesized and developed rapidly for their potential applications in several fields, for instance, photovoltaic devices [40,41], DNA bindings [42,43], sensors [44,45], photo-

sensitizers [46,47], catalysis [48,49], metal-organic framework (MOF) construction [50,51], and many more [52]. Recently, increasing attention has been paid to the synthesis of 4′-substituted terpyridine complexes with potential applications in accessing new classes of functional materials possessing photo-physical and electrochemical properties [53–56]. As terpyridines are generally neutral during complex formation, ancillary ligands like pseudo halides (azido, thiocyanato, etc.) are often employed to sustain electrical neutrality. Azido (N_3^-) and thiocyanato (SCN^-) pseudo halide ions have also been extensively used as bridging ligands in the construction of coordination complexes due to their diversity of bonding modes with 3d metal complexes [57–62]. As a terminal ligand, the coordination mode of SCN^- depends on the electronic nature and oxidation state of the metal ions [63]. Besides, other factors like steric effect, type of solvent, non-coordinated ions and even electronic nature of the auxiliary ligands can influence the coordination mode of the thiocyanato ligand, particularly when the metal ion has intermediate hard−soft acid character [64]. Azido and thiocyanato copper(II) complexes with trigonal bipyramidal (TBP) or square pyramidal (SP) geometry have already gained much attention for the last few years but, there still remains much more work to be explored.

Among other investigated metals, Cu(II) containing complexes have witnessed increasing attention due to their promising applications in various fields such as catalysis, energy harvesting devices, medicinal chemistry, *etc.* within the last decade [65–72]. After iron and zinc, copper is the third most abundant transition metal in the human body and plays an important role in hemopoiesis, metabolism, growth and immune system [73,74]. Most importantly, the reversible change of the oxidation state of Cu(I)/Cu(II) couple under physiological conditions has promoted the development of metal complexes with an active redox chemistry within cancerous cells [75,76]. Besides, compared to other common metal ions, Cu(II) ion exhibits high binding constant with various ligands in chemical and biological systems [77,78].

Keeping all these factors in mind, two new Cu(II) complexes have been synthesized based on 4-(1-methylimidazole)-2,6-di(pyrazinyl)pyridine (**NL**) with auxiliary ligands azido (for complex **1**) and thiocyanato (for complex **2**) in aqueous medium. Both the complexes adopt distorted square pyramidal (SP) geometry where the title ligand, (**NL**) acts as an NNN-tridentate ligand. In both the complexes, the ligand (**NL**) coordinates the Cu(II) ion through three coplanar ligating sites involving one pyridyl nitrogen atom (N3) and two pyrazinyl nitrogen atoms (N5 and N6) forming two five-membered chelate rings (Scheme 2.1). The metallo-aromatic nature of the chelate rings gives rise to the possibility of alternative π-

systems which play an important role in producing various supramolecular architectures for both the complexes in the solid state. Interestingly, a dimer is shaped by two symmetrically equivalent lone pair•••π(chelate ring) interactions between lone pair on azide nitrogen atom (N8) and Cg(2) chelate ring in complex **1**. From the structural database survey, it is evident that the lone pair•••π(chelate ring) interactions involving halogen atoms (Cl, Br, I) are common but to the best of my knowledge the engagement of pnictogen atom like nitrogen in lone pair•••π(chelate ring) interaction is comparatively less familiar [127–131].

In complex **1**, the perchlorate anion is involved in the formation of a tetrameric anion−water cluster, $[(ClO_4)_2–(H_2O)_2]^{2-}$, which is less frequent. To my knowledge, a few perchlorate−water tetrameric clusters have been characterized in the solid state [79–81]. For complex **2**, the influence of π•••π(chelate ring) and sulphur(lone pair)•••π interactions have been well established in the crystal packing. Finally, the present work utilizes DFT calculations and several computational tools (QTAIM and NCI Plot) to analyze the non-covalent interactions focusing on lone pair•••π(chelate ring) and π•••π(chelate ring) interactions in stabilizing the solid state architectures of both the complexes. However, the mutual interactions of the hydrogen bonds in the perchlorate−water cluster have also been evaluated energetically and showed how it influences the crystal packing of complex **1** in the solid state.
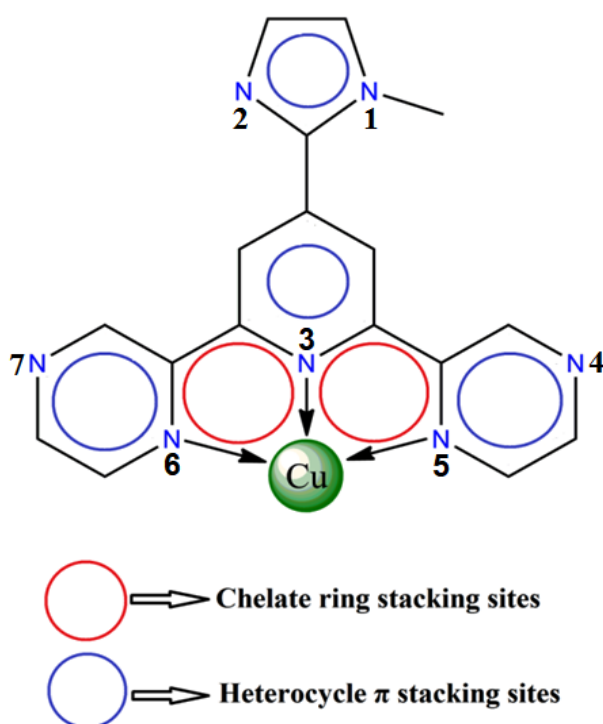
Scheme 2.1. Schematic representation of π stacking sites for both the complexes.

2.2. EXPERIMENTAL SECTION

2.2.1. Materials and apparatus

All the chemical reagents (analytical grade) and solvents (spectroscopic grade) were purchased from commercial suppliers and used without any further purification. Freshly boiled double distilled water was used throughout the synthetic procedure and all the reactions were carried out under aerobic conditions. Elemental analyses (C, H and N) were performed using a PerkinElmer 2400 Series-II CHN analyzer, USA, elemental analyzer. ESI mass spectra were obtained from a Water HRMS model XEVO-G2QTOF#YCA351 spectrometer. ^{1}H NMR and ^{13}C NMR spectra were obtained from Bruker spectrometer (300 MHz) with CDCl$_3$ solvent using trimethylsilane (TMS) as an internal standard. Fourier transform infrared (FT-IR) spectra were recorded on a Perkin Elmer LX-1 FT-IR spectrophotometer (4000−400 cm^{-1}) by using a modern diamond attenuated total reflectance (ATR) accessory method.

2.2.2. Synthesis of 4-(1-methylimidazole)-2,6-di(pyrazinyl)pyridine [NL]

Acetylpyrazine (0.305 g, 2.5 mmol) was added into 30 mL ethanolic solution of 1-methyl imidazole-2-carboxaldehyde (0.11 g, 1 mmol). 3 mL of 1 (M) aqueous solution of NaOH was added drop wise into the reaction mixture at room temperature (Scheme 2.2). Then 5 mL aqueous NH$_3$ (35%) solution was discharged into the basic solution at a time. The reaction mixture was then refluxed for 3 hours. After completion of the reaction, solution was cooled at room temperature. A light-yellow solid formed which was collected by filtration and washed repeatedly with coldwater and dried in air.
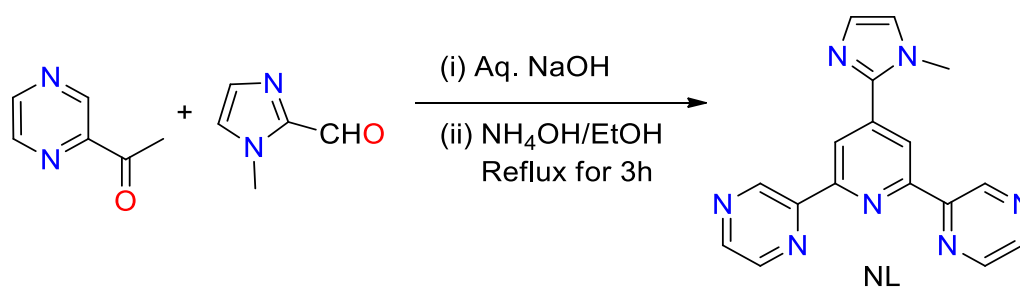
Scheme 2.2. Synthetic route for the ligand, **NL**.

The desired product was obtained with good yield and acceptable purity, Yield 0.214 g (68%). Anal. calc. for C$_{17}$H$_{13}$N$_7$, C 64.75, H 4.16, N 31.09. Found: C 64.12, H 3.89, N 30.79 %. ^{1}H NMR (300 MHz, CDCl$_3$): δ (ppm) = 9.85 (s, 2H), 8.83 (s, 2H), 8.65 (s, 4H), 7.24 (s, 1H), 7.09 (s, 1H), 3.99 (s, 3H) (Fig. 2.1). ^{13}C NMR (75 MHz, CDCl$_3$): δ (ppm) =154.50,

150.46, 144.93, 143.70, 143.48, 140.37, 129.60, 124.24, 120.55, 35.17 (Fig. 2.2). Main FT-IR absorptions, (KBr, cm^{-1}): 1980(s), 1606(vs), 1570(vs), 1519(s), 1464(s), 1456(s), 1419(s), 1371(vs), 1292(s), 1257(s), 1224(s), 1120(vs) (Fig. 2.3). ESI-MS: m/z 316.12, calcd. for $[C_{17}H_{13}N_7 + H]^+$ 316.13 (Fig. 2.4).
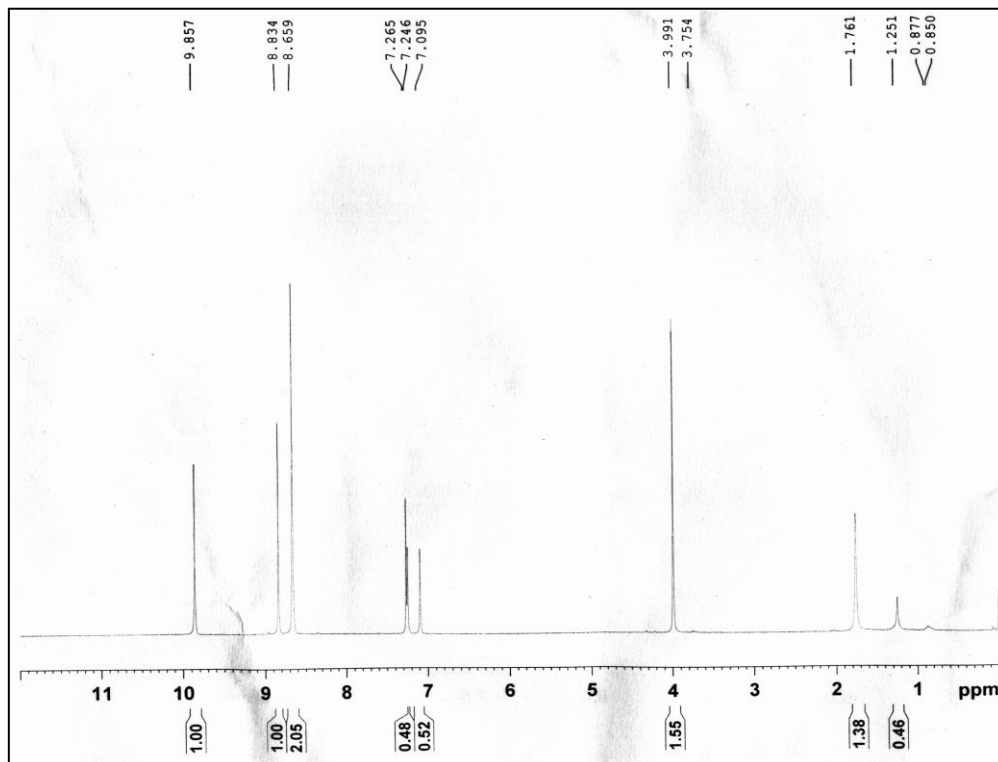
Fig. 2.1. ^{1}H NMR spectrum of **NL** in CDCl$_3$ solution.
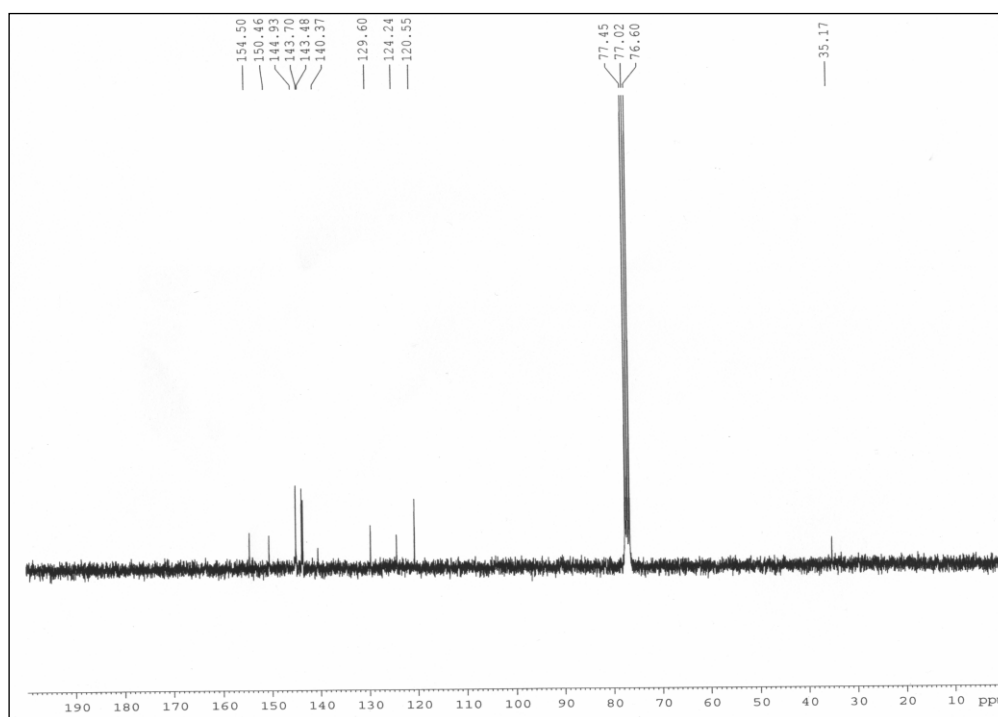
Fig. 2.2. ^{13}C NMR spectrum of **NL** in CDCl$_3$ solution.
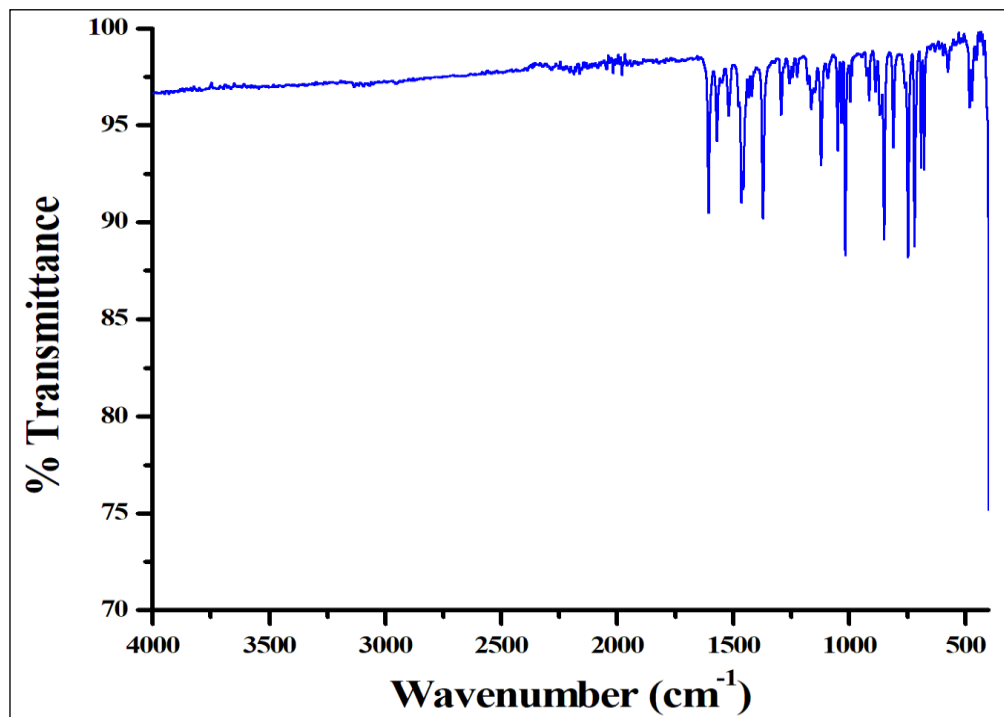
Fig. 2.3. FT-IR spectrum of **NL**.
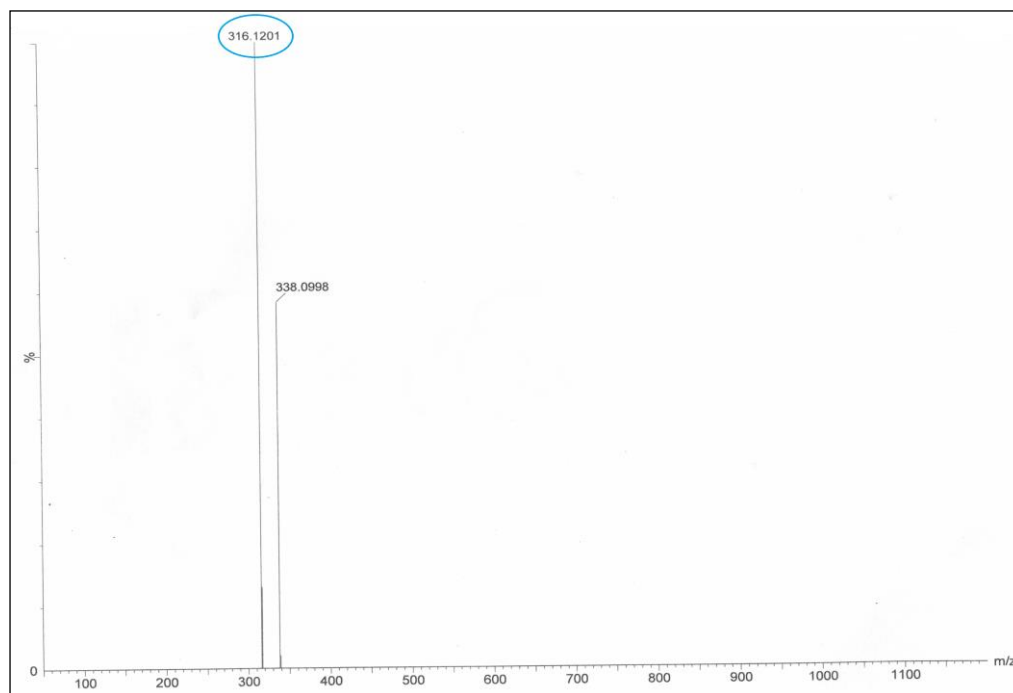
Fig. 2.4. ESI-mass spectrum of **NL**.

2.2.3. Synthesis of [Cu(NL)(N₃)(OH₂)]ClO₄·H₂O (Complex 1)

An aqueous suspension (15 mL) of the ligand, **NL** (0.0315 g, 0.1 mmol) was added drop wise to 15 mL of aqueous Cu(ClO₄)₂·6H₂O (0.0370 g, 0.1 mmol) solution with constant stirring. An aqueous solution (5 mL) of NaN₃ (0.0065 g, 0.1 mmol) was added and stirred for 3 hours (Scheme 2.3). Then the solution was filtered and the filtrate was left for slow evaporation without any disturbance. After one-week, deep green X-ray quality crystals of complex **1** were isolated (yield: 68%). Solubility of the complex was checked in some common solvents for further applications and found to be insoluble in water and methanol whereas completely soluble in acetonitrile, DMSO and DMF. Anal. calc. for $C_{17}H_{17}CuN_{10}ClO_6$: C, 36.70; H, 3.08; N, 25.17. Found: C, 36.63; H, 2.99; N, 25.13%. Main FT-IR absorptions, (KBr, cm^{-1}): 3543(w), 3469(s), 3229(w), 3139(vs), 3102(s), 2050(vs), 1614(vs), 1590(s), 1557(s), 1496(s), 1470(vs), 1433(s), 1408(s), 1340(s), 1299(s), 1283(s), 1227(s) (Fig. 2.5).
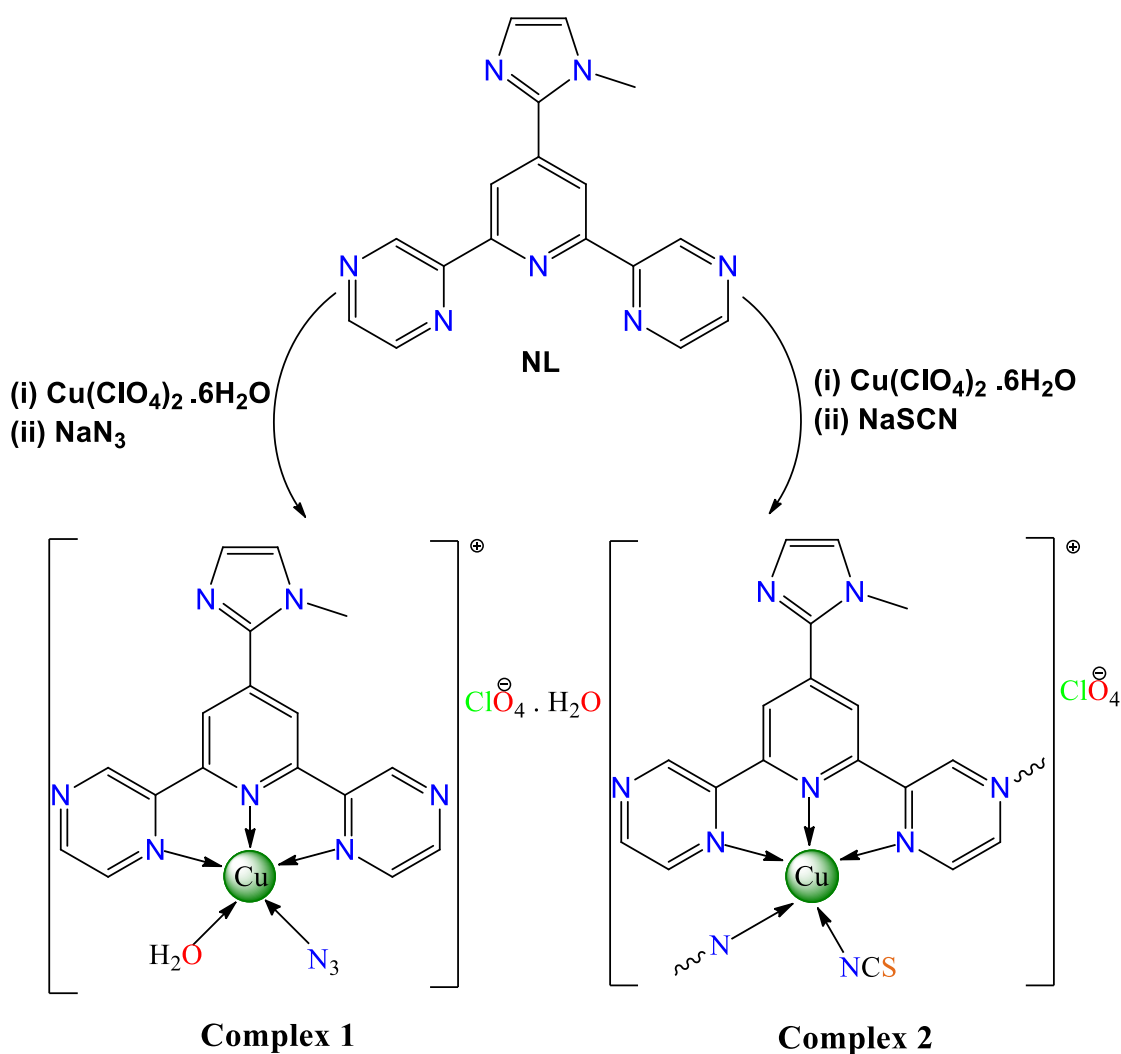
Scheme 2.3. Schematic representations of the synthesis of complexes **1** and **2**.

2.2.4. Synthesis of {[Cu(NL)(μ-NL)NCS]ClO₄}ₙ (Complex 2)

An aqueous suspension (15 mL) of the ligand, **NL** (0.0315 g, 0.1 mmol) was added drop wise to 15 mL aqueous Cu(ClO₄)₂·6H₂O (0.0370 g, 0.1 mmol) solution at stirring condition. An aqueous solution (5 mL) of NaSCN (0.0081 g, 0.1 mmol) was added and stirred for 4 hours (Scheme 2.3). Then the solution was filtered and the filtrate was left undisturbed for slow evaporation. Two weeks later, deep brown X-ray quality crystals of complex **2** were obtained (yield: 63%). The complex **2** was insoluble in water and methanol, partly soluble in acetonitrile and completely soluble in DMSO as well as in DMF. Anal. calc. for $C_{18}H_{13}CuN_8SClO_4$: C, 40.30; H, 2.44; N, 20.89. Found: C, 40.25; H, 2.39; N, 20.85%. Main FT-IR absorptions, (KBr, cm⁻¹): 3218(s), 3114(bs), 2100(vs), 2047(vs), 1611(s), 1599(s), 1554(s), 1497(s), 1470(s), 1423(s), 1406(s), 1332(vs), 1298(s), 1288(s), 1225(s) (Fig. 2.5). (*Caution! Salts of perchlorate and azide are potentially explosive. Only small amounts of materials should be prepared and to be handled with extreme care*).
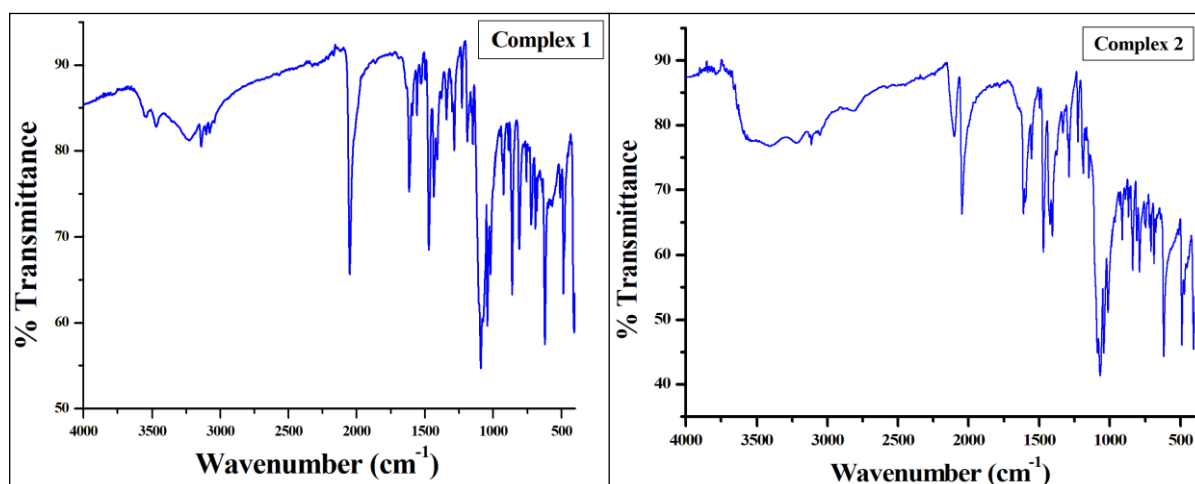
Fig. 2.5. FT-IR spectra for complexes **1** and **2**

2.2.5. X-ray crystallography analysis

Single crystal X-ray data were collected by using a Bruker SMART APEX II CCD area detector equipped with a graphite monochromated Mo Kα radiation ($\lambda = 0.71073$ Å) source in φ and ω scan mode at 296 K for both the complexes. Cell parameter refinement and data reduction for both the complexes were carried out using a Bruker SMART APEX II instrument and Bruker SAINT Software [82]. The crystal structures of both the complexes were solved by SHELXT-2014/5 and refined by full-matrix least squares on F^2 techniques using the SHELXL-2016/6 crystallographic software package [83,84]. The CIFs have been deposited with CCDC No. 2096470 (Complex **1**) and CCDC No. 2096471 (Complex **2**). Selected crystal structure refinement parameters for **1** and **2** are given in Table 2.1.

Table 2.1. Crystal data and structure refinement parameters for complexes 1 and 2

Structure	Complex **1**	Complex **2**
CCDC No.	2096470	2096471
Empirical formula	$C_{17}H_{17}N_{10}CuClO_6$	$C_{18}H_{13}N_8CuSClO_4$
Formula Weight	556.41	536.42
Temperature (K)	296	296
Wavelength (Å)	0.71073	0.71073
Crystal system	Triclinic	Monoclinic
space group	P$\bar{1}$	P 2_1/c
a, b, c (Å)	8.9072(6), 10.3327(8), 13.1658(9)	7.2922(6), 10.1306(8), 27.451(2)
α, β, γ (°)	107.373(2), 104.076(2), 97.873(2)	90, 93.037(2), 90
Volume (Å^3)	1092.59(14)	2025.1(3)
Z / Density (calc.) (Mg/m^3)	2 / 1.691	4 / 1.759
Absorption coefficient (mm^{-1})	1.182	1.361
F(000)	566.0	1084.0
Crystal size (mm^3)	$0.09 \times 0.12 \times 0.18$	$0.08 \times 0.13 \times 0.19$
θ range for data collection	2.120 to 27.146	2.143 to 27.237
Completeness to θ (%)	100%	100%
Absorption correction	Multi-scan	Multi-scan
Max. and min. transmission	0.899 and 0.843	0.897 and 0.809
Refinement method	Full-matrix least-squares on F^2	Full-matrix least-squares on F^2
Data/parameters	4825 / 321	4513 / 299
Goodness-of-fit on F^2	1.029	0.997
Final R indices [I > 2σ(I)]	$R_1 = 0.0428$, $wR_2 = 0.1141$	$R_1 = 0.0418$, $wR_2 = 0.1938$
R indices (all data)	$R_1 = 0.0472$, $wR_2 = 0.1181$	$R_1 = 0.0512$, $wR_2 = 0.2129$
Largest diff. peak and hole (e.Å^{-3})	0.762 and -0.507	0.751 and -1.172

$R_1 = \sum ||F_o| - |F_c|| / \sum |F_o|$, $wR_2 = [\sum\{(F_o^2 - F_c^2)^2\}/\sum\{w(F_o^2)^2\}]^{1/2}$ $w = 1/\{\sigma^2(F_o^2) + (aP)^2 + bP\}$, $P = (F_o^2 + 2F_c^2)/3$, where, a = 0.0604 and b = 1.3233 for complex **1**; a = 0.2000 and b = 0.0100 for complex **2**.

2.2.6. Computational methods

The non-covalent interactions were analysed energetically using Gaussian-16 [85] at the PBE0-D3/def2-TZVP level of theory. The binding energies have been corrected using the Boys and Bernardi counterpoise method [86]. The Grimme's D3 dispersion correction has been also used in the calculations [87]. To evaluate the interactions in the solid state, the crystallographic coordinates were used and only the position of the hydrogen bonds has been optimized. This methodology [88,89] and level of theory [90–100] (functional and basis set) have been previously used to analyze non-covalent interactions in the solid state. The interaction energies were estimated by calculating the difference between the energies of the

isolated monomers and the ones of their assembly. For the calculations, the monomeric Cu(II) species were considered as doublets (one unpaired electron) and the dimers as triplets (two unpaired alpha electrons). The NCI plot [101] isosurfaces have been used to characterize non-covalent interactions. They correspond to both favourable and unfavourable interactions, as differentiated by the sign of the second density Hessian Eigen value and defined by the isosurface colour. The colour scheme is a red-yellow-green-blue scale with red for ρ^+_{cut} (repulsive) and blue for ρ^-_{cut} (attractive).

2.2.7. Tau (τ) parameter calculations for complex 1 and complex 2

The structures with five coordination number can have either square pyramidal or triangular bipyramidal geometry around the metal center. In order to discriminate between these two geometries, tau (τ) parameter was proposed by Addison and co-workers [102]. According to this, the τ parameter ranges between 0 and 1 at the extreme values giving a perfect square pyramidal and triangular bipyramidal structures, respectively. The closer the τ parameter to 0, the more similar it is to square pyramidal geometry.

$$\tau = (\beta-\alpha) / 60 \text{ ……….. (1)}$$

Where, β is the first greatest angle and α is the second greatest angle of the coordination center. For complex **1**: $\beta = 159.22(11)$, and $\alpha = 157.94(9)$ (Table 3). Hence, calculated value of $\tau = 0.0213$. For complex **2**: $\beta = 165.49(11)$, and $\alpha = 158.18(8)$ (Table 6). Hence, calculated value of $\tau = 0.1218$.

Here, the τ values are close to 0 (0.0213 and 0.1218) which indicate almost square pyramidal geometry for both the complexes. Besides, deviations from the basal planes (0.259 Å for complex **1** and 0.203 for complex **2**) also indicate the distortion from the square-pyramidal geometry.

2.3. RESULTS AND DISCUSSION

2.3.1. IR spectroscopic characterization

The molecular structures of the title complexes have been established by single crystal X-ray analysis and supported by IR spectroscopy. The IR spectrum of complex **1** shows typical $\nu(OH)$ vibrations in the $3543-3229$ cm^{-1} range for both coordinated and non-coordinated water molecules. Besides, the complex **1** displays a very sharp $\nu_{as}(N_3)$ band with maximum at 2050 cm^{-1}, while that at 1340 cm^{-1} is presumably associated with the $\nu_s(N_3)$ vibration (Fig. 2.5). The presence of auxiliary NCS ligand in complex **2** is confirmed with the detection of a

very intense $\nu_{as}(CN)$ band at 2047 cm^{-1} with a shoulder at 2100 cm^{-1}, which are typical for the terminal N-bonded isothiocyanate moieties [57,103−106]. In addition, the $\nu(CH)$ vibrations are detected in the range of 3218−3102 cm^{-1} for both the complexes. The observed stretching frequencies for $\nu_{as}(N_3)$ and $\nu_{as}(CN)$ in present complexes (**1** and **2**) have a good agreement with some reported Cu(II) complexes which are summarized in Table 2.2.

Table 2.2. A brief comparison of $\nu_{as}(N_3)$ and $\nu_{as}(CN)$ vibrations in some reported Cu(II) complexes

Cu(II) complexes	$\nu_{as}(N_3)$ (cm^{-1})	$\nu_{as}(CN)$ (cm^{-1})	References
[Cu(μ-N$_3$)(μ-PTA)]$_n$ (**3**)	2047	−	103
[Cu$_2$(μ-Hbdea)$_2$(N$_3$)$_2$] (**4**)	2065	−	104
[Cu$_2$(μ-Hedea)$_2$(N$_3$)$_2$]·(H$_2$O)$_{0.25}$ (**5**)	2068	−	105
[Cu$_4$I$_4$(μ-N$_3$)$_2$(N$_3$)$_4$(μ-PTA-Me)$_2$(PTA-Me)$_2$] (**6**)	2054	−	106
[Cu$_2$(μ-Hmdea)$_2$(NCS)$_2$] (**9**)	−	2084	105
[Cu(cyclen-tpam)(NCS)]ClO$_4$·3H$_2$O (**7**)	−	2093	57
[Cu(bdmpzpy)(NCS)$_2$] (**8**)	−	2069	57
Cu(Mepea)(NCS)$_2$ (**10**)	−	2072	57
[Cu(NL)(N$_3$)(OH$_2$)]ClO$_4$·H$_2$O (**1**)	2050	−	Present work
{[Cu(NL)(μ-NL)NCS]ClO$_4$}$_n$ (**2**)	−	2047	Present work

2.3.2. Structural description of complex 1

The asymmetric unit of complex **1** with the atom numbering scheme is shown in Fig. 2.6. The formula unit of complex **1** shows one monomeric cationic [Cu(C$_{17}$H$_{13}$N$_7$)(N$_3$)(H$_2$O)]$^+$ unit, one non-coordinated perchlorate anion and one non-coordinated water molecule. The complex crystallizes in a triclinic system with the space group P$\bar{1}$ and its unit cell contains two formula units. The selected bond lengths (Å) and bond angles (°) are scheduled in Table 3. The coordination mode around the metal center can be best described as a distorted square pyramid [τ value is 0.0213 (ideally 0 for perfect square pyramidal geometry and 1 for trigonal bipyramidal geometry), eq 1] where the equatorial plane is shaped by the three pyrazinyl nitrogen atoms (N3, N5 and N6) of the ligand (**NL**) and one nitrogen atom (N8) of azide anion. The apical position is occupied by one oxygen atom (O5) of a water molecule. Here the ligand (**NL**) is able to bind the Cu(II) ion to produce two five-membered chelate rings, (Cu1/N3/C7/C17/N6) and (Cu1/N3/C8/C10/N5) having bite angles 79.28(9)° (<N3−Cu1−N6) and 79.42(8)° (<N3−Cu1−N5) respectively. The average distance of Cu−N bonds in the equatorial plane is 1.988 Å [Cu1−N5 = 2.042(2) Å, Cu1−N6 = 2.044(2) Å,

Cu1─N3 = 1.9431(19) Å and Cu1─N8 = 1.923(3) Å]. The axial Cu–O bond is comparatively longer [Cu1─O5 = 2.224(2) Å] than the equatorial Cu─N bonds and is expected as the axial bond utilizes more 'p' character of the orbital in forming the bond, which makes the axially coordinated water oxygen atom more electronegative [107]. The Cu(II) ion is deviated by a distance of 0.259 Å towards the axial oxygen atom (O5) of water from the equatorial plane (N3, N5, N6 and N8). The dipositive charge on the metal centre is stabilized by one coordinated azide anion and one non-coordinated perchlorate anion.
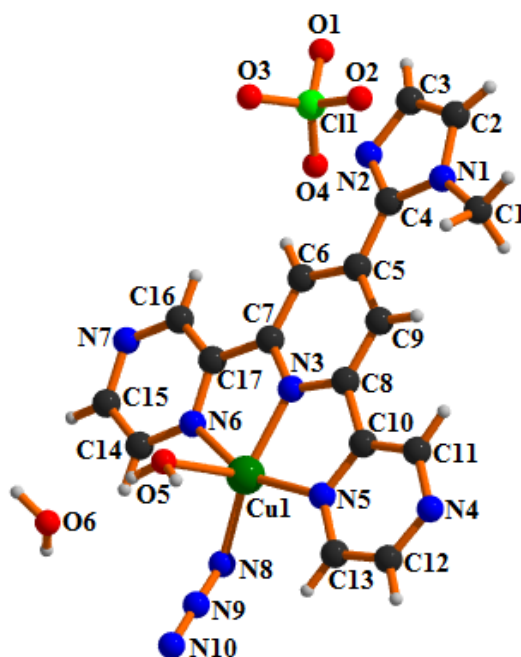
Fig. 2.6. Asymmetric unit of Complex **1**.

Table 2.3. Selected bond distances [Å] and bond angles (°) for complex 1

Bonds	Distance (Å)	Bond angles	Value (°)
Cu1─O5	2.224(2)	O5─Cu1─N3	102.89(8)
Cu1─N3	1.9431(19)	O5─Cu1─N5	98.54(8)
Cu1─N5	2.042(2)	O5─Cu1─N6	91.73(9)
Cu1─N6	2.044(2)	O5─Cu1─N8	97.68(10)
Cu1─N8	1.923(3)	N3─Cu1─N5	79.42(8)
		N3─Cu1─N6	79.28(9)
		N3─Cu1─N8	159.22(11)
		N5─Cu1─N6	157.94(9)
		N5─Cu1─N8	100.54(10)
		N6─Cu1─N8	97.34(10)

The solid-state structure of complex **1** is stabilized through the combination of C─H•••N, C─H•••O, O─H•••N, O─H•••O hydrogen bonds along with π•••π stacking and lone pair•••π (chelate ring) interactions (Table 2.4 and 2.5). In the first architecture (Fig. 2.7), the

monomeric unit of complex **1** propagates to produce a 1-D polymeric chain through a π•••π interaction (Table 2.4) between Cg(3) of one unit with Cg(5) of the other unit with a ring separation distance of 3.4928(19) Å.

Table 2.4. Geometrical parameters (Å, °) for the π-stacking interactions for complex 1

Cg(i)•••Cg(j)	Cg(i)•••Cg(j) [Å]	α (°)	B (°)	γ (°)	Cg(i)– Perp [Å]	Cg(j)– Perp [Å]	Symmetry
Cg(3)[1]•••Cg(6)	3.642(2)	4.11	26.19	28.42	3.203	3.268	-x,1-y,1-z
Cg(3)[1]•••Cg(5)	3.4928(19)	6.70	17.96	13.74	3.393	3.323	-1+x,y,z
Cg(6)[1]•••Cg(3)	3.642(2)	4.11	28.42	26.19	3.268	3.203	-x,1-y,1-z
Cg(5)[1]•••Cg(6)	3.8956(18)	2.64	29.80	27.49	3.456	3.381	1-x,2-y,1-z
Cg(5)[1]•••Cg(3)	3.4928(19)	6.70	13.74	17.96	3.323	3.393	1+x,y,z
Cg(6)[1]•••Cg(5)	3.8957(18)	2.64	27.49	29.80	3.381	3.456	1-x,2-y,1-z

Cg(i) and Cg(j) denotes centroid of ith and j[th] ring respectively. For Complex **1**: Cg(3) is the centroid of [N1/C2/C3/N2/C4] ring; Cg(5) is the centroid of [N4/C11/C10/N5/C13/C12] ring; and Cg(6) is the centroid of [N6/C14/C15/N7/C16/C17] ring.
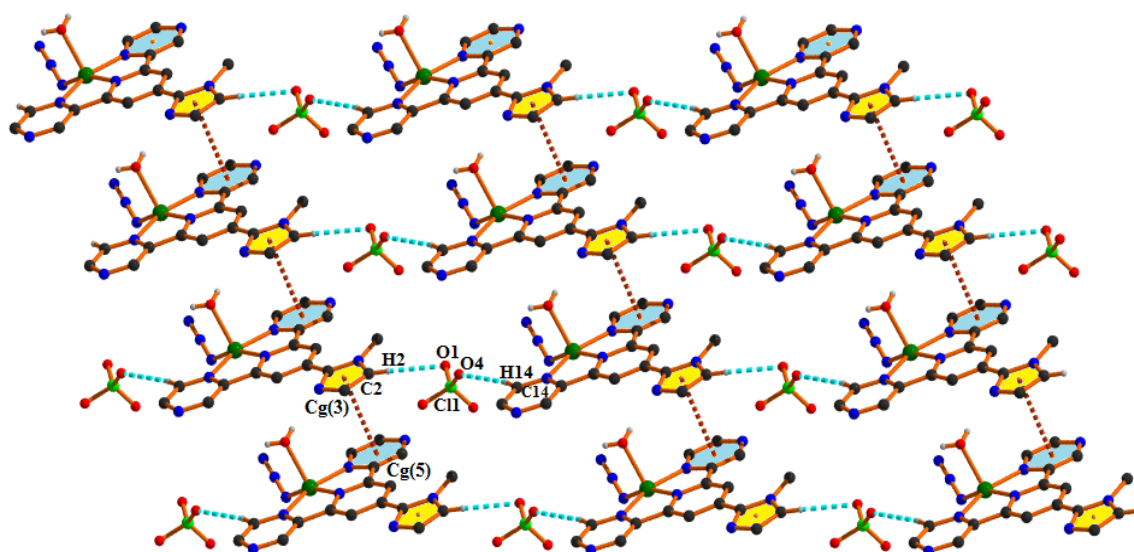
Fig. 2.7. Perspective view of the formation of a 2-D architecture through π•••π stacking and C─H•••O hydrogen bonding interactions in complex **1**.

Now, perchlorate ions connect these parallel 1-D chains through C2─H2•••O1 (169°) and C14─H14•••O4 (154°) hydrogen bonding interactions at (-x, 1-y, 2-z) and (1-x, 1-y, 1-z) respectively; thus leading to the formation of a 2-D architecture in the bc-plane.

Table 2.5. Geometrical parameters for the hydrogen bonds of complex 1

D─H•••A	D–H [Å]	H•••A [Å]	D•••A [Å]	D–H•••A [°]	Symmetry
O5─H5A•••O6	0.8500	1.9100	2.755(3)	175.00	─
O5─H5B•••N2	0.8500	2.0000	2.811(3)	160.00	1+x, y, z
O6─H6A•••O2	0.8500	2.0000	2.839(6)	169.00	x, y, -1+z
O6─H6B•••O4	0.8500	2.2300	3.006(8)	153.00	1-x, 1-y, 1-z
C1─H1B•••N4	0.9600	2.6200	3.351(4)	133.00	1-x, 2-y, 2-z
C1─H1C•••O3	0.9600	2.5600	3.471(10)	158.00	x, 1+y, z
C2─H2•••O1	0.9300	2.5200	3.435(7)	169.00	-x, 1-y, 2-z
C14─H14•••O4	0.9300	2.4500	3.312(9)	154.00	1-x, 1-y, 1-z
C13─H13•••N10	0.9300	2.5300	3.204(5)	130.00	2-x, 2-y, 1-z

A different 2-D layer is generated through π•••π stacking and C─H•••N hydrogen bonding interactions (Fig. 2.8) for complex **1**. The self-complementary nature leads the molecules to form a dimer through π•••π interaction between Cg(5) and Cg(6) of two different units. The inter-planar spacing between Cg(5) and Cg(6) is 3.8956(18) Å. Interconnection of the dimers through another self-complementary Cg(3)─Cg(6) interaction (π•••π stacking) which leads to form an infinite chain along the [010] direction. The separation distance between Cg(3) and Cg(6) is 3.642(2) Å.
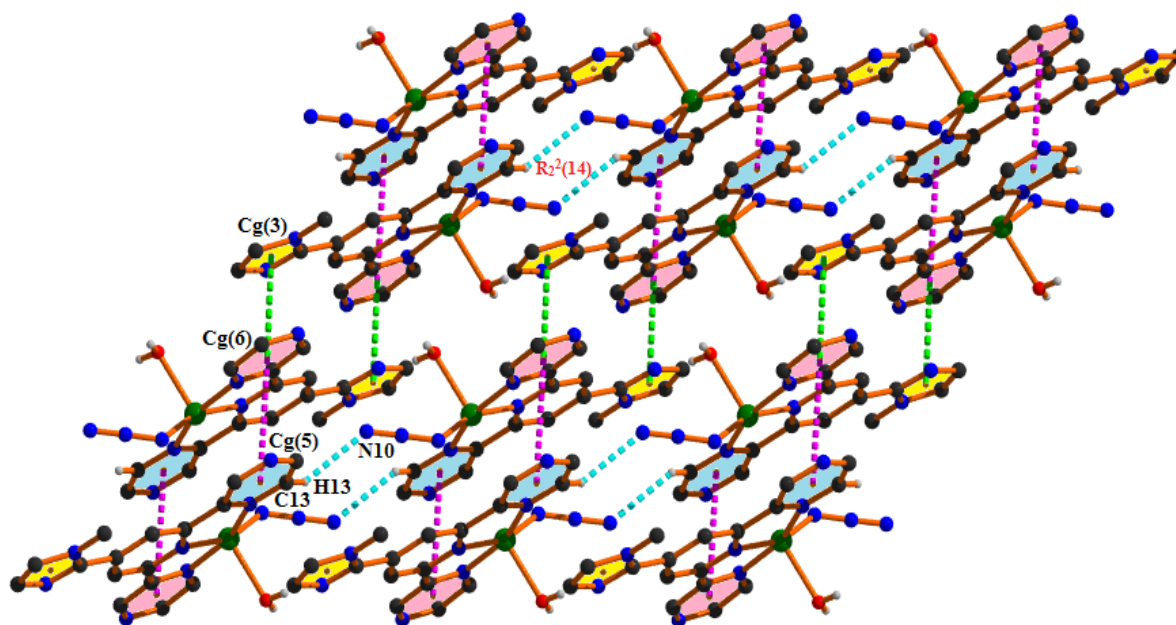
Fig. 2.8. Perspective view of 2-D supramolecular network through π•••π stacking and C─H•••N hydrogen bonding interactions in complex **1**.

Due to the self-complementary nature, the parallel chains are again interlinked through weak C13─H13•••N10 hydrogen bond by generating a $R_2^2(14)$ ring motif. Here, the

aromatic fragment (C13─H13) of one unit acts as donor to the azide nitrogen atom (N10) of adjacent unit at (2-x, 2-y, 1-z) with an angle of 130°. All these interactions are cumulatively associated to extrapolate the dimensionality from 1-D to 2-D in the ab-plane (Fig. 2.8).

A comprehensive analysis exhibits a dimeric distribution (shown in Fig. 2.9) that is formed by two symmetrically equivalent lone pair•••π(chelate ring) interaction in complex **1**. Here, two monomeric units are arranged almost in opposite orientation one above the other to achieve a self complementary lone pair•••π(chelate ring) interaction between lone pair on azide nitrogen atom (N8) and Cg(2) chelate ring (Cu1/N3/C8/C10/N5) having a shortest separation distance of 3.070 Å. The Cu•••Cu separation in this dimeric integrity is 3.917 Å which suggests that there may be some type of weak metal•••metal interaction to stabilize this dimeric form [108].
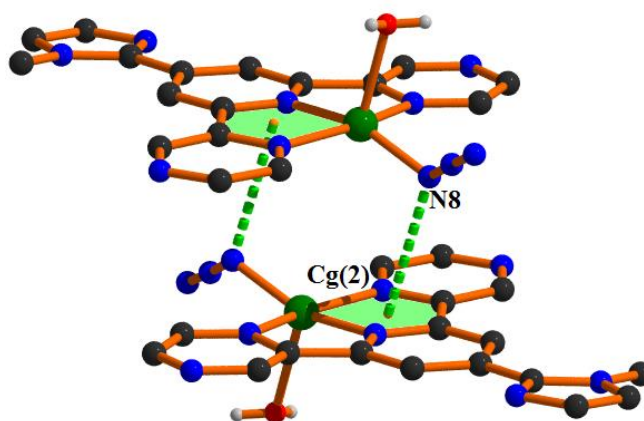
Fig. 2.9. Dimeric distribution in complex **1** through lone pair•••π(chelate ring) interactions.

The solvent water molecules not only tie up themselves for the formation of clusters but also suitable anions participate in the assembly process to satisfy donor─acceptor balance and thus construct anion─water clusters [109,110]. It is worth mentioning that, the behavior of hydrated anion is quite different from that of bare anion or anion in nonpolar media. Thus, studies of anion─water clusters are vitally important in understanding the hydration phenomena of both organic and inorganic anions in nature as well as in biochemistry. In complex **1**, a chair-like perchlorate–water tetrameric cluster, $[(ClO_4)_2–(H_2O)_2]^{2-}$, is decorated due to the self-complementary nature of intermolecular hydrogen bonding interactions between two free water molecules and two perchlorate anions (as depicted in Fig. 2.10). Here, the non-coordinated water oxygen atom O(6) acts as double donor to the oxygen atoms O(2) and O(4) of perchlorate ion in the complex at (169°) and (153°) respectively; thus forming a $R_4^4(12)$ ring motif (Table 2.5). It was well established that the lower H•••A separation and the D–H•••A angle close to 180º indicate the stronger hydrogen bonding

interaction. Here, the O6─H6A•••O2 interaction is relatively stronger than that of O6─H6B•••O4 interaction as the former interaction has lower H•••O distance (2.0 Å) compared to other (2.23 Å) and O–H•••O angle close to 180º. The O•••O separation distances within the tetramer in the range of 2.839(6)–3.006(8) Å, which is longer than the value in ice I_c (2.75 Å) and ice I_h (2.759 Å), but can be compared with the corresponding values observed in liquid water (2.854 Å) [111,112]. Interestingly, the perchlorate─water cluster helps in growth of the molecular crystal by filling the void spaces present in complex **1** (as shown in Fig. 2.11). The mutual influence of the hydrogen bonding interactions in the perchlorate─water cluster has been studied by means of QTAIM analysis (as shown in Fig. 2.22).
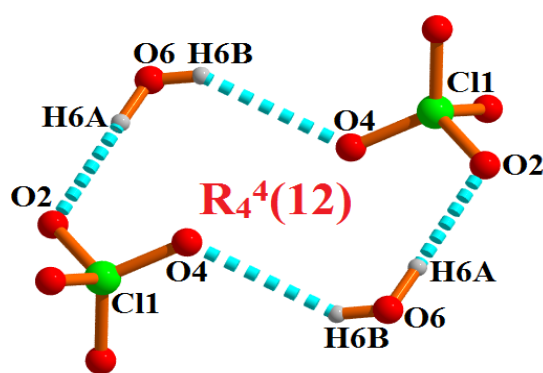
Fig. 2.10. Formation of anion–water cluster by strong O─H•••O hydrogen bonding interactions in complex **1**.
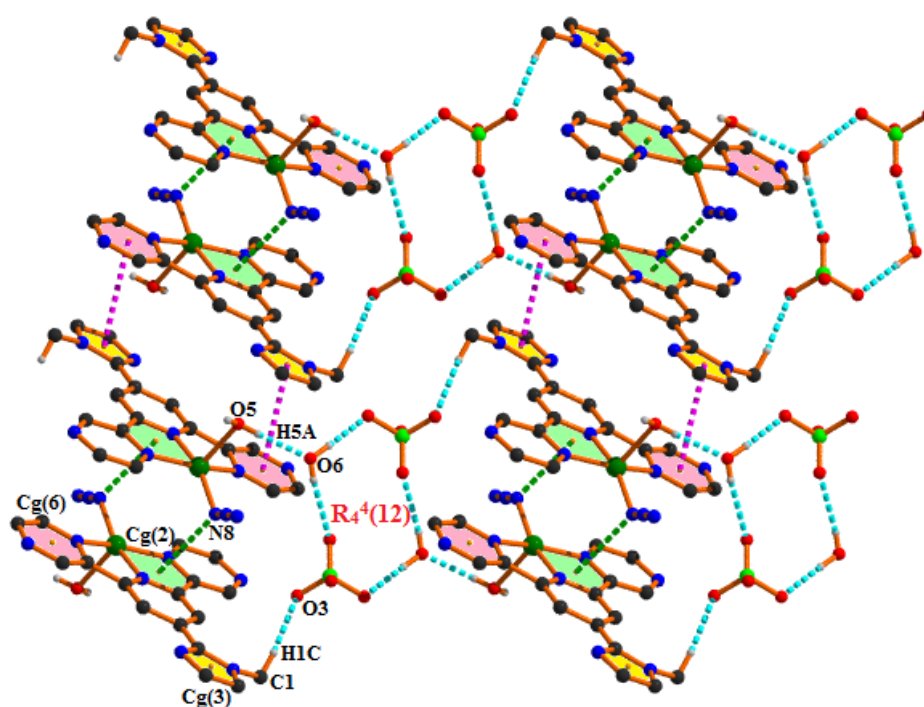
Fig. 2.11. Perspective view of 2-D arrangement incorporating π•••π, lone pair•••π(chelate ring) and hydrogen bonding interactions in complex **1**.

The lone pair•••π(chelate ring) along with π•••π stacking and hydrogen bonding interactions play a decisive role in building the supramolecular arrangement (Fig. 2.11). The dimeric units (as depicted in Fig. 2.9) are interlinked by a self complementary π•••π interaction between Cg(3) and Cg(6) of two different units leading the formation of a 1-D chain along [010] direction. The separation distance between Cg(3) and Cg(6) ring centriods is 3.642(2) Å (Table 2.4).

Now, these 1-D parallel chains are further connected by the anion–water cluster (shown in Fig. 2.10) to generate the 2-D arrangement in the bc-plane. Here, the water-anion clusters are interconnected with the dimeric units by the self complementary strong O5─H5A•••O6 (175°) and comparatively weak C1─H1C•••O3 (158°) hydrogen bonding interactions (Table 2.5) as shown in Fig. 2.11.

In addition, two monomeric units of complex **1** are interconnected by the self complementary C1─H1B•••N4 (133°) hydrogen bonding interactions (Table 2.5) to form another dimer having $R_2^2(20)$ ring motif (Fig. 2.12). The dimeric units are further interlinked through the self complementary O5─H5B•••N2 [165(5)°] hydrogen bonding interactions where coordinated water oxygen atom (O5) acts as donor to the imidazole nitrogen atom (N2) in the molecule at (1+x, y, z). Repetition of this $R_2^2(20)$ ring motif along [100] direction leads the molecules to generate a 1-D tape as shown in Fig. 2.12.
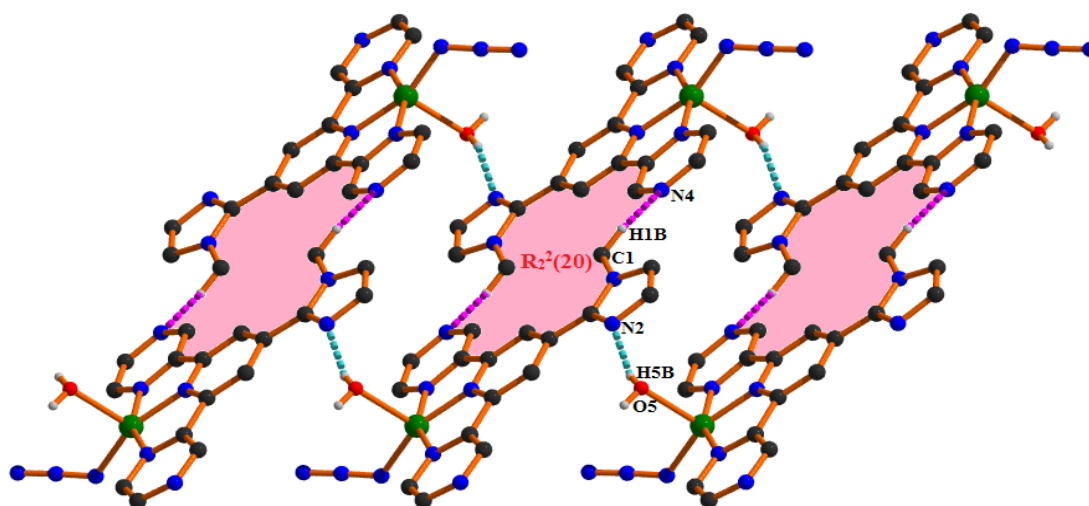
Fig. 2.12. Formation of 1-D tape by hydrogen bonding interactions in complex **1**.

2.3.3. Structural description of complex 2

The complex **2** is a coordination polymer (Fig. 2.13) and the asymmetric unit of the complex with the atom numbering scheme is depicted in Fig. 2.13. In this polymeric chain the asymmetric units are connected along the (010) direction through pyrazine nitrogen atom

(N4) of the second ligand (**NL**). Single-crystal X-ray diffraction study shows that the complex **2** adopts a monoclinic system with the space group $P2_1/c$ and its unit cell contains four formula units. The important bond lengths (Å) and bond angles (°) are included in Table 2.6. In the complex, the central Cu(II) ion is situated in a distorted square pyramidal geometry ($\tau = 0.1218$, eq 1) where the equatorial plane is formed by the three pyrazinyl nitrogen atoms (N3, N5 and N6) of the ligand (**NL**) and one nitrogen atom (N8) of thiocyanate anion. The apical position is occupied by another nitrogen atom (N4) of the second **NL** ligand. Here, two five-membered chelate rings [(Cu1/N3/C7/C17/N6) and (Cu1/N3/C8/C10/N5)] are formed with bite angles 80.11(9)° (for <N3—Cu1—N6) and 79.08(8)° (for <N3—Cu1—N5) respectively. The average distance of Cu—N bonds in the equatorial plane is 1.996 Å [Cu1—N6 = 2.050(2) Å, Cu1—N3 = 1.932(2) Å, Cu1—N5 = 2.066(2) Å and Cu1—N8 = 1.937(3) Å]. The Cu(II) ion is deviated by a distance of 0.204 Å towards the apical nitrogen atom (N4^b, b = 1−x, 1/2+y, 3/2−z) from the equatorial plane (N3, N5, N6 and N8). The axial Cu—N bond length is comparatively larger [Cu1—N4^b = 2.277(2) Å] than the other equatorial Cu—N bonds likely due to the more 'p' character of the orbital involved in the axial bond. The electrical charge on the metal centre is taken care by one coordinated thiocyanate ion and one non-coordinated perchlorate ion.
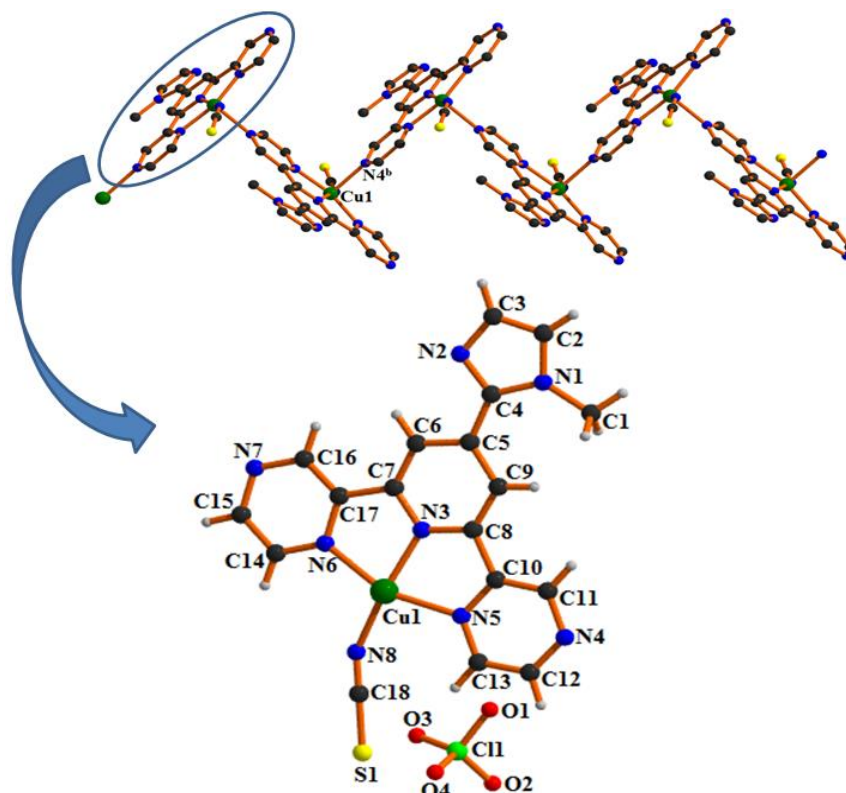
Fig. 2.13. One-dimensional (1-D) zigzag polymeric chain along the [010] direction and the asymmetric unit of complex **2**.

Table 2.6. Selected bond distances [Å] and bond angles (°) for complex 2

Bonds	Distance (Å)	Bond angles	Value (°)
Cu1—N3	1.932(2)	N3—Cu1—N5	79.08(8)
Cu1—N5	2.066(2)	N3—Cu1—N6	80.11(9)
Cu1—N6	2.050(2)	N3—Cu1—N8	165.49(11)
Cu1—N8	1.937(3)	N3—Cu1—N4_b	98.19(8)
Cu1—N4_b	2.277(2)	N5—Cu1—N6	158.18(8)
		N5—Cu1—N8	98.27(11)
		N4_b—Cu1—N5	92.87(8)
		N6—Cu1—N8	100.23(11)
		N4_b—Cu1—N6	96.53(8)
		N4_b—Cu1—N8	96.18(11)

a = 1−x, −1/2+y, 3/2−z; b = 1−x, 1/2+y, 3/2−z

In the solid state, the complex **2** is stabilized through C—H•••O hydrogen bonds in addition with π•••π stacking, π•••π (chelate ring), anion•••π and lone pair•••π interactions (Tables 2.7–2.9).

Table 2.7. Geometrical parameters (Å, °) for the π-stacking interactions for complex 2

Cg(i)•••Cg(j)	Cg(i)•••Cg(j) [Å]	α (°)	B (°)	γ (°)	Cg(i)–Perp [Å]	Cg(j)–Perp [Å]	Symmetry
Cg(1)[1]•••Cg(3)	3.4980(16)	9.88	13.15	6.24	3.477	3.406	-1+x, y, z
Cg(3)[1]•••Cg(1)	3.4980(16)	9.88	6.24	13.15	3.406	3.477	1+x, y, z
Cg(3)[1]•••Cg(3)	3.3969(19)	0.02	10.90	10.90	3.336	3.336	2-x, 1-y, 1-z
Cg(3)[1]•••Cg(6)	3.6803(18)	11.50	32.35	22.62	3.397	3.109	1+x, y, z
Cg(6)[1]•••Cg(3)	3.6804(18)	11.50	22.62	32.35	3.109	3.397	-1+x, y, z
Cg(1)[1]•••Cg(3)	3.4980(16)	9.88	13.15	6.24	3.477	3.406	-1+x, y, z

Cg(i) and Cg(j) denotes centroid of ith and jth ring respectively. For complex **2**: Cg(1) is the centroid of [Cu1/N3/C7/C17/N6] ring; Cg(3) is the centroid of [N1/C2/C3/N2/C4] ring; and Cg(6) is the centroid of [N6/C14/C15/N7/C16/C17] ring.

Table 2.8. Geometrical parameters (Å, °) for the lone pair•••π /anion•••π interactions for the complex 2

Y–X(I)•••Cg(J)	X•••Cg [Å]	Y•••Cg [Å]	Y–X•••Cg (°)	Symmetry
C(18)—S(1)[1]•••Cg(5)	3.5192(15)	4.355(3)	110.53(11)	-1+x, y, z
C(18)—S(1)[1]•••Cg(5)	3.5668(15)	4.047(3)	95.28(10)	-x, 1/2+y, 3/2-z
Cl(1)—O(1)[2]•••Cg(6)	3.022(3)	3.8600(14)	115.52(16)	1-x, -1/2+y, 3/2-z

For complex **2**: Cg(5) is the centroid of [N4/C11/C10/N5/C13/C12] ring; and Cg(6) is the centroid of [N6/C14/C15/N7/C16/C17] ring.

The parallel 1-D zigzag chains are interlinked through face to face π•••π interaction to build a 2-D layered structure (Fig. 2.14) in the bc-plane. The π•••π interaction was executed between Cg(3) of one complex unit and Cg(3) of the other unit with the shortest centroid–centroid distance of 3.3969(19) Å (Table 2.7).

Table 2.9. Geometrical parameters for the hydrogen bonds of complex 2

D–H•••A	D–H [Å]	H•••A [Å]	D•••A [Å]	D–H•••A [°]	Symmetry
C11—H11•••O3	0.9300	2.5500	3.106(6)	119.00	1-x, -1/2+y, 3/2-z
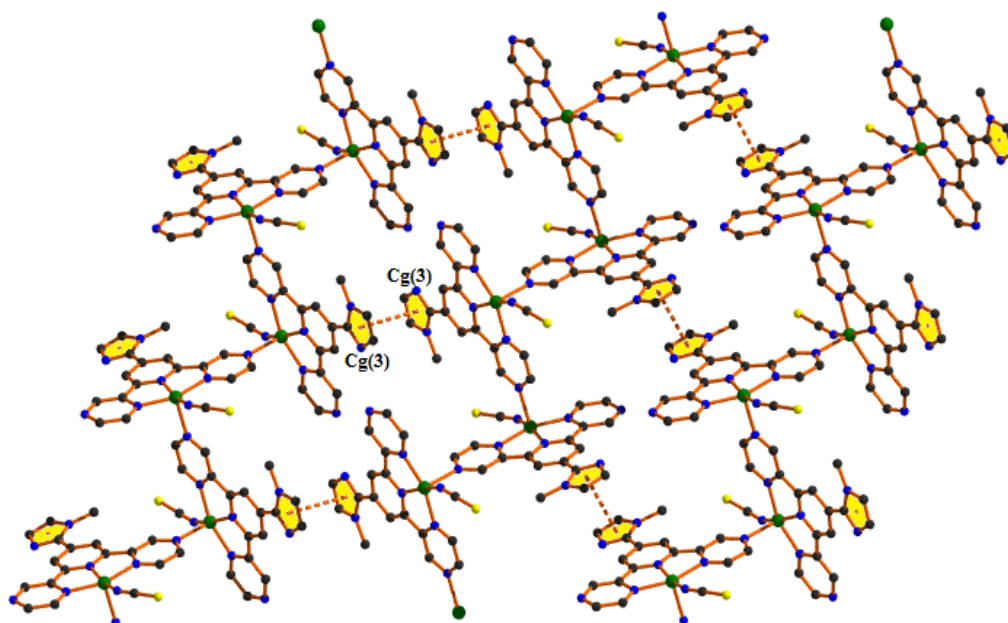
Fig. 2.14. Perspective view of 2-D layer generated through π•••π interactions in complex **2** (aromatic hydrogen atoms have been omitted for clarity).

Fig. 2.15 shows that the 1-D parallel chains are interlinked through the self-complementary π•••π stacking interactions between Cg(3) of one complex unit and Cg(6) of the other unit to form another two-dimensional (2-D) assembly in the ab-plane having an inter-planar spacing of 3.6803(18) Å (Table 2.7).

Again, the 2-D assembly is further stabilized by the lone pair•••π interactions (shown in Fig. 2.16). The sulfur atom (S1) approaches (bifurcated) towards π-faces of two different Cg(5) units at (-1+x, y, z) and (-x, 1/2+y, 3/2-z) with angles of 110.53(11)° and 95.28(10)° respectively (Table 2.8). For having a good sulphur(lone pair)•••π interaction, the S•••π distance should be less than the sum of their van der Waals radii (3.70 Å). Here, the average distance between sulfur atom (S1) and Cg(5) centroid is 3.543 Å; thus suggesting a significant lone pair•••π interaction. Though the sulphur(lone pair)•••π interaction is

comparatively less frequent but it has been well appreciated in biological and model systems [113–116].
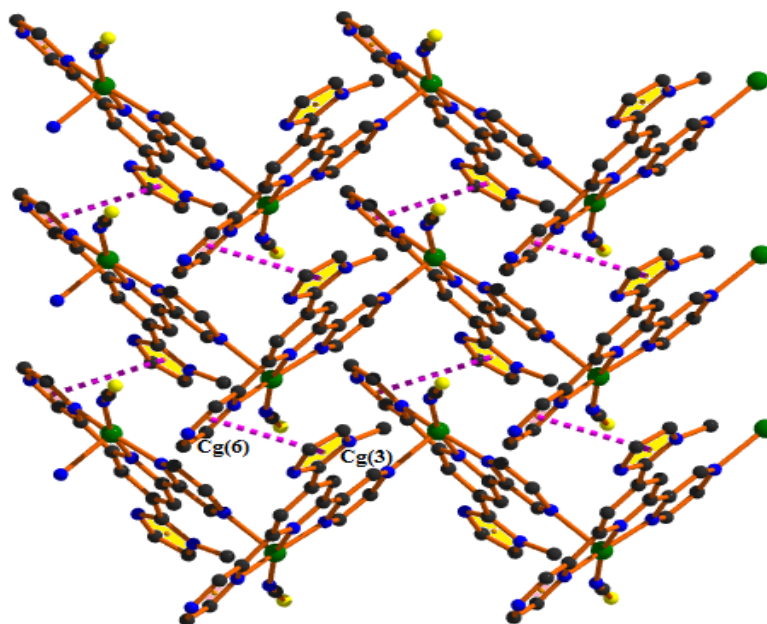
Fig. 2.15. Formation of a 2-D assembly through π•••π interactions in complex **2** (aromatic hydrogen atoms have been omitted for clarity).
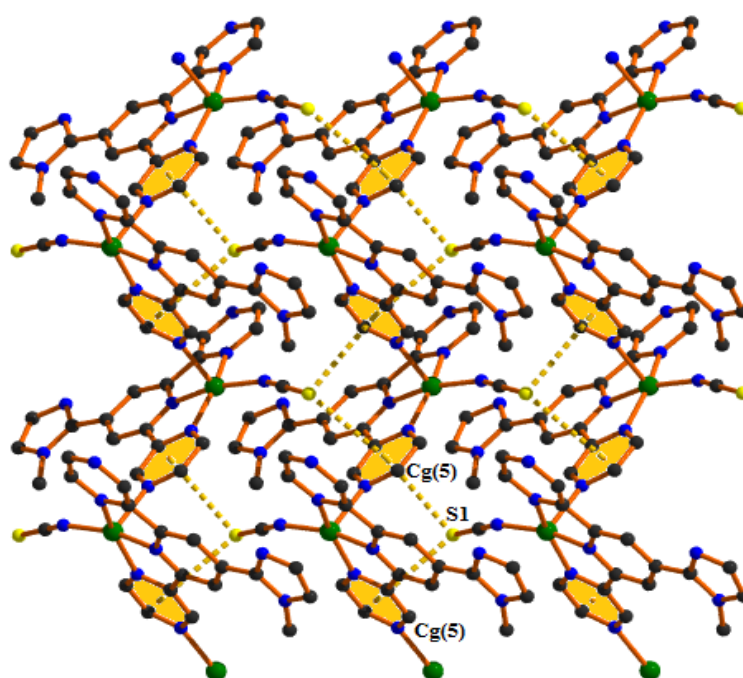
Fig. 2.16. Perspective view of 2-D architecture through sulphur(lone pair)•••π interactions in complex **2** (aromatic hydrogen atoms have been omitted for clarity).

In the Fig. 2.17, the complex units of **2** (extracted from the polymeric chain) ensure to propagate a 1-D polymeric chain through π•••π(chelate ring) interaction (shown by orange dotted lines) between Cg(3) of one unit and Cg(1) (chelate ring) of the adjacent unit separated

at a distance of 3.4980(16) Å (Table 2.7). The parallel chains are interconnected through C11─H11•••O3 (119°) hydrogen bond (shown in aqua dotted line) and anion•••π interaction (shown in pink dotted line). The said anion•••π interaction involves one oxygen atom (O1) of the ClO_4^- anion and Cg(6) of the adjacent complex unit at (1-x, -1/2+y, 3/2-z) with a shortest separation distance of 3.022(3) Å.
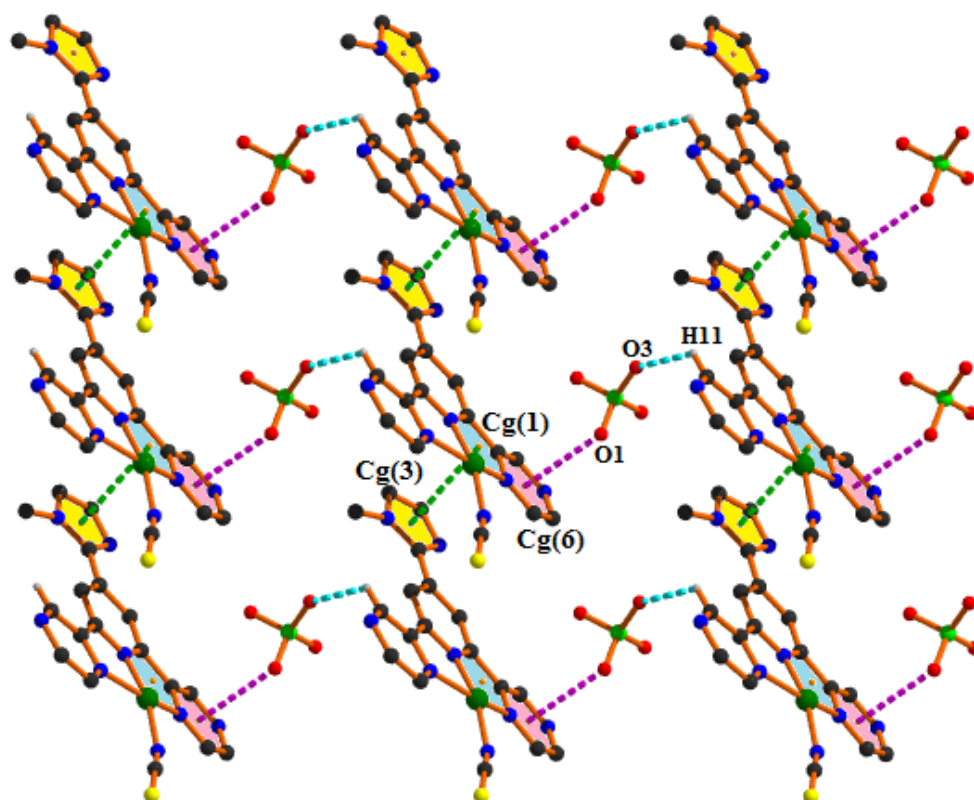
Fig. 2.17. Perspective view of 2-D architecture incorporating π•••π, anion•••π and C─H•••O hydrogen bonding interactions in complex **2** (other aromatic hydrogen atoms have been omitted for clarity).

Therefore, the influence of the unconventional π•••π(chelate ring) interactions along with anion•••π and C─H•••O hydrogen bonding interactions is responsible in building the extended 2-D architecture in the ab-plane (as shown in Fig. 2.17).

2.3.4. Theoretical studies

PBE0-D3/def2-TZVP calculations have been used to study the chelate ring (CR) interactions described above that are relevant for the crystal packing of complex **1**. Complex **2** is a polymer and its solid-state architecture is basically governed by coordination bonds. In this case the theoretical study is limited to the characterization of the interactions described above in Fig. 2.17 using the NCI plot index analysis.

The molecular electrostatic potential (MEP) surface of complex **1** (including the counter ion and water molecule) has been firstly computed to analyze the most nucleophilic and electrophilic parts of the molecules. As expected, the most negative MEP values are located at the perchlorate anion (–74 kcal/mol). The MEP values at the N-atoms of the azido ligand are also negative (–15 kcal/mol). The maximum MEP value (+75 kcal/mol) is located in a cleft that is under the influence of two aromatic H-atoms and one aliphatic H-atom (methyl group of the imidazole ring). The MEP values over the aromatic rings of the ligand are also large and positive, ranging from +21 to +47 kcal/mol.
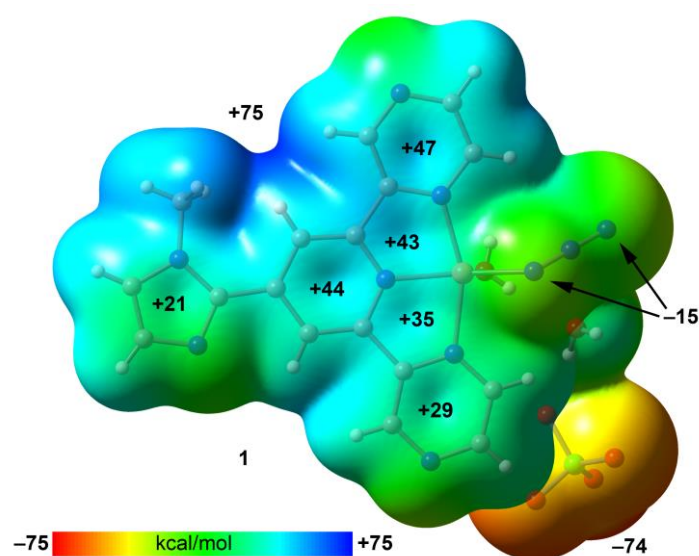
Fig. 2.18. MEP surface (isosurface 0.001 a.u.) of complex**1** at the PBE0-D3/def2-TZVP level of theory. The MEP values at selected points of the surfaces are given in kcal/mol.

The MEP value over the chelate ring that is more distant from the perchlorate anion is also large and positive (+43 kcal/mol), thus adequate for interacting with electron rich atoms (as shown in Fig. 2.18). The ion-pair nature of complex **1** anticipates a dominant role of electrostatic effects in its crystal packing. This is supported by the MEP surface analysis which shows the maximum and minimum MEP values located at the cationic and anionic moieties, respectively. In general, pure electrostatic forces are very strong and non-directional. Therefore, the final orientation of the cations and anions in the solid state is often influenced by other forces that are weaker but able to tune the final geometry of the assemblies found in their crystal structure.

As aforesaid in the structural description of **1** (Fig. 2.9), this complex forms interesting self-assembled dimers governed by the formation of two symmetrically equivalent lp•••π(CR) interactions. This DFT study is mainly focused on the investigation of this interaction. Fig. 2.19 shows the self-assembled dimer where, in addition to the lp•••π(CR)

interactions, two anti-parallel displaced and conventional π•••π interactions are formed. The dimerization energy is very large (–26.6 kcal/mol) due to the contribution of both types of π-stacking interactions. It should be mentioned that this interaction has been computed as a dimer where each monomeric fragment includes the water molecule and the perchlorate counter ion. Therefore, the hydrogen bonds are not evaluated (considered as previously formed). In an effort to evaluate the contribution of the lp•••π(CR) interaction, a reduced model (where the ligand has been simplified) has been used (see Fig. 2.19b). Consequently, the energy is only reduced to –21.9 kcal/mol that is a rough estimation of the lp•••π(CR) interaction. Such large interaction energy agrees well with the MEP surface analysis shown in Fig. 18 that evidences a large and positive MEP value over the chelate ring and negative at the azido ligand. Therefore, it dominates the formation of this dimer. The contribution of the conventional π•••π interactions can be estimated by difference, i.e. –4.7 kcal/mol, that is significantly weaker than the lp•••π(CR) interactions with the shortest centroid-to-centroid distances (see Fig. 2.19a).
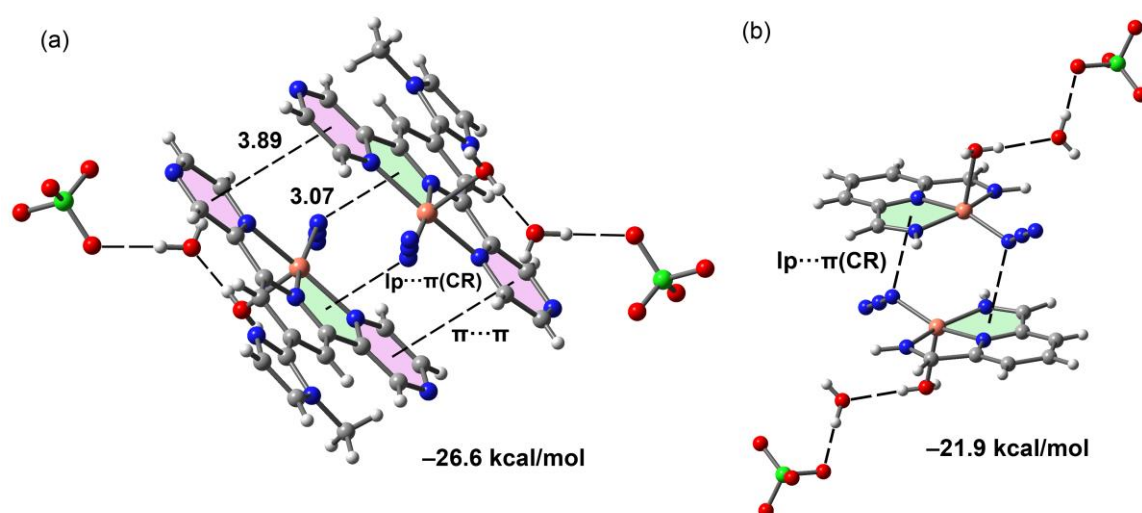
Fig. 2.19. (a) Dimer of complex **1**, π-stacking interactions shown as black dashed lines (distances in Å) (b) Reduced model of complex **1** used to estimate the lp•••π(CR) interaction.

The large dimerization energy obtained for the dimer of **1** is comparable to other interactions where anti-parallel π-stacking interactions in metal complexes with large and conjugated π-systems. It has been rationalized considering the large dipole moments of the metal complexes that are very polarized. For instances π-stacking interactions ranging from –25 to –35 kcal/mol have been reported for similar systems [117–125].

In addition, the "Non-covalent Interaction plot" (NCI plot) index has also been computed in order to characterize both types of π-π stacking interactions in complex **1**. The

NCI plot index is an intuitive visualization index that facilitates the visualization of non-covalent interactions and shows which molecular regions interact. The colour scheme is a red-yellow-green-blue scale with red (repulsive) and blue (attractive). Yellow and green surfaces correspond to weak repulsive and weak attractive interactions, respectively. Fig. 2.20 shows the NCI plot index analysis of the self-assembled dimer of complex **1** using two different perspectives.
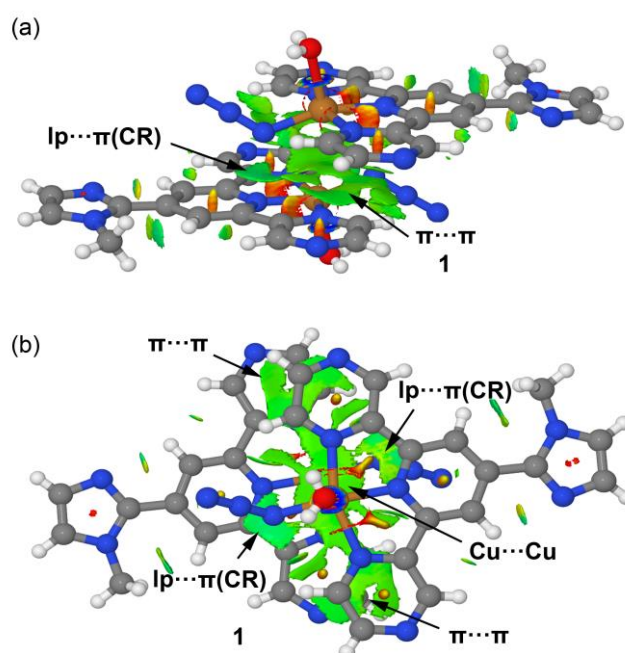
Fig. 2.20. NCI surface of the π-stacked assembly complex **1** using perspective (a) and on-top views (b) The gradient cut-off is ρ = 0.04 a.u., isosurface s = 0.35, and the color scale is −0.04 a.u.< ρ < 0.04 a.u.

The NCI plot reveals the formation of green and extended isosurfaces upon dimerization that are located between the chelate rings and the N-atoms of the azido ligand, thus confirming the existence of the unconventional lp•••π(CR) interaction. Moreover, the NCI plot also shows green isosurfaces located between the pyrazine aromatic rings, thus also confirming the existence of anti-parallel and displaced π•••π stacking interactions.

The NCI plot analysis also reveals a large and green isosurface between both Cu(II) ion, thus suggesting some type of metal•••metal interaction that likely contributes to the large dimerization energy of the reduced model shown in Fig. 2.19b.

Besides, the cambridge structural database (CSD) has been explored in order to investigate the prevalence of N_3•••π(CR) interaction in Cu complexes with five membered (unsaturated) chelate rings. Only five structures have been found in the CSD presenting similar LP•••π(CR) interactions, which are summarized in Table 2.10. The LP•••π(CR)

interactions were not described by their original authors. The Cg•••N distances are gathered in Table 10, which range from 2.938 to 3.016 Å, similar to the distance observed in complex **1** (3.070 Å). Two representative structures from this search are represented in Fig. 2.21.

Table 2.10. CSD reference codes of some Cu-complexes exhibiting N₃•••π(CR) interactions

Ref. code	d(Cg•••N), Å	Reference
FIBGIH	2.964	126
KAHXID	2.940	127
KEYKAU	3.000	128
KUCFIZ	2.938	129
LEXPAH	3.016	130
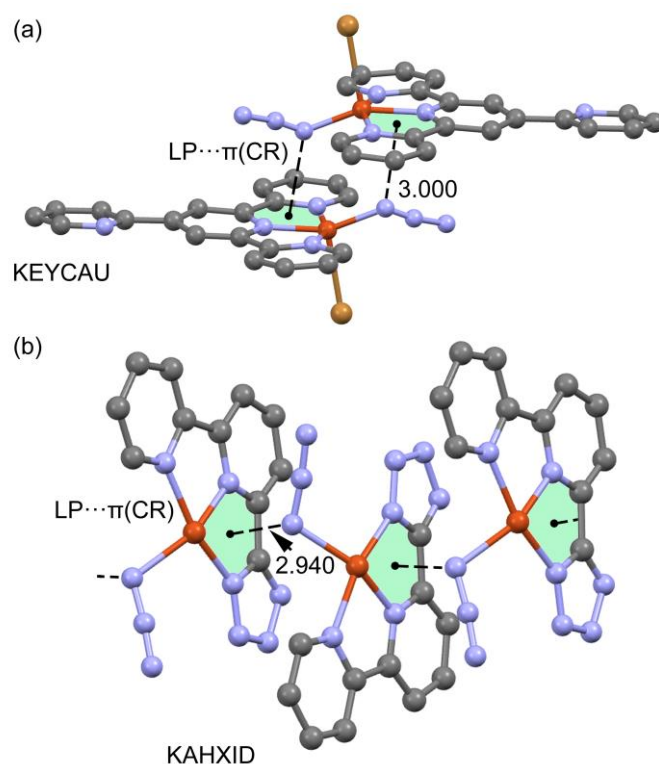
Fig. 2.21. Partial views of the solid state X-ray structures of refcodes KEYCAU (a) and KAHXID (b). Distances in Å. H-atoms omitted for clarity.

In KEYCAU structure, a self-assembled dimer is formed in the solid state that is very similar to that found in complex **1** (see Fig. 2.9) where two symmetrically equivalent LP•••π(CR) interactions are formed. The other structure forms infinite 1D supramolecular assemblies in the solid state where the complex propagates in one direction due to the formation of the LP•••π(CR) interactions. It is interesting to highlight that in all structures the LP-donor N-atom is the one that is coordinated to the Cu-atom.

The hydrogen-bonding network (anion−water cluster) described above in Fig. 2.10 has been also analysed theoretically using the quantum theory of atoms in molecules (QTAIM). The distribution of bond critical points and bond paths is represented in Fig. 2.22 along with the individual hydrogen-bond formation energies derived from the potential energy density predictor ($E_{dis} = \frac{1}{2} * V_r$) proposed by Espinosa et al. [131] Each hydrogen-bond is characterized by a bond critical point connecting the H to the O-atom. The stronger hydrogen-bond corresponds to the one established between the coordinated and uncoordinated water molecules (5.4 kcal/mol) likely to the enhanced acidity of the water protons due to the coordination to Cu(II) metal centre.

The uncoordinated water molecule also establishes two additional hydrogen-bonds as donor with the perchlorate anions, one is strong (5.3 kcal/mol) and the other is more modest (2.7 kcal/mol) in agreement with the experimental bond angles as well as separation distances (Table 2.5). Finally, the QTAIM analysis further discloses the existence of C–H•••O interactions between one aromatic H-atom of the ligand and the perchlorate anion. The interaction energy of this hydrogen-bond is the weakest one (2.0 kcal/mol). The total formation energy of this assembly is very large (–30.8 kcal/mol), thus confirming the importance of these hydrogen-bonding network in the crystal packing of complex **1**, in addition to the anti-parallel π-stacking interactions described in Fig. 2.19.
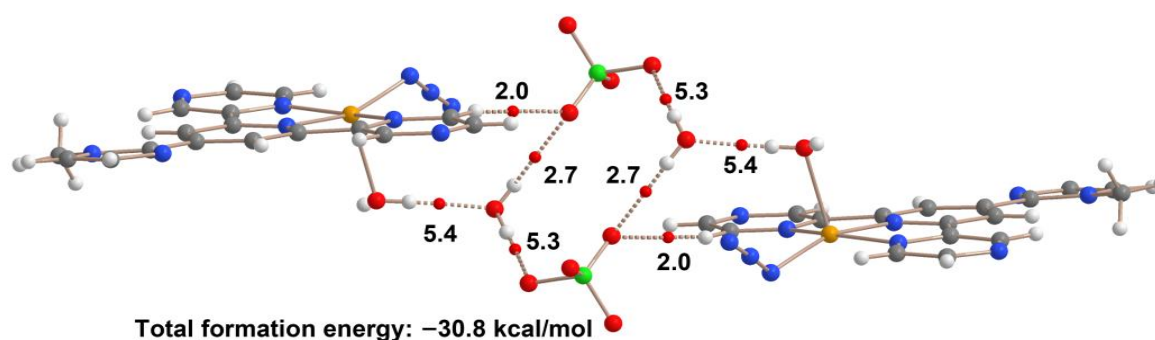
Fig. 2.22. QTAIM distribution of intermolecular bond critical points (small red spheres) and bond paths in the H-bonding assembly complex **1**. The dissociation energy of each hydrogen-bond is indicated adjacent to each bond critical point.

Since complex **2** is a coordination polymer, a dimeric model extracted from the polymeric chain has been used (see Fig. 2.23), where pyrazine rings act as apical ligands for the Cu-atoms. The NCI plot analysis of the dimer is represented in Fig. 2.23 that reveals that the SCN ligand establishes conventional lp–π interactions with the aromatic rings. Since there

is not a NCI plot isosurface located between the chelate ring and the SCN ligand, this analysis suggests that the chelate ring is not involved in the binding mechanism. In contrast, it reveals the existence of $\pi \cdots \pi$(CR) interactions involving the five membered imidazole ring and the chelate ring (see Fig. 2.23b). It is characterized by a green and extended NCI plot index isosurface that embraces the chelate ring and part of the fused pyrazine ring.
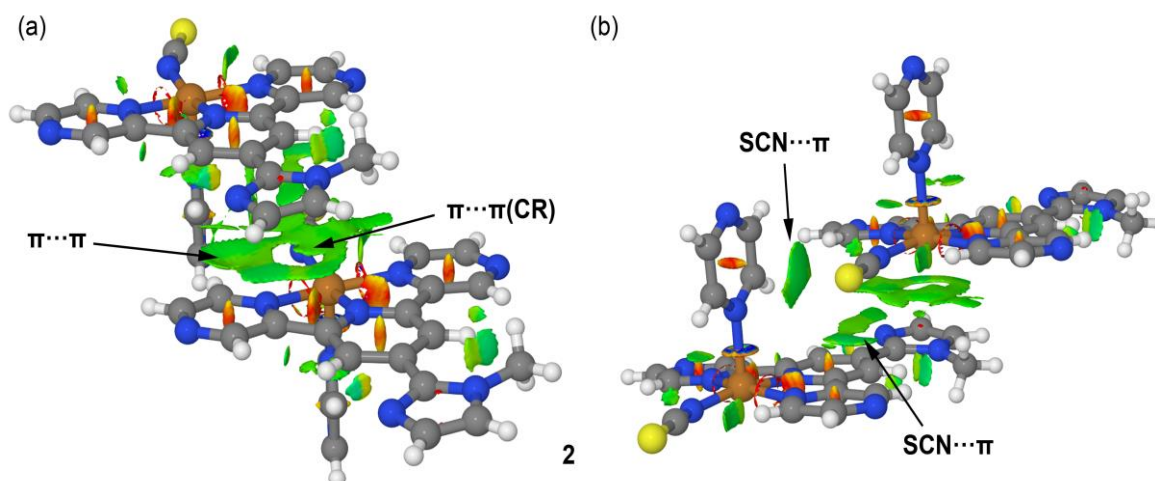
Fig. 2.23. NCI surface of the π-stacked assembly complex **2** using two different perspective views (a,b), (the gradient cut-off is ρ = 0.04 a.u., isosurface s = 0.35, and the color scale is −0.04a.u. < ρ < 0.04 a.u).

2.4. CONCLUSION

In conclusion, two Cu(II) complexes (complexes **1** and **2**) have been successfully synthesized using 4-(1-methylimidazole)-2,6-di(pyrazinyl)pyridineas the backbone ligand with two different auxiliary ligands, established their solid-state crystal structures by single crystal X-ray diffraction study and explored the non-covalent interactions associated with their crystal structures. The structural insights reveal that intermolecular hydrogen bonding (C─H•••N, C─H•••O, O─H•••N, O─H•••O), π•••π, π•••π(chelate ring), anion•••π, lone pair•••π and lone pair•••π(chelate ring) interactions play a significant role in crystal packing of the complexes in the solid state.

A DFT study has been used to evaluate the cooperative influence of unconventional lone pair•••π(chelate ring) and conventional π•••π stacking interactions in the dimeric distribution of complex **1** quantitatively and demonstrating that the former is stronger. Besides, the large formation energy of the perchlorate-water cluster (–30.8 kcal/mol) confirms its decisive role in the self assembly of complex **1**. The sulfur (lone pair)•••π and π•••π(chelate ring) interactions play a lead role in the crystal packing of complex **2**. The NCI plot index also exhibits the involvement of chelate ring to stabilize the crystal structures of the complexes significantly. Therefore, the present study undoubtedly helps to gain knowledge in this rising area of supramolecular chemistry. Finally, the CSD search discloses the existence of lone pair(N_3)•••π(chelate ring) in a few structures.

REFERENCES

1. A. Ciesielski, C. A. Palma, M. Bonini and P. Samorì, *Adv. Mater.*, 2010, **22**, 3506–3520.

2. D. Trauner, *Angew. Chem., Int. Ed.*, 2017, **57**, 4177–4191.

3. K. Geng, T. He, R. Liu, S. Dalapati, K. T. Tan, Z. Li, S. Tao, Y. Gong, Q. Jiang and D. Jiang, *Chem. Rev.*, 2020, 120, 8814–8933.

4. G. R. Desiraju, J. J. Vittal, A. Ramanan, Crystal Engineering: A Textbook, World Scientific Pub. Co. Inc., Singapore, 2011.

5. G. R. Desiraju, *J. Am. Chem. Soc.*, 2013, **135**, 9952–9967.

6. M. Mirzaei, H. Eshtiagh-Hosseini, Z. Karrabi, K. Molčanov, E. Eydizadeh, J. T. Mague, A. Bauzá and A. Frontera, *CrystEngComm*, 2014, 16, 5352–5363.

7. J. J. Novoa, Intermolecular Interactions. Crystals: Fundamentals of Crystal Engineering, The Royal Society of Chemistry, London, 2018.

8. M. D. Allendorf and V. Stavila, *CrystEngComm*, 2015, **17**, 229–246.

9. A. K. Nangia and G. R. Desiraju, *Angew. Chem., Int. Ed.*, 2019, **58**, 4100–4107.

10. I. Gospodinov, K. V. Domasevitch, C. C. Unger, T. M. Klapötke and J. Stierstorfer, *Cryst. Growth Des.*, 2020, **20**, 755–764.

11. N. R. Mote and S. H. Chikkali, *Chem.–Asian J.*, 2018, **13**, 3623–3646.

12. R. Bu, Y. Xiong, X. Wei, H. Li and C. Zhang, *Cryst. Growth Des.*, 2019, **19**, 5981–5997.

13. M. Madni, M. N. Ahmed, M. Hafeez, M. Ashfaq, M. N. Tahir, D. M. Gil, B. Galmés, S. Hameed and A. Frontera, *New J. Chem.*, 2020, **44**, 14592–14603.

14. S. Pramanik, S. Pathak, S. Jana, M. Mondol, A. Frontera and S. Mukhopadhyay, *New J. Chem.*, 2021, **45**, 12108–12119.

15. P. Manna, S. K. Seth, A. Das, J. Hemming, R. Prendergast, M. Helliwell, S. R. Choudhury, A. Frontera and S. Mukhopadhyay, *Inorg. Chem.*, 2012, **51**, 3557–3571.

16. L. A. Barrios, G. Aromi, A. Frontera, D. Quinonero, P. M. Deya, P. Gamez, O. Roubeau, E. J. Shotton and S. J. Teat, *Inorg. Chem.*, 2008, **47**, 5873−5881.

17. C. Garau, D. Quiñonero, A. Frontera, P. Ballester, A. Costa and P. M. Deyà, *Org. Lett.*, 2003, **5**, 2227−2229.

18. I. A. Rather, S. A. Wagay and R. Ali, *Coord. Chem. Rev.*, 2020, **415**, 213327–213387.

19. P. Pal, A. Hossain, R. M. Gomila, A. Frontera and S. Mukhopadhyay, *New J. Chem.*, 2021, **45**, 11689–11696.

20. C. Jia, H. Miao and B. P. Hay, *Cryst. Growth Des.*, 2019, **19**, 6806–6821.

21. M. Savastano, C. García-Gallarín, M. D. López de la Torre, C. Bazzicalupi, A. Bianchi and M. Melguizo, *Coord. Chem. Rev.*, 2019, **397**, 112–137.

22. J. Kozelka, Eur. Biophys. J. 46 (2017) 729–737.

23. M. Chawla, E. Chermak, Q. Zhang, J. M. Bujnicki and R. Oliva L. Cavallo, *Nucleic Acids Res.*, 2017, **45**, 11019–11032.

24. K. Kalra, S. Gorle, L. Cavallo, R. Oliva and M. Chawla, *Nucleic Acids Res.*, 2020, **48**, 5825–5838.

25. S. Maity, T. K. Ghosh, R. M. Gomila, A. Frontera and A. Ghosh, *CrystEngComm*, 2020, **22**, 7673–7683.

26. S. Mirdya, S. Roy, S. Chatterjee, A. Bauza, A. Frontera and S. Chattopadhyay, *Cryst. Growth Des.*, 2019, **19**, 5869–5881.

27. D. P. Malenov, G. V. Janjić, V. B. Medaković, M. B. Hall and S. D. Zarić, *Coord. Chem. Rev.*, 2017, **345**, 318–341.

28. D. P. Malenov, D. Ž. Veljković, M. B. Hall, E. N. Brothers and S. D. Zarić, *Phys. Chem. Chem. Phys.*, 2019, **21**, 1198–1206.

29. D. P. Malenov and S. D. Zarić, *Dalton Trans*., 2019, **48**, 6328–6332.

30. S. L. Tan, S. M. Lee, K. M. Lo, A. Otero-de-la-Roza and E. R. T. Tiekink, *CrystEngComm*, 2021, **23**, 119–130.

31. T. Maity, H. Mandal, A. Bauza, B. C. Samanta, A. Frontera and S. K. Seth, *New J. Chem*., 2018, **42**, 10202–10213.

32. E. R. T. Tiekink, *CrystEngComm*, 2020, **22**, 7308–7333.

33. B. Dutta, S. M. Pratik, S. Jana, C. Sinha, A. Datta and M. H. Mir, *ChemistrySelect*, 2018, **3**, 4289–4291.

34. E. R. T. Tiekink, *CrystEngComm*, 2021, **23**, 904–928.

35. H. Masui, *Coord. Chem. Rev.*, 2001, **219**, 957–992.

36. A. Castiñeiras, A. G. Sicilia-Zafra, J. M. Gonzáles-Pérez, D. Choquesillo-Lazarte, and J. Niclós-Gutiérrez, *Inorg. Chem.*, 2002, **41**, 6956–6959.

37. L. Wang, B. Song, S. Khalife, Y. Li, L.-J. Ming, S. Bai, Y. Xu, H. Yu, M. Wang, H. Wang and X. Li, *J. Am. Chem. Soc.*, 2020, **142**, 1811–1821.

38. G. Baronea, G. Gennaroa, A. M. Giuliania and M. Giustini, *RSC Adv.*, 2016, **6**, 4936–4945.

39. A. Wild, A. Winter, F. Schlütter and U. S. Schubert, *Chem. Soc. Rev.*, 2011, **40**, 1459–1511.

40. D. Saccone, C. Magistris, N. Barbero, P. Quagliotto, C. Barolo and G. Viscardi, *Materials*, 2016, **9**, 137–174.

41. P. Liu, G. Shi and X. Chen, *Front. Chem.*, 2020, **8**, 923–929.

42. M. M. Milutinović, S. K. C. Elmroth, G. Davidović, A. Rilak, O. Klisurić, I. Bratsos and Ž. D. Bugarčić, *Dalton Trans.*, 2017, **46**, 2360–2369.

43. C. Li, F. Xu, Y. Zhao, W. Zheng, W. Zeng, Q. Luo, Z. Wang, K. Wu, J. Du and F. Wang, *Front. Chem.*, 2020, **8**, 210–224.

44. C. Bai, F. H. Wei, H. M. Hu, L. Yan, X. Wang and G. L. Xue, *J. Lumin.*, 2020, **227**, 117545–117555.

45. P. Pal, T. Ganguly, S. Das and S. Baitalik, *Dalton Trans.*, 2021, **50**, 186–196.

46. Y. Wang, X. W. Gao, J. Li and D. Chao, *Chem. Commun.*, 2020, **56**, 12170–12173.

47. R. Fernández-Terán and L. Sévery, *Inorg. Chem.*, 2021, **60**, 1334–1343.

48. C. Wei, Y. He, X. Shi and Z. Song, *Coord. Chem. Rev.*, 2019, **385**, 1–19.

49. A. Winter and U. S. Schubert, *ChemCatChem*, 2020, **12**, 1–52.

50. M. Elcheikh Mahmoud, H. Audi, A. Assoud, T. H. Ghaddar and M. Hmadeh, *J. Am. Chem. Soc.*, 2019, **141**, 7115–7121.

51. D. Luo, T. Zuo, J. Zheng, Z.-H. Long, X. -Z. Wang, Y.-L. Huang, X.-P. Zhou and D. Li, *Mater. Chem. Front.*, 2021, **5**, 2777–2782.

52. B. Z. Momeni, F. Rahimi, M. Torrei and F. Rominger, *Appl. Organometal. Chem.*, 2020, **34**, 5613–5635.

53. A. M. Maron, K. Choroba, J. G. Małecki, S. Kula and E. Malicka, *Polyhedron*, 2020, **182**, 114502–114511.

54. B. Z. Momeni, S. K. Anari, M. Torrei and J. Janczak, *Appl. Organometal. Chem.*, 2021, **35**, 6179–6201.

55. E. U. Mughal, M. Mirzaei, A. Sadiq, S. Fatima, A. Naseem, N. Naeem, N. Fatima, S. Kausar, A. A. Altaf, M. N. Zafar and B. A. Khan, *R. Soc. Open Sci.*, 2020, **7**, 201208–201239.

56. S. M. Elahi, M. Raizada, P. K. Sahu and S. Konar, *Chem. Eur. J.*, 2021, **27**, 5858–5870.

57. F. A. Mautner, J. H. Albering, E. V. Harrelson, A. A. Gallo and S. S. Massoud, *J. Mol. Struct.*, 2011, **1006**, 570–575.

58. S. S. Massoud, M. Dubin, A. E. Guilbeau, M. Spell, R. Vicente, P. Wilfling, R. C. Fischer and F. A. Mautner, *Polyhedron*, 2014, **78**, 135–140.

59. F. A. Mautner, M. Traber, P. Jantscher, R. C. Fischer, K. Reichmann, R. Vicente, N. Arafat and S. S. Massoud, *Polyhedron*, 2019, **161**, 309–316.

60. A. Di Santo, H. Perez, G. A. Echeverria, O. E. Piro, R. A. Iglesias, R. E. Carbonio, A. Ben Altabef and D. M. Gil, *RSC Adv.*, 2018, **8**, 23891–23902.

61. M. Mondal, S. Jana, M. G. B. Drew and A. Ghosh, *Polymer*, 2020, **204**, 122815–122824.

62. P. Ghorai, P. Brandão, S. Benmansour, C. J. G. García and A. Saha, *Polyhedron*, 2020, **188**, 114708–114715.

63. C. D. Mekuimemba, F. Conan, A. J. Mota, M. A. Palacios, E. Colacio and S. Triki, *Inorg. Chem.*, 2018, **57**, 2184–2192.

64. K. Vrieze, G. Van Koten, In Comprehensive Coordination Chemistry; Pergamon Oxford, 1987; Vol. 2, p 225.

65. E. I. Solomon, D. E. Heppner, E. M. Johnston, J. W. Ginsbach, J. Cirera, M. Qayyum, M. T. Kieber-Emmons, C. H. Kjaergaard, R. G. Hadt and L. Tian, *Chem. Rev.*, 2014, **114**, 3659–3853.

66. K. Choroba, B. Machura, S. Kula, L. R. Raposo, A. R. Fernandes, R. Kruszynski, K. Erfurt, L. S. Shul, Y. N. Kozlov and G. B. Shul, *Dalton Trans.*, 2019, **48**, 12656–12673.

67. R. Nasani, M. Saha, S. M. Mobin, L. M. D. R. S. Martins, A. J. L. Pombeiro, A. M. Kirillov and S. Mukhopadhyay, *Dalton Trans.*, 2014, **43**, 9944–9954.

68. Z. Ma, L. Wei, E. C. B. A. Alegria, L. M. D. R. S. Martins, M. F. C. G. da Silva and A. J. L. Pombeiro, *Dalton Trans.*, 2014, **43**, 4048–4058.

69. J. Z. Gu, M. Wen, Y. Cai, Z. F. Shi, A. S. Arol, M. V. Kirillova and A. M. Kirillov, *Inorg. Chem.*, 2019, **58**, 2403–2412.

70. K. Choroba, B. Machura, A. Szlapa-Kula, J. G. Malecki, L. Raposo, C. Roma Rodrigues, S. Cordeiro, P. V. Baptista and A. R. Fernandes, *Eur. J. Med. Chem.*, 2021, **218**, 113404−113423.

71. Y. Liu, S. C. Yiu, C. L. Ho and W. Y. Wong, *Coord. Chem. Rev.*, 2018, **375**, 514–557.

72. C. Icsel, V. T. Yilmaz, S. Aydinlik and M. Aygun, *Eur. J. Med. Chem.*, 2020, **202**, 112535–112545.

73. C. Wu, J. Wang, J. Shen, C. Zhang, Z. Wu and H. Zhou, *Tetrahedron*, 2017, **73**, 5715–5719.

74. H. Q. Li, X. Q. Sun, T. Zheng, Z. X. Xu, Y. X. Song and X. H. Gu, *Sens. Actuators, B*, 2019, **279**, 400–409.

75. A. Hussain, M. F. AlAjmi, T. Rehman, S. Amir, F. M. Husain, A. Alsalme, M. A. Siddiqui, A. A. AlKhedhairy and R. A. Khan, *Sci. Rep.*, 2019, **9**, 5237–5254.

76. J. Karges, K. Xiong, O. Blacque, H. Chao and G. Gasser, *Inorg. Chim. Acta*, 2021, **516**, 120137–120143.

77. F. Cheng, N. Tang, K. Miao and F. Wang, *Z. Anorg. Allg. Chem.*, 2014, **640**, 1816–1821.

78. Y. Q. Pan, X. Xu, Y. Zhang, Y. Zhang and W. K. Dong, *Spectrochim. Acta, Part A*, 2020, **229**, 117927–117937.

79. Z. -Y. Li, J. -S. Yang, R. -B. Liu, J. -J. Zhang, S. -Q. Liu, J. Nia and C. -Y. Duan, *Dalton Trans.*, 2012, 41, 13264−13267.

80. S. S. Bhat, V. K. Revankar, N. Shivalingegowda and N. K. Lokanath, *Acta Crystallogr. C*, 2017, **73(9)**, 710−717.

81. T. Mandal, A. Dey, S. Pathak, M. M. Islam, S. Konar, J. Ortega-Castro, S. K. Seth, P. P. Ray, A. Frontera and S. Mukhopadhyay, *RSC Adv.*, 2019, **9**, 9663–9677.

82. Bruker, SMART *v*5.631, Bruker AXS Inc., Madison, WI, USA, 2001.

83. G. M. Sheldrick, SHELXT-2014, University of Göttingen, 2014.

84. G. M. Sheldrick, *Acta Crystallogr., Sect. C: Struct. Chem.*, 2015, **71**, 3–8.

85. M. J. Frisch, G. W. Trucks, H. B. Schlegel, G. E. Scuseria, M. A. Robb, J. R. Cheeseman, G. Scalmani, V. Barone, B. Mennucci, G. A. Petersson, H. Nakatsuj, M. Caricato, X. Li, H. P. Hratchian, A. F. Iamaylov, J. Bloino, G. Zheng, J. L. Sonnenberg, M. Hada, M. Ehara, K. Toyota, R. Fukuda, J. Hasegawa, M. Ishida, T. Nakajima, Y. Honda, O. Kitao, H. Nakai, T. Vreven, J. A. Montgomery Jr, J. E. Peralta, F. Ogliaro, M. Bearpark, J. J. Heyd, E. Brothers, K. N. Kudin, V. N. Staroverov, R. Kobayashi, J. Normand, K. Raghavachari, A. Rendell, J. C. Burant, S. S. Lyengar, J. Tomasi, M. Cossi, N. Rega, J. M. Millam, M. Klene, J. E. Knox, J. B. Cross, V. Bakken, C. Adamo, J. Jaramillo, R. Gomperts, R. E. Stratmann, O. Yazyev, A. J. Austin, R. Cammi, C. Pomelli, J. W. Ochterski, R. L. Martin, K. Morokuma, V. G. Zakrzewski, G. A. Voth, P. Salvador, J. J. Dannenberg, S. Dapprich, A. D. Daniels, O. Farkas, J. B. Foresman, J. V. Ortiz, J. Cioslowski and D. J. Fox, Gaussian 09, Revision A.1, Gaussian Inc., Wallingford CT, 2016.

86. S. F. Boys and F. Bernardi, *Mol. Phys.*, 1970, **19**, 553–556.

87. S. Grimme, J. Antony, S. Ehrlich and H. Krieg, *J. Chem. Phys.*, 2010, **132**, 154104–154123.

88. P. Manna, S. K. Seth, M. Mitra, S. R. Choudhury, A. Bauzá, A. Frontera, S. Mukhopadhyay, *Cryst. Growth Des.*, 2014, **14**, 5812–5821.

89. M. Mirzaei, H. Eshtiagh-Hosseini, Z. Bolouri, Z. Rahmati, A. Esmaeilzadeh, A. Hassanpoor, A. Bauza, P. Ballester, M. Barceló-Oliver, J. T. Mague, B. Notash and A. Frontera, *Cryst. Growth Des.*, 2015, **15**, 1351–1361.

90. Y. V. Torubaev, I. V. Skabitsky, A. V. Rozhkov, B. Galmes, A. Frontera and V. Yu. Kukushkin, *Inorg. Chem. Front.*, 2021, **8**, 4965−4975.

91. V. V. Suslonov, N. S. Soldatova, D. M. Ivanov, B. Galmes, A. Frontera, G. Resnati, P. S. Postnikov, V. Yu. Kukushkin, N. A. Bokach, *Cryst. Growth Des.*, 2021, **21**, 5360−5372.

92. A. V. Rozhkov, I. V. Ananyev, A. A. Petrov, B. Galmes, A. Frontera, N. A. Bokach and V. Yu. Kukushkin, *Cryst. Growth Des.*, 2021, **21**, 4073−4082.

93. S. V. Baykov, K. K. Geyl, D. M. Ivanov, R. M. Gomila, A. Frontera and V. Yu. Kukushkin, *Chem. Asian J.*, 2021, **16**, 1445−1455.

94. L. E. Zelenkov, A. A. Eliseeva, S. V. Baykov, V. V. Suslonov, B. Galmes, A. Frontera, V. Yu. Kukushkin, D. M. Ivanov and N. A. Bokach, *Inorg. Chem. Front.*, 2021, **8**, 2505−2517.

95. Z. M. Efimenko, A. A. Eliseeva, D. M. Ivanov, B. Galmes, A. Frontera, N. A. Bokach and V. Yu. Kukushkin, *Cryst. Growth Des.*, 2021, **21**, 588−596.

96. L. E. Zelenkov, D. M. Ivanov, E. K. Sadykov, N, A. Bokach, B. Galmes, A. Frontera and V. Yu. Kukushkin, *Cryst. Growth Des.*, 2020, **20**, 6956−6965.

97. N. S. Soldatova, P. S. Postnikov, V. V. Suslonov, T. Yu. Kissler, D. M. Ivanov, M. S. Yusubov, B. Galmes, A. Frontera and V. Yu. Kukushkin, *Org. Chem. Front.*, 2020, **7**, 2230−2242.

98. A. V. Rozhkov, A. A. Eliseeva, S. V. Baykov, B. Galmes, A. Frontera and V. Yu. Kukushkin, *Cryst. Growth Des.*, 2020, **20**, 5908−5921.

99. A. V. Rozhkov, I. V. Ananyev, R. M. Gomila, A. Frontera and V. Yu Kukushkin, *Inorg. Chem.*, 2020, **59**, 9308−9314.

100. E. A. Katlenok, M. Haukka, O. V. Levin, A. Frontera and V. Yu. Kukushkin, *Chem. Eur. J.*, 2020, **26**, 7692−7701.

101. J. Contreras-García, E. R. Johnson, S. Keinan, R. Chaudret, J. -P. Piquemal, D. N. Beratan and W. Yang, *J. Chem. Theory Comput.*, 2011, **7**, 625–632.

102. A. W. Addison, T. N. Rao, J. Reedijk, J. Rijn, G. C. Verschoor, *J. Chem. Soc., Dalton Trans.*, 1984, **7**, 1349–1356.

103. Ł. Jaremko, A. M. Kirillov, P. Smoleński, A. J. L. Pombeiro, *Cryst. Growth Des.*, 2009, **9**, 3006−3010.

104. K. R. Gruenwald, A. M. Kirillov, M. Haukka, J. Sanchiz and A. J. L. Pombeiro, *Dalton Trans.*, 2009, 2109−2120.

105. P. J. Figiel, A. M. Kirillov, M. F. C. Guedes da Silva, J. Lasri and A. J. L. Pombeiro, *Dalton Trans.*, 2010, **39**, 9879−9888.

106. A. M. Kirillov, P. Smolenski, Z. Ma, M. F. C. Guedes da Silva, M. Haukka and A. J. L. Pombeiro, *Organometallics*, 2009, **28**, 6425−6431.

107. P. Pal, K. Das, A. Hossain, A. Frontera, S. Mukhopadhyay, *New J. Chem.*, 2020, **44**, 7310–7318.

108. S. Das, G. P. Muthukumaragopal, S. Pal and S. Pal, *New J. Chem.*, 2003, **27**, 1102–1107.

109. M. N. Hoque, U. Manna and G. Das, *Polyhedron*, 2016, **119**, 307–316.

110. M. N. Hoque and G. Das, *CrystEngComm*, 2017, **19**, 1343–1360.

111. S. R. Choudhury, A. D. Jana, E. Colacio, H. M. Lee, G. Mostafa and S. Mukhopadhyay, *Cryst. Growth & Des.*, 2007, **7**, 212–214.

112. S. Pramanik, S. Konar, K. Chakraborty, T. Pal, S. Das, S. Chatterjee, M. Dolai and S. Pathak, *J. Mol. Struct.*, 2020, **1206**, 127663–127670.

113. K. N. M. Daeffler, H. A. Lester, D. A. Dougherty, J. Am. Chem. Soc. 134 (2012) 14890–14896.

114. R. F. N. Silva, A. C. S. Sacco, I. Caracelli, J. Zukerman-Schpector and E. R. T. Tiekink, *Z. Kristallogr.*, 2018, **233**, 531–537.

115. T. P. Tauer, M. E. Derrick and C. D. Sherrill, *J. Phys. Chem. A*, 2005, **109**, 191–196.

116. Y. H. Peng, F. Y. Liao, C. T. Tseng, R. Kuppusamy, A. S. Li, C. H. Chen, Y. S. Fan, S. Y. Wang, M. H. Wu, C. C. Hsueh and J. Y. Chang, *J. Med. Chem.*, 2020, **63(4),** 1642–1659.

117. H. Nath, P. Sharma, R. M. Gomila, A. Frontera, M. Barcelo-Oliver, A. K. Verma, K. Dutta and M. K. Bhattacharyya, *J. Mol. Struct.*, 2021, **1245**, 131038.

118. A. Das, P. Sharma, A. Frontera, M. Barcelo-Oliver, A. K. Verma, R. S. Ahmed, S. Hussain and M. K. Bhattacharyya, *New J. Chem.*, 2021, **45**, 13040−13055.

119. P. Sharma, H. Nath, A. Frontera, M. Barcelo-Oliver, A. K. Verma, S. Hussain and M. K. Bhattacharyya, *New J. Chem.*, 2021, **45**, 8269−8282.

120. J. C. Belmont-Sanchez, M. E. Garcia-Rubino, A. Frontera, J. M. Gonzalez-Perez, A. Castineiras and J. Niclos-Gutierrez, *Crystals*, 2021, **11**, 48–63.

121. M. K. Bhattacharyya, D. Dutta, S. M. Nashre-ul-Islam, A. Frontera, P. Sharma, A. K. Verma and A. Das, *Inorg. Chim. Acta*, 2020, **501**, 119233.

122. M. N. Ahmed, M. Arif, F. Jabeen, H. A Khan, K. A. Yasin, M. N. Tahir, A. Franconetti and A. Frontera, *New J. Chem.*, 2019, **43**, 8122−8131.

123. A. Najafi, M. Mirzaei, A. Bauza, J. T. Mague and A. Frontera, *Inorg. Chem. Comm.*, 2017, **83**, 24−26.

124. D. Debnath, S. Roy, A. Purkayastha, A. Bauza, R. Choudhury, R. Ganguly, A. Frontera and T. K. Misra, *J. Mol. Struct.*, 2017, **1141**, 225−236.

125. H. Andleeb, I. Khan, S. Hameed, A. Bauza, A. Frontera, M. N. Tahir and J. Simpson, *ActaCryst.*, 2018, **C74**, 816−829.

126. J. D. Woodward, R. V. Backov, K. A. Abboud, D. Dai, H. -J. Koo, M. -H. Whangbo, M. W. Meisel and D. R. Talham, *Inorg. Chem.*, 2005, **44**, 638–648.

127. J. -Y. Tsao, J. -D. Tsai and C. -I. Yang, *Dalton Trans.*, 2016, **45**, 3388–3397.

128. J. -N. Li, *Synth. React. Inorg.*, *Met. -Org.*, *Nano-Met. Chem.*, 2013, **43**, 832–839.

129. B.-L. Liu, N. Wu, C.-P. Li and J. Chen, *Transition Met. Chem.*, 2015, **40**, 341–345.

130. Y. -Y. Zhu, C. Cui, N. Li, B. -W. Wang, Z. -M. Wang and S. Gao, *Eur. J. Inorg. Chem.*, 2013, 3101−3111.

131. E. Espinosa, E. Molins and C. Lecomte, *Chem. Phys. Lett.*, 1998, **285**, 170–173.

CHAPTER 3

Supramolecular and theoretical perspectives of two Cu(II) complexes: on the importance of π•••π and C—H•••Cl interactions
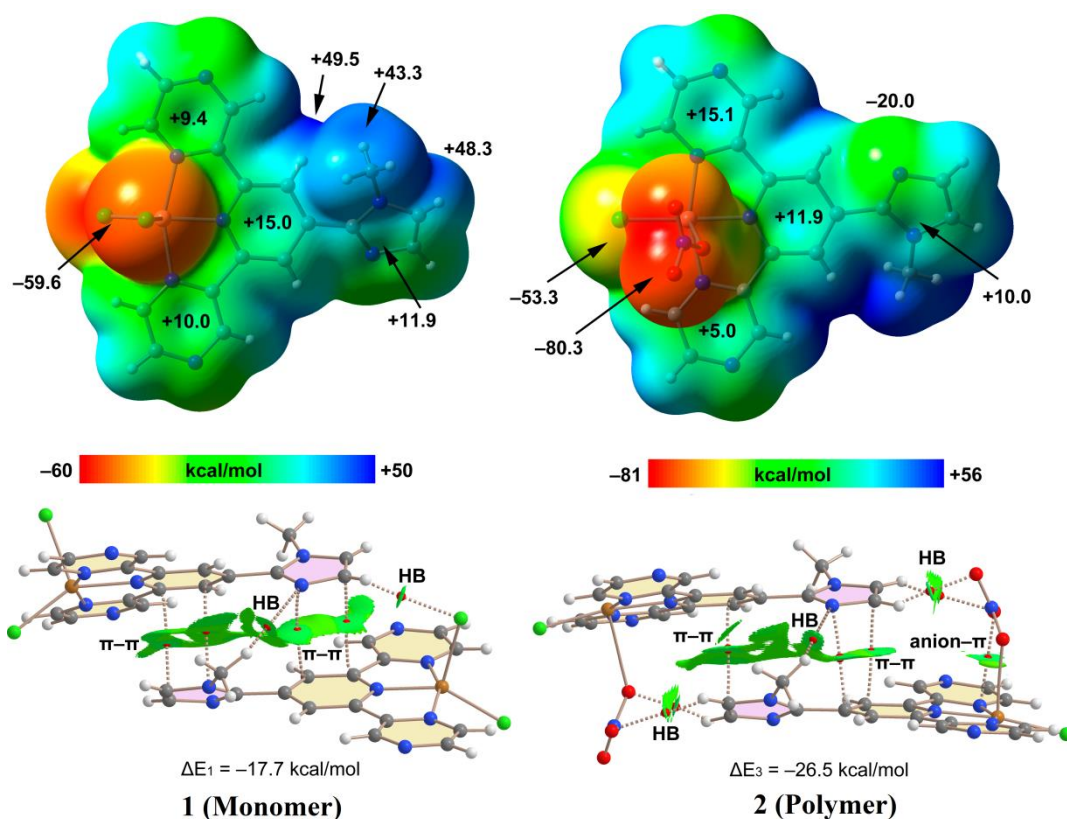
3.1. INTRODUCTION

In the context of crystal packing, crystal engineering aims at understanding of intermolecular interactions that prevail in molecular solids [1,2]. The expansion of crystal engineering as a research field has been accompanied by significant interest in the nature of intermolecular interactions and their subsequent use in the formation of solid-state architectures [3–5]. Engineering strategies not only rely on hydrogen bonding and coordination bonds, but also use interactions of comparatively lower strength such as halogen bonds, π•••π stacking, cation•••π, anion•••π, C—H•••π, lone pair•••π and similar ones actively as well as in conjugation [6–12]. Besides, intermolecular interactions drive the molecular recognition and self-assembly process in both chemical and biological systems [13–20]. For coordination compounds the construction of molecular architectures also depend on the coordination geometry of metal ions [21]. Hydrogen bonding interaction is the heart of supramolecular chemistry and is considered as most imperative non-covalent interaction during self assemble processes [22–24]. The hydrogen bond of the types O—H•••O/Cl/N and N—H•••O/N/Cl are strong enough compared to van der Waals force [25].

Besides the classical hydrogen bonding (Y—H•••A, Y and A = N, O, F) interactions, non-classical hydrogen bonding interactions have arrested notable attention on a number of fronts [26–30]. Non-classical hydrogen bonding interaction involves less polar C—H donor in the presence of unshared-pair bearing atoms (N, O, X where X = F, Cl, Br, I) [31]. The strength of the H•••N/O/X interaction is proportional to the polarization of the donor C—H and the charge of the acceptor heteroatom [32]. For heterocyclic rings like pyridine, pyrimidine or alike, such C—H polarization is more effective. In addition, the hydrogen bond acceptor capability of inorganic halide (M—X) is comparatively stronger than organic halide (C—X) [33,34]. Among non-classical hydrogen bonding (C—H•••N/O/X) interactions, the C—H•••Cl interaction has attracted interest in the broad field of materials chemistry, C—H activation, ion transport, anion recognition, and in constructing molecular architectures [35–43]. For a superior C—H•••Cl interaction, the H•••Cl distance should be less than the sum of the van der Waals radii (2.95 Å) of the hydrogen atom and the neutral chlorine atom [44]. In this work such distances are in the range of 2.49 to 2.83 Å.

Terpyridines or polypyridines have been widely explored as chelating ligands for d-block metal ions for their strong electron affinity [45–48]. Oligopyridine motifs can be utilized to prepare highly stable metal complexes [49]. Terpyridine based metal complexes have drawn keen interest in contemporary research in the fields of supramolecular chemistry and this knowledge is extended to application of material science [50,51]. They have

interesting magnetic and optoelectronic properties like electrocatalysis, hydrogen evolution, *etc.* [52–59]. Terpyridine metal complexes are also employed as the active layer to fabricate resistive switching memory devices, fluorescent probes for pyrophosphate (PPi) detection, and photo-functional nanomaterials [60–66]. Specially, Cu(II) complexes containing heterocyclic ligands have received increasing attention because of their promising applications in catalysis, energy harvesting devices as well as in medicinal chemistry within the last decades [67–74]. Being the third most abundant transition metal (after iron and zinc) in the human body, copper plays an important role in hemopoiesis, metabolism, growth and immune system [75,76]. Additionally, compared to other common metal ions, Cu(II) ion exhibits high binding constant with various ligands [77,78].

Considering the importance of the terpyridine metal complex systems, two Cu(II) complexes have been prepared using newly synthesized 4-(1-methylimidazole)-2,6-di(pyrazinyl)pyridine as terpyridine ligand (**NL**). The synthesis and characterization of the ligand (**NL**) has been discussed in chapter II (see Experimental Section). Complex **1** is formed by reacting with $CuCl_2.2H_2O$ and **NL** in aqueous medium whereas complex **2** is synthesized by treating of $Cu(NO_3)_2.3H_2O$ with **NL** in presence of hydrochloric acid in water. Both the complexes have been synthesized strategically so that at least one chloride ion should be attached with the metal centers. Single-crystal X-ray analysis shows that complex **1** adopts a distorted square pyramidal geometry where complex **2** is a distorted octahedral. It is noted that the change in the auxiliary anion exhibits structural variations in the present complexes substantially. In complex **1**, two different 2D arrangements are observed through intermolecular π•••π stacking and C─H•••Cl hydrogen bonding interactions. Besides, a 2D layer is observed by only C─H•••Cl hydrogen bonding interactions. Complex **2** exhibits a 1D polymeric chain (through nitrate bridge) which was extended utilizing π•••π and hydrogen bonding (C─H•••O, C─H•••Cl) interactions. The 2D fingerprint plots associated with the Hirshfeld surfaces facilitate a comparison of non-classical hydrogen bonding interactions by quantifying them in an effective visual manner. The present work combines experiment and theory (DFT calculations) to explore the non-covalent interactions and their interplay leading the solid state architectures of complex **1** and **2**. The MEP (molecular electrostatic potential) surface analysis also agrees well with the ability of both the complexes to establish the non-classical C─H•••N/O/Cl hydrogen bonding interactions in the solid state. In particular, the influence of π•••π stacking interactions along with the existence of C─H•••Cl hydrogen bonds triggered by terminal M─Cl bonds have been well established in the self assembly of both the complexes.

3.2. EXPERIMENTAL SECTION

3.2.1. Materials and apparatus

All the chemical reagents (analytical grade) and solvents (spectroscopic grade) are procured from commercial suppliers and used as received. Freshly prepared doubly distilled water was used throughout the synthetic procedure and all the reactions were carried out under aerobic conditions. Elemental analyses (C, H and N) were performed using a PerkinElmer 2400 Series-II CHN analyzer, USA elemental analyzer. Fourier transform infrared (FTIR) spectra were recorded on a Perkin Elmer LX-1 FT-IR spectrophotometer (4000−400 cm^{-1}) by using a modern diamond attenuated total reflectance (ATR) accessory.

3.2.2. Synthesis of [Cu(NL)Cl$_2$] (Complex 1)

An aqueous suspension (15 mL) of the ligand, **NL** (0.315 g, 1.0 mmol) was added drop wise to an aqueous solution (15 mL) of CuCl$_2$.2H$_2$O (0.170 g, 1.0 mmol) with constant stirring for 3 hours (Scheme 3.1) when a bright green coloured solution was resulted. The solution was then filtered and the filtrate was kept undisturbed for slow evaporation. After one week, light green X-ray quality crystals of **1** were obtained from the mother liquor (yield: 68%). Solubility of the complex was checked in various solvents for further applications and found to be insoluble in water but partly soluble in acetonitrile and methanol whereas completely soluble in DMSO and DMF. Anal. calc. for C$_{17}$H$_{13}$N$_7$CuCl$_2$: C, 45.40; H, 2.91; N, 21.80. Found: C, 45.35; H, 2.88; N, 21.76%. Main FTIR absorptions, (KBr, cm^{-1}): 3345(bs), 3093(s), 3022(s), 1609(vs), 1557(s), 1495(s), 1463(vs), 1438(s), 1410(s), 1316(s), 1296(s), 1278(vs), 1223(s) (Fig. 3.1).

3.2.3. Synthesis of [Cu(NL)(Cl)(μ-ONO$_2$)]$_n$ (Complex 2)

Complex **2** was synthesized by reacting Cu(NO$_3$)$_2$.3H$_2$O (0.241 g, 1.0 mmol) with the title ligand, **NL**,(0.315 g, 1.0 mmol) in water (30 mL) at 60°C with constant stirring. After around two hours of constant stirring the reaction mixture became turbid, the turbidity was removed by the addition of few drops of dilute hydrochloric acid and the reaction mixture was stirred continuously for another one hour (Scheme 3.1). The resultant solution was then filtered and the filtrate was left without any disturbance. Suitable single crystals for X-ray analysis were obtained after three weeks (yield: 62%). The complex **2** was insoluble in water, partly soluble in methanol and completely soluble in DMSO, DMF as well as in acetonitrile. Anal. calc. for C$_{17}$H$_{13}$N$_8$CuClO$_3$: C, 42.87; H, 2.75; N, 23.52. Found: C, 42.83; H, 2.71; N, 23.49%. Main FTIR absorptions, (KBr, cm^{-1}): 3213(w), 3118(s), 3094(s), 3058(s), 3030(s), 1986(s),

1748(s), 1608(vs), 1591(s), 1557(vs), 1469(s), 1446(s), 1434(s), 1402(s), 1372(s), 1318(s) (Fig. 3.1).
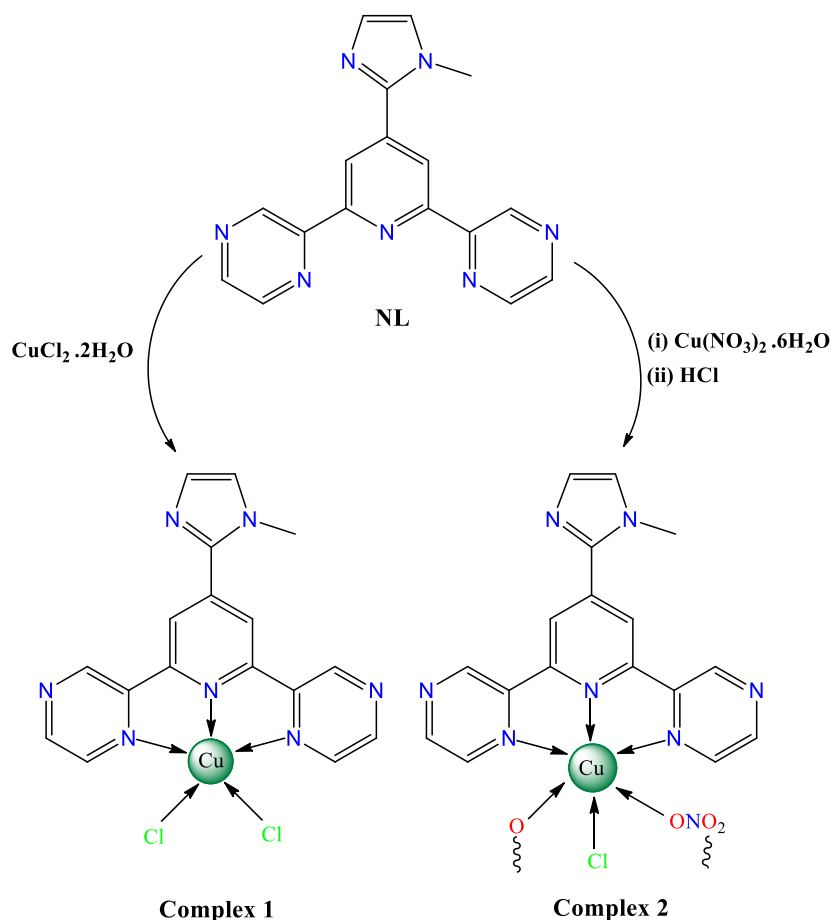
Scheme 3.1. Schematic representations of the synthesis of complexes **1** and **2**.
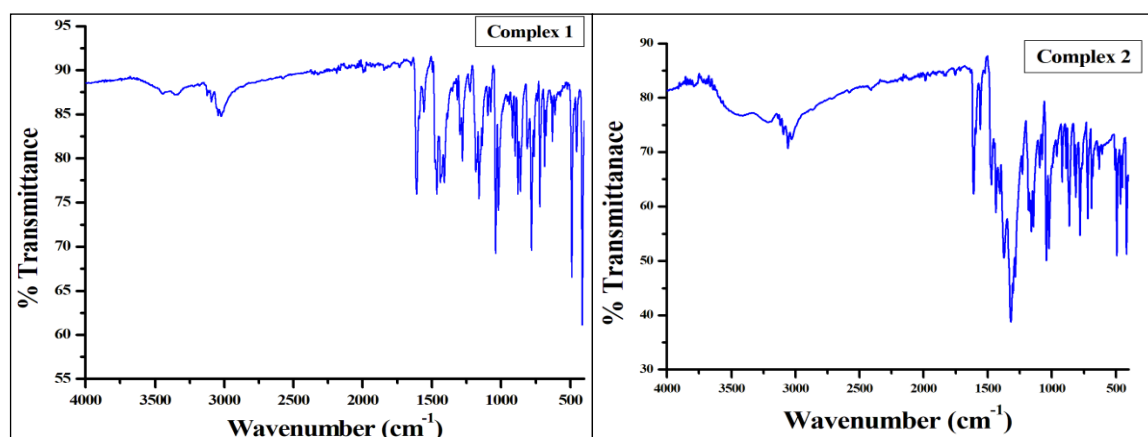
Fig. 3.1. FT-IR spectra for complexes **1** and **2**.

3.2.4. X-ray crystallographic analysis

Single crystal X-ray data of both the complexes were collected using a Bruker SMART APEX II CCD area detector equipped with a graphite monochromated Mo Ka radiation (λ = 0.71073 Å) source in φ and ω scan mode at 273(2) K. Cell parameter refinement and data

reduction were carried out using a Bruker SMART APEX II instrument and Bruker SMART and Bruker SAINT Software [79] for both the complexes. The crystal structures of both the complexes were solved by SHELXT-2014/5 and refined by full-matrix least squares on F^2 techniques using the SHELXL-2016/6 crystallographic software package [80,81]. CCDC 2107292 (for **1**) and 2107293 (for **2**) contain the supplementary crystallographic data for this work. Selected crystal data for complex **1** and complex **2** are given in Table 3.1.

Table 3.1. Crystal data and structure refinement parameters for complexes 1 and 2

Structure	Complex 1	Complex 2
Empirical formula	$C_{17}H_{13}N_7CuCl_2$	$C_{17}H_{13}N_8CuClO_3$
Formula Weight	449.79	476.35
Temperature (K)	273(2)	273(2)
Wavelength (Å)	0.71073	0.71073
Crystal system	Orthorhombic	Orthorhombic
space group	P $2_12_12_1$	P $2_12_12_1$
a, b, c (Å)	7.0900(5), 15.0538(11), 16.4613(12)	6.9172(9), 15.1342(19), 17.174(2)
α, β, γ (°)	90, 90, 90	90, 90, 90
Volume (Å^3)	1756.9(2)	1797.9(4)
Z / Density (calc.) (Mg/m^3)	4 / 1.701	4 / 1.760
Absorption coefficient (mm^{-1})	1.566	1.405
F(000)	908.0	964.0
Crystal size (mm^3)	$0.09 \times 0.14 \times 0.19$	$0.08 \times 0.13 \times 0.19$
θ range for data collection	1.833 to 27.169	1.794 to 27.173
Completeness to θ (%)	100%	100%
Absorption correction	Multi-scan	Multi-scan
Max. and min. transmission	0.869 and 0.769	0.894 and 0.803
Refinement method	Full-matrix least-squares on F^2	Full-matrix least-squares on F^2
Data/parameters	3883 / 288	3979 / 272
Goodness-of-fit on F^2	0.790	0.883
Final R indices [I > 2σ(I)]	R$_1$ = 0.0223, wR$_2$ = 0.0756	R$_1$ = 0.0348, wR$_2$ = 0.1067
R indices (all data)	R$_1$ = 0.0265, wR$_2$ = 0.0881	R$_1$ = 0.0383, wR$_2$ = 0.1122
Largest diff. peak and hole (e.Å^{-3})	0.644 and -0.850	0.485 and -0.382

$R_1=\sum||F_o|-|F_c||/\sum|F_o|$, wR$_2 = [\sum\{(F_o^2-F_c^2)^2\}/\sum\{w(F_o^2)^2\}]^{1/2}$ $w = 1/\{\sigma^2(F_o^2) + (aP)^2 + bP\}$, $P = (F_o^2 + 2F_c^2)/3$ where, a =0.1000, b =0.2438 for complex **1** and a =0.1000, b = 0.8005 for complex **2**.

3.2.5. Hirshfeld surface analysis

Hirshfeld surfaces [82–84] and the associated two-dimensional (2D) fingerprint [85–87] plots were obtained using Crystal Explorer [88] with bond lengths to hydrogen atoms set to standard values. Two distances, d_e (the distance from the point to the nearest nucleus external to the surface) and d_i (the distance to the nearest nucleus internal to the surface), are defined for each point on the Hirshfeld surface. The normalized contact distance (d_{norm}) based on d_e and d_i is defined as:

$$d_{norm} = \frac{(d_i - r_i^{vdw})}{r_i^{vdw}} + \frac{(d_e - r_e^{vdw})}{r_e^{vdw}}$$

where r_i^{vdw} and r_e^{vdw} are the van der Waals radii of the atoms. The d_{norm} value is negative or positive depending on intermolecular contacts being shorter or longer than the van der Waals separations. The parameter d_{norm} displays a surface with a red-white-blue colour design, where bright red spots highlight shorter contacts, white areas in the same surface correspond to contacts around the van der Waals separation and blue regions are devoid of close contacts. For a given CIF, the Hirshfeld surface is said to be unique [89].

3.2.6. Computational methods

The non-covalent interactions were analysed energetically using Gaussian-16 at the PBE0-D3/def2-TZVP level of theory [90]. The binding energies have been corrected using the Boys and Bernardi counterpoise method [91]. The Grimme's D3 dispersion correction has been also used in the calculations [92]. To evaluate the interactions in the solid state, the crystallographic coordinates were used and only the position of the hydrogen bonds has been optimized. This methodology and level of theory has been previously used to analyze non-covalent interactions in the solid state [93,94]. The interaction energies were estimated by calculating the difference between the energies of the isolated monomers and the ones of their assembly. The NCI plot [95] isosurfaces have been used to characterize non-covalent interactions. They correspond to both favourable and unfavourable interactions, as differentiated by the sign of the second density Hessian eigenvalue and defined by the isosurface colour. The colour scheme is a red-yellow-green-blue scale with red for ρ^+_{cut} (repulsive) and blue for ρ^-_{cut} (attractive). The Bader's [96] Quantum Theory of "atoms-in-molecules" (QTAIM) was also used to characterize the interactions. For these calculations, the same level of theory and the program AIMAll have been used [97].

3.2.7. Tau (τ) parameter calculation for complex 1

The structures with five coordination number can have either square pyramidal or triangular bipyramidal geometry around the metal center. In order to discriminate between these two geometries, tau (τ) parameter was proposed by Addison and co-workers [98]. According to this, the τ parameter ranges between 0 and 1 at the extreme values giving a perfect square pyramidal and triangular bipyramidal structures, respectively. The closer the τ parameter to 0, the more similar it is to square pyramidal geometry.

$$\tau = (\beta - \alpha) / 60 \text{ ……….. (1)}$$

Where, β is the first greatest angle and α is the second greatest angle of the coordination center.

For complex **1:** $\beta = 157.23(10)$, and $\alpha = 144.19(7)$ (Table 2). Hence, calculated value of $\tau = 0.217$.

3.3. RESULTS AND DISCUSSION

3.3.1. Structural description of complex 1

The asymmetric unit of complex **1** with the atom numbering scheme is shown in Fig. 3.2. The complex crystallizes in an orthorhombic system with the space group $P2_12_12_1$ and its unit cell comprises of four complex units. The selected bond lengths (Å) and bond angles (°) are scheduled in Table 3.2. Complex **1** shows one mononuclear [Cu(**NL**)Cl$_2$] unit where tridentate ligand, **NL** is a 4-(1-methylimidazole)-2,6-di(pyrazinyl)pyridine molecule. The coordination mode around the metal center can be best described as a distorted square pyramid (the τ value is 0.217, see equation 1) where the three pyrazinyl nitrogen atoms (N4, N5 and N6) of the title ligand (**NL**) and one chloride ion (Cl1) generate the basal plane while the axial position is occupied by another chloride ion (Cl2). The average Cu─N bond distance is 2.026 Å [Cu1─N4 = 2.051(2) Å, Cu1─N5 = 1.963(2) Å and Cu1─N6 = 2.064(2) Å]. The axial chloride (Cl2) is positioned somewhere at a longer distance [Cu1─Cl2 = 2.3629(10)Å] than the equatorial one [Cu1─Cl1 = 2.2495(9)Å] likely due to the less 's' character of the orbital engaged in the coordination bond, which makes the axially coordinated chloride anion more electronegative (stronger hydrogen bond acceptor) [43]. The Cu(II) ion is shifted by a distance of 0.437 Å towards the axial Cl2 atom from the basal plane (N4, N5, N6 and Cl1). The imidazole ring is twisted by an angle of 34.81° from the plane of central pyridine ring of the title ligand, **NL**. The electrical charge on the Cu(II) ion is compensated by two coordinated chloride ions (Cl1 and Cl2).
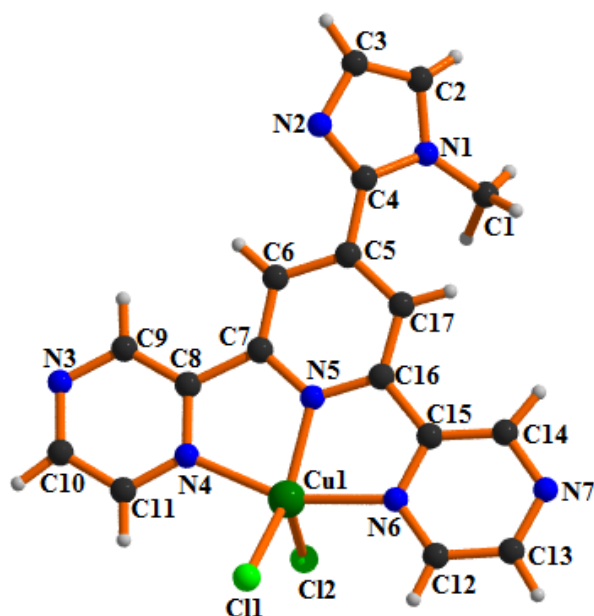
Fig. 3.2. Asymmetric unit of complex **1**.

Table 3.2. Selected bond distances [Å] and bond angles (°) for complex 1

Bonds	Distance (Å)	Bond angles	Value (°)
Cu1—Cl1	2.2495(9)	Cl1—Cu1—Cl2	110.32(3)
Cu1—Cl2	2.3629(10)	Cl1—Cu1—N4	94.99(8)
Cu1—N4	2.051(2)	Cl1—Cu1—N5	144.19(7)
Cu1—N5	1.963(2)	Cl1—Cu1—N6	99.45(8)
Cu1—N6	2.064(2)	Cl2—Cu1—N4	97.91(8)
		Cl2—Cu1—N5	105.48(7)
		Cl2—Cu1—N6	93.48(8)
		N4—Cu1—N5	79.20(9)
		N4—Cu1—N6	157.23(10)
		N5—Cu1—N6	78.79(9)

The complex units of **1** form a one dimensional polymeric chain (ladder type) through the self-complementary π•••π interactions (Table 3.3) between Cg(3) of one unit with Cg(5) of the other unit and *vice versa*. The interplanar separation distances between consecutive Cg(3) and Cg(5) centroids are 3.5021(18) Å and 3.6867(18) Å but the alternate distances are same. Interestingly, the parallel chains are oriented in such a manner that hydrogen H13 (attached with pyrazine C13) of one unit faces the Cl2 atom at (-1/2+x, 3/2-y, 2-z) of the other unit forming hydrogen bonding interaction (shown by green dotted lines)which generates a 2-D supramolecular framework(wave like) in the *ac*-plane (Fig. 3.3).
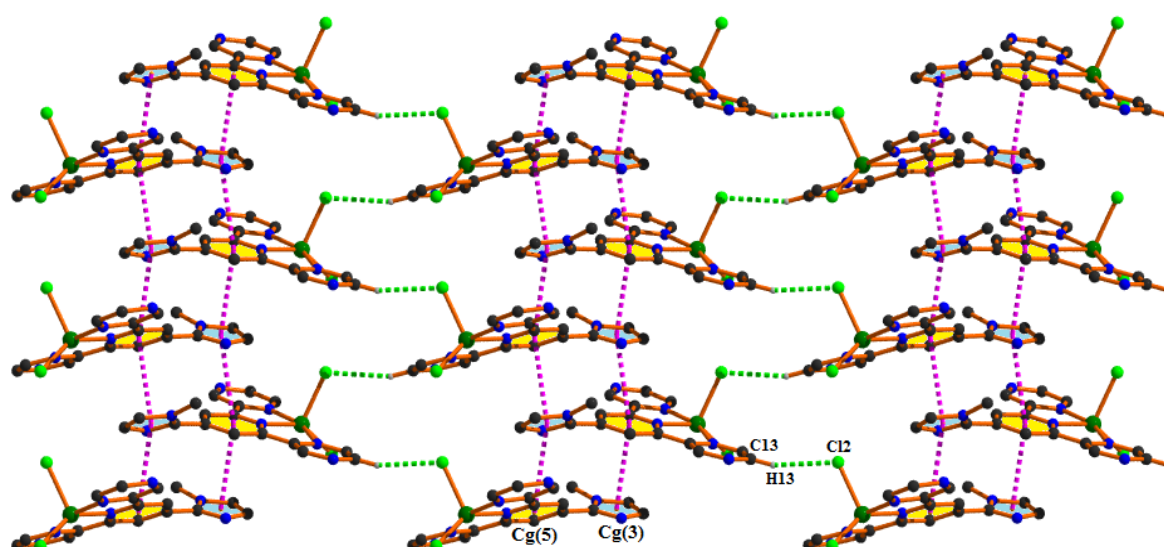
Fig. 3.3. Perspective view of 2-D architecture (wave like) incorporating π•••π and C—H•••Cl hydrogen bonding interactions in complex **1**(other aromatic hydrogen atoms have been omitted for clarity).

Table 3.3. Geometrical parameters (Å, °) for the π-stacking interactions for complex 1

Cg(i)•••Cg(j)	Cg(i)•••Cg(j) [Å]	α (°)	β (°)	γ (°)	Cg(i) – perp [Å]	Cg(j) – perp [Å]	Symmetry
Cg(3)[1]•••Cg(5)	3.6866(18)	2.71	25.29	26.00	3.313	3.333	-1/2+x,3/2-y,1-z
Cg(3)[1]•••Cg(5)	3.5021(18)	2.71	11.40	10.17	3.447	3.433	1/2+x,3/2-y,1-z
Cg(4)[1]•••Cg(6)	3.958(2)	22.80	19.20	41.05	2.985	3.738	-x,-1/2+y,3/2-z
Cg(5)[1]•••Cg(3)	3.5020(18)	2.71	10.17	11.40	3.433	3.447	-1/2+x,3/2-y,1-z
Cg(5)[1]•••Cg(3)	3.6867(18)	2.71	26.00	25.29	3.333	3.313	1/2+x,3/2-y,1-z
Cg(6)[1]•••Cg(4)	3.958(2)	22.80	41.05	19.20	3.738	2.985	-x,1/2+y,3/2-z

Cg(i) and Cg(j) denotes centroid of ith and j^{th} ring respectively. For complex **1**: Cg(3) is the centroid of [N1/C2/C3/N2/C4] ring; Cg(4) is the centroid of [N3/C9/C8/N4/C11/C10] ring; Cg(5) is the centroid of [N5/C7/C6/C5/C17/C16] ring; and Cg(6) is the centroid of [N6/C12/C13/N7/C14/C15] ring.

Table 3.4. Geometrical parameters for the hydrogen bonds of complex 1

D—H•••A	D—H [Å]	H•••A [Å]	D•••A [Å]	D—H•••A [°]	Symmetry
C6—H6•••Cl1	0.9300	2.8200	3.741(3)	171.00	1/2-x, 1-y, -1/2+z
C9—H9•••Cl1	0.92(3)	2.55(3)	3.464(3)	176(3)	1/2-x, 1-y, -1/2+z
C10—H10•••Cl2	0.97(5)	2.76(5)	3.567(3)	142(4)	1-x, -1/2+y, 3/2-z
C13—H13•••Cl2	0.98(3)	2.83(3)	3.770(3)	162(3)	-1/2+x, 3/2-y, 2-z
C14—H14•••Cl1	0.99(5)	2.80(5)	3.651(3)	145(4)	-x, 1/2+y, 3/2-z
C17—H17•••Cl1	0.93(4)	2.81(4)	3.682(3)	157(3)	-x, 1/2+y, 3/2-z

Another 2-D layer is shaped in complex **1** using π•••π and hydrogen bonding interactions (Fig. 3.4). Firstly, a one dimensional (1-D) zigzag polymeric chain is formed by the π•••π interaction between Cg(4) of one complex unit and Cg(6) of the other unit with a ring centroid separation of 3.958(2) Å (Table 3.3). Now, the intermolecular hydrogen bond [C10─H10•••Cl2] connects the parallel chains at (1-x, -1/2+y, 3/2-z) to form the 2-D supramolecular network in the *ab*-plane. The existence of C─H•••Cl interactions triggered by charge-assisted terminal M─Cl bonds, has been well referred in recent times [43,99].
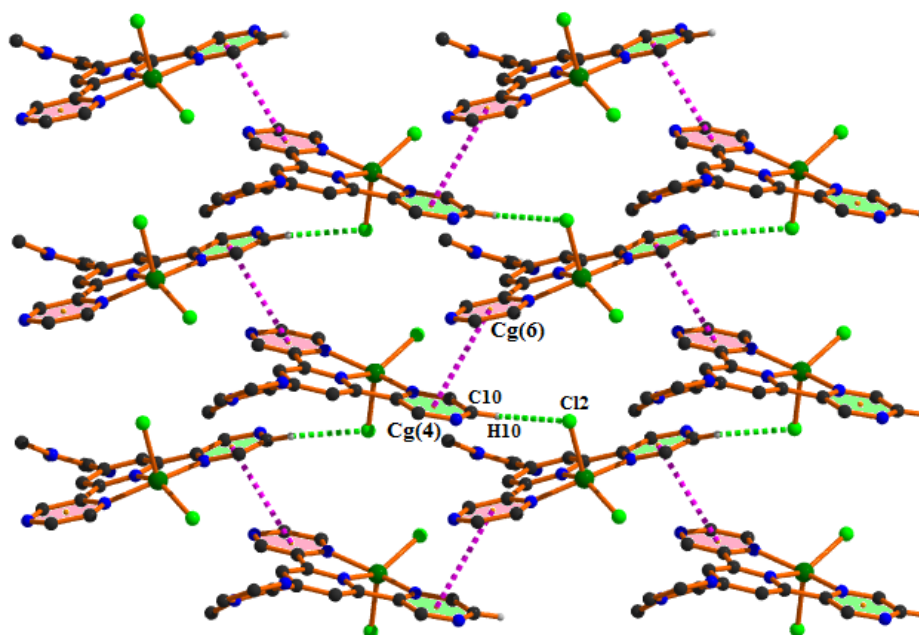
Fig. 3.4. 2-D layer generated through π•••π and C─H•••Cl hydrogen bonding interactions in complex **1**(other aromatic hydrogen atoms have been omitted for clarity).

The formation of a 2-D supramolecular architecture (Fig. 3.5) is ensured by various C─H•••Cl interactions (Table 3.4). Through a closer look it is evident that the mononuclear units are propagated to form a 1-D polymeric chain through two intermolecular hydrogen bonding [C6─H6•••Cl1 at an angle of 171° and C9─H9•••Cl1 at an angle of 176(3)°] interactions (shown by pink dotted lines) incorporating the terminal chloride ion (Cl1). In association with these intermolecular hydrogen bonding interactions other two intermolecular hydrogen bonding [C14─H14•••Cl1 at an angle of 145(4)° and C17─H17•••Cl1 at an angle of 157(3)°] interactions(shown by green dotted lines) are involved to extend the dimensionality to 2-D in the *ac*-plane.

In addition, a 1D chain is generated through C1─H1C•••Cl2 interactions as depicted in Fig. 6. Here, the methyl C1─H1C acts as a donor to the axial Cl2 atom (stronger H bond acceptor).
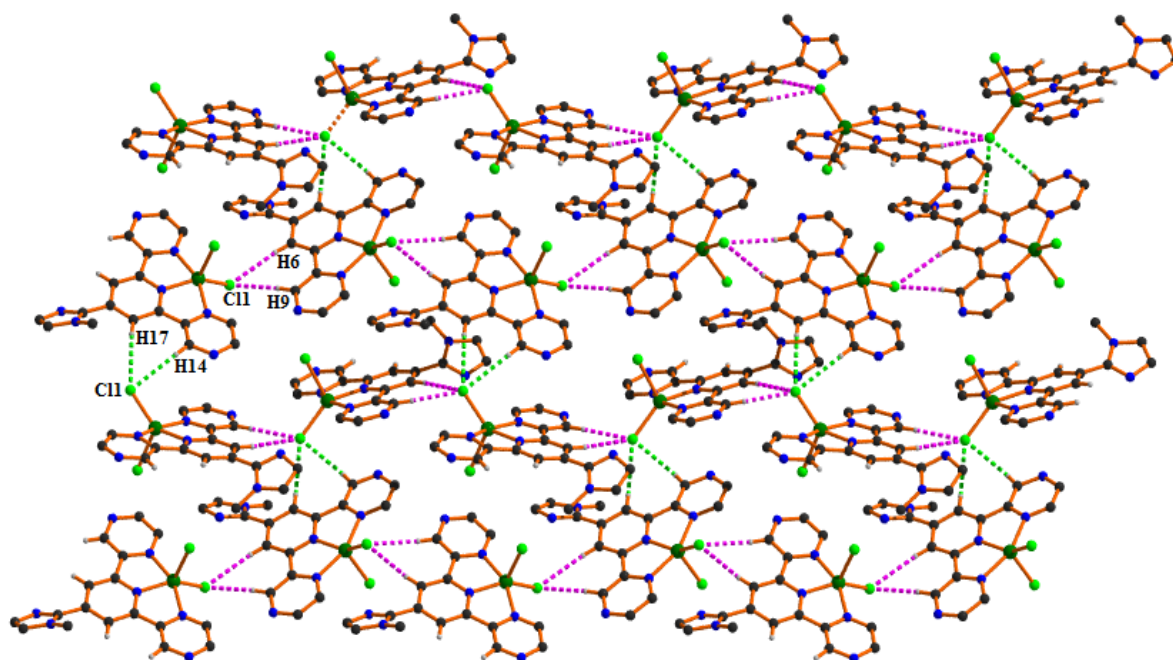
Fig. 3.5. Formation of 2-D network comprising C─H•••Cl hydrogen bonding interactions in complex **1** (other aromatic hydrogen atoms have been omitted for clarity).
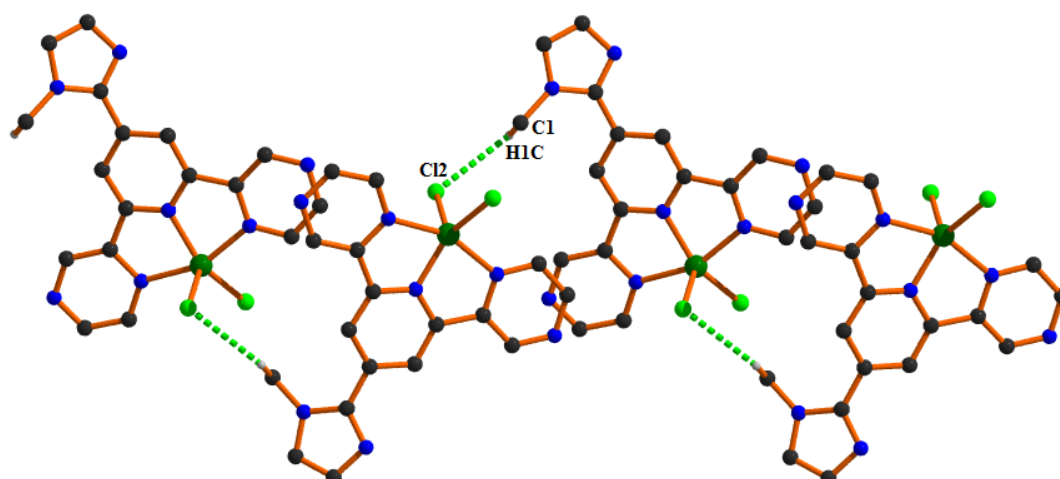
Fig. 3.6. Propagation of 1D chain along [010] direction by C─H•••Cl hydrogen bonding interactions in complex **1** (other aromatic hydrogen atoms have been omitted for clarity).

3.3.2. Structural description of complex 2

Complex **2** is basically a 1D coordination polymer (Fig. 3.7) and the perspective view of the asymmetric unit of the complex with atom numbering scheme is shown in Fig. 3.7. Single-crystal X-ray diffraction study shows that the complex adopts an orthorhombic system with the space group *P2₁2₁2₁* and its unit cell contains four complex units. The important bond lengths (Å) and bond angles (°) are included in Table 3.5. In this complex, the nitrate anion connects the Cu(II) centres along [100] direction by utilizing two different oxygen atoms (O1

and O2) to form the 1D polymeric chain. Here, the 1D chain can be classified within a 2C1 topological type [100,101]. The central Cu(II) ion is situated in a distorted octahedral geometry where the basal plane is formed by the three pyrazinyl nitrogen atoms (N4, N5 and N6) of the title ligand (**NL**) and one chloride ion (Cl1). The *trans* axial positions are occupied by two oxygen atoms (O1 and O2) of the nitrate ion. In the basal plane, the Cu—N bond lengths vary from 1.938(3) to 2.049(3) Å, whereas the axial Cu—O bond lengths [2.498(5)Å and 2.641(4) Å] are much longer than the equatorial bond lengths, suggesting a pronounced Jahn−Teller effect. The imidazole ring is twisted by an angle of 24.41° from the plane of central pyridine ring of the title ligand, **NL**. The electrical charge on the metal center is stabilized by one coordinated chloride ion and one coordinated nitrate (NO_3^-) ion.

Fig. 3.7. One-dimensional (1-D) zigzag polymeric chain along the [010] direction and the asymmetric unit of Complex **2**.

In the complex **2**, the parallel chains are interconnected in a zigzag fashion through π••π interaction between Cg(4) and Cg(6) of two units to generate a supramolecular framework in *ab*-plane (Fig. 3.8). The ring centroid separation between Cg(4) and Cg(6) is 3.826(3) Å (Table 3.6).

Table 3.5. Selected bond distances [Å] and bond angles (°) for complex 2

Bonds	Distance (Å)	Bond angles	Value (°)
Cu1─Cl1	2.1922(13)	Cl1─Cu1─O1	102.68(12)
Cu1─O1	2.498(5)	Cl1─Cu1─N4	97.18(10)
Cu1─N4	2.031(3)	Cl1─Cu1─N5	170.47(11)
Cu1─N5	1.938(3)	Cl1─Cu1─N6	103.20(10)
Cu1─N6	2.049(3)	Cl1─Cu1─O2_b	90.11(15)
Cu1─O2_b	2.641(4)	O1─Cu1─N4	97.98(15)
		O1─Cu1─N5	86.77(15)
		O1─Cu1─N6	79.06(14)
		O1─Cu1─O2_b	152.10(17)
		N4─Cu1─N5	79.98(13)
		N4─Cu1─N6	159.58(13)
		O2_b─Cu1─N4	104.97(17)
		N5─Cu1─N6	79.67(13)
		O2_b─Cu1─N5	81.91(18)
		O2_b─Cu1─N6	73.88(17)

b = 1+x, y, z
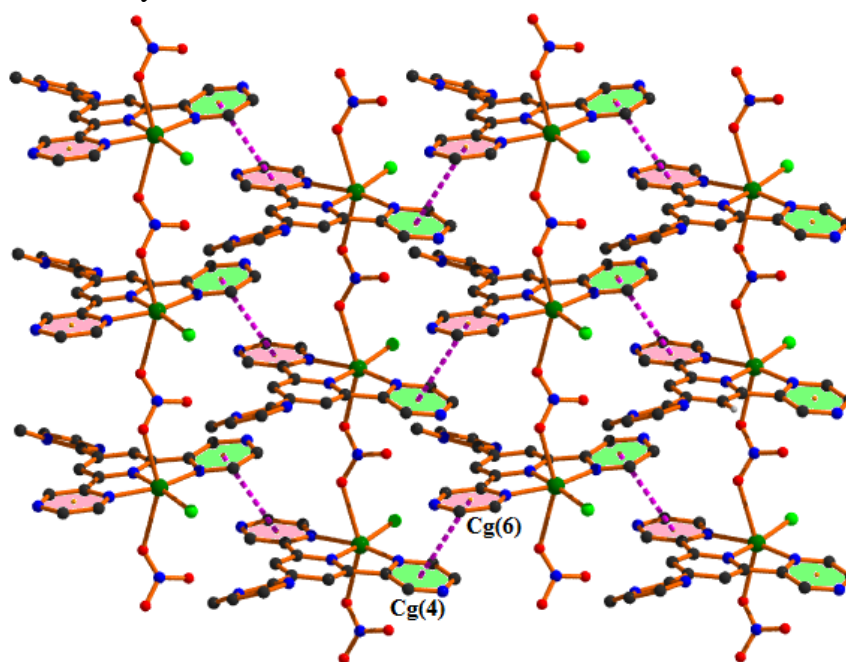
Fig. 3.8. Perspective view of 2-D architecture through π•••π interactions in complex **2** (other aromatic hydrogen atoms have been omitted for clarity).

In another architecture (Fig. 3.9), the parallel chains are interconnected through C14─H14•••O3 hydrogen bonding interaction (Table 3.7) forming a two-dimensional (2-D) supramolecular network which is further strengthened by the C─H•••Cl hydrogen bond at (2-x, 1/2+y, 1/2-z) between the coordinated chlorine atom (Cl1) and methyl hydrogen atom (H1B) of the adjacent molecule (as depicted in Fig. 3.9).
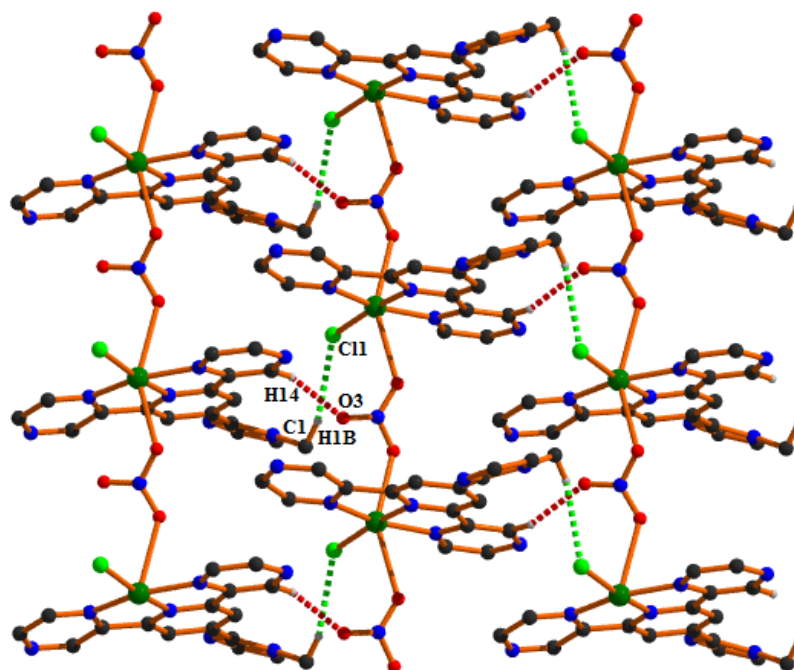
Fig. 3.9. Perspective view of 2-D architecture generated through C─H•••Cl and C─H•••O hydrogen bonding interactions in complex **2** (other aromatic hydrogen atoms have been omitted for clarity).

Table 3.6. Geometrical parameters (Å, °) for the π-stacking interactions for complex 2

Cg(i)•••Cg(j)	Cg(i)•••Cg(j) [Å]	α (°)	β (°)	γ (°)	Cg(i)–perp [Å]	Cg(j)–perp [Å]	Symmetry
Cg(3)[1]•••Cg(5)	3.733(3)	8.82	21.64	19.55	3.518	3.470	-1/2+x,3/2-y,1-z
Cg(3)[1]•••Cg(5)	3.905(3)	8.82	35.72	31.68	3.323	3.170	1/2+x,3/2-y,1-z
Cg(4)[1]•••Cg(6)	3.826(3)	12.83	22.32	34.29	3.161	3.539	2-x,-1/2+y,1/2-z
Cg(5)[1]•••Cg(3)	3.905(3)	8.82	31.68	3.170	35.72	3.323	-1/2+x,3/2-y,1-z
Cg(5)[1]•••Cg(3)	3.733(3)	8.82	19.55	21.64	3.470	3.518	1/2+x,3/2-y,1-z
Cg(6)[1]•••Cg(4)	3.825(3)	12.83	34.29	22.32	3.538	3.160	2-x,1/2+y,1/2-z

Cg(i) and Cg(j) denotes centroid of ith and j[th] ring respectively. For complex **2**: Cg(3) is the centroid of [N1/C2/C3/N2/C4] ring; Cg(4) is the centroid of [N3/C9/C8/N4/C11/C10] ring; Cg(5) is the centroid of [N5/C7/C6/C5/C17/C16] ring; and Cg(6) is the centroid of [N6/C12/C13/N7/C14/C15] ring.

This 2D architecture (Fig. 3.9) is further stabilized through the non-classical C─H•••O hydrogen bonding and intramolecular anion•••π interactions synergistically as shown in Fig. 3.10. Here the π-lobes of pyrazine have been oriented in such a fashion so that it could able to form the above mentioned intramolecular anion•••π interaction with nitrate O3 atom that in turn reinforce to form the C1─H1B•••O3 hydrogen bonding interaction and play a pivotal role from supramolecular perspective in the solid state architecture of complex **2**.

Table 3.7. Geometrical parameters for the hydrogen bonds of complex 2

D─H•••A	D─H [Å]	H•••A [Å]	D•••A [Å]	D─H•••A [°]	Symmetry
C1─H1B•••Cl1	0.9600	2.7600	3.611(6)	148.00	2-x, 1/2+y, 1/2-z
C9─H9•••Cl1	0.9300	2.4900	3.409(5)	168.00	3/2-x, 1-y, 1/2+z
C3─H3•••O2	0.9300	2.5500	3.221(8)	129.00	1/2+x,3/2-y,1-z
C14─H14•••O3	0.9300	2.2300	3.073(7)	151.00	1-x, 1/2+y, 1/2-z
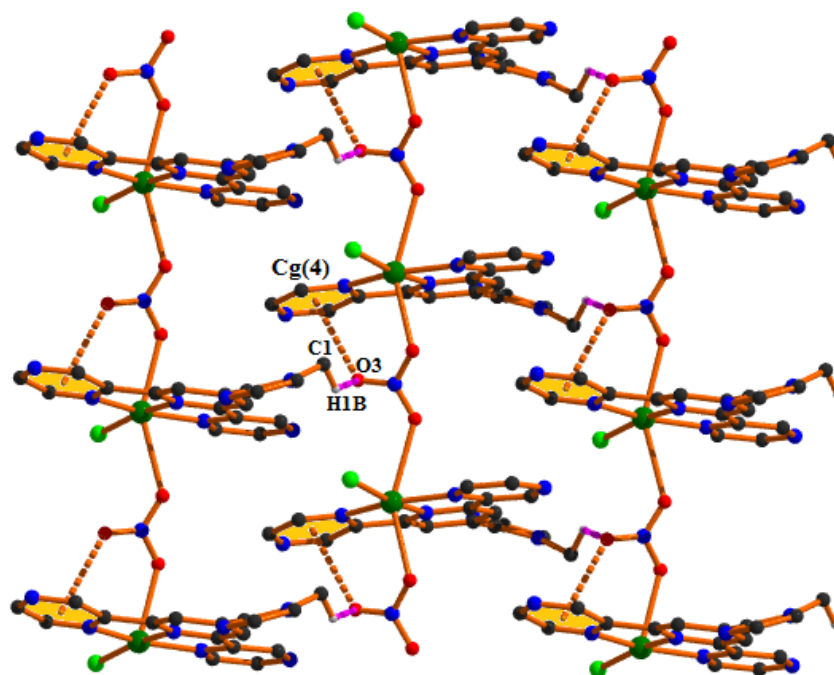
Fig. 3.10. Perspective view of 2D architecture through C─H•••O hydrogen bonding and intramolecular anion•••π interactions in complex **2** (other aromatic H atoms have been omitted for clarity).

Due to their self-complementary nature, complex units (extracted from the polymeric chain) are interconnected along [100] direction through π•••π stacking interactions to form a 1-D zigzag chain. Here, the complex units are arranged in a face-to-face fashion to avail the π•••π stacking interaction between Cg(3) and Cg(5) of two units. As the crystal structure of complex **2** is departed from the ideal planarity, the Cg(3)─Cg(5) distances are not identical [3.733(3) Å and 3.905(3) Å] (Table 3.6). But, the alternate interplanar separation distances between Cg(3) and Cg(5) units are the same in the 1-D zigzag chain. Now, these parallel chains are interlinked by the C9─H9•••Cl1 (168°) hydrogen bond at (3/2-x, 1-y, 1/2+z) to build the 2-D (*ac*-plane) network (Fig. 3.11) which is further extended in the *bc*-plane. Now, these two planes are repeating themselves to enhance the dimensionality from 2-D to 3-D (Fig. 3.12).
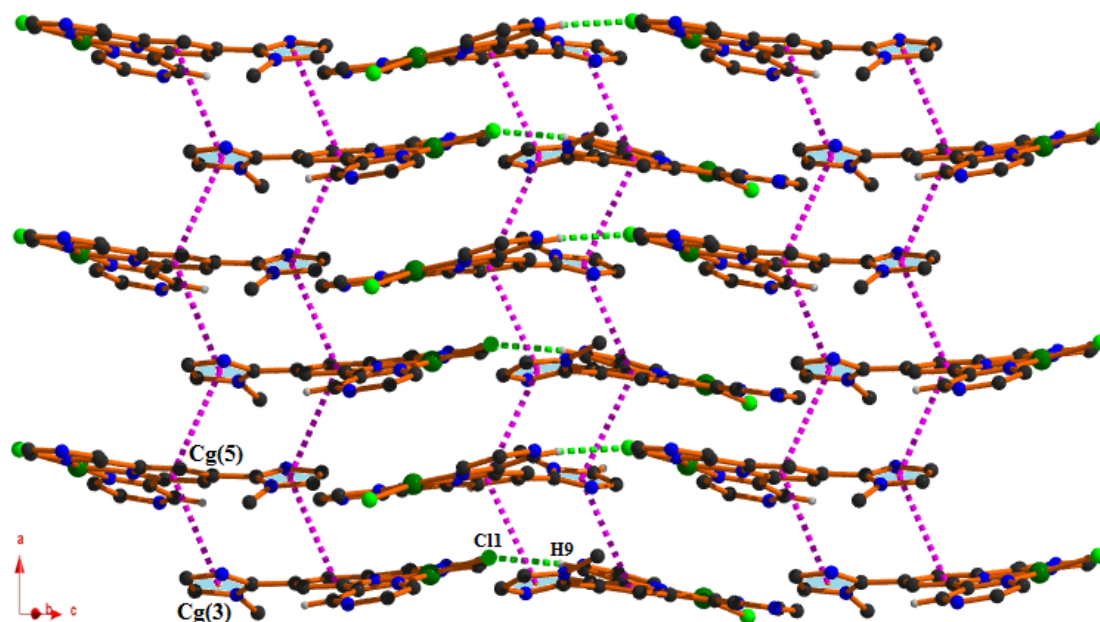
Fig. 3.11. Perspective view of 2-D network generated through π•••π and hydrogen bonding interactions in complex **2**(axial bonds and other aromatic hydrogen atoms have been omitted for clarity).
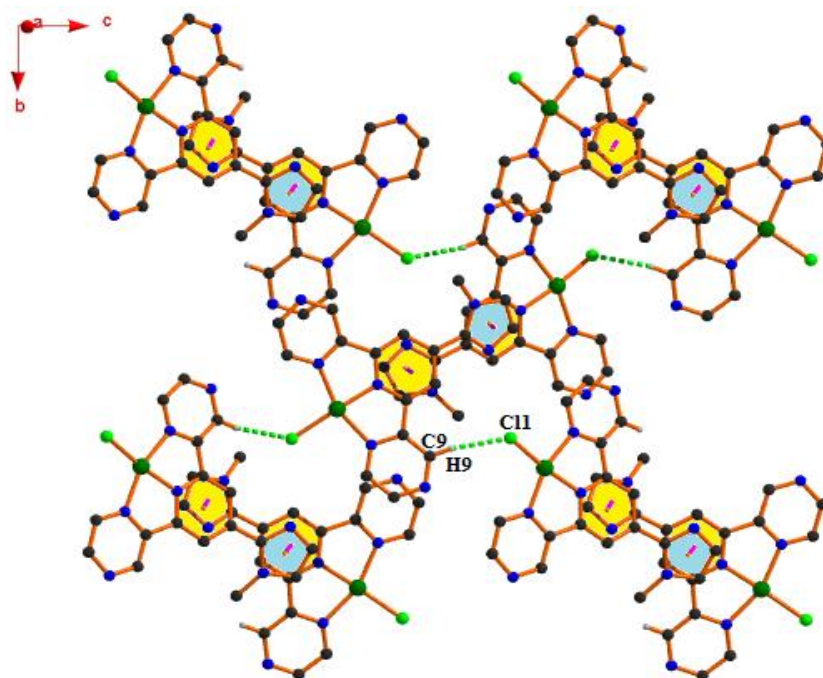
Fig. 3.12. Formation of extended network in the *bc*-plane in complex **2** (axial bonds and other aromatic hydrogen atoms have been omitted for clarity).

Besides, it was observed that the polymeric chains are interconnected in a self-complementary manner through C3─H3•••O2 hydrogen bonding interactions at (1/2+x, 3/2-y, 1-z) to generate a 1D tape along the [100] direction (Fig. 3.13). This molecular integrity

(1D tape) has been stabilized in collaboration with a comparatively weak C1—H1C•••N2 hydrogen bonding interactions.
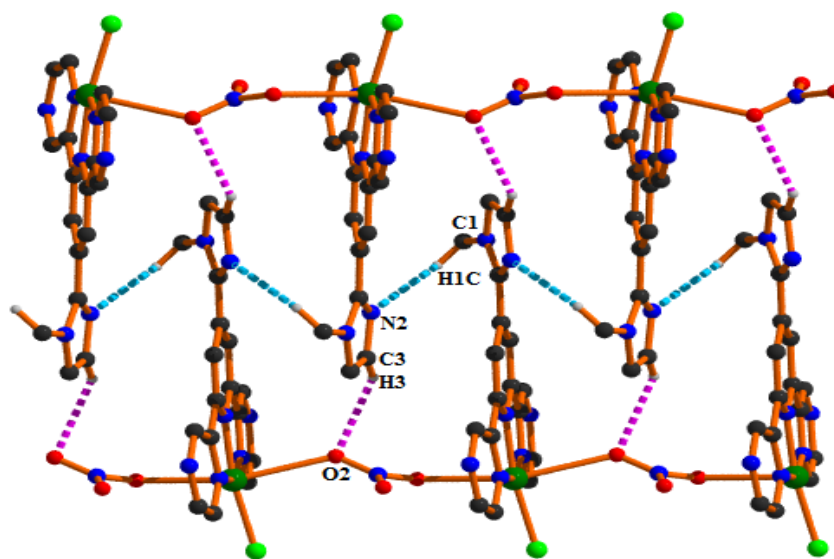
Fig. 3.13. Formation of a 1D tape through C—H•••N and C—H•••O hydrogen bonding interactions in complex **2** (other aromatic hydrogen atoms have been omitted for clarity).

3.3.3. A brief comparison on structural and supramolecular features of some related Cu(II) complexes available in structural database

In this regard a brief comparative review has been carried out on the crystallographic and supramolecular aspects of some related Cu(II) complexes derived from substituted terpyridine ligands reported earlier (Table 3.8 and Table 3.9 respectively). The 4′ substitution on terpyridine moiety was made by 4-pyridyl (**3**), phenyl (**4**), benzoic acid (**5**), 2-pyridyl (**6**), 3-pyridyl (**7**), quinoline-2-yl (**8**), quinoline-4-yl (**9**) in comparison to the present 1-methylimidazole analogue (**1** and **2**). Here, it is interesting to note that these substituents do not participate in direct coordination with the metal ions but may impart some electronic inputs so that their ability to participate in supramolecular interactions may vary. Except complex **2**, all other complexes reported in Table 8 are distorted square pyramidal (as evident from Addison parameter, τ). Among all square pyramidal complexes except **4** and **5**, the ligands act as a N_3Cl_2 donor chromophore where all the three nitrogens came from terpyridine part and one chloride occupy equatorial positions. Finally, the square pyramidal geometry was completed by coordination with another chloride ion axially. In complex **4**, one of the outer pyrazinyl-N atoms takes part in further complexation and forms a square planar moiety (as N_2Cl_2) around another Cu(II) that in turn forms a discrete trinuclear complex rather than a coordination polymer. In complex **5**, the equatorial positions were occupied by

three nitrogens from terpyridine part and one oxygen atom from benzoic acid moiety. In comparison to other reported complexes (**3–9**), the complex (**1**) shows a maximum deviation of central Cu(II) ion from the basal plane (0.437 Å) and results in the shortest axial Cu─Cl bond length (2.363 Å) among **1–9**.

Table 3.8. A brief comparison of structural features of substituted terpyridine derived Cu(II) complexes

Complex	Geometry	Donor chromophore(s)	Axial bond length(s) (Å)	Shifting of central metal from basal plane (Å)	Reference
$C_{20}H_{15}Cl_2CuN_7$ (**3**)	Square pyradimal (τ=0.018)	N_3Cl_2	2.421	0.320	102
$C_{38}H_{26}Cl_6Cu_3N_{10}$ (**4**)	Square pyradimal (τ=0.013) and square planner	N_3Cl_2 and N_2Cl_2	2.491	0.310	103
$C_{20}H_{12}ClCuN_5O_2$, 2.25(H_2O) (**5**)	Square pyradimal (τ=0.27)	N_3OCl	2.507	0.117	104
$C_{18}H_{12}Cl_2CuN_6$ (**6**)	Square pyradimal (τ=0.034)	N_3Cl_2	2.464	0.328	105
$C_{18}H_{12}Cl_2CuN_6$ (**7**)	Square pyradimal (τ=0.064)	N_3Cl_2	2.443	0.353	105
$C_{22}H_{16}Cl_2CuN_6O$ (**8**)	Square pyradimal (τ=0.014)	N_3Cl_2	2.508	0.316	67
$C_{23}H_{18}Cl_2CuN_6O$ (**9**)	Square pyradimal (τ=0.090)	N_3Cl_2	2.444	0.335	67
$C_{17}H_{13}N_7CuCl_2$ (**1**)	Square pyradimal (τ=0.217)	N_3Cl_2	2.363	0.437	Present work
$C_{17}H_{13}N_8CuClO_3$ (**2**)	Distorted octahedral	N_3O_2Cl	2.498 and 2.641	0.082	Present work

Here in all other reported complexes (**3–9**), the substituent bears a six membered ring and in the present work a five membered ring (1-methylimidazole) has been strategically used. The five membered ring may put some stereo-electronic restriction at the square plane so that the

central Cu(II) ion is shifted maximum toward axial chloride with respect to that in the analogous six membered ring substitution and consequently results in the shortest axial Cu─Cl distance.

Substitution on terpyridine moiety not only affects the geometry of the coordination complex but also controls self-assembly process [67]. From supramolecular point of view it was evident that in all complexes (mentioned in Table 3.9) π•••π and C─H•••Cl interactions play a crucial role in forming the solid state architectures.

Table 3.9. A brief comparison of π•••π and C─H•••Cl hydrogen bonding interactions in substituted terpyridine derived Cu(II) complexes

Complex	π•••π distance(s) (Å)	H•••Cl distance(s) (Å)	References
$C_{20}H_{15}Cl_2CuN_7$ (**3**)	3.6894(16), 3.6139(17), 3.5590(18), 3.8731(18)	2.8200, 2.5900, 2.7600, 2.4400	102
$C_{38}H_{26}Cl_6Cu_3N_{10}$ (**4**)	3.377(3), 3.891(3), 3.908(3), 3.851(3)	2.7900, 2.8000, 2.6500, 2.5400	103
$C_{20}H_{12}ClCuN_5O_2$, 2.25(H_2O) (**5**)	3.7762(17)	2.6700	104
$C_{18}H_{12}Cl_2CuN_6$ (**6**)	3.518(3)	2.6500, 2.6700, 2.7300, 2.6200	105
$C_{18}H_{12}Cl_2CuN_6$ (**7**)	3.524(5), 3.815(4), 3.781(5), 3.740(5)	2.7300, 2.7800, 2.6600	105
$C_{22}H_{16}Cl_2CuN_6O$ (**8**)	3.6577(18), 3.8775(16), 3.6104(15)	2.7400, 2.7600, 2.8000	67
$C_{23}H_{18}Cl_2CuN_6O$ (**9**)	3.9847(13), 3.9986(14), 3.8486(15)	2.6100, 2.7100, 2.8200,	67
$C_{17}H_{13}N_7CuCl_2$ (**1**)	3.5020(18), 3.6867(18), 3.958(2)	2.55(3), 2.76(5), 2.80(5), 2.8200	Present work
$C_{17}H_{13}N_8CuClO_3$ (**2**)	3.733(3), 3.826(3), 3.905(3)	2.4900, 2.7600	Present work

The enhanced π electron density of terpyridine moiety acts as a electron rich zone that interacts with electron deficient π moiety (caused by coordination of nitrogens of the terpyridine ring) to form a π•••π stacking interaction. Generally, the C─H bond becomes silent in hydrogen bonding interactions except when electron withdrawing group is attached with carbon to make it electron deficient. The coordination of pyridine nitrogens to central Cu(II) ion makes the rings sufficiently electron deficient and introduces some protonic character to the H atom of the C─H bond that in turn exhibits several C─H•••Cl hydrogen bonding interactions found in the reported complexes (Table 3.9). The H•••Cl distance was found to be second shortest in complex **2** (2.49 Å) just next to that in complex **3** (2.44 Å)

among other complexes suggesting a strong C─H•••Cl interaction. The π•••π separations in this present work ranges 3.5020(18)─3.905(3) Å which are comparable to the tabulated complexes (**3–9**) (Table 3.9). Though the authors [67,102–105] reported the existence of π•••π and C─H•••Cl interactions, but any theoretical studies (DFT) along with MEP and NCI plot were not performed to quantify the interaction energies. Here, besides recognizing the structure guiding role of π•••π and C─H•••Cl interactions, the relevant theoretical studies have been successfully carried out mainly focusing on these interactions in the solid state.

3.3.4. Hirshfeld surface

The Hirshfeld surface of the title complexes were mapped over d_{norm} (range: −0.29 to 1.13 Å), d_i, d_e, shape index and curvedness (Fig.s 3.14 and 3.15). The surfaces were made transparent to enable visualization of the molecular moiety around which they are calculated.

Fig. 3.14. Hirshfeld surfaces mapped with (a) d_{norm} (b) d_e (c) d_i (d) shape-index and (e) curvedness for the complex **1**.

Furthermore, the 2D fingerprint plots represent all intermolecular interactions those are involved within the structures (Fig.s 3.16 and 3.17). To quantify each individual contact, the full-fingerprint plots in unique visual mode for both the complexes have been demonstrated. The intermolecular interactions appear as distinct spikes in the 2D fingerprint plot shows the different spikes with their corresponding interactions.

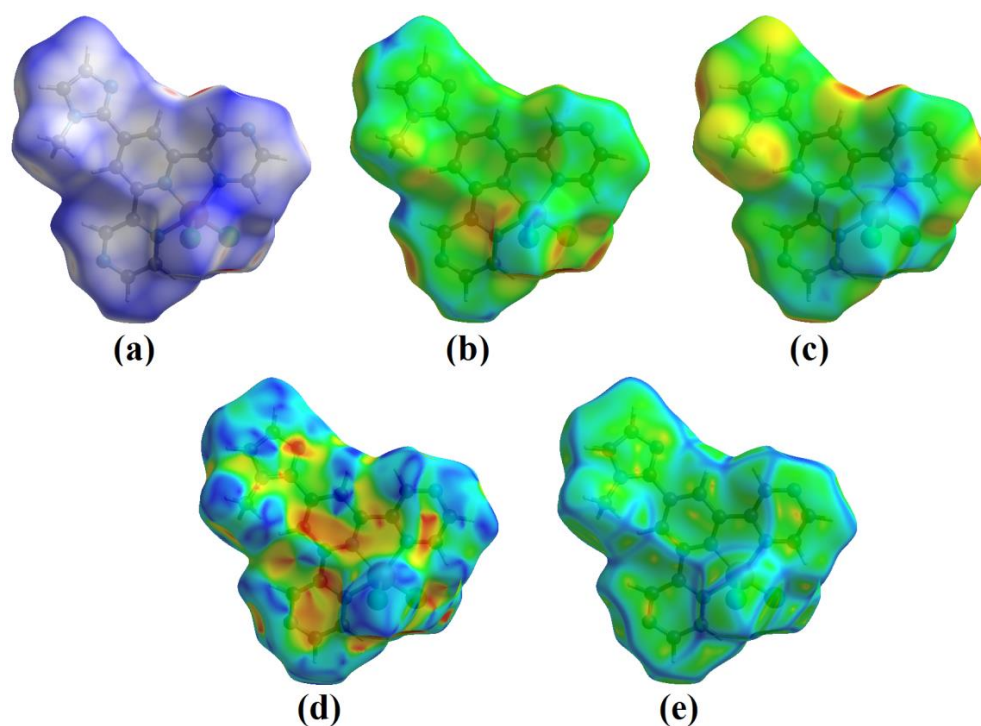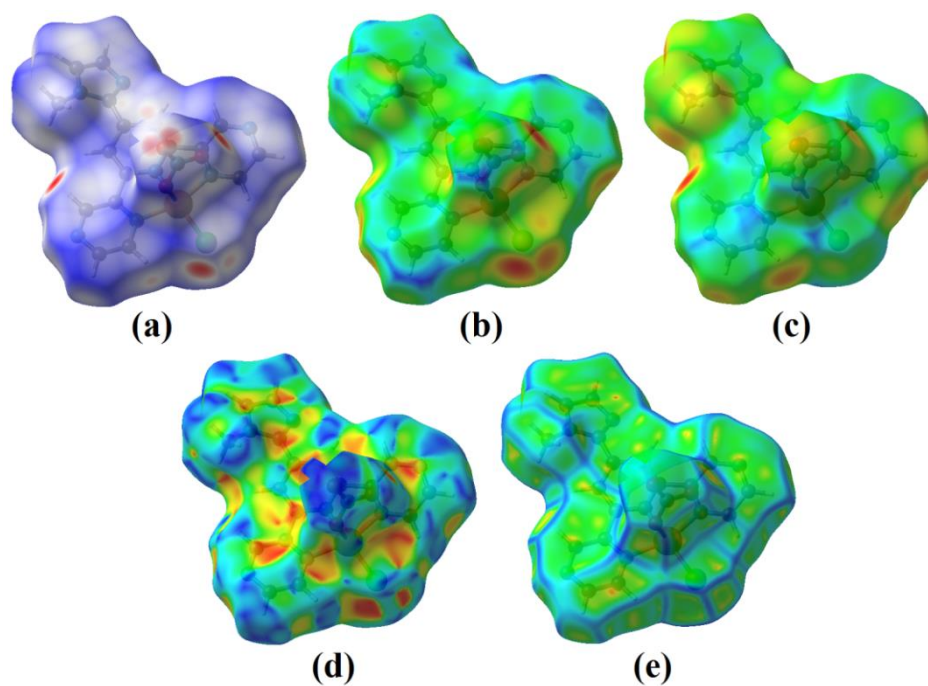**Fig. 3.15.** Hirshfeld surfaces mapped with (a) d_{norm} (b) d_e (c) d_i (d) shape-index and (e) curvedness for the complex **2**.
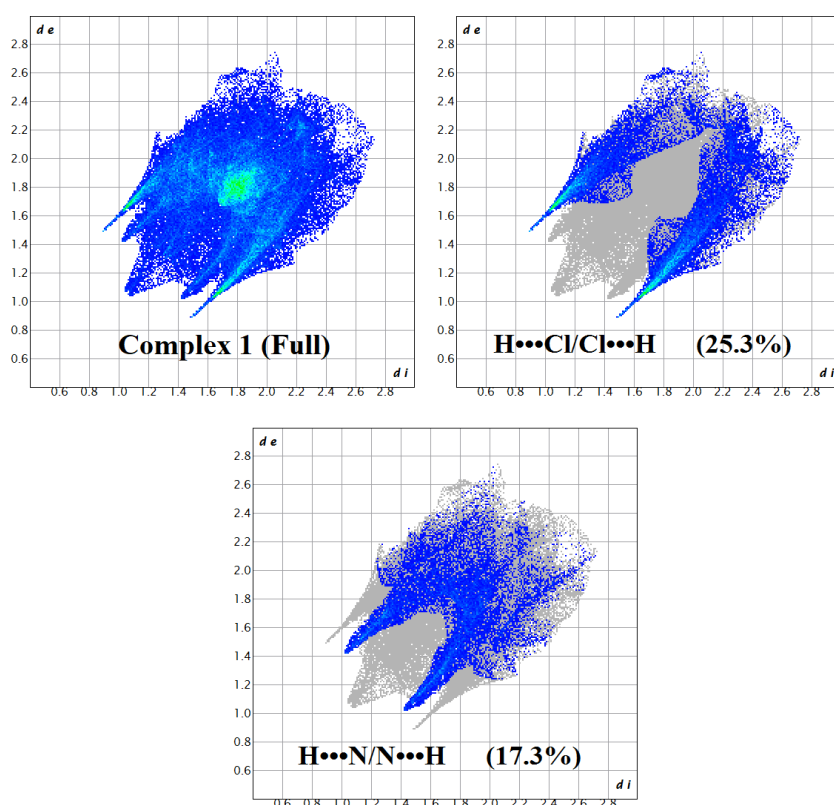
Fig. 3.16. Fingerprint plots (Full) and decomposed plots for each individual interaction in complex **1**.

The main non-classical hydrogen bonding interaction is observed for complex **1** between hydrogen and chlorine atoms. In complex **2**, the major interaction is obtained between hydrogen and oxygen atoms.

The H•••Cl/Cl•••H contacts contributed 25.3% in complex **1** whereas that contribution is 10.4% to the total Hirshfeld surface area for complex **2**. Other visible spot in Hirshfeld surface of complex **1** correspond to H•••N/N•••H contacts (17.3%). The proportions of H•••O/O•••Hand H•••N/N•••H interactions of the Hirshfeld surface of complex **2** comprise 19.1% and 15.9%, respectively (Fig. 3.17).
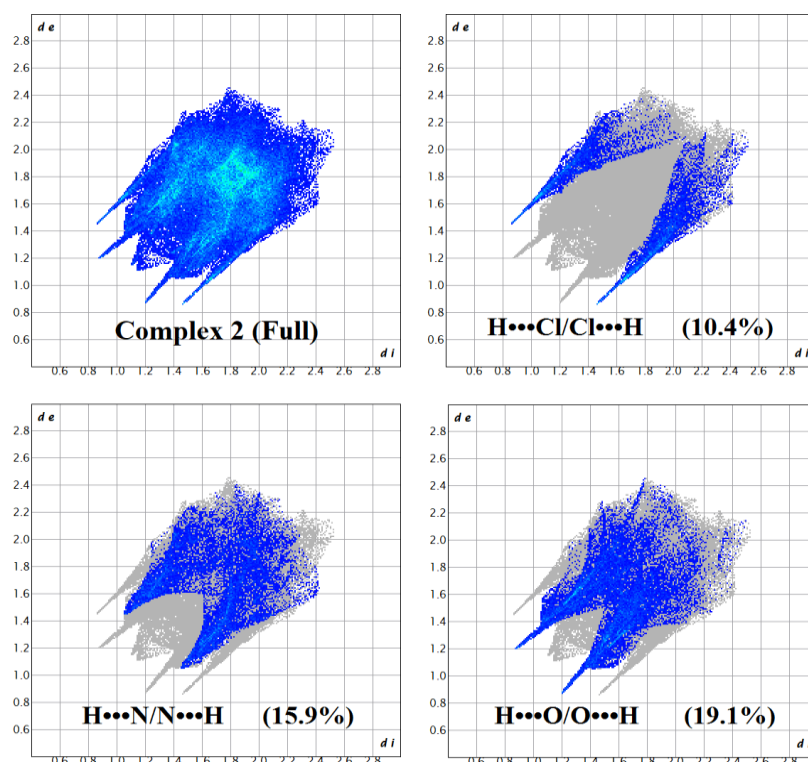
Fig. 3.17. Fingerprint plots (Full) and decomposed plots for each individual interaction in complex **2**.

3.3.5. Theoretical studies

PBE0-D3/def2-TZVP calculations have been used to analyze and rationalize the hydrogen-bonding and the π-stacking interactions described above in Fig.s 3.7−3.10 and Fig.s 3.12−3.17 that are relevant for the crystal packing of complexes **1** and **2**. The molecular electrostatic potential (MEP) surfaces of complex **1** and complex **2** (monomeric fragment) have been initially obtained to investigate the most electron poor and electron rich parts of the molecules (see Fig. 3.18). As expected, the most negative MEP values are located at the anionic co-ligands, that is the axial Cl in **1** and nitrate in **2** (–59.6 and –80.3 kcal/mol). The MEP values at the equatorial Cl atoms in **1** and **2** are –39.5 and –30.1 kcal/mol, respectively (see Figs. 3.18b, d), more positive than those at the axial positions. The MEP values at the

non-coordinated N-atoms of the organic ligand range from –16.9 to –22.9 kcal/mol in complexes **1** and **2**. In both complexes, the maximum MEP value (+49.5 kcal/mol in **1** and 55.0 kcal/mol in **2**) is located in a cleft that is under the influence of two aromatic H-atoms and one aliphatic H-atom (methyl group of the imidazole ring). The MEP values above and below the aromatic rings of the ligand are positive. Interestingly, they are significantly more positive in the side opposite to the axial ligand (ranging from +15 to +30 kcal/mol) than in the same side of the axial ligand (ranging from +5 to +15 kcal/mol. The MEP values over the accessible chelate rings are also positive and larger in complex **2**. The MEP surface analysis explains the ability of both complexes to establish CH•••X (X = N, O, and Cl) H-bonding interactions in the solid state.

As aforementioned in the structural description of **1** (Fig. 3.3), this complex forms π•••π interactions where the five membered ring of one complex is stacked over the central six-membered pyridine ring of the adjacent one and *vice versa*.

Fig. 3.18. Two "on-top" vies of the MEP surfaces (isosurface 0.001 a.u.) of complex **1** (a,b) and a monomeric model of complex **2** (c,d) at the PBE0-D3/def2-TZVP level of theory. The MEP values at selected points of the surfaces are given in kcal/mol.

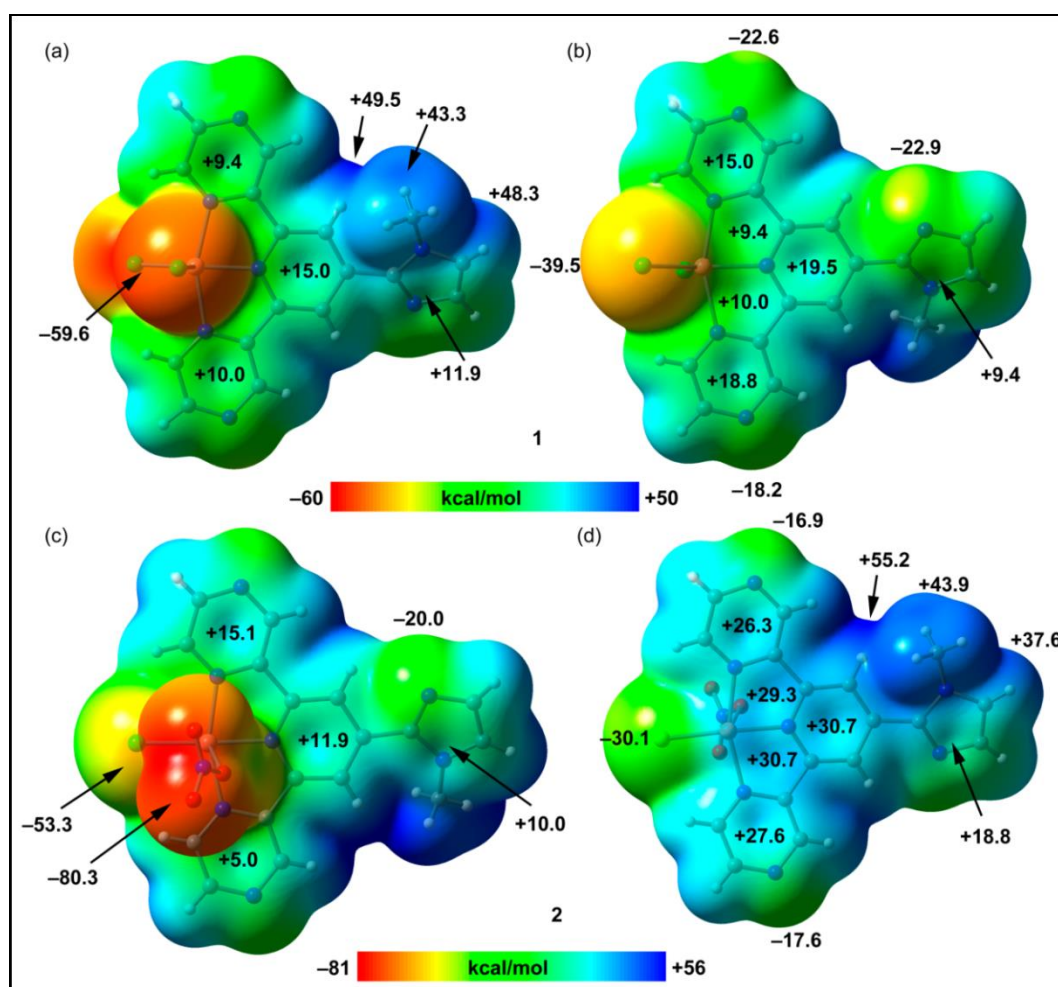In the present DFT study the main focus is on this interaction, where, in good agreement with the MEP surface analysis, the most π-acidic surface of the ligand interacts with the least acidic one to minimize the electrostatic repulsion.

Fig. 3.19a shows a dimer extracted from the solid state of complex **1** where, in addition to the π•••π interactions, two hydrogen bonding interactions (C–H•••N and C–H•••Cl) are formed. The dimerization energy is very large ($\Delta E_1 = -17.7$ kcal/mol) due to the contribution of both types of interactions (HB and π•••π). This assembly have also been analysed using a combination of QTAIM and NCI plot index computational methods since they are very convenient to reveal non-covalent interactions in real space. The NCI plot index is an intuitive visualization index that facilitates the visualization of non-covalent interactions and shows which molecular regions interact. The colour scheme is a red-yellow-green-blue scale with red (repulsive) and blue (attractive). Yellow and green surfaces correspond to weak repulsive and weak attractive interactions, respectively. The hydrogen-bonds are characterized by a bond critical point (represented as a red sphere), bond path connecting the H to the N or Cl-atoms. The green NCI plot isosurfaces that characterize the hydrogen-bonds are located between the H and N, Cl atoms coincident to the position of the bond CPs. The π•••π stacking interactions are characterized by two bond critical points (CPs) and bond paths connecting one N atom and one C-atom of the imidazole ring to two carbon atoms of the pyridine ring. Moreover, green and extended isosurfaces are located between the imidazole and pyridine rings, also confirming the existence of the π•••π stacking interactions.

Fig. 3.19. Combined QTAIM analysis (bond CPs in red) and NCI surfaces of the π-stacked (a) and CH_3•••Cl (b) assemblies of complex **1**. The gradient cut-off is ρ = 0.04 a.u., isosurface s = 0.5, and the colour scale is -0.04 a.u. $< (\text{sign}\lambda_2)\rho < 0.04$ a.u. only intermolecular contacts are shown.

Fig. 3.19b shows a similar QTAIM/NCI plot analysis performed for a different dimer extracted from the solid state. It has been studied to analyse the possibility of the formation of

a Cl•••CH₃ tetrel bonding interaction between the Cl atom and the C-atom of the methyl group. That is, one coordinated chlorine atom (Cl2) and the methyl carbon atom (C1) of imidazole ring have a separation distance of 3.332 Å, that is shorter than their sum of van der Waals radii (3.45 Å), thus suggesting the possibility of a C•••Cl tetrel bonding interaction, that has been described in similar systems [106–108]. However, the combined QTAIM/NCI plot analysis reveals that this interaction is more likely a C–H•••Cl hydrogen bond (the interaction is highlighted by a yellow circle in Fig. 3.19b) characterized by a bond CP, bond path and green isosurface located mostly between one H-atom of the methyl group and the Cl-atom. The NCI plot and QTAIM analyses also disclose the existence of π•••π stacking interactions between two pyrimidine rings and additional C–H•••Cl contacts characterized by the corresponding bond CPs and bond paths. The dimerization energy is similar ($\Delta E_2 = -19.7$ kcal/mol) to that of the other dimer and confirms the energetic significance of the π•••π stacking and C–H•••Cl interactions in the solid state of complex **1**.

A similar study has been performed in complex **2**. However, since complex **2** is a coordination polymer, dimeric models have been used extracted from the polymeric chain (see Fig. 3.20). The fact that similar assemblies are observed in the solid state of both complexes in spite of the polymeric nature of complex **2** and monomeric nature of **1** supports the relevance of both assemblies.
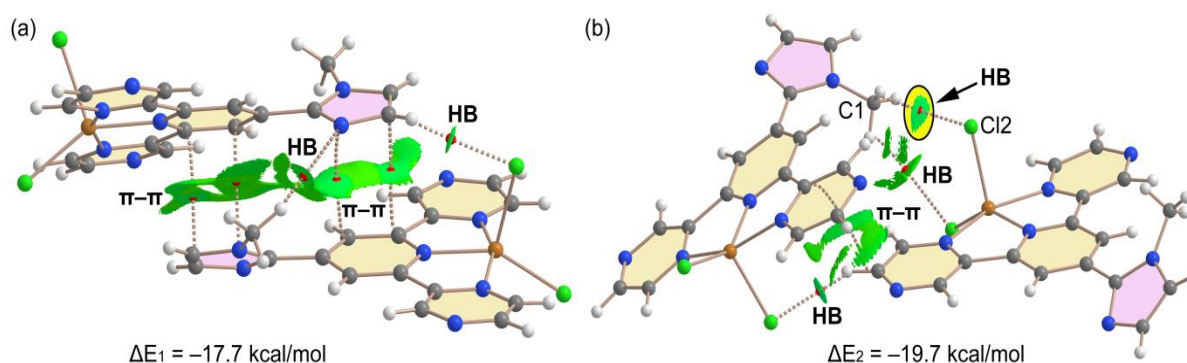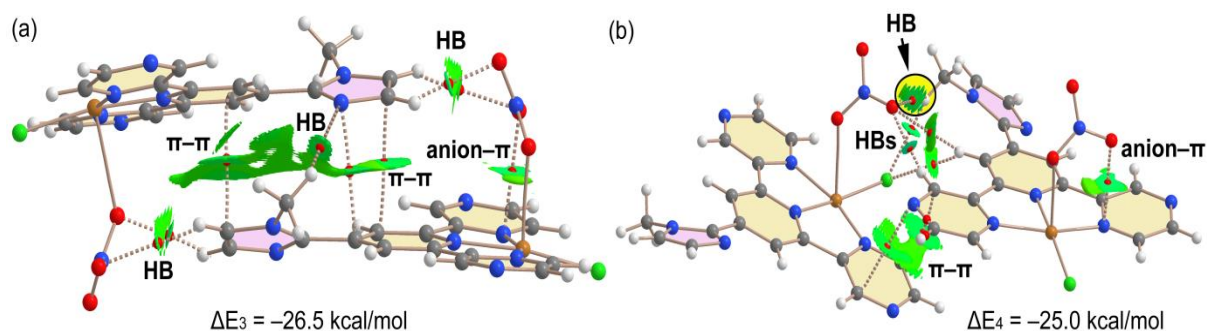

Fig. 3.20. Combined QTAIM analysis (bond CPs in red) and NCI surfaces of the π-stacked (a) and CH₃•••O (b) assemblies of complex **2**. The gradient cut-off is $\rho = 0.04$ a.u., isosurface s = 0.5, and the colour scale is -0.04 a.u. < (signλ₂)ρ < 0.04 a.u. only intermolecular interactions are shown apart from the anion–π interaction.

Fig. 3.20a shows the model π•••π dimer extracted from the solid state of complex **2** where, in addition to the π•••π interactions, a C–H•••N and four C–H•••O hydrogen bonding interactions are formed. This assembly is quite similar to the one discussed above for complex **1** (Fig. 3.19a). The dimerization energy is larger ($\Delta E_3 = -26.5$ kcal/mol) due to a major number of hydrogen bonds. The QTAIM and NCI plot index analyses reveal that the

π•••π stacking interactions are characterized by three bond critical points (CPs) and bond paths interconnecting the five and six membered rings of both complexes. Moreover, green and extended isosurfaces are located between the imidazole and pyridine rings, also confirming the existence and attractive nature of the π•••π stacking interactions.

In complex **2**, the possibility of the formation of an O•••CH$_3$X tetrel bonding interaction between the nitrate's O3 atom and the C-atom of the methyl group has also been analysed. In this case the O•••C distance is 3.313 Å, thus shorter than the sum of O and C van der Waals radii (3.22 Å). But, the combined QTAIM/NCI plot analysis reveals that this interaction is indeed a hydrogen bond (the interaction is highlighted by a yellow circle in Fig. 3.20b) characterized by a bond CP, bond path and green isosurface connecting the H-atom of the methyl group to the O-atom.

The NCI plot and QTAIM analyses also disclose the existence of π•••π stacking interactions between two pyrimidine rings and additional C–H•••O contacts characterized by the corresponding bond CPs and bond paths. The dimerization energy is similar (ΔE$_4$ = –25 kcal/mol) to that of the other dimer (Fig. 3.20a) and larger than the equivalent dimer of complex **1** Fig. 3.19b). This agrees well with the larger MEP values observed at the nitrato than at the chlorido anionic ligands in complexes **2** and **1** (Fig. 3.18).

It should be emphasized that in Figs. 3.19 and 3.20 only intermolecular interactions are represented apart from the intramolecular anion–π interaction observed in complex **2** (Fig. 3.20). This interaction is characterized by a bond CP connecting an O-atom belonging to nitrate and the N-atom of the pyrazine ring. The anion–π is also revealed by the NCI plot analysis that shows a medium size isosurface between the O-atom and the coordinated N-atom of the pyrazine ring. The isosurface extends toward two aromatic C-atoms and the Cu atom directly bonded to the N-atom.

3.4. CONCLUSION

In conclusion, two Cu(II) complexes (complexes **1** and **2**) have been synthesized using a newly synthesized 4-(1-methylimidazole)-2,6-di(pyrazinyl)pyridine (**NL**) moiety as the backbone ligand and characterized by spectroscopic and single crystal X-ray diffraction methods. The structural insights reveal that π•••π stacking and non-classical hydrogen bonding (C─H•••O, N, Cl) interactions play a key role in stabilizing the supramolecular architectures of both the complexes in the solid state. A thorough analysis of Hirshfeld surface and associated 2D fingerprint plots has been carried out to explore the nature of all those non-classical hydrogen bonding interactions and their relative contributions in building the supramolecular architectures.

The energetic features of these interactions have been analyzed by using DFT calculations and the intricate network of non-covalent contacts has been characterized by using a combination of QTAIM and NCI plot computational tools. The MEP values also have a good agreement to rationalize the π•••π stacking and CH•••X (X = N, O, and Cl) hydrogen bonding interactions for both the complexes in the solid state.

REFERENCES

1. J. J. Novoa, *Intermolecular Interactions in Crystals: Fundamentals of Crystal Engineering*, RSC, Cambridge, 2018.

2. A. Nangia and G. Desiraju, *Angew. Chem.*, 2019, **58**, 4100–4107.

3. J. T. Hupp, *Nat. Chem.*, 2010, **2**, 432.

4. A. S. Mahadevi and G. N. Sastry, *Chem. Rev.*, 2016, **116**, 2775–2825.

5. A. K. Ghosh, A. Hazra, A. Mondal and P. Banerjee, *Inorg. Chim. Acta*, 2019, **488**, 86–119.

6. M. Saccone L. Catalano, *J. Phys. Chem. B*, 2019, **123(44)**, 9281–9290.

7. R. Bu, Y. Xiong, X. Wei, H. Li and C. Zhang, *Cryst. Growth Des.*, 2019, **19**, 5981–5997.

8. R. Thakuria, N. K. Nath and B. K. Saha, *Cryst. Growth Des.*, 2019, **19**, 523–528.

9. A. S. Mahadevi and G. N. Sastry, *Chem. Rev.*, 2013, **113**, 2100–2138.

10. C. Zhao, P. Li, M. D. Smith, P. J. Pelle chia and K. D. Shimizu, *Org. Lett.*, 2014, **16**, 3520–3523.

11. C. Jia, H. Miao and B. P. Hay, *Cryst. Growth Des.*, 2019, **19**, 6806.

12. S. Pramanik, S. Pathak, S. Jana, M. Mondol, A. Frontera, and S. Mukhopadhyay, *New J. Chem.*, 2021**, 45**, 12108−12119.

13. D. A. Uhlenheuer, K. Petkau and L. Brunsveld, *Chem. Soc. Rev.*, 2010, **39**, 2817.

14. M. Kolle, P. M. Salgard-Cunha, M. R. J. Scherer, F. Huang, P. Vukusic, S. Mahajan, J. J. Baumberg and U. Steiner, *Nat. Nanotechnol.*, 2010, **5(7)**, 511–515.

15. J. Steed and J. L. Atwood, *Supramolecular Chemistry*, John Wiley, New York, 2001.

16. A. J. Neel, M. J. Hilton, M. S. Sigman and F. D. Toste, *Nature*, 2017, **543**, 637–646.

17. A. S. Mahadevi and G. N. Sastry, *Chem. Rev.*, 2016, **116**, 2775–2825.

18. R. R. Knowles and E. N. Jacobsen, *Proc. Natl. Acad. Sci. U. S. A.*, 2010, **107**, 20678–20685.

19. V. K. Pal, R. Jain and S. Roy, *Langmuir*, 2020, **36**, 1003–1013.

20. H. A. Nkabyo, I. Barnard, K. R. Koch and R. C. Luckay, *Coord. Chem. Rev.*, 2021, **427**, 213588–213611.

21. P. Mukherjee, M. G. B. Drew, C. J. Gomez-García and A. Ghosh, *Inorg. Chem.*, 2009, **48**, 5848–5860.

22. X. Zhang, L. Zhou, C. Wang, Y. Li, Y. Wu, M. Zhang and Q. Yin, *Cryst. Growth Des.*, 2017, **17**, 6151–6157.

23. Y. Hirao, S. Seo, and T. Kubo, *J. Phys. Chem. C*, 2019, **123**, 20928−20935.

24. Z. Yang, Y. Wang, X. Liu, R. T. Vanderlinden, R. Ni, X. Li and P. J. Stang, *J. Am. Chem. Soc.*, 2020, **142**, 13689−13694.

25. F. Biedermann and H. J. Schneider, *Chem. Rev.*, 2016, **116**, 5216–5300.

26. G. S. Nichol and W. Clegg, *Cryst. Growth Des.*, 2009, **9**, 1844–1850.

27. D. F. Back, M. Hörner, F. Broch and G. M. de Oliveira, *Polyhedron*, 2012, **31**, 558–564.

28. M. J. Ajitha and K.-W. Huang, *Synthesis*, 2016, **48**, 3449–3458.

29. L. M. Eytel, H. A. Fargher, M. M. Haley and D. W. Johnson, *Chem. Commun.*, 2019, **55**, 5195–5206.

30. M. Kumar and J. S. Francisco, *J. Am. Chem. Soc.*, 2020, **142**, 6001−6006.

31. G. R. Desiraju and T. Steiner, *The Weak Hydrogen Bond in Structural Chemistry and Biology*, Oxford Univ. Press, Oxford, 1999, chapter. 2 and 3.

32. R. C. Johnston and P. H.-Y. Cheong, *Org. Biomol. Chem.*, 2013, **11**, 5057–5064.

33. L. Brammer, E. A. Bruton and P. Sherwood, *Cryst. Growth Des.*, 2001, **1**, 277–290.

34. F. Zordan, L. Brammer and P. Sherwood, *J. Am. Chem. Soc.*, 2005, **127**, 5979–5989.

35. U. Bentrup, M. Feist and E. Kemnitz, *Prog. Solid State Chem.*, 1999, **27**, 75–129.

36. M. Albrecht, P. Dani, M. Lutz, A. L. Spek and G. van Koten, *J. Am. Chem. Soc.*, 2000, **122**, 11822–11833.

37. S. Chen, S. Zhang, C. Bao, C. Wang, Q. Lin and L. Zhu, *Chem. Commun.*, 2016, **52**, 13132–13135.

38. H. Juwarker, J. M. Lenhardt, D. M. Pham and S. L. Craig, *Angew. Chem., Int. Ed.*, 2008, **47**, 3740–3743.

39. B. W. Tresca, L. N. Zakharov, C. N. Carroll, D. W. Johnson and M. M. Haley, *Chem. Commun.*, 2013, **49**, 7240–7242.

40. J. Cai and J. L. Sessler, *Chem. Soc. Rev.*, 2014, **43**, 6198–6213.

41. A. C. Moro, F. W. Watanabe, S. R. Ananias, A. E. Mauro, A. V. G. Netto, A. P. R. Lima, J. G. Ferreira and R. H. A. Santos, *Inorg. Chem. Commun.*, 2006, **9**, 493–496.

42. W. Jacob and R. Mukherjee, *J. Chem. Sci.*, 2008, **120**, 447–453.

43. P. Pal, K. Das, A. Hossain, A. Frontera and S. Mukhopadhyay, *New J. Chem.*, 2020, **44**, 7310–7318.

44. G. Aullon, D. Bellamy, A. G. Orpen, L. Brammer and E. A. Bruton, *Chem. Commun.*, 1998, 653–654.

45. H. Zhu, J. Fan, B. Wang and X. Peng, *Chem. Soc. Rev.*, 2015, **44**, 4337–4366.

46. L. Zhang, C. -J. Li, J. -E. He, Y. -Y. Chen, S.-R. Zheng, J. Fan and W. -G. Zhang, *J. Solid State Chem.*, 2016, **233**, 444–454.

47. A. Bocian, D. Brykczyńska, M. Kubicki, Z. Hnatejko, M. Wałęsa-Chorab, A. Gorczyński and V. Patroniak, *Polyhedron*, 2019, **157**, 249–261.

48. C. E. Housecroft, and E. C. Constable, *Chem. Commun.*, 2020, **56**, 10786–10794.

49. A. Haque, R. Ilmi, I. J. Al-Busaidiand and M. S. Khan, *Coord. Chem. Rev.*, 2017, **350**, 320–339.

50. S. Chakraborty and G. R. Newkome, *Chem. Soc. Rev.*, 2018, **47**, 3991–4016.

51. Y. Wang, D. Astruc and A. S. Abd-El-Aziz, *Chem. Soc. Rev.*, 2019, **48**, 558–636.

52. C.-J. Yao, Y.-W. Zhong, H.-J. Nie, H. D. Abruña and J. Yao, *J. Am. Chem. Soc.*, 2011, **133**, 20720–20723.

53. N. Elgrishi, M. B. Chambers, V. Artero and M. Fontecave, *Phys. Chem. Chem. Phys.*, 2014, **16**, 13635–13644.

54. B. Das, A. Orthaber, S. Ott and A. Thapper, *Chem. Commun.*, 2015, **51**, 13074–13077.

55. K. Takada, R. Sakamoto, S.-T. Yi, S. Katagiri, T. Kambe and H. Nishihara, *J. Am. Chem. Soc.*, 2015, **137**, 4681–4689.

56. S. Elmas, W. Beelders, S. J. Bradley, R. Kroon, G. Laufersky, M. Andersson and T. Nann, *ACS Sustainable Chem. Eng.*, 2017, **5**, 10206–10214.

57. Y. Kuai, W. Li, Y. Dong, W.-Y. Wong, S. Yan, Y. Dai and C. Zhang, *Dalton Trans.*, 2019, **48**, 15121–15126.

58. S. K. Padhi, E. Ahmad, S. Rai, and B. Panda, *Polyhedron*, 2020, **187**, 114677–114690.

59. S. Rai, S. K. Padhi, *Electrochim. Acta*, 2020, **364**, 137277–137291.

60. J.-H. Tang, T.-G. Sun, J.-Y. Shao, Z.-L. Gong and Y.-W. Zhong, *Chem. Commun.*, 2017, **53**, 11925–11928.

61. P. Wang, H. L. Wang, Y. Fang, H. Li, J. H. He, J. Y. Ji, Y. Y. Li, Q. F. Xu, J. W. Zheng and J. M. Lu, *ACS Appl. Mater. Interfaces*, 2017, **9**, 32930–32938.

62. S. Y. Jiao, K. Li, W. Zhang, Y. H. Liu, Z. Huang and X. Q. Yu, *Dalton Trans.*, 2015, **44**, 1358–1365.

63. D. Chao and S. Ni, *Sci. Rep.*, 2016, **6**, 1–8.

64. V. D. Singh, R. S. Singh, R. P. Paitandi, B. K. Dwivedi, B. Maiti and D. S. Pandey, *J. Phys. Chem. C*, 2018, **122**, 5178–5187.

65. T. Tsukamoto, K. Takada, R. Sakamoto, R. Matsuoka, R. Toyoda, H. Maeda, T. Yagi, M. Nishikawa, N. Shinjo, S. Amano, T. Iokawa, N. Ishibashi, T. Oi, K. Kanayama, R. Kinugawa, Y. Koda, T. Komura, S. Nakajima, R. Fukuyama, N. Fuse, M. Mizui, M. Miyasaki, Y. Yamashita, K. Yamada, W. Zhang, R. Han, W. Liu, T. Tsubomura and H. Nishihara, *J. Am. Chem. Soc.*, 2017, **139**, 5359–5366.

66. S. Roy and C. Chakraborty, *ACS Appl. Mater. Interfaces*, 2020, **12**, 35181−35192.

67. K. Choroba, B. Machura, S. Kula, L. R. Raposo, A. R. Fernandes, R. Kruszynski, K. Erfurt, L. S. Shul, Y. N. Kozlov and G. B. Shul, *Dalton Trans.*, 2019, **48**, 12656–12673.

68. R. Nasani, M. Saha, S. M. Mobin, L. M. D. R. S. Martins, A. J. L. Pombeiro, A. M. Kirillov and S. Mukhopadhyay, *Dalton Trans.*, 2014, **43**, 9944–9954.

69. Z. Ma, L. Wei, E. C. B. A. Alegria, L. M. D. R. S. Martins, M. F. C. G. da Silva and A. J. L. Pombeiro, *Dalton Trans.*, 2014, **43**, 4048–4058.

70. J. Z. Gu, M. Wen, Y. Cai, Z. F. Shi, A. S. Arol, M. V. Kirillova and A. M. Kirillov, *Inorg. Chem.*, 2019, **58**, 2403–2412.

71. C. Wei, Y. He, X. Shi and Z. Song, *Coord. Chem. Rev.*, 2019, **385**, 1–19.

72. Y. Liu, S. C. Yiu, C. L. Ho and W. Y. Wong, *Coord. Chem. Rev.*, 2018, **375**, 514–557.

73. C. Icsel, V. T. Yilmaz, S. Aydinlik and M. Aygun, *Dalton Trans.,* 2020, **49**, 7842–7851.

74. J. Karges, K. Xiong, O. Blacque, H.Chao, G. Gasser, *Inorganica Chimica Acta*, 2021, **516**, 120137.

75. C. Wu, J. Wang, J. Shen, C. Zhang, Z. Wu and H. Zhou, *Tetrahedron*, 2017, **73**, 5715–5719.

76. H. Q. Li, X. Q. Sun, T. Zheng, Z. X. Xu, Y. X. Song and X. H. Gu, *Sens. Actuators, B*, 2019, **279**, 400–409.

77. F. Cheng, N. Tang, K. Miao and F. Wang, *Z. Anorg. Allg. Chem.*, 2014, **640**, 1816–1821.

78. Y. Q. Pan, X. Xu, Y. Zhang, Y. Zhang and W. K. Dong, *Spectrochim. Acta, Part A*, 2020, **229**, 117927.

79. *Bruker, SMART v5.631*, Bruker AXS Inc., Madison, WI, USA, 2001.

80. G. M. Sheldrick, *SHELXT-2014*, University of Göttingen, 2014.

81. G. M. Sheldrick, *Acta Crystallogr., Sect. C: Struct. Chem.*, 2015, **71**, 3–8.

82. M. A. Spackman and D. Jayatilaka, *CrystEngComm*, 2009, **11**, 19−32.

83. F. L. Hirshfeld. *Theor. Chim. Acta*, 1977, **44**, 129−138.

84. H. F. Clausen, M. S. Chevallier, M. A. Spackman and B. B. Iversen, *New J. Chem.*, 2010, **34**, 193–199.

85. A. L. Rohl, M. Moret, W. Kaminsky, K. Claborn, J. J. Mckinnon and B. Kahr, *Cryst. Growth Des.*, 2008, **8**, 4517–4525.

86. A. Parkin, G. Barr, W. Dong, C. J. Gilmore, D. Jayatilaka, J. J. McKinnon, M. A. Spackman and C. C. Wilson, *CrystEngComm*, 2007, **9**, 648–652.

87. M. A. Spackman and J. J. McKinnon, *CrystEngComm*, 2002, **4**, 378–392.

88. S. K. Wolff, D. J. Grimwood, J. J. McKinnon, D. Jayatilaka and M. A. Spackman, *Crystal Explorer 3.1*, University of Western Australia, Perth, Australia, 2007.

89. J. J. McKinnon, M. A. Spackman and A. S. Mitchell, *Acta Crystallogr., Sect. B: Struct. Sci.*, 2004, **60**, 627–668.

90. M. J. Frisch, G. W. Trucks, H. B. Schlegel, G. E. Scuseria, M. A. Robb, J. R. Cheeseman, G. Scalmani, V. Barone, G. A. Petersson, H. Nakatsuji, X. Li, M. Caricato, A. Marenich, J. Bloino, B. G. Janesko, R. Gomperts, B. Mennucci, H. P. Hratchian, J. V. Ortiz, A. F. Izmaylov, J. L. Sonnenberg, D. Williams-Young, F. Ding, F. Lipparini, F. Egidi, J. Goings, B. Peng, A. Petrone, T. Henderson, D. Ranasinghe, V. G. Zakrzewski, J. Gao, N. Rega, G. Zheng, W. Liang, M. Hada, M. Ehara, K. Toyota, R. Fukuda, J. Hasegawa, M. Ishida, T. Nakajima, Y. Honda, O. Kitao, H. Nakai, T. Vreven, K. Throssell, J. A. Montgomery, Jr., J. E. Peralta, F. Ogliaro, M. Bearpark, J. J. Heyd, E. Brothers, K. N. Kudin, V. N. Staroverov, T. Keith, R. Kobayashi, J. Normand, K. Raghavachari, A. Rendell, J. C. Burant, S. S. Iyengar, J. Tomasi, M. Cossi, J. M. Millam, M. Klene, C. Adamo, R. Cammi, J. W. Ochterski, R. L. Martin, K. Morokuma, O. Farkas, J. B. Foresman, D. J. Fox, Gaussian 16 (Revision A.03), Gaussian Inc., Wallingford CT, 2016.

91. S. F. Boys and F. Bernardi, *Mol. Phys.*, 1970, **19**, 553–566.

92. S. Grimme, J. Antony, S. Ehrlich and H. Krieg, *J. Chem. Phys.*, 2010, **132**, 154104–154123.

93. P. Manna, S. K. Seth, M. Mitra, S. R. Choudhury, A. Bauzá, A. Frontera and S. Mukhopadhyay, *Cryst. Growth Des.*, 2014, **14**, 5812–5821.

94. M. Mirzaei, H. Eshtiagh-Hosseini, Z. Bolouri, Z. Rahmati, A. Esmaeilzadeh, A. Hassanpoor, A. Bauza, P. Ballester, M. Barceló-Oliver, J. T. Mague, B. Notash and A. Frontera, *Cryst. Growth Des.*, 2015, **15**, 1351–1361.

95. J. Contreras-García, E. R. Johnson, S. Keinan, R. Chaudret, J.-P. Piquemal, D. N. Beratan and W. Yang, *J. Chem. Theory Comput.*, 2011, **7**, 625–632

96. R. F. W. Bader, *Chem. Rev.*, 1991, **91**, 893–928.

97. T. A. Keith, *AIMAll (Version 19.02.13)*, TK Gristmill Software, Overland Park KS, USA, 2019 (aim.tkgristmill.com).

98. A. W. Addison, T. N. Rao, J. Reedijk, J. Rijn and G. C. Verschoor, *J. Chem. Soc., Dalton Trans.*, 1984, **7**, 1349–1356.

99. P. Pal, K. Das, A. Hossain, R. M. Gomila, A. Frontera and S. Mukhopadhyay, *New J. Chem.*, 2021, **45**, 11689−11696.

100. J. Z. Gu, X. X. Liang, Y. H. Cui, J. Wu, Z. F. Shi and A. M. Kirillov, *CrystEngComm*, 2017, **19**, 2570–2588.

101. Z. Gu, Y. Cai, M. Wen, Z. F. Shi and A. M. Kirillov, *Dalton Trans.*, 2018, **47**, 14327–14339.

102. R. G. Miller and S. Brooker, *Inorg. Chem.*, 2015, **54**, 5398–5409.

103. Z. Yin, G. Zhang, T. Phoenix, S. Zheng and J. C. Fettinger, *RSC Adv.*, 2015, **5**, 36156–36166.

104. R. Hao, L. Li, S. Zhu, Z. H. Wang, X. J. Zhao, and E. C. Yang, *J. Mol. Struct.*, 2019, **1176**, 376–385.

105. H. R. Khavasi, and M. Esmaeili, *Cryst. Growth Des.* 2019, **19**, 4369–4377.

106. A. Frontera, *C*, 2020, **6**, 60–74.

107. A. Daolio, P. Scilabra, G. Terraneo and G. Resnati, *Coord. Chem. Rev.*, 2020, **413**, 213265–213284.

108. M. M. Ayhan, E. Özcan, B. Dedeoglu, Y. Chumakov, Y. Zorlu and B. Coşut, *CrystEngComm*, 2021, **23**, 268–272.

CHAPTER 4

Syntheses, crystal structures and photo-response properties of two new Ni(II) complexes

Complex 1

Complex 2
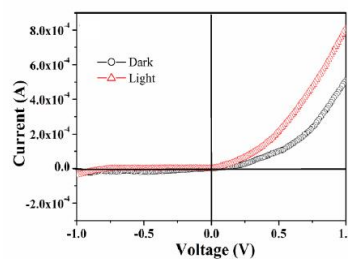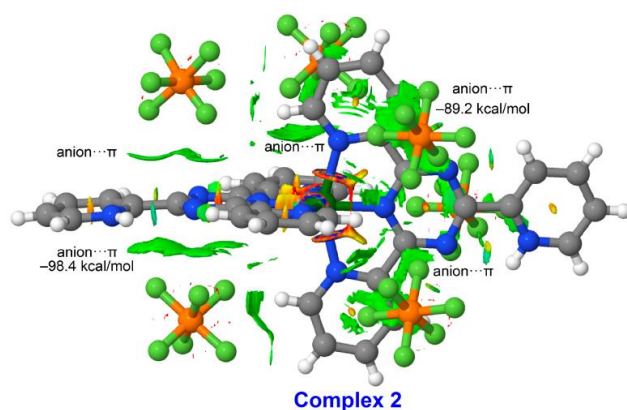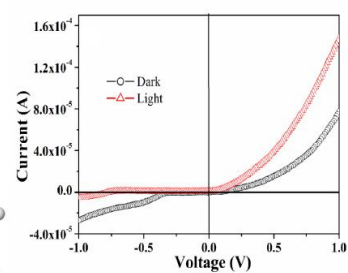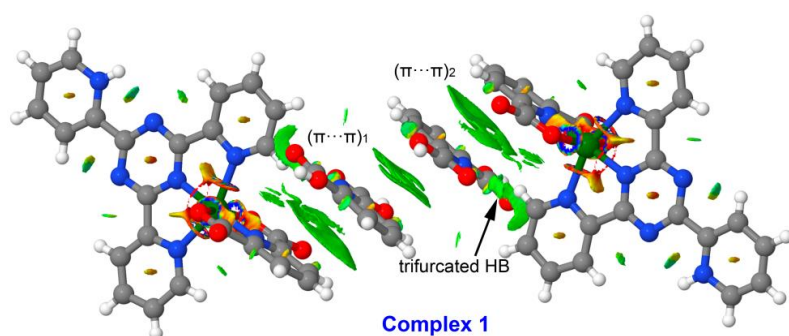
4.1. INTRODUCTION

In recent times, the field of coordination compounds and crystal engineering has matured enough and assisted to design and synthesis of materials with precise solid-state intriguing properties [1−8]. Beyond their syntheses, researchers are now focusing on their potential applications as functional materials like in heterogeneous catalysis, nanotechnology, gas adsorption, gas evolution, optoelectronics, drug delivery, sensors, fuel cell, dye degradation and many more [9−30]. In this context, crystal engineers often help to explore the self-assembly processes after combination of various metals and heterocycle based organic ligands and guide to find out the relationship between the structure and properties of molecules in a programmed way [31,32].

Molecular architectures are the resultant of the mutual interactions to exhibit broad range of different dimensional frameworks (0D, 1D, 2D and 3D) through variety of interactions [33−35]. The interactions associated with aromatic-π systems like $\pi \bullet\bullet\bullet \pi$, lone pair$\bullet\bullet\bullet\pi$, cation$\bullet\bullet\bullet\pi$, anion$\bullet\bullet\bullet\pi$, CH$\bullet\bullet\bullet\pi$, anion$\bullet\bullet\bullet\pi^+$, $\pi\bullet\bullet\bullet\pi^+$, $\pi^+\bullet\bullet\bullet\pi^+$, *etc*. along with comparatively strong hydrogen bonding interactions have been vastly analyzed for the building of various architectures in solid state [36−45]. The counter ions, solvent molecules and electronic nature of auxiliary ligands are also responsible for the organized architectures [46−48].

2,4,6-tri(pyridin-2-yl)-1,3,5-s-triazine or their structural analogues play a pivotal role in metallo-supramolecular chemistry and have drawn much attention in the fields of coordination chemistry as well as materials science [49−51]. The chelating aptitude of the 2,4,6-tri(pyridin-2-yl)-1,3,5-s-triazine increases the stability of the metal complexes, and planarity of the ligand with π stacking ability leads to robust intercalative interactions of the complexes in biological systems [52−54]. Besides, binding constant determines the strength of the interaction between metal and ligand and controls the formation of coordination complexes thermodynamically and a competition might arise if more than one ligand is present to bind with a specific metal ion [55,56]. As a result, there is less number of complexes reported in literature with two different chelating ligands in one pot [57−61].

In addition, majority of coordination complexes are electrical insulators and discrete in nature. However, there are some reports of ordered coordination complexes that exhibit enhanced electron transport and rectifying nature under light illumination [62−69]. It is demonstrated that structural and electronic properties of coordination complexes can be tuned strategically by changing metal ions and organic linkers. As the conductivities of coordination complexes are generally low, hence fabrication of electronic devices becomes a

challenging task using such complexes. Beyond structural stability, thermal and chemical stability are also to be considered for successful implement of coordination complexes in device making.

Considering the above facts, two nickel complexes namely, $[Ni(C_{18}H_{13}N_6)(C_7H_3NO_4)](C_7H_5NO_4)Cl \cdot H_2O$ (complex **1**) and $[Ni(C_{18}H_{13}N_6)_2](PF_6)_4 \cdot H_2O$ (complex **2**) have been synthesised purposefully based on 2,4,6-tri(pyridin-2-yl)-1,3,5-s-triazine moiety. Initially nickel(II) reacts with two different ligands (2,4,6-tri(pyridin-2-yl)-1,3,5-triazine and pyridine-2,6-dicarboxylic acid) in one pot to get octahedral complex **1** where both triazine moiety and pyridine-2,6-dicarboxylic acid act as tridentate ligands. Complex **2** is obtained when Ni(II) is treated with 2,4,6-tri(pyridin-2-yl)-1,3,5-*s*-triazine only as a ligand in the molar ratio 1:2. Though the number of complexes built from *s*-triazine derivatives has been reported in recent years, there still remains much more work to be explored. The structural features, supramolecular aspects of the complexes **1** and **2** with the help of single crystal X-ray diffraction analysis along with their electrical conductivities have been explored. The solid-state structure of complex **1** comprises a combination of C—H•••N, C—H•••O, C—H•••Cl, N—H•••O, O—H•••O and O—H•••Cl hydrogen bonds along with π•••π, π•••π⁺ and lone pair•••π interactions. Complex **2** is stabilized by a combination of C—H•••F, N—H•••O and O—H•••F hydrogen bonds along with π•••π, C—H•••π, anion•••π, π⁺•••π⁺ and anion•••π⁺ interactions. Particular attention has been given to different types of π-stacking interactions in complex **1**, involving uncoordinated di-picolinic acids, coordinated and uncoordinated di-picolinic acid and between the extended π-surface of 2,4,6-tri(pyridin-2-yl)-1,3,5-s-triazine. These interactions have been evaluated energetically using DFT calculations and characterized using the NCI plot index analysis. Moreover, multitude anion–π interactions observed in complex **2** have been characterized using the NCI plot index analysis.

Additionally, to make a clear view on charge transportation a detail I−V analysis is carried out by making thin films of the title complexes. Several device parameters like carrier mobility, carrier concentration, transit time, diffusion coefficient, diffusion length, ideality factor have been measured considering SBD characteristics. Change in auxiliary ligands alters the structural variations, supramolecular behaviours and electrical properties of both the complexes significantly. An improvement in device performance has been observed for the complex **2** compared to complex **1**.

4.2. EXPERIMENTAL SECTION

4.2.1. Materials and apparatus

All the chemicals [2,4,6-tri(pyridin-2-yl)-1,3,5-s-triazine, dipicolinic acid, Ni(II) chloride hexahydrate, and ammonium hexafluorophosphate] were purchased from Sigma-Aldrich Chemical Company, USA and used without further purification. All the reactions were carried out under aerobic environments and doubly distilled water was used throughout.

Elemental analyses (C, H and N) were performed using a PerkinElmer 2400 Series-II CHN analyzer. Fourier transform infrared (FTIR) spectra of **1** and **2** were recorded on a Perkin Elmer LX-1 FTIR spectrophotometer ($4000-400$ cm^{-1}) by using a modern diamond attenuated total reflectance (ATR) accessory method. UV−vis absorption spectra were obtained using UV-1700 PharmaSpec UV−vis spectrophotometer (SHIMADZU). Electrical characterization was carried out with Keithley 4200 I-V instrument in the voltage range of -1 to $+1$ V. Single-crystal X-ray data collections of complex **1** and complex **2** were completed using single crystal X-ray diffractometer (Bruker Smart Apex II).

4.2.2. Synthesis of complex 1

Nickel(II) chloride hexa-hydrate (0.237 g, 1.0 mmol) was dissolved in 15 mL of water and allowed to react with 2,4,6-tri(pyridin-2-yl)-1,3,5-s-triazine (0.312 g, 1.0 mmol) in water-ethanol (8 : 2, v/v) medium (20 mL) at 60 °C with continues stirring. A warm aqueous solution (15 mL) of dipicolinic acid (0.334 g, 2.0 mmol) was added dropwise to the above solution at stirring conditions (Scheme 4.1). After 4 hrs of constant stirring at 60 °C, the resulting solution was cooled, filtered and left unperturbed for slow evaporation at room temperature. Block-shaped brown coloured single crystals were obtained after one week. The crystals were separated by filtration, washed with cold water, and then dried in air, yield 0.495 g (65%). Anal. Calcd. for $C_{32}H_{23}N_8NiClO_9$ (complex **1**): C, 51.96; H, 2.86; N, 15.15%. Found: C, 51.92; H, 2.81; N, 15.14%. Main FTIR absorptions, (KBr, cm-1): 3364 (w), 3097 (vs), 2781 (s), 2621 (s), 1727 (vs), 1621 (s), 1573 (s), 1557 (vs), 1480 (s), 1453 (s), 1429 (s), 1400 (s), 1384 (s) (Fig. 4.1).

4.2.3. Synthesis of complex 2

Complex **2** was synthesized by dissolving Nickel(II) chloride hexahydrate (0.237 g, 1.0 mmol) in 15 mL of water and allowed to react with 2,4,6-tri(pyridin-2-yl)-1,3,5-s-triazine (0.624 g, 2.0 mmol) in water-ethanol (8 : 2, v/v) medium (20 mL) at 60 °C with stirring. A few drops of HCl were added into resulting turbid solution to get the clear solution. A warm

aqueous solution (15 mL) of ammonium hexafluorophosphate (0.652 g, 4.0 mmol) was added drop wise to the above solution and stirred for another 3 hrs (Scheme 4.1). The resultant solution was then cooled, filtered, and left for slow evaporation at room temperature without any disturbance. The yielded block shaped, deep brown coloured single crystals were obtained after two weeks. The crystals were separated by filtration, washed with cold water and air dried; yield 0.796 g (62%). Anal. Calcd. for $C_{36}H_{28}N_{12}NiOF_{24}P_4$ (complex **2**): C, 34.17; H, 2.07; N, 13.28%. Found: C, 34.21; H, 2.04; N, 13.23%. Main FTIR absorptions, (KBr, cm−1): 3454 (w), 3031 (s), 1740 (s), 1635 (s), 1611 (s), 1578 (vs), 1562 (vs), 1530 (vs), 1487 (s), 1473 (s), 1455 (s), 1439 (s), 1399 (s), 1377 (s), 1313 (s) (Fig. 4.1).
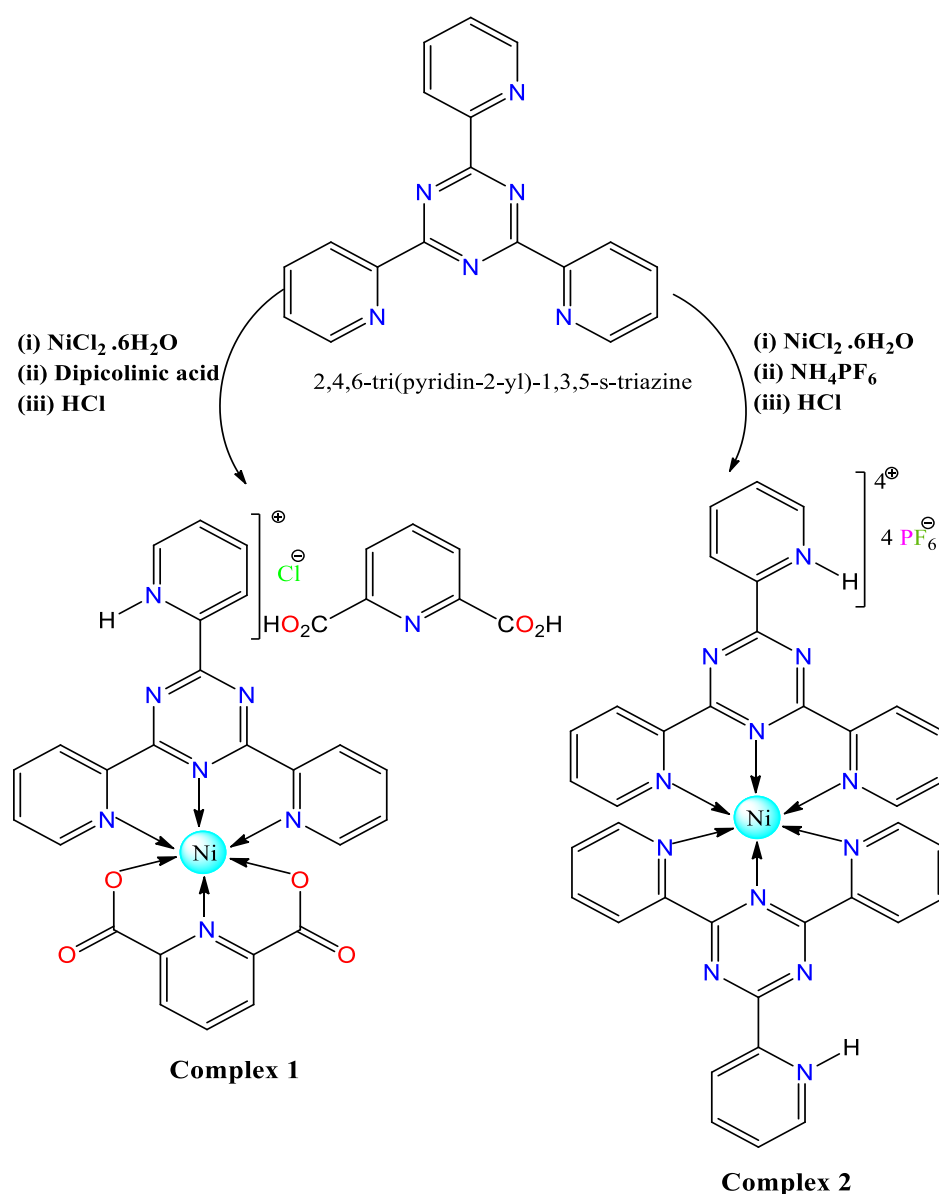
Scheme 4.1. Schematic representations of the synthesis of complexes **1** and **2**.
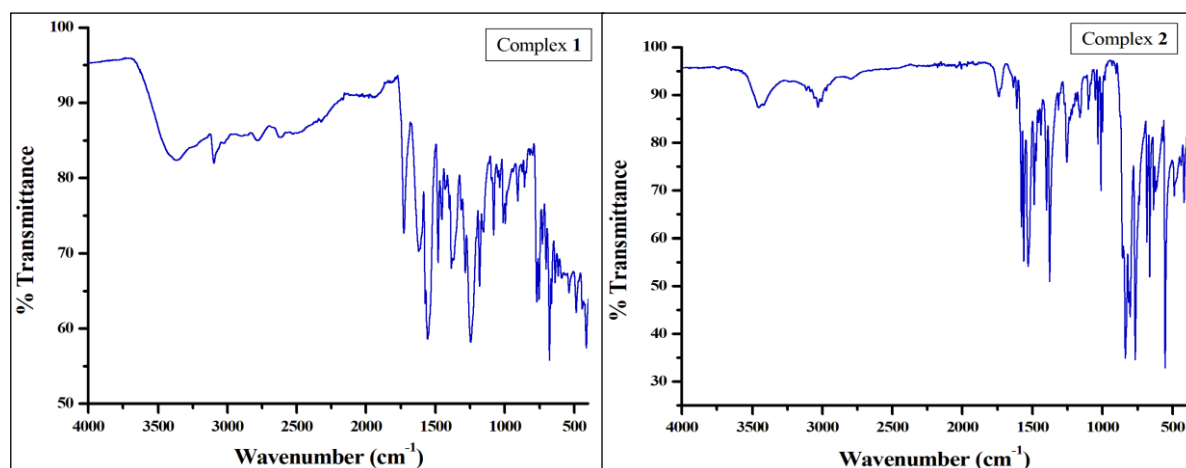
Fig. 4.1. FT-IR spectra for complex **1** and complex **2**.

4.2.4. X-ray crystallographic analysis

Single crystal X-ray data collections for both the complexes were done using a Bruker SMART APEX II CCD area detector equipped with a graphite monochromated Mo Ka radiation (l = 0.71073 A) source in φ and ω scan mode at 273(2) K. Cell parameter refinement and data reduction were carried out using a Bruker SMART APEX II instrument and Bruker SMART and Bruker SAINT Software for both the complexes [70]. The structure of all the complexes was solved by conventional direct methods and refined by full matrix least-squares methods using F^2 data. SHELXL-2014/7 was used for the refinement of the both the structures [71]. CCDC 2052738 (for **1**) and 2052737 (for **2**) include additional crystallographic information. Selected crystal data and structure refinement parametersfor **1** and **2** are given in Table 4.1.

4.2.5. Computational methods

The calculations of the monomers and dimers (shown in Figs. 7, 8, 9) were performed at the DFT level theory using the PBE0-D3 method, and the def2-SVP basis set, with the help of the Gaussian-16 [72–75]. The topological analysis of the electron density distribution has been examined using the noncovalent interaction plot (NCI Plot) using the AIMAll program [76–79]. The estimation of the individual XB energies was done using the potential energy density (V_r) predictor as recently proposed in the literature (E = $0.778V_r$) for the PBE0 functional [80]. The MEP surfaces were computed at the same level of theory by means of the Gaussian-16 program.

Table 4.1. Crystal data and structure refinement parameters for complexes 1 and 2

Complex	**1** (2052738)	**2** (2052737)
Empirical formula	$C_{32}H_{22}N_8NiClO_9$	$C_{36}H_{28}N_{12}NiF_{24}OP_4$
Formula Weight	757.72	1283.27
Temperature (K)	273(2)	273(2)
Wavelength (Å)	0.71073	0.71073
Crystal system	Triclinic	Triclinic
space group	P$\bar{1}$	P$\bar{1}$
a, b, c (Å)	8.4334(14), 13.968(2), 18.311(3)	9.0874(14), 9.5574(16), 28.115(4)
α, β, γ (°)	102.822(5), 101.380(5), 94.631(4)	83.970(4), 86.039(4), 88.258(4)
Volume (Å^3)	2044.3(6)	2421.8(7)
Z / Density (calc.) (Mg/m^3)	2 / 1.231	2 / 1.760
Absorption coefficient (mm^{-1})	0.595	0.673
F(000)	776	1280
Crystal size (mm^3)	$0.18 \times 0.25 \times 0.3$	$0.18 \times 0.25 \times 0.3$
θ range for data collection	2.122 to 27.170	2.143 to 27.133
Completeness to θ (%)	100%	100%
Absorption correction	EMPIRICAL	EMPIRICAL
Max. and min. transmission	0.898 and 0.837	0.886 and 0.817
Refinement method	Full-matrix least-squares on F^2	Full-matrix least-squares on F^2
Data/parameters	9047 / 465	10688 / 706
Goodness-of-fit on F^2	1.089	1.049
Final R indices [I > 2σ(I)]	$R_1 = 0.0715$, $wR_2 = 0.2167$	$R_1 = 0.0883$, $wR_2 = 0.2395$
R indices (all data)	$R_1 = 0.0897$, $wR_2 = 0.2294$	$R_1 = 0.1171$, $wR_2 = 0.2647$
Largest diff. peak and hole (e.Å^{-3})	0.931 and -0.920	0.901 and -0.876

$R_1 = \sum || F_o| - |F_c|| / \sum |F_o|$, $wR_2 = [\sum\{(F_o^2 - F_c^2)^2\}/\sum\{w(F_o^2)^2\}]^{1/2}$ $w = 1/\{\sigma^2(F_o^2) + (aP)^2 + bP\}$ where, $P = (F_o^2 + 2F_c^2)/3$, a = 0.1176; b = 2.4644 for complex **1** and a = 0.1206; b = 7.4829 for complex **2**

4.2.6. Fabrication of thin film and FTO/complex/Ag junction

The prime criterion of device making is small size of synthesized materials. As the thin film technology bridges in between macro systems and molecular systems where size of the material is substantially reduced and is welcomed for device fabrication. With this simplification precursor complexes are turned into thin film. Here, both precursor complexes were taken into account to deposit on FTO substrates (resistance 8-10 Ω/cm^2, surface area 1.0 $\times$ 1.0 cm^2) by spin-coating method. Before the deposition FTO substrates were properly washed, first by soap-water and then with running distilled water. After that these were ultrasonicated for an hour and degreased and thereafter they were shifted in a hot air oven for

proper drying (almost 2 hours). About 4 mg of each complex was then dispersed in DMF in 1:5 ratios and ultrasonicated again for an hour. Now with a micropipette few drops of this solution were dropped onto the centre of FTO and spinned at 700 rpm and then 1000 rpm for 2 and 4 minutes respectively. The resulting films were dried in inert atmosphere and kept in desiccators. Thicknesses of the films were measured to be 2 µm by surface profilometer (Bruker Contour G). To fabricate the sandwich device, two contacts were made one from FTO (bottom contact) and other from contact metal Ag (FTO/complex/Ag) and shadow mask was used to maintain the effective area of 7×10^{-2} cm^2.

4.3. RESULTS AND DISCUSSION

4.3.1. Structural description of complex 1

Single-crystal X-ray diffraction study shows that the asymmetric unit of complex **1** comprises a monomeric cationic [Ni(C$_{18}$H$_{13}$N$_6$)(C$_7$H$_3$NO$_4$)]$^+$ unit, one non-coordinated dipicolinic acid, one non-coordinated chloride ion and one non-coordinated water molecule (Fig. 4.2). The complex adopts the triclinic system with the space group $P\bar{1}$ and its unit cell is composed of two asymmetric units. The selected bond lengths and bond angles are summarized in Table 4.2.

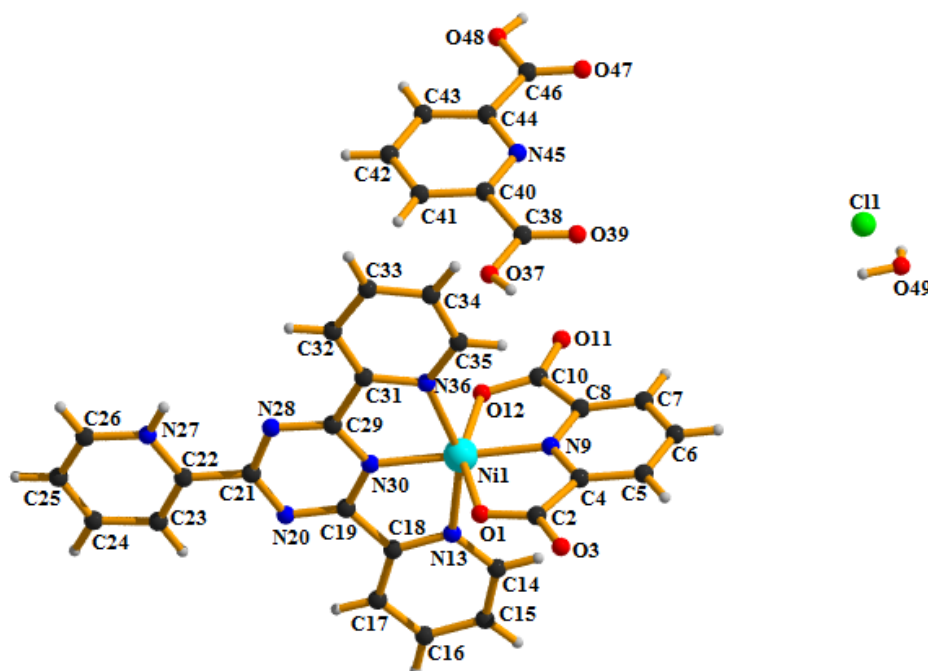**Fig. 4.2.** Asymmetric unit of complex **1**

In the monomeric cationic [Ni(C$_{18}$H$_{13}$N$_6$)(C$_7$H$_3$NO$_4$)]$^+$ unit, Ni(II) ion occupies distorted octahedron structure, where three nitrogen donor atoms (N13, N30 and N36) of triazine based

ligand and another nitrogen atom (N9) of dipicolinate construct the basal plane. Two oxygen atoms O1, at distance 2.170(3) Å and O12, at distance 2.109(3) Å of same acid ligand are *trans* di-axially coordinated to metal ion. The lower value of *trans* axial angle O1−Ni1−O12 [155.94(11)°] induces distortion in octahedral geometry. The Ni−N bond distances in the basal plane are in the range of 1.960(3) to 2.140(3) Å. The Ni(II) ion is almost placed (deviation, 0.009 Å) in the same mean coordination plane of (N13, N30, N36, and N9). One N atom (N27) of the monomeric unit is protonated. A non-coordinated chloride anion is present to neutralize the charge of the complex.

Table 4.2. Selected bond distances [Å] and bond angles (°) for complex 1

Bonds	Distance (Å)	Bond angles	Value (°)
Ni1−O1	2.170(3)	O1−Ni1−O12	155.94(11)
Ni1−O12	2.109(3)	O1−Ni1−N9	77.42(12)
Ni1−N9	1.960(3)	O1−Ni1−N13	91.92(11)
Ni1−N13	2.140(3)	O1−Ni1−N30	102.46(12)
Ni1−N30	1.974(3)	O1−Ni1−N36	92.71(11)
Ni1−N36	2.117(3)	O12−Ni1−N9	78.52(12)
		O12−Ni1−N13	94.04(12)
		O12−Ni1−N30	101.59(12)
		O12−Ni1−N36	91.91(13)
		N9−Ni1−N13	103.44(13)
		N9−Ni1−N30	179.41(14)
		N9−Ni1−N36	102.14(13)
		N13−Ni1−N30	77.13(13)
		N13−Ni1−N36	154.40(13)
		N30−Ni1−N36	77.29(13)

The monomeric cationic unit of complex **1** extends to make certain a 1-D polymeric chain through a π•••π interaction between Cg(6) and Cg(9) of two units along [100] direction (Fig. 4.3).
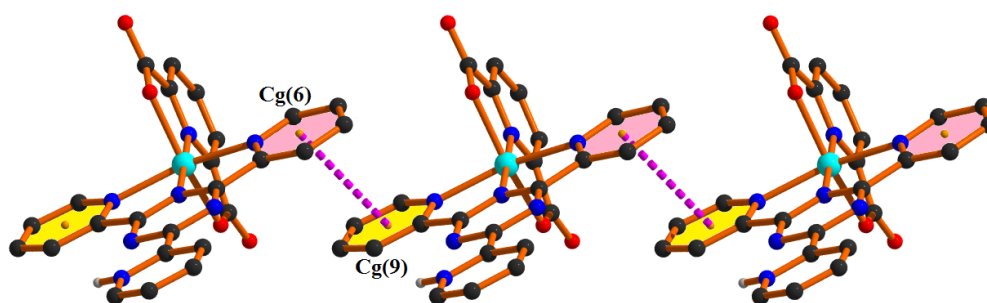

Fig. 4.3. 1D polymeric chain through a π•••π interaction (aromatic hydrogen atoms have been omitted for clarity).

The two parallel chains are then interconnected through the self-complementary $\pi\bullet\bullet\bullet\pi^+$ interaction (Table 4.3) between Cg(9) of one unit and Cg(8) of the other unit, thus forming a 1-D tape (Fig. 4.4). The ring centroid separation distances of Cg(6)─Cg(9) and Cg(8)─Cg(9) are 3.715(3) Å and 3.561(3) Å respectively.
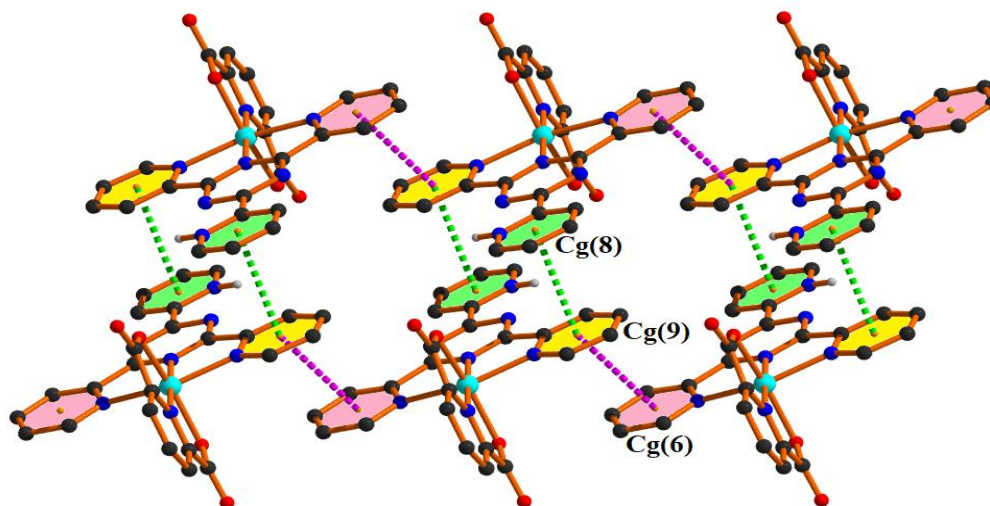

Fig. 4.4. Perspective view of the extended supramolecular networks in complex **1** through $\pi\cdots\pi$ and $\pi\cdots\pi^+$ interactions (aromatic hydrogen atoms have been omitted for clarity).

This supramolecular architecture (1D tape) is further extended through the self complementary lone pair$\bullet\bullet\bullet\pi$ interactions (Table 4.4) between Cg(5) of one unit and carboxyl oxygen atom (O11) of the other unit and vice versa. Thus the $\pi\bullet\bullet\bullet\pi$ interaction along with these $\pi\bullet\bullet\bullet\pi^+$ and lone pair$\bullet\bullet\bullet\pi$ interaction enhance the dimensionality from 1-D to 2-D in the ac-plane (Fig. 4.5).

Table 4.3. Geometrical parameters (Å, °) for the π-stacking interactions for complex 1

Cg(i)•••Cg(j)	Cg(i)•••Cg(j) [Å]	α (°)	β (°)	γ (°)	Cg(i)–perp[Å]	Cg(j)–perp[Å]	Symmetry
Cg(5)[1]•••Cg(10)	3.764(3)	7.54	27.86	23.34	3.456	3.327	2-x, 1-y, 1-z
Cg(6)[1]•••Cg(9)	3.715(3)	2.46	18.70	19.80	3.495	3.519	-1+x, y, z
Cg(8)[1]•••Cg(9)	3.561(3)	2.35	13.85	15.89	3.425	3.458	1-x, 1-y, -z
Cg(9)[1]•••Cg(6)	3.715(3)	2.46	19.80	18.70	3.518	3.495	1+x, y, z
Cg(9)[1]•••Cg(8)	3.561(3)	2.35	15.89	13.85	3.458	3.425	1-x, 1-y, -z
Cg(10)[2]•••Cg(5)	3.765(3)	7.54	23.34	27.86	3.328	3.456	2-x, 1-y, 1-z

Cg(i) and Cg(j) denotes centroid of ith and jth ring respectively. For complex **1**: Cg(5) is the centroid of [N9/C4/C5/C6/C7/C8] ring; Cg(6) is the centroid of [N13/C14/C15/C16/C17/C18] ring; Cg(8) is the centroid of [N27/C22/C23/C24/C25/C26] ring; Cg(9) is the centroid of [N36/C31/C32/C33/C34/C35] ring; and Cg(10) is the centroid of [N45/C40/C41/C42/C43/C44] ring.
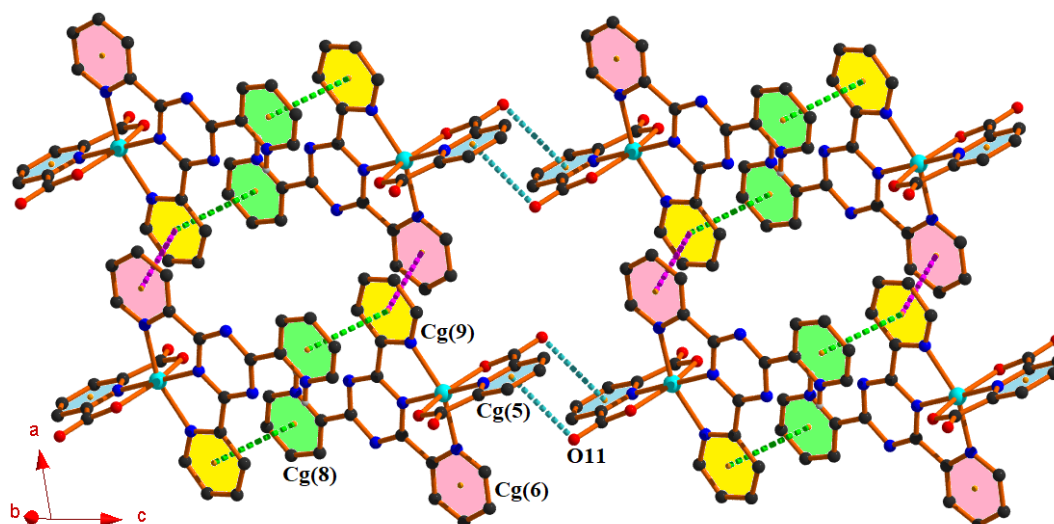
Fig. 4.5. 2-D layer of **1** incorporating π•••π, π•••π$^+$ and lone pair•••π interactions (aromatic hydrogen atoms have been omitted for clarity).

Table 4.4. Geometrical parameters (Å, °) for lone pair•••π interactions for complex 1

Y–X(I)•••Cg(J)	X•••Cg [Å]	Y•••Cg [Å]	Y–X•••Cg (°)	Symmetry
C(10)−O(11)[1]•••Cg(5)	3.493(4)	4.090(5)	110.2(3)	1-x, 1-y, 1-z
C(38)−O(39)[2]•••Cg(1)	3.989(6)	4.734(5)	123.1(5)	1-x, 1-y, 1-z
C(38)−O(39)[2]•••Cg(5)	3.918(7)	4.152(6)	93.2(4)	1-x, 1-y, 1-z
C(46)−O(47)[2]•••Cg(1)	3.546(5)	4.031(5)	105.4(3)	2-x, 1-y, 1-z

Cg(j) denotes centroid of jth ring of the title complexes. For complex **1**: Cg(1) is the centroid of [Ni1/O1/C2/C4/N9] ring; and Cg(5) is the centroid of [N9/C4/C5/C6/C7/C8] ring.
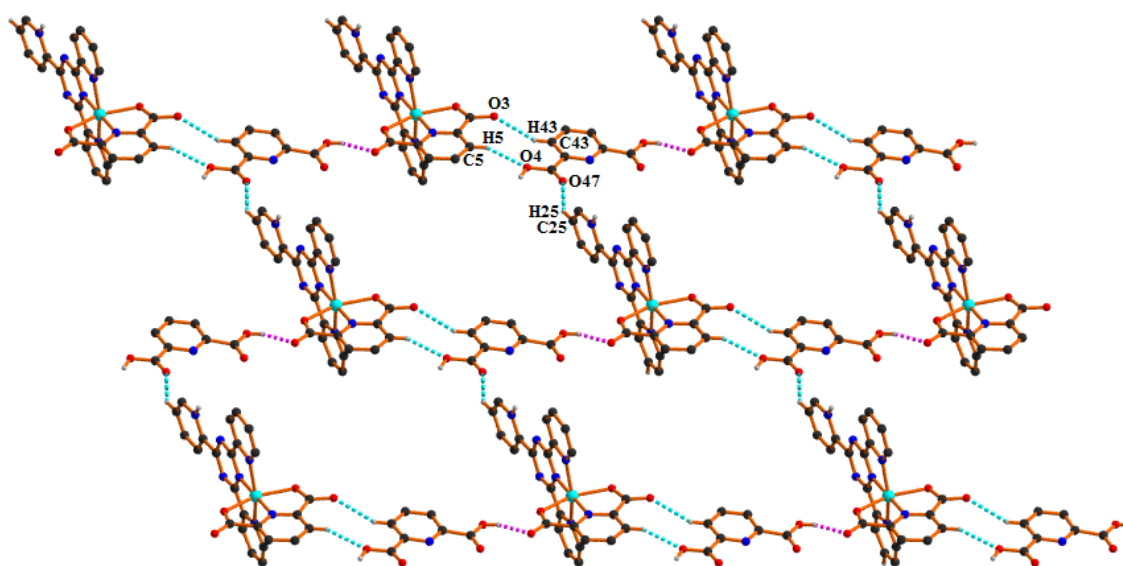

Fig. 4.6. Perspective view of the 2-D layer of **1** incorporating hydrogen bonding interactions (other aromatic hydrogen atoms have been omitted for clarity).

A different 2-D layer (Fig. 4.6) is fashioned in complex **1** using two different types of hydrogen bonding interactions (Table 4.5). Here, the monomeric cationic unit interacts with non-coordinated dipicolinic acid through C5─H5•••O48 (154°) and C43─H43•••O3 (149°) hydrogen bonding interactions to form a dimer having a $R_2^2(10)$ ring motif which is repeated through O37─H37•••O11 (164°) hydrogen bonds for the propagation of a one-dimensional (1-D) polymeric chain. This parallel 1-D chains are interlinked using C25─H25•••O47 (149°) hydrogen bonding interaction to produce a 2-D layer (brick-wall like) in the bc-plane (as shown in Fig. 4.6).

Table 4.5. Geometrical parameters for the hydrogen bonds of complex 1

D─H•••A	D–H [Å]	H•••A [Å]	D•••A [Å]	D–H•••A [°]	Symmetry
N27─H27•••O49	0.8600	2.3100	3.111(6)	155.00	x, y, -1+z
O37─H37•••O11	0.8200	1.8000	2.598(6)	164.00	─
O49─H49B•••Cl1	0.8500	2.2100	3.010(6)	157.00	─
C5─H5•••O48	0.9300	2.4300	3.286(7)	154.00	-1+x, 1+y, z
C14─H14•••O39	0.9300	2.5100	3.212(7)	133.00	1-x, 1-y, 1-z
C23─H23•••Cl1	0.9300	2.3900	3.230(7)	150.00	-1+x, y, -1+z
C25─H25•••O47	0.9300	2.2900	3.127(6)	149.00	-1+x, y, -1+z
C26─H26•••O1	0.9300	2.5400	3.325(8)	142.00	1-x, 1-y, -z
C35─H35•••N45	0.9300	2.4900	3.362(5)	157.00	2-x, 1-y, 1-z
C43─H43•••O3	0.9300	2.5800	3.412(7)	149.00	1+x, -1+y, z

A comprehensive analysis reveals that four different types of intermolecular hydrogen bonding interactions (C─H•••O, C─H•••Cl, N─H•••O, and O─H•••Cl) are involved in the formation of a 1-D tape (Fig. 4.7).
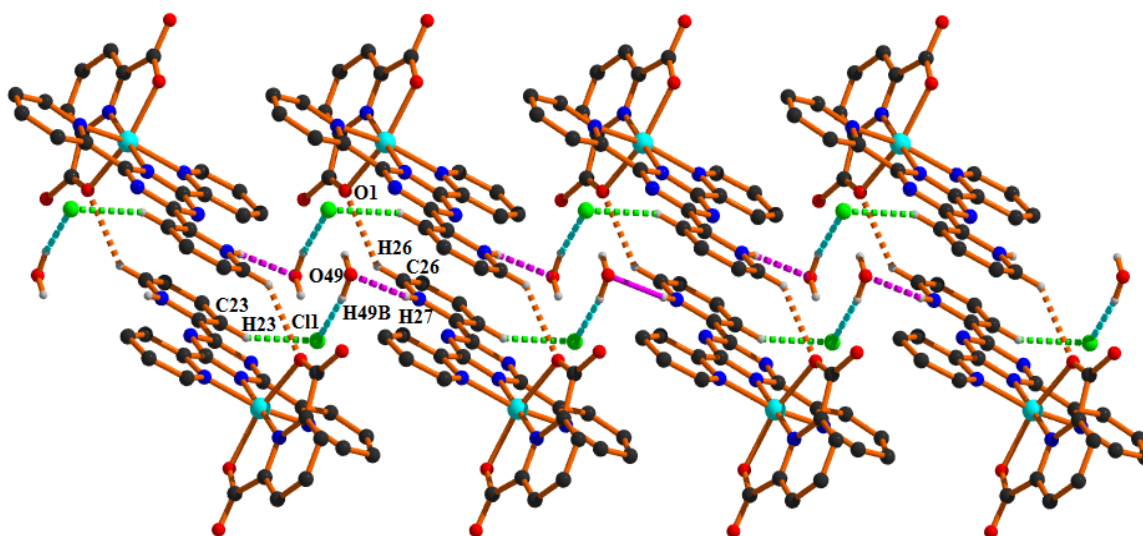

Fig. 4.7. Formation of 1-D tape through hydrogen bonding interactions in complex **1** (other aromatic hydrogen atoms have been omitted for clarity).

The first type of intermolecular hydrogen bonding (shown by green dotted line) was shaped between the C23─H23 fragment of one monomeric cationic unit and the non-coordinated chlorine atom (Cl1). The second type of intermolecular hydrogen bonding (shown by aqua dotted line) was formed by the O49─H49B of the non-coordinated water molecule and the non-coordinated chlorine atom (Cl1). The third type of intermolecular hydrogen bonding (shown by pink dotted line) was shaped by the N27─H27 fragment of one unit and O atom (O49) of the non-coordinated water molecule. These three hydrogen bonding interactions played a significant role to form a one-dimensional (1-D) polymeric chain along [100] direction. The two parallel chains are then interconnected through the self-complementary C26─H26•••O1 (type four) bonds (shown by orange dotted line) for the formation of 1-D tape (as shown in the Fig. 4.7).

There is also a dimeric distribution in complex **1** using π•••π interaction between Cg(5) of one complex moiety and Cg(10) of the non-coordinated dipicolinic acid (Fig. 4.8). The dimeric integrity is further stabilized through carbonyl(lp)•••π and C35─H35•••N45 hydrogen bonding interactions.

Here, carbonyl oxygen atom (O47) approaches towards the π face of Cg(1) chelate ring at (2-x, 1-y, 1-z) to form the said (lp)•••π interaction. Then, another carbonyl oxygen atom (O39) interacts simultaneously with Cg(1) and Cg(5) of adjacent dimeric unit to form a 1-D polymeric chain which is further strengthened by C14─H14•••O39 hydrogen bond (as depicted in Fig. 4.8).
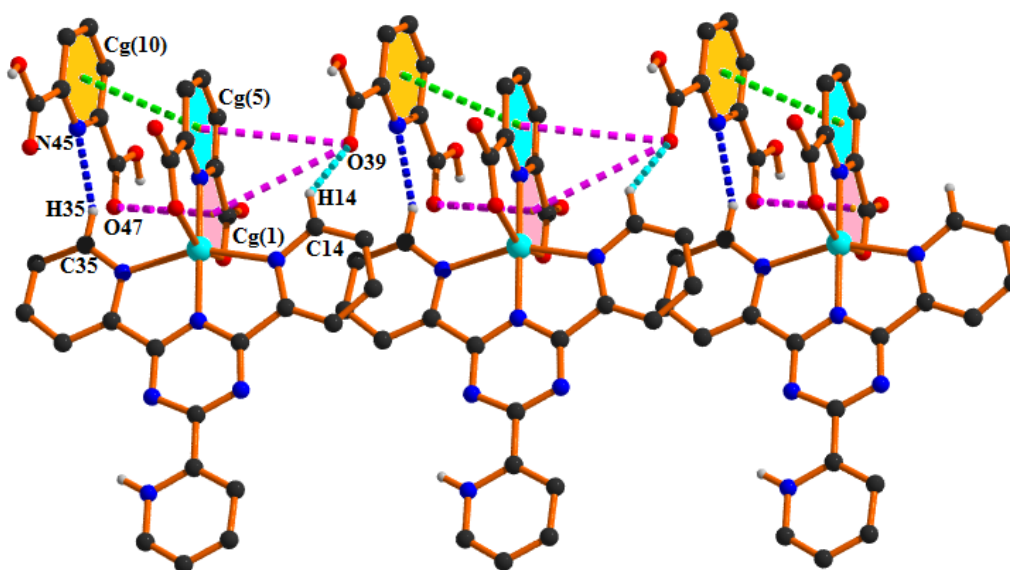

Fig. 4.8. Propagation 1-D of polymeric chain through π•••π / lone pair•••π / hydrogen bonding interactions in complex **1** (other aromatic hydrogen atoms have been omitted for clarity).

4.3.2. Structural description of complex 2

The asymmetric unit of complex **2** contains one monomeric cationic $[Ni(C_{18}H_{13}N_6)_2]^{4+}$ unit, four non-coordinated hexafluorophosphate anions and one non-coordinated water molecule (Fig. 4.9). The complex crystallizes in the triclinic system having space group $P\bar{1}$ and its unit cell is consisting of two asymmetric units. The selected bond lengths and bond angles are summarized in Table 4.6.
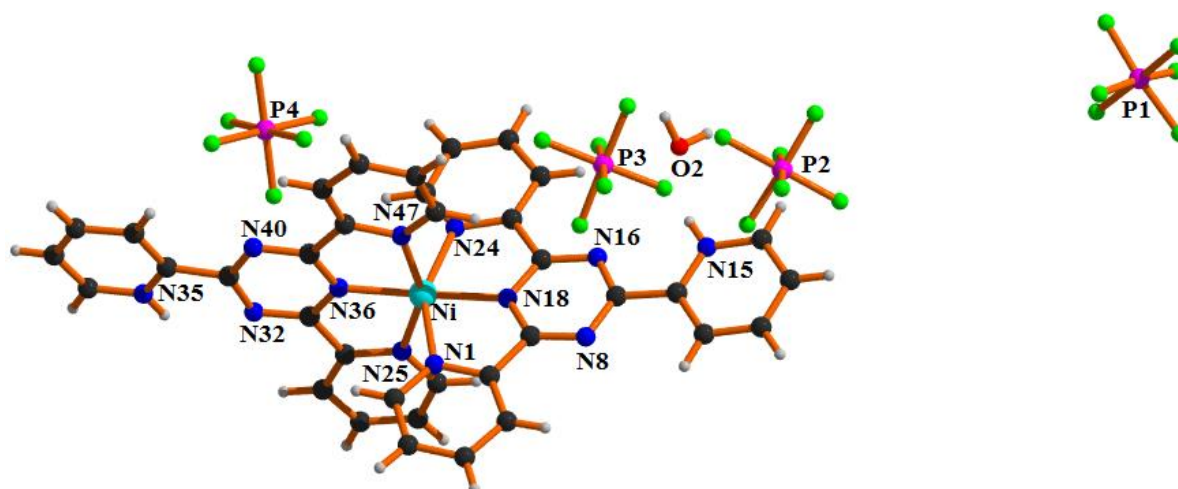
Fig. 4.9. Asymmetric unit of complex **2**

Table 4.6. Selected bond distances [Å] and bond angles (°) for complex 2

Bonds	Distance (Å)	Bond angles	Value (°)
Ni1−N1	2.156(5)	N1−Ni1−N18	76.84(17)
Ni1−N18	1.995(4)	N1−Ni1−N24	152.65(16)
Ni1−N24	2.177(4)	N1−Ni1−N25	92.41(16)
Ni1−N25	2.159(5)	N1−Ni1−N36	103.10(17)
Ni1−N36	1.990(4)	N1−Ni1−N47	92.73(18)
Ni1−N47	2.149(5)	N18−Ni1−N24	75.86(15)
		N18−Ni1−N25	106.29(17)
		N18−Ni1−N36	177.48(18)
		N18−Ni1−N47	100.83(18)
		N24−Ni1−N25	93.64(16)
		N24−Ni1−N36	104.24(16)
		N24−Ni1−N47	93.93(17)
		N25−Ni1−N36	76.23(17)
		N25−Ni1−N47	152.86(17)
		N36−Ni1−N47	76.65(18)

In this monomeric cationic $[Ni(C_{18}H_{13}N_6)_2]^{4+}$ unit, the Ni(II) ion possesses a distorted octahedron where the six coordination mode around the metal centre are satisfied by six N atoms (N1, N18, N24, N25, N36 and N47) from the two triazine based ligands. The four N

atoms (N1, N18, N24 and N36) are involved to construct the basal plane and other two N atoms (N25 and N47) are axially coordinated to the metal ion. The Ni−N distances in the basal plane are in the range of 1.990(4) to 2.177(4) Å. The *trans* angle, N25−Ni1−N47 is distorted with the value of 152.86(17)° and the metal ion almost sits (deviation, 0.01 Å) in the mean coordination plane of (N25, N36, N47, N18). Two nitrogen atoms (N15 and N35) in the monomeric unit of complex **2** are protonated. These two monopositively charged N-centeres along with a Ni(II) ion induce overall tetra-positive charge, which is compensated by four non coordinated hexafluorophosphate anions.

The monomeric cationic unit of complex **2** propagates to make certain a 1-D polymeric chain (Fig. 4.10) through a π•••π stacking interaction (Table 4.7) between Cg(9) and Cg(12) of two different unit along [100] direction having a separation distance of 3.957(3) Å. This 1-D array is further extended to 2-D layers through the C─H•••π interaction (Table 4.8) at (x, -1+y, z) between C4─H4 fragment of one unit with Cg(9) of the other unit in the (110) plane (Fig. 4.11).
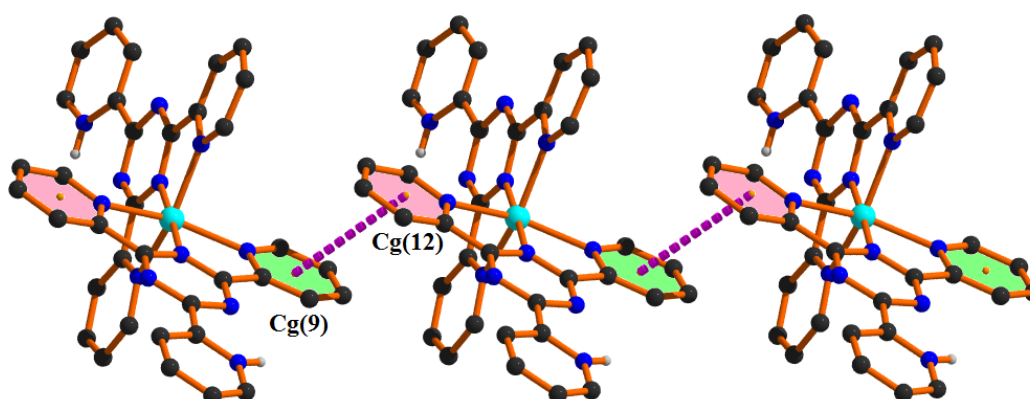
Fig. 4.10. 1-D polymeric chain through a π•••π interaction in complex **2** (aromatic hydrogen atoms have been omitted for clarity).

Table 4.7. Geometrical parameters (Å, °) for the π-stacking interactions for complex 2

Cg(i)•••Cg(j)	Cg(i)•••Cg(j) [Å]	α (°)	β (°)	γ (°)	Cg(i)–Perp [Å]	Cg(j)–Perp [Å]	Symmetry
Cg(7)[1] •••Cg(7)	3.635(4)	0.04	14.69	14.69	3.516	3.516	1-x, -y, 1-z
Cg(9)[1]•••Cg(12)	3.957(3)	4.24	29.07	24.83	3.591	3.458	1+x, y, z
Cg(12)[1]•••Cg(9)	3.956(3)	4.24	24.83	29.07	3.458	3.591	-1+x, y, z

Cg(i) and Cg(j) denotes centroid of ith and j[th] ring respectively. For Complex **2**: Cg(7) is the centroid of [N15/C10/C11/C12/C13/C14] ring; Cg(9) is the centroid of [N25/C26/C27/C28/C29/C30] ring; and Cg(12) is the centroid of [N47/C42/C43/C44/C45/C46] ring.

Table 4.8. Geometrical parameters (Å,°) for the C−H•••π interactions for the complex 2

X–H(I)•••Cg(J)	H•••Cg [Å]	X•••Cg [Å]	X–H•••Cg (°)	Symmetry
C(4)−H(4)[1]•••Cg(9)	2.82	3.738(7)	169	x, -1+y, z

For complex **2**: Cg(9) is the centroid of [N25/C26/C27/C28/C29/C30] ring.
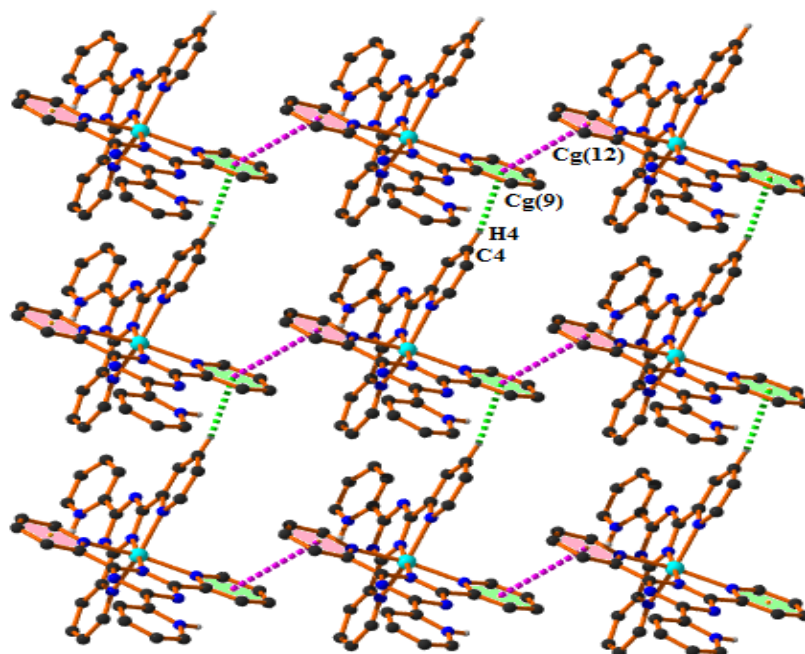
Fig. 4.11. Perspective view of 2-D layer generated through π•••π and C─H•••π interactions in complex **2** (other aromatic hydrogen atoms have been omitted for clarity).

A different 2-D layer (Fig. 4.12) is constructed in complex **2** by using hydrogen bonding, π^+•••π^+, and anion•••π (Table 4.9) interactions.

Table 4.9. Geometrical parameters (Å, °) for the anion•••π interactions for complex 2

Y–X(I)•••Cg(J)	X•••Cg [Å]	Y•••Cg [Å]	Y–X•••Cg (°)	Symmetry
P(2)−F(9)[3]•••Cg(8)	3.329(8)	4.462(3)	128.0(4)	1-x, 1-y, 1-z
P(3)−F(15)[4]•••Cg(6)	2.999(5)	4.337(2)	140.6(3)	x, y, z
P(3)−F(17)[4]•••Cg(1)	3.743(6)	4.693(3)	118.3(3)	-1+x, y, z
P(3)−F(17)[4]•••Cg(5)	3.316(6)	4.419(3)	125.9(3)	-1+x, y, z
P(3)−F(18)[4]•••Cg(7)	3.282(7)	4.611(3)	142.6(4)	x, y, z
P(4)−F(19)[5]•••Cg(5)	3.747(9)	4.485(3)	108.3(4)	x, 1+y, z
P(4)−F(22)[5]•••Cg(5)	3.636(8)	4.485(3)	112.7(3)	x, 1+y, z
P(4)−F(22)[5]•••Cg(10)	3.012(7)	4.086(3)	122.9(3)	x, y, z
P(4)−F(23)[5]•••Cg(12)	3.203(7)	4.203(3)	119.7(4)	x, 1+y, z
P(4)−F(24)[5]•••Cg(10)	3.454(7)	4.086(3)	102.2(3)	x, y, z

Cg(j) denotes centroid of jth ring of the title complexes. For complex **2**: Cg(1) is the centroid of [Ni1/N1//C6/C7/N18] ring; Cg(5) is the centroid of [N1/C2/C3/C4/C5/C6] ring; Cg(6) is the centroid of [N8/C7/N18/C17/N16/C9] ring; Cg(7) is the centroid of

[N15/C10/C11/C12/C13/C14] ring; Cg(8) is the centroid of [N24/C19/C20/C21/C22/C23] ring; Cg(10) is the centroid of [N32/C31/N36/C41/N40/C33] ring; and Cg(12) is the centroid of [N47/C42/C43/C44/C45/C46] ring.

Here, two monomeric cationic units are connected through anion•••π interactions via two F atoms (F19 and F23) with Cg(5) and Cg(12) of first unit respectively and one F atom (F24) with Cg(10) of second unit for the propagation of a one-dimensional (1-D) polymeric chain that is again interconnected by the self-complementary C38─H38•••F1 and C44─H44•••F6 hydrogen bonds (Table 4.10), thus forming a 1-D tape. This 1-D tape is further extended to 2-D layers through the π^+•••π^+ interaction between Cg(7) of one unit with Cg(7) of the other unit having a inter-planar spacing of 3.635(4) Å.
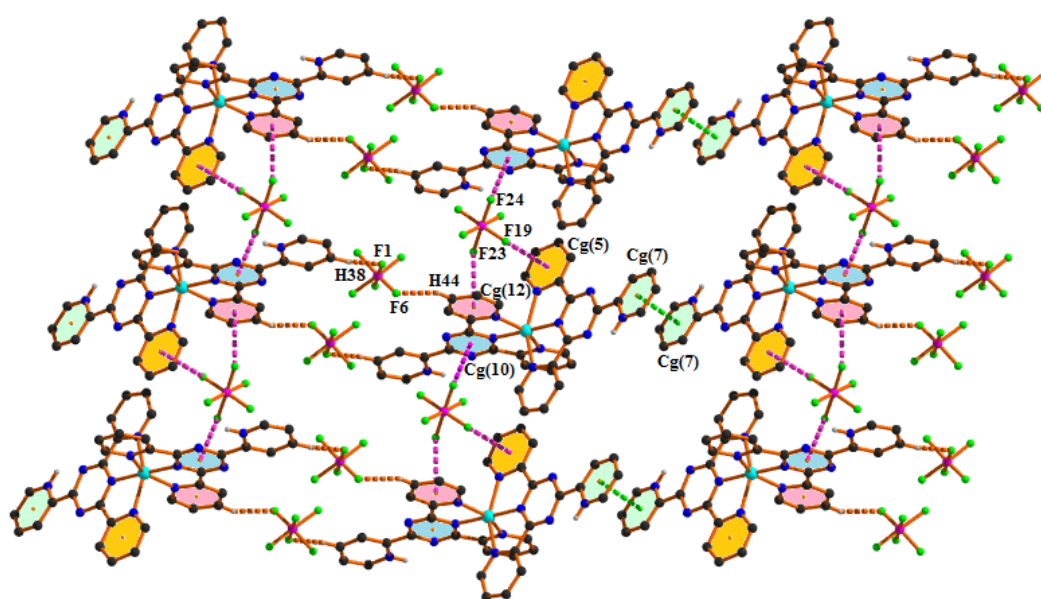
Fig. 4.12. Perspective view of 2-D architecture incorporating anion•••π / π^+•••π^+ / hydrogen bonding interactions in complex **2** (other aromatic hydrogen atoms have been omitted for clarity).

Table 4.10. Geometrical parameters for the hydrogen bonds of complex 2

D–H•••A	D–H [Å]	H•••A [Å]	D•••A [Å]	D–H•••A [°]	Symmetry
O2─H2B•••F10	0.8500	2.4100	2.995(8)	127.00	–
O2─H2B•••F12	0.8500	2.3700	2.990(8)	130.00	–
N15─H15•••O2	0.8600	1.9200	2.717(8)	154.00	–
C2─H2•••F6	0.9300	2.5300	3.444(13)	167.00	1-x, 1-y, 1-z
C13─H13•••F13	0.9300	2.5400	3.166(8)	124.00	-x, -y, 1-z
C14─H14•••F18	0.9300	2.4900	3.286(9)	143.00	-x, -y, 1-z
C38─H38•••F1	0.9300	2.2000	3.08(2)	157.00	x, y, -1+z
C39─H39•••F4	0.9300	2.5400	3.252(16)	133.00	x, y, -1+z
C44─H44•••F6	0.9300	2.5100	3.400(14)	161.00	-x, 1-y, 1-z
C45─H45•••F17	0.9300	2.4500	3.089(10)	126.00	–
C46─H46•••F15	0.9300	2.5300	3.431(8)	164.00	–

In addition, one-dimensional (1-D) tape is formed in complex **2** using anion•••π and hydrogen bonding interactions (Fig. 4.13). Firstly, monomeric cationic units are connected through anion•••π interactions via one F atom (F15) with Cg(6) of one unit and one F atom (F17) with Cg(5) of another unit for the propagation of a one-dimensional (1-D) polymeric chain along [100] direction. Due to the self complementary nature, the two parallel chains are interlinked through another anion•••π interaction via one F atom (F9) with Cg(8) of one monomeric unit and three hydrogen bonding [P2─F10•••O2, P2─F12•••O2 and N15─H15•••H2B] interactions, thus resulting a 1-D tape (as shown in Fig. 4.13).
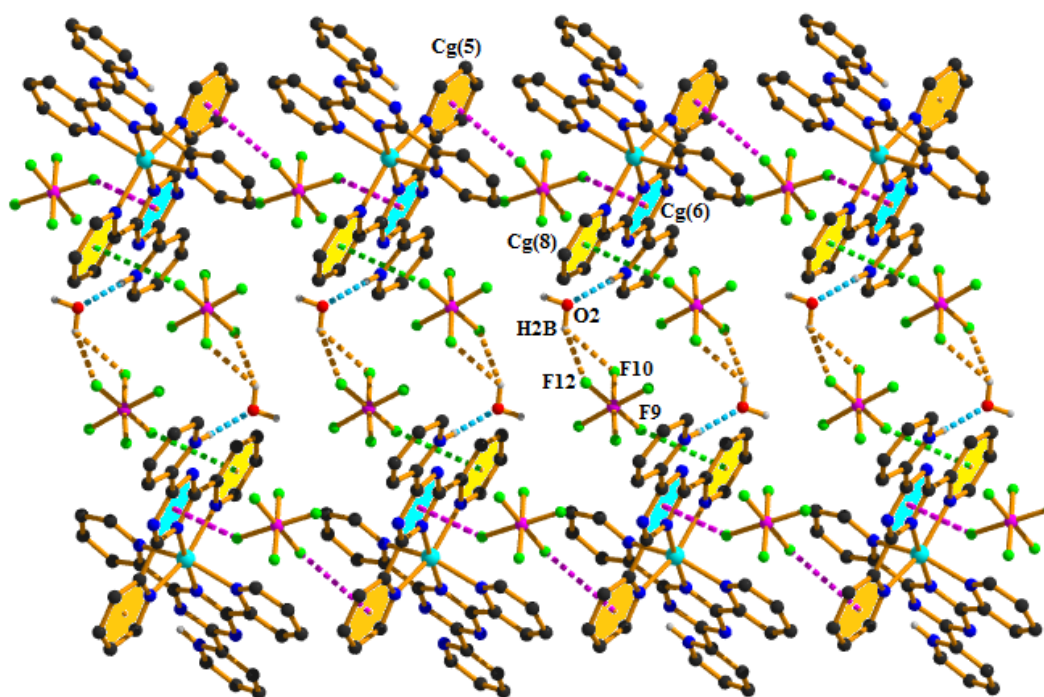
Fig. 4.13. Perspective view of 1-D tape generated through incorporating anion•••π and hydrogen bonding interactions in complex **2** (aromatic hydrogen atoms have been omitted for clarity).

Another two-dimensional (2-D) layer (Fig. 4.14) is formed in complex **2** using anion•••π and anion•••π$^+$ interactions. Here, monomeric cationic units are connected through anion•••π interactions via one F atom (F22) with Cg(5) of first unit and Cg(10) of second unit for the propagation of a one-dimensional (1-D) polymeric chain. Now, this 1-D chain is further extended to 2-D layers (110) through another anion•••π interaction [via one F atom (F17) with Cg(5) of one unit] and anion•••π$^+$ interaction [via one F atom (F18) with Cg(7) of the other unit]. In addition, the crystal structure of **2** reveals the existence of various intermolecular hydrogen bonding interactions in the solid state leading to the organization of one-dimensional (1-D) zigzag polymeric chain along [001] direction (Fig. 4.15).
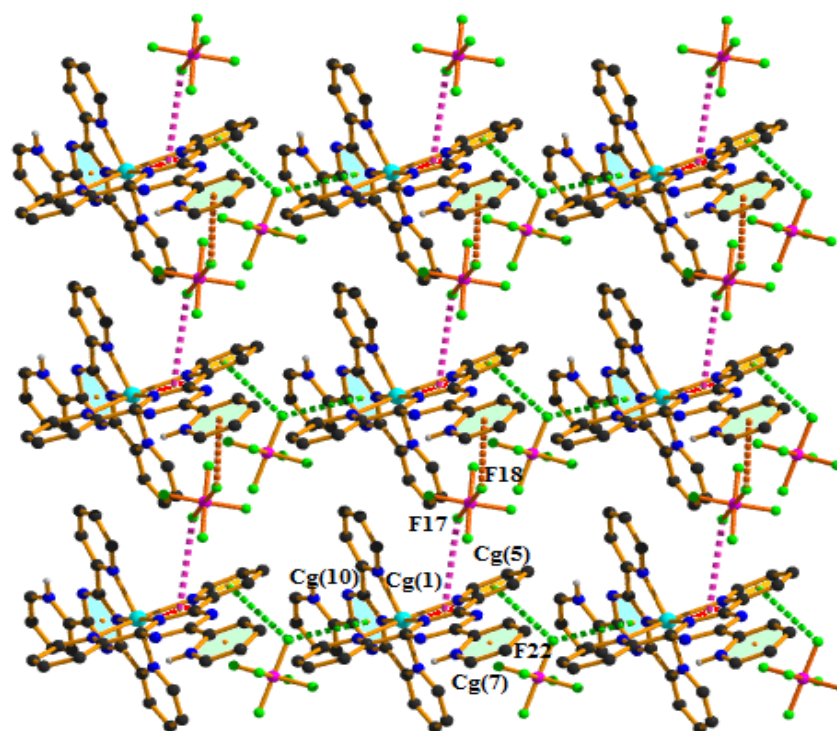
Fig. 4.14. Perspective view of 2-D layer incorporating anion•••π and anion•••π⁺ interactions in complex **2**(aromatic hydrogen atoms have been omitted for clarity).

Here, two monomeric cationic units are interconnected through the self complementary C13─H13•••F13, C14─H14•••F18, C45─H45•••F17 and C46─H46•••F15 hydrogen bonds (shown in green dotted lines); thus generating two different $R_2^2(7)$ ring motifs.

Now these dimeric units are repeated in a zigzag fashion via another two intermolecular hydrogen bonding [C2─H2•••F6 and C39─H39•••F4] interactions which are self complementary in nature (shown in pink dotted lines).
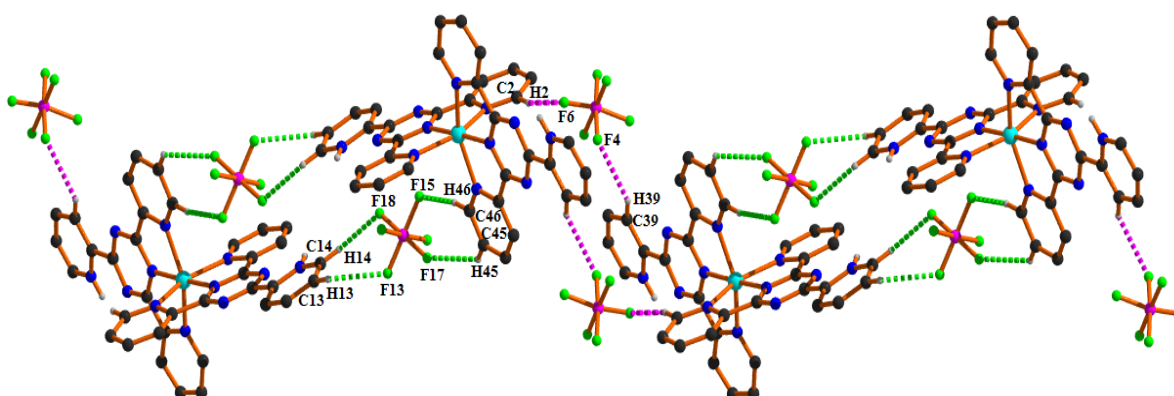
Fig. 4.15. One-dimensional (1-D) zigzag polymeric chain through C─H•••F hydrogen bonding interactions in complex **2** (other aromatic hydrogen atoms have been omitted for clarity).

4.3.3. Theoretical studies

The theoretical study is mainly focused to the study on the analysis of the π-stacking assemblies in complex **1** and anion···π interactions in complex **2**. Fig. 4.16a shows a partial view of the X-ray structure of **1** where the π•••π/π•••π/π•••π four-component assembly is highlighted. Two different types of π-stacking are formed: (i) a non-conventional one, denoted as (π•••π)$_1$, established between two non-coordinated dipicolinic acids, where the exocyclic carboxylic group of one ligand interacts with the π-cloud of the adjacent ligand, and vice versa. (ii) A conventional one, denoted as (π•••π)$_2$, where the aromatic rings of the coordinated and non-coordinated dipicolinic acids interact. The latter is expected to be stronger due to the larger polarization of the π-system as a consequence of the coordination of the ligand to the Ni(II) metal center. The formation energy of this assembly is very large ($\Delta E_{assembly}$ = –52.4 kcal/mol) thus confirming the relevance of the cooperative π•••π/π•••π/π•••π interactions in the solid state of **1**. In order to compare both types of π-stacking and also the existence of cooperativity effects, additional calculations have been performed, which are summarized in Fig. 4.16 b,c.
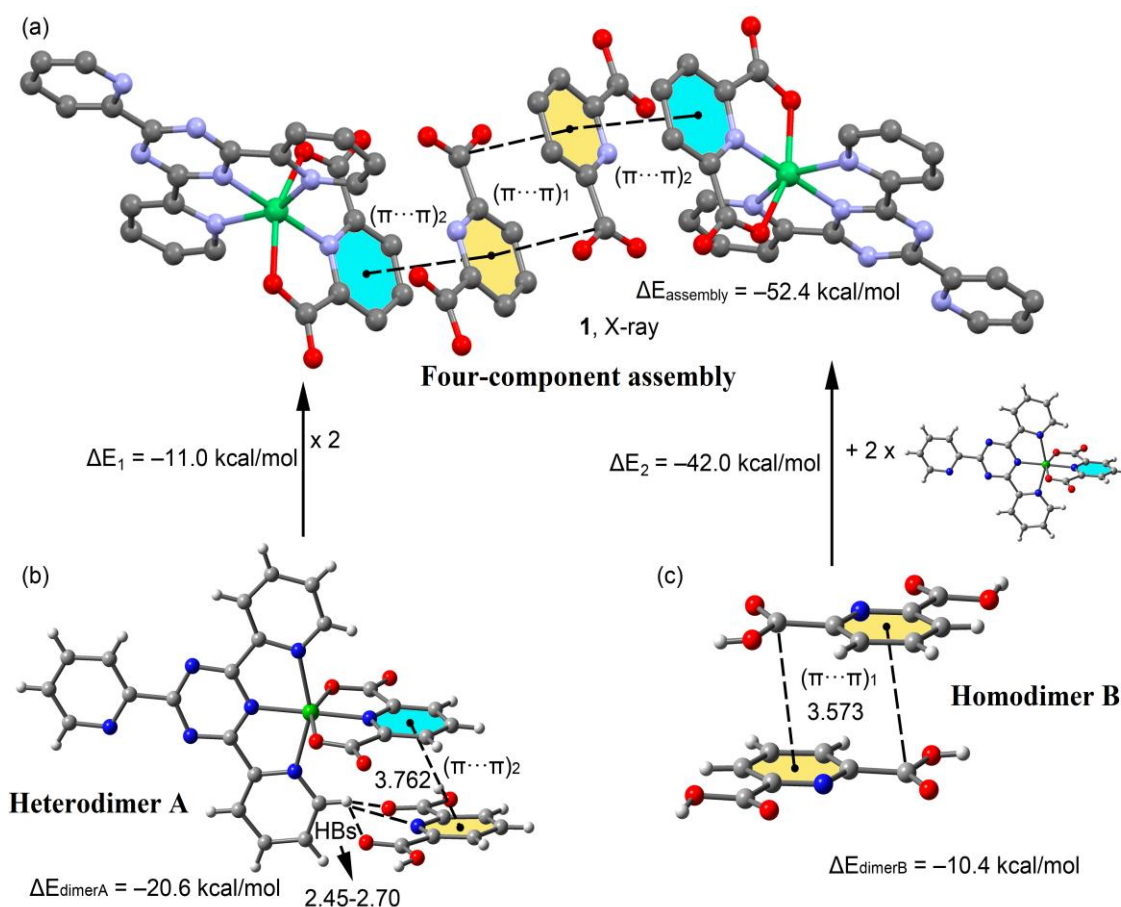

Fig. 4.16. (a) Partial view of the X-ray structure of **1** (H-atoms omitted for clarity). Theoretical models (b,c) used to evaluate the interaction energies. Distances are in Å.

It can be observed that the interaction energies of heterodimer **A** (Fig. 4.16b) and homodimer **B** (Fig. 4.16c) are $\Delta E_{heterodimerA}$ = –20.6 kcal/mol and $\Delta E_{homodimerB}$ = –10.4 kcal/mol, respectively, thus confirming the fact that $(\pi\bullet\bullet\bullet\pi)_2$ binding mode is stronger. This larger dimerization energy is also due to the formation of a trifurcated H-bond between one aromatic C–H group and two O-atoms and one N-atom of the dipicolinic acid (see dashed lines in Fig. 4.16b). In order to investigate the existence of cooperativity effects, the formation energy of the tetramer have also been computed by using heterodimer **A** as starting point, which is ΔE_1 = –11.0 kcal/mol.

The comparison of this formation energy with the one of homodimer **B** ($\Delta E_{homodimerB}$ = –10.4 kcal/mol) gives information about the influence of $(\pi\bullet\bullet\bullet\pi)_2$ on the strength of $(\pi\bullet\bullet\bullet\pi)_1$. Consequently, the $(\pi\bullet\bullet\bullet\pi)_1$ is reinforced by 0.6 kcal/mol due to its coexistence with $(\pi\bullet\bullet\bullet\pi)_2$, thus confirming the existence of cooperativity effects. Similarly, the formation energy of the four-component assembly have also been computed using homodimer **B** as starting point. The formation energy is ΔE_2 = –42.0 kcal/mol that accounts for two symmetrically equivalent $(\pi\bullet\bullet\bullet\pi)_2$ interactions. The comparison of this interaction energy with twice the dimerization energy of heterodimer **A** (2 x $\Delta E_{heterodimerA}$ = –41.2 kcal/mol reveals that the $(\pi\bullet\bullet\bullet\pi)_2$ interactions are reinforced by 0.8 kcal/mol as a consequence of the presence of the $(\pi\bullet\bullet\bullet\pi)_1$.

The non-covalent interaction plot index (NCI Plot) have also been used to characterize the $\pi\bullet\bullet\bullet\pi/\pi\bullet\bullet\bullet\pi/\pi\bullet\bullet\bullet\pi$ assembly in **1**. The NCI plot is an intuitive method that shows which spatial regions between molecules interact. Consequently, it is very convenient to analyze non-covalent interactions. Moreover, it gives hints regarding the strength of the interactions by using a color code, where green is used for weak interactions and yellow for repulsive ones. Strongly attractive and repulsive interactions are represented by blue and red colors, respectively.

The NCI plot of the four-component assembly is given in Fig. 4.17, which confirms the existence of the $\pi\bullet\bullet\bullet\pi$ stacking interactions that are characterized by large and green isosurfaces. In case of $(\pi\bullet\bullet\bullet\pi)_1$, the isosurfaces embrace the carboxylic groups, thus confirming their participation in the π-stacking interaction. In case of $(\pi\bullet\bullet\bullet\pi)_2$ binding mode, the isosurface is more extended, evidencing a larger overlap of the π-systems. Moreover, the existence of the trifurcated C–H$\bullet\bullet\bullet$O, N, O interaction is also confirmed by the presence of a green isosurface located between the H-atom and the three electron donor atoms belonging to the dipicolinic acid.
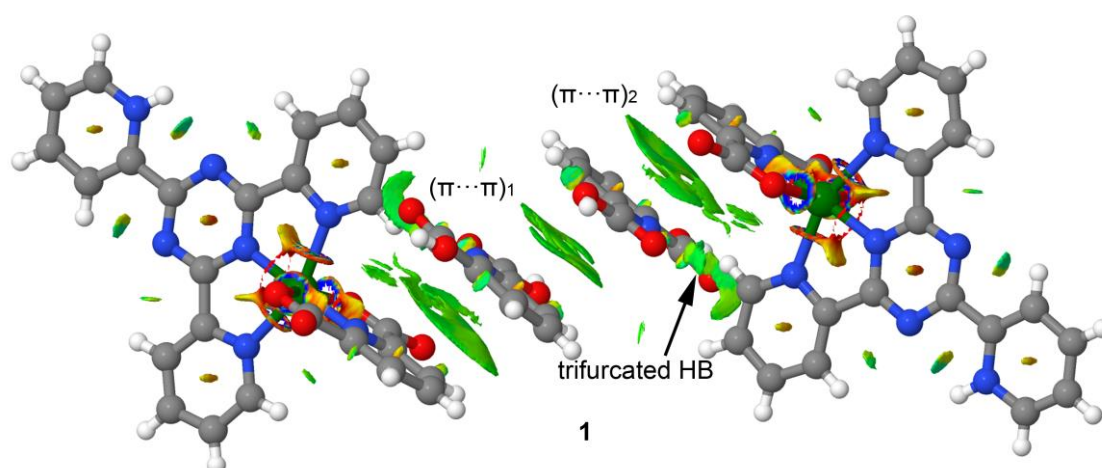
Fig. 4.17. NCI Plot of the four-component assembly of **1**. Isosurface 0.4 a.u. Density cut-off 0.04 a.u. Color scale –0.035 a.u. ≤ sign(λ2)ρ ≤ 0.035 a.u.

Finally, anion•••π interactions observed in the solid state of complex **2** have also been studied the by using the NCI Plot index, as shown in Fig. 4.18. The NCI plot representation shows that up to six PF_6^- anions concurrently form anion–π interactions with the extended and π-acidic rings of the Ni(II)-coordinated 2,4,6-tri(pyridin-2-yl)-1,3,5-s-triazine ligands. Due to the protonation of the ligand, the anion•••π interactions are very strong. Two of them as representative contacts have been evaluated, (as shown in Fig. 4.18) and the interaction energies are –98.4 and –89.2 kcal/mol, which are in the range of previously reported anion–$π^+$ interactions [81].
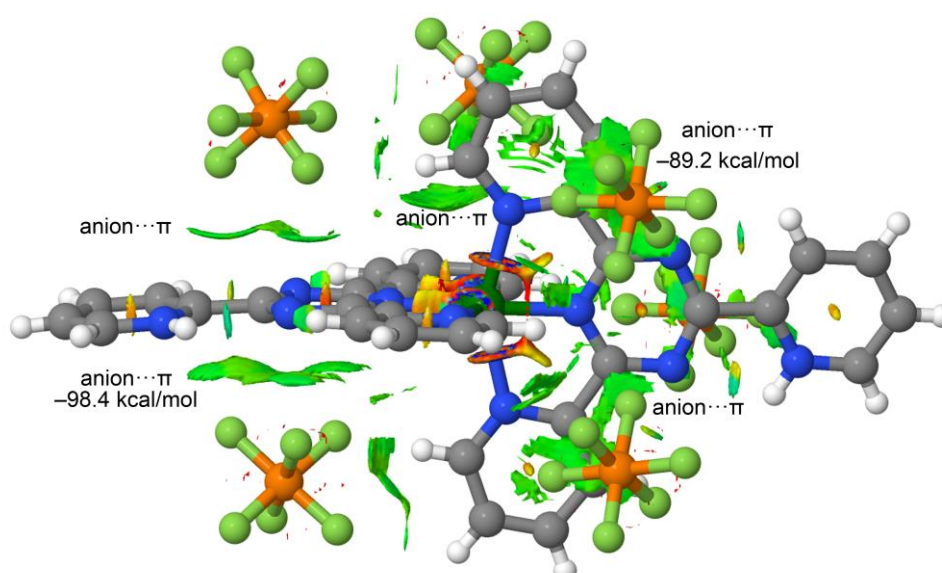
Fig. 4.18. NCI Plot of complex **2** surrounded by six PF_6^- anions establishing anion–π interactions. Isosurface 0.4 a.u. Density cut-off 0.04 a.u. Color scale –0.035 a.u. ≤ sign(λ₂)ρ ≤ 0.035 a.u.

4.3.4. Optical studies

UV-vis absorption spectra were taken to calculate the band gap of the complexes and to know the type of absorption. Fig. 4.19 (a) and (b) show UV-Vis absorption spectra of complex **1** and **2** respectively. Almost similar sharp visible range absorptions are observed for both complexes. To calculate band gap energy conventional Tauc's relation was used

$$(\alpha h\nu) \propto (h\nu - E_g)^n \qquad (1)$$

Where, α represents absorption coefficient; $h\nu$ is photon energy; E_g represents band gap of material and coefficient 'n' is for direct band-to-band transition having value ½. Now plotting $(\alpha h\nu)^2$ *vs* $h\nu$ and extrapolating the linear portion of the curve gives the corresponding optical band gap of the complex. The band gaps (E_g) were calculated to 3.89 and 3.76 eV for complexes **1** and **2** respectively and it was shown in the inset of Fig. 4.19. The wide band gap of both complexes falls under semiconductor regime and is an indication of device making properties.

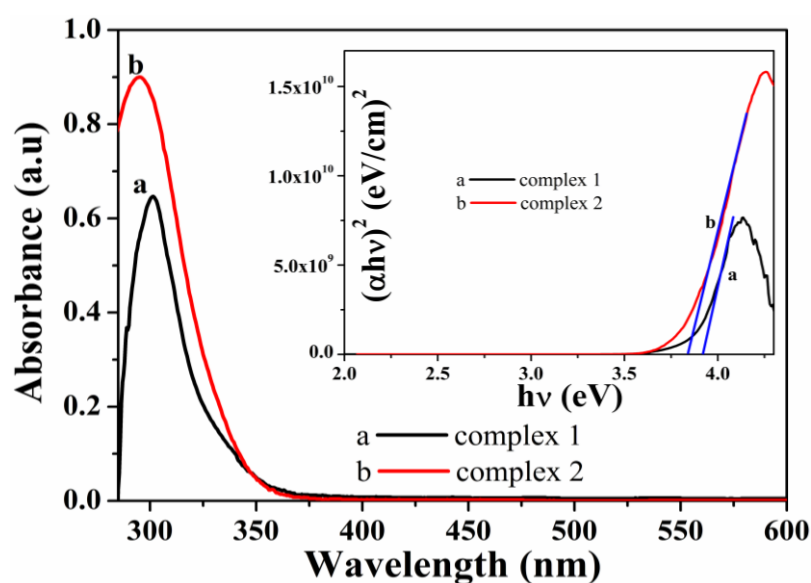**Fig. 4.19.** UV-Vis spectrum of (a) complex **1** inset: band gap (b) complex **2** and; inset: band gap.

4.3.5. Electrical measurements

Electrical measurements were performed at room temperature under dark and illumination condition (Sun light) in the voltage range of −1 to +1 V. Fig. 4.20 represents characteristics current–voltage (I–V) curves of the devices under dark and illumination conditions. I–V

nature of both complexes shows non-linear rectifying nature which indicates materials are of p type and that form Schottky junction with n type FTO substrate.

The nature of the I–V curve represents the rectifying behaviour, similar to the Schottky Barrier Diode (SBD). It indicates that the rectifying nature is highly influenced under illumination of incident radiation. The current rectification i.e. the On/Off ratio of the device 1 under dark and photo-illumination were found to be 2.95 and 31.31 at ±1 V whereas for device 2 the rectification ration enhanced to 31.32 and 54.93 under dark and illumination conditions respectively. Conductivity measurement of the devices further indicates enhanced electron transportation property of device 2 under light condition. Room temperature conductivity for device 1 was calculated to be $2.4×10^{-6}$ S cm^{-1} and $6.0×10^{-6}$ S cm^{-1} under dark and light condition respectively, whereas for device 2 under same condition the conductivity increased to $1.48×10^{-5}$ S cm^{-1} and $3.24×10^{-5}$ S cm^{-1}. The outcome indicates significant photoresponse of the device 2 compared to device 1.
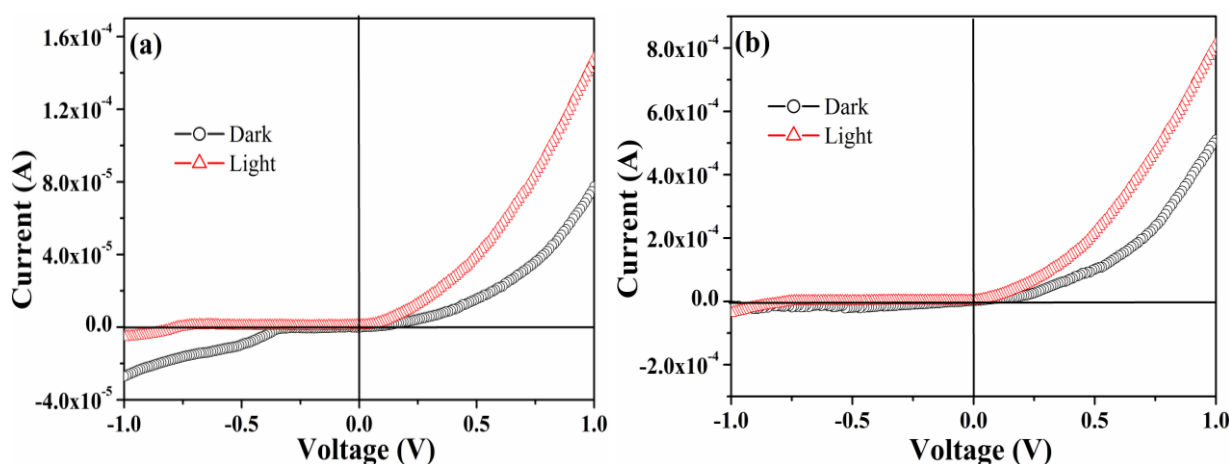
Fig. 4.20. I–V characteristic curve of (a) device 1 under dark and illumination conditions, (b) device 2 under dark and illumination.

To investigate the predominant charge transportation mechanism, these I–V curves are must be carefully analysed. The non-linear I–V nature of the devices arises due to different types of charge transportation mechanisms and which can be explained by the established model of Richardson-Schottky or Poole-Frankel [82]. Thermal activation of electrons over the metal-semiconductor interface results Schottky emission in presence of applied field [83]. To get a clear understanding into the charge transport mechanism thermionic emission theory has been adapted to quantitatively analyse the I-V plots where device parameters were verified by Cheung's standard equation [84].

$$I = I_0 \left[exp\left(\frac{qV}{\eta kT}\right) - 1 \right] \tag{2}$$

Here, I and I_0 are forward and reverse saturation current, V and q are applied potential and electron's charge, k and T are Boltzmann constant and absolute temperature, η represents ideality factor of SBD. Saturation current (I_0) can be expressed as

$$I_0 = AA^*T^2 \exp\left(\frac{-q\Phi_B}{KT}\right) \qquad (3)$$

Where the terms ϕ_B represents barrier height; 'A' and 'A*' are diode area and Richardson constant, respectively. For both devices diode area was fixed as 7×10^{-2} cm^2, and the effective Richardson constant was taken as 32 A K^{-2} cm^{-2}. Now, I−V characteristics can also be represented as

$$I = I_0 \left[\exp\left(\frac{q(V - IR_s)}{\eta kT}\right)\right] \qquad (4)$$

Where the term IR$_S$ stands for voltage drop across the series resistance can be calculated from the following equation:

$$\frac{dv}{d(lnI)} = \frac{\eta kT}{q} + IR_s \qquad (5)$$

Equation (9) can also be expressed as a function of 'I' by the following form

$$H(I) = IR_S + \eta\Phi_B \qquad (6)$$

Hence series resistance (Rs) can be measured and tallied by above two consecutive equations H(I) can also be represented by the following equation

$$H(I) = V - \left(\frac{\eta kT}{q}\right)\ln\left(\frac{I}{AA^*T^2}\right) \qquad (7)$$

Now using equation 5, dV/d(ln I) versus I (Fig. 4.21) is plotted to measure series resistance (R$_S$) from the slope and ideality factor (η) from the intercept (under dark and light illumination). The calculated ideality factor (η) values for device 1 are 2.81 and 1.79 respectively under dark and light conditions whereas for device 2 the η values become 2.53 and 1.41 under same condition. Hence with the irradiation of incident radiation the device 2 goes more towards ideality.

Deviation of η values from ideality (η = 1) is an indication of improper metal-semiconductor junction which results from trapping states in the interface. Structural disorderness of complex plays a significant role; more clutter structure brings more trapping

states and thereby easily deviates from ideal value. There are some reports on SBD device analysis that impose some other factors like surface contamination, barrier tunnelling etc., responsible for non ideality [85,86].
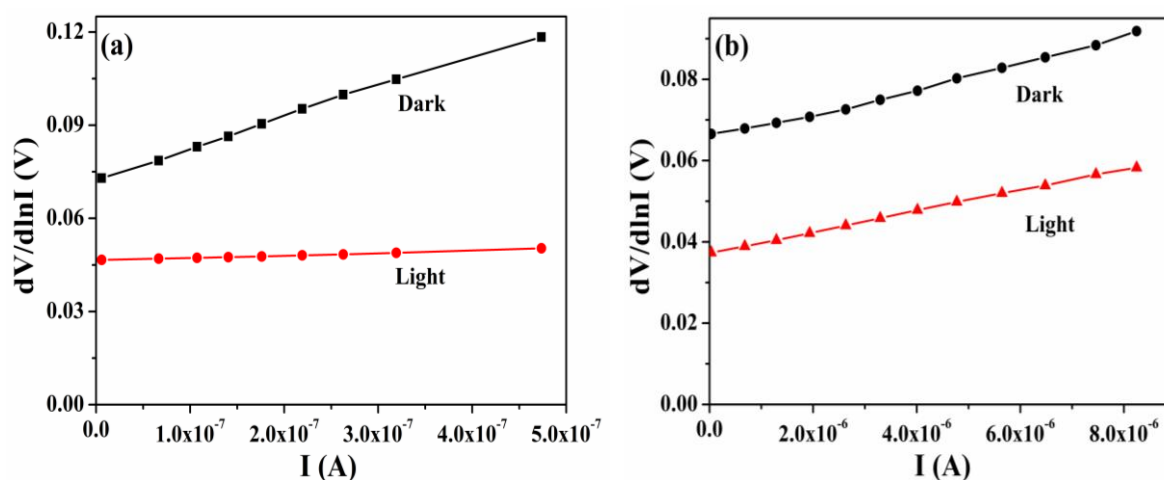
Fig. 4.21 dV/dln I vs. I plot under dark and illumination conditions for (a) complex **1** and (b) complex **2**.

The potential barrier height (Φ_B) values are calculated from the intercepts of H(V) vs. I plot of both devices (Fig. 4.22) using equation 6. The 'H' values are calculated by means of η values obtained from Fig. 4.21 using equation (5).
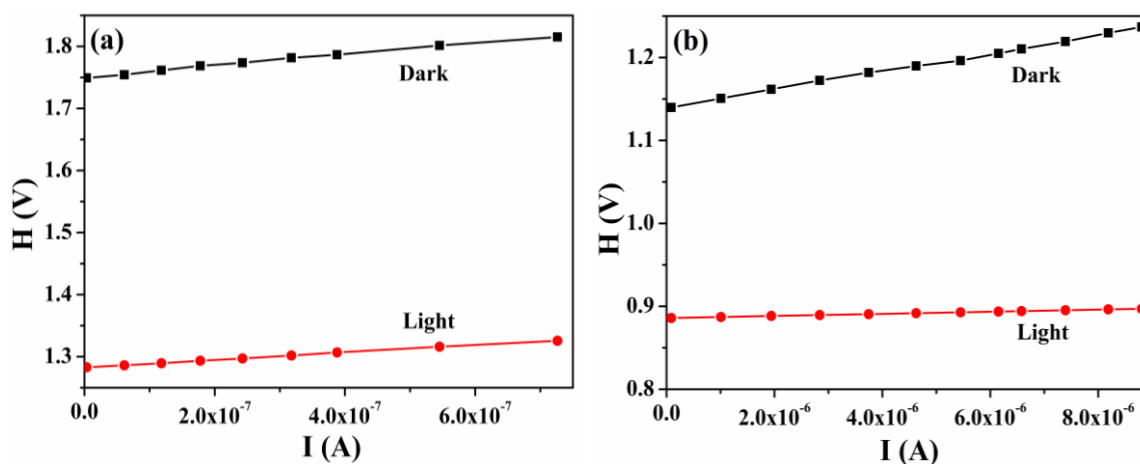
Fig. 4.22. H (V) vs I plot under dark and illumination condition for (a) device 1 and (b) device 2.

To make a depth on charge transport phenomenon of carrier transport through the interface of the MS junction, the log-log plot i.e., log(I) versus log(V) was analyzed (Fig. 4.23). Presence of two distinct regions in the log-log plot ensures different conduction mechanisms are being operating here. Now applying power law ($I \propto V^m$) (where m is slope value) on log-log plot the governing mechanism prevailing in carrier conduction can be

specified. By analyzing slope values 'm' two distinct zones can be separated out, m ≥ 2 indicates a space-charge-limited-current (SCLC) region whereas being less than or equal to 1 (m ≤ 1) indicates ohmic zone [87,88]. Fig. 4.23 represents log (I) vs. log (V) plot of device 1 and 2 in absence and presence of light. Presence of two separate regions indicates that different conduction mechanisms are prevailing here. At region-I i.e., at low bias voltage, the complex exhibits ohmic nature (I ∝V).
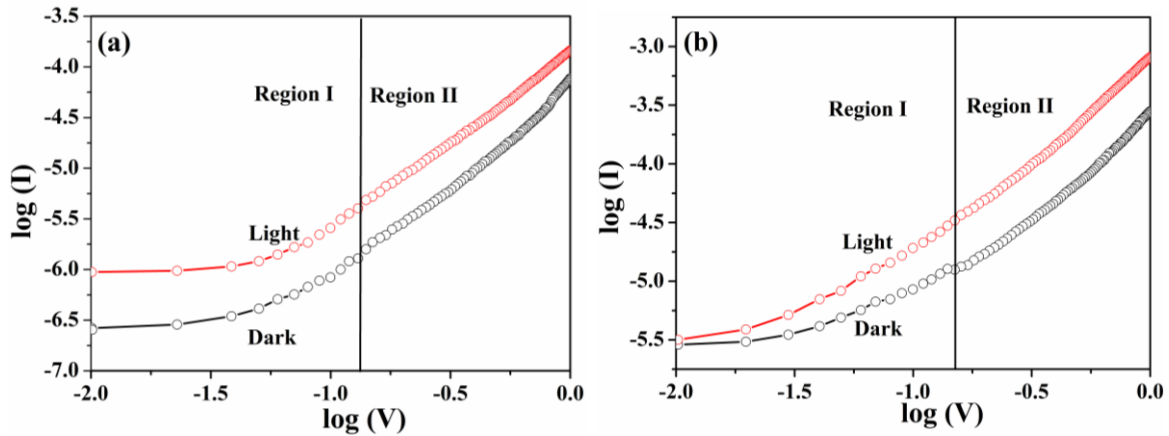
Fig. 4.23. log (I) vs. log (V) plot under dark and illumination conditions for (a) device 1 (b) and device 2.

The I–V characteristic in this region can be imposed to thermionic emission. Just after that the I–V curve obeys power law behaviour (I ∝ V^m) and it is assigned as region II. In region II, the current is ruled by the space charge limited current (SCLC) which is proportional to the square of applied voltage (I ∝ V^2) [89,90]. This SCLC region gives several important device performances like carrier concentration (N), carrier mobility (μ_{eff}), diffusion coefficient (D), diffusion length (L_D), transit time (τ), *etc*.

Dielectric constants of the complexes were measured from the saturation capacitance (C) value of capacitance vs. frequency plot (Fig. 4.24) by using the following equation [91].

$$\varepsilon_r = \frac{1}{\varepsilon_0} \cdot \frac{C.L}{A} \qquad (8)$$

Here, L is thickness of deposited material and A is diode area.

The measured relative dielectric constants of the material were calculated to be 32.26 and 6.45 for complex **1** and **2** respectively. Comparatively low dielectric constant of complex **2** suggests its preferential use in power generation to minimize electric power loss.
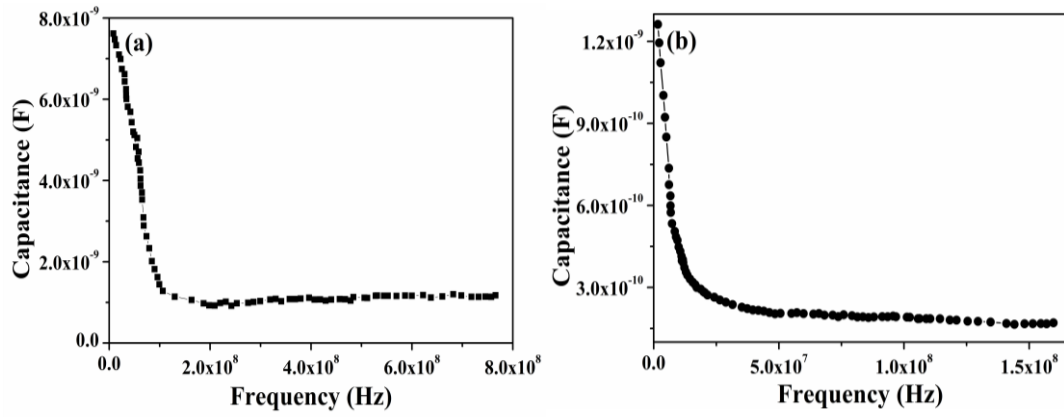
Fig. 4.24. Capacitance *vs.* Frequency plot of (a) device 1 and (b) device 2.

Effective carrier mobility (μ_{eff}) of both devices have been calculated from I vs. V^2 (Fig. 4.25) plot by employing Mott–Gurney equation (11) [92].

$$J = \frac{9\mu_{eff}\varepsilon_0\varepsilon_r}{8}\left(\frac{V^2}{d^3}\right) \tag{9}$$

Here J is current density, ε_0 and ε_r is permittivity of vacuum and relative dielectric constant of complex respectively. The device made of complex 2 has the higher mobility (5.36×10^{-4}cm^2 V^{-1} s^{-1}) than complex 1 (3.19×10^{-4}cm^2 V^{-1} s^{-1}).
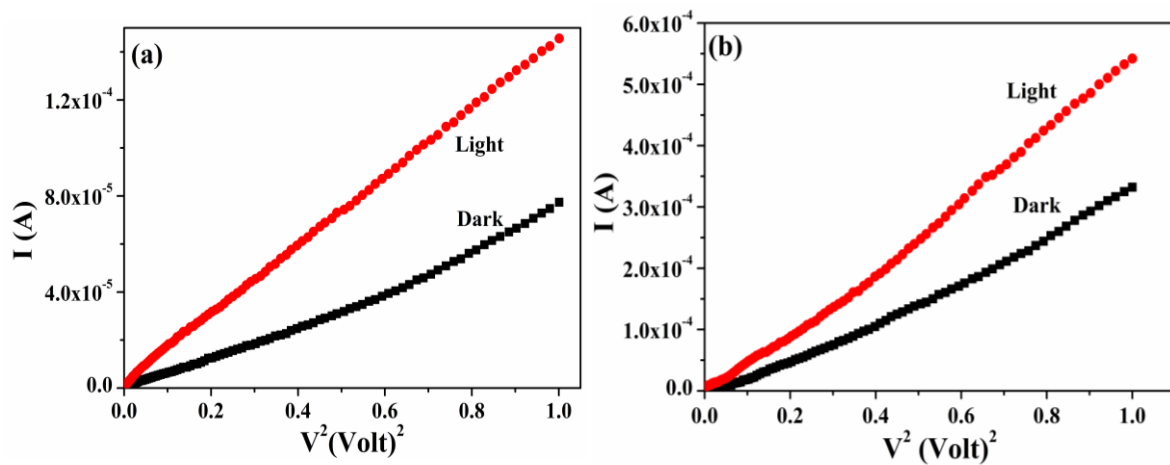
Fig. 4.25. I vs V^2 graph for complex **1** under (a) dark and (b) illumination conditions and I vs V^2 graph of complex **2** under (c) dark and (d) illumination conditions.

Other important device performance like carrier concentration (N), carrier mobility (μ_{eff}), diffusion coefficient (D), diffusion length (L_D), transit time (τ) etc. are calculated using the following set of equations.

$$N = \frac{\sigma}{q\mu_{eff}} \tag{10}$$

$$\tau = \frac{9\varepsilon_0\varepsilon_r A}{8d}\left(\frac{V}{I}\right) \qquad (11)$$

$$\mu_{ef} = \frac{qD}{kT} \qquad (12)$$

$$L_D = \sqrt{2D\tau} \qquad (13)$$

Table 4.11. Device parameter for complex 1

Condition	on/off	Conductivity δ(S cm^{-1})	ideality factor (η)	dv/dlnI Rs (k ohm)	H Rs (k ohm)	barrier height (Φ)$_B$	transit time t$\times10^{-9}$ (s)	D $\times10^{-6}$	L$_D$ $\times10^{-7}$	Mobility μ_{eff} $\times10^{-5}$ (cm^2 V^{-1} s^{-1})
Dark	2.95	2.45$\times10^{-3}$	2.81	9.63	9.40	0.64	8.31	3.69	2.476	7.14
Light	31.31	6.06$\times10^{-3}$	1.79	5.58	5.18	0.70	6.3	18.45	2.584	14.30

Table 4.12. Device parameter for complex 2

Condition	on/off	Conductivity δ(S cm^{-1})	ideality factor (η)	dv/dlnI Rs (k ohm)	H Rs (k ohm)	barrier height (Φ)$_B$	transit time t$\times10^{-9}$ (s)	D $\times10^{-6}$	L$_D$ $\times10^{-7}$	Mobility μ_{eff} $\times10^{-5}$ (cm^2 V^{-1} s^{-1})
Dark	31.21	1.54$\times10^{-2}$	2.53	3.11	2.64	0.73	7.2	8.25	3.447	3.19
Light	54.93	3.24$\times10^{-2}$	1.44	2.58	2.17	0.60	5.7	13.86	3.976	5.36

The better performance of a SBD device can be categorised by high value of N, μ_{eff} and L$_D$. All device parameters for both the devices are listed in Table 4.11 (complex **1**) and Table 4.12 (complex **2**). From the detail analysis with respect to device performance it can be concluded that the device 2 made from complex **2** is quite better than 1.

A comparison of the conductivities of recently reported Ni(II) based complexes with our synthesized complexes **1** and **2** (Table 4.13) shows that the present materials have enough potentiality in optoelectronic applications.

Table 4.13. Conductivity data reported for single crystals of Ni-based complexes at room temperature

Ni(II) complexes	Electrical conductivity (S cm^{-1})	Reference
$[Ni_2(C_4N_2H_3S)_4]_n$	5×10^{-3}	93
$C_{20}H_{10}N_4NiHg_2S_4$	2.18×10^{-10}	94
$Ni_2(C_{22}H_{20}N_6O_4)_n$	2.15×10^{-11}	95
$C_{10}H_{23}N_4O_8SClNi$	2.14×10^{-9}	96
$C_{60}H_{54}Br_4N_4Ni_2O_{13}$	3.57×10^{-4}	97
$Ni(BzO_4[16]octaeneN_4)](ClO_4)_2$	6.97×10^{-4}	98
$C_{52}H_{40}F_2N_8NiS_2$	9.81×10^{-9}	99
$C_{32}H_2N_8NiClO_9$ (Complex **1**)	6.0×10^{-6}	Present work
$C_{36}H_{28}N_{12}NiOF_{24}P_4$ (Complex **2**)	3.24×10^{-5}	Present work

4.4. CONCLUSION

Two nickel (II) complexes have been synthesized successfully and characterised where both triazine moiety and pyridine-2,6-dicarboxylic acid act as ligands for complex **1** and only triazine moiety binds Ni(II) in complex **2**. In the synthesized metal ligand frameworks, various supramolecular interactions specially π···π stacking, anion•••π interactions along with lone pair•••π, C—H•••π, anion•••π$^+$, π•••π$^+$, π$^+$•••π$^+$ and hydrogen bonding interactions are present. These imperative interactions are responsible in the construction of extended networks in the solid state architectures of **1** and **2**. Theoretical (DFT) calculations have been used to evaluate π-stacking behaviors energetically in the four-component assembly π•••π/π•••π/π•••π of complex **1** and various anion•••π interactions in complex **2**.

Finally, the interactions have been analyzed using the NCI plot indexes. The practical application of both the complexes has been initiated by fabricating SBD device using silver as metal contact. The devices made from complexes **1** and **2** exhibit non-linear rectifying behaviour under dark and light illumination at an applied potential of ±1.0 V. The measured device parameters e.g., mobility, transit time, carrier diffusion length, and ideality factor confirm complex **2** as better SBD compared to complex **1**. A likely explanation for this behaviour can be related to the presence of extensive π•••π stacking and a large number of counter-ions in complex **2**. Conductivity measurement of the devices further indicated enhanced charge transportation property of device 2 than device 1 under illumination condition. In fact, both Ni(II) coordination complexes reported herein illustrate reasonably higher electrical conductivities than other Ni-based complexes reported in the literature.

REFERENCES

1. A. K. Nangia and G. R. Desiraju, *Angew. Chem., Int. Ed.*, 2019, **58**, 4100–4107.

2. M. Du, C. -P. Li, C. -S. Liu and S. -M. Fang, *Coord. Chem. Rev.*, 2013, **257**, 1282−1305.

3. K. B. Thapa, Y. -F. Hsu, H. -C. Lin and J. -D. Chen, *CrystEngComm*, 2015, **17**, 7574–7582.

4. S. Konar, *Inorg. Chem. Commun.*, 2014, **49**, 76–78.

5. L. -P. Xue, Z. -H. Li, L. -F. Ma and L. -Y. Wang, *CrystEngComm*, 2015, **17**, 6441−6449.

6. S. Radi, M. El-Massaoudi, H. Benaissa, N. N. Adarsh, M. Ferbinteanu, E. Devlin, Y. Sanakis and Y. Garcia, *New J. Chem.*, 2017, **41**, 8232–8241.

7. J. Z. Gu, Y. Cai, X. X. Liang, J. Wu, Z. F. Shi and A. M. Kirillov, *CrystEngComm*, 2018, **20**, 906−916.

8. S. Jia, Z. Gao, N. Tian, Z. Li, J. Gong, J. Wang and S. Rohani, *Chem. Eng. Res. Des.*, 2021, **166**, 268–280.

9. B. Gole, A. K. Bar, A. Mallick, R. Banerjee and P. S. Mukherjee, *Chem. Commun.*, 2013, **49**, 7439−7441.

10. X.-Q. Guo, C. Huang, H.-Y. Yang, Z.-C. Shao, K. Gao, N. Qin, G.-X. Li, J. Wu and H.-W. Hou, *Dalton Trans.*, 2018, **47**, 16895−16901.

11. J. Z. Gu, M. Wen, Y. Cai, Z. F. Shi, A. S. Arol, M. V. Kirillova and A. M. Kirillov, *Inorg. Chem.*, 2019, **58**, 2403−2412.

12. K. J. Lee, J. H. Lee, S. Jeoung and H. R. Moon, *Acc. Chem. Res.*, 2017, **50**, 2684–2692.

13. A. C. Kizzie, A. G. Wong-Foy and A. J. Matzger, *Langmuir*, 2011, **27**, 6368–6373.

14. K. S. Song, D. Kim, K. Polychronopoulou and A. Coskun, *ACS Appl. Mater. Interfaces*, 2016, **8**, 26860–26867.

15. S. Mondal and P. Dastidar, *Cryst. Growth Des.*, 2019, **19**, 470−478.

16. K. Biradha, A. Goswami and R. Moi, *Chem. Commun.*, 2020, **56**, 10824−10842.

17. B. Dutta, R. Jana, A. K. Bhanja, P. P. Ray, C. Sinha and M. H. Mir, *Inorg. Chem.*, 2019, **58**, 2686–2694.

18. P. Ghorai, A. Dey, A. Hazra, B. Dutta, P. Brandao, P. P. Ray, P. Banerjee and A. Saha, *Cryst. Growth Des.*, 2019, **11**, 6431–6447.

19. B. Deka, T. Sarkar, S. Banerjee, A. Kumar, S. Mukherjee, S. Deka, K. K. Saikia and A. Hussain, *Dalton Trans.*, 2017, **46**, 396–409.

20. Q.-P. Qin, Z.-F. Wang, S.-L. Wang, D.-M. Luo, B.-Q. Zou, P.-F. Yao, M.-X. Tan and H. Liang, *Eur. J. Med. Chem.*, 2019, **170**, 195–202.

21. D. Das and K. Biradha, *Cryst. Growth Des.*, 2018, **18**, 3683−3692.

22. B. Parmar, K. K. Bisht, Y. Rachuri and E. Suresh, *Inorg. Chem. Front.*, 2020, **7**, 1082–1107.

23. J.-L. Zhu, P. Zhu, H.-T. Chen, M. Yan and K.-L. Zhang, *CrystEngComm*, 2021, **23**, 1929–1941.

24. G. Xu, P. Nie, H. Dou, B. Ding, L. Li and X. Zhang, *Mater. Today*, 2017, **20**, 191–209.

25. M. Inukai, S. Horike, T. Itakura, R. Shinozaki, N. Ogiwara, D. Umeyama, S. Nagarkar, Y. Nishiyama, M. Malon, A. Hayashi, T. Ohhara, R. Kiyanagi and S. Kitagawa, *J. Am. Chem. Soc.*, 2016, **138**, 8505–8511.

26. M. Guergueb, S. Nasri, J. Brahmi, F. Loiseau, F. Molton, T. Roisnel, V. Guerineau, I. Turowska-Tyrk, K. Aouadi and H. Nasri, *RSC Adv.*, 2020, **10**, 6900–6918.

27. M. Dai, H. X. Li and J. P. Lang, *CrystEngComm*, 2015, **17**, 4741–4753.

28. J. Huo, D. Yu, H. Li, B. Luo and N. Arulsamy, *RSC Adv.*, 2019, **9**, 39323−39331.

29. J. Liu, D. Xie, W. Shi and P. Cheng, *Chem. Soc. Rev.*, 2020, **49**, 1624–1642.

30. J. B. Gilroy and E. Otten, *Chem. Soc. Rev.*, 2020, **49**, 85–113.

31. N. Li, R. Feng, J. Zhu, Z. Chang, X. -H. Bu, *Coord. Chem. Rev.*, 2018, **375**, 558–586.

32. X. Q. Liang, R. K. Gupta, Y. W. Li, H. Y. Ma, L. N. Gao, C. H. Tung and D. Sun, *Inorg. Chem.*, 2020, **59**, 2680–2688.

33. J. Kim, B. L. Chen, T. M. Reineke, H. L. Li, M. Eddaoudi, D. B. Moler, M. O'Keeffe and O. M. Yaghi, *J. Am. Chem. Soc.*, 2001, **123**, 8239−8247.

34. Y. N. Gong, C. B. Liu, H. L. Wen, L. S. Yan, Z. Q. Xiong and L. Ding, *New J. Chem.*, 2011, **35**, 865−875.

35. G. Mahmoudi, F. A. Afkhami, E. Zangrando, W. Kaminsky, A. Frontera and D. A. Safin, *J. Mol. Struct.*, 2021, **1224**, 129188−129196.

36. A. Nijamudheen, D. Jose, A. Shine and A. Datta, *J. Phys. Chem. Lett.*, 2012, **3**, 1493–1496.

37. O. Perraud, V. Robert, H. Gornitzka, A. Martinez and J.-P. Dutasta, *Angew. Chem., Int. Ed.*, 2012, **51**, 504–508.

38. M. K. Bhattacharyya, D. Dutta, S. M. N. Islam, A. Frontera, P. Sharma, A. K. Verma and A. Das, *Inorg. Chim. Acta*, 2020, **501**, 119233−119247.

39. M. Mitra, P. Manna, A. Bauzá, P. Ballester, S. K. Seth, S. R. Choudhury, A. Frontera and S. Mukhopadhyay, *J. Phys. Chem. B*, 2014, **118**, 14713–14726.

40. A. Das, S. R. Choudhury, B. Dey, S. K. Yalamanchili, M. Helliwell, P. Gamez, S. Mukhopadhyay, C. Estarellas and A. Frontera, *J. Phys. Chem. B*, 2010, **114**, 4998–5009.

41. A. Das, S. R. Choudhury, C. Estarellas, B. Dey, A. Frontera, J. Hemming, M. Helliwell, P. Gamez, S. Mukhopadhyay, *CrystEngComm*, 2011, **13**, 4519–4527.

42. L. A. Barrios, G. Aromi, A. Frontera, D. Quiñonero, P. M. Deya, P.Gamez, O. Roubeau, E. J. Shotton, S. J. Teat, *Inorg. Chem.*, 2008, **47**, 5873–5881.

43. C.Garau, D. Quiñonero, A. Frontera, P. Ballester, A. Costa, P. M.Deyà, *Org. Lett.*, 2003, **5**, 2227–2229.

44. P. Manna, S. K. Seth, M. Mitra, A. Das, N. J. Singh, S. R. Choudhury, T. Kar and S. Mukhopadhyay, *CrystEngComm*, 2013, **15**, 7879–7886.

45. S. Pramanik, S. Konar, K. Chakraborty T. Pal, S. Das, S. Chatterjee, M. Dolai, S. Pathak, *J. Mol. Struct.*, 2020, **1206**,127663−127670.

46. J. J. Liu, S. B. Xia, Y. L. Duan, T. Liu, F. X. Cheng and C. K. Sun, *Polymer*, 2018, **10**, 165−176.

47. P. Thuéry and J. Harrowfield, *CrystEngComm*, 2015, **17**, 4006−4018.

48. Y. Rachuri, B. Parmar, K. K. Bisht and E. Suresh, *Dalton Trans.*, 2017, **46**, 3623−3630.

49. S. E. Domínguez, F. E. M. Vieyra and F. Fagalde, *Dalton Trans.*, 2020, **49**, 12742−12755.

50. Z.Azarkamanzad, F. Farzaneh, M. Maghami and J. Simpson, *New J. Chem.*, 2019, **43**, 12020–12031.

51. A. H. Sun, Q. Wei, A. P. Fu, S. D. Han, J. H. Li and G. M. Wang, *Dalton Trans.*, 2018, **47**, 6965–6972.

52. K. Abdi, H. Hadadzadeh, M. Salimi, J. Simpson and A. D. Khalaji, *Polyhedron*, 2012, **44**, 101–112.

53. D. A. Safin, J. M. Frost and M. Murugesu, *Dalton Trans.*, 2015, **44**, 20287−20294.

54. M. Maghami, F. Farzaneh, J. Simpson, M. Ghiasi, M. Azarkish, *J. Mol. Struct.*, 2015, **1093**, 24–32.

55. D. K. Maity, S. Ghosh, K. Otake, H. Kitagawa and D. Ghoshal, *Inorg. Chem.*, 2019, **58**, 12943−12953.

56. S. Bala, A. De, A. Adhikary, S. Saha, S. Akhtar, K. S. Das, M. -L. Tong, and R. Mondal, *Cryst. Growth Des.*, 2020, **20**, 5698−5708.

57. C. W. Machan, M. Adelhardt, A. A. Sarjeant, C. L. Stern, J. Sutter, K. Meyer and C. A. Mirkin, *J. Am. Chem. Soc.*, 2012, **134**, 16921–16924.

58. I. Kumar, P. Bhattacharya and K. H. Whitmire, *Organometallics*, 2014, **33**, 2906–2909.

59. K. Ghosh, A. Banerjee, A. Bauzá, A. Frontera and S. Chattopadhyay, *RSC Adv.*, 2018, **8**, 28216–28237.

60. Q.-P. Qin, Z. -F. Wang, M. -X. Tan, X. -L. Huang, H. -H. Zou, B. -Q. Zou, B. -B. Shi and S. -H. Zhang, *Metallomics*, 2019, **11**, 1005–1015.

61. M. D. Olawale, J. O. Obaleyeb and E. O. Oladelec, *New J. Chem.*, 2020, **44**, 18780−18791.

62. K. Sinziger, S. Hünig, M. Jopp, D. Bauer, W. Bietsch, J. U. von Schütz, H. C. Wolf, R. K. Kremer, T. Metzenthin, R. Bau, S. I. Khan, A. Lindbaum, C. L. Lengauer and E. Tillmans, *J. Am. Chem. Soc.*, 1993, **115**, 7696−7705.

63. R. Kato, H. Kobayashi, A. Kobayashi, T. Mori and H. Inokuchi, *Chem. Lett.*, 1987, **16**, 1579−1582.

64. R. Kato, H. Kobayashi and A. Kobayashi, *J. Am. Chem. Soc.*, 1989, **111**, 5224−5232.

65. S. Hünig and P. Erk, *Adv. Mater.*, 1991, **3**, 225−236.

66. D. Asakura, C. H. Li, Y. Mizuno, M. Okubo, H. Zhou and D. R. Talham, *J. Am. Chem. Soc.*, 2013, **135**, 2793–2799.

67. L. Welte, A. Calzolari, R. di Felice, F. Zamora and J. Gómez-Herrero, *Nat. Nanotechol.*, 2010, **5**, 110–115.

68. W. Shi, G. Wu, X. Yong, T. Deng, J. S. Wang, J. C. Zheng, J. Xu, M. B. Sullivan and S. W. Yang, *ACS Appl. Mater. Interfaces*, 2018, **10**, 35306–35315.

69. V. Rubio-Giménez, S. Tatay and C. Martí-Gastaldo, *Chem. Soc. Rev.*, 2020, **49**, 5601–5638.

70. *Bruker, SMART v5.631*, Bruker AXS Inc., Madison, WI, USA, 2001.

71. G. M. Sheldrick, *SHELXL-2014/7: Program for the Solution of Crystal Structures*, University of Gottingen, Gottingen, Germany, 2014.

72. C. Adamo and V. Barone, *J. Chem. Phys.*, 1999, **110**, 6158–6170.

73. S. Grimme, J. Antony, S. Ehrlich and H. Krieg, *J. Chem. Phys.*, 2010, **132**, 154104−154124.

74. F. Weigend, *Phys. Chem. Chem. Phys.*, 2006, **8**, 1057–1065.

75. M. J. Frisch, G. W. Trucks, H. B. Schlegel, G. E. Scuseria, M. A. Robb, J. R. Cheeseman, G. Scalmani, V. Barone, B. Mennucci, G. A. Petersson, H. Nakatsuj, M. Caricato, X. Li, H. P. Hratchian, A. F. Iamaylov, J. Bloino, G. Zheng, J. L. Sonnenberg, M. Hada, M. Ehara, K. Toyota, R. Fukuda, J. Hasegawa, M. Ishida, T. Nakajima, Y. Honda, O. Kitao, H. Nakai, T. Vreven, J. A. Montgomery Jr, J. E. Peralta, F. Ogliaro, M. Bearpark, J. J. Heyd, E. Brothers, K. N. Kudin, V. N. Staroverov, R. Kobayashi, J. Normand, K. Raghavachari, A. Rendell, J. C. Burant, S. S. Lyengar, J. Tomasi, M. Cossi, N. Rega, J. M. Millam, M. Klene, J. E. Knox, J. B. Cross, V. Bakken, C. Adamo, J. Jaramillo, R. Gomperts, R. E. Stratmann, O. Yazyev, A. J. Austin, R. Cammi, C. Pomelli, J. W. Ochterski, R. L. Martin, K. Morokuma, V. G. Zakrzewski, G. A. Voth, P. Salvador, J. J. Dannenberg, S. Dapprich, A. D. Daniels, O. Farkas, J. B. Foresman, J. V. Ortiz, J. Cioslowski and D. J. Fox, *Gaussian 09, Revision A.1*, Gaussian Inc., Wallingford CT, 2016.

76. R. F. W. Bader, *Chem. Rev.*, 1991, **91**, 893−928.

77. E. R. Johnson, S. Keinan, P. Mori-Sánchez, J. Contreras-García, A. J. Cohen and W. Yang, *J. Am. Chem. Soc.*, 2010, **132**, 6498–6506.

78. J. Contreras-García, E. R. Johnson, S. Keinan, R. Chaudret, J. -P. Piquemal, D. N. Beratan and W. Yang, *J. Chem. Theory Comput.*, 2011, **7**, 625–632.

79. T. A. Keith, *AIMALL (Version 19.02.13)*, TK Gristmill Software, Overl. Park KS, USA, 2019.

80. L. E. Zelenkov, D. M. Ivanov, K. Sadykov, N. A. Bokach, B. Galmes, A. Frontera, V. Yu. Kukushkin and Yu. Vadim, *Cryst. Growth Des.*, 2020, **20**, 6956–6965.

81. P. Manna, S. K. Seth, M. Mitra, S. R. Choudhury, A. Bauzá, A. Frontera and S. Mukhopadhyay, *Cryst. Growth Des.*, 2014, **14**, 5812–5821.

82. S.M. Sze, Physics of Semiconductor Devices (Wiley, New York, 1969), p. 496.

83. J. G. Simmons, *Phys. Rev.*, 1967, 155, 657–660.

84. S. K. Cheung and N. W. Cheung, *Appl. Phys. Lett.*, 1986, **49**, 85–87.

85. M. W. Allen, S. M. Durbin, *Appl. Phys. Lett.*, 2008, **92**,12110–113.

86. D. T. Quan, H. Hbib, *Solid-State Electron.*, 1993,**36***,* 339–344.

87. A. Jain, P. Kumar, S. C. Jain, V. Kumar, R. Kaur and R. M. Mehra, *J. Appl. Phys.*, 2007, **102**, 094505−094511.

88. S. Aydogan, M. Saglam and A. Turut, *J. Phys.: Condens. Matter*, 2006, **18**, 2665–2676.

89. Z. Ahmad and M. H. Sayyad, *Physica E*, 2009, **41**, 631−634.

90. P. Kumar, S. C. Jain, V. Kumar, S. Chand, and R. P. Tandon, *J. Appl. Phys.*, 2009, **105**, 104507−104514.

91. S. Suresh, *Int. J. Phys. Sci.*, 2013, **8**, 1121–1127.

92. P. W. M. Blom, M. J. M. D. Jong, M. G. V. Munster, *Phys. Rev. B: Condens. Matter Mater. Phys.*, 1997, **55**, 656–659.

93. Y. Zhao, M. Hong, Y. Liang, R. Cao, W. Li, J. Weng and S. Lu, *Chem. Commun.*, 2001, 1020−1021.

94. N. Singh and V. K. Singh, *Transition Met. Chem.*, 2001, **26**, 435−439.

95. J. T. Makode, A. R. Yaul, S. G. Bhadange, and A. S. Aswar, *Russ. J. Inorg. Chem.*, 2009, **54**, 1372−1377.

96. M. S. Refat, I. M. El Deen, M. A. Zein, A. M. A. Adam, M. I. Kobeasy, *Int. J. Electrochem. Sci.*, 2013, **8**, 9894−9917.

97. İ. Gönül, *Inorg. Chim. Acta*, 2019, **495**, 119027−119034.

98. M. E. Sánchez-Vergaraa, B. Molinab, A. Hernández-Garcíaa, J. R. Álvarez-Badaa, and R. Salcedoc, *Semiconductors*, 2020, **54**, 441−449.

99. U. M. Osman, S. Silvarajoo, K. H. Kamarudin, M. I. M. Tahir, H. C. Kwong, *J. Mol. Struct.*, 2021, **1223**, 128994−129003.

CHAPTER 5

Experimental and theoretical studies of a reversible fluorescent probe for sequental detection of aluminum (Al³⁺) and bifluoride (HF₂⁻) ions in solution as well as in living HepG2 cells
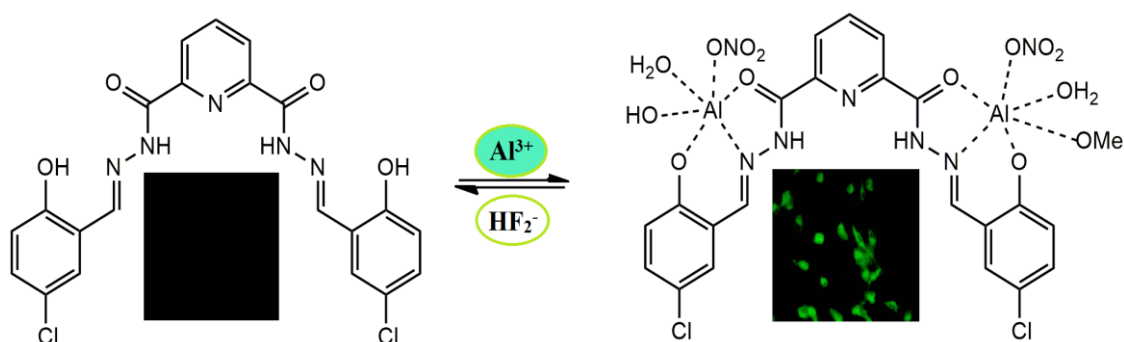
5.1. INTRODUCTION

Aluminum is the third most abundant (8.3% by weight) element (after oxygen and silicon) of the surface of the earth and is extensively attached to our daily life in the form of food packaging, water purification, cooking utensils, pharmaceuticals, manufacturing of computers, cars, *etc.* [1–6]. Aluminum compounds are also frequently utilized in the paper industry, dye productions, textile industry, cosmetic preparations, alimentary industry and many more [7,8]. Thus, there is a good chance of accumulation of aluminum ion (Al^{3+}) in food chain, resulting toxicity towards human health. But, according to a WHO (World Health Organization) report, the tolerable daily intake of aluminum in the human body is about 3–10 mg and the acceptable weekly aluminum dietary intake is about 7 mg/kg^{-1} per week of the body weight [9,10]. Accumulation of excessive amounts of this metal results some serious diseases like Alzheimer's disease, myopathy, Parkinson's disease, osteoporosis, headaches, anemia, chronic renal failure, bone softening, kidney damage and even breast cancer [11–20]. At lower pH, the solubility of aluminum minerals increases, resulting in an increase of available Al^{3+} ions which affect plants' usual growth and development, ultimate hampering agricultural production [21,22]. Therefore, the detection of aluminum ion is essential in various samples connected to drinking water, foodstuff, medicine, *etc*.

But, the easy detection of aluminum ion is still a difficult task because of its poor coordination ability, strong hydration tendency and the lack of spectroscopic characteristics [23]. A several numbers of analytical techniques have been utilized for the detection of aluminum ions, such as atomic absorption spectrometry (AAS), inductively coupled plasma-atomic emission spectrometry (ICP-AES), inductively coupled plasma-mass spectrometry (ICP-MS), nanoparticle-based sensors, ion selective membrane, and some electrochemical methods [24–34]. But these techniques are limited to the laboratory due to high equipment cost, less sensitive, requirement for trained persons, time consuming and complicated. In this context, spectrofluorimetry technique is superior in terms of quick analysis, high selectivity, sensitivity and real-time monitoring with rapid response time. Being a hard metal ion, Al^{3+} prefers hard donor sites for coordination, so the Schiff base ligands with N and O donor centre are considered to be suitable probes for Al^{3+} detection [35–40]. Hydrazide or its derivatives have been extensively used in several research fields due to their facile syntheses, good chelating capability and tunable electronic properties [41].

Anions play a crucial role in the area of supramolecular chemistry, especially in environmental, chemical, medical and biological systems. Among other anions, the semi-

ionic, three-center four-electron (3c-4e) bonding bifluoride ions (HF_2^-) recognition is of growing interest because of its widespread applications including etching of borosilicates glass capillary columns, insecticides, fluorometric detection of ultra-trace levels of beryllium in occupational hygiene samples, preparation of borane derivatives and molten salts [42−44]. So far, a few chemosensors have been reported for bifluoride ions [45−47]. Hence, it is an urgent requirement for fluorescent and biocompatible probes for selective and sensitive detection of bifluoride ions with rapid response through easy spectral analysis. Besides, the implementation of fluorescent chemosensors for anions in aqueous solution is still a major challenge due to strong hydration tendencies of anions. This problem could be solved by using the metal displacement strategy.

This chapter presents a simple pyridine-dicarbohydrazide based colorimetric and fluorometric chemosensor (**L**) which can selectively detect Al^{3+} ions in organo aqueous solution. In presence of Al^{3+} ions, probe **L** exhibited visible color changes and fluorescence enhancement (20-fold) due to Al^{3+} induced chelation-enhanced fluorescence (CHEF) effects. The chemosensor **L** revealed high selectivity toward Al^{3+} ions by "turn-on" fluorescence among the other competitive metal ions examined with a detection limit of 0.8 µM. The probe **L** was found to bind with Al^{3+} ions in a 1: 2 (probe: metal) stoichiometric fashion, with the association constant (K_a) of 4.26×10^4 M^{-1}. In addition, DFT and TDDFT calculations were carried out to recognize the binding nature and electronic properties of the probe **L** and its Al^{3+}-complex. Furthermore, *in situ* prepared [**L**-Al^{3+}] complex was able to detect HF_2^- anions via a metal displacement approach. The bioimaging application of Al^{3+} and HF_2^- were also implemented in the living human liver cancer cells (Hep G2).

5.2. EXPERIMENTAL SECTION

5.2.1. Materials and apparatus

All the chemical reagents and solvents (analytical and spectroscopic grades) were procured from commercial suppliers and used without additional purification. Millipore water was used throughout the experiment. Nitrate salts of Al^{3+} and Ag^+, chloride salts of metal ions (Na^+, K^+, Cr^{3+}, Cd^{2+}, Fe^{2+}, Zn^{2+}, Hg^{2+}, Pb^{2+}), perchlorate salts of metal ions (Ni^{2+}, Mn^{2+}, Cu^{2+}, Fe^{2+}, Co^{2+}), terabutyl ammonium salts of F^-, Br^-, AcO^-, HSO_4^- and sodium salts of HF_2^-, PPi, Pi, NO_3^- were used for the experiments.

Elemental analyses (C, H and N) were performed using a PerkinElmer 2400 Series-II CHN elemental analyzer. ESI mass spectra were obtained from a Water HRMS model

XEVO-G2QTOF#YCA351 spectrometer. ^{1}H NMR and ^{13}C NMR spectra were obtained from Bruker spectrometer (400 MHz) and ^{1}H NMR titration spectra were obtained from Bruker spectrometer (300 MHz) with DMSO-d_6 solvent using trimethylsilane (TMS) as an internal standard. Fourier transform infrared (FT-IR) spectra were recorded on a Perkin Elmer LX-1 FT-IR spectrophotometer ($4000-400$ cm^{-1}) by using a modern diamond attenuated total reflectance (ATR) accessory method. UV−vis absorption spectra were obtained using UV-1700 PharmaSpec UV−vis spectrophotometer (SHIMADZU). Fluorescence emission spectra were carried out using a Horiba Jobin Yvon Fluoromax-4P spectrofluorometer. Single crystal structures were obtained using single-crystal X-ray diffractometer (Bruker Smart Apex II). The cells were imaged by using Zetasizer fluorescence microscope (Leica).

5.2.2. Synthesis of bis(2-hydroxy-4-chlorobenzaldehyde)-2,6-pyridinedicarbohydrazone (L)

2,6-pyridinedicarbohydrazide (**1**) was synthesized following a reported method (as shown in Scheme 5.1) [48]. Then a mixture of 2,6-pyridinedicarbohydrazide (0.19 g, 1.0 mmol) and 2-hydroxy-4-chlorobenzaldehyde (0.36 g, 2.3 mmol) was refluxed in methanol for 5 h. A light yellow solid formed was filtered off and dried in vacuum (yield 0.39 g (84%). m.p. > 200°C).
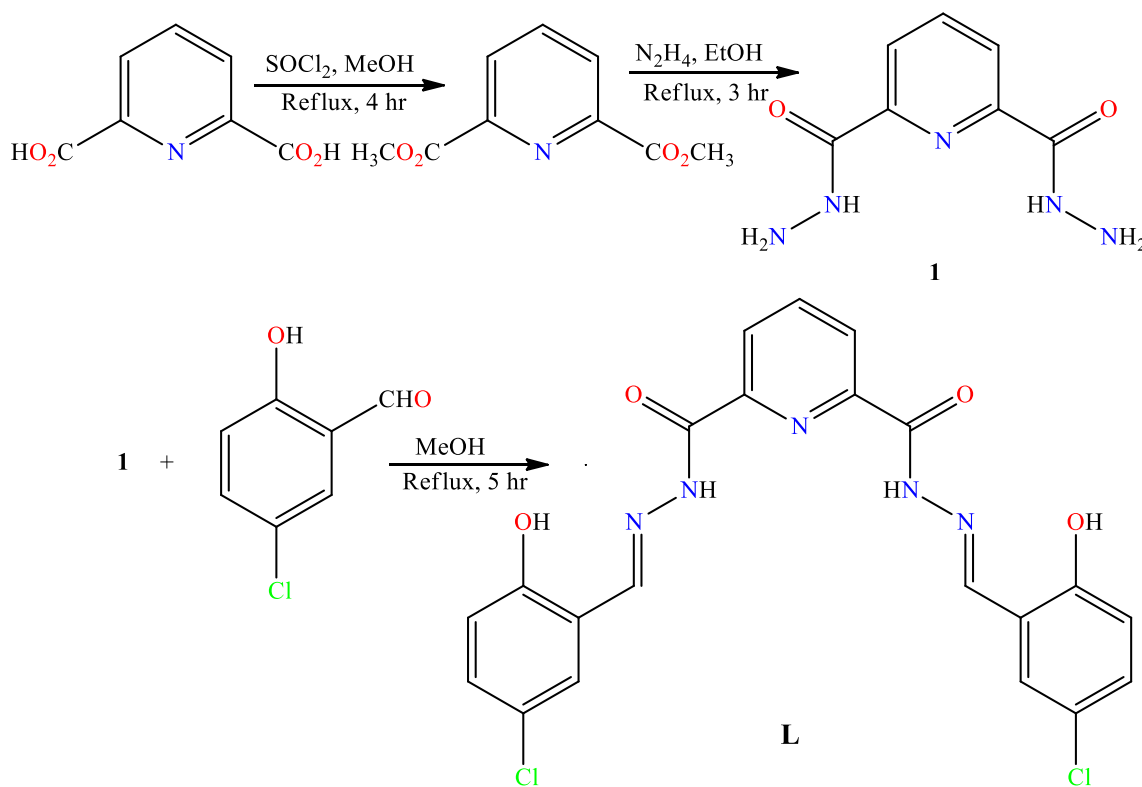
Scheme 5.1. Synthetic route for chemosensor **L**

Anal. Calcd. for $C_{21}H_{15}Cl_2N_5O_4$, C 53.41, H 3.20, N 14.83. Found: C 54.12, H 4.01, N 15.23 %. ^{1}H NMR (400 MHz, DMSO-d_6): δ = 12.47 (s, 2H), 11.09 (s, 2H), 8.88 (s, 2H), 8.35 (d, J = 7.2 Hz, 2H), 8.28 (m, 1H), 7.92 (s, 3H), 7.75 (d, J = 2.4 Hz, 2H), 7.34 (m, 6.8 Hz, 2H), 6.97 (d, J = 8.8 Hz, 2H) (Fig. 5.1).
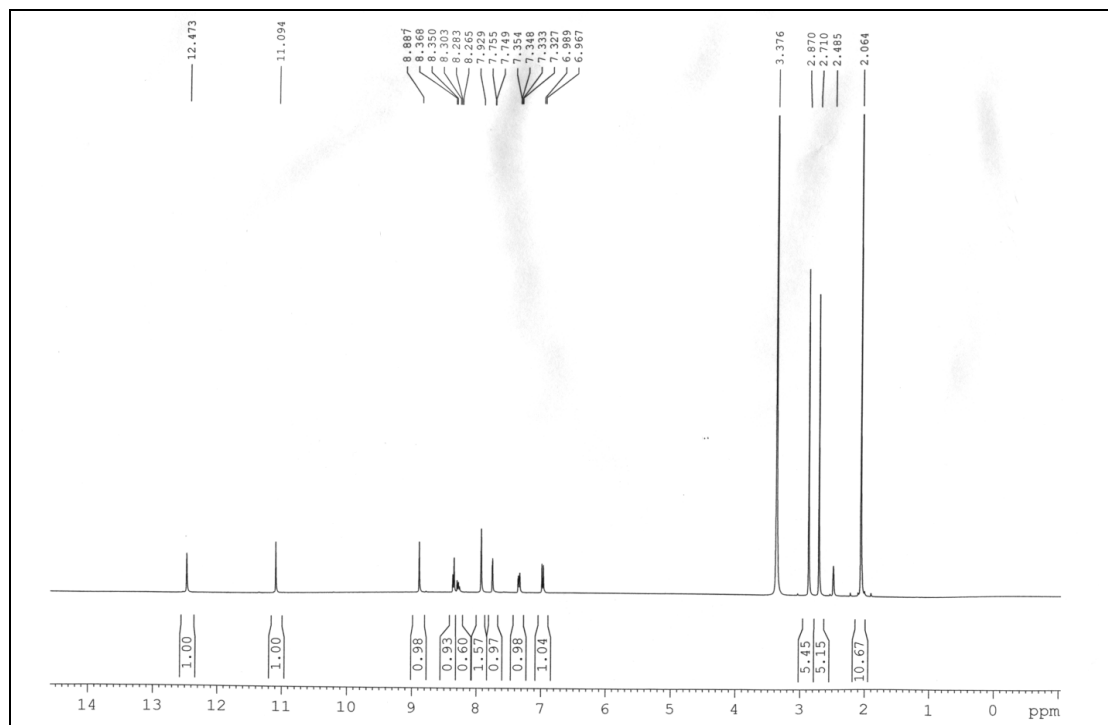

Fig. 5.2. ^{1}H NMR spectrum of **L** in DMSO-d_6 solution.
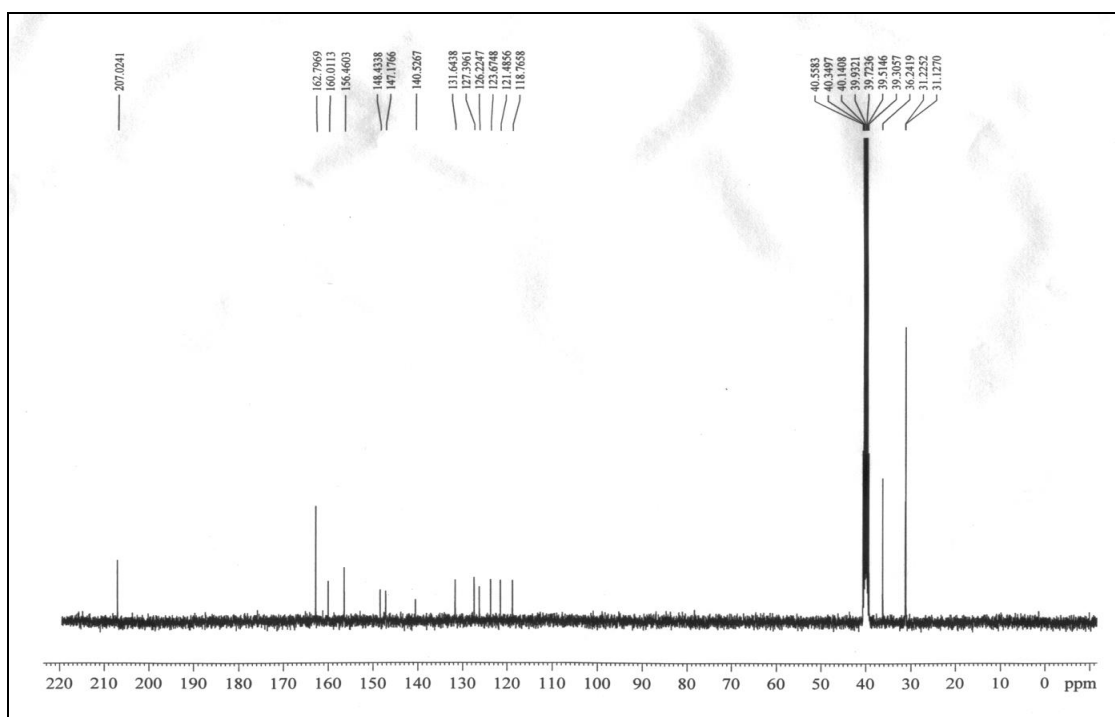
Fig. 5.3. ^{13}C NMR spectrum of **L** in DMSO-d_6 solution.

^{13}C NMR (100 MHz, DMSO-d_6): δ = 207.02 (for C=O of DMF), 162.79, 160.01, 156.46, 148.43, 147.17, 140.52, 131.64, 127.39, 126.22, 123.67, 121.48, 118.76, 31.17 (Fig. 5.2). Main FT-IR absorptions (KBr, cm^{-1}): 3472, 3248, 1657, 1621, 1538, 1481, 1353, 1264, 1187, 1089, 1000, 950, 824, 716, 608, 560 (Fig. 5.3).

Fig. 5.4. FT-IR spectrum of **L**.

Fig. 5.4. ESI-mass spectrum of **L**.

ESI-MS: m/z 472.11, calcd. for $[C_{21}H_{15}Cl_2N_5O_4 + H]^+$ 472.06 (Fig. 5.4). Crystals suitable for X-ray structural determination were obtained by slow evaporation of DMF solution.
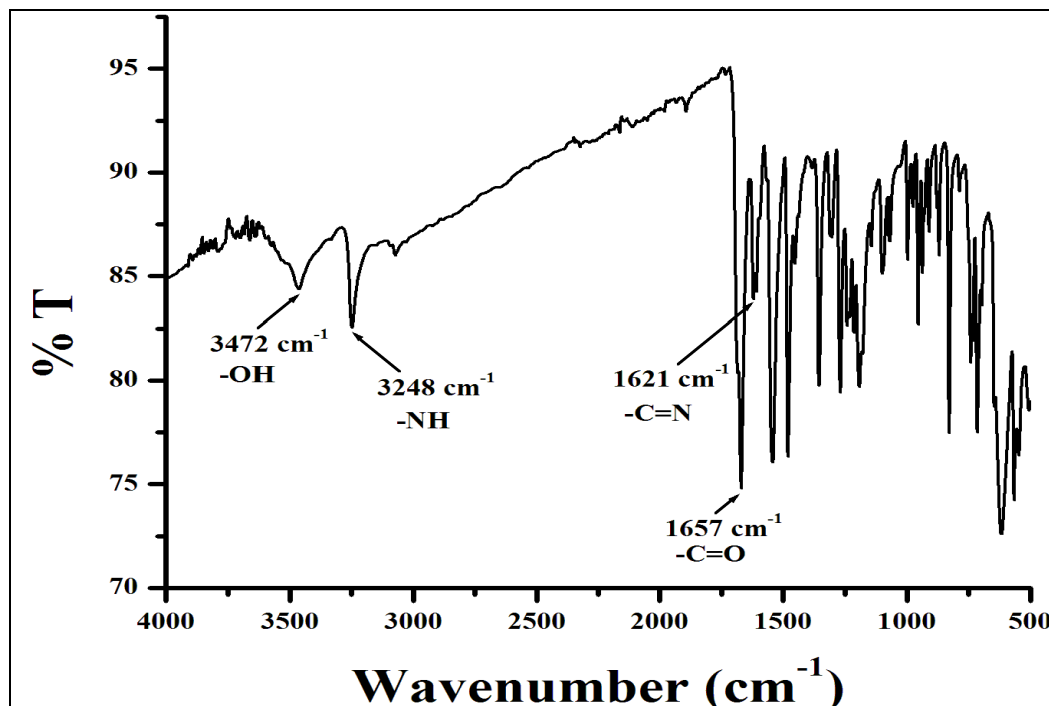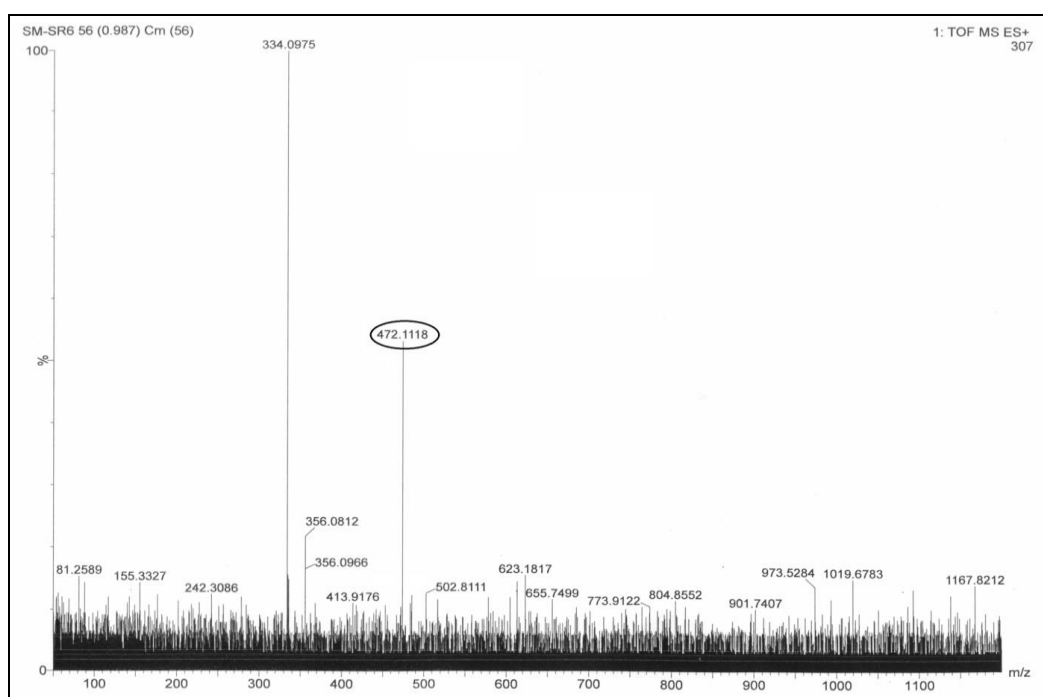
5.2.3. Single-crystal X-ray crystallographic analysis of the chemosensor (L)

Single crystal X-ray data collections were made using a Bruker SMART APEX II CCD area detector equipped with a graphite monochromated Mo Ka radiation ($\lambda = 0.71073$ Å) source in φ and ω scan mode at 273 K. Cell parameter refinement and data reduction was carried out using a Bruker SMART APEX II instrument and Bruker SAINT Software [49]. The crystal structure of the probe was solved by conventional direct methods and refined by full matrix least-squares methods using F^2 data. SHELXT-2014/5 was used for the structure solution of the probe [50]. The CIF has been deposited with CCDC No. 1979155. Selected crystal data for the probe, **L** are given in Table 5.1. The chemical structure of the chemosensor (**L**) is given in Fig. 5.5. Some selected bond lengths and bond angles are included in Table 5.2.

Table 5.1. Crystal data and structure refinement parameters for chemosensor, L

Structure	Chemosensor, L
Empirical formula	$C_{48}H_{46}Cl_4N_{12}O_{12}$
Formula Weight	1124.77
Temperature (K)	273(2)
Wavelength (Å)	0.71073
Crystal system	Triclinic
space group	$P\bar{1}$
a, b, c (Å)	13.8336(11), 14.4635(11), 15.3548(12)
α, β, γ (°)	66.622(2), 71.512(2), 85.747(3)
Volume (Å^3)	2669.8(4)
Z / Density (calc.) (Mg/m^3)	2 / 1.399
Absorption coefficient (mm^{-1})	0.293
F(000)	1164.0
Crystal size (mm^3)	$0.08 \times 0.13 \times 0.19$
θ range for data collection	1.802 to 27.121
Completeness to θ (%)	100%
Absorption correction	multi-scan
Max. and min. transmission	0.977 and 0.955
Refinement method	Full-matrix least-squares on F^2
Data/parameters	11722/ 753
Goodness-of-fit on F^2	1.110
Final R indices [I > 2σ(I)]	$R_1 = 0.0534$, $w\text{R}_2 = 0.1636$
R indices (all data)	$R_1 = 0.0765$, $w\text{R}_2 = 0.1886$
Largest diff. peak and hole (e.Å^{-3})	0.780 and -0.588

$R_1 = \sum || F_o| - |F_c|| / \sum |F_o|$, $wR_2 = [\sum\{(F_o^2 - F_c^2)^2\} / \sum\{w(F_o^2)^2\}]^{1/2}$ $w = 1/\{\sigma^2(F_o^2) + (aP)^2 + bP\}$ where, a = 0.1000 and b = 0.6180. P = $(F_o^2 + 2F_c^2)/3$ for the probe, **L**.
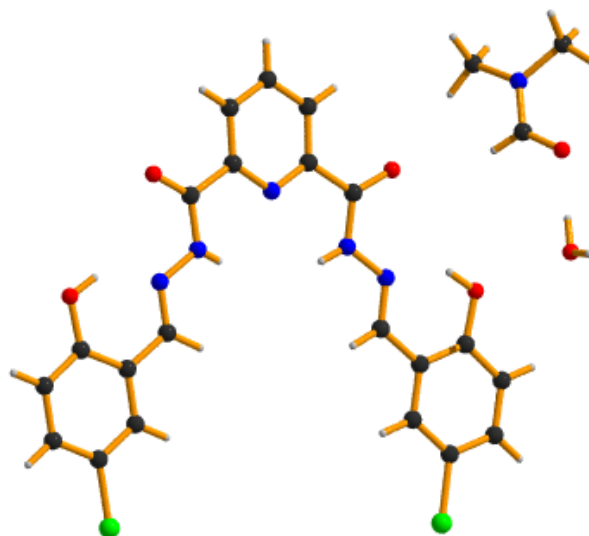

Fig. 5.5. Chemical structure of the chemosensor (**L**).

Table 5.2. Some selected bond length and bond angles of L

Bond	Length(Å)	Bond angle	Values (°)
Cl(1)—C(18)	1.739(3)	C(1)—O(1)—H(1)	112(2)
Cl(2)—C(4)	1.736(3)	C(21)—O(4)—H(15)	110(3)
O(1)—C(1)	1.363(3)	N(2)—N(1)—C(15)	117.69(19)
O(2)—C(8)	1.216(3)	N(1)—N(2)—C(14)	118.93(19)
O(3)—C(14)	1.220(3)	N(5)—N(4)—C(8)	118.6(2)
O(4)—C(21)	1.351(3)	N(4)—N(5)—C(7)	118.17(19)
O(1)—H(1)	0.82(3)	N(1)—N(2)—H(10)	119(2)
O(4)—H(15)	0.90(4)	C(14)—N(2)—H(10)	123(2)
N(1)—N(2)	1.374(3)	N(5)—N(4)—H(6)	120(2)
N(1)—C(15)	1.273(3)	C(8)—N(4)—H(6)	120(2)
N(2)—C(14)	1.347(3)	O(1)—C(1)—C(6)	122.0(2)
N(4)—N(5)	1.359(3)	O(1)—C(1)—C(2)	118.2(2)
N(4)—C(8)	1.356(4)	O(2)—C(8)—N(4)	123.6(2)
N(5)—C(7)	1.279(3)	O(3)—C(14)—N(2)	123.3(2)
N(2)—H(10)	0.80(3)	O(2)—C(8)—C(9)	122.2(2)
N(4)—H(6)	0.72(2)	O(3)—C(14)—C(13)	122.1(2)

5.2.4. General method of UV−vis and fluorescence spectral studies

For UV–vis and fluorescence titrations, stock solution of sensor, **L** (c = 2×10^{-5} M) was prepared in DMSO-H_2O (8:2, v/v, 10 mM HEPES buffer, pH 7.4) solution. Solutions of 2×10^{-4} metal salts of the respective cations and anions were prepared in Millipore water. In titration experiments, solution of the chemosensor (4×10^{-5} M) was filled each time in a

quartz optical cell of 1.00 cm optical path length, and the metal ion stock solutions were added into the quartz optical cell gradually by using a micropipette. Spectral data were recorded at 1 min after the addition of the ions.

5.2.5. Computational methods

All the geometries for **L** and **L**-2Al^{3+} were optimized by using density functional theory (DFT) at the Becke's three-parameter hybrid exchange functional and the Lee−Yang−Parr correlation functional (B3LYP) in combination with Pople's spilt-valence basis set 6-31+G(d, p) basis set [51−54]. Harmonic vibrational frequencies also computed to confirm the optimized structures as local minima (no imaginary frequency). The effect of solvent (dimethyl sulfoxide) was considered by using self-consistent reaction field (SCRF) procedure with the integral equation formalism polarized continuum model (IEF-PCM) [55−59]. Time dependent DFT calculation were also conducted at the same level of theory specifying the keyword TD (N states=50, root=1) [60,61]. All the computations have been carried out in Gaussian 16 program [62].

5.2.6. Cell imaging studies

5.2.6.1. Cell line culture

Human liver cancer cell line Hep G2 cells and Human lung fibroblast cells, WI-38 were collected from National Center for Cell Science (NCCS) Pune, India. The cells were grown in DMEM (Dulbecco's Modified Eagle Medium) with 10% FBS (Fetal Bovine Serum), penicillin/streptomycin (100 units/ml) at 37ºC and 5% CO_2. All the treatments were performed at 37ºC and at a cell density allowing exponential growth.

5.2.6.2. Cellular imaging

The Hep G2 cells were grown in a cover slip for more than 24h. Then, the Hep G2 cells were treated with 10µM of probe **L** for 30 min followed by addition and incubation with 10µM Al(NO$_3$)$_3$ solution and then with NaHF$_2$ solution. The cells were washed with 1 X PBS. Lastly, they were then mounted on a glass slide and fluorescent images were taken from the Leica fluorescence microscope.

5.3. RESULTS AND DISCUSSION

5.3.1. UV-vis and fluorescence studies

The spectroscopic properties of the probe **L** were investigated by monitoring absorption and fluorescence changes in presence of several metal ions, such as K^+, Na^+, Mg^{2+}, Ca^{2+}, Pb^{2+}, Pd^{2+}, Cd^{2+}, Hg^{2+}, Zn^{2+}, Cu^{2+}, Al^{3+}, Ag^+, Fe^{2+}, Co^{2+}, Ni^{2+} and Mn^{2+} in DMSO:H_2O (8:2, v/v, 10 mM HEPES buffer, pH 7.4) solution at room temperature. As illustrated in Fig. 5.6, the free probe **L** displayed a maximal absorption peak at 345 nm which corresponds to π-π* transition from the conjugated moiety of **L**. However, upon gradual addition of Al^{3+} ion to the solution of **L**, the initial absorption band at 345 nm decreased and a simultaneous increase at 402 nm with a red shift of 57 nm was observed, accompanied by a naked eye color change from colorless to light yellow. The clear isosbestic point at 370 nm undoubtedly indicates the formation of Al^{3+} complex in the binary mixture. Again, chemosensor **L** did not exhibit any noteworthy changes in absorption spectra with the addition of a number of competitive metal ions, signifying the high selectivity of this probe for Al^{3+} ion.
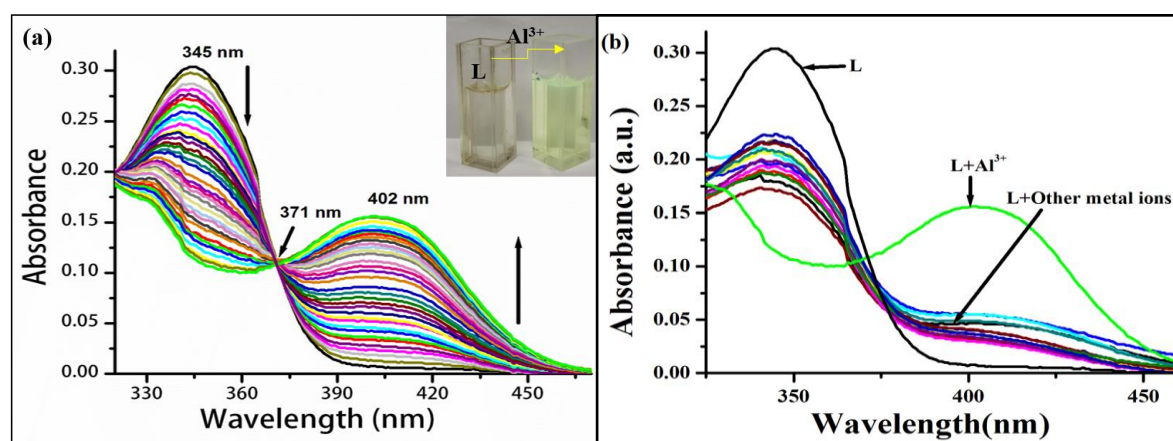

Fig. 5.6. (a) The UV-vis absorption spectra of **L** (c = 2 × 10^{-5} M) in presence of Al^{3+} (c = 2 × 10^{-4} M) ions in DMSO-H_2O (8:2, v/v, 10 mM HEPES buffer, pH 7.4) solution. Inset: Color change after addition of Al^{3+} to probe **L**. (b) Absorption spectra of **L** in presence of different metal ions.

As shown in Fig. 5.7a, in absence of Al^{3+} ion, probe **L** showed a very weak emission band centred at 483 nm (λ_{ext} = 371 nm) in DMSO-H_2O (8:2, v/v, 10 mM HEPES buffer, pH 7.4). This weak emission of probe **L** is due to the (a) excited state intramolecular proton transfer (ESIPT) from the −OH group to the imine nitrogen (b) photoinduced electron transfer effect from the lone pair of imine nitrogen and (c) isomerization of the −HC=N (imine) bond [63−65]. However, treatment of probe **L** with 3 equivalent Al^{3+} ions induced a gradual increase in fluorescence (20-fold) along with a blue shift of 7 nm having highest emission intensity at 476 nm and a color change from dark to greenish-blue under UV light.

This significant fluorescence 'turn-on' in presence of Al^{3+} ions might be explained by the formation of a complex between the probe **L** and Al^{3+} through the coordination of two "O" and one "N" atom. This inhibits both the ESIPT and PET processes as well as C=N isomerization resulting in a distinctive chelation enhanced fluorescence (CHEF) effect. The selectivity of chemosensor **L** towards different metal cations was examined under identical working conditions.

As shown in Fig. 5.7b, probe **L** demonstrated strong fluorescence response at 476 nm, while the other cations [K^+, Na^+, Mg^{2+}, Ca^{2+}, Pb^{2+}, Pd^{2+}, Cd^{2+}, Hg^{2+}, Zn^{2+}, Cu^{2+}, Ag^+, Fe^{2+}, Co^{2+}, Ni^{2+} and Mn^{2+}] did not cause any remarkable emission spectral changes. In order to further evaluate the practical capability of probe **L** as Al^{3+} selective fluorescent chemosensor, competitive experiments on addition of Al^{3+} ions to the solution of **L** in presence of excess equivalent of other individual metal ions were conducted. The increase in fluorescence intensity induced by mixing Al^{3+} ions with other miscellaneous cations was comparable to that elicited by Al^{3+} alone, indicating stable complexation between **L** and Al^{3+}. The above results indicate high selectivity of probe **L** for Al^{3+} over other commonly coexistent cations in organo-aqueous solution.
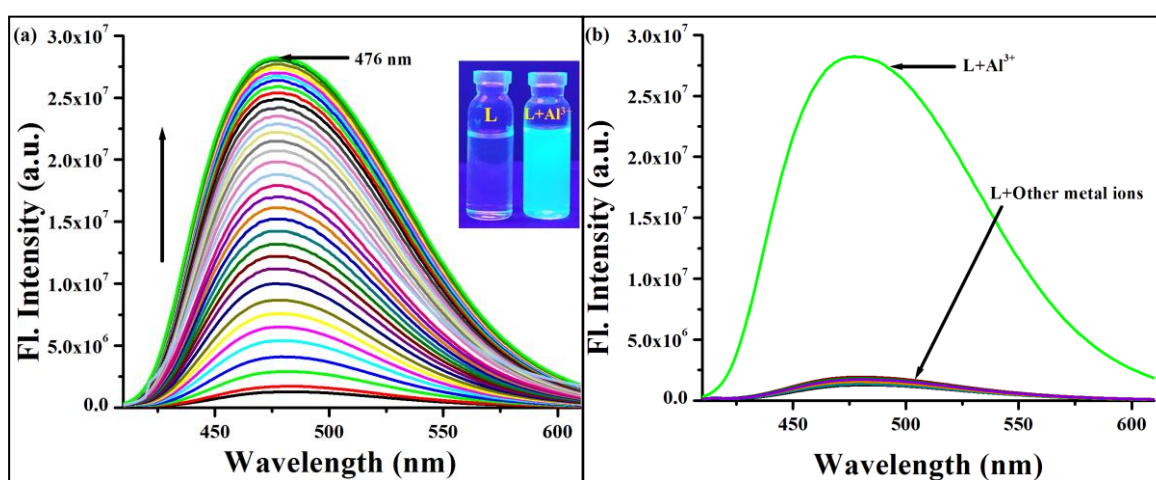

Fig. 5.7. (a) Changes in fluorescence spectra of **L** ($c = 2 \times 10^{-5}$ M) in presence of different amount of Al^{3+} ($c = 2 \times 10^{-4}$ M) ions in DMSO-H_2O (8:2, v/v, 10 mM HEPES buffer, pH 7.4) solution. Inset: Fluorescence change after addition of Al^{3+} to probe **L**. (b) Fluorescence response of **L** to different metal ions.

5.3.2. Binding constant calculation using fluorescence titration data

The binding constant (K_a) of **L** for Al^{3+} was evaluated using the Benesi−Hildebrand (B−H) plot using equation 1 [66−68].

$$1/(I - I_0) = 1/K_a(I_{max} - I_0)[\,Al^{3+}] + 1/(I_{max} - I_0) \quad (1)$$

where, I_0, I_{max}, and I represent the emission intensity of free **L**, the maximum emission intensity observed in the presence of added metal ion at 476 nm for Al^{3+} (λ_{ext} = 371 nm), and experimentally measured emission intensity at a certain concentration of the metal ion added, respectively. The association constant (K_a) was graphically evaluated by plotting $1/(I - I_0)$ vs. $1/[Al^{3+}]$ as shown in Fig. 5.8. From the fluorescence titration profile, the binding constant (K_a) of **L** with Al^{3+} ion was determined to be 4.26×10^4 M^{-2} (R^2 = 0.982), which points out a strong binding affinity of Al^{3+} to probe **L**.
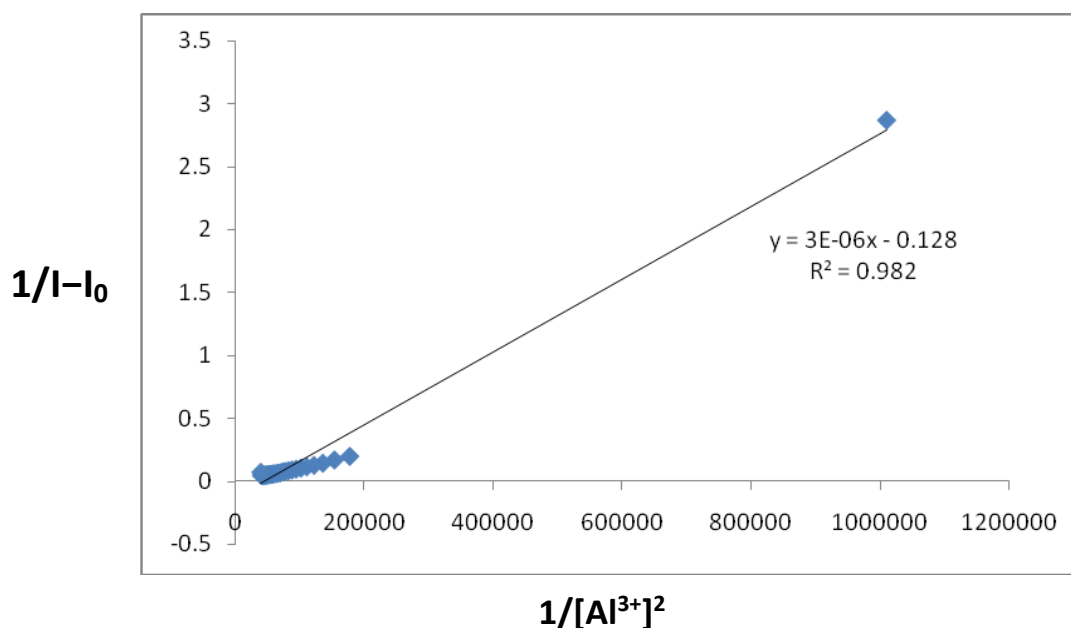

Fig. 5.8. Bensei-Hildebrand plot obtained from the Fluorescence (emission calculated from 476 nm) studies. Binding constant (K_a = 4.26×10^4 M^{-2}) curve of sensor **L** with Al^{3+} determined by fluorescence method.
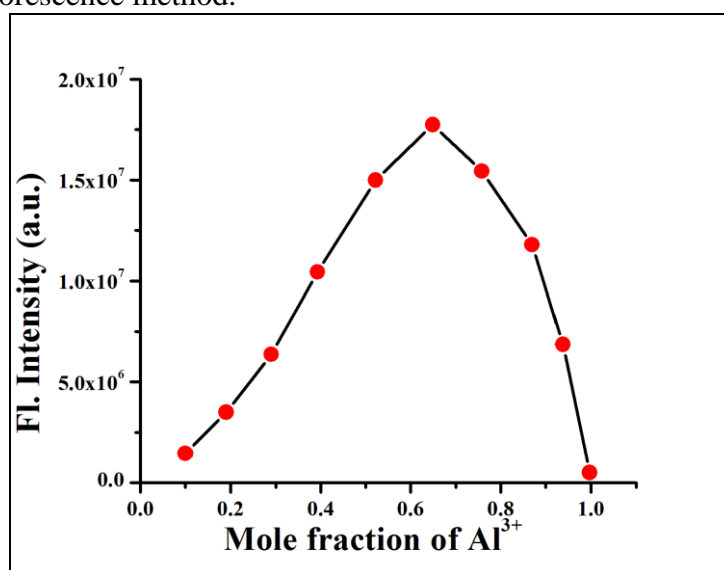

Fig. 5.9. Fluorescence Job's plot for **L** with Al^{3+} in DMSO/H_2O solution (8:2, v/v, 10 mM HEPES buffer, pH 7.4). ([H] = [G] = 4×10^{-5} M).

The Job's plot revealed that 1:2 stoichiometry is the most probable binding mode between **L** and Al^{3+} ions (Fig. 5.9). To attain such type of stoichiometry, imine nitrogen, carbonyl oxygen and phenolic oxygen atoms are the most likely binding sites for Al^{3+} ions.

To know the probable binding sites, ^{1}H NMR titration was performed by gradual addition of nitrate salt of Al^{3+} ions to a DMSO-d_6 solution of **L** (Fig. 5.10). The result shows that the intensity of the proton signal corresponding to the hydroxyl group (–OH) at 11.08 ppm, which is the most likely binding site for Al^{3+} ions, decreases significantly relative to that of other protons upon exposure to Al^{3+} ions.
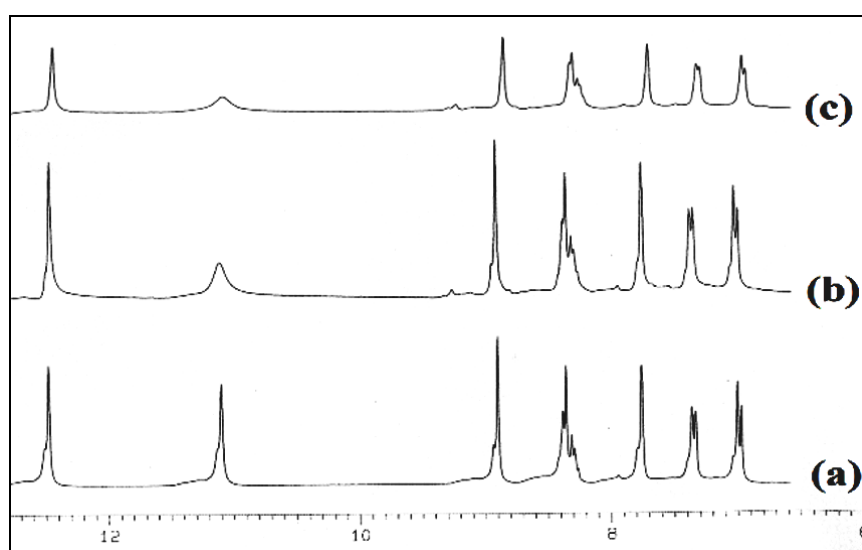

Fig. 5.10. ^{1}HNMR spectra in DMSO-d_6: (a) **L** only (b) **L** and 1 equiv. of Al^{3+} (c) **L** and 2 equiv. of Al^{3+}.

In addition, IR spectrum of **L**-Al^{3+} complex (Fig. 5.11) shows shifted frequency value and a new signal for NO_3^- at 1349 cm^{-1}.
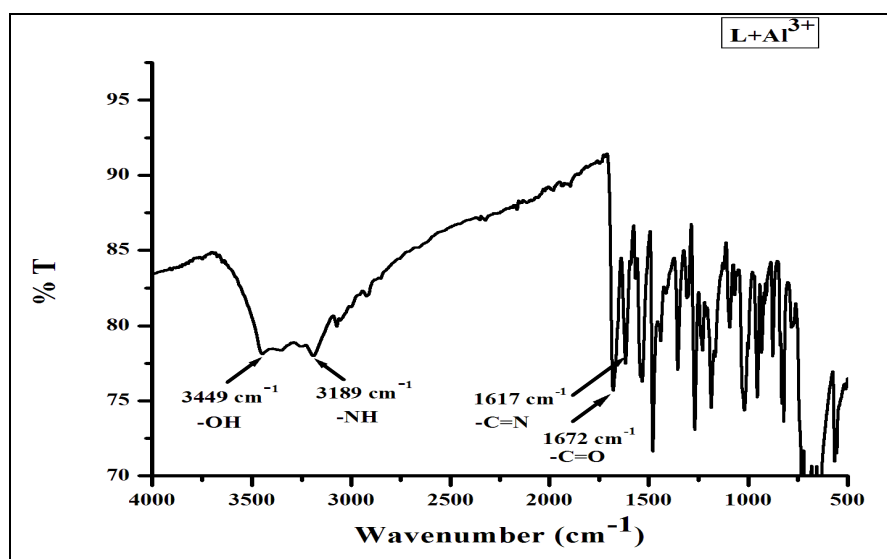

Fig. 5.11. FT-IR spectrum of **L**-Al^{3+} complex.

The spectrum shows ν(NH), 3189(s); ν(C=O), 1672(s); ν(C=N), 1617 cm^{-1} but the ν(OH) appears as a broad signal at 3449 cm^{-1}. This result shows that the −OH is the most probable binding site for Al^{3+} ions.

5.3.3. Calculation of detection limit

The detection limit (DL) of **L** for Al^{3+} was determined using the following equation 2 [69,70].

$$DL = K* Sb1/S \qquad (2)$$

Where K = 2 or 3 (3 was taken in this case); Sb1 is the standard deviation of the blank solution; S is the slope of the calibration curve as shown in Fig. 5.12.
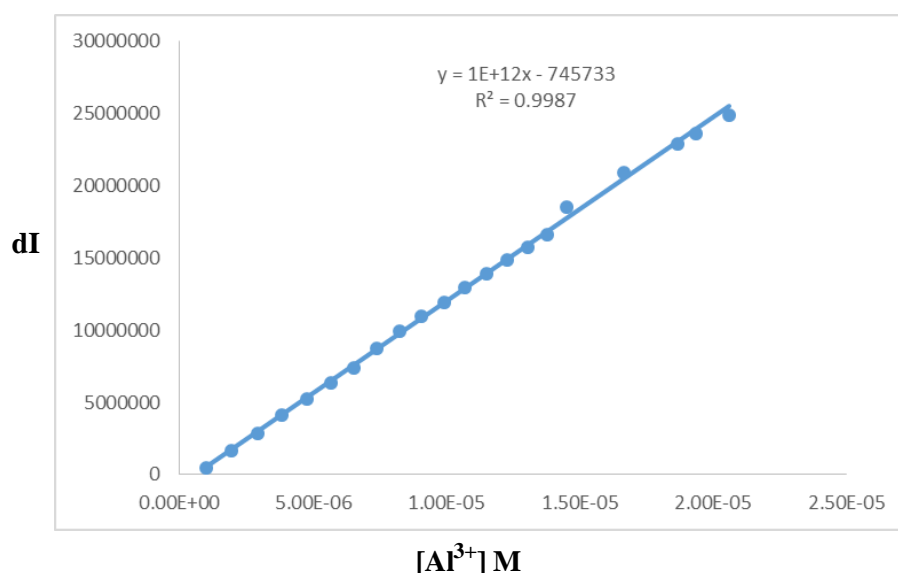

$$y = 1E+12x - 745733$$
$$R^2 = 0.9987$$

Fig. 5.12. Calibration curve for fluorescence titration of **L** with Al^{3+}

The fluorescence intensity of the **L** at 476 nm exhibited a good linear relationship (R^2 = 0.998) with the Al^{3+} concentration ranging from 0.99 µM to 20.6 µM. The slope (S) and the standard deviation (Sb1) of the graph are 1×10^{12} and 274989.74356, respectively. Thus, using the formula (equation 2), the detection limit (DL) was calculated as 0.8249×10^{-6} M = 0.8249 µM.

It is noteworthy to mention that the chemosensor (**L**) has interesting analytical features like its easy synthetic route with good yield and reasonably low detection limit for Al^{3+} ion with no interference from a number of cations in comparison to reported methods (Table 5.3).

Table 5.3. Summary of representative fluorescent probes for Al^{3+}

Paper	Al^{3+} detection limit	Interferences (cation/anion)	Any other remark	Present work
1. *J. Photochem. Photobiol.*, A, 2017, **332**, 101.	1.62 μM	PPi	Starting materials are not readily available.	Starting materials are commercially available.There is no interference from a number of cations.
2. *Dalton Trans.*, 2015, **44**, 18902.	6.86×10^{-7} M	No	Starting materials are not readily available.	Starting materials are commercially available.
3. *Sens. Actuators*, B, 2015, **208**, 159.	$(13.7 \pm 0.17) \times 10^{-7}$ M	No	Starting materials are not readily available.	Starting materials are commercially available.
4. *Tetrahedron*, 2014, **35**, 5580.	0.33 μM	Fe^{3+}, Hg^{2+}, Pb^{2+}, and Zn^{2+}	Starting materials are not readily available.	There is no interference from a number of cations.
5. *Sens. Actuators*, B, 2014, **195**, 98.	1.0×10^{-6} M	Ni^{2+}	Starting materials are commercially available.	There is no interference from a number of cations. LOD is 0.8249 μM
6. *J. Lumin.*, 2015, **158**, 401.	$(9.82\pm0.27) \times 10^{-6}$ M	No	Starting materials are commercially available.	LOD is 0.8249 μM
7. *J. Lumin.*, 2016, **172**, 124.	0.08 μM	Cu^{2+}, Fe^{2+} and Fe^{3+}	Starting materials are commercially available.	There is no interference from a number of cations.
8. *J. Photochem. Photobiol. A*, 2020, **392**, 112427.	0.16 μM	No	Multistep reaction.	Comparatively less reaction steps.
9. *Synth. Met.*, 2020, **262**, 116334.	2×10^{-6} M	No	Starting materials are not commercially available.	Starting materials are commercially available. LOD is 0.8249 μM
10. *Photochem. Photobiol. Sci.*, 2020, **19**, 931.	54 nM	No	Starting materials are not commercially available.	Starting materials are commercially available.

Reversibility is an essential feature of a probe to be used as a chemosensor to detect particular anion. Interestingly, the *in situ* generated **L**-2Al^{3+} complex displayed fluorescence "turn-off" behavior only in presence of HF$_2^-$ ion. Now, to inspect this, when an excess amount of NaHF$_2$ solution was added to the solution containing **L**-2Al^{3+} complex system, the

emission band at 476 nm was gradually decreased, accompanied by the emission color changes from deep blue to dark (Fig. 5.13a). However, various common anions such as Cl^-, Br^-, AcO^-, CO_3^{2-}, N_3^-, HCO_3^-, NO_2^-, SO_4^{2-}, $H_2PO_4^-$ did not produce any noticeable results under the similar conditions except F^-. Fluoride ion decreases the fluorescence intensity but only by a small extent compared to HF_2^- ion (Fig. 5.13b). The added fluoride source (TBAF) could be hydrolyzed, and a small amount of HF_2^- may be generated in situ to assist the quenching of emission of **L**-$2Al^{3+}$ complex; thus, a quenching response might be observed [71].
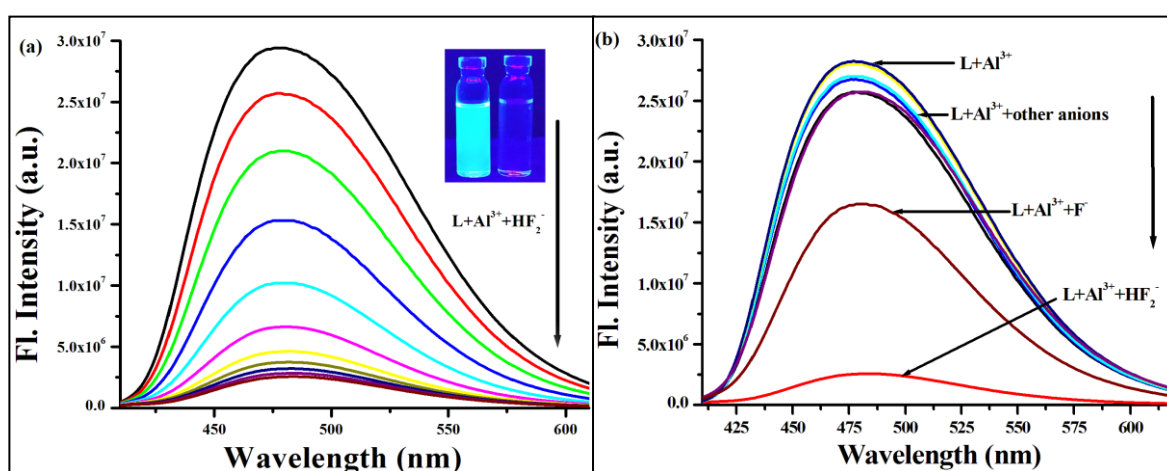

Fig. 5.13. (a) Fluorescence titrations of **L**-$2Al^{3+}$ complex with sodium salt of bifluoride in DMSO-H_2O (8:2, v/v, 10 mM HEPES buffer, pH 7.4) solution (λ_{ext} = 370 nm). Inset: Fluorescence photographs of **L**+Al^{3+} and **L**+Al^{3+}+HF_2^-. (b) Changes in the fluorescence spectra of **L**-$2Al^{3+}$ complex in presence of different anions.

Such fluorometric changes was mainly due to the removal of Al^{3+} from **L**-$2Al^{3+}$ system followed by the regeneration of probe **L** as shown in Scheme 5.2.
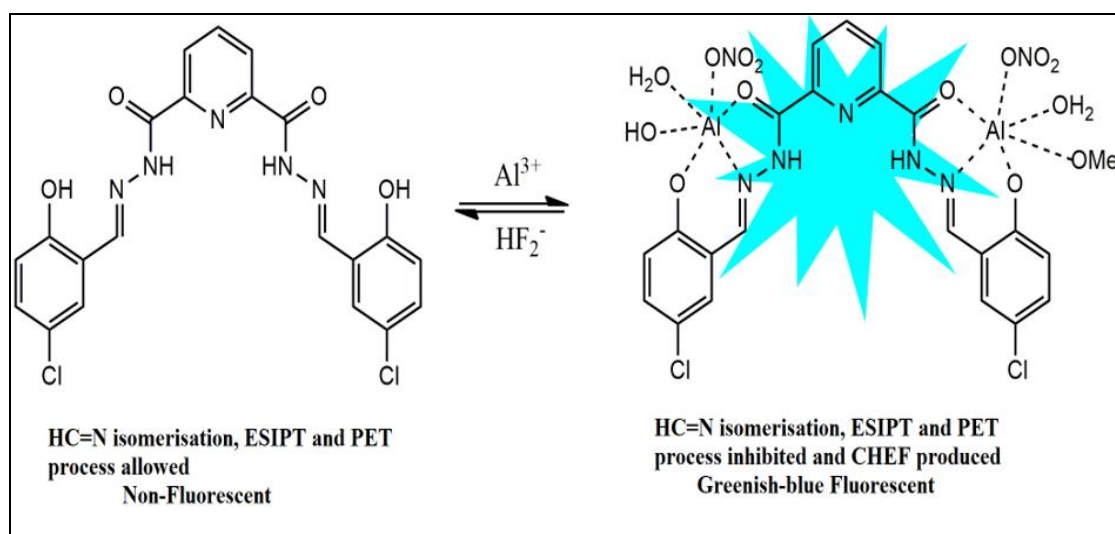
Scheme 5.2. Proposed sensing mechanism for detection of Al^{3+} by probe **L**

These properties indicate that **L**-2Al^{3+} ensemble are employed as an "on-off" fluorescent sensor for bifluoride ion.

In addition, the reversible and reusable behavior of probe **L** was also verified by performing four alternate cycles of fluorescence titration of **L** with Al^{3+} followed by addition of HF$_2^-$ as shown in Fig. 5.14. Moreover, from the fluorescence titration experiment, a good linear relationship ($R^2 = 0.989$) of fluorescence intensity versus the HF$_2^-$ concentration was found over a range of 0.99 to 6.5 µM (Fig. 5.15).
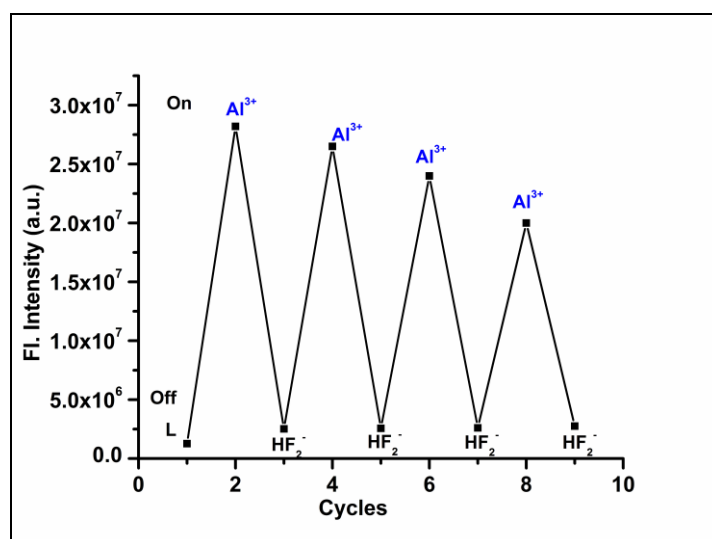

Fig. 5.14. Reversible changes in fluorescence intensity of probe **L** at 476 nm (DMSO-H$_2$O, 8:2, v/v, 10 mM HEPES buffer, pH 7.4) upon alternate addition of Al^{3+} and HF$_2^-$ solution up to four cycles.
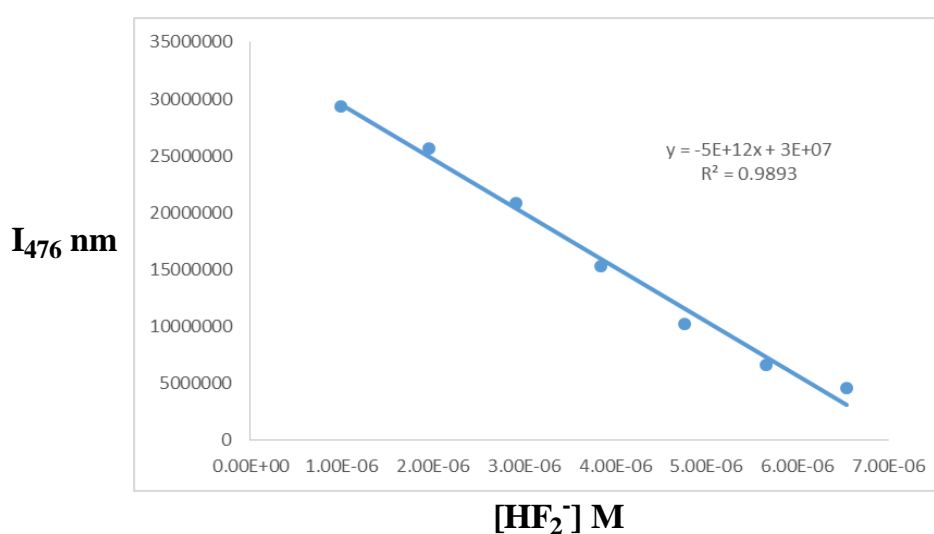

Fig. 5.15. Plot of the fluorescence intensity at 476 nm versus the concentration of HF$_2^-$.

However, incremental addition of HF_2^- ion into the solution of *in situ* generated **L**-$2Al^{3+}$ complex led to a gradual decrease in absorption band at 394 nm and a concomitant increase in the intensity of a new absorption band centered at 344 nm (Fig. 5.16a). It is also noticeable that the common ions did not lead to any significant changes in the absorption spectra as shown in Fig. 5.16b.
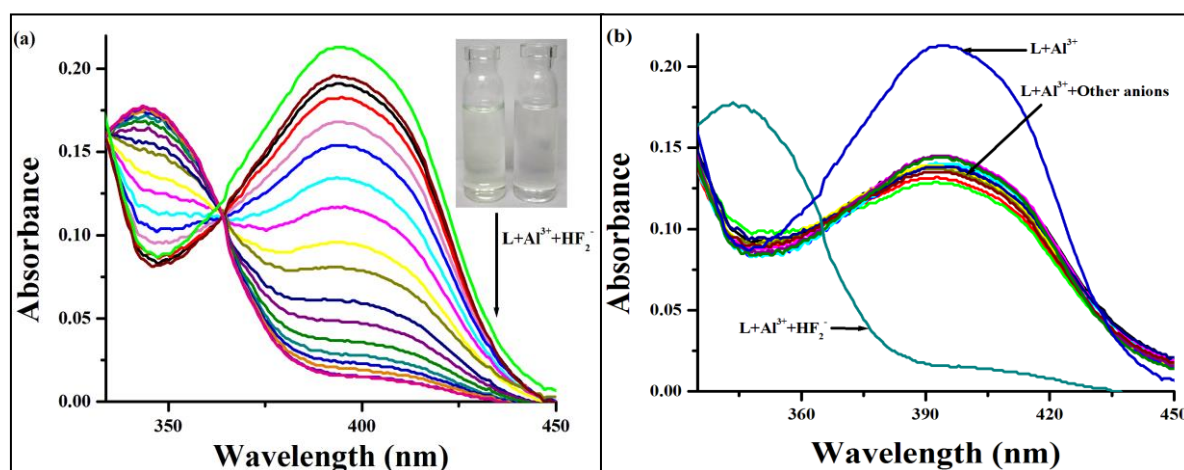

Fig. 5.16. (a) UV-vis absorption spectra of **L**-$2Al^{3+}$ complex with sodium salt of bifluoride in DMSO-H_2O (8:2, v/v, 10 mM HEPES buffer, pH 7.4) solution. Inset: Color change after addition of HF_2^- to **L**+Al^{3+}. (b) Changes in the absorption spectra of **L**-$2Al^{3+}$ complex in presence of different anions.

5.3.4. pH studies

5.3.4.1. Effect of pH on the absorption study

To investigate the suitable pH range in which sensor, **L** can effectively detect Al^{3+}, a pH titration of **L** was carried out. The ligand is enriched with basic nitrogen centers as well as sensitive proton donor sites (-OH, -NH). At acidic pH, the ligand is protonated and shows low absorbance ratio (A_{402}/A_{345}) but at basic pH deprotonation occurred and absorbance ratio (A_{402}/A_{345}) is increased. Addition of Al^{3+} resulted in a high absorbance ratio in a pH range of 6 to 9. At acidic pH (at pH <6), **L** is weakly coordinated to Al^{3+} and shows low absorbance ratio. At pH>9, the absorbance ratio is decreased due to the formation of colloidal $Al(OH)_3$. These observations indicate that the pH range of 6 to 9 is suitable for monitoring Al^{3+} by the chemosensor, **L** (Fig. 5.17).

5.3.4.2. Effect of pH on the emission study

In this experiment, the fluorescence intensity of **L** at 476 nm, in the absence and presence of equivalent amount of Al^{3+} in DMSO-H_2O (8:2v/v) solvent at excitation wavelength of 370 nm, was measured. Fig. 5.18 shows that the probe (**L**) is weakly emissive in the wide range

of pH (3−13). The low emission intensity of L-Al^{3+} complex at pH<6 was presumably due to the free **L** that remains uncoordinated to Al^{3+}. At pH>9, Al^{3+} is converted to $Al(OH)_3$ and $Al(OH)_4^-$, leaving the sensor almost in its free anionic form in the solution. At pH ~ 7 the sensor is deprotonated and the resulting dianionic ligand forms a chelate complex with Al^{3+}, leading to the fluorescence enhancement via CHEF mechanism (as depicted in Scheme 5.2). Therefore, **L** sensor is capable of being used for selective detection of Al^{3+} at physiological pH, and can be a suitable candidate for biological applications.
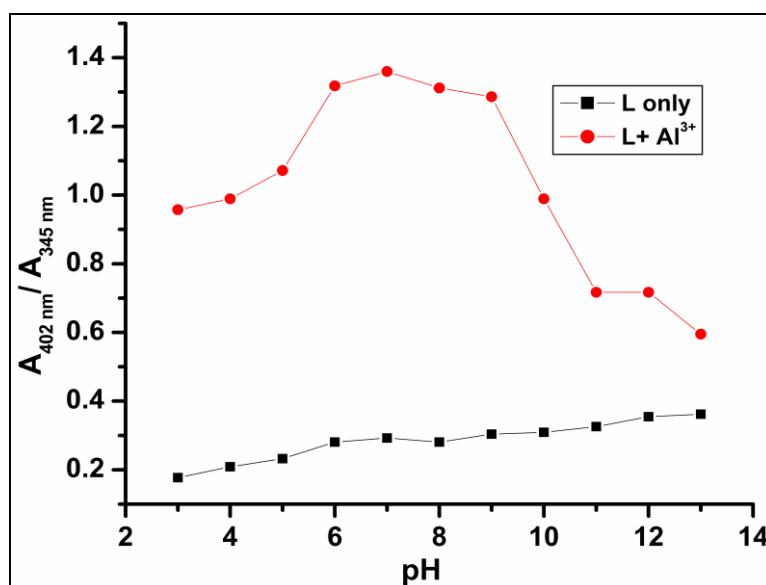

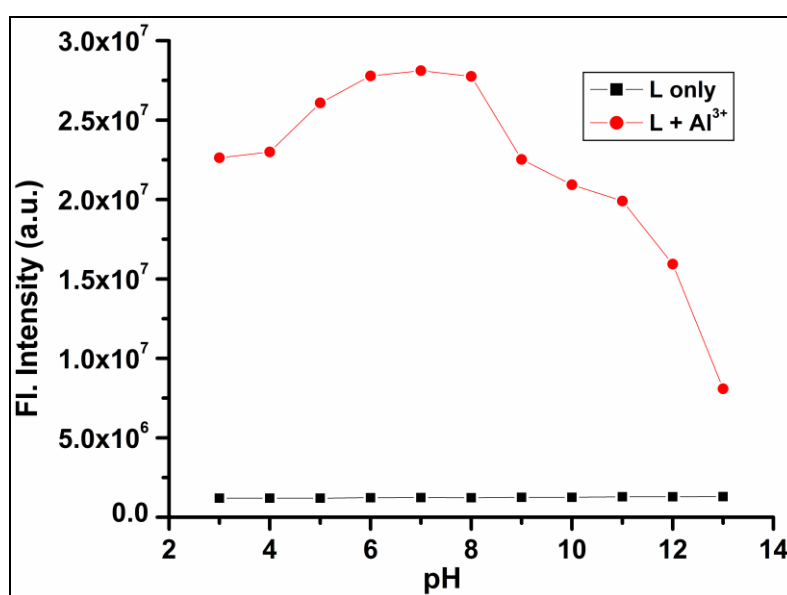**Fig. 5.17.** Influence of pH on absorbance ratio (A_{402}/A_{345}) of **L** in the absence and presence of Al^{3+}.

Fig. 5.18. Fluorescence emission (at λ_{max} = 476 nm) spectral changes of **L** and **L**+Al^{3+} complex with pH variations.

5.3.5. Theoretical studies

In order to know the optimized geometry of **L** and **L**-2Al^{3+} and the binding interactions between probe **L** and Al^{3+}, density functional theory (DFT) calculations were carried out with the B3LYP/6-311+G(d,p) basis set using the Gaussian 16 program. The energy optimized structures of **L** and Al-complex were presented in Fig. 5.19.
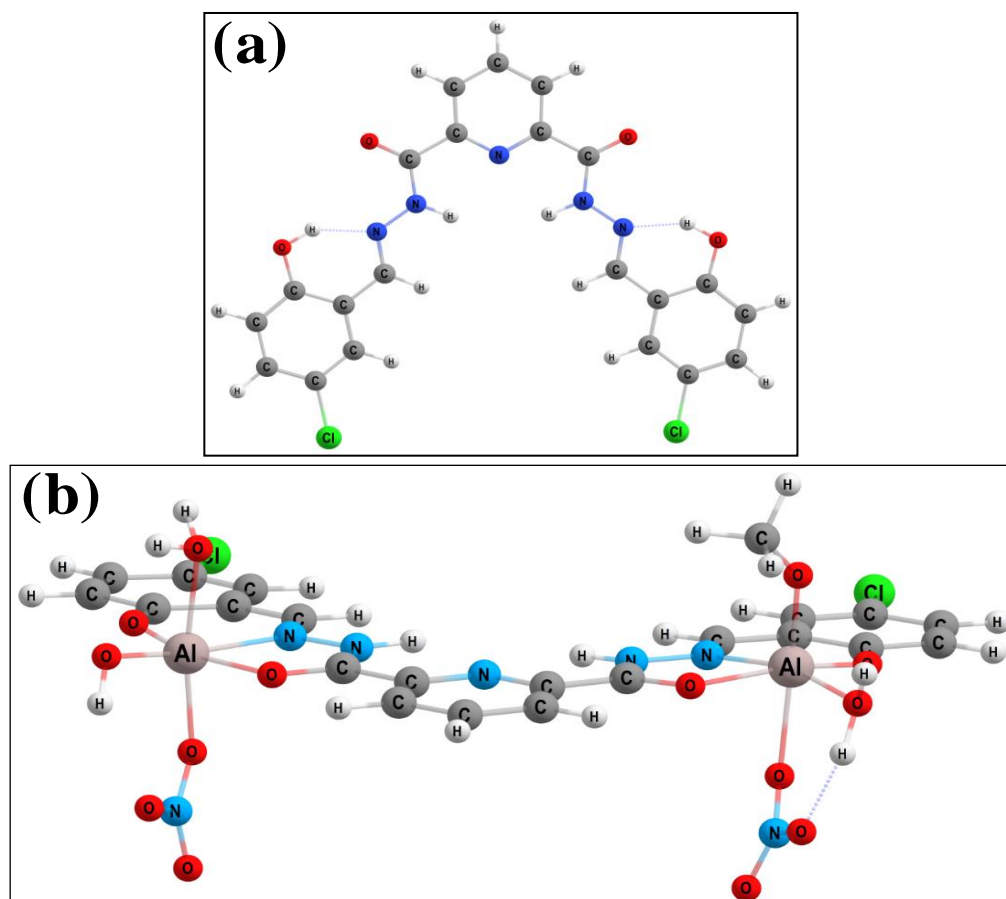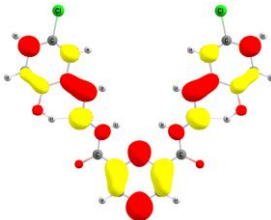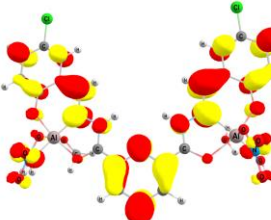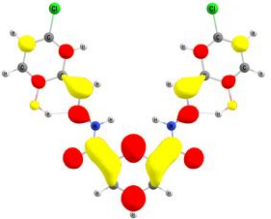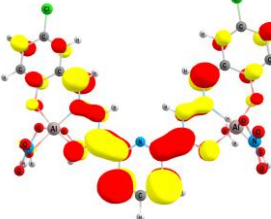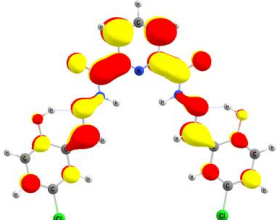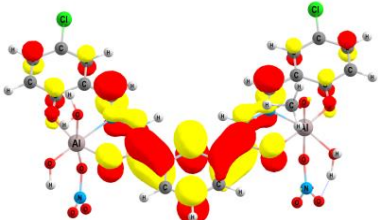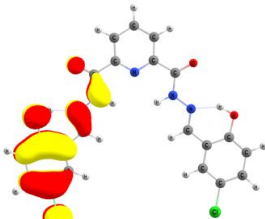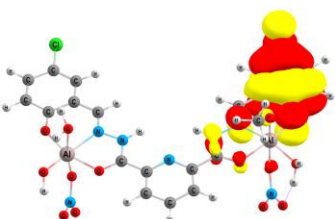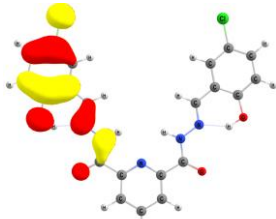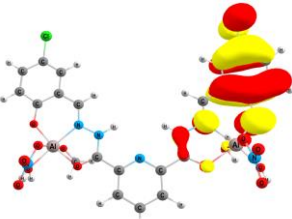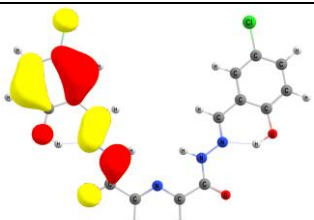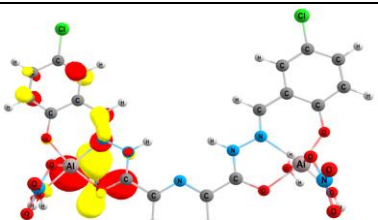
Fig. 5.19. The calculated energy minimized structures of **L** and **L-2Al^{3+}** complex.

Table 5.4. Energies of the important molecular orbitals in Au

Orbital	L	L-2Al^{3+}
HOMO	-0.23351	-0.22925
HOMO-1	-0.23352	-0.23089
HOMO-2	-0.25807	-0.25262
LUMO	-0.09260	-0.11303
LUMO-1	-0.09004	-0.11272
LUMO-2	-0.06651	-0.08224

The highest occupied molecular orbital (HOMO), lowest unoccupied molecular orbital (LUMO) energies (Table 5.4) and spatial distribution of **L** and **L**-2Al^{3+} were also calculated (Table 5.5).

Table 5.5. Molecular orbital plots of L and L–2Al³⁺

L	L–2Al³⁺
LUMO+2	
LUMO+1	
LUMO	
HOMO	
HOMO-1	
HOMO-2	

As shown in Fig. 5.20, the HOMO-LUMO energy gap of probe **L** was considerably reduced from 3.83 eV (88.4 kcal/mol) to 3.16 eV (72.9 kcal/mol) in the **L**-2Al^{3+} complex (Table 5.6), establishing that **L** formed stable complex with Al^{3+} ion and supports the red-shifting of the absorption band (λ_{max}) in the UV-Vis absorption spectra [72,73].
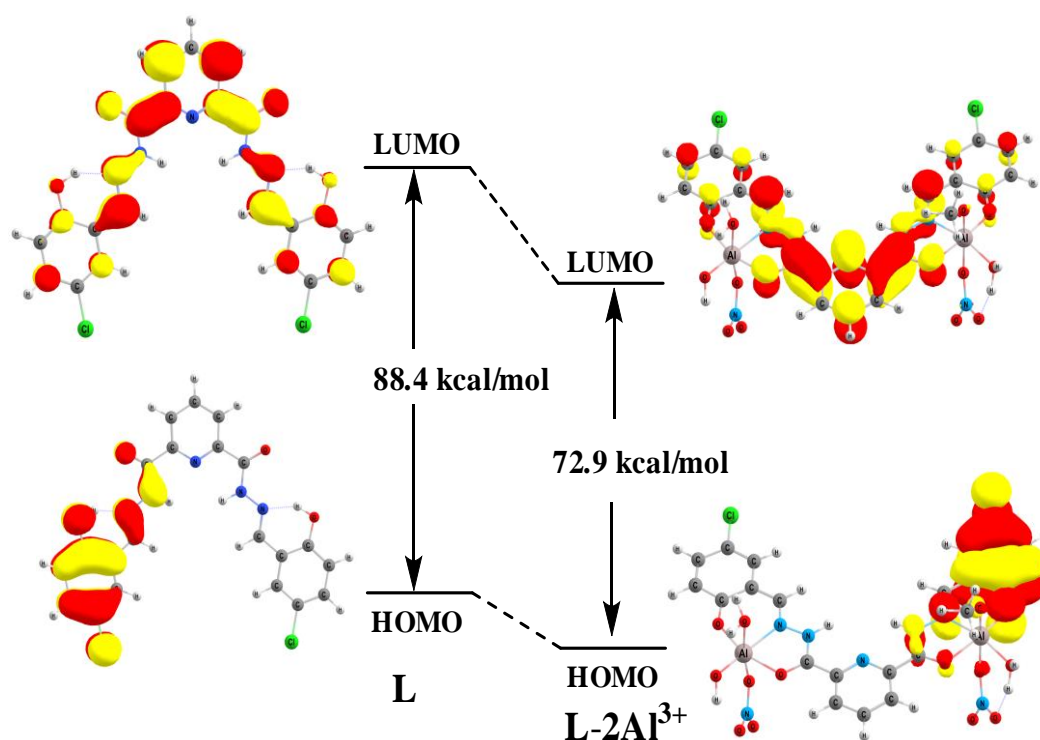
Fig. 5.20. HOMO and LUMO distributions of **L** and **L-2Al^{3+}** complex.

Table 5.6. Energies of the highest occupied molecular orbital (HOMO) and lowest unoccupied molecular orbital (LUMO)

Species	E$_{HOMO}$ (a.u)	E$_{LUMO}$ (a.u)	ΔE (a.u)	ΔE (eV)	ΔE (kcal/mol)
L	-0.23351	-0.0926	0.14091	3.83	88.4
L-2Al^{3+}	-0.22925	-0.11303	0.11622	3.16	72.9

Moreover TDDFT calculations were performed on the optimized geometries to explain the electronic properties of probe **L** and its Al-complex. Table 5.7 showed the details of the vertical excitation energies, oscillator frequencies and wavelengths and from these data it was found that the computed vertical transitions were analogous with the experimentally observed UV−vis bands.

Table 5.7. Calculated excitation energies (Ev), oscillator strengths (F), contributions for Al-complex

Species	Electronic Transition	Excitation Energy	f	Contributions
L	$S_0 \rightarrow S_1$	3.1938 eV 388.21 nm	0.2353	HOMO→ LUMO (64%) HOMO-3 → LUMO+1 (31%)
	$S_0 \rightarrow S_7$	3.9695 eV 312.34 nm	0.2148	HOMO -4→ LUMO (69%)
L-2Al^{3+}	$S_0 \rightarrow S_1$	2.6986 eV 459.44 nm	0.2646	HOMO → LUMO (49%) HOMO → LUMO+1 (32%)
	$S_0 \rightarrow S_{10}$	3.7387 eV 331.62 nm	0.3280	HOMO-3→ LUMO (58%)
	$S_0 \rightarrow S_{15}$	3.8651 eV 320.78 nm	0.4837	HOMO-3→ LUMO+1 (41%)

5.3.6. Cell survivability assay

Cell survivability of the ligand were studied for human lung fibroblast cells, WI38 following reported procedure [74,75]. In brief, viability of WI-38 cells after exposure to various concentrations of probe **L** was assessed by MTT assay (Fig. 5.21). The cells were seeded in 96-well plates at 1×10^4 cells per well and exposed to probe **L** at concentrations of 0 µM, 20 µM, 40 µM, 60 µM, 80 µM, 100 µM for 24 hrs. After incubation cells were washed with 1×PBS twice and incubated with MTT solution (450µg/ml) for 3-4 hrs at 37ºC. The resulting formazan crystals were dissolved in an MTT solubilization buffer and the absorbance was measured at 570 nm by using a spectrophotometer (BioTek) and the value was compared with control cells. The probe was applied in Hep G2 cells (Human liver cancer cell line) for fluorescence imaging of intracellular Al^{3+} ions to investigate its application in biological system.
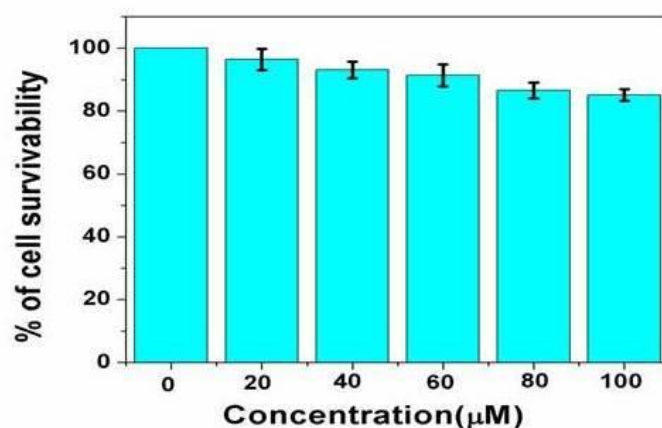
Fig. 5.21. Cell survivability of WI-38 cells exposed to the probe **L**.

First, Hep G2 cells were treated with probe **L** (10 µM) for 30 min at 37°C and then washed with PBS buffer to remove excess probe. After that, the treated cells were incubated with Al^{3+} ions (10 µM) for another 30 min at 37°C.

Then, these incubated cells were washed again with PBS buffer and images were recorded using a fluorescence microscope. Hep G2 cells treated with only probe **L** displayed no fluorescence signal, whereas an intense green fluorescence signal was detected in the intracellular area when stained with **L** followed by $Al(NO_3)_3$. Again, this bright fluorescence signal disappeared when the cells were treated with $NaHF_2$ (10 µM) solution (Fig. 5.22).

Furthermore, there were no gross morphological changes in bright-field images of cells, suggesting that the cells remained viable throughout the imaging studies. The above results established the good cell-membrane permeability of **L** and that it could be employed in living cells for *in vitro* imaging of Al^{3+} and HF_2^- ions. Additionally, the MTT assay determined that probe **L** displayed very low cytotoxicity toward living cells.
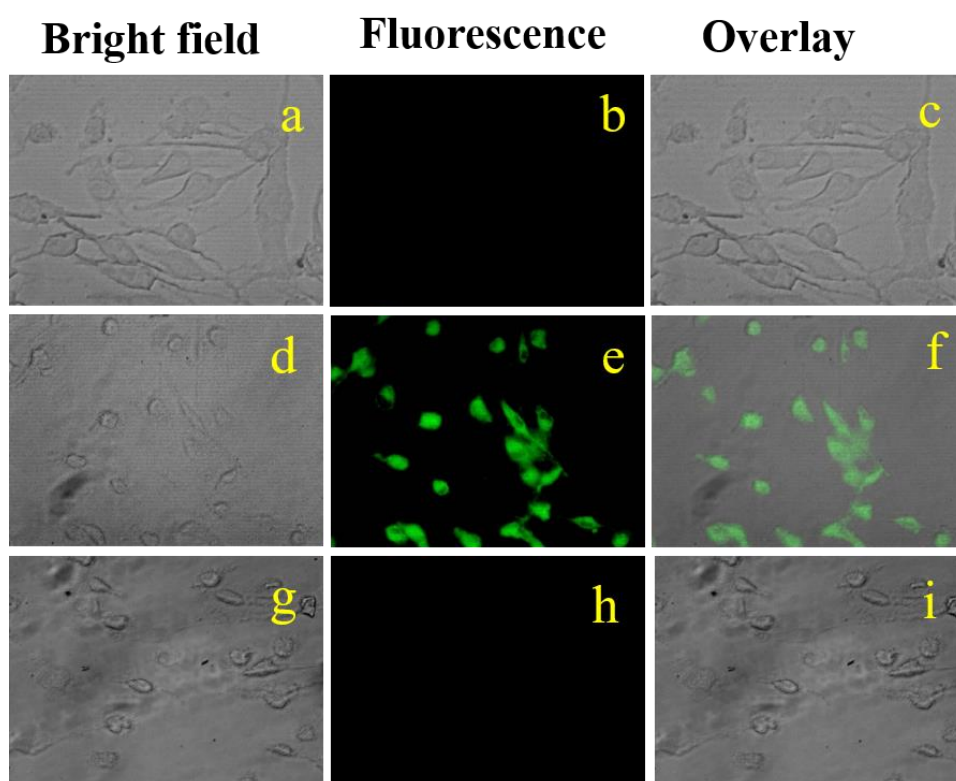
Fig. 5.22. Bright field, fluorescence and overlay images of Hep G2 cells. (a-c) cells were incubated with 10 μM probe **L** for 30 min, (d-f) followed by addition and incubation with 10 μM Al^{3+} for another 30 min and (g-i) then with $NaHF_2$ for 30 minutes.

5.4. CONCLUSION

In conclusion, a simple colorimetric and fluorometric chemosensor, **L**, was designed and successfully synthesized based on pyridine-dicarbohydrazide. The chemosensor **L** shows both color and switch-on emission response to Al^{3+} ions in organo aqueous solution as a result of metal enhanced chelation effect (CHEF) inhibiting the PET, ESIPT and C=N isomerization processes. With a detection limit of $0.8\mu M$, this chemosensor displays high selectivity for Al^{3+} ions over other 18 commonly coexistent metal ions. The stoichiometry of the **L**-Al^{3+} is determined to be 1:2 (**L**: Al^{3+}) and is confirmed by Job's plot analysis. The association constant for **L** with Al^{3+} is found to be 4.26×10^4 M^{-2} on the basis of fluorescence studies, proposing a strong binding affinity for Al^{3+}. Besides, the *in situ* prepared **L**-$2Al^{3+}$ complex can be utilized for the detection of HF_2^- ions *via* the displacement approach and it exhibits a "turn-off" type of fluorescence response. Moreover, the detection of Al^{3+} and HF_2^- ions was also carried out in HepG2 cells to demonstrate the "off-on-off" fluorescence cellular image. It proves that molecule penetrates to cell and thus it is applicable to biological system.

REFERENCES

1. A. C. Sedgwick, L. Wu, H.-H. Han, S. D. Bull, X.-P. He, T. D. James, J. L. Sessler, B. Z. Tang, H. Tian and J. Yoon, *Chem. Soc. Rev.*, 2018, **47**, 8842–8880.

2. S. Sen, T. Mukherjee, B. Chattopadhyay, A. Moirangthem, A. Basu, J. Marek and P. Chattopadhyay, *Analyst*, 2012, **137**, 3975–3981.

3. S. H. Kim, H. S. Choi, J. Kim, S. J. Lee, D. T. Quang and J. S. Kim, *Org. Lett.*, 2010, **12**, 560–563.

4. R. A. Yokel, *Food Chem. Toxicol.*, 2008, **46**, 2261–2266.

5. R. J. Lakowicz, Principles of Fluorescence Spectroscopy, 3rd ed.; Springer: New York, 2006; p xxvi.

6. B. Valeur and I. Leray, *Coord. Chem. Rev.*, 2000, **205**, 3−40.

7. D. Krewski, R. A. Yokel, E. Nieboer, D. Borchelt, J. Cohen, J. Harry, S. Kacew, J. Lindsay, A. M. Mahfouz and V. Rondeau, *J. Toxicol. Environ. Health, Part B*, 2007, **10**, 1–269.

8. M. J. Cullen, M. J. Allwood, D. M. ambach, *Environ. Sci. Technol.*, 2012, **46**, 13048−13055.

9. T. Khan, S. Vaidya, D. S. Mhatre and A. Datta, *J. Phys. Chem. B*, 2016, **120**, 10319–10326.

10. A. K. Mahapatra, S. S. Ali, K. Maiti, A. K. Manna, R. Maji, S. Mondal, M. R. Uddin, S. Mandal and P. A. Sahoo, *RSC Adv.*, 2015, **5**, 81203–81211.

11. M. R. Wills and J. Savory, *Lancet*, 1983, **2**, 29–34.

12. C. A. Shaw and L. Tomljenovic, *Immunol. Res.*, 2013, **56**, 304–316.

13. G. Berthon, *Coord. Chem. Rev.*, 2002, **228**, 319–341.

14. A. C. Alfrey, *Adv. Clin. Chem.*, 1983, **23**, 69–91.

15. A. M. Pierides, W. G. Edwards Jr, U. X. Cullum Jr, J. T McCall and H. A. Ellis, *Kidney Int.*, 1980, **18**, 115–124.

16. T. P. Flaten, *Brain Res. Bull.*, 2001, **55**, 187–196.

17. M. Yasui, T. Kihira and K. Ota, *Neurotoxicology*, 1992, **13**, 593–600.

18. P. Nayak, *Environ. Res.*, 2002, **89**, 101–115.

19. B. Wang, W. Xing, Y. Zhao and X. Deng, *Environ. Toxicol. Pharmacol.*, 2010, **29**, 308–313.

20. P. D. Darbre, *J. Inorg. Biochem.*, 2005, **99**, 1912–1919.

21. C. S. Cronan, W. J. Walker and P. R. Bloom, *Nature*, 1986, **324**, 140–143.

22. J. Barcelo and C. Poschenrieder, *Environ. Exp. Bot.*, 2002, **48**, 75–92.

23. V. Kumar, A. Kumar, U. Diwan, Ramesh Shweta, S.K. Srivastava, *Sens. Actuators, B*, 2015, **207**, 650–657.

24. M. Frankowski, A. Zioła-Frankowska, and J. Siepak, *Talanta*, 2010, **80**, 2120–2126.

25. G. Tangen, T. Wickstrom, S. Lierhagen, R. Vogt, W. Lund, *Environ. Sci. Technol.*, 2002, **36**, 5421–5425.

26. M. Rezaee, Y. Yamini, A. Khanchi, M. Faraji and A. Saleh, *J. Hazard. Mater.*, 2010, **178**, 766–770.

27. A. Sanz-Medel, A. B. Soldado Caabezuelo, R. Milačič and T. Bantan Polak, *Coord. Chem. Rev.*, 2002, **228**, 373–383.

28. Y. C. Chen, I. L. Lee, Y. M. Sung and S. P. Wu, *Talanta*, 2013, **117**, 70–74.

29. V. K. Gupta, A. K. Jain and P. Kumar, *Sens. Actuators, B*, 2006, **120**, 259–265.

30. V. K. Gupta, B. Sethi, N. Upadhyay, S. Kumar, R. Singh and L. P. Singh, *Int. J. Electrochem. Sci.*, 2011, **6**, 650–663.

31. V. K. Gupta, R. Jain, and K. M. Pal, *Int. J. Electrochem. Sci.*, 2010, **5**, 1164−1178.

32. H. Wang, Z. Yu, Z. Wang, H. Hao, Y. Chen and P. Wan, *Electroanalysis*, 2011, **23**, 1095–1099.

33. S. Samanta, B. Nath and J. B. Baruah, *Inorg. Chem. Commun.*, 2012, **22**, 98–100.

34. J. F. G. Reyes, P. O. Barrales, and A. M. Diaz, *Talanta*, 2005, **65**, 1203-1208.

35. J. C. Qin, L. Fan, T. R. Li and Z. Y. Yang, *Synth. Met.*, 2015, **199**, 179–186.

36. S. Sinha, B. Chowdhury, and P. Ghosh, *Inorg. Chem.*, 2016, **55**, 9212–9220.

37. A. Sahana, A. Banerjee, S. Lohar, B. Sarkar, S. K. Mukhopadhyay and Debasis Das, *Inorg. Chem.*, 2013, **52**, 3627–3633.

38. S. Kim, J. Y. Noh, K. Y. Kim, J. H. Kim, H. K. Kang, S.-W. Nam, S. H. Kim, S. Park, C. Kim and J. Kim, *Inorg. Chem.*, 2012, **51**, 3597–3602.

39. V. Saini, R. Krishnan and B. Khungar, *Photochem. Photobiol. Sci.,* 2020, **19(7)**, 931−942.

40. P. Ghorai, K. Pal, P. Karmakar and A. Saha, *Dalton Trans.*, 2020, **49**, 4758−4773.

41. M. Wang, C. Cheng, C. Li, D. Wu, J. Song, J. Wang, X. Zhou, H. Xiang and J. Liu, *J. Mater. Chem. C*, 2019, **7**, 6767–6778.

42. K. Ashley, A. Agrawal, J. Cronin, J. Tonazzi, T. M. McCleskey, A. K. Burrell and D. S. Ehler, *Anal. Chim. Acta*, 2007, **584**, 281–286.

43. T. L. Peters, T. J. Nestrlck, L. L. Lamparski and R. H, Sthel, *Anal. Chem.*, 1982, **51**, 2397–2398.

44. C. R. Wade, A. E. J. Broomsgrove, S. Aldridge and F. o. P. Gabbaï, *Chem. Rev.*, 2010, **110**, 3958–3984.

45. K. Murugesan, V. Jeyasingh, S. Lakshminarayanan, S. Narayanan, S. Ramasamy, I. V. M. V. Enoch, and L. Piramuthu, *Spectrochim. Acta, Part A*, 2019, **209**, 165−169.

46. A. Ghorai, S. S. Thakur and G. K. Patra, *RSC Adv.*, 2016, **6**, 108717–108725.

47. K. Dutta, R. C. Deka and D. K. Das, *J. Fluoresc.*, 2013, **23**, 823−828.

48. N. Yadav, A. K. Singh, *New J. Chem.*, 2018, **42**, 6023−6033.

49. *Bruker, SMART v5.631*, Bruker AXS Inc., Madison, WI, USA, 2001.

50. G. M. Sheldrick, *SHELXT-2014*, University of Göttingen, 2014.

51. A. D. Becke, *J. Chem. Phys.*, 1993, **98**, 5648−5662.

52. C. T. Lee, W. T. Yang and R. G. Parr, *Phys. Rev. B*, 1988, **37**, 785−789.

53. B. Miehlich, A. Savin, H. Stoll and H. Preuss, *Chem. Phys. Lett.*, 1989, **157**, 200−206.

54. J. D. Dill, J. A. Pople, *J. Chem. Phys.*, 1975, **62**, 2921−2923.

55. J. Tomasi, and M. Persico, *Chem. Rev.*, 1994, **94**, 2027−2094.

56. M. Cossi, V. Barone, R. Cammi and J. Tomasi, *Chem. Phys. Lett.*, 1996, **255**, 327−335.

57. V. Barone, M. Cossi and J. Tomasi, *J. Chem. Phys.*, 1997, **107**, 3210−3221.

58. V. Barone, M. Cossi and J. Tomasi, *J. Comput. Chem.*, 1998, **19**, 404−417.

59. M. Cossi and V. Barone, *J. Chem. Phys.*, 1998, **109**, 6246−6254.

60. R. Bauernschmitt and R. Ahlrichs, *Chem. Phys. Lett.*, 1996, **256**, 454−464.

61. R. E. Stratmann, G. E. Scuseria, and M. J. Frisch, *J. Chem. Phys.*, 1998, **109**, 8218−8224.

62. Gaussian 16, Revision B.01, M. J. Frisch, G. W. Trucks, H. B. Schlegel, G. E. Scuseria, M. A. Robb, J. R. Cheeseman, G. Scalmani, V. Barone, G. A. Petersson, H. Nakatsuji, X. Li, M. Caricato, A. V. Marenich, J. Bloino, B. G. Janesko, R. Gomperts, B. Mennucci, H. P. Hratchian, J. V. Ortiz, A. F. Izmaylov, J. L. Sonnenberg, D. Williams-Young, F. Ding, F. Lipparini, F. Egidi, J. Goings, B. Peng, A. Petrone, T. Henderson, D. Ranasinghe, V. G. Zakrzewski, J. Gao, N. Rega, G. Zheng, W. Liang, M. Hada, M. Ehara, K. Toyota, R. Fukuda, J. Hasegawa, M. Ishida, T. Nakajima, Y. Honda, O. Kitao, H. Nakai, T. Vreven, K. Throssell, J. A. Montgomery, Jr., J. E.

Peralta, F. Ogliaro, M. J. Bearpark, J. J. Heyd, E. N. Brothers, K. N. Kudin, V. N. Staroverov, T. A. Keith, R. Kobayashi, J. Normand, K. Raghavachari, A. P. Rendell, J. C. Burant, S. S. Iyengar, J. Tomasi, M. Cossi, J. M. Millam, M. Klene, C. Adamo, R. Cammi, J. W. Ochterski, R. L. Martin, K. Morokuma, O. Farkas, J. B. Foresman, and D. J. Fox, Gaussian, Inc., Wallingford CT, 2016.

63. N. Xiao, L. Xie, X. Zhi and C. Fang, *Inorg. Chem. Commun.*, 2018, **89**, 13–17.

64. J. Wang and Y.Pang, *RSC Adv.*, 2014, **4**, 5845–5848.

65. S. K. Asthana, A. Kumar, Neeraj, Shweta, S. K. Hira, P. P. Manna, and K. K. Upadhyay, *Inorg. Chem. Commun.*, 2017, **56**, 3315–3323.

66. C. Yang, L. Liu, T. W. Mu and Q.-X. Guo, *Anal. Sci.*, 2000, **16**, 537–539.

67. H. A. Benesi and J. H. Hildebrand, *J. Am. Chem. Soc.*, 1949, **71**, 2703−2707.

68. Y. Shiraishi, S. Sumiya, Y. Kohono and T. Hirai, *J. Org. Chem.*, 2008, **73**, 8571–8574.

69. L. L. Long, D. D. Zhang, X. F. Li, J. F. Zhang, C. Zhang and L. P. Zhou, *Anal. Chim. Acta*, 2013, **775**, 100–105.

70. T. Mandal, A. Hossain, A. Dhara, A. A. Masum, S. Konar, S. K. Manna, S. K. Seth, S. Pathak and S. Mukhopadhyay, *Photochem. Photobiol. Sci.*, 2018, **17**, 1068–1074.

71. R. Purkait and C. Sinha, *New J. Chem.,* 2019, **43**, 9815−9823.

72. R. Purkait, A. Dey, S. Dey, P. P. Ray, and C. Sinha, *New J. Chem.*, 2019, **43**, 14979−14990.

73. P. B. Thale, P. N. Borase and G. S. Shankarling, *Inorg. Chem. Front.*, 2016, **3**, 977–984.

74. A. Samui, K. Pal, P. Karmakar and S. K. Sahu, *Mater. Sci. Eng. C*, 2019, **98**, 772–781.

75. K. Pal, S. Roy, P. K. Parida, A. Dutta, S. Bardhan, S. Das, K. Jana and P. Karmakar, *Mater. Sci. Eng. C*, 2019, **95**, 204–216.

CHAPTER 6

Crystallographic, theoretical and antibacterial studies of two Zn(II) complexes derived from a new hydrazone ligand

Complex 1

Complex 2

6.1. INTRODUCTION

The field of non-covalent interactions (NCIs) is extensive and covers the whole of science. The NCIs involving hydrogen bonding, halogen bonding, π•••π stacking, lone pair•••π, cation•••π, anion•••π, C–H•••π, N–H•••π, O–H•••π interactions have attracted recent interest to elucidate the outstanding importance of these weak forces in controlling the structure and function of macromolecules [1–7]. A deep understanding of these weak interactions is essential to go forward in many fields, especially in crystal growth and crystal engineering [8]. Recently, much attention has also been given on π-hole interactions owing to their cooperative participation in chemical reactions, crystal engineering as well as in biological applications. Theoreticians have established that the distribution of the electron density around covalently bonded atoms is not isotropic, i.e., the atoms develop some regions of higher and lower electron density [9]. A π–hole can be defined as positive electrostatic potential on unoccupied π* orbitals, which have capability to interact with some electron-dense region (anion, Lewis base, π-system, *etc.*) [10,11]. It is typically located above and below to the molecular framework of π-systems, such as carbonyls or conjugated π-acidic systems such as hexafluorobenzene [12]. One of the promising but comparatively less studied system is the imidic C=N group, acting as a Lewis acid (π–hole donor) [13–15]. Thus, there are much of works on the π-hole interactions involving the imidic C=N moiety is yet to be explored.

Schiff base ligands with nitrogen or oxygen donor atoms are a good class of organic compounds that play an important role by serving as chelating ligands in the main groups and transition metal coordination chemistry [16,17]. The diverse role of transition metal complexes of Schiff base ligands in inorganic, metallo-organic and biochemistry have received considerable attention owing to their stability in different oxidative and reductive conditions [18,19]. Hydrazone ligands are a special type of Schiff bases which can accommodate with different coordination modes according to the demand of variable geometries and valences of metal ions in coordination complexes [20]. Due to the presence of the N─H functionality adjacent to the azomethine (C=N) chromophore, they can form interesting hydrogen bonded self assembly in metal complexes [21]. However, in the metal-coordinated hydrazone ligand, the electron withdrawing N─H group induces acidity to the imidic C=N bond which can interact with electron rich atoms and develop distinct supramolecular interaction [22]. The interaction of these donor ligands and metal ions gives complexes of different geometries and literature survey reveals that these complexes are

potentially more biologically active such as anticancer, antifungal, antibacterial, anti-malarial, anti-inflammatory, antiviral, and antipyretic properties [23–25]. It should be noted that metal chelation can tremendously influence the antimicrobial/bioactive behavior of the organic ligands [26]. Thus, various transition metal complexes have been synthesized in this field.

After iron, zinc (Zn) is the second most abundant trace element in the human body and is one of the most important micro-elements for human physiology [27]. Zn^{2+} (d^{10} configuration) has zero ligand field stabilization energy that can support a variable coordination geometry around the metal centre (zinc) and assist fast exchange of ligands [28,29]. Besides, due to the lack of redox activity of divalent zinc ion, it eliminates any chances of free radical reactions and makes it crucial for the body's antioxidant protection system [27]. However, a random mix of transition metal components such as Co-M (M = Zn, Cu, Fe) was reported in several studies to enhance the catalyst efficiency [30]. The importance of zinc in biological systems is related to its unique chemical properties. It plays an important role in the catalytic activity of various enzymes, protein synthesis, DNA synthesis, immune functions and determines the conformations of many proteins through binding in the active sites. This makes zinc as essential element for all cellular functions and development of all forms of life. Compared to other metal-based drugs, Zn(II) complexes generally exert lower toxicity and have fewer side effects [31]. In the last few years different classes of zinc coordination complexes have shown a good potential in diverse applications, including in nonlinear optics, in photo-catalysis, as anti-inflammatory, anti-diabetic, antimicrobial, antioxidant, antitumor agents and in several diseases [32–40].

To explore the non-covalent interactions in coordination compounds, herein, two Zn(II) complexes (**1** and **2**) using newly synthesized [(1-methylimidazol-2-yl)methylene]isonicotinohydrazide [H**L**] ligand have been designed and prepared in aqueous medium. Single crystal X-ray analysis shows that complex **1** is a distorted octahedral whereas complex **2** is a distorted tetrahedral in nature. The complex **1** shows π•••π, O─H•••π and hydrogen bonding interactions that are responsible to form various supramolecular architectures. Interestingly, the non-coordinated water molecules are interconnected through hydrogen bonds to form a tetrameric water cluster which has significant role in stabilizing molecular structure of complex **1**. The solid-state structure of complex **2** is stabilized through π•••π$^+$ stacking, lone pair•••π/π$^+$ and various types of hydrogen bonding interactions which are responsible to form various supramolecular architectures. More importantly, the imidic

C=N bond of the Zn(II)-coordinated hydrazone ligand is able to interact favorably with electron rich oxygen atom of non coordinated water molecule (O••π-hole interaction) in complex **2**, which is a rare example. Another interesting phenomenon is that the π-system of the –NNHCO– group takes part in the stacking interaction to give additional stability in the complex **2**. These NCIs have been confirmed using combined QTAIM/NCI plot analysis and supported by MEP surface analysis. Moreover, the cooperative and energetic features of both conventional and unconventional interactions have also been evaluated by means of DFT calculations. In addition, the antibacterial activities of H**L** and its complex (**2**) were tested against Gram-negative (*Escherichia coli*) and Gram-positive (*Staphylococcus aureus*) bacteria.

6.2. EXPERIMENTAL SECTION

6.2.1. Materials and apparatus

All the chemicals (analytical grade) and solvents (spectroscopic grade) were purchased from commercial suppliers and used without any further purification. Freshly prepared double distilled water was used throughout the synthetic procedure and all the reactions were carried out under aerobic conditions. Elemental analyses (C, H and N) were performed using a PerkinElmer 2400 Series-II CHN analyzer, USA elemental analyzer. ESI mass spectra were obtained from a Water HRMS model XEVO-G2QTOF#YCA351 spectrometer. ^{1}H NMR spectrum was obtained from Bruker spectrometer (400 MHz) with DMSO-d_6 solvent using trimethylsilane (TMS) as an internal standard. Fourier transform infrared (FT-IR) spectra were recorded on a Perkin Elmer LX-1 FT-IR spectrophotometer (4000−400 cm^{-1}) by using a modern diamond attenuated total reflectance (ATR) accessory method. Single crystal structures were performed using single-crystal X-ray diffractometer (Bruker Smart Apex II).

6.2.2. Synthesis of [(1-methylimidazol-2-yl)methylene]isonicotinohydrazide [HL]

Isonicotinic hydrazide (0.137 g, 1 mmol) was added into 30 mL ethanolic solution of 1-methyl imidazole-2-carboxaldehyde (0.11 g, 1 mmol). The reaction mixture was then refluxed for 3 hours (Scheme 6.1). After completion of the reaction, solution was cooled at room temperature. A light yellow solid formed which was collected by filtration and washed repeatedly with cold water and dried in air. The desired product was obtained with good yield and acceptable purity. Yield 0.174 g (76%). The ligand (H**L**) is soluble in water ($S_{25^\circ C} \approx$ 3.3 mg/mL), methanol ($S_{25^\circ C} \approx$ 4.2 mg/mL) and acetonitrile ($S25 \degree C \approx$ 3.8 mg/mL) as well as

in DMSO ($S_{25°C} \approx 5.1$ mg/mL). Anal. calcd. for $C_{11}H_{12}N_5O$, C 57.63, H 4.84, N 30.55. Found: C 57.61, H 4.83, N 30.52 %. ^{1}H NMR (400 MHz, CDCl$_3$): δ (ppm) = 12.11 (s, 1H), 8.78 (d, *J* = 6 Hz 2H), 8.42 (s, 1H), 7.81 (d, *J* = 6 Hz, 2H), 7.35 (d, *J* = 6 Hz, 2H), 7.08 (d, *J* = 7 Hz, 2H), 3.97 (s, 3H) (Fig. 6.1). Main FT-IR absorptions, (KBr, cm^{-1}): 3210(bs), 3118(s), 3101(vs), 3054(s), 1683(s), 1456(vs), 1625(s), 1613(vs), 1602(s), 1556(s), 1525(s), 1499(s), 1471(s), 1437(s), 1412(s) (Fig. 6.2). ESI-MS: m/z 252.150, 230.181; Calcd. for [$C_{11}H_{12}N_5O$ + Na$^+$] = 252.089, [$C_{11}H_{12}N_5O$ + H$^+$] = 230.10 (Fig. 6.3).
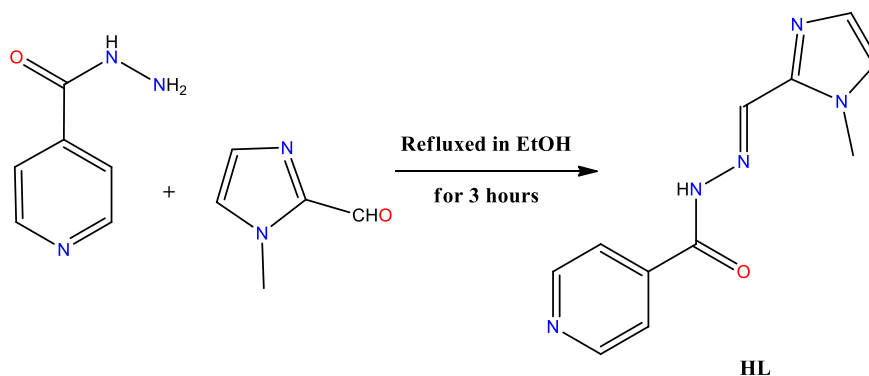
Scheme 6.1. Synthetic route for the ligand, H**L**
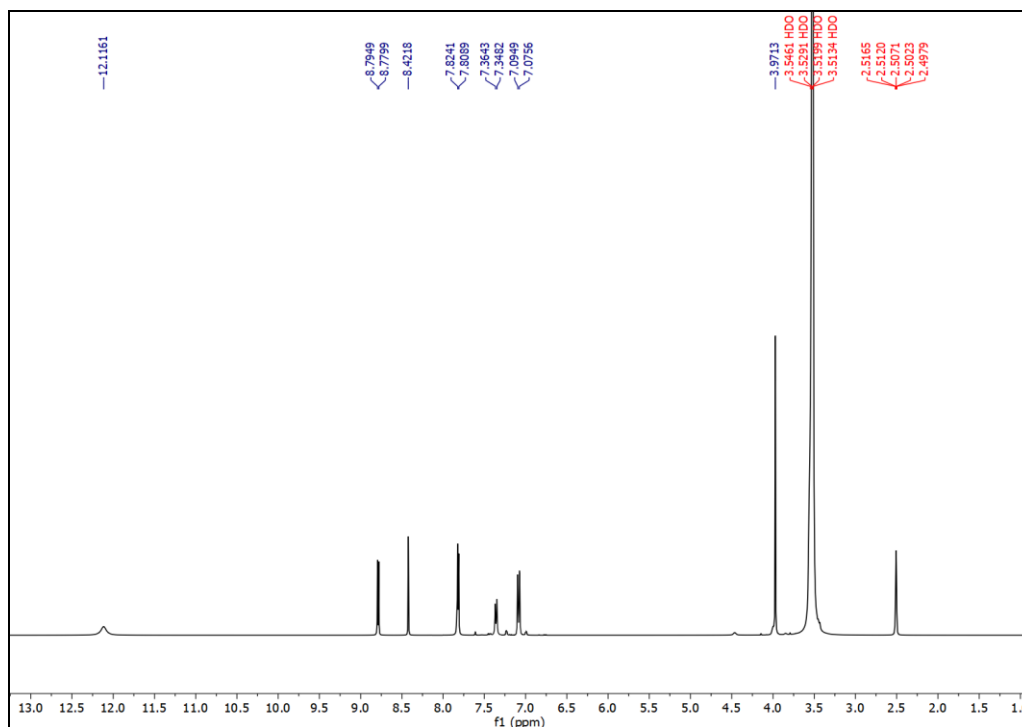
Fig. 6.1. ^{1}H NMR spectrum of H**L**
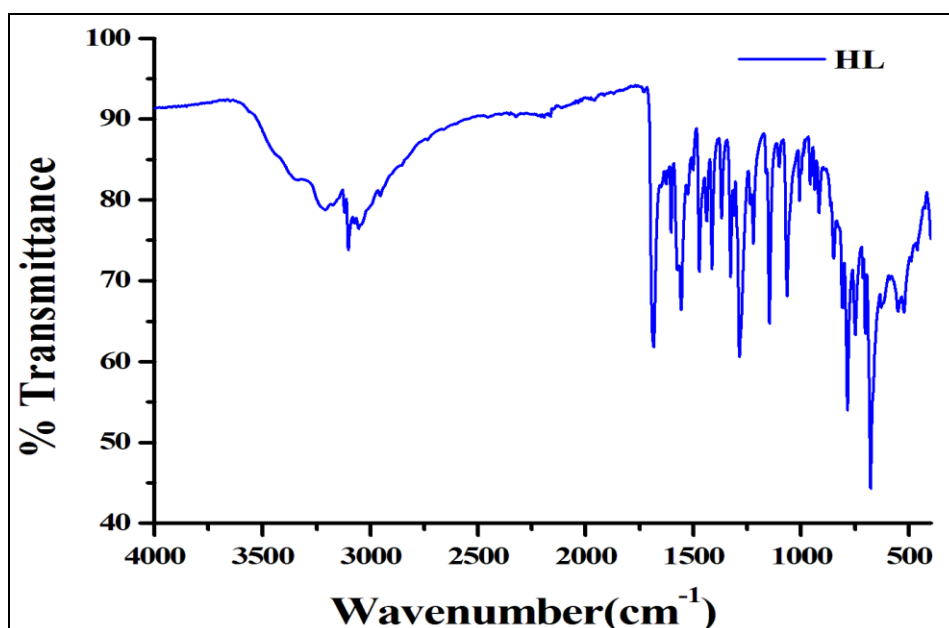
Fig. 6.2. FT-IR spectrum of H**L**
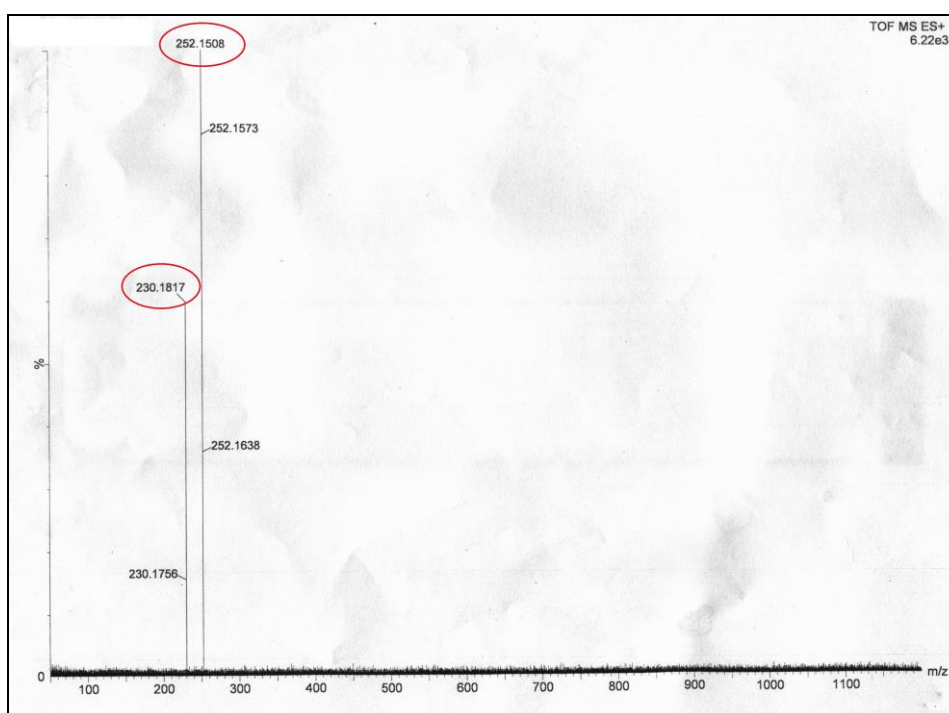
Fig. 6.3. ESI mass spectrum of H**L**

6.2.3. Synthesis of [Zn(L)₂]·2H₂O (Complex 1)

An aqueous suspension (20 mL) of the ligand, H**L** (0.229 g, 1 mmol) was added to 20 mL of aqueous $Zn(NO_3)_2 \cdot 6H_2O$ (0.297 g, 1 mmol) solution with constant stirring (Scheme 6.2). A clear bright yellow solution was appeared after 3 hours of constant stirring. Then the solution was filtered and the filtrate was left for slow evaporation without any disturbance. After one

week, yellow coloured X-ray quality crystals of **1** were isolated (yield: 65%). The complex **1** is sparingly soluble in water ($S_{25°C} \approx 0.5$ mg/mL), slightly soluble in methanol ($S_{25°C} \approx 1.3$ mg/mL) and acetonitrile ($S_{25°C} \approx 0.9$ mg/mL) whereas completely soluble in DMSO ($S_{25°C} \approx 5.3$ mg/mL). Anal. calcd. for $C_{11}H_{14}N_5O_3Zn$: C, 40.08; H, 4.28; N, 21.25. Found: C, 40.05; H, 4.26; N, 21.21%. Main FT-IR absorptions, (KBr, cm^{-1}): 3564(w), 3359(w), 3118(vs), 3098(vs), 3045(s), 2955(s), 1946(s), 1791(s), 1704(s), 1634(vs), 1604(s), 1595(s), 1565(vs), 1500(s), 1489(s), 1469(s), 1456(s), 1415(vs) (Fig. 6.4).

6.2.4. Synthesis of [Zn(H₂L)Cl₃]·H₂O (Complex 2)

Complex **2** was synthesised by reacting an aqueous suspension (20 mL) of the ligand, **HL** (0.229 g, 1 mmol) with 20 mL aqueous $ZnCl_2$ (0.136 g, 1 mmol) solution at stirring condition. The solution became turbid after one hour of constant stirring (Scheme 6.2). Two drops of 1 (M) HCl were added into the resultant turbid solution to obtain a clear pale yellow solution. Then the solution was filtered and the filtrate was left undisturbed for slow evaporation. Two weeks later, deep yellow X-ray quality crystals of **2** were obtained (yield: 68%). The complex **2** is soluble in water ($S_{25°C} \approx 5.7$ mg/mL), methanol ($S_{25°C} \approx 3.7$ mg/mL) and acetonitrile (S25 ° C ≈ 3.4 mg/mL) as well as in DMSO ($S_{25°C} \approx 6.5$ mg/mL). Anal. calcd. for $C_{11}H_{14}Cl_3N_5O_2Zn$: C, 31.46; H, 3.36; N, 16.67. Found: C, 31.44; H, 3.35; N, 16.64%. Main FT-IR absorptions, (KBr, cm^{-1}): 3507(s), 3402(s), 3200(s), 3144(vs), 3102(s), 3059(vs), 1979(s), 1673(vs), 1620v(s), 1544(vs), 1498(s), 1475(vs), 1422(vs) (Fig. 6.4).
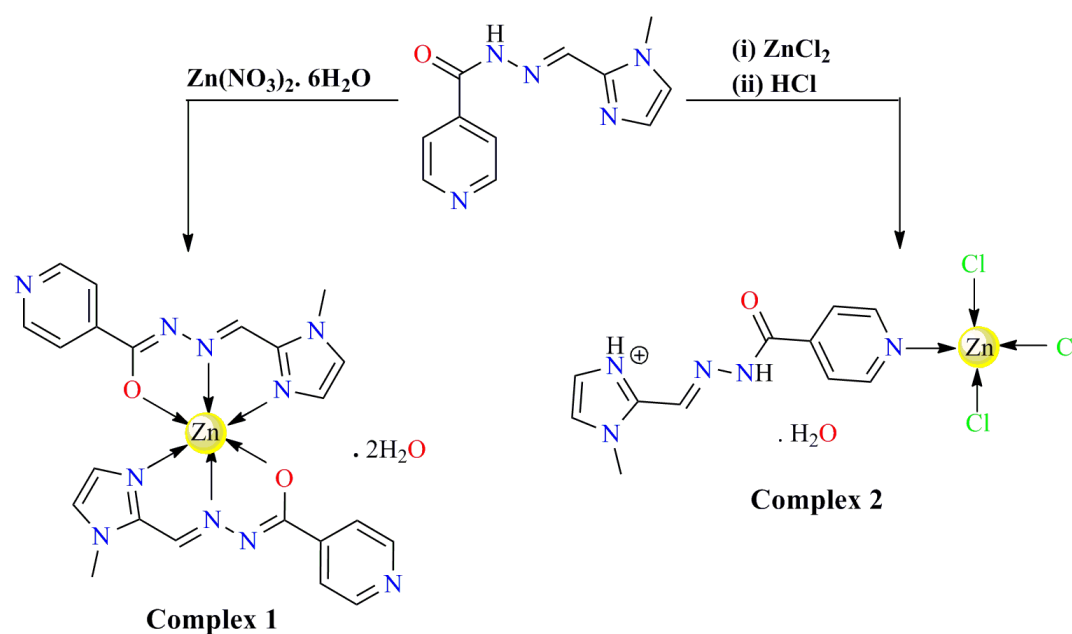
Scheme 6.2. Schematic representation of the synthesis of the title complexes
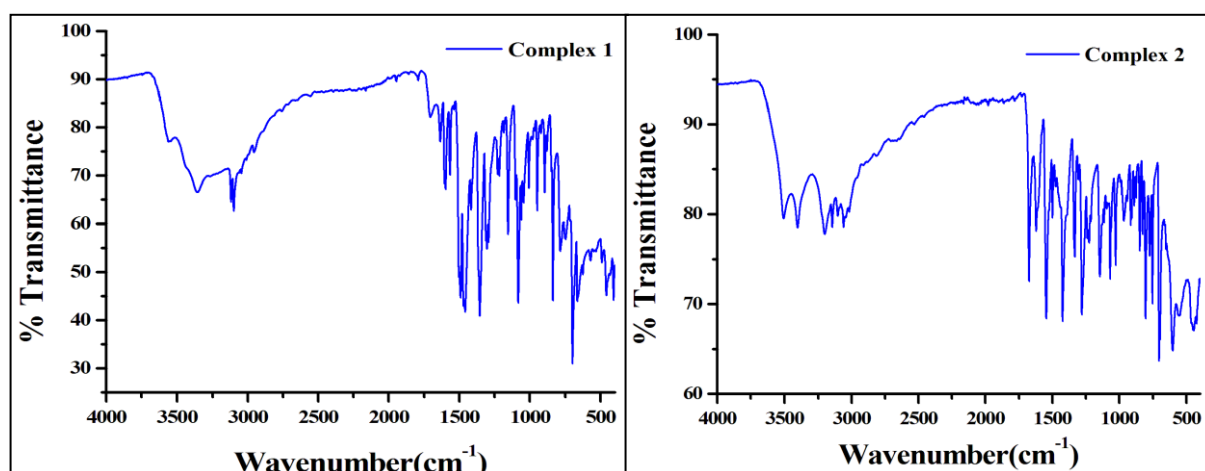
Fig. 6.4. FT-IR spectra for complex **1** and **2**

6.2.5. X-ray crystallographic analysis

Single crystal X-ray data collections were made using a Bruker SMART APEX II CCD area detector equipped with a graphite monochromated Mo Ka radiation (λ = 0.71073 Å) source in φ and ω scan mode at 296 K for both the complexes. Cell parameter refinement and data reduction for both the complexes were carried out using a Bruker SMART APEX II instrument, Bruker SMART and Bruker SAINT Software [41]. The crystal structures of the title compounds were solved by intrinsic phasing method using SHELXT-2014/5 and refined by full-matrix least squares on F^2 techniques using the SHELXL-2016/6 crystallographic software package [42]. The CIFs have been deposited with CCDC No. 2209945 (complex **1**) and CCDC No. 2209946 (complex **2**). Selected crystal data for **1** and **2** are given in Table 6.1.

6.2.6. Computational methods

The calculations of the non-covalent interactions were carried out using the Gaussian-16 [43] and the PBE0-D3/def2-TZVP level of theory [44,45] and the crystallographic coordinates. The interaction energies have been computed by calculating the difference between the energies of isolated monomers and their assembly. The interaction energies are corrected for the basis set superposition error (BSSE) employing the methodology proposed by Boys–Bernardi [46]. The Bader's "Atoms in molecules" theory (QTAIM) [47] has been used to study the interactions by means of the AIMAll calculation package [48]. The molecular electrostatic potential surfaces have been computed using the Gaussian-16 software and the 0.001 a.u. isovalue. To reveal the interactions in real space, NCIPLOT index [49] have been used based on the reduced density gradient (RDG) isosurfaces that are derived from the

electronic density and its first derivative. The sign of the second Hessian eigenvalue times the electron density [*i.e.*, sign $(\lambda 2)\rho$ in atomic units] enables the identification of attractive/stabilizing (blue-green coloured isosurfaces) or repulsive (yellow-red coloured isosurfaces) interactions using 3D-Plots [50].

Table 6.1. Crystal data and structure refinement parameters for complexes 1 and 2

Structure	Complex **1**	Complex **2**
Empirical formula	$C_{22}H_{28}N_{10}O_6Zn$	$C_{11}H_{14}Cl_3N_5O_2Zn$
Formula Weight	593.93	420.01
Temperature (K)	296	296
Wavelength (Å)	0.71073	0.71073
Crystal system	Monoclinic	Monoclinic
space group	C2/c	P 21/c
a, b, c (Å)	23.393(5), 8.6036(19), 13.597(3)	9.473(4), 13.927(6), 13.293(5)
α, β, γ (°)	90, 107.497(7), 90	90, 105.063(5), 90
Volume (Å^3)	2610.0(10)	1693.5(12)
Z / Density (calc.) (Mg/m^3)	4 / 1.512	4 / 1.647
Absorption coefficient (mm^{-1})	0.999	1.935
F(000)	1232	848
Crystal size (mm^3)	$0.08 \times 0.14 \times 0.19$	$0.09 \times 0.13 \times 0.19$
θ range for data collection	1.833 to 27.169	2.158 to 27.842
Completeness to θ (%)	100%	100%
Absorption correction	Multi-scan	Multi-scan
Max. and min. transmission	0.923 and 0.845	0.840 and 0.747
Refinement method	Full-matrix least-squares on F^2	Full-matrix least-squares on F^2
Data/parameters	2933 / 184	4022 / 203
Goodness-of-fit on F^2	0.972	0.971
Final R indices [I > 2σ(I)]	R$_1$ = 0.0363, wR$_2$ = 0.0842	R$_1$ = 0.0346, wR$_2$ = 0.0715
R indices (all data)	R$_1$ = 0.0573, wR$_2$ = 0.0880	R$_1$ = 0.0608, wR$_2$ = 0.0804
Largest diff. peak and hole (e.Å^{-3})	0.387 and -0.353	0.273 and -0.339

$R_1 = \sum ||F_o|-|F_c||/\sum|F_o|$, $wR_2 = [\sum\{(F_o^2-F_c^2)^2\}/\sum\{w(F_o^2)^2\}]^{1/2}$ $w = 1/\{\sigma^2(F_o^2) + (aP)^2 + bP\}$, $P = (F_o^2 + 2F_c^2)/3$ where, a =0.0511, b =0.0 for complex **1** and a = 0.0339, b = 0.6250 for complex **2**.

6.2.7. Bacterial strains and culture conditions

Properly distinguished cells of *E. coli DH5α* (K12) and *S. aureus* (ATCC 29737) were obtained from National Institute of Cholera and Enteric Diseases (NICED), Kolkata, India. Cultures were nourished on Luria Broth (LB). The bacteria were cultured overnight in 3 ml of LB in shaker at 37 °C prior to incubation with complex **2**, ligand **HL**, and positive control $ZnCl_2$ until the absorbance of the culture reached 1.0 at 600 nm, indicating colony formation of 10^9 CFU (colony-forming unit) ml^{-1}. Sterile broth was used to dilute the overnight cultures to 10^7 CFU ml^{-1}.

6.2.8. Antibacterial activity study

Complex **1** was sparingly soluble in water whereas the ligand (**HL**) and the complex **2** were completely soluble in water. Thus, the antibacterial study for the complex **1** was not performed. The antibacterial activity of $ZnCl_2$ and complex **2** was confirmed through determination of minimum inhibitory concentration (MIC). The lowest concentration of antimicrobial agent at which no growth is observed in medium is termed as MIC. 3 ml of LB was taken in test tubes and each of them were inoculated with overnight cultures of the bacteria and thereafter various concentrations of complex **2** (0 mM–5 mM), ligand **HL** (0 mM–5 mM) and $ZnCl_2$ (0 mM–5 mM) were added in every test tube. The tubes were shaken at 37 °C for 24 h and the absorbances were measured at 600 nm to determine bacterial growth.

6.3. RESULTS AND DISCUSSION

6.3.1. Structural description of complex 1

The perspective view of complex **1** with atom numbering scheme is displayed in Fig. 6.5. The single crystal X-ray diffraction study shows that the asymmetric unit of complex **1** consists of one-half of $[Zn(L)_2]$ unit (the other half being generated by an inversion center) and two non-coordinated water molecules. The complex **1** crystallizes in a monoclinic system with the space group *C*2/c. The metal centric bond lengths and bond angles are summarized in Table 6.2. During complex formation, ligand undergoes lactam-lactim tautomerism and the deprotonated mono-negative ligand (**L**⁻) resulting in the formation of first order inner metallic complex. Here, the ligand acts as *ONN* tridentate chelating ligand through O1, N3 and N2 atoms that occupy the respective meridional planes resulting a distorted octahedral geometry around Zn(II) ion. The great distortion from regular octahedral geometry is mainly

due to the formation of four planar 5-membered chelate rings having bite angles in the range from 72.42(6)° to 76.76(6)°. The average Zn–N and Zn–O bond distances are 2.1388 Å and 2.1877 Å respectively which are in the range found for similar kind of octahedral Zn(II) complexes. The electrical charge on the metal centre is stabilized by the two deprotonated Schiff base ligand (**L⁻**).
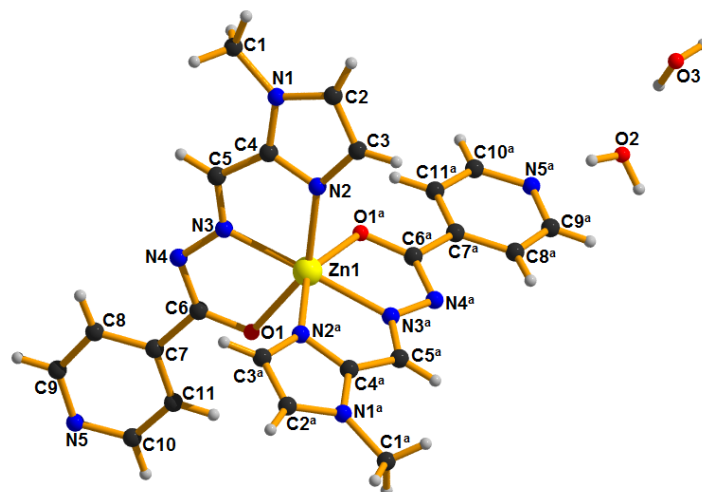
Fig. 6.5. Perspective view of the complex **1**.

Table 6.2. Selected bond distances [Å] and bond angles (°) for complex 1

Bonds	Distance (Å)	Bond angles	Value (°)
Zn1—O1	2.1877(15)	O1—Zn1—N2	149.17(6)
Zn1—N2	2.1806(17)	O1—Zn1—N3	72.42(6)
Zn1—N3	2.0971(17)	O1—Zn1—O1_a	97.64(5)
Zn1—O1_a	2.1877(15)	O1—Zn1—N2_a	89.26(6)
Zn1—N2_a	2.1806(17)	O1—Zn1—N3_a	101.52(6)
Zn1—N3_a	2.0971(17)	N2—Zn1—N3	76.76(6)
		O1_a—Zn1—N2	89.26(6)
		N2—Zn1—N2_a	100.07(6)
		N2—Zn1—N3_a	109.20(6)
		O1_a —Zn1—N3	101.52(6)
		N2_a—Zn1—N3	109.20(6)
		N3—Zn1—N3_a	171.09(6)
		O1_a—Zn1— N2_a	149.17(6)
		N2—Zn1—N3_a	109.20(6)
		O1_a —Zn1—N3	101.52(6)
		O1_a—Zn1—N3_a	72.42(6)
		N2_a—Zn1—N3_a	76.76(6)

a = 1-x, y, 3/2-z

Complex **1** is stabilized through π•••π stacking, O—H•••π and hydrogen bonding (C—H•••O, O—H•••N and O—H•••O) interactions (Tables 6.3–6.5) that are responsible to form various

supramolecular architectures. In complex **1**, the non-coordinated water molecules interact among themselves through two different self-complementary hydrogen bonding interactions (O3─H3A•••O2 and O3─H3B•••O2) to form a tetrameric water cluster having a $R_4^2(8)$ ring motif (Fig. 2). These water clusters connect the monomeric units of complex **1** by O2─H2A•••N5 (169°) hydrogen bonding interactions to produce a 1D zigzag polymeric chain as depicted in Fig. 6.6.
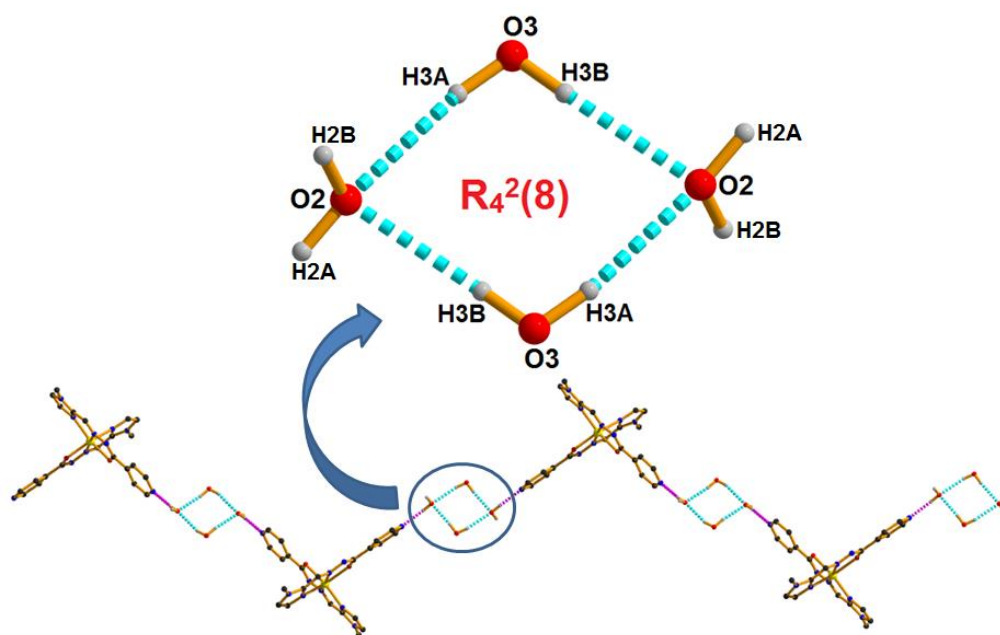
Fig. 6.6. Formation of 1D zigzag polymeric chain and perspective view of water cluster through hydrogen bonding interactions in complex **1**.

Table 6.3. Geometrical parameters for the hydrogen bonds of complex 1

D─H•••A	D─H [Å]	H•••A [Å]	D•••A [Å]	D─H•••A [°]	Symmetry
O2─H2A•••N5	0.8500	1.9900	2.832(2)	169.00	–
O2─H2B•••O1	0.8500	2.0600	2.859(2)	157.00	x,1-y,-1/2+z
O3─H3A•••O2	0.8500	2.1700	2.993(3)	162.00	1/2-x,1/2-y,-z
O3─H3B•••O2	0.8500	2.0800	2.920(3)	171.00	–
C2─H2•••O3	0.9300	2.5800	3.476(3)	163.00	1-x,2-y,1-z
O2─H2A•••N5	0.8500	1.9900	2.832(2)	169.00	–

Bulk water is assumed to be a combination of various small water clusters like dimers, trimers, tetramers, pentamers, hexamers, *etc* [51]. Water clusters are smaller assemblies of a limited number of water molecules and they are very interesting for analysis as they can reveal the nature of host–guest interactions at the molecular level [52]. Among the water clusters, the cyclic water tetramer is particularly interesting as it plays a vital role in

understanding the two-structure model of liquid water and ice [53]. The study of the possible structures of water clusters in different surroundings is important to understand the nature of water–water interactions in the ice or bulk water as well as in many biological and chemical processes [54]. Water tetramers encapsulated within different metal complex hosts have been reported by several researchers [51,52,55–57]. In this work, the water tetramer may be assigned to have a D_{2h} symmetry.

In another structure metallic moieties are connected through π•••π interactions [Cg(5)•••Cg(6)] and form dimeric structures which are further connected through chelate ring•••π interactions [Cg(1)•••Cg(6) and Cg(3)•••Cg(6)] and generates a 2D layered structure in *bc* plane as shown in Fig. 6.7. The interplaner spacing of Cg(5)•••Cg(6), Cg(1)•••Cg(6) and Cg(3)•••Cg(6) are 3.8699(14) Å, 3.8699(14) Å and 3.8699(14) Å respectfully.
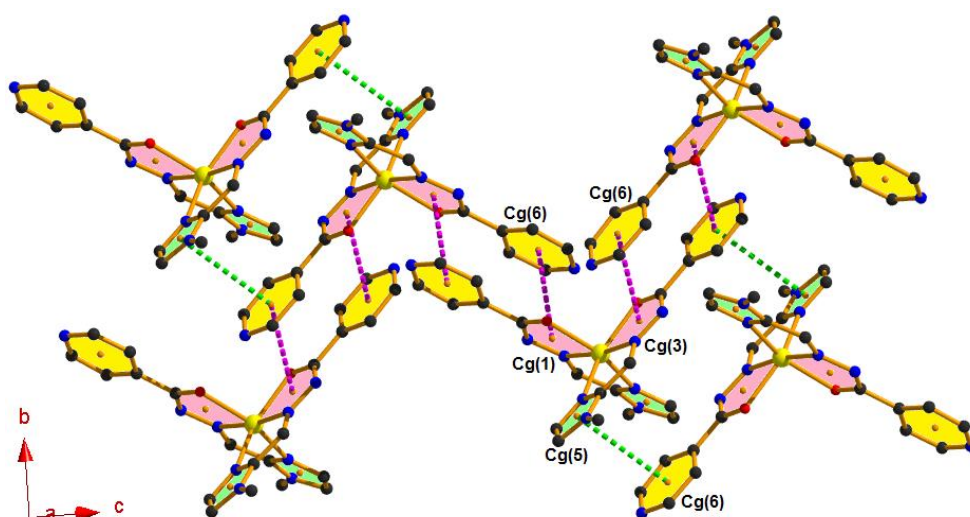
Fig. 6.7. Formation of supramolecular assembly through π•••π interactions in complex **1**

Table 6.4. Geometrical parameters (Å, °) for the π-stacking interactions for complex 1

Cg(i)•••Cg(j)	Cg(i)•••Cg(j) [Å]	α (°)	β (°)	γ (°)	Cg(i)–Perp [Å]	Cg(j)–Perp [Å]	Symmetry
Cg(1)[1]•••Cg(6)	3.8699(14)	5.38	34.13	29.52	3.367	3.203	1-x,1-y,1-z
Cg(3)[1]•••Cg(6)	3.8699(14)	5.38	34.13	29.52	3.367	3.203	x,1-y,1/2+z
Cg(5)[1]•••Cg(6)	3.8786(14)	11.45	25.24	36.36	3.123	3.508	1-x,2-y,1-z
Cg(6)[1]•••Cg(1)	3.8699(14)	5.38	29.52	34.13	3.203	3.368	1-x,1-y,1-z
Cg(6)[1]•••Cg(3)	3.8699(14)	5.38	29.52	34.13	3.203	3.368	x,1-y,-1/2+z
Cg(6)[1]•••Cg(5)	3.8786(14)	11.45	36.36	25.24	3.508	3.123	1-x,2-y,1-z

Cg(i) and Cg(j) denotes centroid of ith and jth ring respectively. For complex **1**: Cg(1) is the centroid of [Zn1/O1/C6/N4/N3] ring; Cg(3) is the centroid of [Zn1/O1_a/C6_a/N4_a/N3_a]

ring; Cg(5) is the centroid of [N1/C2/C3/N2/C4] ring; and Cg(6) is the centroid of [N5/C9/C8/C7/C11/C10] ring.

Interestingly, the water cluster helps in growth of the molecular crystal by filling the void spaces present in complex **1** through O2─H2B•••O1 and O2─H2B•••Cg(2) [O─H••π] hydrogen bonding interactions (Fig. 6.8). Here, the hydrogen atom (H2B) of water molecule interacts simultaneously with carbonyl oxygen (O1) and Cg(2) of the same monomeric unit in a bifurcated manner to produce 1D chain. Such parallel chains are further connected through weak C2─H2•••O3 interactions symbiotically to generate the 2D architecture as shown in Fig. 6.8.
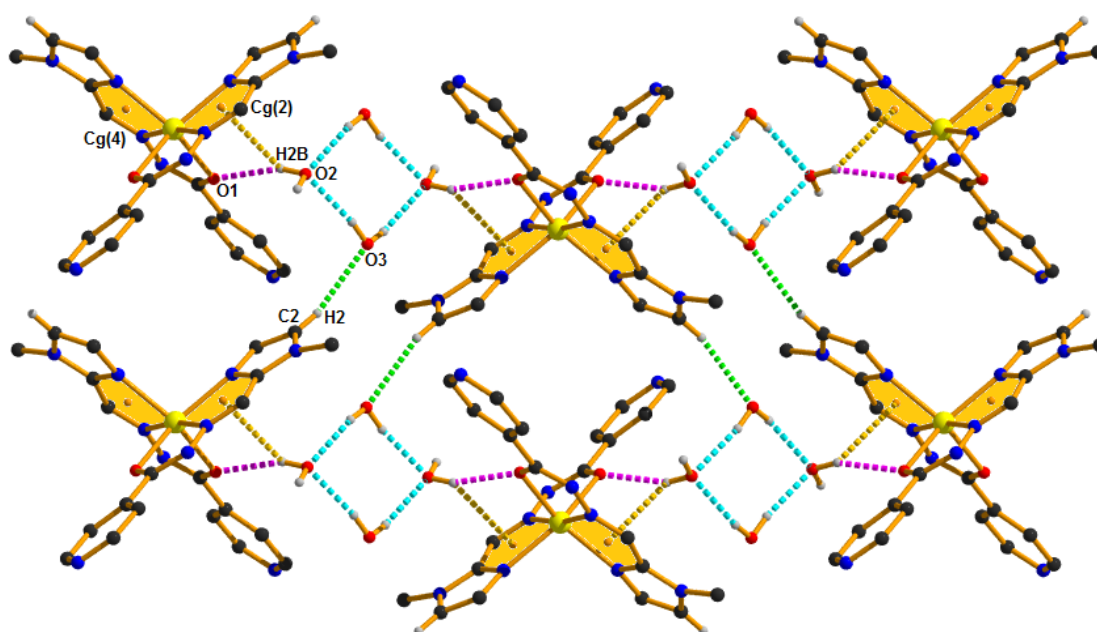
Fig. 6.8. Perspective view of the formation of a 2-D architecture through O─H•••π and hydrogen bonding interactions in complex **1**

Table 6.5. Geometrical parameters (Å,°) for the O─H•••π interaction for the complex 1

X─H(I)•••Cg(J)	H•••Cg [Å]	X•••Cg [Å]	X─H•••Cg (°)	Symmetry
O(2)H(2B)─[2]•••Cg(2)	2.93	3.343(2)	112	1-x,1-y,1-z
O(2)H(2B)─[2]•••Cg(4)	2.93	3.343(2)	112	x,1-y,-1/2+z

For Complex **1**: Cg(2) is the centroid of [Zn1/N2/C4/C5/N3] ring and Cg(4) is the centroid of [Zn1/N2_a/C4_a/C5_a/N3_a] ring.

The spacefill model (Fig. 6.9) reveals how the tetrameric water cluster helps in growth of the molecular crystal by filling the void spaces present in complex **1**.
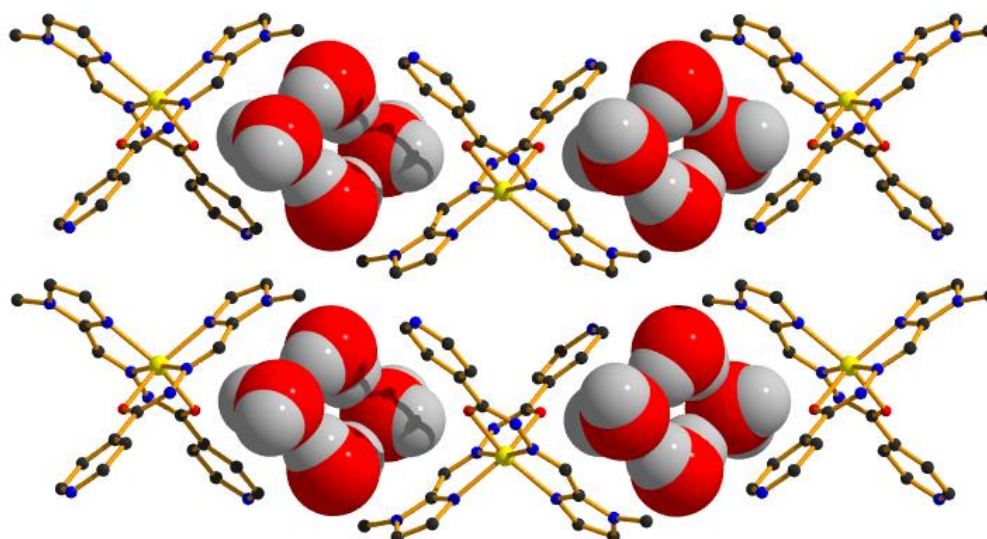
Fig. 6.9. Filling of void spaces through water cluster present in complex **1**

6.3.2. Structural description of complex 2

The perspective view of complex **2** with the atom numbering scheme is shown in Fig. 6.10. The asymmetric unit of the complex **2** shows one [Zn(H$_2$**L**)Cl$_3$] unit and one non-coordinated water molecule. Structural investigation shows that the complex adopts monoclinic crystal system with *P* 2$_1$/c space group and its unit cell comprises of four asymmetric units. The metal centric bond lengths and bond angles are included in Table 6.6. Protonation of the imidazole nitrogen atom (N2) prohibits the chelating ability of the Schiff base ligand (H**L**) and thus behaves as a simple monodentate ligand instead of *ONN* tridentate chelating ligand towards Zn(II) ion. The Zn(II) ion is in a distorted tetrahedral environment completed by one pyridine nitrogen atom (N5) of the protonated Schiff base ligand (H$_2$**L**$^+$) and three chloride anions (Cl1, Cl2 and Cl3).
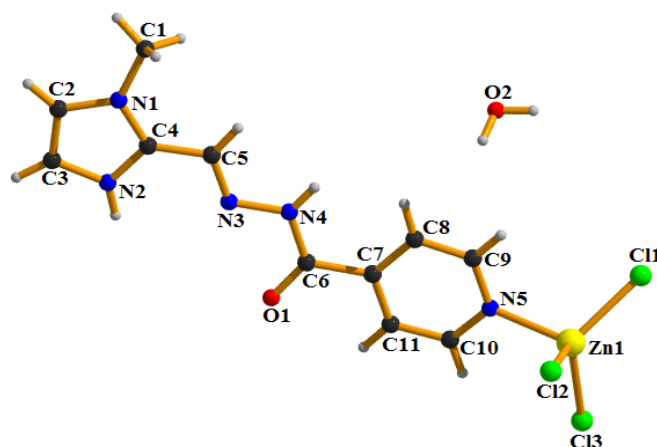
Fig. 6.10. Perspective view of the complex **2**.

The degree of distortion of the Zn(II) ion can be expressed by the parameter of τ_4 ($\tau_4 = 0.88$; $\tau_4 = 0$ for a square planar geometry and $\tau_4 = 1$ for a tetrahedral geometry).[58] The bond angles around the metal center are ranging from 101.88(6)° to 119.21(3)° that signify the deviation from ideal tetrahedral geometry. The overall tripositive charge of the complex is satisfied by the three chloride ions.

Table 6.6. Selected bond distances [Å] and bond angles (°) for complex 2

Bonds	Distance (Å)	Bond angles	Value (°)
Zn1—Cl1	2.2165(13)	Cl1—Zn1—Cl2	110.54(3)
Zn1—Cl2	2.2873(12)	Cl1—Zn1—Cl3	119.21(3)
Zn1—Cl3	2.2583(12)	Cl1—Zn1—N5	110.26(6)
Zn1—N5	2.068(2)	Cl2—Zn1—Cl3	109.01(3)
		Cl2—Zn1—N5	101.88(6)
		Cl3—Zn1—N5	104.41(6)

The solid-state structure of complex **2** is stabilized through π•••π stacking, lone pair•••π and various types of hydrogen bonding (C—H•••Cl, N—H•••O, N—H•••Cl, O—H•••N, O—H•••O and O—H•••Cl) interactions (Tables 6.7–6.9).

The self-complementary nature of complex **2** results a 2D architecture involving π•••π$^+$ and lone pair•••π$^+$ interactions (Fig. 6.11). Here, the oxygen atom (O1) of carbonyl group (attached with one complex unit) interacts with Cg(1) of adjacent protonated imidazole ring (π$^+$) that in turn interacts with Cg(2) of another unit having interplanar spacing of 3.710(2) Å. Hence the combined effect of lone pair•••π$^+$ and π•••π$^+$ interactions mutually strengthens each other.

Table 6.7. Geometrical parameters (Å, °) for the π-stacking interactions for complex 2

Cg(i)•••Cg(j)	Cg(i)•••Cg(j) [Å]	α (°)	β (°)	γ (°)	Cg(i)–perp [Å]	Cg(j)–perp [Å]	Symmetry
Cg(1)[1]•••Cg(2)	3.710(2)	8.41	29.78	21.63	3.448	3.220	2-x,-1/2+y,3/2-z
Cg(2)[1]•••Cg(1)	3.710(2)	8.41	21.63	29.78	3.220	3.448	2-x,1/2+y,3/2-z

Cg(i) and Cg(j) denotes centroid of ith and jth ring respectively. For complex **2**: Cg(1) is the centroid of [N1/C2/C3/N2/C4] ring and Cg(2) is the centroid of [N5/C9/C8/C7/C11/C10] ring.
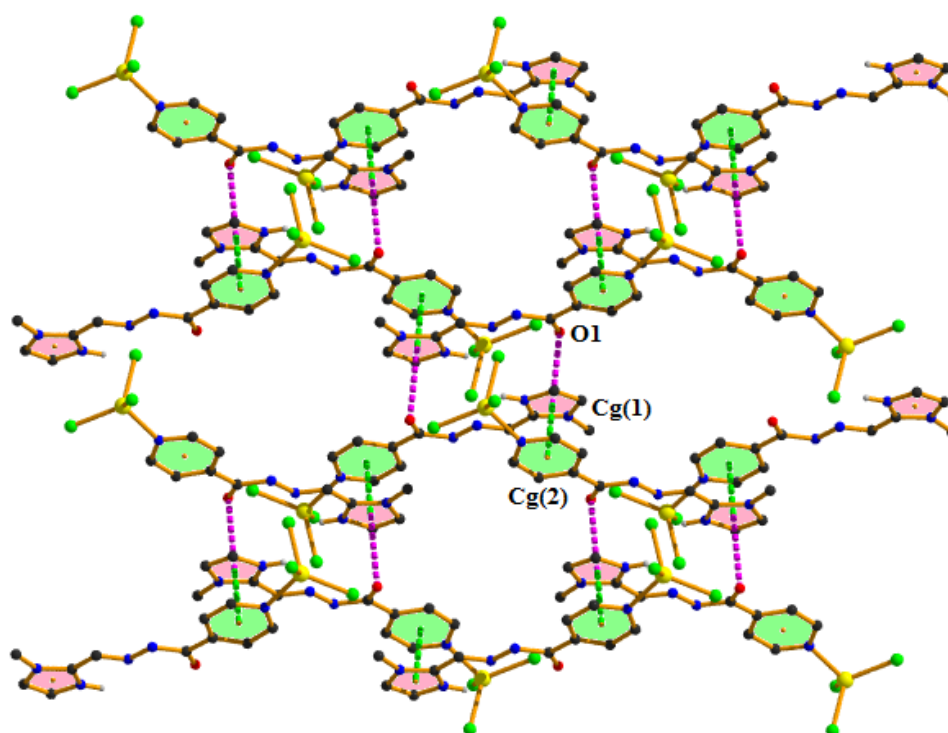
Fig. 6.11. Perspective view of the formation of a 2-D architecture through π•••π⁺ stacking and lone pair•••π⁺ interactions in complex **2**.

Table 6.8. Geometrical parameters (Å, °) for the lone pair•••π interactions for the complex 2

Y–X(I)•••Cg(J)	X•••Cg [Å]	Y•••Cg [Å]	Y–X•••Cg (°)	Symmetry
Zn(1)─Cl(3)[1]•••Cg(2)	3.608(2)	4.622(2)	101.49(3)	1-x,2-y,1-z
C(6)─O(1)[1]•••Cg(1)	3.186(3)	3.320(3)	85.49(15)	2-x,1-y,1-z

For complex **2**: Cg(1) is the centroid of [N1/C2/C3/N2/C4] ring and Cg(2) is the centroid of [N5/C9/C8/C7/C11/C10] ring.

A different 2D supramolecular network is generated incorporating lone pair•••π and hydrogen bonding interactions (Fig. 6.12). Here, the coordinated chlorine atom (Cl2) interacts with the complex unit through two different intermolecular hydrogen bonding (C5─H5•••Cl2 and N4─H4C•••Cl2) interactions that lead to the formation of an $R_2^1(6)$ ring motif. Now, these ring motifs are further connected through the self-complementary lone pair•••π interactions where the lone pair of coordinated chlorine atom (Cl3) faces towards the Cg(2) ring of the adjacent unit at (1-x,2-y,1-z) with an angle of 101.49(3)°. Thus lone pair•••π interactions along with these two types of intermolecular hydrogen bonding interactions enhance the dimensionality from 1D to 2D as shown in Fig. 6.12.
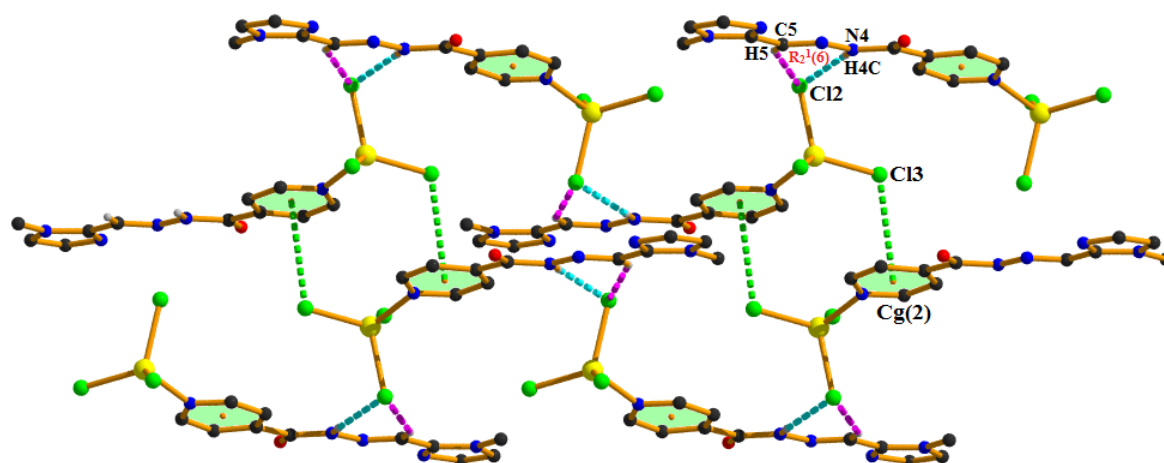
Fig. 6.12. Perspective view of 2-D supramolecular network through lone pair•••π and hydrogen bonding interactions in complex **2**.

Table 6.9. Geometrical parameters for the hydrogen bonds of complex 2

D─H•••A	D─H [Å]	H•••A [Å]	D•••A [Å]	D─H•••A [°]	Symmetry
O2─H2A•••O1	0.8500	2.0500	2.879(3)	167.00	-1+x,y,z
O2─H2A•••N3	0.8500	2.4700	2.982(3)	120.00	-1+x,y,z
O2─H2B•••Cl3	0.8500	2.5000	3.347(3)	175.00	1-x,-1/2+y,3/2-z
N2─H2C•••O2	0.8600	1.9700	2.821(3)	173.00	1+x,y,z
N4─H4C•••Cl2	0.8600	2.5100	3.303(3)	154.00	1-x,-1/2+y,3/2-z
C5─H5•••Cl2	0.9300	2.7200	3.526(3)	145.00	1-x,-1/2+y,3/2-z

In complex **2**, the non-coordinated water molecule interacts with the complex unit by the three different intermolecular hydrogen bonding (N2─H2C•••O2, O2─H2A•••N3, O2─H2A•••O1) interactions that lead to the formation of two different types of synthons, namely, $R_2^2(7)$ [A] and $R_1^2(5)$ [B]. These two synthons (A and B) are further connected by another type of intermolecular hydrogen bonding (O2─H2B•••Cl3) interactions to form a 1D zigzag polymeric chain (Fig. 6.13).

Now, the adjacent chains interact themselves through unconventional O2•••C5 contact (tetrel bond) in a self-complementary manner to produce 2D layered assembly in *bc*-plane (Fig. 6.13). Here, the oxygen atom (O2) of water molecule is also close to the carbon atom (C5) of the C=N bond, *i.e.* 3.132 Å (shorter than the sum of their van der Waals radii 3.22 Å) [59] which indicates a significant O•••π-hole interaction. Protonation of the nitrogen atom (N2) of the imidazole ring enhances the positive potential over the C=N bond favoring π-hole interaction with electron rich oxygen atom (O2), which is strongly supported by MEP surface analysis as well as by the QTAIM/NCI plot in the theoretical part.

Fig. 6.13. Formation of 2-D layered assembly through O•••π-hole and hydrogen bonding interactions in complex **2**.

6.3.3. Theoretical studies

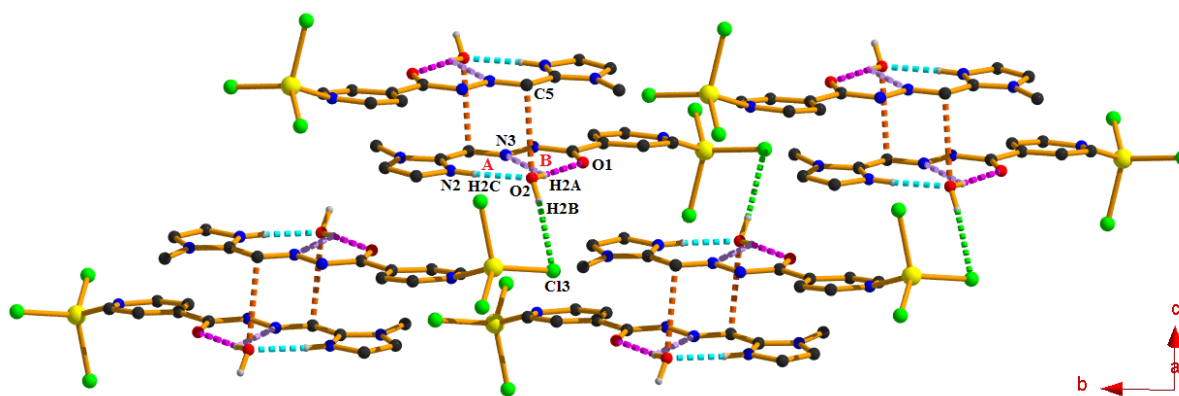The theoretical study is devoted to the analysis the hydrogen bonds involving the co-crystallized water molecules, both in the water cluster and between the water and the ligands. Moreover, the influence of the water molecules on the electronic structure of the ligands and their ability to form π-stacking interactions has also been analysed.

At first the MEP surfaces of the complexes **1** and **2** with and without the hydrogen-bonded water molecules have been computed. The MEP surfaces of **1**·H_2O and **1** are represented in Fig. 6.14, evidencing that the MEP minimum is located at the pyridine N-atom followed by the coordinated O-atom of the hydrazide ligand. The hydrogen-bonded water molecule slightly affects the MEP values over the aromatic rings, making the MEP values more positive. That is, the MEP value over the pyridine ring changes from –19.5 kcal/mol in **1** to –11.9 kcal/mol in **1**·H_2O and that over the imidazole ring increases from 6.9 kcal/mol in **1** (Fig. 14b) to 13.1 kcal/mol in **1**·H_2O. The different electronic nature of both rings supports the formation of the π-stacking assemblies described in Fig. 6.7 where the pyridine ring is stacked over the imidazole ring, which is electrostatically favoured.

The MEP surfaces of **2**·H_2O and **2** are represented in Fig. 6.15, showing that the MEP minimum is located at the chlorido ligands of Zn^{2+}, as expected. The MEP maximum is located at the NH of the hydrazide group in **2**·H_2O and in the imidazole group in **2**. In this complex, the MEP over the imidazole ring is very large and positive due to its protonation. The MEP over this ring is only slightly reduced by the formation of the hydrogen-bond with the water molecule. The effect of the hydrogen-bonded water on the pyridine ring is also small, slightly changing the MEP value from –6.2 kcal/mol in **2** to –3.6 kcal/mol in **2**·H_2O. Finally, it is worth mentioning that the MEP value over the C-atom of the C=N bond is large

and positive (+56.2 kcal/mol in **2**·H$_2$O), thus adequate for interacting with electron rich atoms, as further analysed below.
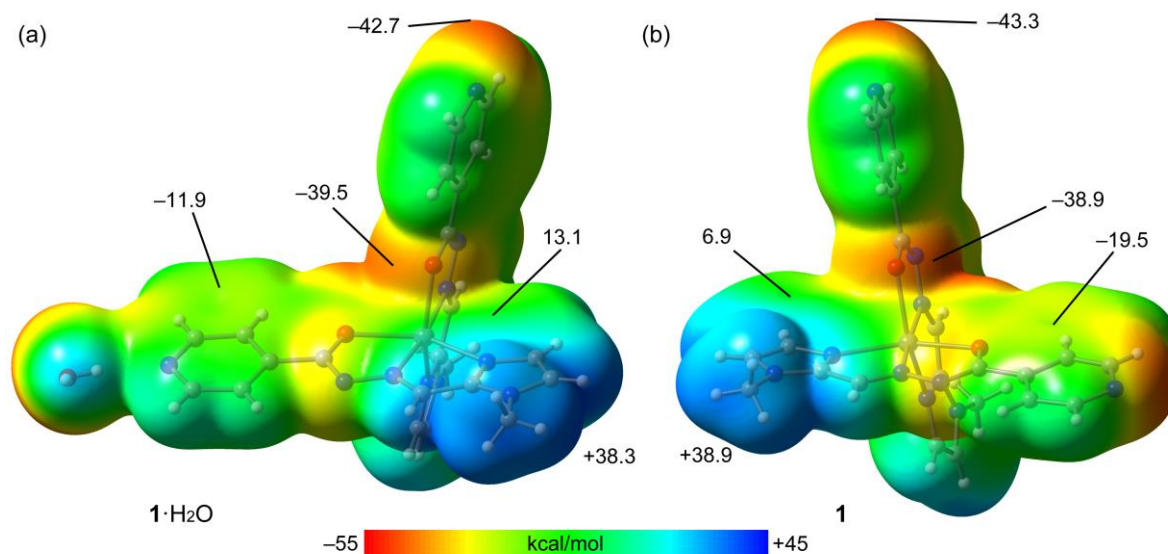
Fig. 6.14. MEP surface of complexes **1**·H$_2$O (a) and **1** (b). Isovalue 0.001 a.u. The energies at selected points of the surfaces are given in kcal/mol. Level of theory: PBE0-D3/def2-TZVP.
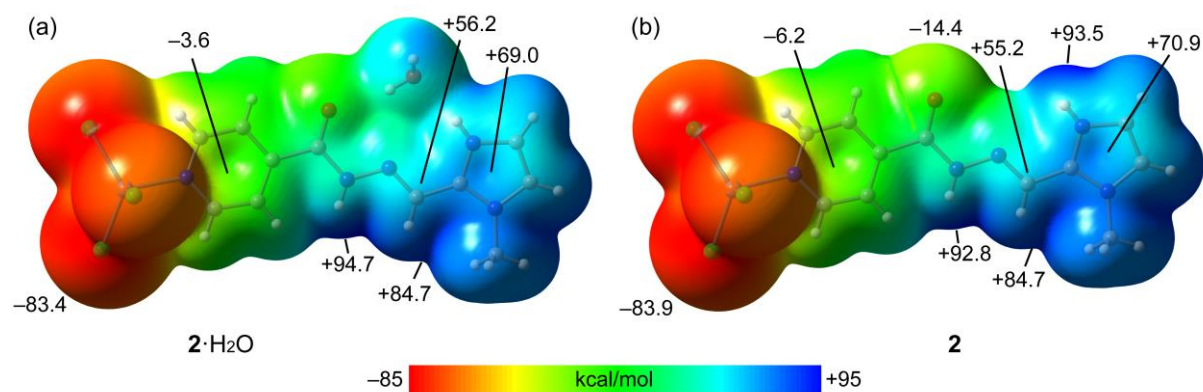
Fig. 6.15. MEP surface of complexes **2**·H$_2$O (a) and **2** (b). Isovalue 0.001 a.u. The energies at selected points of the surfaces are given in kcal/mol. Level of theory: PBE0-D3/def2-TZVP.

The strength of the different hydrogen-bonds involving the water molecules has been studied using the QTAIM method for the water cluster in **1** and also for the **1**·H$_2$O and **2**·H$_2$O dimers. Each hydrogen-bond is characterized by a bond critical point CP, (represented as a small red sphere) and a bond path (dashed bond) connecting the H–atoms to the O/N-atoms (see Fig. 6.16). The energetic results are also indicated in Fig. 11, disclosing the strong nature of the O–H•••N and N–H•••O H-bonds in **1**·H$_2$O and **2**·H$_2$O dimers, respectively (–6.1 kcal/mol in **1** and –6.0 kcal/mol in **2**). The QTAIM analysis confirms the existence of the three hydrogen-bonds in the **2**·H$_2$O dimer connecting the water molecule to the ligand. Due

to the worse directionality and longer distance, the O–H•••N is the weakest one (Fig. 6.16c). The total interaction energy is very large (–12.2 kcal/mol) due to the contribution of the three hydrogen-bonds and fixing the position of the water molecule and explaining the co-crystallization. Regarding the water cluster of **1**, the individual O–H•••O hydrogen-bonds are in general weaker than those observed between water and the ligands, however the binding energy is significant (–12.6 kcal/mol) and similar to those previously reported for this type of clusters [60].
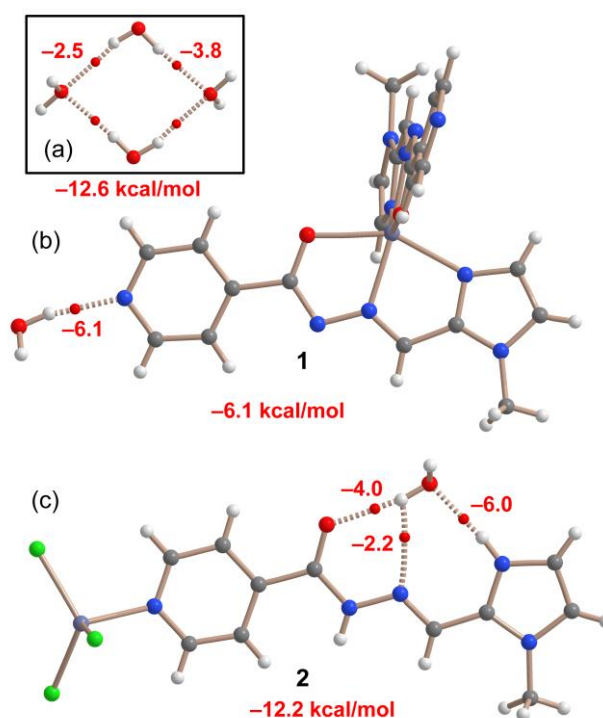
Fig. 6.16. QTAIM analysis (bond CPs in red) of the water cluster (a), **1**·H_2O dimer (b) and **2**·H_2O (c). The individual and total hydrogen-bond energies are indicated next to the bond CPs. Only intermolecular bond CPs and bond paths are represented.

The influence of the water molecule on the π-stacked dimers observed in the solid state of **1** and described in Fig. 6.7 have also been studied. To do so, the binding energies of the dimers with and without the presence of the hydrogen-bonded water molecule, have been computed as indicated in Fig. 6.17. Moreover, the combined QTAIM/NCI plot analysis of the dimer is also included in Fig. 6.17. The NCI plot, via the representation of the reduced density gradient (RDG) isosurfaces, is very convenient to represent non-covalent interactions in real space. The QTAIM/NCI plot analysis confirms the existence of the pyridine•••imidazole π-stacking interactions, characterized by two bond CPs, bond paths and extended green RDG isosurfaces. Moreover, the analysis also shows the participation of the

chelate ring (CR) interactions, since two atoms of the five membered CRs are connected via two bond CPs, bond paths and green RDG isosurfaces. Other ancillary interactions are also observed like C–H•••π and C–H•••N contacts, both characterized by the corresponding bond CPs, bond paths and green isosurfaces. This intricate combination of interactions explains the large interaction energy of this assembly ($\Delta E_1 = -23.6$ kcal/mol) and confirms its relevance in the solid state of complex **1**. The binding energy without the presence of the hydrogen-bonded water molecules is only reduced to $\Delta E_2 = -22.7$ kcal/mol, thus suggesting that the water molecule slightly reinforces the stacking, in line with the small differences observed in the MEP values over the aromatic rings (see Fig. 6.14).

Fig. 6.17. QTAIM analysis of intermolecular bond CPs (red spheres) and bond paths (dashed lines) of **1**·H_2O. Only intermolecular interactions are shown. Settings for the NCI plot are: RDG = 0.5, ρ cut-off = 0.04 a.u., color scale -0.04 a.u. $\leq$ (signλ$_2$)ρ $\leq$ 0.04 a.u.

A similar analysis has been performed for complex **2** (see Fig. 6.18), showing a different behaviour. That is, the binding energy of the π-stacked dimer is strongly influenced by the presence of the water molecule. This is due to the formation of an extra interaction (O•••C) where the O-atom of the water molecule is located over the imidic C-atom, thus forming a O•••π-hole contact. This is strongly supported by the QTAIM/NCI plot analysis, that shows a bond CP, bond path and green isosurface connecting the O and C-atoms. The difference between the dimerization energies (with and without water) is –6 kcal/mol; thus disclosing that such contacts are energetically significant and further contributes to the stabilization of the assembly. Moreover, the extended RDG isosurface located between the imidazole ring and the hydrazido group suggests that the π-system of the –NNHCO– groups participate in the stacking interaction.
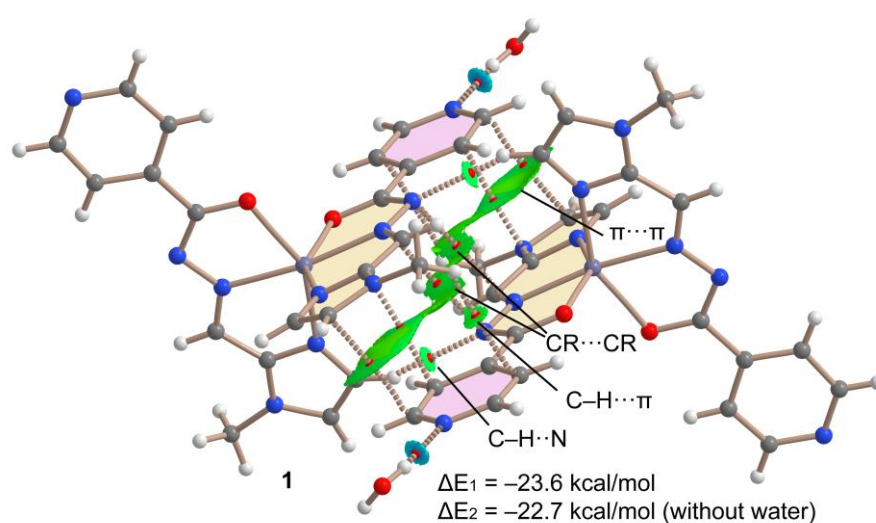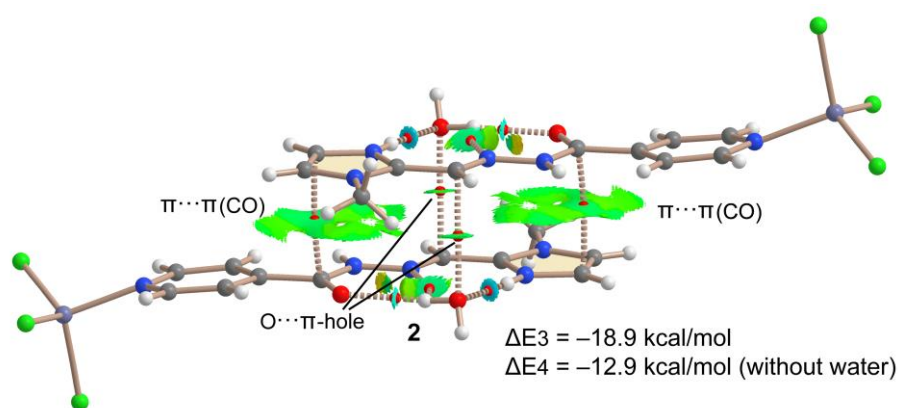
Fig. 6.18. QTAIM analysis of intermolecular bond CPs (red spheres) and bond paths (dashed lines) of **2**·H_2O. Only intermolecular interactions are shown. Settings for the NCI plot are: RDG = 0.5, ρ cut-off = 0.04 a.u., color scale −0.04 a.u. ≤ (signλ_2)ρ ≤ 0.04 a.u.

6.3.4. Antibacterial effects of complex 2

Minimum inhibitory concentration affirms the antibacterial activity of complex **2** and positive control $ZnCl_2$ on both Gram-positive and Gram-negative bacteria as shown in Fig. 6.19. Lower concentration of complex **2** (1.89 mM) completely inhibits the growth of gram-positive bacteria whereas higher concentration (2.64 mM) of the same was needed to inhibit the growth of gram-negative bacteria.

The MIC of $ZnCl_2$ required to inhibit the growth of *S. aureus* and *E. coli* was found to be 2.93 mM and 3.34 mM respectively, indicating complex **2** has higher antibacterial activity than $ZnCl_2$. However, ligand H**L** did not show any cytotoxic activity. The finding suggest that complex **2** has more antibacterial effect on gram-positive *S. aureus* strain than gram-negative *E. coli* strain due to the different nature of their cell walls. The cell walls of gram-positive bacteria are composed of a thick peptidoglycan layer and teichoic acid which allows various molecules including complex **2** to penetrate unlike gram-negative bacteria which inhibits the penetration of any external molecule due to presence of a unique protective outer membrane and a thin peptidoglycan layer in its cell wall.

The higher percentage in bar graph indicates biocompatibility whereas lower percentage shows enhanced cell mortality. The decrease in the number of active bacterial cells on the treatment with complex **2** can be ascribed on the basis of lipophilicity and cell permeability [61]. The interaction between Zn(II) ion and cell membrane through electrostatic forces destroy the plasma membrane and cause leakage of intracellular material [62].

Moreover, protonation of the hydrazone ligand (H**L**) diminishes its chelation property and makes the complex **2** more polar that prefers stronger interactions with the amino acids /

proteins in bacteria. Another concept is that the metal complex can hampers the process of respiration of cells, which lead to the blockage in the synthesis of proteins causing the death of bacteria [63].
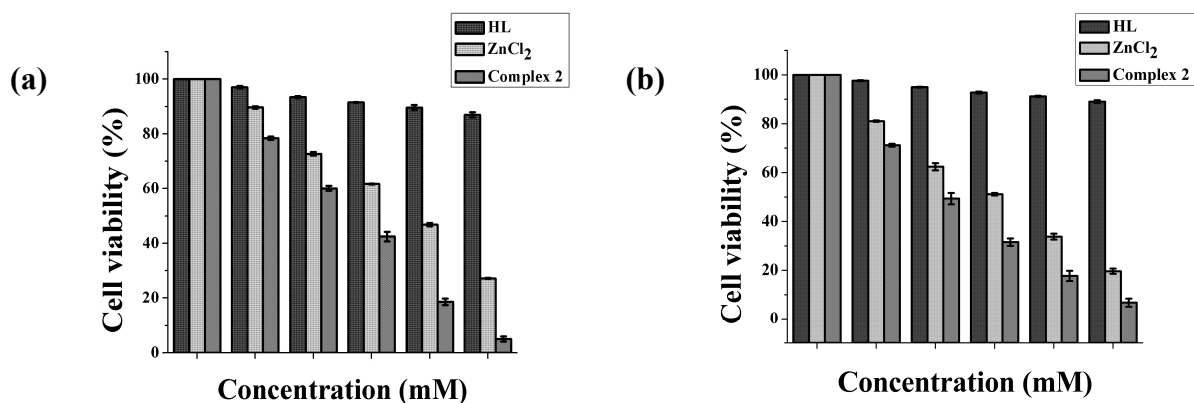
Fig. 6.19. Determination of minimum inhibitory concentration of ligand **HL** and the complex **2** toward (a) *E. coli DH5α* strain and (b) *S. aureus* strain. The results are the mean ± SD of two independent experiments.

6.4. CONCLUSION

In conclusion, two Zn(II) complexes (complexes **1** and **2**) have been synthesized using [(1-methylimidazol-2-yl)methylene]isonicotinohydrazide [**HL**] as the backbone ligand with two different metal salts, crystallographically characterized and explored the non-covalent interactions related with their crystal structures. The DFT study discloses the importance of the water lattice molecules in the solid state of complexes **1** and **2**. The energetic features of the hydrogen-bonds have been studied, either interacting with the hydrogen-bond donor and acceptor groups of the ligands or forming the tetrameric water cluster.

Moreover, their influence on the stacking assemblies of complexes **1** and **2** has been studied both energetically and using MEP surfaces, showing a strong influence in **2** due to the formation of additional π-hole O•••C tetrel bonds. The QTAIM analysis further confirms that the π-system of the –NNHCO– groups participate in the stacking interaction to give the additional stability to the complex **2**. Besides, the complex **2** shows better antibacterial activity against the Gram-positive *S. aureus* (1.89 mM) over the Gram-negative *E. coli DH5α* (2.64 mM) bacteria whereas the ligand (**HL**) exhibits no such activity.

REFERENCES

1. K. T. Mahmudov, M. N. Kopylovich, M. F. C. Guedes da Silva and A. J. L. Pombeiro, *Coord. Chem. Rev.*, 2017, **354**, 54–72.

2. I. A. Rather, S. A. Wagay and R. Ali, *Coord. Chem. Rev.*, 2020, **415**, 213327–213387.

3. M. Mitra, P. Manna, A. Bauzá, P. Ballester, S. K. Seth, S. R. Choudhury, A. Frontera and S. Mukhopadhyay, *J. Phys. Chem. B*, 2014, **118**, 14713–14726.

4. K. T. Mahmudov, A. V. Gurbanov, F. I. Guseinov and M. F. C. Guedes da Silva, *Coord. Chem. Rev.*, 2019, **387**, 32–46.

5. S. Jena, J. Dutta, K. D. Tulsiyan, A. K. Sahu, S. S. Choudhury and H. S. Biswal, *Chem. Soc. Rev.*, 2022, **51**, 4261–4286.

6. S. Pramanik, S. Pathak, S. Jana, M. Mondol, A. Frontera and S. Mukhopadhyay, *New J. Chem.*, 2021, **45**, 12108–12119.

7. N. Mohan, K. P. Vijayalakshmi, N. Koga and C. H. Suresh, *J. Comput. Chem.*, 2010, **31**, 2874–2882.

8. G. R. Desiraju, *J. Am. Chem. Soc.*, 2013, **135**, 9952–9967.

9. P. Politzer, J. S. Murray and T. Clark, *Phys. Chem. Chem. Phys.*, 2013, **15**, 11178–11189.

10. D. Dutta, P. Sharma, A. Frontera, A. Gogoi, A. K. Verma, D. Dutta, B. Sarma and M. K. Bhattacharyya, *New J. Chem.*, 2020, **44**, 20021–20038.

11. P. Politzer, J. S. Murray and T. Clark, *J. Phys. Chem. A*, 2019, **123**, 10123–10130.

12. A. Bauzá, A. V. Sharko, G. A. Senchyk, E. B. Rusanov, A. Frontera and K. V. Domasevitch, *CrystEngComm*, 2017, **19**, 1933–1937.

13. T. Basak, A. Bhattacharyya, M. Das, K. Harms, A. Bauzá, A. Frontera and S. Chattopadhyay, *ChemistrySelect*, 2017, **2**, 6286–6295.

14. A. Bhattacharyya, M. Das, A. Bauzá, S. Herrero, R. González-Prieto, A. Frontera and S. Chattopadhyay, *New J. Chem.*, 2017, **41**, 13585–13592.

15. D. Sadhukhan, M. Maiti, A. Bauzá, A. Frontera, E. Garribba and C. J. Gomez-García, *Inorganica Chim. Acta*, 2019, **484**, 95–103.

16. S. Shaygan, H. Pasdar, N. Foroughifar, M. Davallo and F. Motiee, *Appl. Sci.*, 2018, **8**(3), 385–397.

17. C. Verma and M. A. Quraishi, *Coord. Chem. Rev.*, 2021, **446**, 214105–214127.

18. W. Al Zoubi and Y. G. Ko, *Appl. Organomet. Chem.*, 2017, **31**(3), 3574–3586.

19. K. Ghosh, A. Banerjee, A. Bauzá, A. Frontera and S. Chattopadhyay, *RSC Adv.*, 2018, **8**(49), 28216–28237.

20. D. K. Kölmel and E. T. Kool, *Chem. Rev.*, 2017, **117**, 10358–10376.

21. D. Sadhukhan, A. Ray, G. Pilet, G. M. Rosair, E. Garribba, A. Nonat, L. J. Charbonnière and S. Mitra, *Bull. Chem. Soc. Jpn.*, 2011, **84**(7), 764–777.

22. D. Sadhukhan, M. Maiti, A. Bauzá, A. Frontera, E. Garribba and C. J. Gomez-García, *Inorganica Chim. Acta*, 2019, **484**, 95–103.

23. B. D. Nath, M. M. Islam, M. R. Karim, S. Rahman, M. A. A. Shaikh, P. E. Georghiou and M. Menelaou, *ChemistrySelect*, 2022, **7(14)**, 202104290.

24. Y. Gou, J. Li, B. Fan, B. Xu, M. Zhou and F. Yang, *Eur. J. Med. Chem.*, 2017, **134**, 207–217.

25. M. A. Malik, O. A. Dar, P. Gull, M. Y. Wani and A. A. Hashmi, *MedChemComm*, 2018, **9(3)**, 409–436.

26. M. Streater, P. D. Taylor, R. C. Hider and J. Porter, *J. Med. Chem.*, 1990, **33(6)**, 1749–1755.

27. M. Porchia, M. Pellei, F. Del Bello and C. Santini, *Molecules*, 2020, **25(24)**, 5814.

28. S. Adhikari, T. Bhattacharjee, R. J. Butcher, M. Porchia, M. De Franco, C. Marzano, V. Gandin and F. Tisato, *Inorganica Chim. Acta*, 2019, **498**, 119098.

29. M. V. Kirillova, A. M. Kirillov, M. F. C. G. da Silva, M. N. Kopylovich, J. J. F. da Silva and A. J. Pombeiro, *Inorganica Chim. Acta*, 2008, **361**(6), 1728–1737.

30. X. Luo, R. Abazari, M. Tahir, W. K. Fan, A. Kumar, T. Kalhorizadeh, A. M. Kirillov, A. R. Amani-Ghadim, J. Chen and Y. Zhou, *Coord. Chem. Rev.*, 2022, **461**, 214505.

31. J. B. Araškov, A. Višnjevac, J. Popović, V. Blagojević, H. S. Fernandes, S. F. Sousa, I. Novaković, J. M. Padrón, B. B. Holló, M. Monge and M. Rodríguez-Castillo, *CrystEngComm*, 2022, **24**(29), 5194–5214.

32. R. Abazari, E. Yazdani, M. Nadafan, A. M. Kirillov, J. Gao, A. M. Slawin and C. L. Carpenter-Warren, *Inorg. Chem.*, 2021, **60**(13), 9700–9708.

33. J. Z. Gu, Y. Cai, X. X. Liang, J. Wu, Z. F. Shi and A. M. Kirillov, *CrystEngComm*, 2018, **20**(7), 906–916.

34. G. Psomas, *Coord. Chem. Rev.*, 2020, **412**, 213259.

35. Y. Deswal, S. Asija, A. Dubey, L. Deswal, D. Kumar, D. K. Jindal and J. Devi, *J. Mol. Struct.*, 2022, **1253**, 132266.

36. K. Chkirate, K. Karrouchi, N. Dege, N. K. Sebbar, A. Ejjoummany, S. Radi, N. N. Adarsh, A. Talbaoui, M. Ferbinteanu, E. M. Essassi and Y. Garcia, *New J. Chem.*, 2020, **44**, 2210–2221.

37. A. Gaber, M. S. Refat, A. A. Belal, I. M. El-Deen, N. Hassan, R. Zakaria, M. Alhomrani, A. S. Alamri, W. F. Alsanie and E. M. Saied, *Molecules*, 2021, **26**(8), 2288.

38. A. Tarushi, X. Totta, A. Papadopoulos, J. Kljun, I. Turel, D. P. Kessissoglou and G. Psomas, *Eur. J. Med. Chem.*, 2014, **74**, 187–198.

39. M. Pellei, F. Del Bello, M. Porchia and C. Santini, *Coord. Chem. Rev.*, 2021, **445**, 214088.

40. B. Kaya, Z. K. Yılmaz, O. Şahin, B. Aslim and B. Ülküseven, *New J. Chem.*, 2020, **44**(22), 9313–9320.

41. *Bruker, SMART v5.631*, Bruker AXS Inc., Madison, WI, USA, 2001.

42. G. M. Sheldrick, *SHELXT-2014*, University of Göttingen, 2014.

43. M. J. Frisch, G. W. Trucks, H. B. Schlegel, G. E. Scuseria, M. A. Robb, J. R. Cheeseman, G. Scalmani, V. Barone, G. A. Petersson, H. Nakatsuji, X. Li, M. Caricato, A. V. Marenich, J. Bloino, B. G. Janesko, R. Gomperts, B. Mennucci, H. P. Hratchian, J. V. Ortiz, A. F. Izmaylov, J. L. Sonnenberg, D. Williams-Young, F. Ding, F. Lipparini, F. Egidi, J. Goings, B. Peng, A. Petrone, T. Henderson, D. Ranasinghe, V. G. Zakrzewski, J. Gao, N. Rega, G. Zheng, W. Liang, M. Hada, M. Ehara, K. Toyota, R. Fukuda, J. Hasegawa, M. Ishida, T. Nakajima, Y. Honda, O. Kitao, H. Nakai, T. Vreven, K. Throssell, J. A. Montgomery, Jr., J. E. Peralta, F. Ogliaro, M. J. Bearpark, J. J. Heyd, E. N. Brothers, K. N. Kudin, V. N. Staroverov, T. A. Keith, R. Kobayashi, J. Normand, K. Raghavachari, A. P. Rendell, J. C. Burant, S. S. Iyengar, J. Tomasi, M. Cossi, J. M. Millam, M. Klene, C. Adamo, R. Cammi, J. W. Ochterski, R. L. Martin, K. Morokuma, O. Farkas, J. B. Foresman, and D. J. Fox, Gaussian 16, Revision C.01, Gaussian, Inc., Wallingford CT, 2016.

44. S. Grimme, J. Antony, S. Ehrlich and H. Krieg, *J. Chem. Phys.*, 2010, **132**, 154104.

45. F. Weigend, *Phys. Chem. Chem. Phys.*, 2006, **8**, 1057−1065.

46. S. F. Boys and F. Bernardi, *Mol. Phys.*, 1970, **19**, 553–566.

47. R. F. W. Bader, *J. Phys. Chem. A*, 1998, **102**, 7314–7323

48. T. A. Keith, AIMAll (Version 13.05.06), TK Gristmill Software, Overland Park, KS, 2013.

49. J. Contreras-García, E. R. Johnson, S. Keinan, R. Chaudret, J.-P. Piquemal, D. N. Beratan and W. Yang, *J. Chem. Theory Comput.*, 2011, **7**, 625–632.

50. E. R. Johnson, S. Keinan, P. Mori-Sánchez, J. Contreras-García, A. J. Cohen and W. Yang, *J. Am. Chem. Soc.*, 2010, **132**, 6498-6506.

51. E. A. Cobar, P.R. Horn, R. G. Bergman and M. Head-Gordon, *Phys. Chem. Chem. Phys.*, 2012, **14**(44), 15328–15339.

52. S. Thakur, A. Frontera and S. Chattopadhyay, *Inorganica Chim. Acta*, 2021, **515**, 120057.

53. B. Dutta, S. R. Ghosh, A. Ray, S. Jana, C. Sinha, S. Das, A. D. Jana and M. H. Mir, *New J. Chem.*, 2020, **44**(37), 15857–15870.

54. B. Bagchi, *Water in Biological and Chemical Processes: From Structure and Dynamics to Function*, Cambridge University Press, Cambridge, 2013.

55. O. Fabelo, J. Pasán, L. Cañadillas-Delgado, F. S. Delgado, A. Labrador, F. Lloret, M. Julve and C. Ruiz-Pérez, *CrystEngComm*, 2008, **10**(12), 1743–1746.

56. D. Sun, M. Z. Xu, S. S. Liu, S. Yuan, H. F. Lu, S. Y. Feng and D. F. Sun, *Dalton Trans.*, 2013, **42**(34), 12324–12333.

57. S. Roy, T. Basak, S. Khan, M. G. Drew, A. Bauzá, A. Frontera and S. Chattopadhyay, *ChemistrySelect*, 2017, **2(29)**, 9336–9343.

58. L. Yang, D. R. Powell and R. P. Houser, *Dalton Trans.*, 2007, 955–964.

59. H. Kruse, K. Mrazikova, L. d'Ascenzo, J. Sponer and P. Auffinger, *Angew. Chem. Int. Ed.*, 2020, **132**(38), 16696–16703.

60. S. Li, A. Azizi, S. R. Kirk and S. Jenkins, *Int. J. Quantum Chem.*, 2020, **120**(19), 26361.

61. R. S. Joseyphus and M. S. Nair, *Mycobiology*, 2008, **36**(2), 93–98.

62. S. Mahato, N. Meheta, M. Kotakonda, M. Joshi, M. Shit, A. R. Choudhury and B. Biswas, *Polyhedron*, 2021, **194**, 114933.

63. H. Kargar, A. A. Ardakani, M. N. Tahir, M. Ashfaq and K. S. Munawar, *J. Mol. Struct.*, 2021, **1233**, 130112.

CHAPTER 7

Exploration of supramolecular and photo-physical properties of tetrachlorometallates [MCl₄²⁻: M = Zn(II), Cd(II) and Hg(II)] with triply protonated 2,4,6 tris-(2-pyridyl)-1,3,5 triazine ligand: a combined experimental and theoretical studies
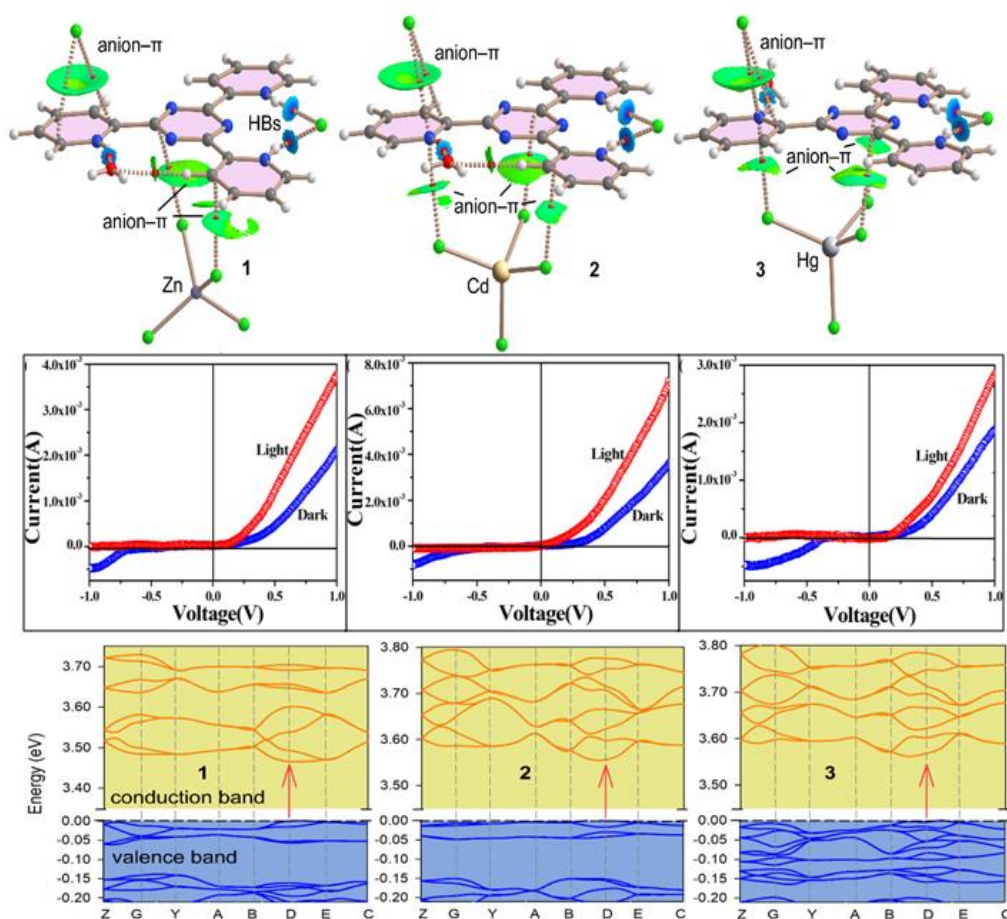
7.1. INTRODUCTION

Recent years have witnessed an immense growth in crystal engineering propelled by numerous non-covalent interactions [1,2]. The basic objective of crystal engineering is to achieve the desired structural topology that requires judicious choice of ligands and metal precursors [3,4]. Based on crystallographic data available in the structural database, new supramolecular synthons have been planned and synthesized accordingly. In general, either cationic or anionic part of the complex (complex cation or complex anion) interacts with oppositely charged counter ions by exploiting several non-covalent interactions like π•••π, cation•••π, anion•••π, hydrogen bonding interactions *etc* [5–7]. Second-sphere coordination has been defined as non-covalent bonding of chemical entities to the first coordination sphere of a transition metal complex. In current research supramolecular interactions directed by organic cations have arrested interest due to their unique structural features related to stacking interactions [8,9] . Recent works of Bowmaker *et al.*, Loeb and his coworkers have proposed that the second-sphere coordination strategies can form selectively and effectively a binding site for anion recognition [10,11]. Some organic-inorganic hybrid complexes constructed by second-sphere coordination strategy are composed of organic cations and anionic metal complexes. 2,4,6-tris(2-pyridyl)-*s*-triazine (tptz) or their analogs are well known neutral binding motifs and can be used in contemporary metallo-supramolecular chemistry [12,13]. Group-12 metal ions in periodic table have d^{10} electronic configuration and does not exhibit any crystal field stabilization and hence their geometrical preference can be guided by steric factors mainly. As both 'π' and 'anion' are electron rich species their interactions have been unacknowledged for a long period. In 2002, Ackorta *et al.*, Deya *et al.* and Mascal *et al*. confirmed the presence of favorable non-covalent interactions between electronic deficient aromatic ring and anions [14–16]. From crystallographic database, it was found that only anion•••π interaction is not able to ensure suitable for structural assembly, but an orchestrated interplay between anion•••π and π•••π or anion•••π and hydrogen-bonding interactions are energetically favorable to construct supramolecular architectures.

Metal–organic hybrids with essentially high conducting properties have grown to be an important research topic owing to its potential applications in electronic devices. Designing of such flexible metal-organic hybrids of organic and inorganic building blocks into a stable structural integrity that plays a significant role in electron transportation which in turn displays a wide spectrum of applications as schottky barrier diode (SBD) in electronics and optoelectronic device [17,18]. SBD is broadly used in photovoltaics [19], batteries

[20,21], sensors [22], super capacitors [23] and transistors [24]. Despite of these advantages, application of most of the metal-organic hybrids is not up to the mark because of incompetent electron transportation (lower conductivity lesser than 10^{-10} S cm^{-1}) between non-redox metal ions and insulated organic ligands [25,26]. Thus, exploring the role of metals in metal-organic hybrids with enhanced conductivity has become a trendy research topic to researchers. However, there are other device parameters like short lifetime, high barrier potential and transit time, low effective mobility and carrier concentration *etc.*, must to be confirmed before fabricating final device. The flexibility of devices depends on assortment of metal ion and binding functionality of the ligands. Therefore before preparing metal-organic hybrids, one has to understand the influence of weak interactions in metal-organic frameworks (MOFs) for easy electron tunneling. Even weak interactions can enhance conductivity by several orders (by electronic delocalization) and linkers with electron-withdrawing or donating groups convey more interactions for making electronically conductive arrangements [27]. By precisely controlling these interactions, the chemist may impart new functions such as high thermal stability, hydrophobicity, charge carrier density and charge mobility to these materials. Li *et al*., and Xia *et al*., successfully fabricated SBD devices with d^{10} metal ions (Zn^{2+}, Cd^{2+}) by using carboxylate linkers [28,29].

Considering the above facts, herein, the syntheses, X-ray structures and supramolecular aspects of Zn (**1**), Cd (**2**) and Hg (**3**) complexes derived from triply protonated 2,4,6 tris-(2-pyridyl)-1,3,5 triazine ligand along with their photophysical properties, have been reported. To ensure the bulk purity of the complexes, single crystal X-ray data have been compared with powder X-ray data.

In this work a strategy have been planned to restrict the ligand 'tptz' not to participate as chelating ligand to form metal complex but should act as an organic cation. In this regard all the peripheral pyridine nitrogen (to restrict the neutral coordination in first coordination sphere) have been protonated maintaining the proper acidic pH of the reaction medium. All these members of group-12 (Zn, Cd and Hg) are able to form tetrachlorometallates [MCl$_4$]$^{2-}$ (M=Zn, Cd, Hg) in presence of dilute hydrochloride acid (Scheme 7.1). In this work the supramolecular interactions between organic salt (tptzH$_3$)$^{3+}$ and the tetrachlorometallate having the general formula (tptzH$_3$)$^{3+}$.Cl$^-$.[MCl$_4$]$^{2-}$.nH$_2$O are described. The geometry of the central metal in the complexes is distorted tetrahedral. Here the tptz ligand is the prime interest because of its large π-conjugation and utilizing these π-based supramolecular interactions one can execute extended architectures. Hence, in this communication hydrogen-

bonding and anion•••π interactions have been found in all these complexes. The structure-directing role of anion–π/ π^+ and hydrogen-bonding interactions has been analyzed by DFT calculation. Structural analysis supported with Hirshfeld surface and fingerprint plots have also been displayed to gain additional insights into the hydrogen bonding interactions for all those complexes. Under illumination condition, the magnitudes of photo physical properties of the complexes improve remarkably although the improvement differs from complex to complex, which have also been analyzed theoretically. To the best of my knowledge it is the first report covering group 12 metals that encompass both supramolecular and photo-physical studies with proper theoretical justification.
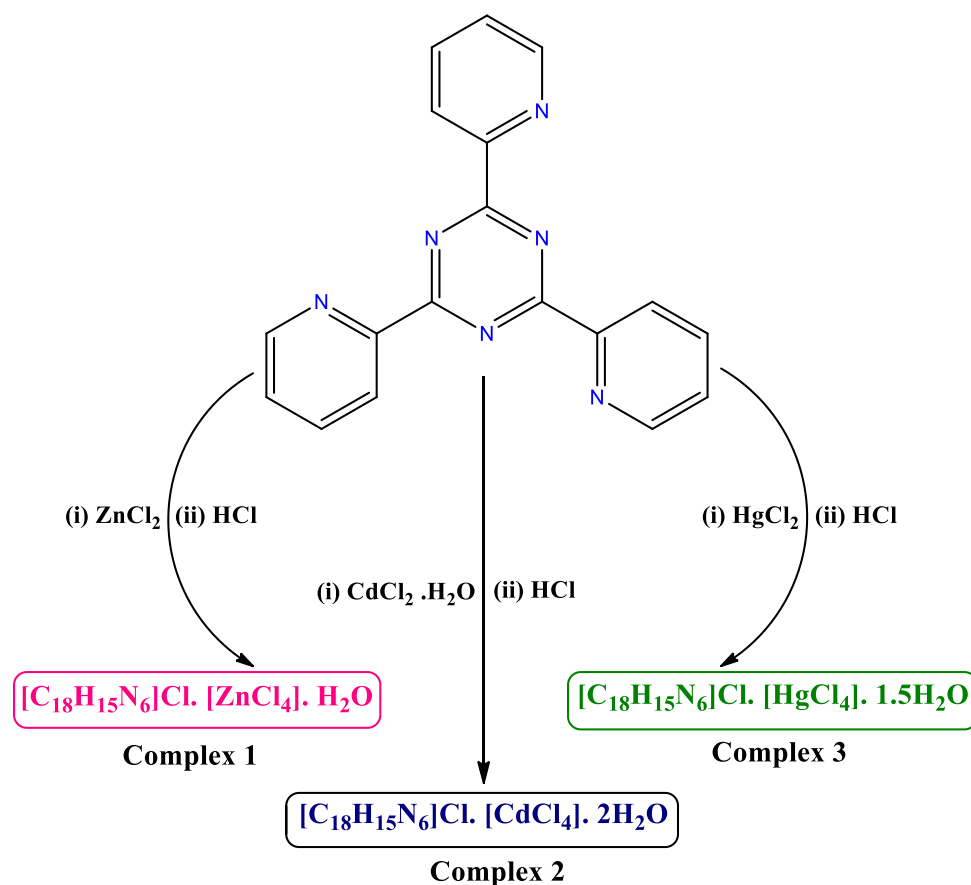
Scheme 7.1. Schematic representation of the synthesis of the title complexes.

7.2. EXPERIMENTAL SECTION

7.2.1. Materials and apparatus

All starting materials were analytical pure grade and 2,4,6-tris(2-pyridyl)-*s*-triazine was purchased from commercial source (Sigma-Aldrich) and used without further purification. All the reactions were carried out under aerobic conditions and in aqueous medium. Freshly boiled, doubly distilled water was used during all the experiment.

Elemental analyses (C, H and N) were performed using a PerkinElmer 2400 Series-II CHN analyzer. Fourier transform-infrared (FT-IR) spectra of complexes **1**, **2** and **3** were recorded using a PerkinElmer LX-1 FTIR spectrophotometer (4000−400 cm⁻¹) by using a modern diamond attenuated total reflectance (ATR) accessory method. UV-vis absorption spectra were obtained using a UV-1900i UV-vis spectrophotometer (SHIMADZU). Single-crystal X-ray data collections of the title complexes were completed using a single crystal X-ray diffractometer (Bruker Smart Apex II). The electrical characterization was carried out using a highly sophisticated I-V analyzer (Keithley 4200) instrument in the voltage range of −1 to +1 V. Powder X-ray diffraction (PXRD) data of the complexes were collected by Bruker D8 advance diffractometer with Cu Kα radiation (λ = 1.5418 Å) generated at 40 kV and 40 mA at a scan rate of 0.2 s per step in the range of 2θ from 10° to 40° under ambient condition.

7.2.2. Synthesis of [tptzH₃]Cl·[ZnCl₄]·H₂O (Complex 1)

An aqueous solution (5 ml) of of $ZnCl_2$ (0.136 g, 1 mmol) was added drop wise to a stirred warm solution (40 °C) of 2,4,6-tris(2-pyridyl)-*s*-triazine (0.312 g, 1 mmol) dissolved in 10 mL of HCl (1 M). After constant stirring of 2 hours, the resulting solution was filtered and the filtrate was left for slow evaporation without any disturbance. Crystals of **1** suitable for X-ray were obtained after two weeks (yield: 73%). Anal. calcd. for $C_{18}H_{15}Cl_5N_6Zn.H_2O$: C, 37.53; H, 2.97; N, 14.59. Found: C, 37.50; H, 2.94; N, 14.56%. Main FT-IR absorptions, (KBr, cm⁻¹): 3458(vs), 3376(vs), 3055(s), 2606(w), 2068(w), 2008(w), 1652(vs), 1615(vs), 1543(vs), 1525(s), 1396(vs),1366(s), 1342(s), 1313(w) (Fig. 7.1).
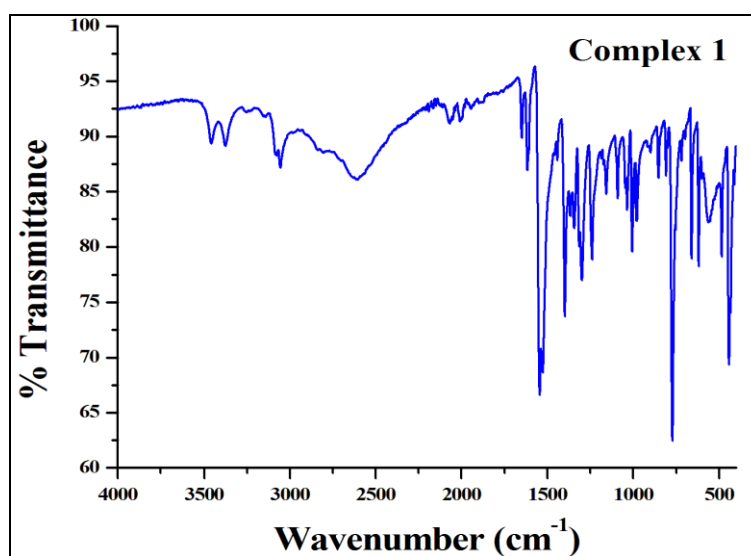
Fig. 7.1. FT-IR spectrum of complex **1**.

7.2.3. Synthesis of [tptzH₃]Cl·[CdCl₄]·2H₂O (Complex 2)

Complex **2** was synthesized using the similar procedure as that of complex **1**. Here aqueous solution of $CdCl_2 \cdot H_2O$ (0.201 g, 1 mmol) was used instead of $ZnCl_2$. After three weeks, block-shaped pale yellow single crystals of **2** were obtained by slow evaporation of the solvent (yield: 72%). Anal. calcd. for $C_{18}H_{15}Cl_5N_6Cd.2H_2O$: C, 33.72; H, 2.99; N, 13.11. Found: C, 33.69; H, 2.94; N, 13.08%. Main FT-IR absorptions, (KBr, cm^{-1}): 3558(s), 3498(vs), 3412(vs), 3081(s), 3055(s), 2517(w), 2069(s), 2000(s), 1940(w), 1643(vs), 1616(vs), 1605(s), 1546(s), 1538(s), 1521(s), 1440(s), 1396(vs), 1366(s), 1344(s), 1300(s) (Fig. 7.2).
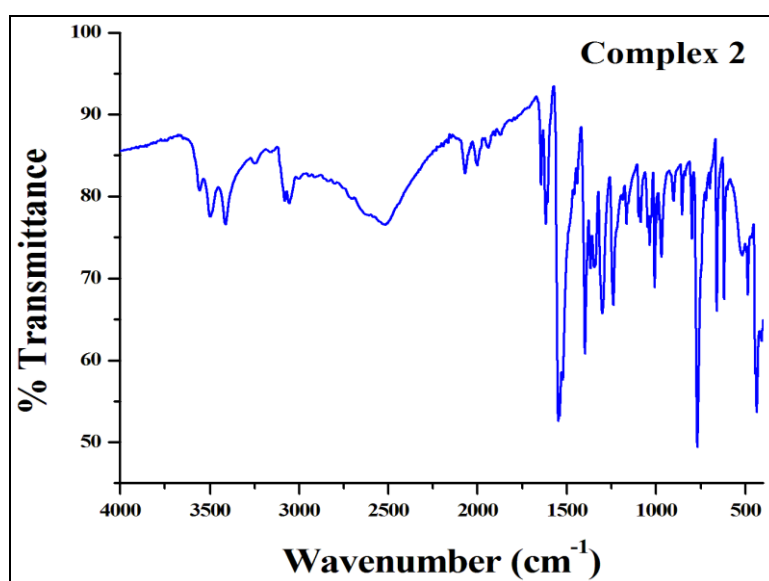
Fig. 7.2. FT-IR spectrum of complex **2**.

7.2.4. Synthesis of [tptzH₃]Cl·[HgCl₄]·1.5H₂O (Complex 3)

Complex **3** was obtained via the same procedure as that for complex **1** using aqueous solution $HgCl_2$ (0.271 g, 1 mmol) instead of $ZnCl_2$. The yellow crystals of **3** suitable for single crystal X-ray diffraction analysis were collected after one month with a yield of 67%. Anal. calc. for $C_{18}H_{15}Cl_5N_6Hg.1.5H_2O$: C, 30.02; H, 2.52; N, 11.67. Found: C, 29.99; H, 2.48; N, 11.65%. Main FT-IR absorptions, (KBr, cm^{-1}): 3562(S), 3506(s), 3380(vs), 3242(s), 3055(s), 2518(w), 2067(s), 2005(s), 1643(s), 1615(vs), 1545(s), 1523(s), 1439(s), 1396(vs), 1366(s), 1344(s) (Fig. 7.3).
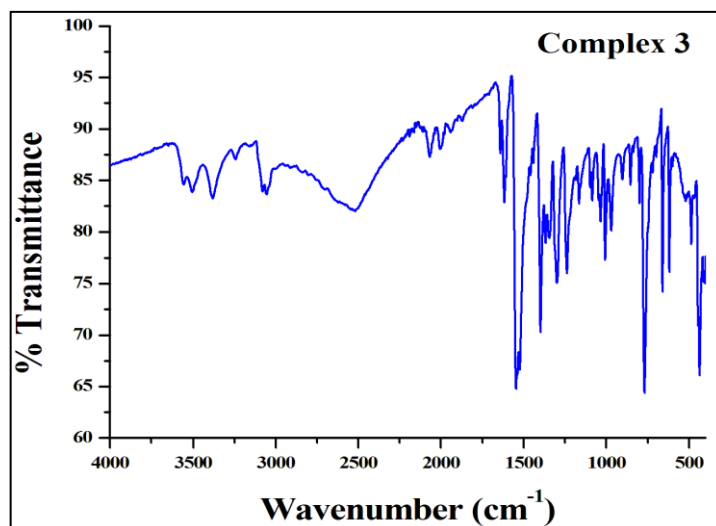
Fig. 7.3. FT-IR spectrum of complex **3**.

7.2.5. X-ray crystallographic analysis

Single crystal X-ray data were collected by using a Bruker SMART APEX II CCD area detector equipped with a graphite monochromated Mo Ka radiation (λ = 0.71073 Å) source in φ and ω scan mode at 295 K for all the complexes. Cell parameter refinement and data reduction for all the complexes were carried out using a Bruker SMART APEX II instrument and Bruker SAINT Software [30]. The crystal structures of the title complexes were solved by intrinsic phasing method using SHELXT-2014/5 and refined by full-matrix least squares on F^2 techniques using the SHELXL-2016/6 crystallographic software package [31,32]. The CIFs have been deposited with CCDC No. 2223679 (complex **1**), CCDC No. 2223680 (complex **2**) and CCDC No. 2223681 (complex **3**). Selected crystal structure refinement parameters for the complexes are given in Table 7.1.

PXRD has been carried out at room temperature with the powdered sample of the complexes (**1**, **2** and **3**). The bulk purity of the complexes has been confirmed by the PXRD pattern analysis. The major peaks of the PXRD pattern of the synthesized complexes match very well with the simulated pattern obtained from the single crystal data, representing phase purity of the bulk as shown in Figs. 7.4, 7.5, and 7.6. The minor shifts and the differences in the intensities might be attributed due to the baseline drift of the PXRD diffractometer and the temperature difference in measuring single crystal diffraction and powder X-ray diffraction [33,34].

Table 7.1. Crystal data and structure refinement parameters for complexes 1, 2 and 3

Complex	1	2	3
Empirical formula	$C_{18}H_{17}Cl_5N_6OZn$	$C_{18}H_{19}Cl_5N_6O_2Cd$	$C_{36}H_{36}Cl_{10}N_{12}O_3Hg_2$
Formula Weight	576.02	641.05	1440.45
Temperature (K)	295	295	295
Wavelength (Å)	0.71073	0.71073	0.71073
Crystal system	Monoclinic	Monoclinic	Monoclinic
space group	P 2_1/n	P 2_1/n	P 2_1/n
a, b, c (Å)	12.2182(10), 14.4158(11), 13.6442(12)	11.2745(8), 14.9594(10), 14.8043(11)	11.2191(10), 14.9507(13), 14.8316(13)
α, β, γ (°)	90, 103.157(3), 90	90, 99.555(2), 90	90, 99.444(3), 90
Volume ($Å^3$)	2340.1(3)	2462.3(3)	2454.0(4)
Z / Density (calc.) (Mg/m^3)	4 / 1.635	4 / 1.729	2 / 1.949
Absorption coefficient (mm^{-1})	1.644	1.457	6.842
F(000)	1160.0	1272.0	1380.0
Crystal size (mm^3)	$0.19 \times 0.13 \times 0.09$	$0.17 \times 0.14 \times 0.08$	$0.19 \times 0.13 \times 0.09$
θ range for data collection	2.021 to 27.188	1.949 to 27.120	1.948 to 27.143
Completeness to θ (%)	100%	100%	100%
Absorption correction	Multi-scan	Multi-scan	Multi-scan
Max. and min. transmission	0.862 and 0.774	0.890 and 0.783	0.540 and 0.358
Refinement method	Full-matrix least-squares on F^2	Full-matrix least-squares on F^2	Full-matrix least-squares on F^2
Data/parameters	5190 / 291	5404 / 295	5400 / 296
Goodness-of-fit on F^2	1.149	1.093	1.107
Final R indices [I > 2σ(I)]	$R_1 = 0.0296$, $wR_2 = 0.0830$	$R_1 = 0.0274$, $wR_2 = 0.0767$	$R_1 = 0.0863$, $wR_2 = 0.2495$
R indices (all data)	$R_1 = 0.0362$, $wR_2 = 0.0943$	$R_1 = 0.0319$, $wR_2 = 0.0796$	$R_1 = 0.1065$, $wR_2 = 0.2763$
Largest diff. peak and hole ($e.Å^{-3}$)	0.613 and -0.501	0.384 and -0.554	4.402 and -4.160

$R_1 = \sum || F_o| - |F_c|| / \sum |F_o|$, $wR_2 = [\sum\{(F_o^2 - F_c^2)^2\}/\sum\{w(F_o^2)^2\}]^{1/2}$ $w = 1/\{\sigma^2(F_o^2) + (aP)^2 + bP\}$; where, $P = (F_o^2 + 2F_c^2)/3$.

For complex **1**: a = 0.0479 and b = 0.9481. For complex **2**: a = 0.0389 and b = 1.4746. For complex **3**: a = 0.2000 and b = 0.9808.
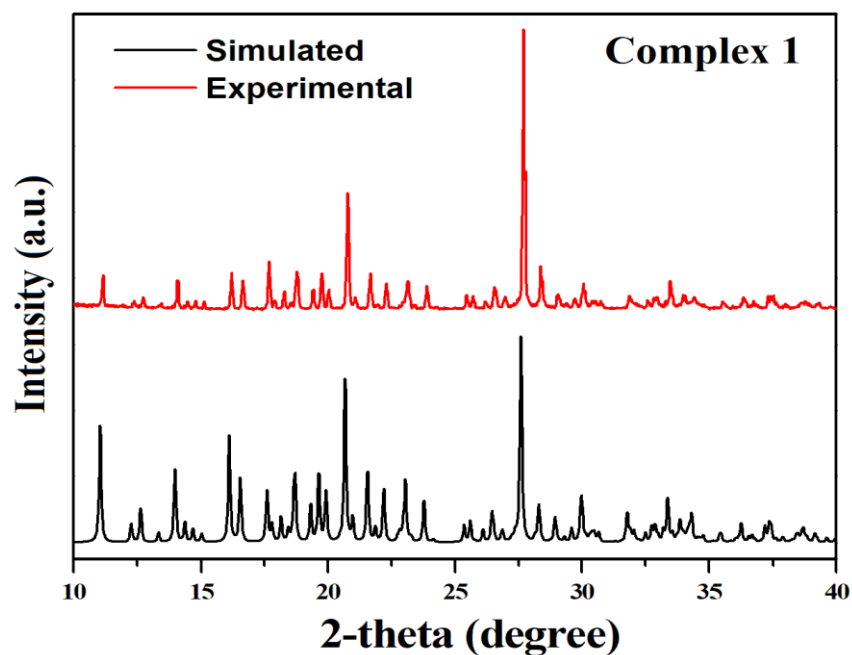
Fig. 7.4. PXRD patterns of experimental powder XRD (red) and simulated pattern from single crystal data (black) for complex **1**.
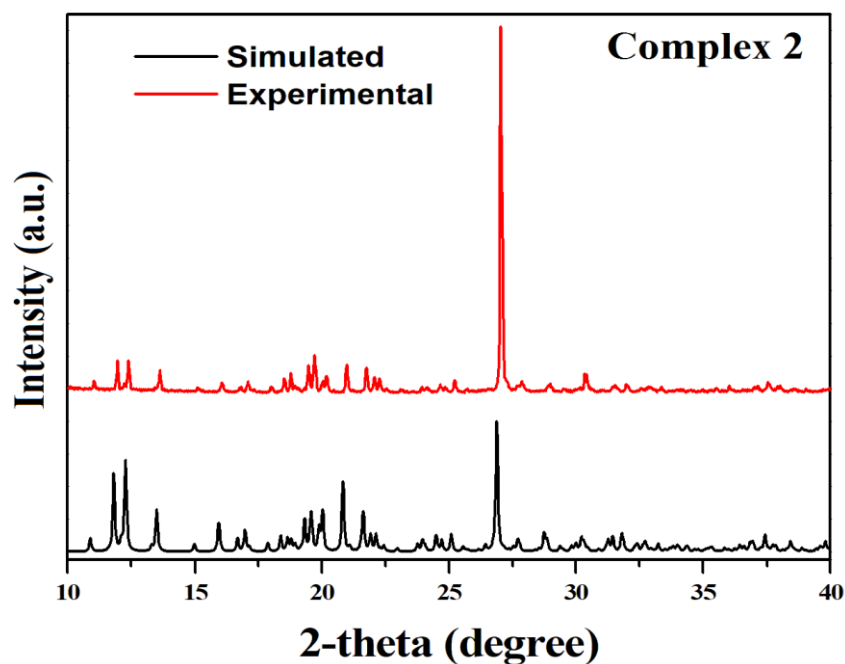
Fig. 7.5. PXRD patterns of experimental powder XRD (red) and simulated pattern from single crystal data (black) for complex **2**.
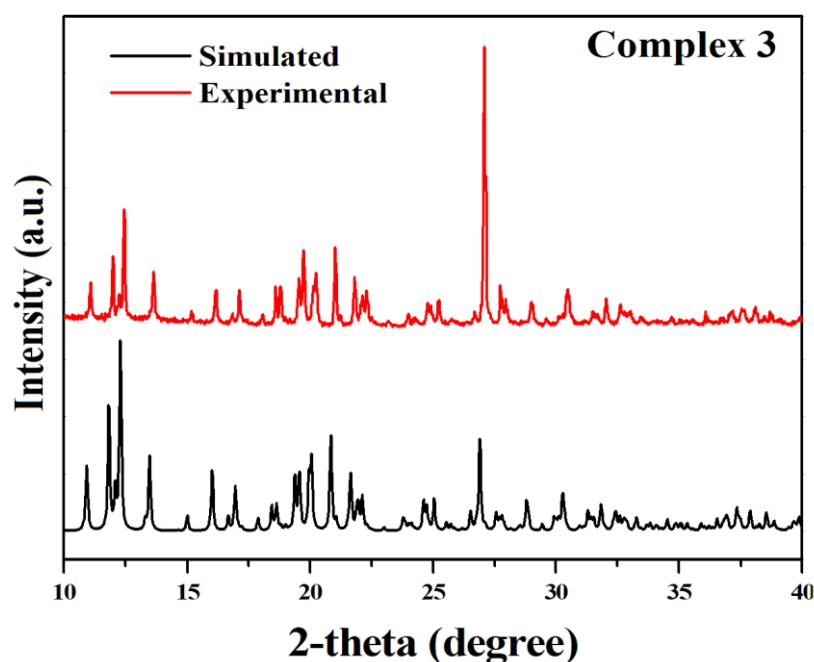
Fig. 7.6. PXRD patterns of experimental powder XRD (red) and simulated pattern from single crystal data (black) for complex **3**.

7.2.6. Hirshfeld surface analysis

Hirshfeld surfaces [35–37] and the related two-dimensional (2D) fingerprint [38–40] plots presented in this paper were generated using Crystal Explorer 21.5 [41], with bond lengths to hydrogen atoms set to standard values. For each point on the Hirshfeld surface, two distances, d_e (the distance from the point to the nearest nucleus external to the surface) and d_i (the distance to the nearest nucleus internal to the surface), are defined. The normalized contact distance (d_{norm}) based on d_e, d_i and the van der Waal radii of the atom is given by the following equation.

$$d_{norm} = \frac{(d_i - r_i^{vdw})}{r_i^{vdw}} + \frac{(d_e - r_e^{vdw})}{r_e^{vdw}}$$

The value of the d_{norm} is negative or positive when intermolecular contacts are shorter or longer than the van der Waals separations, respectively. The parameter d_{norm} displays a surface with a red-white-blue color scheme, where red highlights shorter contacts, white is used for contacts around the van der Waals separation and blue regions are devoid of close contacts. For a given crystal structure and set of spherical atomic electron densities, the Hirshfeld surface is said to be unique [42].

7.2.7. Computational methods

The crystals (**1**, **2**, and **3**) were optimized with the DFT method using the CASTEP program code of Accelrys, Inc [43]. The atomic positions within the crystal were optimized while preserving the experimental unit cell parameters. The optimizations were realized with GGA approximation, PBE functional [44,45], and ultrasoft pseudo-potentials [46] with the relativistic treatment of the Koelling-Harmon [47]. A plane-wave basis set (340 eV cutoff) was used in the Γ points over the Brillouin zone. The energy tolerance for self-consistent field (SCF) convergence was $1 \times 10\text{-}6$ eV/atom for geometric optimization. The Tkatchenko-Scheffler scheme of DFT-D dispersion correction has been included in the calculations [48]. Band Structures and Total and Partial density of states were calculated with HS03 hybrid functional [49]. Band structures follow the k-vector of the first Brillouin zone of the crystals, and the Total and Partial density of states were plotted concerning the Fermi level with a 2X2X2 grid. Norm-conserving pseudo-potentials [43] were used to join a plane-wave basis set (750 eV cutoff) in the G points over the Brillouin zone. The optical properties, including dielectric function and optical conductivity of the crystal, are calculated for plane-polarized light with the polycrystalline approximation. This calculation was realized with GGA approximation, PBE functional [44,45] and norm-conserving pseudo-potentials [49] with the relativistic treatment of the Koelling-Harmon [47]. The final representations were corrected using the scissors operator until the values were obtained with the HSE03 hybrid functional for calculating bands and PDOS. The smearing of 0.2 eV was employed. Molecular orbital calculations used double numerical with polarization (DNP) basis set [50–52] in the all-electron scheme, Γ point set, and PBE functional [44, 45] using the Dmol3 program code of Accelrys, Inc [43].

7.3. RESULTS AND DISCUSSION

7.3.1. Structural description with comparison for complexes 1, 2 and 3

The molecular structures with atom numbering scheme for all the complexes are shown in Figs. 7.7, 7.8 and 7.9). All these complexes are isostructural and bear monoclinic structure with $P\,2_1/n$ space group. All the complexes contain a tetrachlorometallate MCl_4^{2-} (where M = Zn, Cd and Hg), a non-coordinated chloride ion as well as a triply protonated organic moiety (H_3tptz^{3+}) to balance the charge. The product stoichiometry is thus driven by the overall charge balance with H_3tptz^{3+}: MCl_4^{2-}: $Cl^- = 1$: 1: 1. All the three complexes have been hydrated in different extent.
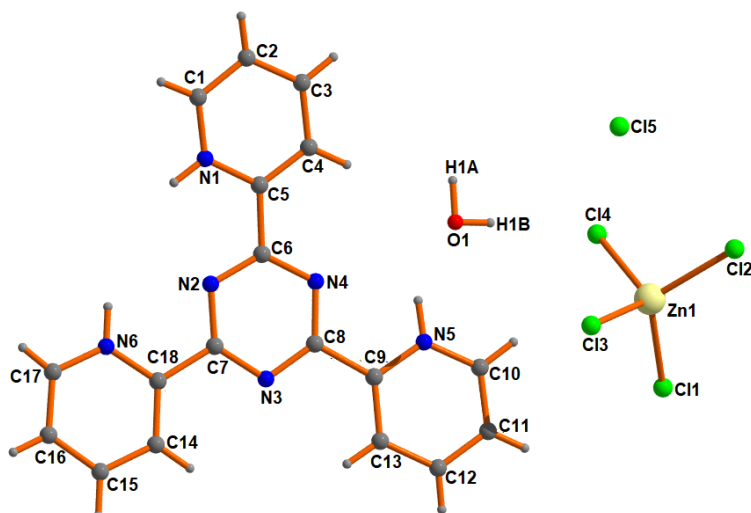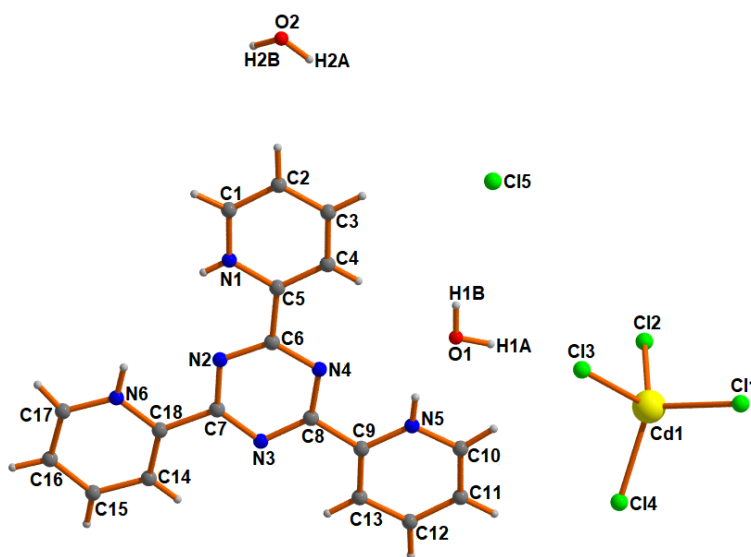
Fig. 7.7. Asymmetric unit of complex **1**.

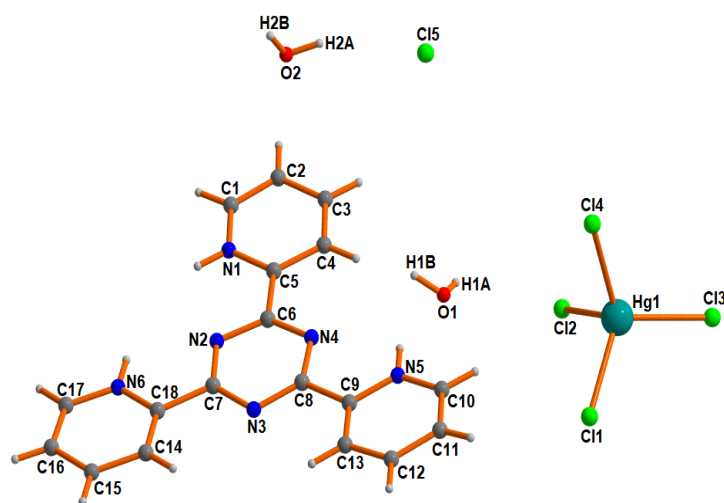**Fig. 7.8.** Asymmetric unit of complex **2**.

Fig. 7.9. Asymmetric unit of complex **3**.

Complex **1** bears one H_2O, complex **2** bears two H_2O and complex **3** bears one and half (1.5) H_2O molecules per asymmetric unit. The important bond lengths and bond angles are gathered in Tables 7.2 and 7.3, respectively for the complexes.

Table 7.2. Selected bond distances [Å] for complexes 1, 2 and 3

Bonds	Distance (Å)	Bonds	Distance (Å)
Complex **1**			
Zn1—Cl4	2.2899(7)	Zn1—Cl2	2.2443(8)
Zn1—Cl1	2.2663(8)	Zn1—Cl3	2.2601(7)
Complex **2**			
Cd1—Cl4	2.4403(8)	Cd1—Cl2	2.4525(8)
Cd1—Cl1	2.4460(8)	Cd1—Cl3	2.4792(8)
Complex **3**			
Hg1—Cl4	2.459(3)	Hg1—Cl2	2.536(3)
Hg1—Cl1	2.450(3)	Hg1—Cl3	2.461(3)

Table 7.3. Selected bond angles [°] for complexes 1, 2 and 3

Bond angles	Value (°)	Bond angles	Value (°)
Complex **1**			
Cl2—Zn1—Cl4	109.07(3)	Cl1—Zn1—Cl2	118.93(3)
Cl3—Zn1—Cl4	111.85(3)	Cl1—Zn1—Cl3	106.61(3)
Cl1—Zn1—Cl4	103.44(3)	Cl2—Zn1—Cl3	106.97(3)
Complex **2**			
Cl2—Cd1—Cl4	114.24(3)	Cl1—Cd1—Cl2	112.17(3)
Cl3—Cd1—Cl4	106.86(3)	Cl1—Cd1—Cl3	104.38(3)
Cl1—Cd1—Cl4	112.44(3)	Cl2—Cd1—Cl3	105.86(3)
Complex **3**			
Cl2—Hg1—Cl4	104.16(11)	Cl1—Hg1—Cl2	105.16(13)
Cl3—Hg1—Cl4	113.76(12)	Cl1—Hg1—Cl3	113.26(13)
Cl1—Hg1—Cl4	115.31(14)	Cl2—Hg1—Cl3	103.55(11)

The asymmetric units of complexes consist of M^{2+} cation (M = Zn, Cd and Hg) coordinated to four chlorido ligands in tetrahedral fashion with ∠ClMCl ranging from 103.44(3)° to 111.85(3)° (for complex **1**), 104.38(3)° to 114.24(3)° (for complex **2**) and 103.55(11)° to 115.31(14)° (for complex **3**). The M—Cl bond distances ranging from 2.2443(8) Å to 2.2899(7) Å (for complex **1**), 2.4403(8) Å to 2.4792(8) Å (for complex **2**) and 2.450(3) Å to 2.536(3) Å (for complex **3**). All M—Cl distances and ∠ClMCl angles are in well agreement with the same as reported earlier [53–55]. The departure from the ideal tetrahedral angle (109º28′) is probably due to stereo-electronic relaxation as a demand of efficient crystal packing by improvising several supramolecular interactions.

Several kinds of hydrogen bonding interactions (both classical and non-classical) namely O–H•••Cl, N–H•••Cl, N–H•••N, N–H•••O, C–H•••Cl and C–H•••O interactions play a very crucial role in stabilizing the structures (Table 7.4).

Table 7.4. Geometrical parameters for the hydrogen bonds of complexes 1, 2 and 3

D−H•••A	D−H [Å]	H•••A [Å]	D•••A [Å]	D−H•••A [°]	Symmetry
Complex **1**					
O1−H1A•••Cl1	0.89(6)	2.27(6)	3.159(2)	176(5)	1/2-x, 1/2+y,1/2-z
O1−H1B•••Cl4	0.78(5)	2.34(5)	3.111(3)	175(4)	-
N1−H1C•••Cl5	0.8600	2.2500	3.062(2)	157.00	1+x,y,z
N1−H1C•••N2	0.8600	2.3200	2.683(2)	106.00	-
N5−H5C•••O1	0.8600	1.9400	2.710(3)	148.00	-
N5−H5C•••N4	0.8600	2.3400	2.702(3)	106.00	-
N6−H6C•••Cl5	0.8600	2.2700	3.066(2)	155.00	1+x,y,z
N6−H6C•••N2	0.8600	2.3000	2.672(3)	106.00	-
C2−H2•••Cl3	0.9300	2.6400	3.554(3)	168.00	1-x,1-y,1-z
C17−H17•••Cl2	0.9300	2.6000	3.439(3)	150.00	3/2+x,3/2-y,1/2+z
C16−H16•••Cl5	0.9300	2.8200	3.637(3)	147.00	3/2-x,1/2+y,3/2-z
C13−H13•••Cl3	0.9300	2.6500	3.500(2)	153.00	1-x,2-y,1-z
Complex **2**					
O1−H1A•••Cl3	0.8500	2.2700	3.110(3)	172.00	-
O1−H1B•••Cl4	0.8500	2.4200	3.225(2)	159.00	1/2-x,1/2+y,1/2-z
N1−H1C•••Cl5	0.8600	2.2300	3.042(2)	157.00	1+x,y,z
N1−H1C•••N2	0.8600	2.3200	2.688(3)	106.00	-
O2−H2A•••Cl1	0.8500	2.2900	3.134(5)	170.00	1/2-x,1/2+y,1/2-z
O2−H2B•••Cl2	0.8500	2.5700	3.299(5)	144.00	1-x,1-y,1-z
N5−H5C•••O1	0.8600	1.9800	2.763(3)	150.00	-
N5−H5C•••N4	0.8600	2.3300	2.692(3)	106.00	-
N6−H6C•••Cl5	0.8600	2.2500	3.054(2)	156.00	1+x,y,z
N6−H6C•••N2	0.8600	2.2900	2.665(3)	107.00	-
C17−H17•••Cl2	0.9300	2.7300	3.619(3)	160.00	3/2+x,1/2-y,1/2+z
C16−H16•••Cl5	0.9300	2.7100	3.533(3)	147.00	3/2-x,-1/2+y,3/2-z
C10−H10•••Cl3	0.9300	2.8200	3.731(3)	166.00	-
Complex **3**					
O1−H1A•••Cl1	0.8500	2.5000	3.220(11)	143.00	3/2-x,-1/2+y,3/2-z
N1−H1C•••Cl5	0.8600	2.2300	3.046(10)	158.00	-1+x,y,z
N1−H1C•••N2	0.8600	2.3400	2.700(12)	105.00	-
O2−H2A•••Cl3	0.8500	2.5200	3.13(2)	129.00	3/2-x, -1/2+y, 3/2-z
N5−H5C•••N4	0.8600	2.3300	2.697(13)	106.00	-
N6−H6C•••Cl5	0.8600	2.2400	3.049(9)	156.00	-1+x,y,z
N6−H6C•••N2	0.8600	2.2700	2.647(13)	107.00	-
N5−H5C•••O1	0.8600	1.9900	2.771(14)	151.00	-
C17−H17•••Cl4	0.9300	2.7400	3.626(13)	160.00	-3/2+x, 3/2-y, -1/2+z
C16−H16•••Cl5	0.9300	2.7100	3.527(14)	147.00	1/2-x, 1/2+y, 1/2-z
C14−H14•••O2	0.9300	2.3100	3.17(3)	153.00	x, 1+y, z
C12−H12•••Cl2	0.9300	2.8300	3.525(13)	133.00	3/2-x, 1/2+y, 3/2-z

In complex **1**, the non-coordinated water molecule acts as a double donor to Cl(1) and Cl(4) of two different $ZnCl_4^{2-}$ ions at an angle of 176(5)º and 175(4)º respectively to produce a 1D zigzag chain along (010) direction (Fig. 7.10).
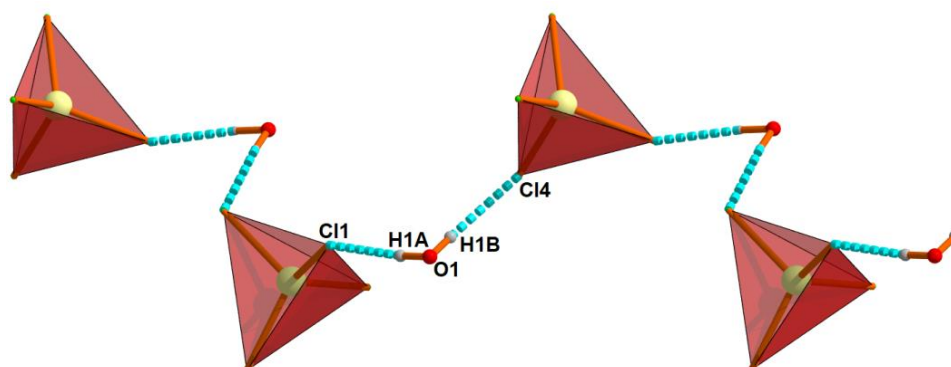
Fig. 7.10. Formation of a 1D water-anion cluster in complex **1**

In complex **2**, two different non-coordinated water molecules are engaged in producing two different 1D water-anion clusters (Figs. 7.11a and 7.11b) that in turn make a 2D extended architecture having $R_8^8(24)$ ring motif in the *bc*-plane (Fig. 7.11c).

Fig. 7.11. (a) Formation of a 1D water-anion cluster along (010) direction. (b) Propagation of another 1D water-anion cluster along (001) direction. (c) Extension of water-anion cluster in *bc*-plane in complex **2**.

The local tetrahedral M^{2+} tetrachloro coordination sphere and non-coordinated chloride ions have participated in hydrogen bonding interactions and help to generate higher dimensionality of the crystal structure in solid state.

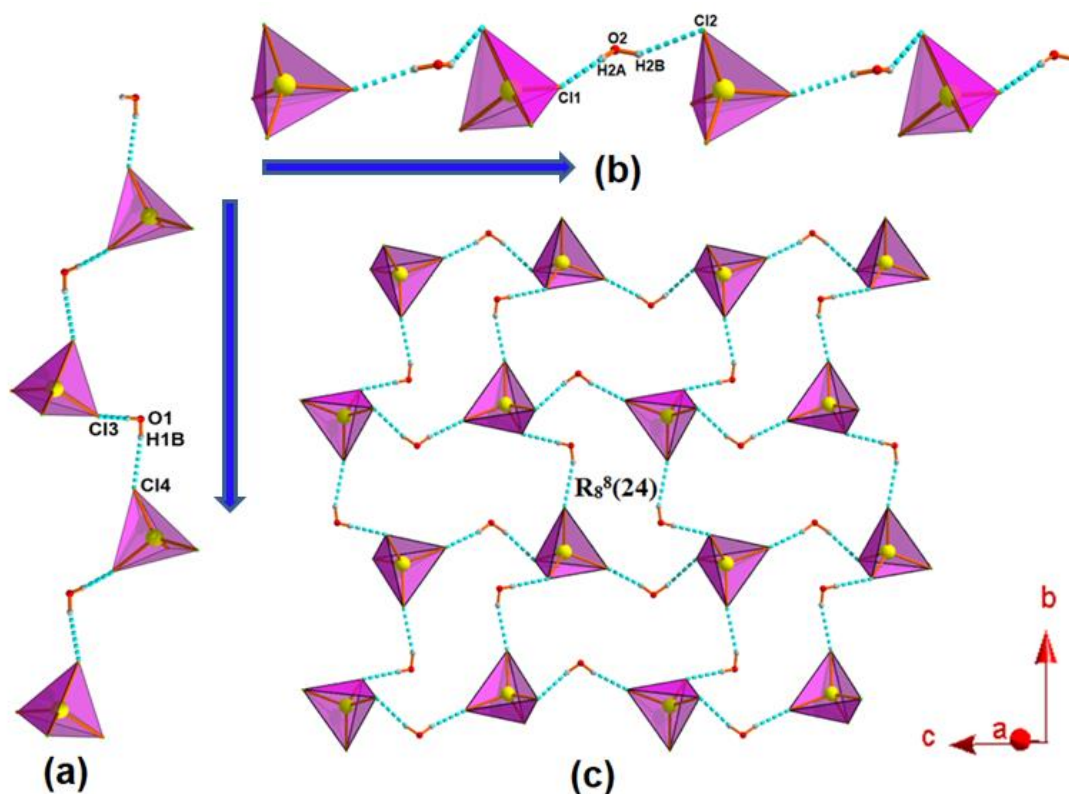In the triply protonated organic moiety (Fig. 7.12), the major coordination site is restricted due to two different intramolecular hydrogen bonding interactions (N1—H1C•••N2 and N6—H6C•••N2). The moderate coordination site is restricted through another intramolecular hydrogen bonding interaction (N5—H5C•••N4) but there are no such interactions in minor coordination site.
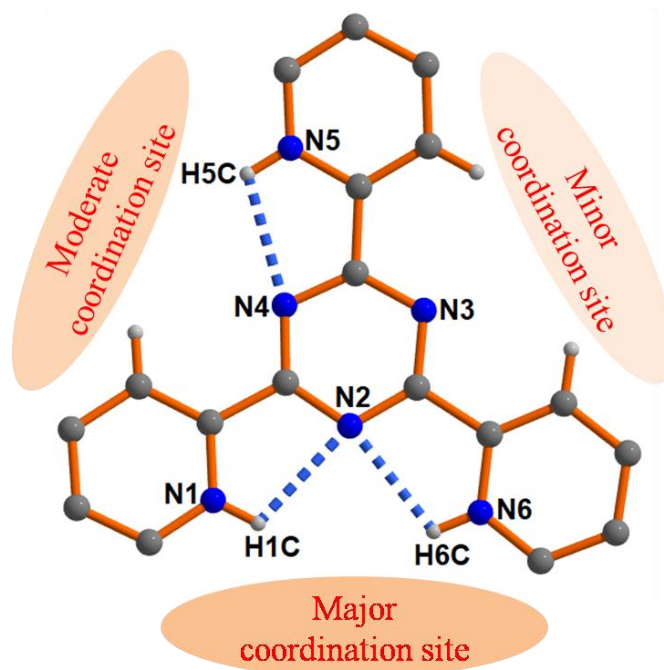
Fig. 7.12. Intramolecular hydrogen bonding interactions restrict the neutral coordination sites of the H_3tptz^{3+} ligand.

However, both protonated pyridine ring protons (N1—H1C and N6—H6C) of the organic moiety further interact with the non-coordinated ionic chloride (Cl5) and generates $R_2^2(4)$ ring motif which is propagated in a zigzag fashion along (010) direction through C16—H16•••Cl5 interaction to produce a 1D chain (Fig. 7.13). This 1D chain is further stabilized by the self-complementary anion•••π^+ interactions of the non-coordinated ionic chloride (Cl5) with Cg(1) and Cg(3) of the protonated moiety as shown in the Fig. 7.13.

The interesting phenomenon is that complexes **2** and **3** also exhibit the exact same architecture (Fig. 7.12) where the non-coordinated chloride ion (Cl5) forms trifurcated hydrogen bonding interactions (N1—H1C•••Cl5, N6—H6C•••Cl5 and C16—H16•••Cl5) and the self-complementary anion•••π^+ interactions to connect the triply protonated moieties.
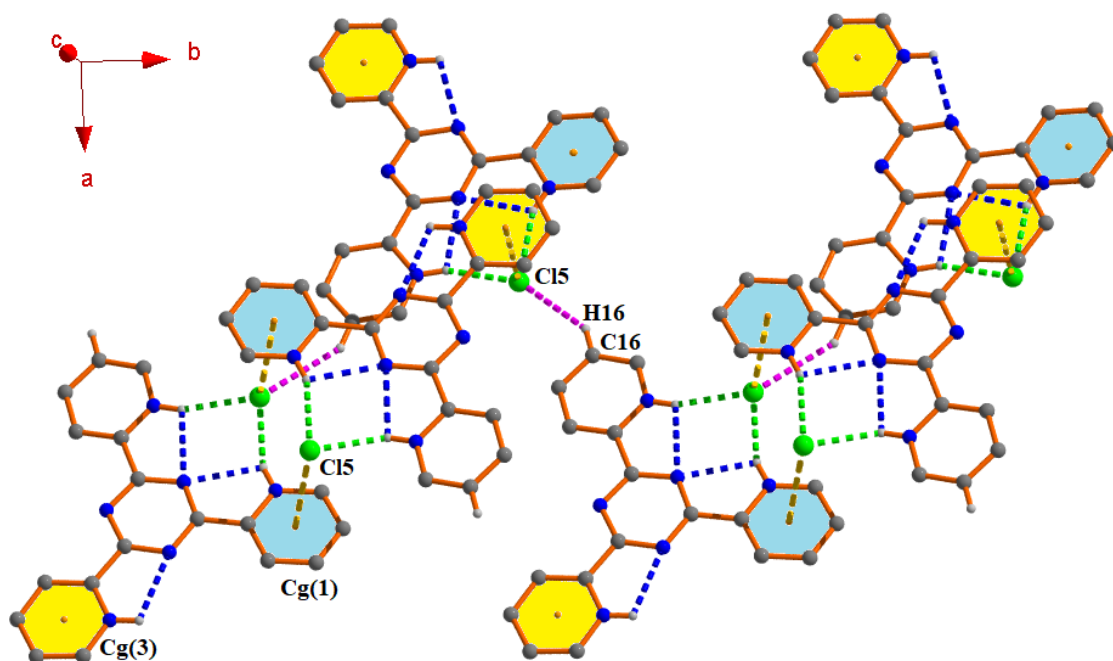
Fig. 7.13. View of 2D layered assembly through anion•••π^+ and hydrogen bonding interactions in complex **1**.

The water-anion clusters play an important role to stabilize various supramolecular architectures for both the complexes (**1** and **2**) in solid state. In complex **1**, triply protonated organic moieties are parallel to each other with intervening water-anion cluster (Fig. 7.10) which connects those organic moieties through strong N5─H5C•••O1 interactions to ensure a 1D tape like architecture (Fig. 7.14).
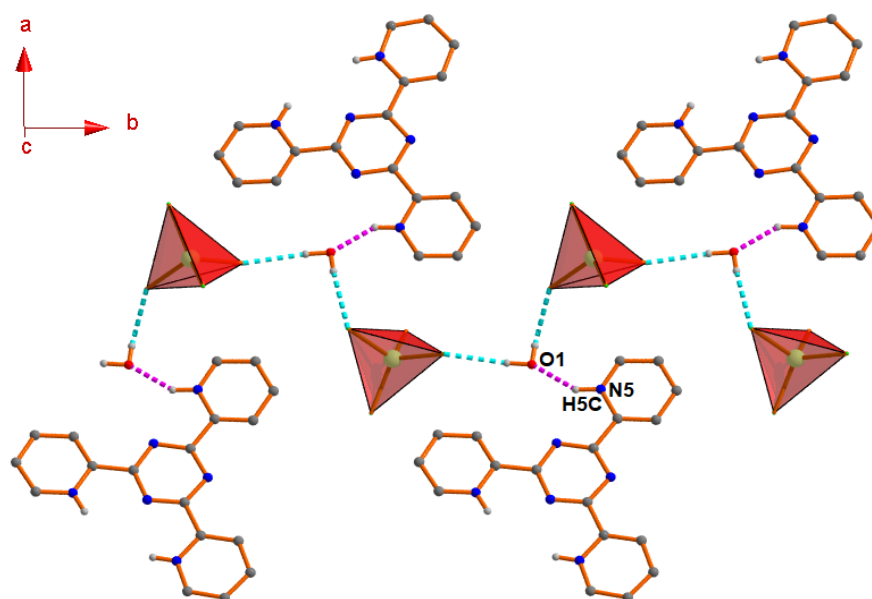
Fig. 7.14. View of 1D tape through hydrogen bonding interactions in complex **1**.

Another interesting phenomenon is that complex **2** also exhibits the architecture (Fig. 7.15) similar to that of complex **1** (Fig. 7.14), where triply protonated organic moieties are stitched with the water-anion cluster (as depicted in Fig. 7.11a).
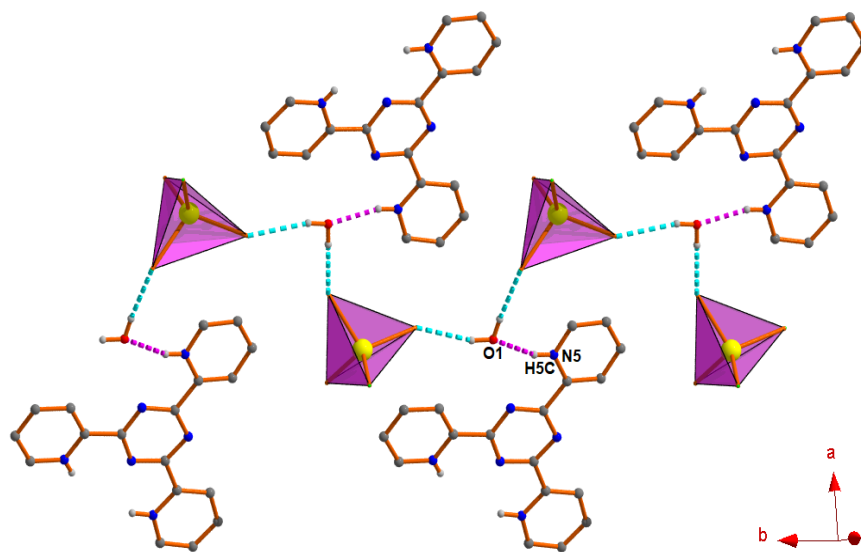
Fig. 7.15. Perspective view of 1D tape through hydrogen bonding interactions in complex **2**.

Besides strong charge-assisted N–H•••O interaction, weak non-classical C–H•••Cl–M hydrogen bonding contacts (between the aromatic ring hydrogen atom and the chloride ligands of the mononuclear complexes) further expand the structures. In complex **1**, the protonated moieties are interlinked through water-anion cluster (Fig. 7.10) and three different C–H•••Cl interactions [C2–H2•••Cl3 (168º), C13–H13•••Cl3 (153º) and C17–H17•••Cl2 (150º)] to produce a 2D layer (Fig. 7.16).
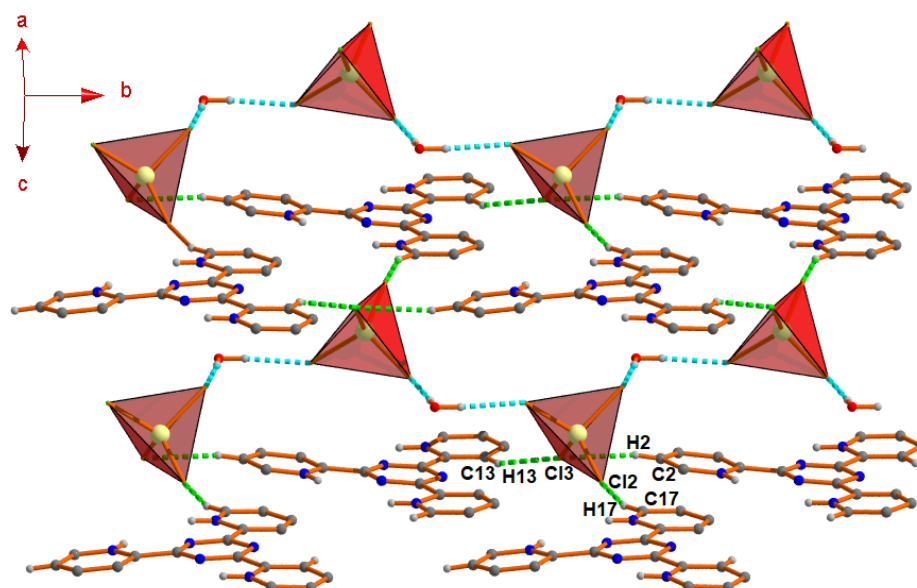
Fig. 7.16. 2D layer through water-anion cluster and C–H•••Cl interactions in complex **1**.

In complex **2**, the protonated organic moieties are arranged such a fashion so that the water-anion cluster (Fig. 7.11b) connects those moieties incorporating two different hydrogen bonding interactions [C10–H10•••Cl3(166º) and C17–H17•••Cl2(160º)] which result a different type of 2D architecture in *ac*-plane (Fig. 7.17).
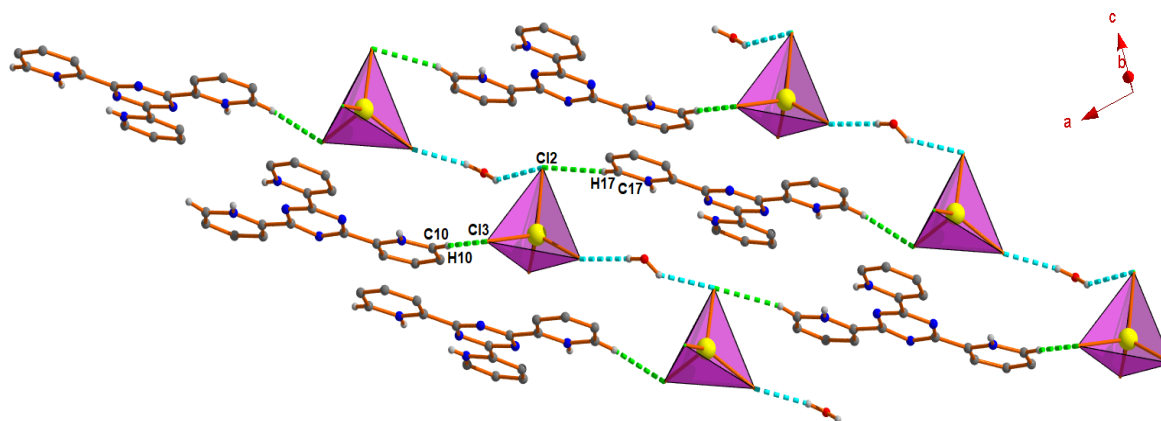
Fig. 7.17. 2D layer incorporating water-anion cluster and C–H•••Cl interactions in **2**.

Beside several hydrogen bonding interactions all four chloride ions attached with group 12 metal ions have engaged in anion•••π and anion•••π^{+} interactions (Table 7.5). Anion•••π interactions are mediated by middle triazine ring whereas protonated peripheral pyridine rings of H$_3$tptz^{3+} are responsible for anion•••π^{+} interactions. From crystallographic database it was evident that anion•••π interactions play significant role in association with either π•••π or hydrogen bonding interactions [6].

When the aromatic π systems adopt positive charges, the positive charges are often found to participate in anion•••π^{+} interaction to strengthen the binding ability than that of conventional anion•••π interaction. But, in this case the anion•••π interaction is stronger compared to anion•••π^{+} interaction. It was evident that generally the central triazine ring participate in anion•••π interaction if the triazine ring is attached with some electron withdrawing groups. Here, in our case the central triazine ring is attached with three protonated pyridine rings that in turn make the central triazine ring sufficiently electron deficient and dictated to take part in strong anion•••π interaction.

In complex **1**, Cl(2) and Cl(4) attached with Zn^{2+} form anion•••π interactions with Cg(2) whereas Zn^{2+} bound Cl(1) and Cl(3) form anion•••π^{+} interactions with Cg(1) and Cg(4) of the H$_3$tptz^{3+} moiety [where Cg(1), Cg(2) and Cg(4) are the centroids of N1C1C2C3C4C5, N2C6N4C8N3C7 and N6C17C16C15C14C18 rings respectively] to form a 1D chain (Fig. 7.18).

Table 7.5. Geometrical parameters (Å, °) for the anion•••π/ anion•••π+ interactions for the title complexes

Y─X(I)•••Cg(J)	X•••Cg [Å]	Y•••Cg [Å]	Y─X•••Cg (°)	Symmetry
Complex **1**				
Zn(1)─Cl(1)[2]•••Cg(1)	3.5819(14)	5.3909(12)	133.11(4)	-1/2+x,3/2-y,-1/2+z
Zn(1)─Cl(2)[2]•••Cg(2)	3.5100(12)	5.3535(10)	135.85(4)	-1+x,y,z
Zn(1)─Cl(3)[2]•••Cg(4)	3.4549(12)	5.0589(11)	123.18(3)	-1+x,y,z
Zn(1)─Cl(4)[2]•••Cg(2)	3.3514(11)	5.1296(9)	129.87(3)	-1/2+x,3/2-y,-1/2+z
Complex **2**				
Cd(1)─Cl(1)[2]•••Cg(3)	3.7195(13)	5.4517(12)	122.98(3)	-1/2+x,1/2-y,-1/2+z
Cd(1)─Cl(2)[2]•••Cg(2)	3.2756(12)	5.6682(10)	163.24(3)	-1+x,y,z
Cd(1)─Cl(3)[2]•••Cg(2)	3.3773(12)	4.4899(10)	98.95(3)	-1/2+x,1/2-y,-1/2+z
Cd(1)─Cl(4)[2]•••Cg(1)	3.6774(15)	5.5519(13)	129.21(3)	-1/2+x,1/2-y,-1/2+z
Complex **3**				
Hg(1)─Cl(1)[2]•••Cg(3)	3.655(7)	5.564(5)	130.40(16)	1/2+x,3/2-y,1/2+z
Hg(1)─Cl(2)[2]•••Cg(2)	3.367(5)	4.505(4)	98.56(11)	1/2+x,3/2-y,1/2+z
Hg(1)─Cl(3)[2]•••Cg(4)	3.710(6)	5.479(5)	123.86(17)	1/2+x,3/2-y,1/2+z
Hg(1)─Cl(4)[2]•••Cg(2)	3.269(5)	5.655(4)	161.48(18)	1+x,y,z

Cg(j) denotes centroid of jth ring of the title complexes. For complex **1**: Cg(1) is the centroid of [N1/C1/C2/C3/C4/C5] ring; Cg(2) is the centroid of [N2/C6/N4/C8/N3/C7] ring; and Cg(4) is the centroid of [N6/C17/C16/C15/C14/C18] ring. For complex **2**: Cg(1) is the centroid of [N1/C1/C2/C3/C4/C5] ring; Cg(2) is the centroid of [N2/C6/N4/C8/N3/C7] ring; and Cg(3) is the centroid of [N5/C9/C13/C12/C11/C10] ring. For complex **3**: Cg(2) is the centroid of [N2/C6/N4/C8/N3/C7] ring; Cg(3) is the centroid of [N5/C9/C13/C12/C11/C10] ring; and Cg(4) is the centroid of [N6/C17/C16/C15/C14/C18] ring.
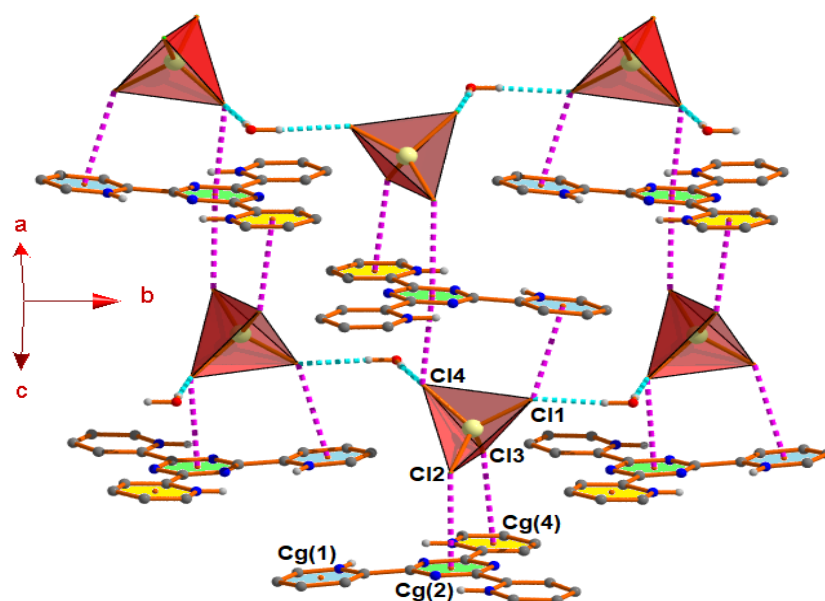
Fig. 7.18. Perspective view of 2D architecture through water-anion cluster, anion•••π and anion•••π+ interactions in complex **1**.

Finally, the non-coordinated water molecule connects $ZnCl_4^{2-}$ ions as a form of water-anion cluster (Fig. 7.10) to extend the dimensionality to 2D. The Zn–Cl•••Cg bipodal anion•••π/π^+ interactions distances ranges from 3.3514(11) Å to 3.5819(14) Å and the corresponding angles are 129.87(3)° and 133.11(4)° respectively.

In complex **2**, Cd(1)–Cl(2) and Cd(1)–Cl(3) form anion•••π interactions with Cg(2) whereas Cl(1) and Cl(4) attached with Cd^{2+} interact with Cg(1) and Cg(3) respectively as anion•••π^+ fashion [where Cg(3) is the centroid of N5C9C13C12C11C10 ring] to ensure a 1D chain (Fig. 7.19). Now the water-anion cluster (Fig. 7.11b) along with these anion•••π and anion•••π^+ interactions enhance the dimensionality from 1D to 2D as depicted in Fig. 7.19.
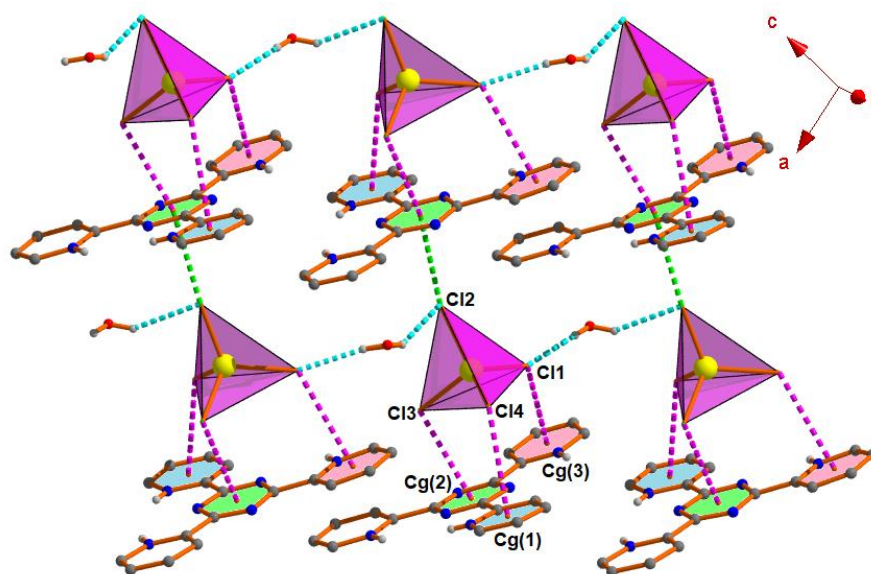
Fig. 7.19. Perspective view of 2D architecture incorporating water-anion cluster, anion•••π and anion•••π^+ interactions in complex **2**.

Here the tripodal anion•••π/π^+ interactions distances ranges from 3.2756(12) Å to 3.7195(13) Å and the corresponding angles are 163.24(3)° and 122.98(3)° respectively.

In complex **3**, the $HgCl_4^{2-}$ ion interacts in similar tripodal anion•••π/π^+ fashion with the protonated organic moieties (as that of complex **2**) to produce a 1D chain. Now the parallel chains are interconnected through C17–H17•••Cl4 (160°) hydrogen bonds to expand the dimensionality to 2D (Fig. 7.20).

Here, Hg(1)–Cl(2) and Hg(1)–Cl(4) form anion•••π interactions with Cg(2) whereas Cl(1) and Cl(3) attached with Hg^{2+} form anion•••π^+ interactions with Cg(3) and Cg(4) respectively. The tripodal anion•••π/π^+ interactions distances in this complex ranges from 3.269(5) Å to 3.710(6) Å and the corresponding angles are 161.48(18)° and 123.86(17)° respectively.
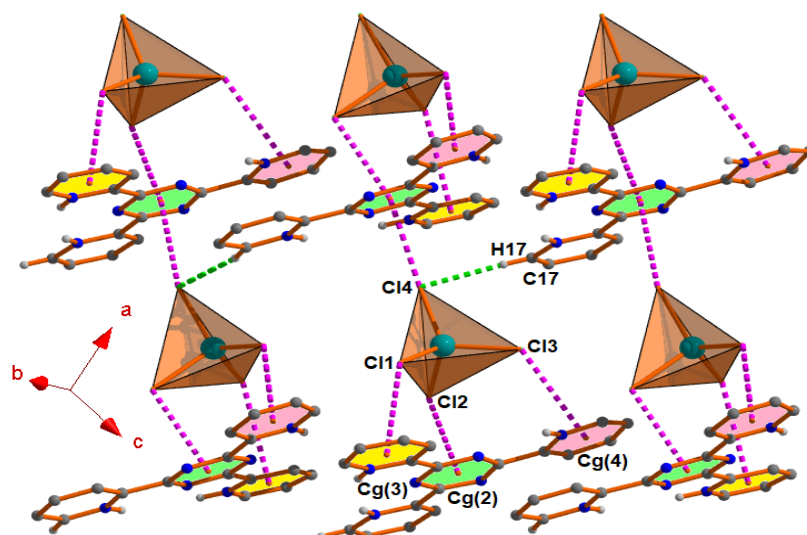
Fig. 7.20. Perspective view of 2D architecture through anion•••π/ anion•••π⁺/ C–H•••Cl interactions in complex **3**.

Besides such tripodal anion•••π/π⁺ interactions, a new supramolecular interaction (O–H•••π⁺ interaction) has been identified in complex **3** (Table 7.6). Fig. 7.21 depicts a different type of 2D architecture which is generated including several hydrogen bonds (C–H•••O, N–H•••O, C–H•••Cl, O–H•••Cl) along with the above mentioned O–H•••π⁺ interactions in complex **3**. Here, one $HgCl_4^{2-}$ ion, one non-coordinated water molecule and one triply protonated moiety are interconnected through C14–H14•••O2, O2–H2A•••Cl3 and C12–H12•••Cl2 interactions that are responsible to form $R_3^3(15)$ ring motif .
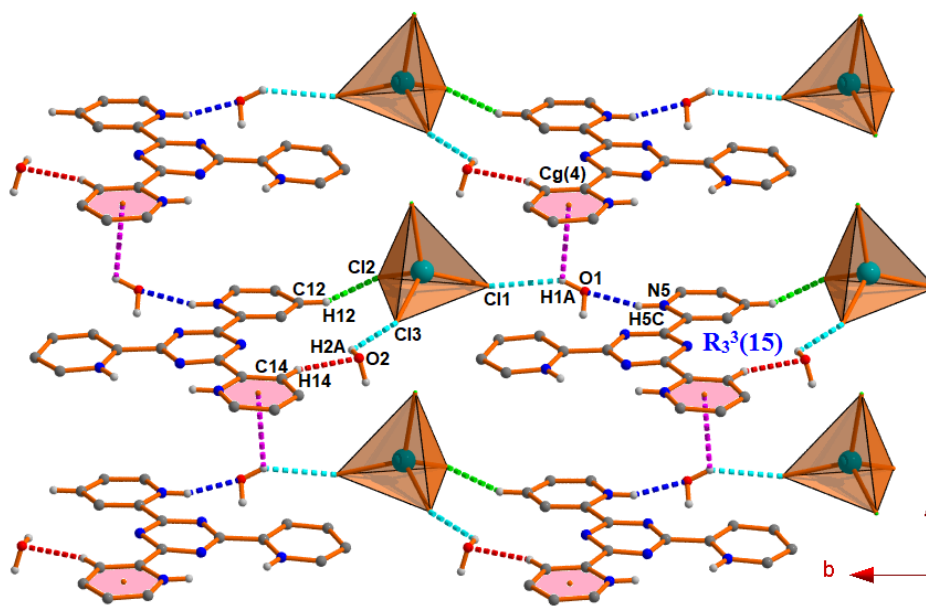
Fig. 7.21. Formation of 2D architecture through both classical and non-classical hydrogen bonding interactions in complex **3**.

Table 7.6. Geometrical parameters (Å,°) for the O─H•••π interaction for the complex 3

X─H(I)•••Cg(J)	H•••Cg [Å]	X•••Cg [Å]	X─H•••Cg (°)	Symmetry
O(1)─H(1A)[3]•••Cg(4)	2.87	3.289(14)	112	1/2+x,3/2-y,1/2+z

For complex **3**: Cg(4) is the centroid of [N6/C17/C16/C15/C14/C18] ring.

Now the ring motifs are further connected through two different hydrogen bonding interactions (N5–H5C•••O1 and O1–H1A•••Cl1) to ensure a 1D chain along (010) direction. In association with the O1–H1A•••Cl1 interaction the O1–H1A fragment of the non-coordinating water molecule is able to form O–H•••π^+ interaction with Cg(4) of the protonated pyridine ring to extend the dimensionality to 2D. Thus the synergistic behavior of these two interactions (O1–H1A•••Cl1 and O–H•••π^+) mutually strengthens each other.

7.3.2. Hirshfeld surface

The Hirshfeld surfaces of the title complexes (**1**−**3**) were mapped over d_{norm}, d_i, d_e, shape index, curvedness and fragment patches (shown in Figs. 7.22, 7.23 and 7.24). The shape-index and curvedness surfaces have been demonstrated to convey the information about each donor–acceptor pair and to measure how much shape effectively splits the surfaces into set of patches respectively. The fragment patches correspond to the environment of the nearest neighbor in the form of color patches on the surface based on the closeness of the adjacent molecules.
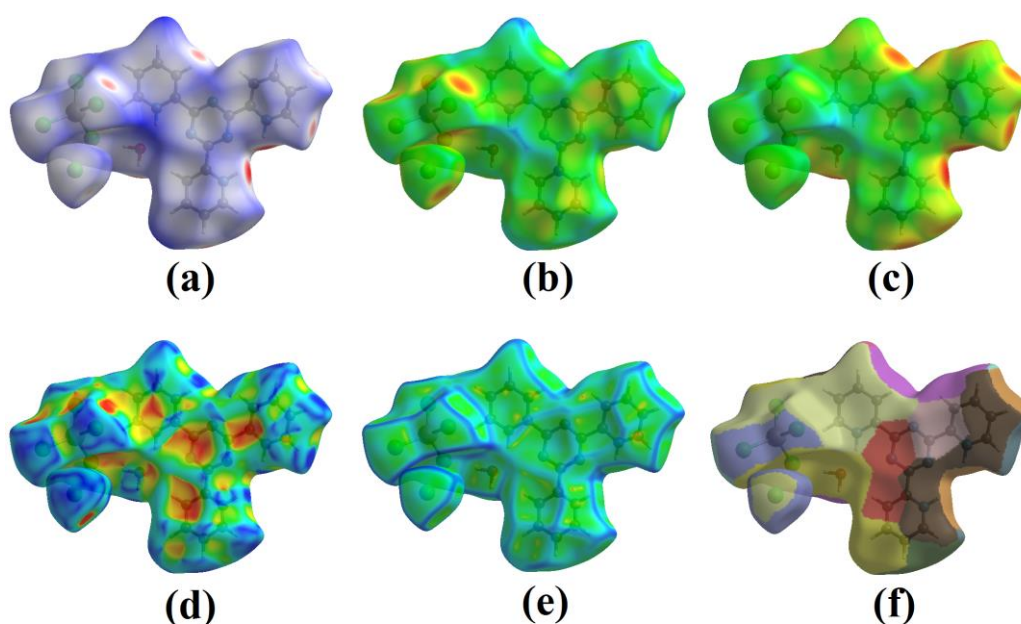
Fig. 7.22. Hirshfeld surfaces mapped with (a) d_{norm} (b) d_e (c) d_i (d) shape-index (e) curvedness and (f) fragment patches for the complex **1**.
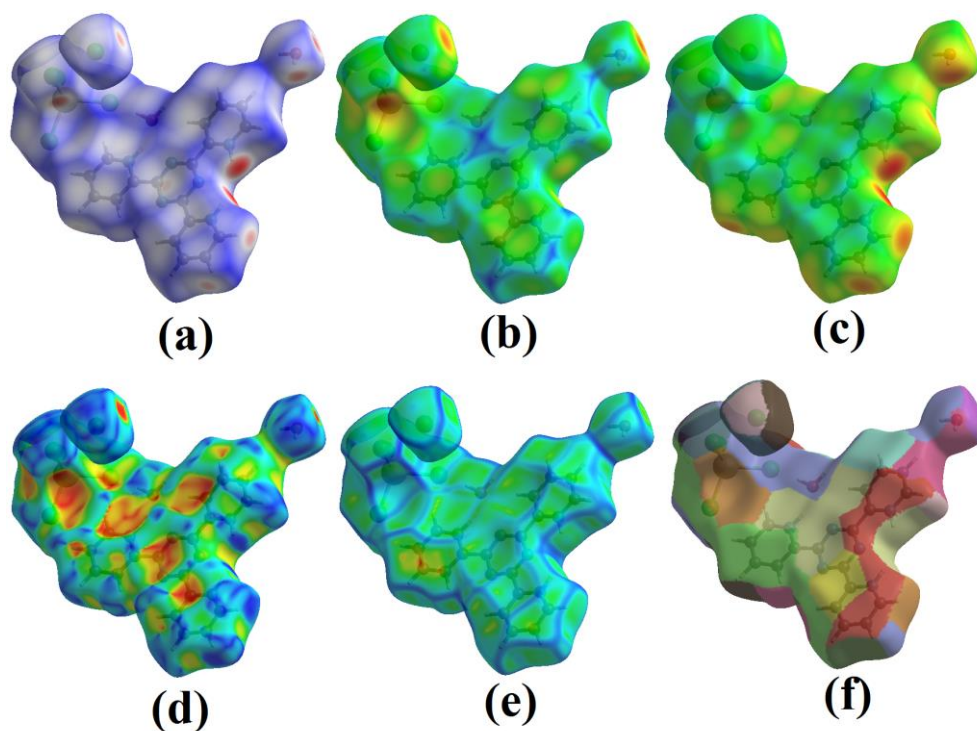
Fig. 7.23. Hirshfeld surfaces mapped with (a) d_{norm} (b) d_e (c) d_i (d) shape-index (e) curvedness and (f) fragment patches for the complex **2**.
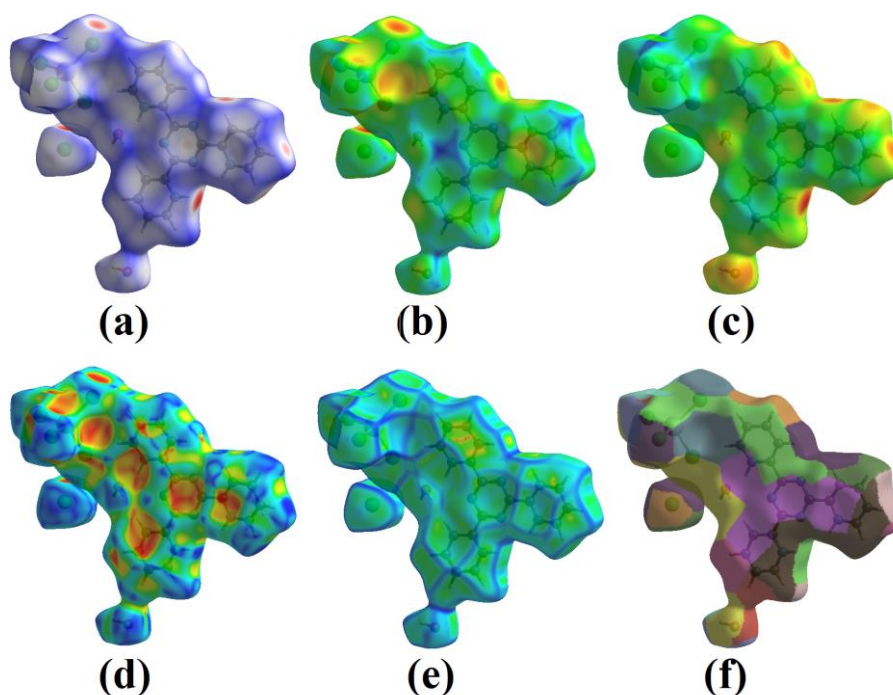
Fig. 7.24. Hirshfeld surfaces mapped with (a) d_{norm} (b) d_e (c) d_i (d) shape-index (e) curvedness and (f) fragment patches for the complex **3**.

The surfaces were made transparent to enable visualization of the molecular moiety, in a similar orientation for all the structures, around which they were calculated. Furthermore, the

combination of d_e and d_i in the form of 2D fingerprint plot represents all intermolecular contacts those are involved within the structures. The intermolecular interactions appear as distinct spikes in the 2D fingerprint plot shows the different spikes with their corresponding interactions. The fingerprint plots can be decomposed to highlight particular atom pair close contacts (Figs. 7.25, 7.26 and 7.27) and the decomposition enables the separation of contributions from different interaction types, which overlap in the full fingerprint.
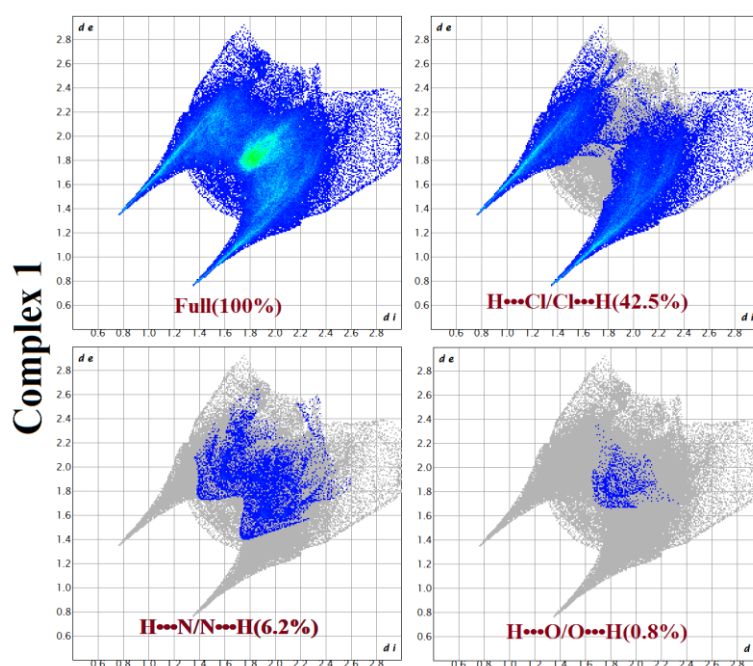
Fig. 7.25. Fingerprint plots (Full) and decomposed plots for each individual interaction in **1**.
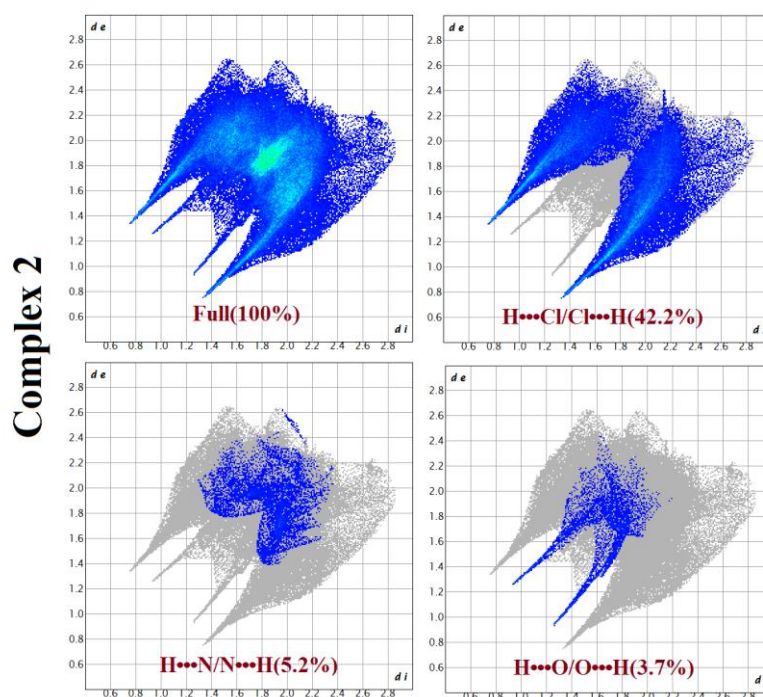
Fig. 7.26. Fingerprint plots (Full) and decomposed plots for each individual interaction in **2**.
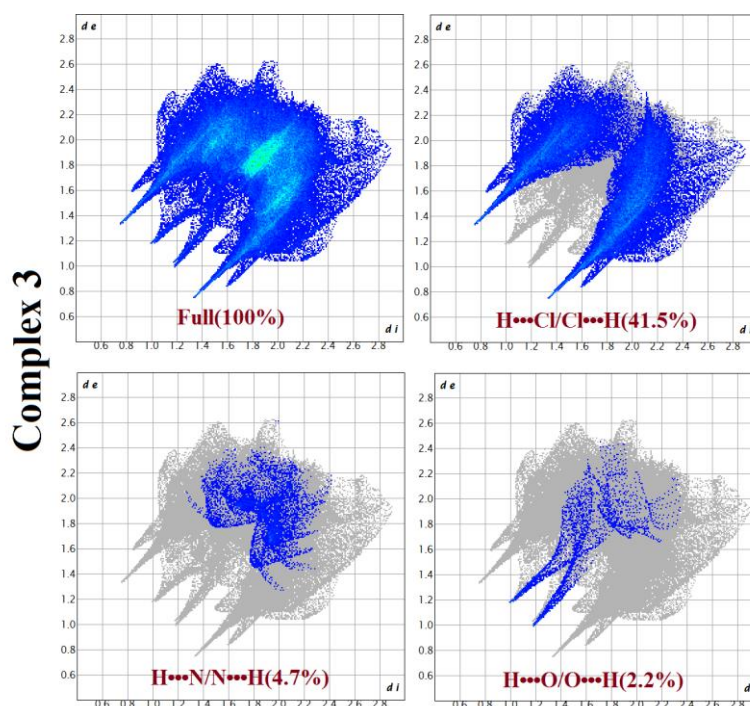
Fig. 7.27. Fingerprint plots (Full) and decomposed plots for each individual interaction in **3**.

For all the title complexes (**1**−**3**), the major non-classical hydrogen bonding interaction is observed between hydrogen and chlorine atoms. The H•••Cl/Cl•••H contacts contributed 42.5%, 42.2% and 41.5% for each complex of the total Hirshfeld surface area of **1**, **2** and **3** respectively.

From the Figures (Figs. 7.25, 7.26 and 7.27), one can see that the contribution of other interactions (H•••N and H•••O) are minimal compared to H•••Cl interactions. The H•••N/N•••H interactions contributed 6.2%, 5.2% and 4.7% whereas the contribution of the H•••O/O•••H contacts were 0.8%, 3.7% and 2.2% to the total Hirshfeld surface area of the complexes (**1**–**3**).

7.3.3. Theoretical study of non-covalent interactions

As detailed above, all complexes reported herein exhibit structure-directing anion–π and hydrogen-bonding interaction between the protonated organic ligand, the counter ions and water molecules. The DFT study is devoted to analyze and compare the interactions in complexes **1**–**3**. First the MEP surfaces of a neutral model of each complex have been computed, that consists of tricationic H_3tptz^{3+} with the hydrogen-bonded Cl^- and one anion–π bonded $[MCl_4]^{2-}$ as counter ions and the hydrogen-bonded water molecule. The MEP surfaces for these models of complexes **1**–**3** are represented in Fig. 7.28, evidencing that the MEP

maxima are located at the H-atoms of the water molecule, ranging from 69 to 75 kcal/mol.
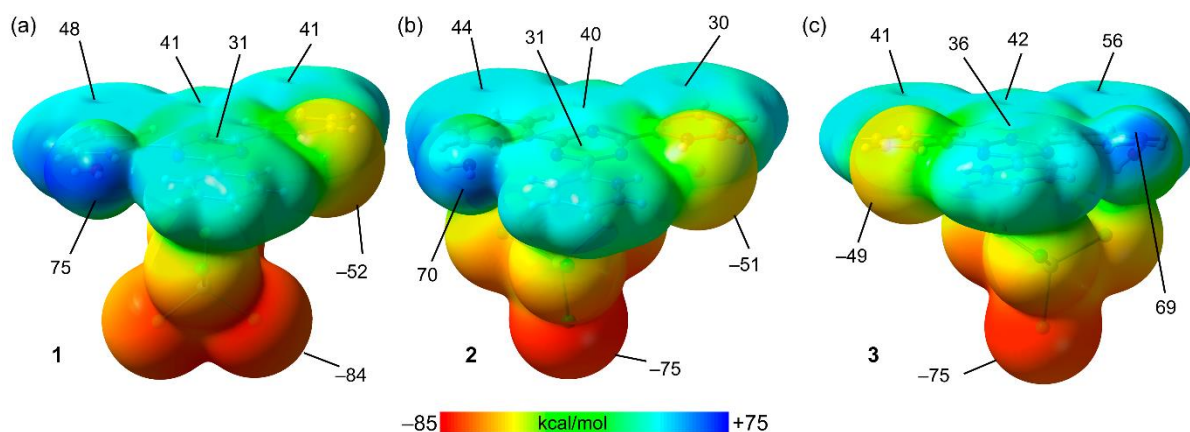
Fig. 7.28. MEP surfaces of complexes **1**–**3** with indication of the values at some points of the surface in kcal/mol.

The MEP values over the aromatic rings of the ligand are also large and positive, ranging from 30 to 56 kcal/mol; thus revealing the existence of an extended π-acidic surface. The MEP minima are located at the $[MCl_4]^{2-}$ counter ions, ranging from –75 to –84 kcal/mol. The MEP is also large and negative at the hydrogen-bonded Cl-atoms, ranging from –49 to –52 kcal/mol. The energies of the anion–π and anion–π⁺ interactions have also been analyzed using DFT calculations and characterized the interactions using a combination of the QTAIM and NCI plot analyses, since they are very convenient to reveal non-covalent interactions in real space. First, the energies of the neutral assemblies have been analyzed, used to construct the MEPs shown in Fig. 7.28 with the Cl⁻ anion (anion–π⁺). That is, the energies summarized in Fig. 7.29 were calculated as dimers, where one monomer is the chloride anion and the other one is the $[(H_3tptz)(Cl)(MCl_4)(H_2O)]$ assembly. The anion–π energies are very large and negative due to the large electrostatic attraction between the anion and the protonated pyridine ring. The stronger energy is found for complex **1** (ΔE_1 = –43.1 kcal/mol), while for complexes **2** and **3** is almost identical, likely due to the similar orientation of the $[MCl_4]^{2-}$ anion at the opposite side of the Cl•••π interaction. The combined QTAIM/NCI Plot analyses for the assemblies of $[(H_3tptz)(Cl)(MCl_4)(H_2O)]$ interacting with Cl⁻ are represented in Fig.7.30, showing that each Cl⁻ anion is connected to the aromatic ligand via two bond critical points (CPs, red spheres) and bond paths (dashed bonds) thus confirming the existence of the anion–π⁺ interactions. The anion–π nature of the interaction is further confirmed by size and shape of the reduced density gradient (RDG) isosurfaces, embracing the region between the π-system and the chlorine atom. The energies of the hydrogen-bonds have also been computed by using the values of the potential energy density (V_r) at the bond

CPs. It can be observed that in all complexes the chloride is connected to the NH groups via bond CPs and bond paths and further characterized by small blue isosurfaces. The water molecule is also connected to one NH bond via a bond CP, bond path and blue isosurface. Moreover, in complexes **1** and **2**, a secondary CH•••O (water) is also established. The energies of the hydrogen-bonds are indicated in red adjacent to the bond CPs.

Fig. 7.29. Combined QTAIM (bond CPs in red and ring CPs in yellow) and NCI plot (RDG = 0.5, color scale −0.03a.u. ≤ sign(λ_2)ρ ≤ 0.03a.u., ρ cut-off = 0.04 a.u.) analysis of the ternary anion–π/HBs assemblies observed in complexes **1** (a), **2** (b) and **3** (d). The dissociation energies of the H-bonds are indicated using a red font close to the bond CPs.

In complexes **2** and **3**, the hydrogen-bond energies are identical, with a total of 10.2 kcal/mol for both NH•••Cl hydrogen-bonds and 5.4 kcal/mol for the NH•••O (water). For complex **1**, the NH•••Cl hydrogen-bonds are slightly weaker (9.5 kcal/mol in total) and the NH•••O (water) hydrogen-bond is stronger 6.3 kcal/mol. The secondary CH•••O (water) contacts are significantly weaker (0.6 kcal/mol for **1** and 0.9 kcal/mol in **2**) in line with the small and green NCI plot isosurface.

The anion–π energies for the assemblies of [(H$_3$tptz)(Cl)(MCl$_4$)(H$_2$O)] with the [MCl$_4$]$^{2−}$ anions have also been evaluated, as detailed in Fig. 7.30. The strongest interaction is observed again for complex **1** (ΔE_4 = −54.9 kcal/mol), while for complexes **2** and **3** the energies are ΔE_4 = −42.7 kcal/mol and ΔE_6 = −44.0 kcal/mol, respectively. This is likely due to the different binding mode observed in **1**, where the two Cl-atoms are pointing to the acidic π-surface of the ligand, whilst in complexes **2** and **3** only one Cl-atom of the anion points to the central ring. In the latter complexes, only one bond CP and bond path connect the anion to the N-atom of the ligand.

However, the shape and extension of the NCI plot isosurface confirms the anion–π nature of this interaction, though the QTAIM analysis only reveals a single Cl•••N contact. In case of complex **1**, two bond CPs and bond paths connect the anion to the ligand, one to the central triazine ring and the other one to one protonated pyridine ring.
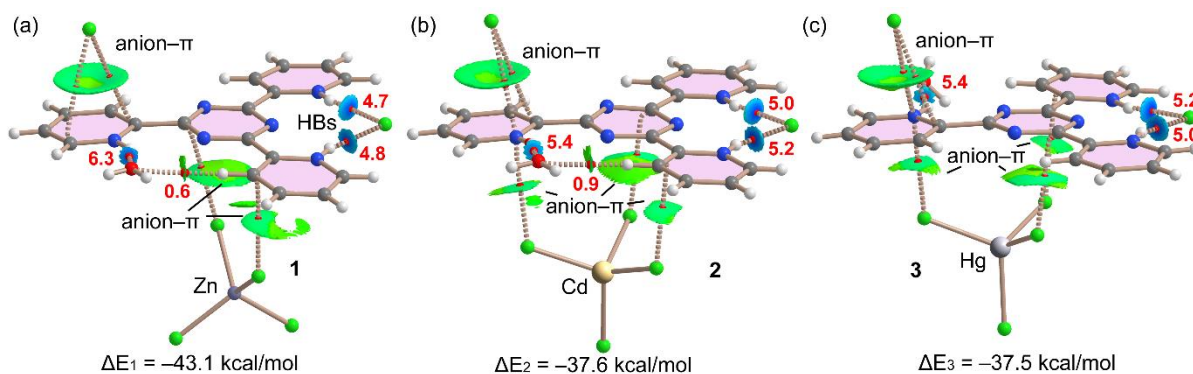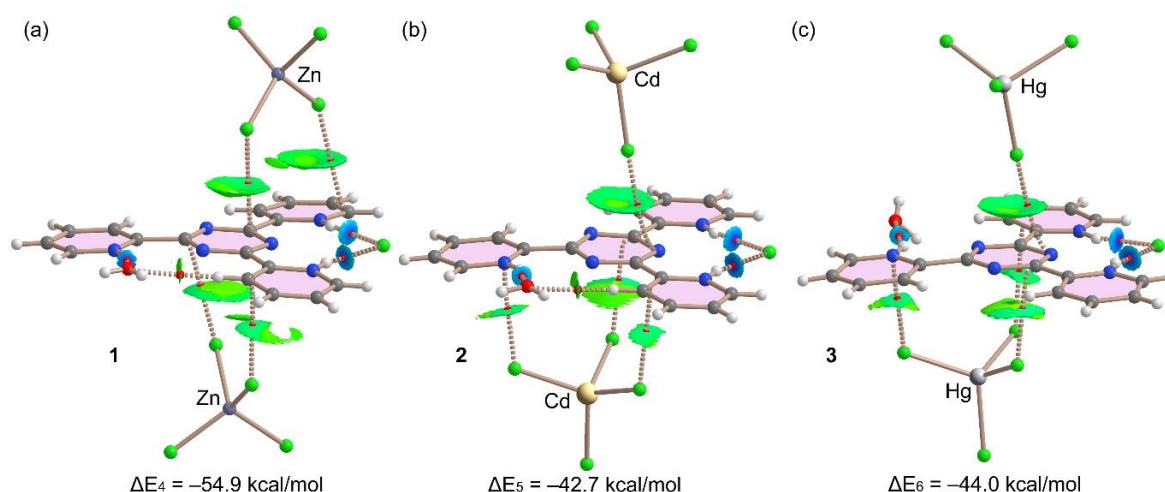
Fig. **7.30.** Combined QTAIM (bond CPs in red and ring CPs in yellow) and NCI plot (RDG = 0.5, color scale –0.03 a.u. ≤ sign(λ_2)ρ ≤ 0.03 a.u., ρ cut-off = 0.04 a.u.) analysis of the anion–π/HBs assemblies observed in complexes **1** (a), **2** (b) and **3** (d).

The interaction energies obtained for the anion–π complexes involving the $[MCl_4]^{2-}$ anions (Fig. 7.30) are stronger than those involving the Cl^- anion (Fig. 7.29) due to their monoanionic nature and consequently, weaker electrostatic attraction.

7.3.4. Optical studies

Figs. 7.31, 7.32 and 7.33 represent Tauc's plot of complex **1** (Zn^{2+} based), **2** (Cd^{2+} based), **3** (Hg^{2+} based) respectively. Using the Tauc's relation band gap energy (E_g) was calculated from the equation

$$(\alpha h\nu) \propto (h\nu - E_g)^n \qquad (1)$$

Here, hν represents photon energy; α as absorption coefficient; n is a coefficient for direct band-to-band transition having value ½. By plotting $(\alpha h\nu)^2$ *vs* $h\nu$ and extrapolating the linear line to the x-axis band gaps were calculated. The E_g was calculated to 3.87, 3.77 and 3.96 eV for complex **1**, **2** and **3** respectively. E_g values suggest that only changing the meat ion has no such broad impact in altering band structure of the complexes. Inset of the figures represent UV-vis absorption spectra of the complexes where no such distinct changes have been noticed for a particular complex.

7.3.5. Thin film fabrication from the precursor complexes

Recent development in SBD fabrication shows that functional materials are must be thin film form for simple use and ease of device parameters. Thin film technology bridges in between

macro and molecular systems where dimension of the material is decreased widely for accurate device fabrication. With this overview thin film preparation from a particular complex has been started. Usually, spin-coating method is ideal to make a film for low cost, minimum material, substrate flexibility, and tunable thickness. In the present work, three precursor complexes (**1-3**) were separately deposited onto properly clean ITO substrates (resistance ~10-12 Ω/sq cm, surface area 1.0×1.0 cm^2) by spin-coating method.
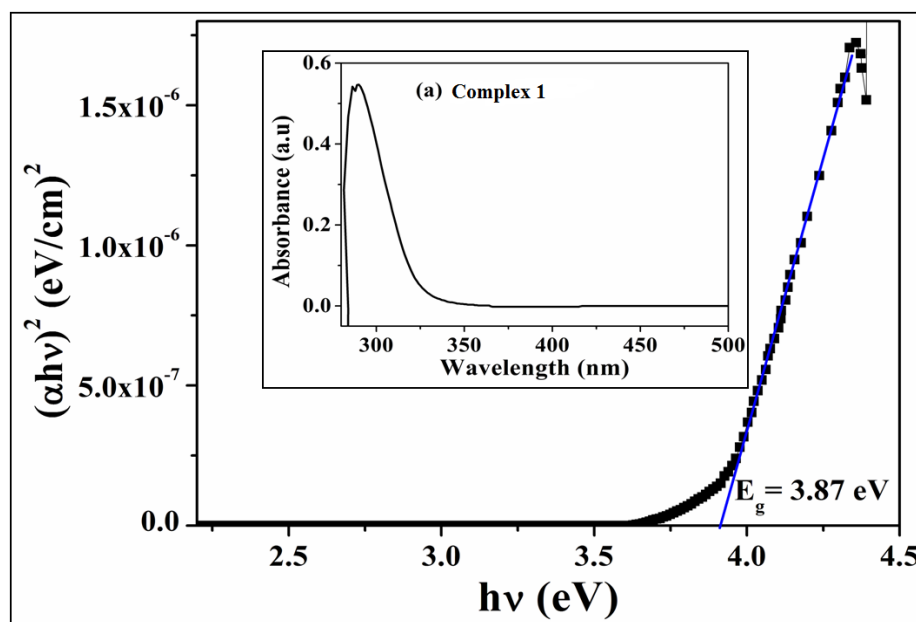
Fig. 7.31. UV-Vis spectrum of complex **1** (inset) and Tauc's plot.
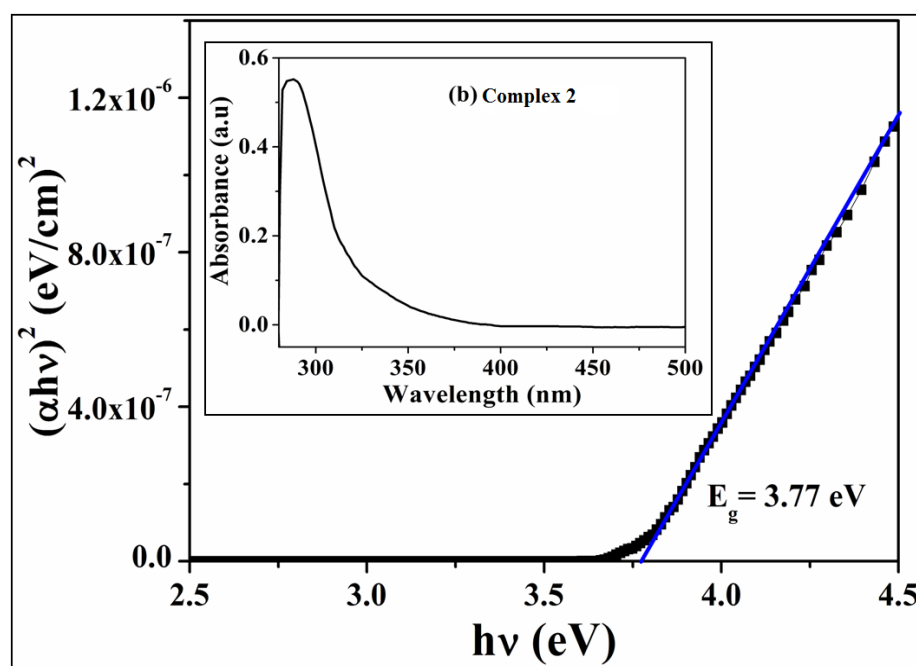
Fig. 7.32. UV-Vis spectrum of complex **2** (inset) and Tauc's plot.
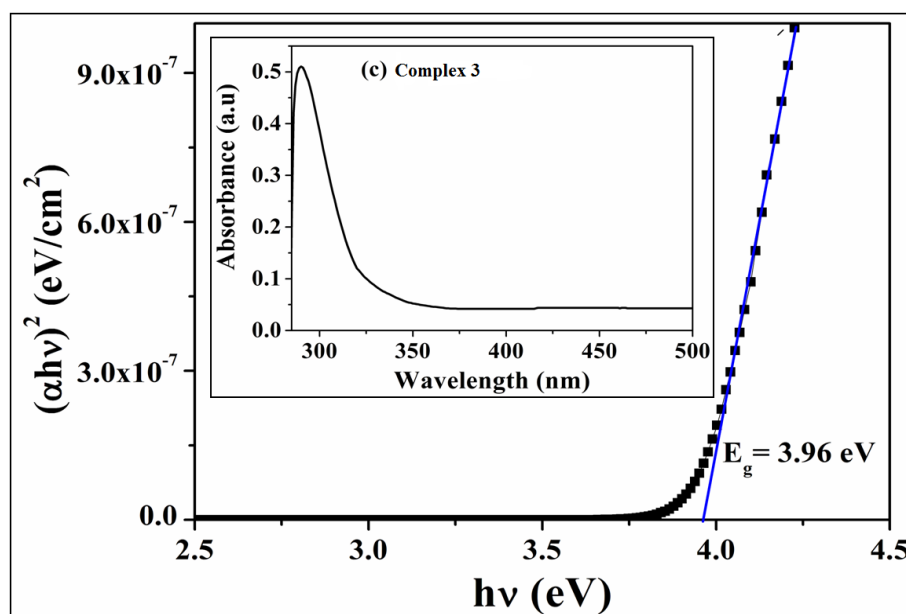
Fig. 7.33. UV-Vis spectrum of complex **3** (inset) and Tauc's plot.

About 3 to 4 mg of each complex were dispersed in DMF (ratio 1:4) and ultrasonicated for 45 minutes. Few drops of this precursor solution were dropped onto the center of ITO and spinned at 700 rpm and then 1000 rpm for 5 and 7 minutes respectively. The resulting thin films were dried in inert atmosphere and reserved in desiccators.

7.3.6. Fabrication of device and electrical properties

To measure the electrical properties related to SBD parameters I−V measurement was carried out by taking ITO substrates as the bottom contact and graphite as the top contact (ITO/complex/graphite). Experiments were performed with highly sophisticated I-V analyzer (Keithley 4200) under dark and illumination conditions in the voltage range of −1 to +1 V. Fig. 7.34(a-c) shows I−V nature of complexes **1**, **2** and **3** respectively. It is obvious that, the I−V nature of complex **2** displays enhanced nonlinear rectifying performance than complex **1** and **3**. The nonlinearity of I−V curve specifies that conduction mechanism is non-ohmic for all complexes (**1-3**) and rectifying nature indicates schottky barrier diode (SBD) characteristics of the devices. Room temperature conductivity of complexes under dark and light conditions has been measured. In presence of light, the conductivity increased from 7.20 to 15.64 S m^{-1} for complex **1**, 10.72 to 22.35 S m^{-1} for complex 2 and 7.89 to 13.5 S m^{-1} for complex **3**. In all the cases the conductivity value was found to increase in presence of light and the higher conductivity of complex **2** compared to **1** and **3** indicates significant photoresponse behavior of device 2. As the complexes show wide band gap hence thermionic

emission theory could be applied to justify the electrical properties [56]. All the I-V's and parameters are quantitatively analyzed and verified by Cheung's equation [57]

$$I = I_0 \left[exp\left(\frac{qV}{\eta kT}\right) - 1 \right] \qquad (2)$$

Where, I_0, saturation current was calculated from the intercept of ln(I) at V = 0 and can be simplified as

$$I_0 = AA^*T^2 \exp\left(\frac{-q\Phi_B}{KT}\right) \qquad (3)$$

Where the terms q, K, T, V, A, A* and η stand for electronic charge, Boltzmann constant, temperature in Kelvin, forward bias voltage, effective diode area, effective Richardson constant and ideality factor respectively. The effective diode area was kept as 8.0×10^{-2} cm^2, and Richardson constant was considered as 32 A K^{-2} cm^{-2} for all the devices. Now, forward I−V characteristics can be expressed as

$$I = I_0 \left[exp\left(\frac{q(V - IR_s)}{\eta kT}\right) \right] \qquad (4)$$

Here, IR$_S$ symbolizes the voltage drop across the series resistance and it can be determined from the following equation

$$\frac{dv}{d(lnI)} = \frac{\eta kT}{q} + IR_s \qquad (5)$$

Equation 5 can also be expressed another way as function of I

$$H(I) = IR_S + \eta\Phi_B \qquad (6)$$

Again, H(I) can also be written using the following equation

$$H(I) = V - \left(\frac{\eta kT}{q}\right) \ln\left(\frac{I}{AA^*T^2}\right) \qquad (7)$$

Fig. 7.35 represents dV/d(ln I) vs I plot for all devices under dark and light condition. The series resistance (R$_S$) and ideality factor (η) for all devices were determined from the slope and intercept of dV/d(ln I) vs I plot. The Rs of the devices (**1** to **3**) was found to be 7.76 and 2.76, 6.78 and 5.63, 0.256 and 5.33 under dark and illumination condition respectively. The low Rs value for device 2 indicates its easy passage of electron tunneling. The ideality factor η of the devices was found to 4.1, 4.0 and 4.13 under dark condition. Under the illumination of light the η value reduced to 1.48, 1.39 and 1.7 for respective devices. From the η values it is clear that the metal semiconductor (MS) junctions of the complexes are not exactly ideal.
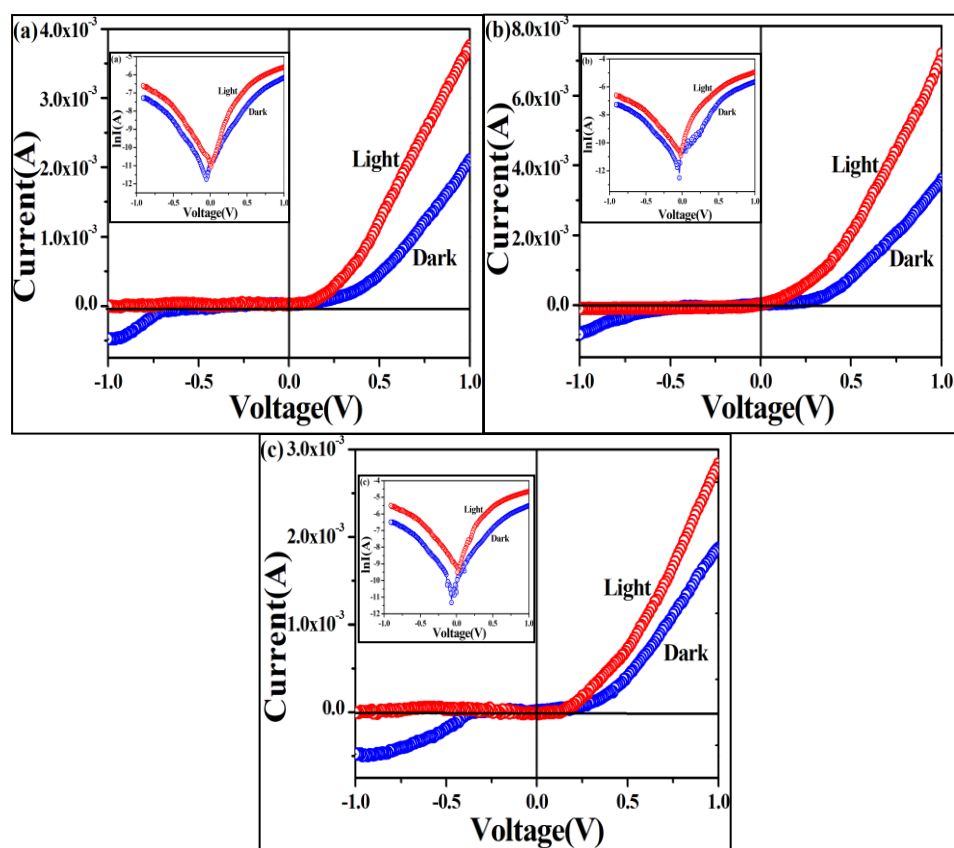
Fig. 7.34. I–V characteristic of complexes **1-3** (a-c) under dark and illumination conditions (a, b, c), inset ln I vs. V plot.
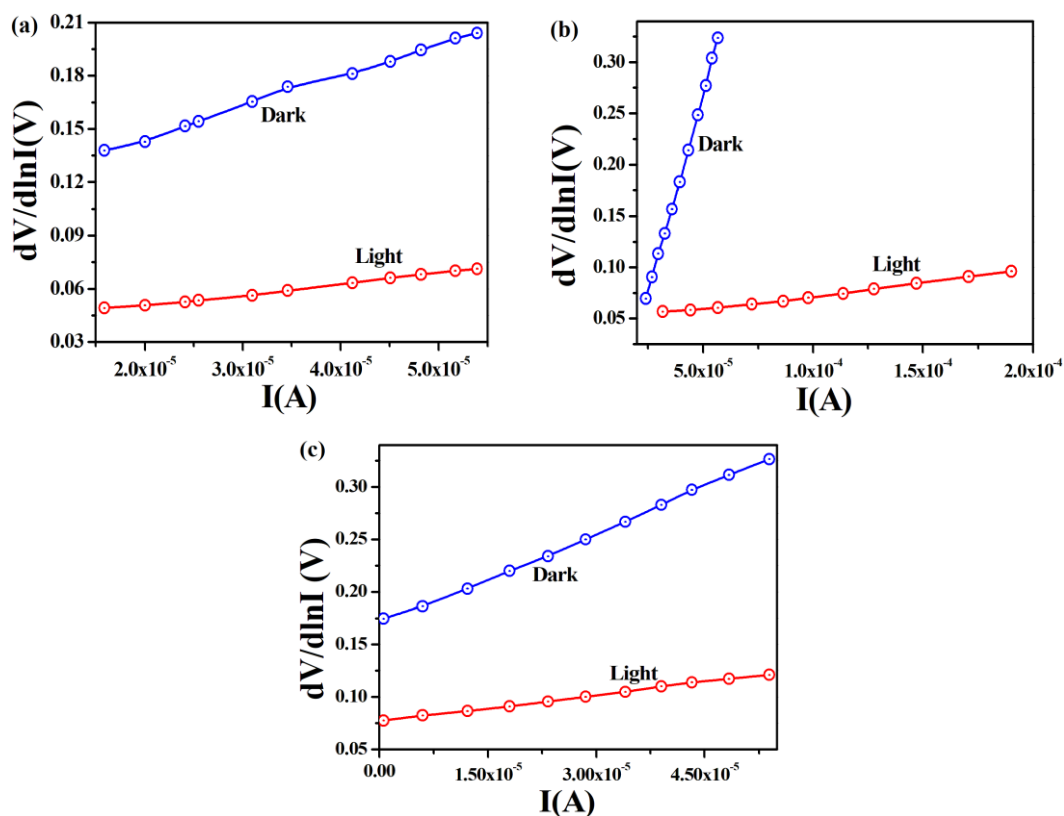
Fig. 7.35. dV/dln I vs. I plot of complexes **1-3** (a-c) under dark and illumination conditions.

Fig. 7.36 represents H(I) vs I plot for all devices under dark and light condition. H(I) vs I plot gives a straight line where intercept along y axis becomes equal to $\eta\phi_B$ and slope gives Rs. Now by using measured η values potential barrier heights (Φ_B) for respective devices were calculated. All the device related parameters *e.g.*, potential height (ϕ_B), ideality factor (η), and series resistance (R_S) are listed in Tables 7.7 and 7.8.
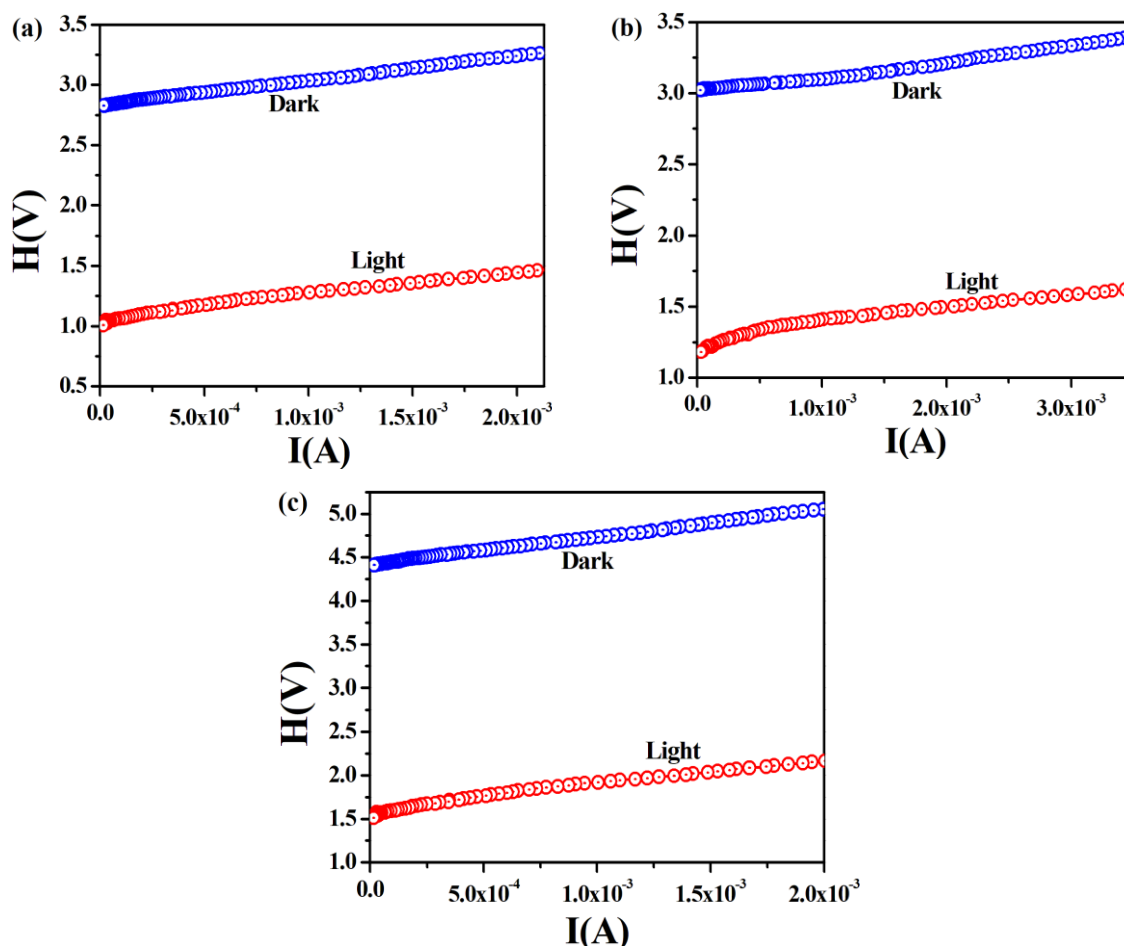
Fig. 7.36. H (I) vs. I plot of complexes **1-3** (a-c) under dark and illumination condition.

Table 7.7.

Device	condition	On /off	conductivity δ (S m^{-1}) $\times 10^{-4}$	photosensitivity	ideality factor η	dv/dlnI Rs (k ohm)	H Rs (k ohm)
1	dark	4.14	7.20	1.78	4.1	7.76	13.1
	light	133	15.64		1.48	5.63	7.67
2	dark	4.54	10.72	2.0	4.0	2.76	6.86
	light	165	22.35		1.39	0.256	4.77
3	dark	4.11	7.89	1.64	4.13	6.78	8.22
	light	123	13.5		1.7	5.33	17.5

To quantify a detail study of charge transport phenomena at the interface of MS junction, space charge limited current (SCLC) theory is introduced. Using this theorem several SBD parameters like carrier mobility (μ_{eff}), carrier concentration (N), diffusion coefficient (D), diffusion length (L_D) and transient response time (τ) have been calculated.

Table 7.8.

Device	condition	barrier height Φ_B	mobility μ_{eff} ($cm^2\,V^{-1}\,s^{-1}$)	transit time $t \times 10^{-12}$ (s)	D $\times 10^{-6}$	L_D $\times 10^{-8}$	carrier concentration $N \times 10^{22}$
1	dark	0.89	1.01×10^{-8}	122.71	2.65	2.52	1.63
	light	0.65	1.58×10^{-8}	100.04	4.16	2.89	2.56
2	dark	0.76	10.5×10^{-4}	112.23	2.76	7.87	1.54
	light	0.43	17.8×10^{-4}	31.60	27.1	13.09	2.94
3	dark	0.96	0.32×10^{-8}	135.63	2.74	2.43	0.94
	light	0.74	1.33×10^{-8}	118.63	6.37	6.33	2.19

To acquire significant outcome with respect to carrier transport phenomenon at the interface of MS junction log(I) vs log(V) plots were drawn for the forward bias (Fig. 7.37). This plot is compared with the power law (I $\propto V^m$) to locate the charge transfer zone in MS junction. The slope 'm' fence the boundary in between ohmic and SCLC region.
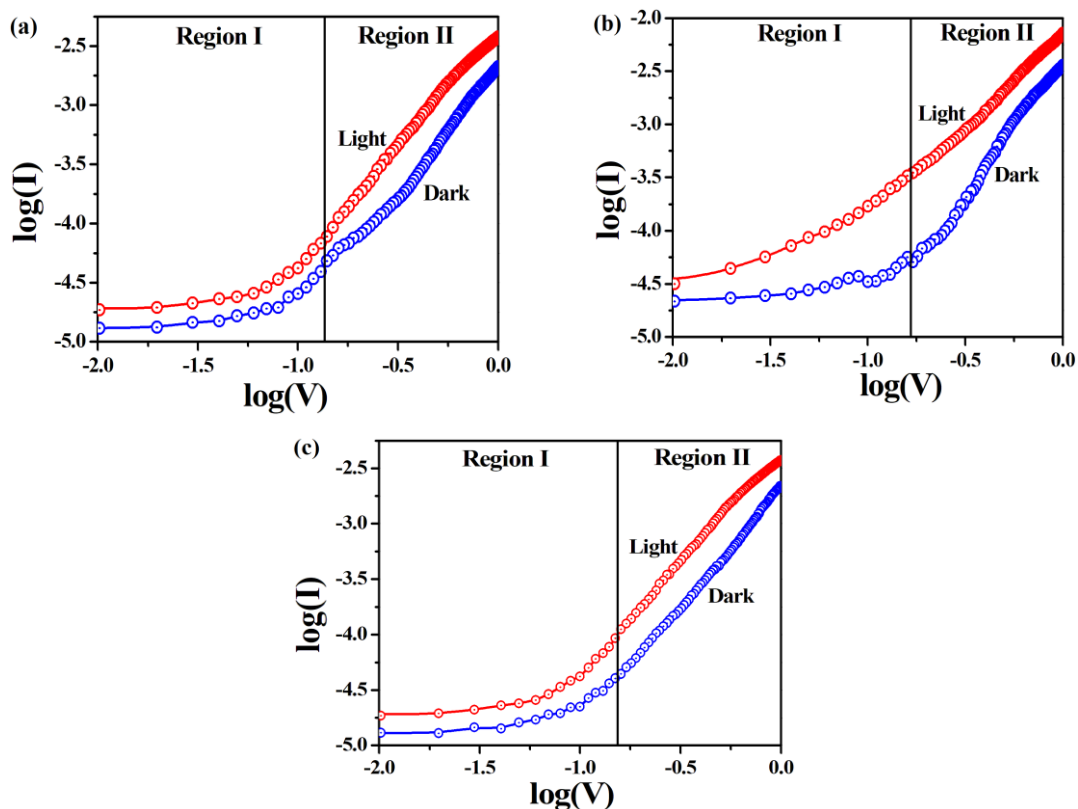
Fig. 7.37. log (I) vs. log (V) plot of complexes **1-3** (a-c) under dark and light condition.

For ohmic nature the m value will be in the range of less than or equal to 1. Further greater than1 or equal to 2 (m $\geq$ 2) indicates a space-charge-limited-current (SCLC) region [58]. Fig. 7.37(a) (b) and (c) represent log-log plot of device 1, 2 and 3 respectively under dark and illumination conditions.

The log-log plot illustrates two distinct linear regions (I and II) of different slopes hence, concludes two different conduction mechanisms are being operated in MS junction. At low potential region I current becomes proportional to applied voltage (I $\propto$ V^2) and hence, the device exhibits an ohmic nature in this zone. Region I attributes thermionic emission where bulk generated electrons are responsible to produce current than the injected free carriers from metal [59,60]. At higher potential, the log-log plot obeys simple power law (I $\propto$V^m) and it is separated as region II. In region II, the current becomes proportional to the square of applied voltage (I $\propto$ V^2), specifies that the current is run by space charge limited current (SCLC) obtained from discrete trapping level [61,62].

From the I vs V^2 graph (Fig. 7.38) and using Mott−Gurney equation [63] carrier mobility (μ_{eff}) was evaluated.

$$J = \frac{9\mu_{eff}\varepsilon_0\varepsilon_r}{8}\frac{V^2}{d^3} \qquad (8)$$

Where, the terms J, ε_0, ε_r and d stands for current density, permittivity of free space, relative dielectric constant of complexes and film thickness.
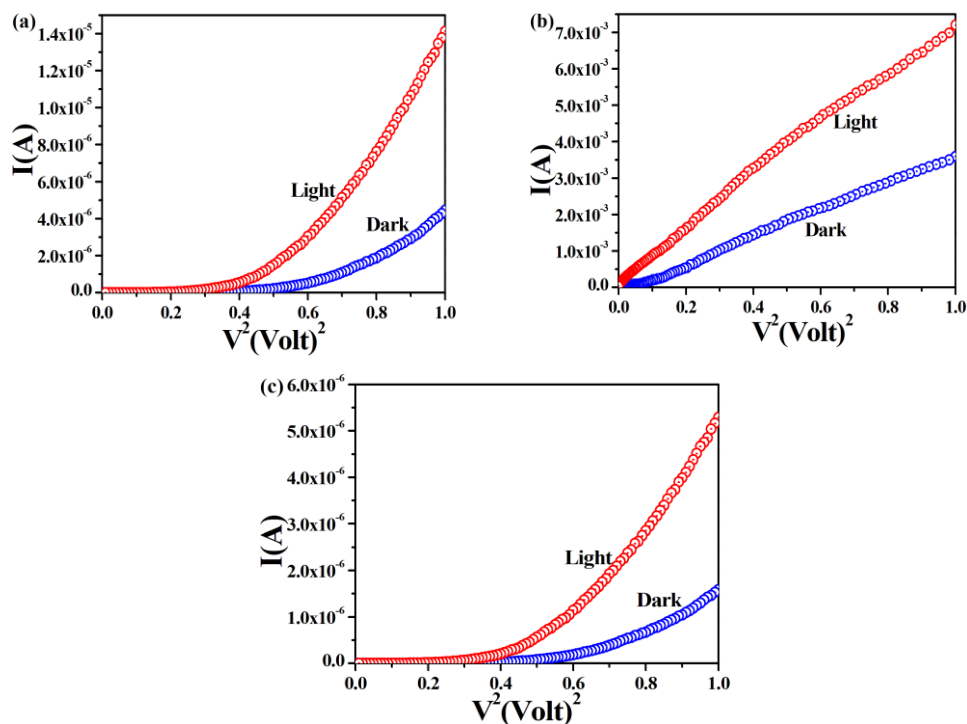
Fig. 7.38. I vs V^2 plot of complexes **1-3** (a-c) under dark and illumination condition.

Thicknesses of the films were about 2 µm for all the devices. Before this measurement dielectric studies were made for all the complexes. Dielectric constants for all the complexes have been calculated from the plots of capacitance *vs.* frequency (Fig. 7.39).
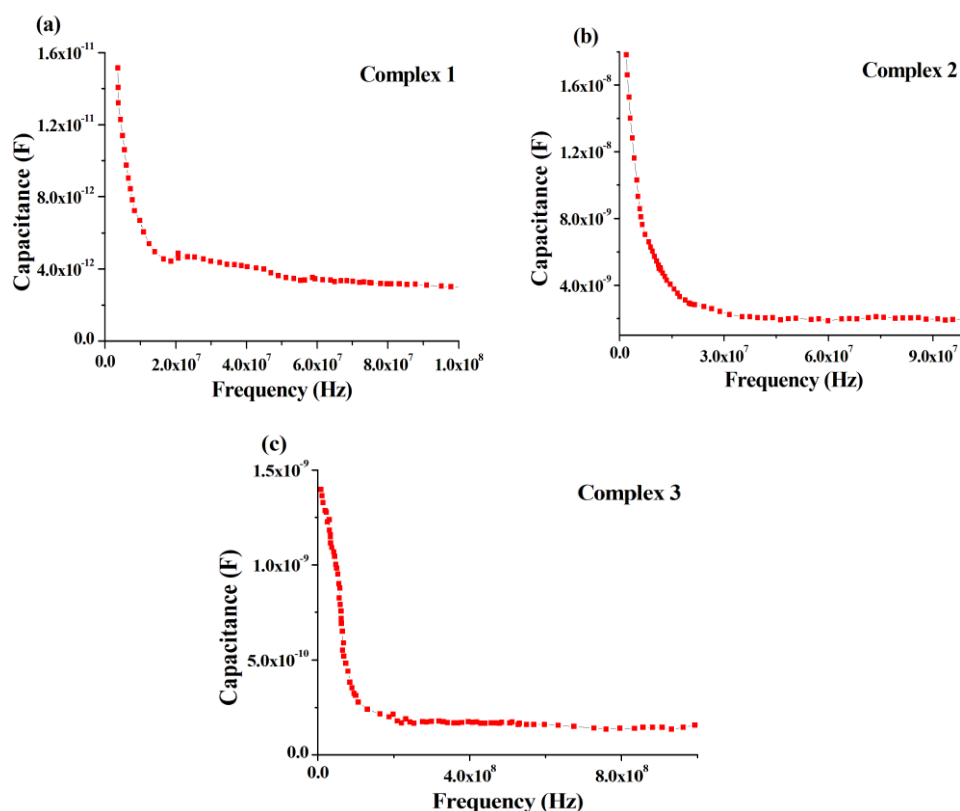
Fig. 7.39. Capacitance *vs.* frequency plots of complexes **1**, **2** and **3**

Capacitance was measured by varying frequency between 1 to 10 kHz, under a constant bias of 1 V. By using the conventional equation [64] relative dielectric constants for complexes **1, 2** and **3** were measured and found 6.23 2.27, and 4.13 respectively. Relatively lower dielectric constant of complex **2** is an indication of its potential use as an optoelectronic device to reduce power loss.

Transit time (τ) of the charge carriers is another important parameter to investigate charge transport across the junction. From the slope of forward I−V curve (Fig. 7.34) τ was calculated using the equation [65].

$$\tau = \frac{9\varepsilon_0\varepsilon_r A}{8d}\left(\frac{V}{I}\right) \tag{9}$$

The details of these parameters are presented in Table 7.8. Higher effective mobility value of device **2** confirms fast charge transport of the material through the MS junction compared to **1** and **3**. Mobility enhancement of the carrier due to light illumination indicates a good photo-

responsivity of the device. The results demonstrate that the charge transport property of the device 2 (made from complex **2**) is better than device **1** and **3**. All of these SBD related parameters implies ultimate supremacy of complex **2**.

7.3.7. Theoretical analysis for photo-physical properties

The solid state structure of the **1**, **2**, and **3** crystals was modeled using DFT methodology and choosing the experimental crystal lattices as a starting point for optimizing the atomic position. Standard band theory was used to determine the adjustment degree between the experimental and theoretical data. Fig. 7.40 shows the band diagram between the crystals in the study. All systems present direct band gap behavior at point D of the Brillouin zone and around 3.50 eV.
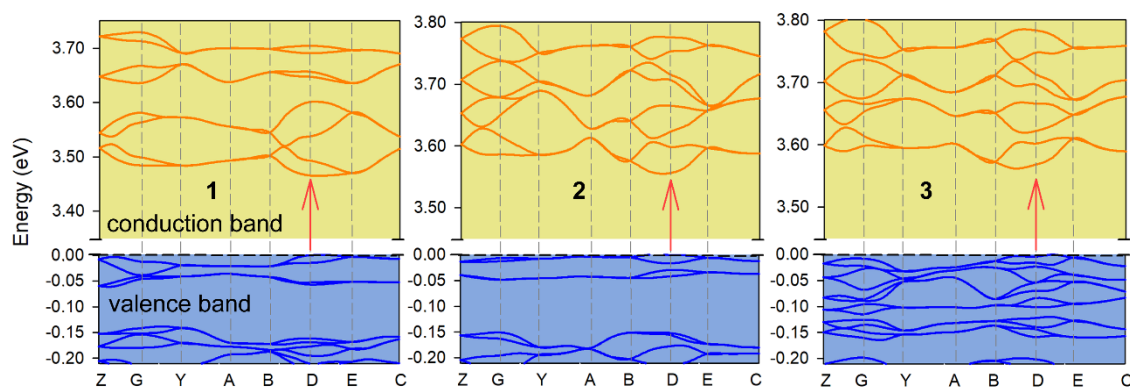
Fig. 7.40. Electronic band structures of the ground state for **1**, **2** and **3** crystals structure. Points of high symmetry in the first Brillouin zone are labeled as follows: Z = (0, 0, 0.5); G = (0, 0, 0); Y = (0, 0.5, 0); A = (-0.5, 0.5, 0); B = (-0.5, 0, 0); D = (-0,5, 0, 0.5); E = (-0.5, 0.5, 0.5); C = (0, 0.5, 0.5). The red arrow marks the band gap.

This is in reasonable agreement with the experimental values that range 3.77 to 3.96 eV, thus evidencing that the DFT method slightly underestimates the band gap values. Nevertheless, the theoretical calculations confirm the semiconductor type and low influence of the metal atom. Fig. 7.41 shows the partial density of states for the three complexes. The plots represent the contribution of $[MCl_4]^{2-}$ (M = Zn, Cd, Hg) and chloride anions and tptz ligand separately.

It is revealed that the p-character of the anions mainly dominates the valence band, and the p-character of the tptz ligands mainly dominates conduction bands. Interestingly, the d-orbitals of the metal centers do not participate neither in the conduction or the valence bands, in line with the negligible effect of the group-12 element on the band gap. This fact is

also verified by calculating the frontier molecular orbitals in all the systems that show the total absence of density at the $[MCl_4]^{2-}$ anions in both frontier orbitals.
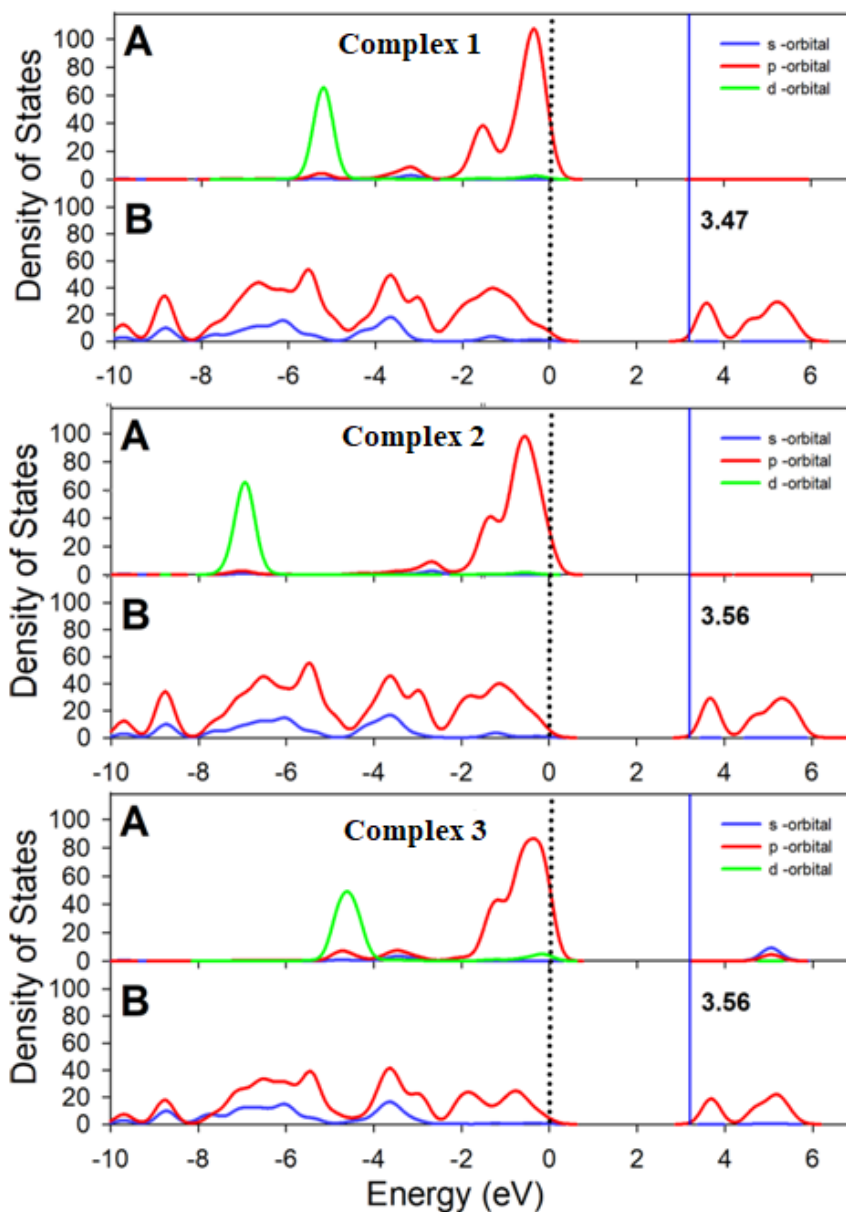
Fig. 7.41. Calculated total and partial density of states of **1**, **2** and **3** crystal cells. Panels show: **1)** A.) $[ZnCl_4]^{2-}$ and Cl^- anions, B.) tptz ligands; **2)** A.) $[CdCl_4]^{2-}$ and Cl^- anions, B.) tptz ligands; **3)** A.) $[HgCl_4]^{2-}$ and and Cl^- anions, B.) tptz ligands. The lines represent the s-orbital character (blue), p-orbital character (red) and d-orbital character (green) of the atoms into the crystal.

Fig. 7.42 shows the HOMO and LUMO of complex **2** as representative crystal structure, since these are almost identical in the three complexes. The HOMO plot in Fig. 7.42 shows the contribution of the p-orbital at the chloride anion, while the LUMO is a π-anti-bonding orbital localized at the tptz ligand.
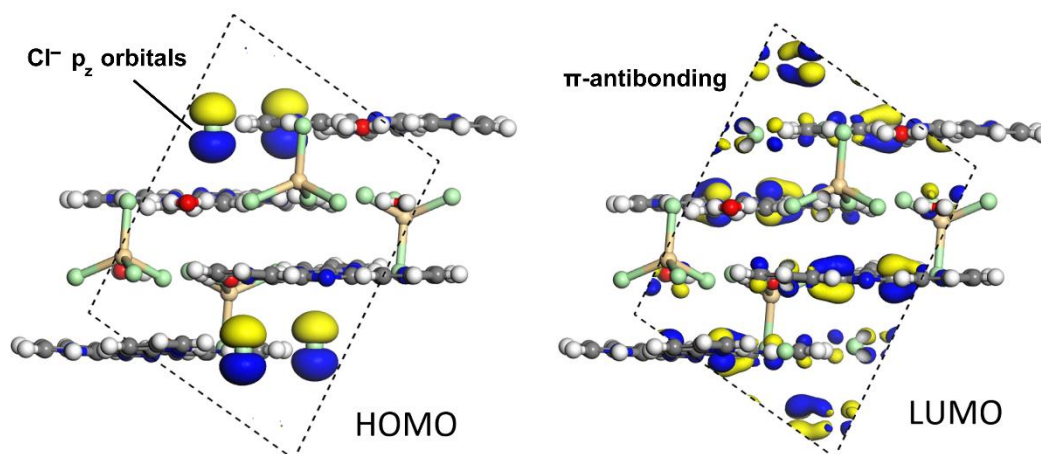
Fig. 7.42. Representation of HOMO-LUMO of complex **2**. The orbitals are represented using the 0.025 a.u. isovalue.

Theoretically it is possible to know the frequency dependence of an incident photon in a material with the calculation of the dielectric function ε (ω) (see Fig. 7.43) [66–71]. A photon-energy range of 0-12 eV have been chosen to calculate the optical response using the band structure. The Fig. 7.43 shows that complexes **1**–**3** have similar dielectric constant diagrams concerning the intensity of their maxima, in agreement with the similar experimental behavior of complexes **1**–**3**.
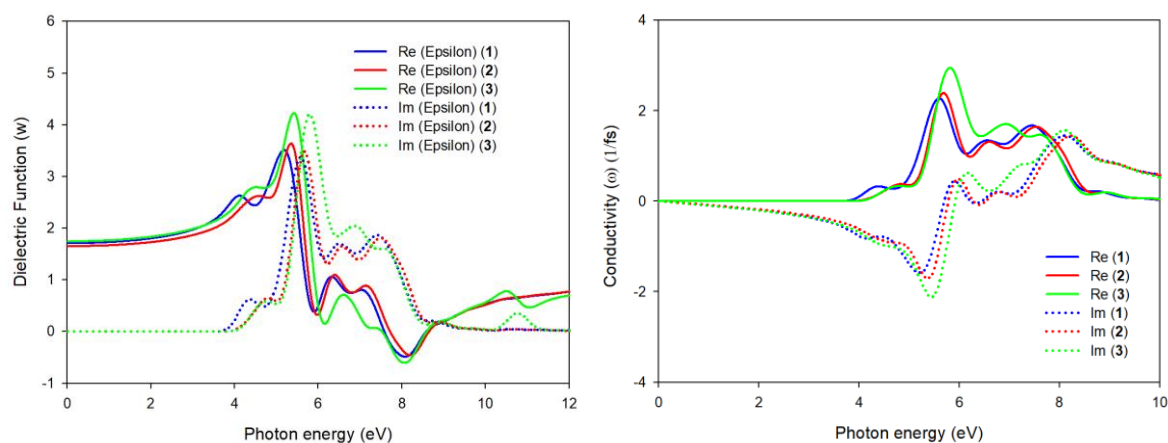
Fig. 7.43. The left panel shows a plot of real (solid line) and imaginary (point lines) parts of the dielectric function versus the photon energy of the **1** (blue line), **2** (red line), and **3** (green line) crystals. The right panel show a plot of real (solid lines) and imaginary (points lines) parts of optical conductivity versus the photon energy of the **1** (blue line), **2** (red line), and **3** (green line) crystal.

The optical conductivity of the material [$\sigma(\omega)$] have also been measured, since it is helpful to analyze how the conductivity of the material changes upon illumination. Moreover, the photoconductivity and hence electrical conductivity of materials increases because of

absorbing photons [66–71]. As a rough approximation, it is possible to relate the optical conductivity of the material with the electrical conductivity measured experimentally, verifying whether any change in its electronic configurations occurs when the material absorbs a photon. These facts can be related to the increased conductivity of these materials when illuminated. However, the results shown in Fig. 7.43 do not explain the fact that complex **2** is superior to **1** and **3** in terms of optical properties. A likely explanation for this could be related to the fabrication of the device like differences in the junctions.

Recently, a number of efforts have been explored to induce conductivity via through-bond (charge transfer occurs through strong orbital overlap bonding between metal centers and organic ligands), extended conjugation (the metals and entire ligands form large delocalized systems) and through-space (involving weak interactions) strategies [72−74]. In this work the charge transportation occurs through the combination of these three strategies. The extended conjugation in the protonated organic moiety (H_3tptz^{3+}) and metal to ligand charge transfer in the M─Cl bonds along with several weak interactions resulting higher conductivity in the title complexes (**1−3**).

Here, such a striking differences of device properties among the complexes can be attributed by two factors: (i) the enhanced electron density of the protonated organic moiety (H_3tptz^{3+}) by partial electron transfer from MCl_4^{2-} and Cl^- anions involved in anion–π/ anion–π^+ interactions and (ii) the possibility of more effective charge transport through the strong hydrogen bonding interactions between the anions and non-coordinated water molecules. In association with the anion–π/ anion–π^+ interactions, the charge transportation occurs more in complex **2** through 2D water-anion cluster than that of complex **1** (through 1D water-anion cluster) and complex **3** (no such water-anion cluster). With this believe it can be simplified that both factors likely contributed to enhance the conductivities as well as the device properties for complex **2** than complexes **1** and **3**.

7.4. CONCLUSION

A series of tetrachlorometallates including Zn (II) (complex **1**), Cd (II) (complex **2**) and Hg (II) (complex **3**) with the help of a triply protonated tptz (H_3tptz^{3+}) ligand, have been successfully synthesized and crystallographically characterized. The crystallographic analysis reveals that anion•••π, anion•••$π^+$ and several hydrogen bonding interactions play crucial role in the stabilization of the self-assembled structure which in turn is responsible for enhancement of dimensionality for all the complexes. The Hirshfeld surfaces and breakdown of the corresponding fingerprint plots of **1−3** structures facilitate a comparison of hydrogen bonding interactions significantly. A DFT study has been used to disclose the interplay among these interactions and compare them towards the stability of the complexes. Furthermore, the interactions were rationalized and analyzed by using MEP surfaces and the combined QTAIM/NCI plot computational tools.

Besides, SBD devices with d^{10} metal series have been fabricated successfully. The devices made from complexes **1**, **2** and **3** exhibit non–ohmic rectifying nature under dark and illumination conditions. The measured device parameters *e.g.*, conductivity, effective mobility, transit time, carrier concentration, diffusion coefficient, diffusion length, and ideality factor authenticate that the complex **2**, made with Cd^{2+} is more ideal as an SBD compared to complex **1** and **3**. Betterment of complex **2** as an SBD was critically explained both by theoretical and supramolecular point of view.

REFERENCES

1. I. O. Koshevoy, M. Krause and A. Klein, *Coord. Chem. Rev.*, 2020, **405**, 213094.

2. R. S. J. Proctor, A. C. Colgan and R. J. Phipps, *Nat. Chem.*, 2020, **12**, 990–1004.

3. A. Bhattacharyya and S. De Sarkar, A. Das. *ACS Catal.*, 2021, **11**, 710−733.

4. V. Guillermand M. Eddaoudi, *Acc. Chem. Res.*, 2021, **54**(17), 3298–3312.

5. E. Kuzniak-Glanowska, J. Kobylarczyk, K. Jedrzejowska, D. Gloszand R. Podgajny, *Dalton Trans.*, 2021, **50**(32), 10999–11015.

6. P. Pal, A. Hossain, R. M. Gomila, A. Fronteraand S. Mukhopadhyay, *New J. Chem.*, 2021, **45**(26), 11689–11696.

7. P. Pal, A. Hossain, A. Frontera and S. Mukhopadhyay, *New J. Chem.*, 2020, **44**(18), 7310–7318.

8. A. Hossain, A. Dey, S. K. Seth and P. P. Ray, *CrystEngComm*, 2021, **23**(19), 3569–3581.

9. S. Pramanik, S. Pathak, S. Jana, M. Mondol, A. Frontera and S. Mukhopadhyay, *New J. Chem.*, 2021, **45**, 12108–12119.

10. G. A. Bowmaker, S. I. Rahajoe, B. W. Skelton and A. H. White, *Z. Anorg. Allg. Chem.*, 2011, **637**, 1361–1370.

11. D. J. Mercer and S. J. Loeb, *Chem. Soc. Rev.*, 2010, **39**(10), 3612–3620.

12. Z. Azarkamanzad, F. Farzaneh, M. Maghami and J. Simpson, *New J. Chem.*, 2019, **43**(30), 12020–12031.

13. S. E. Domínguez, F. E. M. Vieyraand F. Fagalde, *Dalton Trans.*, 2020, **49**(36), 12742–12755.

14. I. Alkorta, I. Rozasand J. Elguero, *J. Am. Chem. Soc.*, 2002, **124**(29), 8593–8598.

15. D. Quiñonero, C. Garau, C. Rotger, A. Frontera, P. Ballester, A. Costa and P. Deyà, *Angew. Chem. Int. Ed.*, 2002, **114**(18), 3539–3542.

16. M. Mascal, A. Armstrong and M. D. Bartberger, *J. Am. Chem. Soc.*, 2002, **124**, 6274–6276.

17. V. Stavila, A. Talin and M. D. Allendorf, *Chem. Soc. Rev.*, 2014, **43**, 5994–6010.

18. A. Dhakshinamoorthy and H. Garcia, *Chem. Soc. Rev.*, 2012, **41**, 5262–5284.

19. J. Liu, W. Zhou, J. Liu, I. Howard, G. Kilibarda, S. Schlabach, D. Coupry, M. Addicoat, S. Yoneda, Y. Tsutsui and T. Sakurai, *Angew. Chem., Int. Ed.*, 2015, **54**, 7441–7445.

20. M. L. Aubrey and J. R. Long, *J. Am. Chem. Soc.*, 2015, **137**, 13594–13602.

21. Z. Zhang, H. Yoshikawa and K. Awaga, *Chem. Mater.*, 2016, **28**, 1298–1303.

22. M. G. Campbell, D. Sheberla, S. F. Liu, T. M. Swager and M. Dincă, *Angew. Chem., Int. Ed.*, 2015, **54**, 4349–4352.

23. K. M. Choi, H. M. Jeong, J. H. Park, Y. B. Zhang, J. K. Kang and O. M. Yaghi, *ACS* Nano, 2014, **8**, 7451–7457.

24. X. Huang, P. Sheng, Z. Tu, F. Zhang, J. Wang, H. Geng, Y. Zou, C. A. Di, Y. Yi, Y. Sun and W. Xu, *Nat. Commun.*, 2015, **6**, 7408.

25. C. H. Hendon, D. Tiana and A. Walsh, *Phys. Chem. Chem. Phys.*, 2012, **14**, 13120–13132.

26. L. Sun, M. G. Campbell and M. Dincă. A*ngew. Chem., Int. Ed.*, 2016, **55**, 3566–3579.

27. K. T. Butler, C. H. Hendon and A. Walsh, *ACS Appl. Mater.* Interfaces, 2014, **6**, 22044–22050.

28. W.J. Li, J. Liu, Z. H. Sun, T. F. Liu, J. Lü, S. Y. Gao, C. He, R. Cao and J. H. Luo, *Nat. Commun.*, 2016, **7**, 11830−11837.

29. T. K. Maji, R. Matsuda and S. Kitagawa, *Nat. Mater.*, 2007, **6**, 142−148.

30. *Bruker, SMART v5.631*, Bruker AXS Inc., Madison, WI, USA, 2001.

31. G. M. Sheldrick, Acta Crystallogr., Sect. A: Found. Adv. 2015, 71, 3−8.

32. G. M. Sheldrick, SHELXL-2016/6, Program for Crystal Structure Solution; University of Göttingen, 2016.

33. C.F.Holder andR. E. Schaak, *ACS* Nano, 2019,**13**, 7359–7365.

34. H. Zhao, B. G. Zhang, X. X. Zhang, S. Wang and B. L. Wu, *Synth. React. Inorg., Met.-Org., Nano-Met. Chem.*, 2015, **45**, 572–580.

35. M.A.Spackman and D. Jayatilaka, *CrystEngComm*, 2009, 11, 19−32.

36. F. L. Hirshfeld, *Theor. Chim.* Acta, 1977, **44**, 129−138.

37. H. F. Clausen, M. S. Chevallier, M. A. Spackman and B. B. Iversen, *New J. Chem.*, 2010, **34**, 193–199.

38. A. L. Rohl, M. Moret, W. Kaminsky, K.Claborn, J. J. McKinnon and B. Kahr, *Cryst. Growth Des.*, 2008, **8**, 4517–4525.

39. A. Parkin, G. Barr, W. Dong, C. J. Gilmore, D. Jayatilaka, J. J. McKinnon, M. A. Spackman and C. C. Wilson, *CrystEngComm*, 2007, **9**, 648–652.

40. M. A. Spackman and J. J. McKinnon, *CrystEngComm*, 2002, **4**, 378–392.

41. P. R. Spackman, M. J. Turner, J. J. McKinnon, S. K. Wolff, D. J. Grimwood, D. Jayatilaka and M. A. Spackman, *J. Appl. Cryst.*, 2021, **54**, 1006–1011.

42. S. J. Clark, M. D. Segall, C. J. Pickard, P. J. Hasnip, M. I. Probert, K. Refson and M. C. Payne, *Z. Kristallogr.*, 2005, **220**, 567−570.

43. J. P. Perdew, K. Burke and M. Ernzerhof, *Phys. Rev. Lett.*, 1996, **77**, 3865−3868.

44. J. P. Perdew, J. A. Chevary, S. H. Vosko, K. A. Jackson, M. R. Pederson, D. J. Singh and C. Fiolhais, *Phys. Rev. B*, 1992, **46**, 6671−6687.

45. D. Vanderbilt, *Phys. Rev. B*, 1990, **41**, 7892−7895.

46. D. D. Koelling and B. N. Harmon, *J. Phys. C: Solid State Phys.*, 1977, **10**, 3107−3114.

47. A. Tkatchenko and M. Scheffler, *Phys. Rev. Lett.*, 2009, **102**, 073005.

48. J. Heyd, G. E. Scuseria and M. Ernzerhof, *J. Chem. Phys.*, 2003, **118**, 8207−8215.

49. B. Delley, *J. Chem. Phys.*, 1990, **92**, 508.

50. B. Delley, *J. Phys. Chem.*, 1996, **100**, 6107.

51. B. Delley, *J. Chem. Phys.*, 2000, **113**, 7756.

52. C. Slabbert and M. Rademeyer, *CrystEngComm*, 2016, **18**, 4555−4579.

53. X. Wang, L. Li, W. L. Duan, J. Tong, H. Y. Guan and F. Guo, *Inorg. Nano-Met. Chem.*, 2016, **46**, 1437−1444.

54. W. Z. Fu, H. Q. Wang, B. Wang, H. J. Duan, X. X. Cui, W. J. Wang, Z. G. Wang, Z. H. Zhang, X. C. Liu and Y. Y. Niu, *Inorg. Nano-Met. Chem.*, 2011, **41**, 272−278.

55. J. J. McKinnon, M. A. Spackman and A. S. Mitchell, *Acta Crystallogr., Sect. B: Struct. Sci.*, 2004, **60**, 627–668.

56. E. H. Rhoderick, Metal Semiconductors Contacts; OxfordUniversity Press: Oxford, U.K., 1978.

57. S. K. Cheung and N. W. Cheung, *Appl. Phys. Lett*.1986,**49**, 85−87.

58. A. A. M. Farag, W. A. Farooq and F. Yakuphanoglu, *Microelectron. Eng.*, 2011, **88**, 2894–2899.

59. Y. S. Ocak, M. Kulakci, T. Kılıçoğlu, R. Turan and K. Akkılıç, *Synth. Met.*, 2009, **159**, 1603–1607.

60. R. Şahingöz, H.A.T.İ. C. E. Kanbur, M. Voigt and C. Soykan, *Synth. Met.*, 2008, **158**, 727–731.

61. Z. Ahmad and M. H. Sayyad,*Phys. E, 2009, **41**, 631–634.

62. A. Jain, P. Kumar, S. C. Jain, V. Kumar, R. Kaur and R. M. Mehra, *J. Appl. Phys.*, 2007, **102**, 094505.

63. P. W. M. Blom and M. J. M. de Jong, M. G. van Munster, *Phys. Rev. B: Condens. Matter Mater. Phys.*, 1997, **55**, R656−R659.

64. S. Sagadevan, *Int. J. Phys. Sci.*, 2013, **8**, 1121–1127.

65. A. Dey, A. Layek, A. Roychowdhury, M. Das, J. Datta, S. Middya, D. Das and P. P. Ray, *RSC Adv.*, 2015, **5**, 36560–36567.

66. T. Mandal, S. Pathak, A.Dey, M. M. Islam, S. K. Seth, A. A. Masum, J. Ortega-Castro, P. P. Ray, A. Frontera and S. Mukhopadhyay, *ACS* Omega, 2019, **4**, 7200–7212.

67. T. Mandal, A. Dey, S. Pathak, M. M. Islam, S. Konar, J. Ortega-Castro, S. K. Seth, P. P. Ray, A. Frontera and S. Mukhopadhyay, *RSC Adv.*, 2019, **9**, 9663.

68. P. Ghorai, A. Dey, P. Brandao, J. Ortega-Castro, A. Bauza, A. Frontera, P. P. Ray and A. Saha, *Dalton Trans.*, 2017, **46**, 13531−13543.

69. S. Halder, A. Dey, A. Bhattacharjee, J. Ortega-Castro, A. Frontera, P. P. Ray and P. Roy, *Dalton Trans.*, 2017, **46**, 11239−11249.

70. S. Halder, A. Dey, J. Ortega-Castro, A. Frontera, P. P. Ray and P. Roy, *J. Phys. Chem. C*, 2016, **120**, 25557−25563.

71. F. Ahmed, J. Ortega-Castro, A Frontera and M. H. Mir, *Dalton Trans.*, 2021, **50**, 270−278.

72. L. S. Xie, G. Skorupskii and M. Dincă, *Chem. Rev.*, 2020, **120**, 8536−8580.

73. P. Thanasekaran, C. H. Su, Y. H. Liu and K. L. Lu, *Coord. Chem. Rev.*, 2021, **442**, 213987.

74. A. Yadav, D. K. Panda, S. Zhang, W. Zhou and S. Saha, *ACS Appl. Mater. Interfaces*, 2020, **12**, 40613−40619.

Appendix

List of Publications

1. Exploration of supramolecular and theoretical aspects of two new Cu(II) complexes: On the importance of lone pair•••π(chelate ring) and π•••π(chelate ring) interactions

   S. Pramanik, S. Pathak, A. Frontera and S. Mukhopadhyay, ***Journal of Molecular Structure, 2022, 1265, 133358.***

2. Syntheses, crystal structures and supramolecular assemblies of two Cu(II) complexes based on a new heterocyclic ligand: insights into C–H•••Cl and π•••π interactions

   S. Pramanik, S. Pathak, A. Frontera and S. Mukhopadhyay, ***CrystEngComm, 2022, 24, 1598-1612.***

3. An experimental and theoretical exploration of supramolecular interactions and photoresponse properties of two Ni(II) complexes

   S. Pramanik, S. Pathak, S. Jana, M. Mondol, A. Frontera, S. Mukhopadhyay, ***New Journal of Chemistry, 2021, 45, 12108–12119.***

4. Chromogenic and fluorogenic "off-on-off" chemosensor for selective and sensitive detection of aluminum (Al^{3+}) and bifluoride (HF_2^-) ions in solution and in living Hep G2 cells: Synthesis, experimental and theoretical studies

   S. Pramanik, S. K. Manna, S. Pathak, D. Mondal, K. Pal and S. Mukhopadhyay, ***New Journal of Chemistry, 2020, 44, 13259–13265.***

5. Revealing the supramolecular features of two Zn(II) complexes derived from a new hydrazone ligand: A combined crystallographic, theoretical and antibacterial studies

   S. Pramanik, A. Hossain, S. Pathak, S. G. Chowdhury, P. Karmakar, A. Frontera, S. Mukhopadhyay, ***CrystEngComm, 2023, DOI: 10.1039/d2ce01445a.***

6. Crystallographic aspects of tetrachlorometallates of group 12 metals [Zn(II), Cd(II) and Hg(II)] with triply protonated 2,4,6 tris-(2-pyridyl)-1,3,5 triazine ligand: special emphasis on theoretical survey of supramolecular and photophysical properties

   S. Pramanik, S. Jana, K. Das, S. Pathak, J. Ortega-Castro, A. Frontera, S. Mukhopadhyay, **Communicated to an *International Journal*, 2023.**

Publications not included in this thesis

7. Investigation of electrical conductance properties, non-covalent interactions and TDDFT calculation of a newly synthesized copper(II) metal complex

   S. Pramanik, S. Konar, K. Chakraborty, T. Pal, S. Das, S. Chatterjee, M. Dolai, S. Pathak, *Journal of Molecular Structure,* **2020, 1206, 127663.**

8. A new strategy to fabricate SnS-SnO2 heterostructure with excellent photoresponse and charge transport properties: Efficient photocatalyst for fast photoreduction of Cr (VI)

   S. Jana, *S. Pramanik*, B. Show, A. Mondal and S. Mukhopadhyay, *Materials Science and Engineering: B*, **2022, 275, 115520.**

9. Rationalization of supramolecular interactions of a newly synthesized binuclear Cu(II) complex derived from 4,4′,6,6′-tetramethyl 2,2′-bipyrimidine ligand through Hirshfeld surface analysis

   S. Pramanik, S. Mukhopadhyay, K. Das, *European Journal of Chemistry*, **2022, 13(4), 393–401.**

10. Synthetic, structural and supramolecular features of a new dithiocyanato-κ-N, κ-S-copper(II) complex: Insights through computational studies

    S. Pramanik, P. Mandal, K. Das, S. Pathak, S. Mukhopadhyay, **Communicated to an *International Journal*, 2023.**

Exploration of supramolecular and theoretical aspects of two new Cu(II) complexes: On the importance of lone pair···π(chelate ring) and π···π(chelate ring) interactions

Samit Pramanik [a], Sudipta Pathak [b], Antonio Frontera [c],*, Subrata Mukhopadhyay [a],*

[a] Department of Chemistry, Jadavpur University, Kolkata 700032, India
[b] Department of Chemistry, Haldia Government College, Debhog, Purba Medinipur 721657, West Bengal, India
[c] Departament de Química, Universitat de les Illes Balears, Crta. de Valldemossa km 7.5, 07122 Palma de Mallorca (Baleares), Spain

A B S T R A C T

An organic ligand, **NL** [4-(1-methylimidazole)-2,6-di(pyrazinyl)pyridine] has been synthesized and characterized by several spectroscopic methods. The ligand (**NL**) was then utilized for the preparation of two complexes, namely, $[Cu(\textbf{NL})(N_3)(H_2O)]ClO_4 \cdot H_2O$ (complex **1**) and $\{[Cu(\textbf{NL})(\mu\text{-}\textbf{NL})NCS]ClO_4\}_n$ (complex **2**). The crystal structures of these complexes have been established by single-crystal X-ray analysis. Complex **2** exhibits a one dimensional (1-D) polymeric chain, whereas complex **1** is a mononuclear one. It is noteworthy that the change in auxiliary ligands exhibit structural variations and different supramolecular behaviors for the present complexes. Mainly, lone pair···π(chelate ring) and π···π(chelate ring) interactions are well investigated in governing the solid state architecture of complex **1** and **2** respectively. Besides, the other non-covalent interactions like π···π stacking, sulphur (lone pair)···π and hydrogen bonding interactions play crucial role in the crystal packing for both the complexes. In complex **1**, a chair-like perchlorate–water tetrameric cluster, $[(ClO_4)_2–(H_2O)_2]^{2-}$ was observed. The aim of this work is to investigate the role of chelate rings in producing supramolecular architectures of both the complexes in the solid state. Theoretical (DFT) calculations including QTAIM and NCI Plot index were carried out to analyze the non-covalent interactions in the solid state for both the complexes.

© 2022 The Author(s). Published by Elsevier B.V.
This is an open access article under the CC BY license (http://creativecommons.org/licenses/by/4.0/)

1. Introduction

Supramolecular chemistry deals with the design, synthesis and self-assembly of well-defined molecular components into tailor-made architectures by using intermolecular interactions [1–3]. Crystal engineers always help to study various intermolecular interactions in the journey from molecule to crystal in the solid state [4–7]. Over the last few years, crystal engineering has matured enough and interplayed between structure and properties of molecules in a programmed way [8–10]. However, finding of new interactions by creative and intellectual way in designing and building crystal architecture is one keen interest in crystal engineering.

Hydrogen bonding has been extensively well studied as it universally exists in both natural and artificial substances [11,12]. Not only hydrogen bonds but also other dispersive interactions

like π···π stacking, anion···π and lone pair···π interactions play a decisive role in nucleation and growth of molecular crystals in recent years [13–21]. Among those, lone pair···π interaction is a significant binding mode which plays a key role in stabilizing the structures of nucleic acids and modulating the recognition of protein DNA and enzyme substrates [22–24]. Recently, the attention has shifted toward more unconventional interactions such as π(arene)···π(chelate ring), π(chelate ring)···π(chelate ring), lone pair···π(chelate ring), C–H···π(chelate ring), etc. interactions which have been proven to have equal or even dominating contributions to molecular crystal formation [25–34]. Chelate rings are recognized to exhibit metallo-aromatic behavior and undoubtedly they can take part in similar interactions to their organic counterparts [35,36]. In the context of supramolecular architecture of coordination compounds, contribution of chelate ring (formed by metal coordination using heterocyclic π-systems) assisted interactions have arrested recent interest of researchers.

As an NNN-tridentate ligand, terpyridine plays an important role in supramolecular chemistry as well in coordination chemistry due to its π stacking ability among themselves and excel-

* Corresponding authors.
  E-mail address: toni.frontera@uib.es (A. Frontera).

lent chelating capability with various metal cations [37]. Terpyridine or their structural analogs show very high binding potentiality towards transition metal ions due to *cis, cis* arrangement of the three nitrogen atoms and dπ−pπ* back bonding of the metal to pyridine rings [38]. However, they always prefer to adopt a planar geometry to achieve maximum conjugation in the complexes [39]. Terpyridine metal complexes have been synthesized and developed rapidly for their potential applications in several fields, for instance, photovoltaic devices [40,41], DNA bindings [42,43], sensors [44,45], photo-sensitizers [46,47], catalysis [48,49], metalorganic framework (MOF) construction [50,51], and many more [52]. Recently, increasing attention has been paid to the synthesis of 4′-substituted terpyridine complexes with potential applications in accessing new classes of functional materials possessing photo-physical and electrochemical properties [53–56]. As terpyridines are generally neutral during complex formation, ancillary ligands like pseudo halides (azido, thiocyanato, etc.) are often employed to sustain electrical neutrality. Azido (N_3^-) and thiocyanato (SCN^-) pseudo halide ions have also been extensively used as bridging ligands in the construction of coordination compounds due to their diversity of bonding modes with 3d metal complexes [57–62]. As a terminal ligand, the coordination mode of SCN^- depends on the electronic nature and oxidation state of the metal ion [63]. Besides, other factors like steric effect, type of solvent, noncoordinated ions and even electronic nature of the auxiliary ligands can influence the coordination mode of the thiocyanato ligand, particularly when the metal ion has intermediate hard−soft acid character [64]. Azido and thiocyanato copper(II) complexes with trigonal bipyramidal (TBP) or square pyramidal (SP) geometry have already gained much attention for the last few years but, there still remains much more work to be explored. Among the investigated metals, Cu(II) containing complexes have received increasing attention due to their promising applications in various fields such as catalysis, energy harvesting devices, medicinal chemistry and in related areas in the recent past [65–72]. After iron and zinc, copper is the third most abundant transition metal in the human body and plays an important role in hemopoiesis, metabolism, growth and immune system [73,74]. Most importantly, the reversible change of the oxidation state of Cu(I)/Cu(II) couple under physiological conditions has promoted the development of metal complexes with an active redox chemistry within cancerous cells [75,76]. Besides, compared to other common metal ions, Cu(II) ion exhibits high binding constant with various ligands in chemical and biological systems [77,78]. Keeping all these factors in mind, two new Cu(II) complexes have been synthesized based on 4-(1-methylimidazole)-2,6-di(pyrazinyl)pyridine (**NL**) with auxiliary ligands azido (for complex **1**) and thiocyanato (for complex **2**) in aqueous medium (Scheme S1). Both the complexes adopt distorted square pyramidal (SP) geometry where the title ligand, (**NL**) acts as an NNN-tridentate ligand. In both the complexes, the ligand (**NL**) coordinates the Cu(II) ion through three coplanar ligating sites involving one pyridyl nitrogen atom (N3) and two pyrazinyl nitrogen atoms (N5 and N6) forming two five-membered chelate rings (Scheme S1). The metallo-aromatic nature of the chelate rings gives rise to the possibility of alternative π-systems which play an important role in producing various supramolecular architectures for both the complexes in the solid state. Interestingly, a dimer is shaped by two symmetrically equivalent lone pair⋯π(chelate ring) interactions between lone pair on azide nitrogen atom (N8) and Cg(2) chelate ring in complex **1**. From the structural database survey, it is evident that the lone pair⋯π(chelate ring) interactions involving halogen atoms (Cl, Br, I) are common but to the best of our knowledge the engagement of pnictogen atom like nitrogen in lone pair⋯π(chelate ring) interaction is comparatively less familiar [127–131]. In complex **1**, the perchlorate anion is involved in the formation of a tetrameric anion−water cluster, $[(ClO_4)_2-(H_2O)_2]^{2-}$,

which is less frequent. To our knowledge, a few perchlorate−water tetrameric clusters have been characterized in the solid state [79–81]. For complex **2**, the influence of π⋯π(chelate ring) and sulphur(lone pair)⋯π interactions have been well established in the crystal packing. Finally, the present work utilizes DFT calculations and several computational tools (QTAIM and NCI Plot) to analyze the noncovalent interactions focusing on lone pair⋯π(chelate ring) and π⋯π(chelate ring) interactions in stabilizing the solid state architectures of both the complexes. We have also evaluated energetically how the presence of the perchlorate−water cluster influences the crystal packing of complex **1** in the solid state.

2. Experimental sections

2.1. Materials and apparatus

All the chemical reagents (analytical grade) and solvents (spectroscopic grade) were purchased from commercial suppliers and used without any further purification. Freshly boiled double distilled water was used throughout the synthetic procedure and all the reactions were carried out under aerobic conditions. Elemental analyses (C, H and N) were performed using a PerkinElmer 2400 Series-II CHN analyzer, USA, elemental analyzer. ESI mass spectra were obtained from a Water HRMS model XEVO-G2QTOF#YCA351 spectrometer. ^{1}H NMR and ^{13}C NMR spectra were obtained from Bruker spectrometer (300 MHz) with CDCl$_3$ solvent using trimethylsilane (TMS) as an internal standard. Fourier transform infrared (FT-IR) spectra were recorded on a Perkin Elmer LX-1 FT-IR spectrophotometer (4000−400 cm^{-1}) by using a modern diamond attenuated total reflectance (ATR) accessory method.

2.2. Syntheses

2.2.1. Synthesis of 4-(1-methylimidazole)-2,6-di(pyrazinyl)pyridine [NL]

Acetylpyrazine (0.305 g, 2.5 mmol) was added into 30 mL ethanolic solution of 1-methyl imidazole-2-carboxaldehyde (0.11 g, 1 mmol). 3 mL of 1 (M) aqueous solution of NaOH was added drop wise into the reaction mixture at room temperature (Scheme 1). Then 5 mL aqueous NH$_3$ (35%) solution was discharged into the basic solution at a time. The reaction mixture was then refluxed for 3 h. After completion of the reaction, solution was cooled at room temperature. A light-yellow solid formed which was collected by filtration and washed repeatedly with coldwater and dried in air. The desired product was obtained with good yield and acceptable purity, Yield 0.214 g (68%). Anal. calc. for C$_{17}$H$_{13}$N$_7$, C 64.75, H 4.16, N 31.09. Found: C 64.12, H 3.89, N 30.79%. ^{1}H NMR (300 MHz, CDCl$_3$): δ (ppm) = 9.85 (s, 2H), 8.83 (s, 2H), 8.65 (s, 4H), 7.24 (s, 1H), 7.09 (s, 1H), 3.99 (s, 3H) (Fig. S1). ^{13}C NMR (75 MHz, CDCl$_3$): δ (ppm) =154.50, 150.46, 144.93, 143.70, 143.48, 140.37, 129.60, 124.24, 120.55, 35.17 (Fig. S2). Main FT-IR absorptions, (KBr, cm^{-1}): 1980(s), 1606(vs), 1570(vs), 1519(s), 1464(s), 1456(s), 1419(s), 1371(vs), 1292(s), 1257(s), 1224(s), 1120(vs) (Fig. S3). ESI-MS: *m/z* 316.12, calcd. for [C$_{17}$H$_{13}$N$_7$ + H]$^+$ 316.13 (Fig. S4).

2.2.2. Synthesis of [Cu(NL)(N$_3$)(OH$_2$)]ClO$_4$·H$_2$O(complex 1)

An aqueous suspension (15 mL) of the ligand, **NL** (0.0315 g, 0.1 mmol) was added drop wise to 15 mL of aqueous Cu(ClO$_4$)$_2$·6H$_2$O (0.0370 g, 0.1 mmol) solution with constant stirring. An aqueous solution (5 mL) of NaN$_3$ (0.0065 g, 0.1 mmol) was added and stirred for 3 h (Scheme 2). Then the solution was filtered and the filtrate was left for slow evaporation without any disturbance. After one-week, deep green X-ray quality crystals of **1** were isolated (yield: 68%). Solubility of the complex was checked in some common solvents for further applications and found to
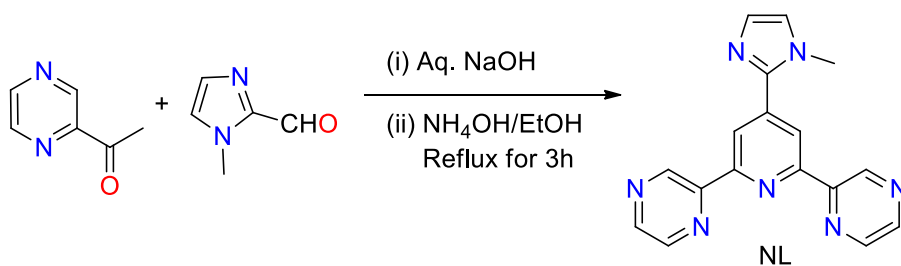
Scheme 1. Synthetic route for the ligand, **NL**.
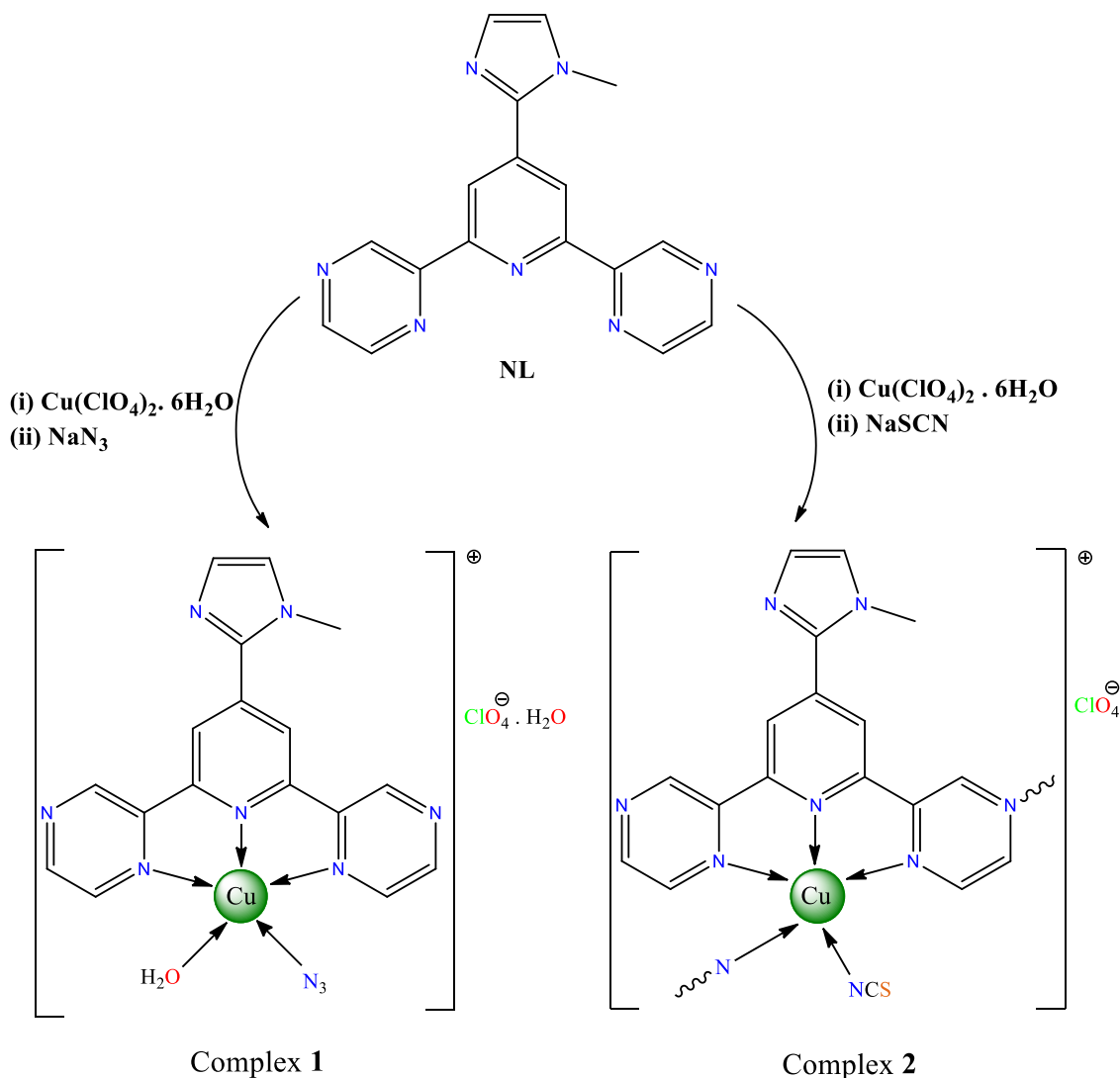
Scheme 2. Schematic representations of the synthesis of complex **1** and **2**.

be insoluble in water and methanol whereas completely soluble in acetonitrile, DMSO and DMF. Anal. calc. for $C_{17}H_{17}CuN_{10}ClO_6$: C, 36.70; H, 3.08; N, 25.17. Found: C, 36.63; H, 2.99; N, 25.13%. Main FT-IR absorptions, (KBr, cm^{-1}): 3543(w), 3469(s), 3229(w), 3139(vs), 3102(s), 2050(vs), 1614(vs), 1590(s), 1557(s), 1496(s), 1470(vs), 1433(s), 1408(s), 1340(s), 1299(s), 1283(s), 1227(s) (Fig. S5).

2.2.3. Synthesis of {[Cu(NL)(μ-NL)NCS]ClO₄}ₙ (complex 2)

An aqueous suspension (15 mL) of the ligand, **NL** (0.0315 g, 0.1 mmol) was added drop wise to 15 mL aqueous Cu(ClO₄)₂·6H₂O (0.0370 g, 0.1 mmol) solution at stirring condition. An aque-

ous solution (5 mL) of NaSCN (0.0081 g, 0.1 mmol) was added and stirred for 4 h (Scheme 2). Then the solution was filtered and the filtrate was left undisturbed for slow evaporation. Two weeks later, deep brown X-ray quality crystals of **2** were obtained (yield: 63%). The complex **2** was insoluble in water and methanol, partly soluble in acetonitrile and completely soluble in DMSO as well as in DMF. Anal. calc. for $C_{18}H_{13}CuN_8SClO_4$: C, 40.30; H, 2.44; N, 20.89. Found: C, 40.25; H, 2.39; N, 20.85%. Main FT-IR absorptions, (KBr, cm^{-1}): 3218(s), 3114(bs), 2100(vs), 2047(vs), 1611(s), 1599(s), 1554(s), 1497(s), 1470(s), 1423(s), 1406(s), 1332(vs), 1298(s), 1288(s), 1225(s) (Fig. S6).

(Caution! Salts of perchlorate and azide are potentially explosive. Only small amounts of materials should be prepared and to be handled with extreme care).

2.3. X-ray crystallography analysis

Single crystal X-ray data were collected by using a Bruker SMART APEX II CCD area detector equipped with a graphite monochromated Mo Ka radiation ($\lambda = 0.71073$ Å) source in φ and ω scan mode at 296 K for both the complexes. Cell parameter refinement and data reduction for both the complexes were carried out using a Bruker SMART APEX II instrument and Bruker SAINT Software [82]. The crystal structures of both the complexes were solved by SHELXT-2014/5 and refined by full-matrix least squares on F^2 techniques using the SHELXL-2016/6 crystallographic software package [83,84]. The CIFs have been deposited with CCDC No. 2096470 (complex **1**) and CCDC No. 2096471 (complex **2**). Selected crystal structure refinement parameters for **1** and **2** are given in Table S1. The important bond lengths and bond angles are included in Tables S2 and S3, respectively for the title complexes.

2.4. Computational methods

The non-covalent interactions were analysed energetically using Gaussian-16 [85] at the PBE0-D3/def2-TZVP level of theory. The binding energies have been corrected using the Boys and Bernardi counterpoise method [86]. The Grimme's D3 dispersion correction has been also used in the calculations [87]. To evaluate the interactions in the solid state, the crystallographic coordinates were used and only the position of the hydrogen bonds has been optimized. This methodology [88,89] and level of theory [90–100] (functional and basis set) have been previously used to analyze non-covalent interactions in the solid state. The interaction energies were estimated by calculating the difference between the energies of the isolated monomers and the ones of their assembly. For the calculations, the monomeric Cu(II) species were considered as doublets (one unpaired electron) and the dimers as triplets (two unpaired alpha electrons). The NCI plot [101] isosurfaces have been used to characterize non-covalent interactions. They correspond to both favorable and unfavorable interactions, as differentiated by the sign of the second density Hessian Eigen value and defined by the isosurface color. The color scheme is a red-yellow-green-blue scale with red for ρ^+_{cut} (repulsive) and blue for ρ^-_{cut} (attractive).

3. Results and discussion

3.1. Synthesis and IR spectroscopic characterization

The copper(II) complexes **1** and **2** were prepared by using newly synthesized 4-(1-methylimidazole)-2,6-di(pyrazinyl)pyridine [**NL**] moiety as the main ligand with different auxiliary ligands (azide anion for **1** and thiocyanato anion for **2**) at room temperature in aqueous medium (Scheme 2). Strategically 1:1:1 molar ratio was maintained to synthesize the mixed ligand complexes (to avoid bis-terpyridine complexes) having product stoichiometry Cu(II): **NL**: N_3^- = 1:1:1 for complex **1** and Cu(II): **NL**: SCN^- = 1:1:1 for complex **2**. Interestingly, when sodium azide (NaN_3) was used as the auxiliary ligand in combination with the **NL** ligand, the formation of the mononuclear complex **1** was observed, while similar reaction condition with sodium thiocyanate ($NaSCN$) results in the 1D coordination polymeric complex **2**. Both the complexes were isolated as air stable green colored crystalline solids in good yields (68% for **1** and 63% for **2**). Hence, the synthesis presented herein composed of copper(II) perchlorate as a metal source and **NL** as a primary ligand, together with easily accessible and cheap auxiliary ligands (N_3^- and SCN^-) in a simple one-

pot synthetic procedure for engineering of diverse metal-organic assemblies in organic-solvent-free medium.

The molecular structures of the title complexes have been established by single crystal X-ray analysis and supported by IR spectroscopy. The IR spectrum of complex **1** shows typical $\nu(OH)$ vibrations in the $3543-3229$ cm^{-1} range for both coordinated and non-coordinated water molecules. Besides, the complex **1** displays a very sharp $\nu_{as}(N_3)$ band with maximum at 2050 cm^{-1}, while that at 1340 cm^{-1} is presumably associated with the $\nu_s(N_3)$ vibration. The presence of auxiliary NCS ligand in complex **2** is confirmed with the detection of a very intense $\nu_{as}(CN)$ band at 2047 cm^{-1} with a shoulder at 2100 cm^{-1}, which are typical for the terminal N-bonded isothiocyanate moieties [57,102–105]. In addition, the $\nu(CH)$ vibrations are detected in the range of $3218-3102$ cm^{-1} for both the complexes. The observed stretching frequencies for $\nu_{as}(N_3)$ and $\nu_{as}(CN)$ in our complexes (**1** and **2**) are in good agreement with some reported Cu(II) complexes which are summarized in Table S4.

3.2. Structural description of complex 1

The asymmetric unit of complex **1** with the atom numbering scheme is shown in Fig. 1. The formula unit of complex **1** shows one monomeric cationic $[Cu(C_{17}H_{13}N_7)(N_3)(H_2O)]^+$ unit, one non-coordinated perchlorate anion and one non-coordinated water molecule. The complex crystallizes in a triclinic system with the space group $P\bar{1}$ and its unit cell contains two formula units. The coordination mode around the metal center can be best described as a distorted square pyramid [τ value [106] is 0.0213 (ideally 0 for perfect square pyramidal geometry and 1 for trigonal bipyramidal geometry), eq S1] where the equatorial plane is shaped by the three pyrazinyl nitrogen atoms (N3,
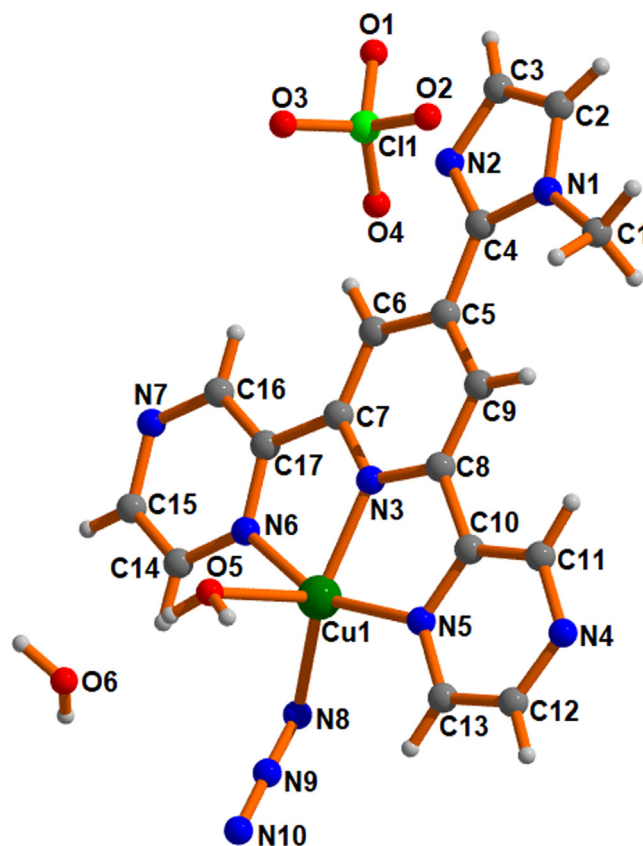

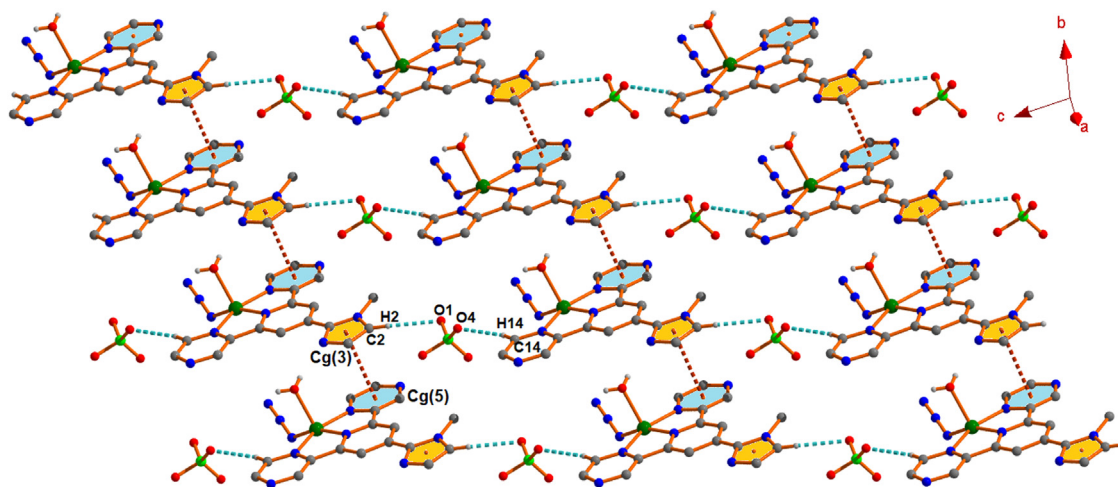**Fig. 1.** Asymmetric unit of complex **1**.

Fig. 2. Perspective view of the formation of a 2-D architecture through $\pi \cdots \pi$ stacking and C–H···O hydrogen bonding interactions in complex **1**.
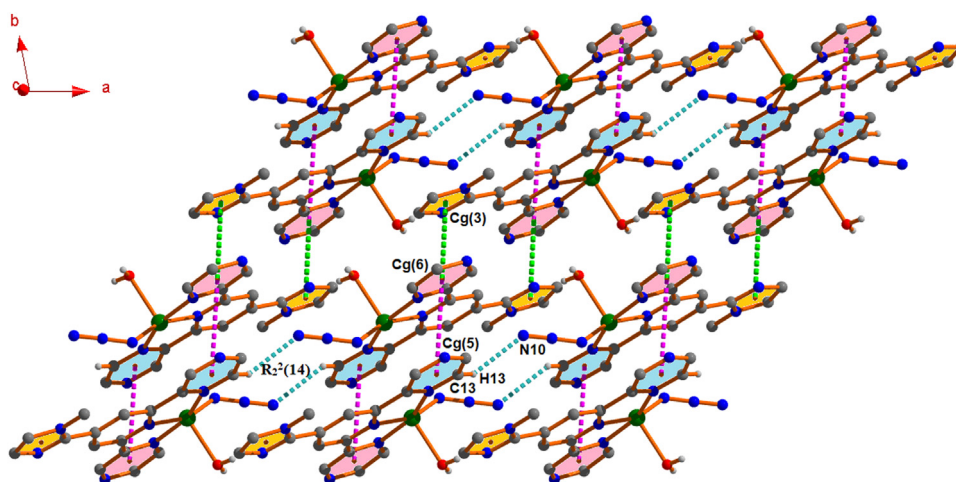

Fig. 3. Perspective view of 2-D supramolecular network through $\pi \cdots \pi$ stacking and C–H···N hydrogen bonding interactions in complex **1**.

N5 and N6) of the ligand (**NL)** and one nitrogen atom (N8) of azide anion. The apical position is occupied by one oxygen atom (O5) of a water molecule. Here the ligand (**NL**) is able to bind the Cu(II) ion to produce two five-membered chelate rings, (Cu1/N3/C7/C17/N6) and (Cu1/N3/C8/C10/N5) having bite angles [N3−Cu1−N6 = 79.28(9)° and N3−Cu1−N5 = 79.42(8)°] respectively. The average distance of Cu−N bonds in the equatorial plane is 1.988 Å [Cu1−N5 = 2.042(2) Å, Cu1−N6 = 2.044(2) Å, Cu1−N3 = 1.9431(19) Å and Cu1−N8 = 1.923(3) Å]. The axial Cu−O bond is comparatively longer [Cu1−O5 = 2.224(2) Å] than the equatorial Cu−N bonds and is expected as the axial bond utilizes more 'p' character of the orbital in forming the bond, which makes the axially coordinated water oxygen atom more electronegative [107]. The Cu(II) ion is deviated by a distance of 0.259 Å towards the axial water oxygen atom (O5) from the equatorial plane (N3, N5, N6 and N8). The dipositive charge on the metal center is stabilized by one coordinated azide anion and one non-coordinated perchlorate anion.

The solid-state structure of complex **1** is stabilized through the combination of C−H···N, C−H···O, O−H···N, O−H···O hydrogen bonds along with $\pi \cdots \pi$ stacking and lone pair···π (chelate ring) interactions (Table S5 and S6). In the first architecture (Fig. 2), the monomeric unit of complex **1** propagates to produce a 1-D polymeric chain through a $\pi \cdots \pi$ interaction (Table S6) between Cg(3) of one unit with Cg(5) of the other unit with a ring separation dis-

tance of 3.4928(19) Å. Now, perchlorate ions connect these parallel 1-D chains through C2−H2···O1 (169°) and C14−H14···O4 (154°) hydrogen bonding interactions at (-x, 1-y, 2-z) and (1-x, 1-y, 1-z) respectively; thus leading to the formation of a 2-D architecture in the *bc*-plane.

A different 2-D layer is generated through $\pi \cdots \pi$ stacking and C−H···N hydrogen bonding interactions (Fig. 3) for complex **1**. The self-complementary nature leads the molecules to form a dimer through $\pi \cdots \pi$ interaction between Cg(5) and Cg(6) of two different units. The inter-planar spacing between Cg(5) and Cg(6) is 3.8956(18) Å. Interconnection of the dimers through another self-complementary Cg(3)−Cg(6) interaction ($\pi \cdots \pi$ stacking) which leads to form an infinite chain along the [010] direction. The separation distance between Cg(3) and Cg(6) is 3.642(2) Å. Due to the self-complementary nature, the parallel chains are again interlinked through weak C13−H13···N10 hydrogen bond by generating a $R_2^2(14)$ ring motif. Here, the aromatic fragment (C13−H13) of one unit acts as donor to the azide nitrogen atom (N10) of adjacent unit at (2-x, 2-y, 1-z) with an angle of 130° All these interactions are cumulatively associated to extrapolate the dimensionality from 1-D to 2-D in the *ab*-plane (as shown in Fig. 3).

A comprehensive analysis exhibits a dimeric distribution (shown in Fig. 4) that is formed by two symmetrically equivalent lone pair···π (chelate ring) interaction in complex **1**. Here, two monomeric units are arranged almost in opposite orienta-
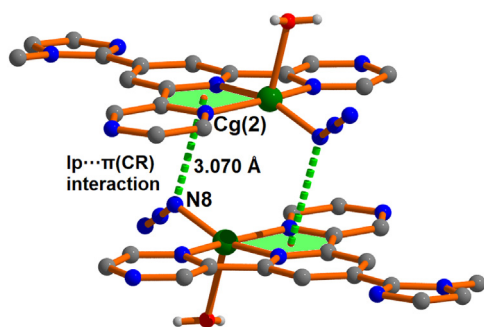
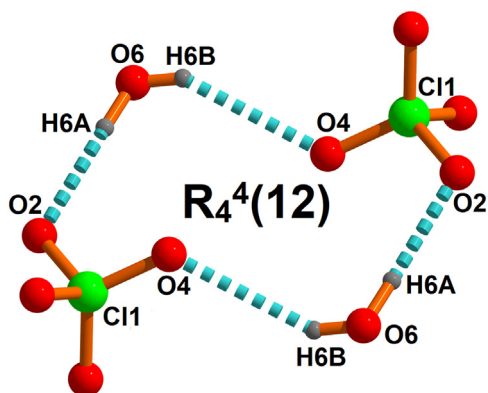**Fig. 4.** Dimeric distribution in complex **1** through lone pair···π(chelate ring) interactions.

Fig. 5. Formation of anion–water cluster by strong O–H···O hydrogen bonding interactions in complex **1**.

tion one above the other to achieve a self complementary lone pair···π(chelate ring) interaction between lone pair on azide nitrogen atom (N8) and Cg(2) chelate ring (Cu1/N3/C8/C10/N5) having a shortest separation distance of 3.070 Å. The Cu···Cu separa-

tion in this dimeric integrity is 3.917 Å which suggests that there may be some type of weak metal···metal interaction to stabilize this dimeric form [108].

The solvent water molecules not only tie up themselves for the formation of clusters but also suitable anions participate in the assembly process to satisfy donor−acceptor balance and thus construct anion−water clusters [109,110]. It is worth mentioning that, the behavior of hydrated anion is quite different from that of bare anion or anion in nonpolar media. Thus, studies of anion−water clusters are vitally important in understanding the hydration phenomena of both organic and inorganic anions in nature as well as in biochemistry. In complex **1**, a chair-like perchlorate–water tetrameric cluster, $[(ClO_4)_2–(H_2O)_2]^{2-}$, is decorated due to the self-complementary nature of intermolecular hydrogen bonding interactions between two free water molecules and two perchlorate anions (as depicted in Fig. 5). Here, the non-coordinated water oxygen atom O(6) acts as double donor to the oxygen atoms O(2) and O(4) of perchlorate ion in the complex at (169°) and (153°) respectively; thus forming a $R_4^4(12)$ ring motif (Table S5). It was well established that the lower H···A separation and the D−H···A angle close to 180° indicate the stronger hydrogen bonding interaction. Here, the O6−H6A···O2 interaction is relatively stronger than that of O6−H6B···O4 interaction as the former interaction has lower H···O distance (2.0 Å) compared to other (2.23 Å) and O−H···O angle close to 180°. The O···O separation distances within the tetramer in the range of 2.839(6)–3.006(8) Å, which is longer than the value in ice I_c (2.75 Å) and ice I_h (2.759 Å), but can be compared with the corresponding values observed in liquid water (2.854 Å) [111,112]. Interestingly, the perchlorate–water cluster helps in growth of the molecular crystal by filling the void spaces present in complex **1** (as shown in Fig. 6). We have studied the mutual influence of the hydrogen bonding interactions in the perchlorate–water cluster by means of QTAIM analysis (shown in Fig. 16).

The lone pair···π(chelate ring) along with π···π stacking and hydrogen bonding interactions play a decisive role in building the supramolecular arrangement (Fig. 6). The dimeric units (as de-

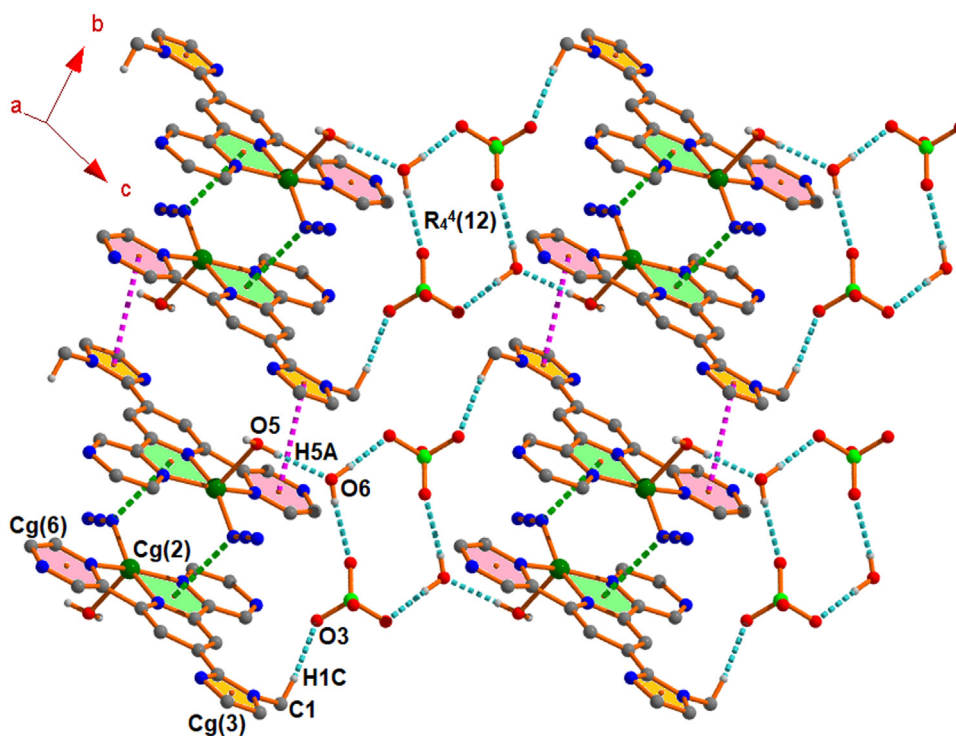**Fig. 6.** Perspective view of 2-D arrangement incorporating π···π, lone pair···π(chelate ring) and hydrogen bonding interactions in complex **1**.
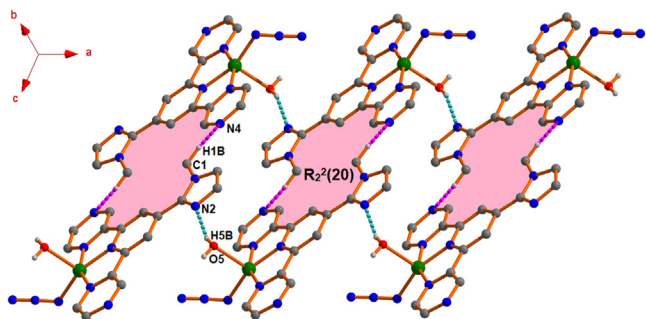
Fig. 7. Formation of 1-D tape by hydrogen bonding interactions in complex **1**.

picted in Fig. 4) are interlinked by a self complementary $\pi \cdots \pi$ interaction between Cg(3) and Cg(6) of two different units leading the formation of a 1-D chain along [010] direction. The separation distance between Cg(3) and Cg(6) ring centriods is 3.642(2) Å (Table S6). Now, these 1-D parallel chains are further connected by the anion–water cluster (shown in Fig. 5) to generate the 2-D arrangement in the *bc*-plane. Here, the water-anion clusters are interconnected with the dimeric units by the self complementary strong O5−H5A⋯O6 (175°) and comparatively weak C1−H1C⋯O3 (158°) hydrogen bonding interactions (Table S5) as shown in Fig. 6.

Two monomeric units of complex **1** are interconnected by the self complementary C1−H1B⋯N4 (133°) hydrogen bonding interactions (Table S5) to form another dimer having $R_2^2(20)$ ring motif (Fig. 7). The dimeric units are further interlinked through the self complementary O5−H5A⋯N2 [165(5)°] hydrogen bonding interactions where coordinated water oxygen atom (O5) acts as donor to the imidazole nitrogen atom (N2) in the molecule at (1 + *x*, y, z). Repetition of this $R_2^2(20)$ ring motif along [100] direction leads the molecules to generate a 1-D tape as shown in Fig. 7.

3.3. Structural description of complex 2

The complex **2** is a coordination polymer (Fig. 8) and the asymmetric unit of the complex with the atom numbering scheme is depicted in Fig. 8. In this polymeric chain the asymmetric units are connected along the (010) direction through pyrazine nitrogen atom (N4) of the second ligand (**NL**). Single-crystal X-ray diffraction study shows that the complex **2** adopts a monoclinic system with the space group $P2_1/c$ and its unit cell contains four formula units. In the complex, the central Cu(II) ion is situated in a distorted square pyramidal geometry (τ = 0.1218, eq S1) where the equatorial plane is formed by the three pyrazinyl nitrogen atoms (N3, N5 and N6) of the ligand (**NL**) and one nitrogen atom (N8) of thiocyanate anion. The apical position is occupied by another nitrogen atom (N4)

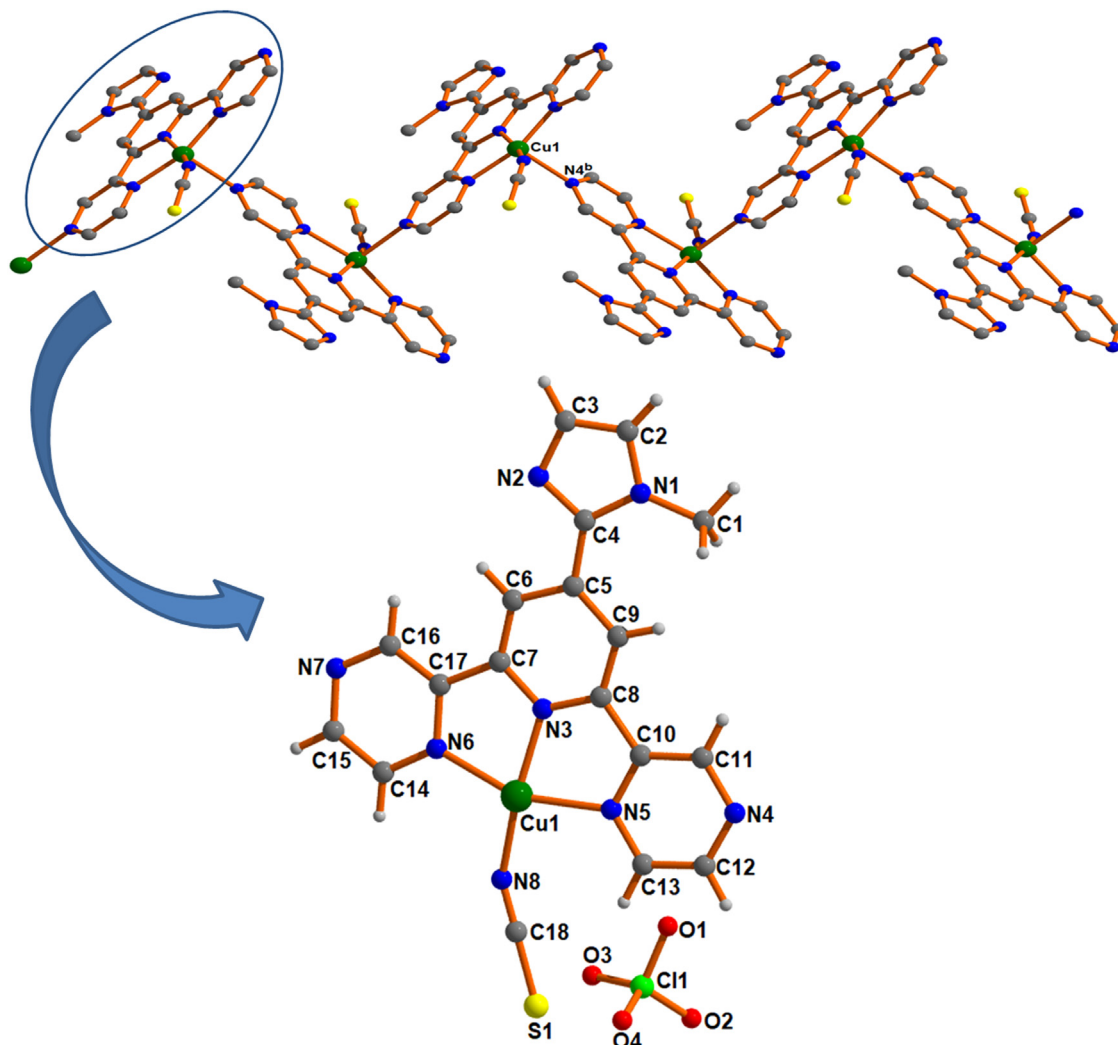**Fig. 8.** One-dimensional (1-D) zigzag polymeric chain along the [010] direction and the asymmetric unit of complex **2**.
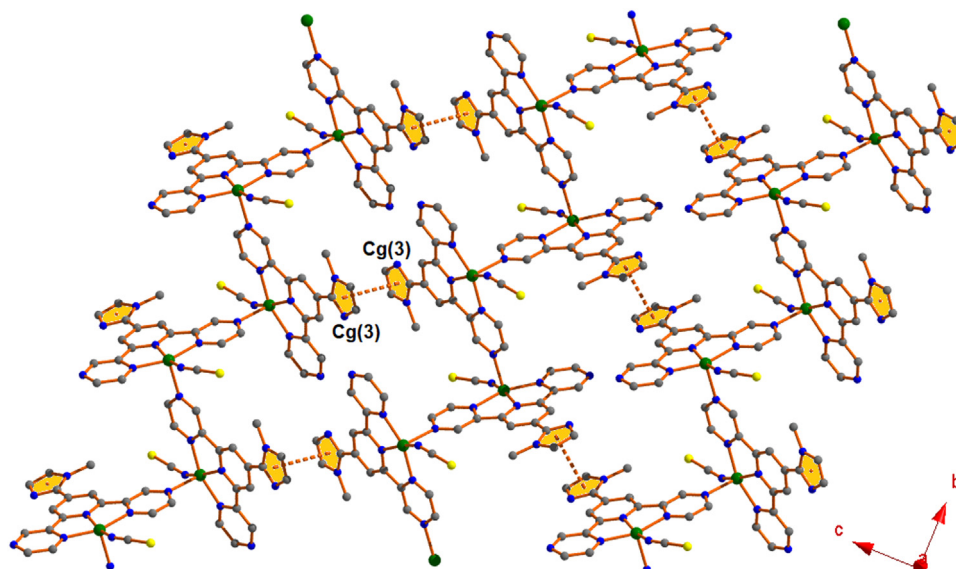
Fig. 9. Perspective view of 2-D layer generated through $\pi\cdots\pi$ interactions in complex **2** (aromatic hydrogen atoms have been omitted for clarity).
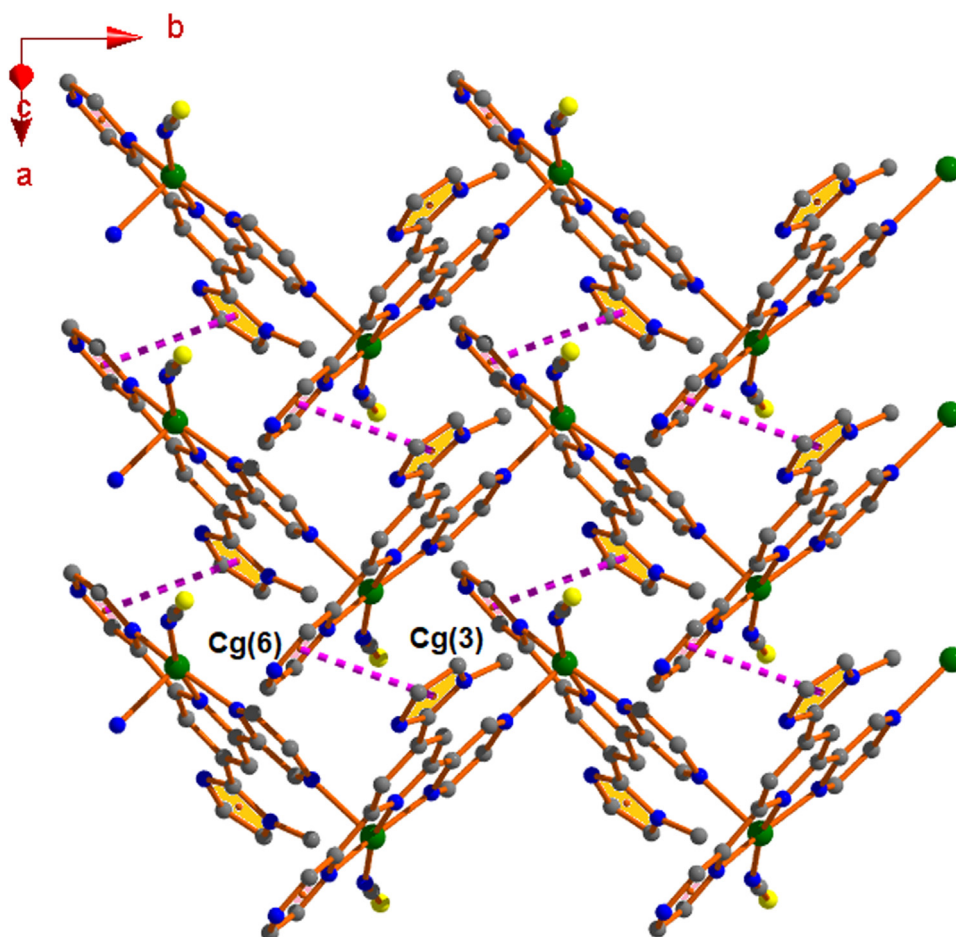
Fig. 10. Formation of a 2-D assembly through $\pi\cdots\pi$ interactions in complex **2** (aromatic hydrogen atoms have been omitted for clarity).

of the second **NL** ligand. Here, two five-membered chelate rings [(Cu1/N3/C7/C17/N6) and (Cu1/N3/C8/C10/N5)] are formed with bite angles [N3−Cu1−N6 = 80.11(9)° and N3−Cu1−N5 = 79.08(8)°] respectively. The average distance of Cu−N bonds in the equatorial plane is 1.996 Å [Cu1−N6 = 2.050(2) Å, Cu1−N3 = 1.932(2) Å, Cu1−N5 = 2.066(2) Å and Cu1−N8 = 1.937(3) Å]. The Cu(II) ion

is deviated by a distance of 0.204 Å towards the apical nitrogen atom (N4^b, b = 1 − x, 1/2 + y, 3/2 − z) from the equatorial plane (N3, N5, N6 and N8). The axial Cu−N bond is comparatively larger [Cu1−N4^b = 2.277(2) Å] than the other equatorial Cu−N bonds likely due to the more 'p' character of the orbital involved in the axial bond. The electrical charge on the metal center is taken care

Fig. 11. Perspective view of 2-D architecture through sulphur(lone pair)···π interactions in complex **2** (aromatic hydrogen atoms have been omitted for clarity).
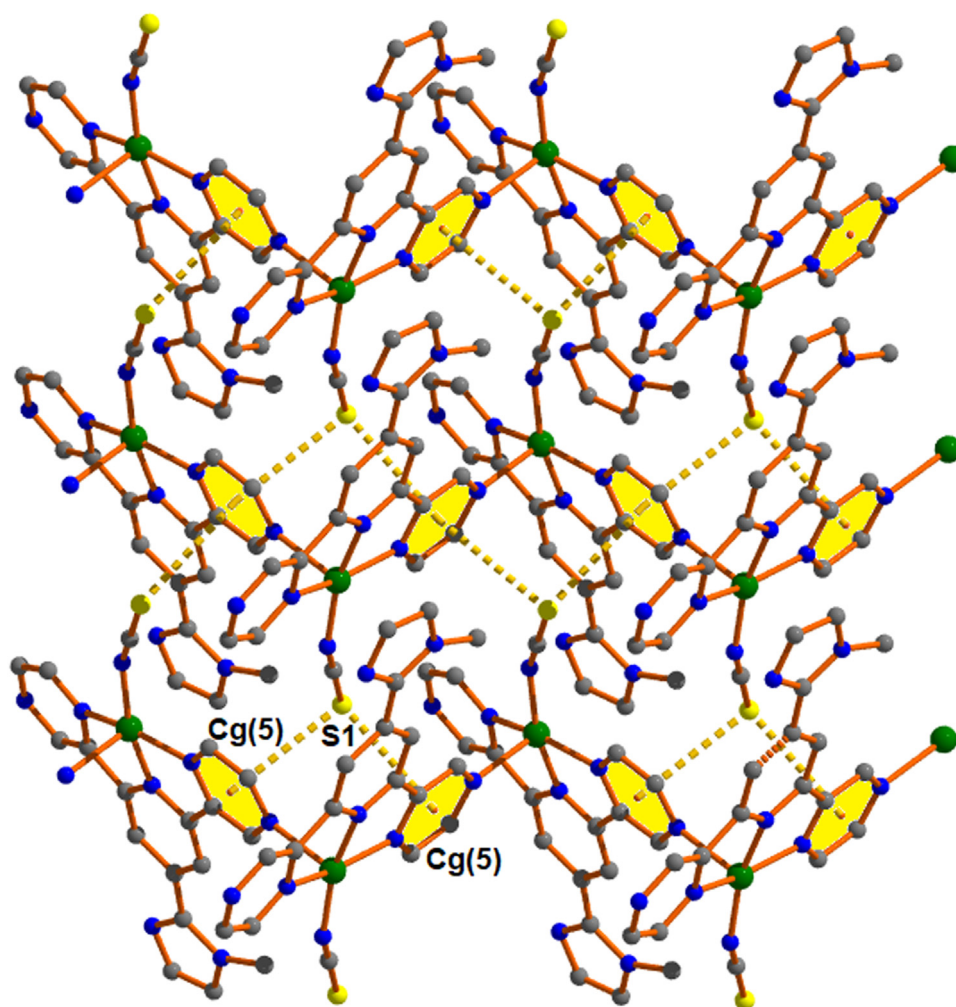
by one coordinated thiocyanate ion and one non-coordinated perchlorate ion.

In the solid state, the complex **2** is stabilized through C−H···O hydrogen bonds in addition with π···π stacking, π···π (chelate ring), anion···π and lone pair···π interactions (Tables S5-S7). The parallel 1-D zigzag chains are interlinked through face to face π···π interaction to build a 2-D layered structure (Fig. 9) in the bc-plane. The π···π interaction was executed between Cg(3) of one complex unit and Cg(3) of the other unit with the shortest centroid–centroid distance of 3.3969(19)Å (Table S5).

Fig. 10 shows that the 1-D parallel chains are interlinked through the self-complementary π···π stacking interactions between Cg(3) of one complex unit and Cg(6) of the other unit to form another two-dimensional (2-D) assembly in the ab-plane having an inter-planar spacing of 3.6803(18) Å (Table S6).

Again, the 2-D assembly is further stabilized by the lone pair···π interactions (shown in Fig. 11). The sulfur atom (S1) approaches (bifurcated) towards π-faces of two different Cg(5) units at ($-1 + x$, y, z) and (-x, 1/2 + y, 3/2-z) with angles of 110.53(11)° and 95.28(10)° respectively (Table S7). For having a good sulphur(lone pair)···π interaction, the S···π distance should be less than the sum of their van der Waals radii (3.70 Å). Here, the average distance between sulfur atom (S1) and Cg(5) centroid is 3.543 Å; thus suggesting a significant lone pair···π interaction. Though the sulphur(lone pair)···π interaction is comparatively less frequent but it has been well appreciated in biological and model systems [113–116].

In the Fig. 12, the complex units of **2** (extracted from the polymeric chain) ensure to propagate a 1-D polymeric chain through π···π (chelate ring) interaction (shown by orange dotted lines) between Cg(3) of one unit and Cg(1) (chelate ring) of the adjacent unit separated at a distance of 3.4980(16) Å (Table S6). The parallel chains are interconnected through C11−H11···O3 (119°) hydrogen bond (shown in aqua dotted line) and anion···π interaction (shown in pink dotted line). The said anion···π interaction involves one oxygen atom (O1) of the ClO_4^- anion and Cg(6) of the adjacent complex unit at (1-x, $-1/2 + y$, 3/2-z) with a shortest separation distance of 3.022(3) Å. Therefore, the influence of the unconventional π···π (chelate ring) interactions along with anion···π and C−H···O hydrogen bonding interactions is responsible in building the extended 2-D architecture in the ab-plane (Fig. 12).

3.4. Theoretical study

PBE0-D3/def2-TZVP calculations have been used to study the chelate ring (CR) interactions described above that are relevant for the crystal packing of compound **1**. Compound **2** is a polymer and its solid-state architecture is basically governed by coordination bonds. In this case the theoretical study is limited to the characterization of the interactions described above in Fig. 12 using the NCI plot index analysis.

The molecular electrostatic potential (MEP) surface of compound **1** (including the counter ion and water molecule) has been firstly computed to analyze the most nucleophilic and electrophilic
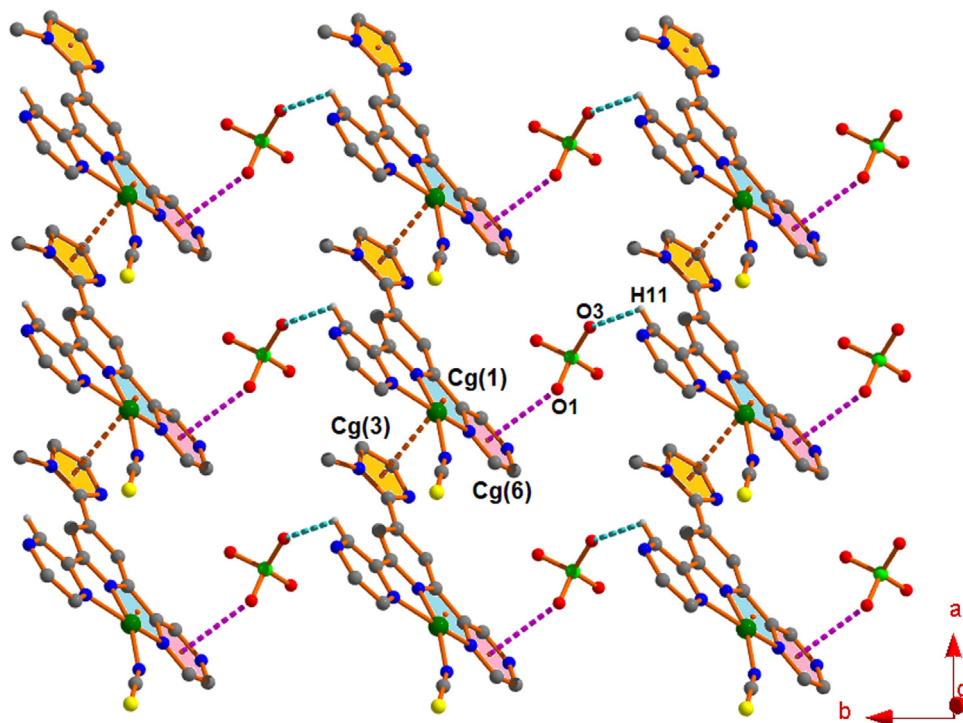
Fig. 12. Perspective view of 2-D architecture incorporating $\pi\cdots\pi$, anion$\cdots\pi$ and C–H$\cdots$O hydrogen bonding interactions in complex **2** (other aromatic hydrogen atoms have been omitted for clarity).

parts of the molecules. As expected, the most negative MEP values are located at the perchlorate anion (−74 kcal/mol). The MEP values at the N-atoms of the azido ligand are also negative (−15 kcal/mol). The maximum MEP value (+75 kcal/mol) is located in a cleft that is under the influence of two aromatic H-atoms and one aliphatic H-atom (methyl group of the imidazole ring). The MEP values over the aromatic rings of the ligand are also large and positive, ranging from +21 to +47 kcal/mol. The MEP value over the chelate ring that is more distant from the perchlorate anion is also large and positive (+43 kcal/mol), thus adequate for interacting with electron rich atoms (as shown in Fig. 13).
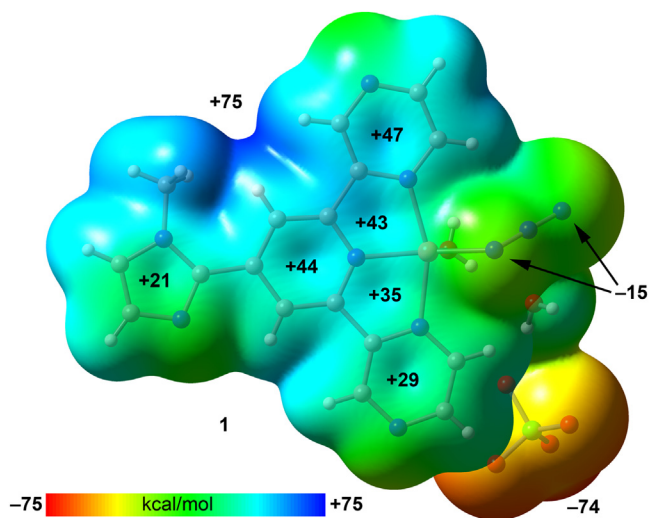
Fig. 13. MEP surface (isosurface 0.001 a.u.) of compound **1** at the PBE0-D3/def2-TZVP level of theory. The MEP values at selected points of the surfaces are given in kcal/mol.

The ion-pair nature of compound **1** anticipates a dominant role of electrostatic effects in its crystal packing. This is supported by the MEP surface analysis which shows the maximum and minimum MEP values located at the cationic and anionic moieties, respectively. In general, pure electrostatic forces are very strong and non-directional. Therefore, the final orientation of the cations and anions in the solid state is often influenced by other forces that are weaker but able to tune the final geometry of the assemblies found in their crystal structure.

As aforesaid in the structural description of **1** (Fig. 4), this compound forms interesting self-assembled dimers governed by the formation of two symmetrically equivalent lp$\cdots\pi$(CR) interactions. This DFT study is mainly focused on the investigation of this interaction. Fig. 14 shows the self-assembled dimer where, in addition to the lp$\cdots\pi$(CR) interactions, two anti-parallel displaced and conventional $\pi\cdots\pi$ interactions are formed. The dimerization energy is very large (−26.6 kcal/mol) due to the contribution of both types of π-stacking interactions. It should be mentioned that this interaction has been computed as a dimer where each monomeric fragment includes the water molecule and the perchlorate counter ion. Therefore, the H-bonds are not evaluated (considered as previously formed). In an effort to evaluate the contribution of the lp$\cdots\pi$(CR) interaction, we have used a reduced model where the ligand has been simplified (see Fig. 14b). Consequently, the energy is only reduced to −21.9 kcal/mol that is a rough estimation of the lp$\cdots\pi$(CR) interaction. Such large interaction energy agrees well with the MEP surface analysis shown in Fig. 13 that evidences a large and positive MEP value over the chelate ring and negative at the azido ligand. Therefore, it dominates the formation of this dimer. The contribution of the conventional $\pi\cdots\pi$ interactions can be estimated by difference, i.e. −4.7 kcal/mol, that is significantly weaker than the lp$\cdots\pi$(CR) interactions with the shortest centroid-to-centroid distances (see Fig. 14a).

The large dimerization energy obtained for the dimer of **1** is comparable to other interactions where anti-parallel π-stacking
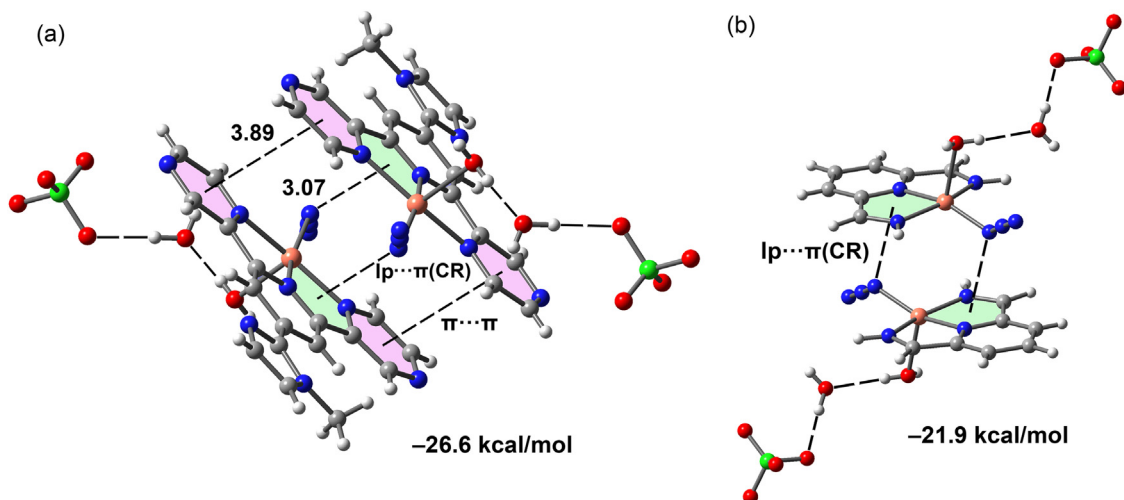
Fig. 14. (a) Dimer of compound **1**, π-stacking interactions shown as black dashed lines (distances in Å) (b) Reduced model of compound **1** used to estimate the lp···π(CR) interaction.

interactions in metal complexes with large and conjugated π-systems. It has been rationalized considering the large dipole moments of the metal complexes that are very polarized. For instances π-stacking interactions ranging from –25 to –35 kcal/mol have been reported for similar systems [117–125].

We have also computed the "Non-covalent Interaction plot" (NCI plot) index in order to characterize both types π-π stacking interactions in compound **1**. The NCI plot index is an intuitive visualization index that facilitates the visualization of non-covalent interactions and shows which molecular regions interact. The color scheme is a red-yellow-green-blue scale with red (repulsive) and blue (attractive). Yellow and green surfaces correspond to weak repulsive and weak attractive interactions, respectively. Fig. 15 shows the NCI plot index analysis of the self-assembled dimer of compound **1** using two different perspectives. The NCI plot reveals the

Fig. 16. Partial views of the solid state X-ray structures of refcodes KEYCAU (a) and KAHXID (b). Distances in Å. H-atoms omitted for clarity.
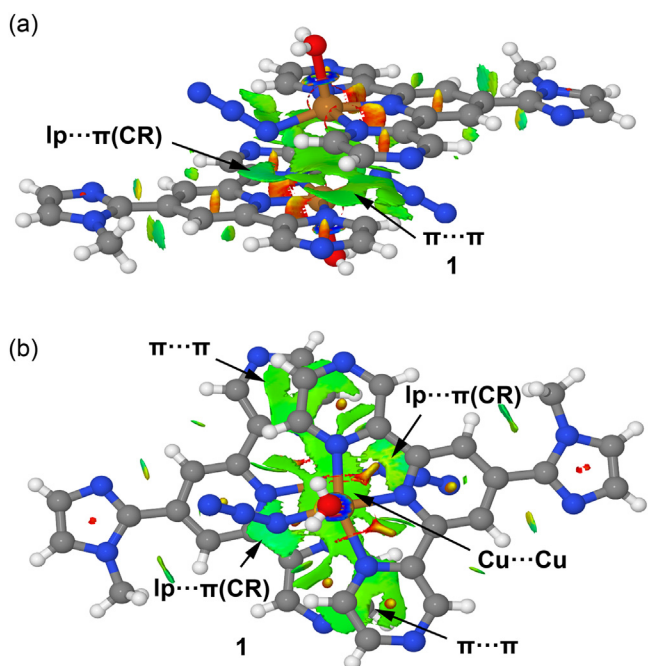
Fig. 15. NCI surface of the π-stacked assembly compound **1** using perspective (a) and on-top views (b) The gradient cut-off is $\rho = 0.04$ a.u., isosurface s = 0.35, and the color scale is -0.04 a.u.$< \rho < 0.04$ a.u.
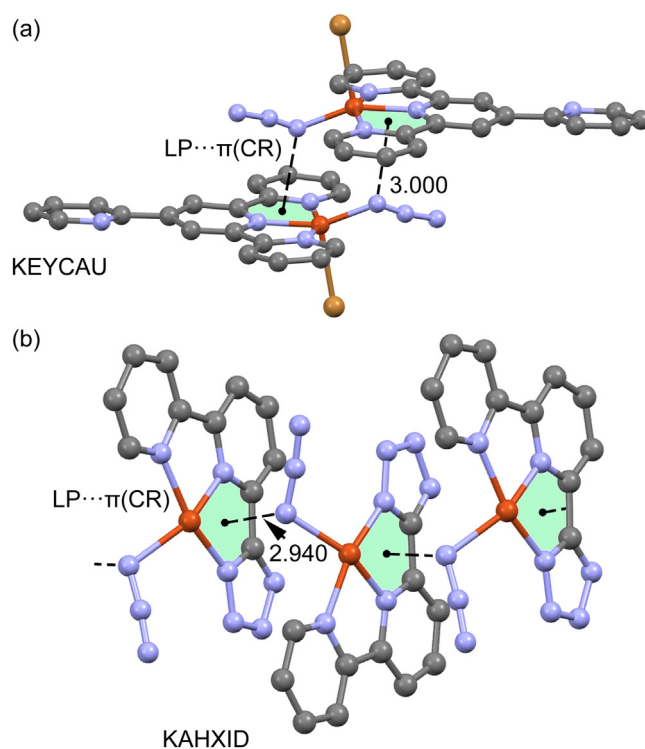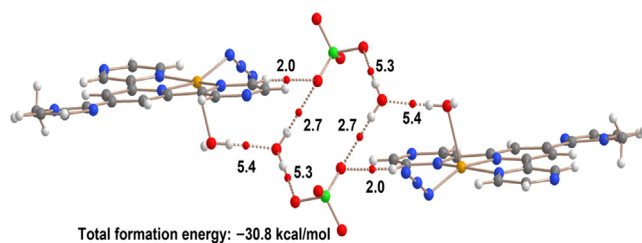
Fig. 17. QTAIM distribution of intermolecular bond critical points (small red spheres) and bond paths in the H-bonding assembly compound **1**. The dissociation energy of each H-bond is indicated adjacent to each bond critical point.
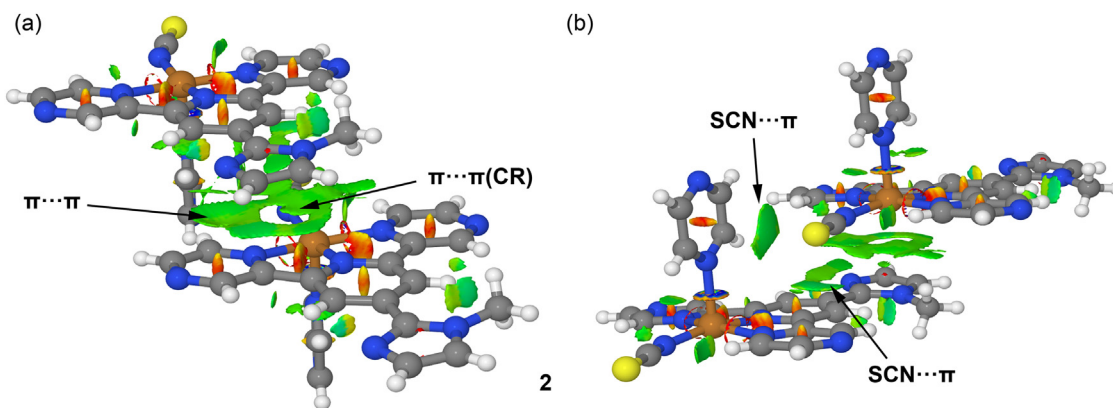
Fig. 18. NCI surface of the π-stacked assembly compound **2** using two different perspective views (a,b), (the gradient cut-off is $\rho = 0.04$ a.u., isosurface $s = 0.35$, and the color scale is -0.04 a.u. $< \rho < 0.04$ a.u).

formation of green and extended isosurfaces upon dimerization that are located between the chelate rings and the N-atoms of the azido ligand, thus confirming the existence of the unconventional lp$\cdots\pi$(CR) interaction. Moreover, the NCI plot also shows green isosurfaces located between the pyrazine aromatic rings, thus also confirming the existence of anti-parallel and displaced $\pi\cdots\pi$ stacking interactions. The NCIplot analysis also reveals a large and green isosurface between both Cu(II) ion, thus suggesting some type of metal$\cdots$metal interaction that likely contributes to the large dimerization energy of the reduced model shown in Fig. 14b.

We have explored the Cambridge structural database (CSD) in order to investigate the prevalence of N$_3\cdots\pi$(CR) interaction in Cu complexes with five membered (unsaturated) chelate rings. We have found only five structures in the CSD presenting similar LP$\cdots$ π(CR) interactions, which are summarized in Table 1. The LP$\cdots$ π(CR) interactions were not described by their original authors. The Cg$\cdots$N distances are gathered in Table 1, which range from 2.938 to 3.016 Å, similar to the distance observed in compound **1** (3.070 Å). Two representative structures from this search are represented in Fig. 16. In KEYCAU structure, a self-assembled dimer is formed in the solid state that is very similar to that found in compound **1** (see Fig. 4) where two symmetrically equivalent LP$\cdots\pi$(CR) interactions are formed. The other structure forms infinite 1D supramolecular assemblies in the solid state where the complex propagates in one direction due to the formation of the LP$\cdots\pi$(CR) interactions. It is interesting to highlight that in all structures the LP-donor N-atom is the one that is coordinated to the Cu-atom.

The H-bonding network (anion−water cluster) described above in Fig. 5 has been also analysed theoretically using the quantum theory of atoms in molecules (QTAIM). The distribution of bond critical points and bond paths is represented in Fig. 17 along with the individual H-bond formation energies derived from the potential energy density predictor ($E_{dis} = \frac{1}{2} * V_r$) proposed by Espinosa et al. [131] Each H-bond is characterized by a bond critical point connecting the H to the O-atom. The stronger H-bond corresponds

to the one established between the coordinated and uncoordinated water molecules (5.4 kcal/mol) likely to the enhanced acidity of the water protons due to the coordination to Cu(II) metal center. The uncoordinated water molecule also establishes two additional H-bonds as donor with the perchlorate anions, one is strong (5.3 kcal/mol) and the other is more modest (2.7 kcal/mol) in agreement with the experimental bond angles as well as separation distances (Table S5). Finally, the QTAIM analysis further discloses the existence of C−H$\cdots$O interactions between one aromatic H-atom of the ligand and the perchlorate anion. The interaction energy of this H-bond is the weakest one (2.0 kcal/mol). The total formation energy of this assembly is very large (–30.8 kcal/mol), thus confirming the importance of these H-bonding network in the crystal packing of compound **1**, in addition to the antiparallel π-stacking interactions described in Fig. 14.

Since compound **2** is a coordination polymer, we have used a dimeric model extracted from the polymeric chain (see Fig. 18) where pyrazine rings act as apical ligands for the Cu-atoms. The NCIplot analysis of the dimer is represented in Fig. 18 that reveals that the SCN ligand establishes conventional lp−π interactions with the aromatic rings. Since there is not a NCIplot isosurface located between the chelate ring and the SCN ligand, this analysis suggests that the chelate ring is not involved in the binding mechanism. In contrast, it reveals the existence of $\pi\cdots\pi$(CR) interactions involving the five membered imidazole ring and the chelate ring (see Fig 18b). It is characterized by a green and extended NCIplot index isosurface that embraces the chelate ring and part of the fused pyrazine ring.

4. Concluding remarks

In conclusion, we have successfully synthesized two Cu(II) complexes (complex **1** and **2**) using 4-(1-methylimidazole)-2,6-di(pyrazinyl)pyridineas the backbone ligand with two different auxiliary ligands, established their solid-state crystal structures by single crystal X-ray diffraction study and explored the noncovalent interactions associated with their crystal structures. The structural insights reveal that intermolecular hydrogen bonding (C−H$\cdots$N, C−H$\cdots$O, O−H$\cdots$N, O−H$\cdots$O), $\pi\cdots\pi$, $\pi\cdots\pi$(chelate ring), anion$\cdots\pi$, lone pair$\cdots\pi$ and lone pair$\cdots\pi$(chelate ring) interactions play a significant role in crystal packing of the complexes in the solid state. A DFT study has been used to evaluate the cooperative influence of unconventional lone pair$\cdots\pi$(CR) and conventional $\pi\cdots\pi$ stacking interactions in the dimeric distribution of complex **1** quantitatively and demonstrating that the former is stronger. Besides, the large formation energy of the perchlorate-water cluster (–30.8 kcal/mol) confirms its decisive role in the self assembly of complex **1**. The

Table 1

CSD reference codes of Cu-complexes exhibiting N$_3\cdots\pi$(CR) interactions. The distance from the N-atom to the ring centroid (Cg) is also indicated.

Ref. code	d(Cg$\cdots$N), Å	Reference
FIBGIH	2.964	[126]
KAHXID	2.940	[127]
KEYKAU	3.000	[128]
KUCFIZ	2.938	[129]
LEXPAH	3.016	[130]

sulfur (lone pair)$\cdots\pi$ and $\pi\cdots\pi$(CR) interactions play a lead role in the crystal packing of complex **2**. The NCI plot index also exhibits the involvement of chelate ring to stabilize the crystal structures of the complexes significantly. Therefore, the present study undoubtedly helps to gain knowledge in this rising area of supramolecular chemistry. Finally, the CSD search discloses the existence of LP(N$_3$)$\cdots\pi$(CR) in a few structures. However, further investigation in this topic will be conducted to extend the analysis to other elements, LP donors and ring sizes.

Declaration of Competing Interest

There are no conflicts to declare.

CRediT authorship contribution statement

Samit P., Sudipta P., A.F. and S.M.: investigation and methodology. A.F.: in silico studies. Samit P., Sudipta P. and S.M.: data curation. A.F. and S.M.: conceptualization, supervision, validation. A.F.: project administration. Samit P., A.F. and S.M. writing – original draft, writing – review and editing.

Acknowledgments

Supplementary materials

CCDC 2096470 and 2096471 contain the supplementary crystallographic data for complex 1 and complex 2 respectively. These data can be obtained free of charge via http://www.ccdc.cam.ac.uk/conts/retrieving.html, or from the Cambridge Crystallographic Data center, 12 Union Road, Cambridge CB2 1EZ, UK; fax: (+44) 1223-336-033; or e-mail: deposit@ccdc.cam.ac.uk.

Supplementary material associated with this article can be found, in the online version, at doi:10.1016/j.molstruc.2022.133358.

References

[1] A. Ciesielski, C.A. Palma, M. Bonini, P. Samorì, Towards supramolecular engineering of functional nanomaterials: pre-programming multi-component 2d self-assembly at solid-liquid interfaces, Adv. Mater. 22 (2010) 3506–3520 https://doi.org/, doi:10.1002/adma.201001582.

[2] D. Trauner, The chemist and the architect, Angew. Chem., Int. Ed. 57 (2017) 4177–4191, doi:10.1002/anie.201708325.

[3] K. Geng, T. He, R. Liu, S. Dalapati, K.T. Tan, Z. Li, S. Tao, Y. Gong, Q. Jiang, D. Jiang, Covalent organic frameworks: design, synthesis, and functions, Chem. Rev. 120 (2020) 8814–8933, doi:10.1021/acs.chemrev.9b00550.

[4] G.R. Desiraju, J.J. Vittal, A. Ramanan, Crystal Engineering: A Textbook, World Scientific Pub. Co. Inc., Singapore, 2011.

[5] G.R. Desiraju, Crystal engineering: from molecule to crystal, J. Am. Chem. Soc. 135 (2013) 9952–9967, doi:10.1021/ja403264c.

[6] M. Mirzaei, H. Eshtiagh-Hosseini, Z. Karrabi, K. Molčanov, E. Eydizadeh, J.T. Mague, A. Bauzá, A. Frontera, Crystal engineering with coordination compounds of Ni^{II}, Co^{II}, and Cr^{III} bearing dipicolinic acid driven by the nature of the noncovalent interactions, CrystEngComm 16 (2014) 5352–5363, doi:10.1039/C4CE00325J.

[7] J.J. Novoa, Intermolecular Interactions. Crystals: Fundamentals of Crystal Engineering, The Royal Society of Chemistry, London, 2018.

[8] M.D. Allendorf, V. Stavila, Crystal engineering, structure–function relationships, and the future of metal–organic frameworks, CrystEngComm 17 (2015) 229–246, doi:10.1039/C4CE01693A.

[9] A.K. Nangia, G.R. Desiraju, Crystal engineering: an outlook for the future, Angew. Chem., Int. Ed. 58 (2019) 4100–4107, doi:10.1002/anie.201811313.

[10] I. Gospodinov, K.V. Domasevitch, C.C. Unger, T.M. Klapötke, J. Stierstorfer, Midway between energetic molecular crystals and high-density energetic salts: crystal engineering with hydrogen bonded chains of polynitro bipyrazoles, Cryst. Growth Des. 20 (2020) 755–764, doi:10.1021/acs.cgd.9b01177.

[11] N.R. Mote, S.H. Chikkali, Hydrogen-bonding-assisted supramolecular metal catalysis, Chem.–Asian J. 13 (2018) 3623–3646, doi:10.1002/asia.201801302.

[12] R. Bu, Y. Xiong, X. Wei, H. Li, C. Zhang, Hydrogen bonding in CHON-containing energetic crystals: a review, Cryst. Growth Des. 19 (2019) 5981–5997, doi:10.1021/acs.cgd.9b00853.

[13] M. Madni, M.N. Ahmed, M. Hafeez, M. Ashfaq, M.N. Tahir, D.M. Gil, B. Galmés, S. Hameed, A. Frontera, Recurrent π–π stacking motifs in three new 4,5-dihydropyrazolyl–thiazole–coumarin hybrids: X-ray characterization, Hirshfeld surface analysis and DFT calculations, New J. Chem. 44 (2020) 14592–14603, doi:10.1039/D0NJ02931A.

[14] S. Pramanik, S. Pathak, S. Jana, M. Mondol, A. Frontera, S. Mukhopadhyay, An experimental and theoretical exploration of supramolecular interactions and photoresponse properties of two Ni(II) complexes, New J. Chem. 45 (2021) 12108–12119, doi:10.1039/D1NJ01363G.

[15] P. Manna, S.K. Seth, A. Das, J. Hemming, R. Prendergast, M. Helliwell, S.R. Choudhury, A. Frontera, S. Mukhopadhyay, Anion induced formation of supramolecular associations involving lone pair-π and anion-π interactions in Co(II) malonate complexes: experimental observations, Hirshfeld surface analyses and DFT studies, Inorg. Chem. 51 (2012) 3557–3571, doi:10.1021/ic202317f.

[16] L.A. Barrios, G. Aromi, A. Frontera, D. Quinonero, P.M. Deya, P. Gamez, O. Roubeau, E.J. Shotton, S.J. Teat, Coordination complexes exhibiting anion$\cdots\pi$ interactions: synthesis, structure, and theoretical studies, Inorg. Chem. 47 (2008) 5873–5881, doi:10.1021/ic800215r.

[17] C. Garau, D. Quiñonero, A. Frontera, P. Ballester, A. Costa, P.M. Deyà, Dual binding mode of s-triazine to anions and cations, Org. Lett. 5 (2003) 2227–2229, doi:10.1021/ol034650u.

[18] A. Rather, S.A. Wagay, R. Ali, Emergence of anion-π interactions: the land of opportunity in supramolecular chemistry and beyond, Coord. Chem. Rev. 415 (2020) 213327–213387, doi:10.1016/j.ccr.2020.213327.

[19] P. Pal, A. Hossain, R.M. Gomila, A. Frontera, S. Mukhopadhyay, Synthesis and crystal structure of the simultaneous binding of Ni(II) cation and chloride by the protonated 2,4,6 tris-(2-pyridyl)-1,3,5 triazine ligand: theoretical investigations of anion$\cdots\pi$, $\pi\cdots\pi$ and hydrogen bonding interactions, New J. Chem. 45 (2021) 11689–11696, doi:10.1039/D1NJ01880A.

[20] C. Jia, H. Miao, B.P. Hay, Crystal structure evidence for the directionality of lone pair–π interactions: fact or fiction? Cryst. Growth Des. 19 (2019) 6806–6821, doi:10.1021/acs.cgd.9b01081.

[21] M. Savastano, C. García-Gallarín, M.D. López de la Torre, C. Bazzicalupi, A. Bianchi, M. Melguizo, Anion-π and lone pair-π interactions with s-tetrazine-based ligands, Coord. Chem. Rev. 397 (2019) 112–137, doi:10.1016/j.ccr.2019.06.016.

[22] J. Kozelka, Lone pair–π interactions in biological systems: occurrence, function, and physical origin, Eur. Biophys. J. 46 (2017) 729–737, doi:10.1007/s00249-017-1210-1.

[23] M. Chawla, E. Chermak, Q. Zhang, J.M. Bujnicki, R. Oliva L. Cavallo, Occurrence and stability of lone pair–π stacking interactions between ribose and nucleobases in functional RNAs, Nucleic Acids Res 45 (2017) 11019–11032, doi:10.1093/nar/gkx757.

[24] K. Kalra, S. Gorle, L. Cavallo, R. Oliva, M. Chawla, Occurrence and stability of lone pair–π and OH–π interactions between water and nucleobases in functional RNAs, Nucleic Acids Res 48 (2020) 5825–5838, doi:10.1093/nar/gkaa345.

[25] S. Maity, T.K. Ghosh, R.M. Gomila, A. Frontera, A. Ghosh, Recurrent π(arene)$\cdots\pi$(chelate ring) motifs in four trinuclear Cu$^{II}_2$M^{II} (M = Cd/Zn) complexes derived from an unsymmetrical N$_2$O$_2$ donor ligand: structural and theoretical investigations, CrystEngComm 22 (2020) 7673–7683, doi:10.1039/D0CE01219J.

[26] S. Mirdya, S. Roy, S. Chatterjee, A. Bauza, A. Frontera, S. Chattopadhyay, Importance of π-interactions involving chelate rings in addition to the tetrel bonds in crystal engineering: a combined experimental and theoretical study on a series of hemi- and holodirected nickel(II)/lead(II) complexes, Cryst. Growth Des. 19 (2019) 5869–5881, doi:10.1021/acs.cgd.9b00881.

[27] D.P. Malenov, G.V. Janjić, V.B. Medaković, M.B. Hall, S.D. Zarić, Noncovalent bonding: Stacking interactions of chelate rings of transition metal complexes, *Coord. Chem. Rev.* 345 (2017) 318–341, doi:10.1016/j.ccr.2016.12.020.

[28] D.P. Malenov, D.Ž. Veljković, M.B. Hall, E.N. Brothers, S.D. Zarić, Influence of chelate ring type on chelate–chelate and chelate–aryl stacking: the case of nickel bis(dithiolene), Phys. Chem. Chem. Phys. 21 (2019) 1198–1206, doi:10.1039/C8CP06312E.

[29] D.P. Malenov, S.D. Zarić, Strong stacking interactions of metal–chelate rings are caused by substantial electrostatic component, Dalton Trans 48 (2019) 6328–6332, doi:10.1039/C9DT00182D.

[30] S.L. Tan, S.M. Lee, K.M. Lo, A. Otero-de-la-Roza, E.R.T. Tiekink, Experimental and computational evidence for a stabilising C–Cl(lone-pair)$\cdots\pi$(chelate-ring) interaction, CrystEngComm 23 (2021) 119–130, doi:10.1039/D0CE01478H.

[31] T. Maity, H. Mandal, A. Bauza, B.C. Samanta, A. Frontera, S.K. Seth, Quantifying conventional C–H$\cdots\pi$(aryl) and unconventional C–H$\cdots\pi$(chelate) interactions in dinuclear Cu(II) complexes: experimental observations, Hirshfeld surface and theoretical DFT study, New J. Chem. 42 (2018) 10202–10213, doi:10.1039/C8NJ00747K.

[32] E.R.T. Tiekink, The remarkable propensity for the formation of C–H$\cdots\pi$(chelate ring) interactions in the crystals of the first-row transition metal dithiocarbamates and the supramolecular architectures they sustain, CrystEngComm 22 (2020) 7308–7333, doi:10.1039/D0CE00289E.

[33] B. Dutta, S.M. Pratik, S. Jana, C. Sinha, A. Datta, M.H. Mir, Novel

Br···π(chelate) interaction in a 1D coordination polymer revealing aromaticity, ChemistrySelect 3 (2018) 4289–4291, doi:10.1002/slct.201800738.

[34] E.R.T. Tiekink, Supramolecular architectures sustained by delocalised C–I···π(arene) interactions in molecular crystals and the propensity of their formation, CrystEngComm 23 (2021) 904–928, doi:10.1039/D0CE01677B.

[35] H. Masui, Metalloaromaticity, Coord. Chem. Rev. 219–221 (2001) 957–992, doi:10.1016/S0010-8545(01)00389-7.

[36] A. Castiñeiras, A.G. Sicilia-Zafra, J.M. Gonzáles-Pérez, D. Choquesillo-Lazarte J. Niclós-Gutiérrez, Intramolecular "aryl–metal chelate ring" π,π-interactions as structural evidence for metalloaromaticity in (aromatic α,α'-diimine)–copper(II) chelates: molecular and crystal structure of aqua(1,10-phenanthroline)(2-benzylmalonato)copper(II) three-hydrate, Inorg. Chem. 41 (2002) 6956–6959, doi:10.1021/ic026004h.

[37] L. Wang, B. Song, S. Khalife, Y. Li, L.-J. Ming, S. Bai, Y. Xu, H. Yu, M. Wang, H. Wang, X. Li, Introducing seven transition metal ions into terpyridine-based supramolecules: self-assembly and dynamic ligand exchange study, J. Am. Chem. Soc. 142 (2020) 1811–1821, doi:10.1021/jacs.9b09497.

[38] G. Baronea, G. Gennaroa, A.M. Giuliania, M. Giustini, Interaction of Cd(II) and Ni(II) terpyridine complexes with model polynucleotides: a multidisciplinary approach, RSC Adv 6 (2016) 4936–4945, doi:10.1039/C5RA24919H.

[39] A. Wild, A. Winter, F. Schlütter, U.S. Schubert, Advances in the field of π-conjugated 2,2′:6′,2″-terpyridines, Chem. Soc. Rev. 40 (2011) 1459–1511, doi:10.1039/C0CS00074D.

[40] D. Saccone, C. Magistris, N. Barbero, P. Quagliotto, C. Barolo, G. Viscardi, Terpyridine and quaterpyridine complexes as sensitizers for photovoltaic applications, Materials 9 (2016) 137–174, doi:10.3390/ma9030137.

[41] P. Liu, G. Shi, X. Chen, Terpyridine-containing π-conjugated polymers for light-emitting and photovoltaic materials, Front. Chem. 8 (2020) 923–929, doi:10.3389/fchem.2020.592055.

[42] M.M. Milutinović, S.K.C. Elmroth, G. Davidović, A. Rilak, O. Klisurić, I. Bratsos, Ž.D. Bugarčić, Kinetic and mechanistic study on the reactions of ruthenium(II) chlorophenyl terpyridine complexes with nucleobases, oligonucleotides and DNA, Dalton Trans. 46 (2017) 2360–2369, doi:10.1039/C6DT04254F.

[43] C. Li, F. Xu, Y. Zhao, W. Zheng, W. Zeng, Q. Luo, Z. Wang, K. Wu, J. Du, F. Wang, Platinum(II) terpyridine anticancer complexes possessing multiple mode of DNA interaction and EGFR inhibiting activity, Front. Chem. 8 (2020) 210–224, doi:10.3389/fchem.2020.00210.

[44] C. Bai, F.H. Wei, H.M. Hu, L. Yan, X. Wang, G.L. Xue, New highly luminescent europium(III) complex covalently bonded with titania-based host via using a terpyridine carboxylate derivative linker for fluorescence sensing, J. Lumin. 227 (2020) 117545–117555, doi:10.1016/j.jlumin.2020.117545.

[45] P. Pal, T. Ganguly, S. Das, S. Baitalik, pH-Responsive colorimetric, emission and redox switches based on Ru(II)–terpyridine complexes, Dalton Trans 50 (2021) 186–196, doi:10.1039/D0DT03537H.

[46] Y. Wang, X.W. Gao, J. Li, D. Chao, Merging an organic TADF photosensitizer and a simple terpyridine–Fe(III) complex for photocatalytic CO$_2$ reduction, Chem. Commun. 56 (2020) 12170–12173, doi:10.1039/D0CC05047D.

[47] R. Fernández-Terán, L. Sévery, Living long and prosperous: productive intraligand charge-transfer states from a rhenium(I) terpyridine photosensitizer with enhanced light absorption, Inorg. Chem. 60 (2021) 1334–1343, doi:10.1021/acs.inorgchem.0c01939.

[48] C. Wei, Y. He, X. Shi, Z. Song, Terpyridine-metal complexes: applications in catalysis and supramolecular chemistry, Coord. Chem. Rev. 385 (2019) 1–19, doi:10.1016/j.ccr.2019.01.005.

[49] A. Winter, U.S. Schubert, Metal-terpyridine complexes in catalytic application–a spotlight on the last decade, ChemCatChem 12 (2020) 1–52, doi:10.1002/cctc.201902290.

[50] M. Elcheikh Mahmoud, H. Audi, A. Assoud, T.H. Ghaddar, M. Hmadeh, Metal–organic framework photocatalyst incorporating bis(4′-(4-carboxyphenyl)-terpyridine)ruthenium(II) for visible-light-driven carbon dioxide reduction, J. Am. Chem. Soc. 141 (2019) 7115–7121, doi:10.1021/jacs.9b01920.

[51] D. Luo, T. Zuo, J. Zheng, Z.-H. Long, X.-Z. Wang, Y.-L. Huang, X.-P. Zhou, D. Li, Enabling photocatalytic activity of [Ru(2,2′:6′,2″-terpyridine)$_2$]$^{2+}$ integrated into a metal–organic framework, Mater. Chem. Front. 5 (2021) 2777–2782, doi:10.1039/D1QM00024A.

[52] B.Z. Momeni, F. Rahimi, M. Torrei, F. Rominger, Hirshfeld surface analysis, luminescence and thermal properties of three first-row transition metal complexes containing 4′-hydroxy-2,2′:6′,2″-terpyridine: application for preparation of nano metal oxides, Appl. Organometal. Chem. 34 (2020) 5613–5635, doi:10.1002/aoc.5613.

[53] A.M. Maron, K. Choroba, J.G. Małecki, S. Kula, E. Malicka, Platinum(II) coordination compound with 4′-[4-(dimethylamino)phenyl]-2,2′:6′,2″-terpyridine–the new insight into the luminescence behavior and substituent effect, Polyhedron 182 (2020) 114502–114511, doi:10.1016/j.poly.2020.114502.

[54] B.Z. Momeni, S.K. Anari, M. Torrei, J. Janczak, Crystal exploring, Hirshfeld surface analysis, and properties of 4′-(furan-2-yl)-2,2′:6′,2″-terpyridine complexes of nickel (II): new precursors for the synthesis of nanoparticles, Appl. Organometal. Chem. 35 (2021) 6179–6201, doi:10.1002/aoc.6179.

[55] E.U. Mughal, M. Mirzaei, A. Sadiq, S. Fatima, A. Naseem, N. Naeem, N. Fatima, S. Kausar, A.A. Altaf, M.N. Zafar, B.A. Khan, Terpyridine-metal complexes: effects of different substituents on their physico-chemical properties and density functional theory studies, R. Soc. Open Sci. 7 (2020) 201208–201239, doi:10.1098/rsos.201208.

[56] S.M. Elahi, M. Raizada, P.K. Sahu, S. Konar, Terpyridine-based 3D metal–organic-frameworks: a structure–property correlation, Chem. Eur. J. 27 (2021) 5858–5870, doi:10.1002/chem.202004651.

[57] F.A. Mautner, J.H. Albering, E.V. Harrelson, A.A. Gallo, S.S. Massoud, N-bonding vs. S-bonding in thiocyanato-copper(II) complexes, J. Mol. Struct. 1006 (2011) 570–575, doi:10.1016/j.molstruc.2011.10.005.

[58] S.S. Massoud, M. Dubin, A.E. Guilbeau, M. Spell, R. Vicente, P. Wilfling, R.C. Fischer, F.A. Mautner, Azido- and thiocyanato-cobalt(II) complexes based pyrazole ligands, Polyhedron 78 (2014) 135–140, doi:10.1016/j.poly.2014.04.025.

[59] F.A. Mautner, M. Traber, P. Jantscher, R.C. Fischer, K. Reichmann, R. Vicente, N. Arafat, S.S. Massoud, Thiocyanato-metal(II) and azido-cobalt(III) complexes with hydroxymethylpyridines, Polyhedron 161 (2019) 309–316, doi:10.1016/j.poly.2019.01.030.

[60] A. Di Santo, H. Perez, G.A. Echeverria, O.E. Piro, R.A. Iglesias, R.E. Carbonio, A. Ben Altabef, D.M. Gil, Exploring weak intermolecular interactions in thiocyanate-bonded Zn(II) and Cd(II) complexes with methylimidazole: crystal structures, Hirshfeld surface analysis and luminescence properties, RSC Adv 8 (2018) 23891–23902, doi:10.1039/C8RA04452J.

[61] M. Mondal, S. Jana, M.G.B. Drew, A. Ghosh, Application of two Cu(II)-azido based 1D coordination polymers in optoelectronic device: structural characterization and experimental studies, Polymer 204 (2020) 122815–122824, doi:10.1016/j.polymer.2020.122815.

[62] P. Ghorai, P. Brandão, S. Benmansour, C.J.G. García, A. Saha, Azido and thiocyanato bridged dinuclear Ni(II) complexes involving 8-aminoquinoline based Schiff base as blocking ligands: Crystal structures, ferromagnetic properties and magneto-structural correlations, Polyhedron 188 (2020) 114708–114715, doi:10.1016/j.poly.2020.114708.

[63] C.D. Mekuimemba, F. Conan, A.J. Mota, M.A. Palacios, E. Colacio, S. Triki, On the magnetic coupling and spin crossover behavior in complexes containing the head-to-tail [Fe^{II}$_2$(μ-SCN)$_2$] bridging unit: a magnetostructural experimental and theoretical study, Inorg. Chem. 57 (2018) 2184–2192, doi:10.1021/acs.inorgchem.7b03082.

[64] K. Vrieze, G. Van Koten, Comprehensive Coordination Chemistry, 2, Pergamon Oxford, 1987, p. 225.

[65] E.I. Solomon, D.E. Heppner, E.M. Johnston, J.W. Ginsbach, J. Cirera, M. Qayyum, M.T. Kieber-Emmons, C.H. Kjaergaard, R.G. Hadt, L. Tian, Copper active sites in biology, Chem. Rev. 114 (2014) 3659–3853, doi:10.1021/cr400327t.

[66] K. Choroba, B. Machura, S. Kula, L.R. Raposo, A.R. Fernandes, R. Kruszynski, K. Erfurt, L.S. Shul, Y.N. Kozlov, G.B. Shul, Copper(II) complexes with 2,2′:6′,2″-terpyridine, 2,6-di(thiazol-2-yl)pyridine and 2,6-di(pyrazin-2-yl)pyridine substituted with quinolines. Synthesis, structure, antiproliferative activity, and catalytic activity in the oxidation of alkanes and alcohols with peroxides, Dalton Trans. 48 (2019) 12656–12673, doi:10.1039/C9DT01922G.

[67] R. Nasani, M. Saha, S.M. Mobin, L.M.D.R.S. Martins, A.J.L. Pombeiro, A.M. Kirillov, S. Mukhopadhyay, Copper–organic frameworks assembled from in situ generated 5-(4-pyridyl)tetrazole building blocks: synthesis, structural features, topological analysis and catalytic oxidation of alcohols, Dalton Trans. 43 (2014) 9944, doi:10.1039/C4DT00531G.

[68] Z. Ma, L. Wei, E.C.B.A. Alegria, L.M.D.R.S. Martins, M.F.C.G. da Silva, A.J.L. Pombeiro, Synthesis and characterization of copper(II) 4′-phenyl-terpyridine compounds and catalytic application for aerobic oxidation of benzylic alcohols, Dalton Trans. 43 (2014) 4048–4058, doi:10.1039/C3DT53054J.

[69] J.Z. Gu, M. Wen, Y. Cai, Z.F. Shi, A.S. Arol, M.V. Kirillova, A.M. Kirillov, Metal–organic architectures assembled from multifunctional polycarboxylates: hydrothermal self-assembly, structures, and catalytic activity in alkane oxidation, Inorg. Chem. 58 (2019) 2403, doi:10.1021/acs.inorgchem.8b02926.

[70] K. Choroba, B. Machura, A. Szlapa-Kula, J.G. Malecki, L. Raposo, S. Cordeiro, P.V. Baptista, A.R. Fernandes, Square planar Au(III), Pt(II) and Cu(II) complexes with quinoline-substituted 2,2′:6′,2″-terpyridine ligands: from in vitro to in vivo biological properties, Eur. J. Med. Chem. 218 (2021) 113404–113423, doi:10.1016/j.ejmech.2021.113404.

[71] Y. Liu, S.C. Yiu, C.L. Ho, W.Y. Wong, Recent advances in copper complexes for electrical/light energy conversion, Coord. Chem. Rev. 375 (2018) 514–557, doi:10.1016/j.ccr.2018.05.010.

[72] C. Icsel, V.T. Yilmaz, S. Aydinlik, M. Aygun, New manganese(II), iron(II), cobalt(II), nickel(II) and copper(II) saccharinate complexes of 2,6-bis(2-benzimidazolyl)pyridine as potential anticancer agents, Eur. J. Med. Chem. 202 (2020) 112535–112545, doi:10.1016/j.ejmech.2020.112535.

[73] C. Wu, J. Wang, J. Shen, C. Zhang, Z. Wu, H. Zhou, A colorimetric quinoline-based chemosensor for sequential detection of copper ion and cyanide anions, Tetrahedron 73 (2017) 5715–5719, doi:10.1016/j.tet.2017.08.010.

[74] H.Q. Li, X.Q. Sun, T. Zheng, Z.X. Xu, Y.X. Song, X.H. Gu, Coumarin-based multifunctional chemosensor for arginine/lysine and Cu^{2+}/Al^{3+} ions and its Cu^{2+} complex as colorimetric and fluorescent sensor for biothiols, Sens. Actuators, B 279 (2019) 400–409, doi:10.1016/j.snb.2018.10.017.

[75] A. Hussain, M.F. AlAjmi, T. Rehman, S. Amir, F.M. Husain, A. Alsalme, M.A. Siddiqui, A.A. AlKhedhairy, R.A. Khan, Copper(II) complexes as potential anticancer and nonsteroidal anti-inflammatory agents: in vitro and in vivo studies, Sci. Rep. 9 (2019) 5237–5254, doi:10.1038/s41598-019-41063-x.

[76] J. Karges, K. Xiong, O. Blacque, H. Chao, G. Gasser, Highly cytotoxic copper(II) terpyridine complexes as anticancer drug candidates, Inorganica Chimica Acta 516 (2021) 120137–120143, doi:10.1016/j.ica.2020.120137.

[77] F. Cheng, N. Tang, K. Miao, F. Wang, A Dinuclear Ruthenium(II) Polypyridyl Complex Containing A terpy-like Fragment for Cu^{2+} Probing, Z. Anorg. Allg. Chem. 640 (2014) 1816–1821, doi:10.1002/zaac.201300662.

[78] Y.Q. Pan, X. Xu, Y. Zhang, Y. Zhang, W.K. Dong, A highly sensitive and selective bis(salamo)-type fluorescent chemosensor for identification of Cu^{2+} and the

continuous recognition of S^{2-}, Arginine and Lysine, Spectrochim. Acta, Part A 229 (2020) 117927–117937, doi:10.1016/j.saa.2019.117927.

[79] Z.-Y. Li, J.-S. Yang, R.-B. Liu, J.-J. Zhang, S.-Q. Liu, J. Nia, C.-Y. Duan, Two one-dimensional compounds based on pyramidal {TbCu₄} units and formate ligand: chair-like [(H₂O)₂(ClO₄)₂]²⁻ clusters and slow relaxation of magnetization, Dalton Trans. 41 (2012) 13264–13267, doi:10.1039/C2DT32147E.

[80] S.S. Bhat, V.K. Revankar, N. Shivalingegowda, N.K. Lokanath, A fluorophore-labelled copper complex: Crystal structure, hybrid cyclic water-perchlorate cluster and biological properties, Acta Crystallogr. C 73 (9) (2017) 710–717, doi:10.1107/S2053229617011639.

[81] T. Mandal, A. Dey, S. Pathak, M.M. Islam, S. Konar, J. Ortega-Castro, S.K. Seth, P.P. Ray, A. Frontera, S. Mukhopadhyay, Structures, photoresponse properties and DNA binding abilities of 4-(4-pyridinyl)-2-pyridone salts, RSC Adv 9 (2019) 9663–9677, doi:10.1039/C9RA00666D.

[82] Bruker, SMART ν5.631, Bruker AXS Inc., Madison, WI, USA, 2001.

[83] G.M. Sheldrick, SHELXT-2014, University of Göttingen, 2014.

[84] G.M. Sheldrick, Crystal structure refinement with SHELXL, Acta Crystallogr., Sect. C: Struct. Chem. 71 (2015) 3–8, doi:10.1107/S2053229614024218.

[85] M.J. Frisch, G.W. Trucks, H.B. Schlegel, G.E. Scuseria, M.A. Robb, J.R. Cheeseman, G. Scalmani, V. Barone, B. Mennucci, G.A. Petersson, H. Nakatsuj, M. Caricato, X. Li, H.P. Hratchian, A.F. Iamaylov, J. Bloino, G. Zheng, J.L. Sonnenberg, M. Hada, M. Ehara, K. Toyota, R. Fukuda, J. Hasegawa, M. Ishida, T. Nakajima, Y. Honda, O. Kitao, H. Nakai, T. Vreven, J.A. Montgomery Jr, J.E. Peralta, F. Ogliaro, M. Bearpark, J.J. Heyd, E. Brothers, K.N. Kudin, V.N. Staroverov, R. Kobayashi, J. Normand, K. Raghavachari, A. Rendell, J.C. Burant, S.S. Lyengar, J. Tomasi, M. Cossi, N. Rega, J.M. Millam, M. Klene, J.E. Knox, J.B. Cross, V. Bakken, C. Adamo, J. Jaramillo, R. Gomperts, R.E. Stratmann, O. Yazyev, A.J. Austin, R. Cammi, C. Pomelli, J.W. Ochterski, R.L. Martin, K. Morokuma, V.G. Zakrzewski, G.A. Voth, P. Salvador, J.J. Dannenberg, S. Dapprich, A.D. Daniels, O. Farkas, J.B. Foresman, J.V. Ortiz, J. Cioslowski, D.J. Fox, Gaussian 09, Revision A.1, Gaussian Inc., Wallingford CT, 2016.

[86] S.F. Boys, F. Bernardi, The calculation of small molecular interactions by the differences of separate total energies. Some procedures with reduced errors, Mol. Phys. 19 (1970) 553–556, doi:10.1080/00268977000101561.

[87] S. Grimme, J. Antony, S. Ehrlich, H. Krieg, A consistent and accurate *ab initio* parametrization of density functional dispersion correction (DFT-D) for the 94 elements H-Pu, J. Chem. Phys. 132 (2010) 154104–154123, doi:10.1063/1.3382344.

[88] P. Manna, S.K. Seth, M. Mitra, S.R. Choudhury, A. Bauzá, A. Frontera, S. Mukhopadhyay, Experimental and computational study of counterintuitive $ClO_4^- \cdots ClO_4^-$ interactions and the interplay between $\pi^+ - \pi$ and anion$\cdots\pi^+$ interactions, Cryst. Growth Des. 14 (2014) 5812–5821, doi:10.1021/cg5014126.

[89] M. Mirzaei, H. Eshtiagh-Hosseini, Z. Bolouri, Z. Rahmati, A. Esmaeilzadeh, A. Hassanpoor, A. Bauza, P. Ballester, M. Barceló-Oliver, J.T. Mague, B. Notash, A. Frontera, Rationalization of noncovalent interactions within six new M^II/8-aminoquinoline supramolecular complexes (M^II = Mn, Cu, and Cd): a combined experimental and theoretical DFT study, Cryst. Growth Des. 15 (2015) 1351–1361, doi:10.1021/cg501752e.

[90] Y.V. Torubaev, I.V. Skabitsky, A.V. Rozhkov, B. Galmes, A. Frontera, V. Yu. Kukushkin, Highly polar stacking interactions wrap inorganics in organics: lone-pair–π-hole interactions between the PdO₄ core and electron-deficient arenes, Inorg. Chem. Front. 8 (2021) 4965–4975, doi:10.1039/D1QI01067K.

[91] V.V. Suslonov, N.S. Soldatova, D.M. Ivanov, B. Galmes, A. Frontera, G. Resnati, P.S. Postnikov, V. Yu. Kukushkin, N.A. Bokach, Diaryliodonium tetrachloroplatinates(II): recognition of a trifurcated metal-involving μ_3-I$\cdots$(Cl, Cl, Pt) halogen bond, Cryst. Growth Des. 21 (2021) 5360–5372, doi:10.1021/acs.cgd.1c00654.

[92] A.V. Rozhkov, I.V. Ananyev, A.A. Petrov, B. Galmes, A. Frontera, N.A. Bokach, V. Yu. Kukushkin, Ligand steric hindrances switch bridging (μ_2-I)$\cdots$O to two-center I$\cdots$O halogen-bonding mode in the assembly of diketonate copper(II) species, Cryst. Growth Des. 21 (2021) 4073–4082, doi:10.1021/acs.cgd.1c00373.

[93] S.V. Baykov, K.K. Geyl, D.M. Ivanov, R.M. Gomila, A. Frontera, V. Yu. Kukushkin, Azine steric hindrances switch halogen bonding to N-arylation upon interplay with σ-hole donating haloarenenitriles, Chem. Asian J. 16 (2021) 1445–1455, doi:10.1002/asia.202100282.

[94] L.E. Zelenkov, A.A. Eliseeva, S.V. Baykov, V.V. Suslonov, B. Galmes, A. Frontera, V. Yu. Kukushkin, D.M. Ivanov, N.A. Bokach, Electron belt-to-σ-hole switch of noncovalently bound iodine(I) atoms in dithiocarbamate metal complexes, Inorg. Chem. Front. 8 (2021) 2505–2517, doi:10.1039/D1QI00314C.

[95] Z.M. Efimenko, A.A. Eliseeva, D.M. Ivanov, B. Galmes, A. Frontera, N.A. Bokach, V. Yu. Kukushkin, Bifurcated μ_2-I$\cdots$(N,O) halogen bonding: the case of (nitrosoguanidinate) Ni^II cocrystals with iodine(I)-based σ-hole donors, Cryst. Growth Des. 21 (2021) 588–596, doi:10.1021/acs.cgd.0c01408.

[96] L.E. Zelenkov, D.M. Ivanov, E.K. Sadykov, A.Bokach N, B. Galmes, A. Frontera, V. Yu. Kukushkin, Semicoordination bond breaking and halogen bond making change the supramolecular architecture of metal-containing aggregates, Cryst. Growth Des. 20 (2020) 6956–6965, doi:10.1021/acs.cgd.0c00999.

[97] N.S. Soldatova, P.S. Postnikov, V.V. Suslonov, T. Yu. Kissler, D.M. Ivanov, M.S. Yusubov, B. Galmes, A. Frontera, V. Yu. Kukushkin, Diaryliodonium as a double σ-hole donor: the dichotomy of thiocyanate halogen bonding provides divergent solid state arylation by diaryliodonium cations, Org. Chem. Front. 7 (2020) 2230–2242, doi:10.1039/D0QO00678E.

[98] A.V. Rozhkov, A.A. Eliseeva, S.V. Baykov, B. Galmes, A. Frontera, V. Yu. Kukushkin, One-pot route to x-perfluoroarenes (X = Br, I) based on Fe^III-assisted C–F functionalization and utilization of these arenes as building

[99] A.V. Rozhkov, I.V. Ananyev, R.M. Gomila, A. Frontera, V. Yu Kukushkin, π-Hole$\cdots$$d_z^2$[Pt^II] interactions with electron-deficient arenes enhance the phosphorescence of Pt^II-based luminophores, Inorg. Chem. 59 (2020) 9308–9314, doi:10.1021/acs.inorgchem.0c01170.

[100] E.A. Katlenok, M. Haukka, O.V. Levin, A. Frontera, V. Yu. Kukushkin, Supramolecular assembly of metal complexes by (aryl)I$\cdots$d [Pt^II] halogen bonds, Chem. Eur. J. 26 (2020) 7692–7701, doi:10.1002/chem.202001196.

[101] J. Contreras-García, E.R. Johnson, S. Keinan, R. Chaudret, J.-P. Piquemal, D.N. Beratan, W. Yang, NCIPLOT: A program for plotting noncovalent interaction regions, J. Chem. Theory Comput. 7 (2011) 625–632, doi:10.1021/ct100641a.

[102] Ł. Jaremko, A.M. Kirillov, P. Smoleński, A.J.L. Pombeiro, Engineering coordination and supramolecular copper–organic networks by aqueous medium self-assembly with 1,3,5-triaza-7-phosphaadamantane (PTA), Cryst. Growth Des. 9 (2009) 3006–3010, doi:10.1021/cg900334w.

[103] K.R. Gruenwald, A.M. Kirillov, M. Haukka, J. Sanchiz, A.J.L. Pombeiro, Mono-, di- and polynuclear copper(II) compounds derived from N-butyldiethanolamine: structural features, magnetism and catalytic activity for the mild peroxidative oxidation of cyclohexane, Dalton Trans. (2009) 2109–2120, doi:10.1039/B813160K.

[104] P.J. Figiel, A.M. Kirillov, M.F.C. Guedes da Silva, J. Lasri, A.J.L. Pombeiro, Self-assembled dicopper(II) diethanolaminate cores for mild aerobic and peroxidative oxidation of alcohols, Dalton Trans 39 (2010) 9879–9888, doi:10.1039/C0DT00472C.

[105] A.M. Kirillov, P. Smolenski, Z. Ma, M.F.C. Guedes da Silva, M. Haukka, A.J.L. Pombeiro, Copper(I) iodide complexes derived from N-alkyl-1,3,5-triaza-7-phosphaadamantanes: synthesis, crystal structures, photoluminescence, and identification of the unprecedented {Cu₃I₅}²⁻ cluster, Organometallics 28 (2009) 6425–6431, doi:10.1021/om900591q.

[106] A.W. Addison, T.N. Rao, J. Reedijk, J. Rijn, G.C. Verschoor, Synthesis, structure, and spectroscopic properties of copper(II) compounds containing nitrogen–sulphur donor ligands; the crystal and molecular structure of aqua[1,7-bis(N-methylbenzimidazol-2′-yl)-2,6-dithiaheptane]copper(II) perchlorate, J. Chem. Soc., Dalton Trans. 7 (1984) 1349–1356, doi:10.1039/DT9840001349.

[107] P. Pal, K. Das, A. Hossain, S. Mukhopadhyay, Supramolecular and theoretical perspectives of 2,2′:6′,2″-terpyridine based Ni(II) and Cu(II) complexes: on the importance of C–H$\cdots$Cl and $\pi\cdots\pi$ interactions, New J. Chem. 44 (2020) 7310–7318, doi:10.1039/D0NJ00094A.

[108] S. Das, G.P. Muthukumaragopal, S. Pal, S. Pal, A one-dimensional assembly of a square-planar copper(II) complex with alternating short and long Cu$\cdots$Cu distances. Metal ion spin-exchange *via* π-π interactions, New J. Chem. 27 (2003) 1102–1107, doi:10.1039/B212399C.

[109] M.N. Hoque, U. Manna, G. Das, Discrepancy in anion coordination directed by isomeric pyridine–urea receptors: solid state recognition of hydrated anions, Polyhedron 119 (2016) 307–316, doi:10.1016/j.poly.2016.09.022.

[110] M.N. Hoque, G. Das, Overview of the strategic approaches for the solid-state recognition of hydrated anions, CrystEngComm 19 (2017) 1343–1360, doi:10.1039/C6CE02438F.

[111] S.R. Choudhury, A.D. Jana, E. Colacio, H.M. Lee, G. Mostafa, S. Mukhopadhyay, Crowned tetrameric spirocyclic water chain: an unusual building block of a supramolecular metal–organic host, Cryst. Growth & Des. 7 (2007) 212–214, doi:10.1021/cg060837r.

[112] S. Pramanik, S. Konar, K. Chakraborty, T. Pal, S. Das, S. Chatterjee, M. Dolai, S. Pathak, Investigation of electrical conductance properties, non-covalent interactions and TDDFT calculation of a newly synthesized copper(II) metal complex, J. Mol. Struct. 1206 (2020) 127663–127670, doi:10.1016/j.molstruc.2019.127663.

[113] K.N.M. Daeffler, H.A. Lester, D.A. Dougherty, Functionally important aromatic–aromatic and sulfur–π interactions in the D2 dopamine receptor, J. Am. Chem. Soc. 134 (2012) 14890–14896, doi:10.1021/ja304560x.

[114] R.F.N. Silva, A.C.S. Sacco, I. Caracelli, J. Zukerman-Schpector, E.R.T. Tiekink, Sulfur(lone-pair)...π interactions with FAD in flavoenzymes, Z. Kristallogr. 233 (2018) 531–537, doi:10.1515/zkri-2018-2064.

[115] T.P. Tauer, M.E. Derrick, C.D. Sherrill, Estimates of the ab initio limit for sulfur–π interactions: the H₂S–benzene dimer, J. Phys. Chem. A 109 (2005) 191–196, doi:10.1021/jp046778e.

[116] Y.H. Peng, F.Y. Liao, C.T. Tseng, R. Kuppusamy, A.S. Li, C.H. Chen, Y.S. Fan, S.Y. Wang, M.H. Wu, C.C. Hsueh, J.Y. Chang, Unique sulfur–aromatic interactions contribute to the binding of potent imidazothiazole indoleamine 2,3-dioxygenase inhibitors, J. Med. Chem. 63 (4) (2020) 1642–1659, doi:10.1021/acs.jmedchem.9b01549.

[117] H. Nath, P. Sharma, R.M. Gomila, A. Frontera, M. Barcelo-Oliver, A.K. Verma, K. Dutta, M.K. Bhattacharyya, Unconventional enclathration of guest adipic acid and energetically significant antiparallel π-stacked ternary assemblies involving unusual regium-π(chelate) contacts in phenanthroline-based Ni(II) and Cu(II) compounds—Antiproliferative evaluation and theoretical studies, J. Mol. Struct. 1245 (2021) 131038, doi:10.1016/j.molstruc.2021.131038.

[118] A. Das, P. Sharma, A. Frontera, M. Barcelo-Oliver, A.K. Verma, R.S. Ahmed, S. Hussain, M.K. Bhattacharyya, Supramolecular assemblies involving biologically relevant antiparallel π-stacking and unconventional solvent driven structural topology in maleato and fumarato bridged Zn(II) coordination polymers: antiproliferative evaluation and theoretical studies, New J. Chem. 45 (2021) 13040–13055, doi:10.1039/D1NJ00619C.

[119] P. Sharma, H. Nath, A. Frontera, M. Barcelo-Oliver, A.K. Verma, S. Hussain, M.K. Bhattacharyya, Biologically relevant unusual cooperative assemblies and fascinating infinite crown-like supramolecular nitrate–water hosts involving guest complex cations in bipyridine and phenanthroline-based Cu(II) coordination compounds: antiproliferative evaluation and theoretical studies, New J. Chem. 45 (2021) 8269–8282, doi:10.1039/D1NJ01004B.

[120] J.C. Belmont-Sanchez, M.E. Garcia-Rubino, A. Frontera, J.M. Gonzalez-Perez, A. Castineiras, J. Niclos-Gutierrez, H-bonds, π-stacking and (water)O-H/π interactions in (μ_4-EDTA)bis(imidazole) dicopper(II) dihydrate, Crystals 11 (2021) 48, doi:10.3390/cryst11010048.

[121] M.K. Bhattacharyya, D. Dutta, S.M. Nashre-ul-Islam, A. Frontera, P. Sharma, A.K. Verma, A. Das, Energetically significant antiparallel π-stacking contacts in Co(II), Ni(II) and Cu(II) coordination compounds of pyridine-2,6-dicarboxylates: Antiproliferative evaluation and theoretical studies, Inorg. Chim. Acta 501 (2020) 119233, doi:10.1016/j.ica.2019.119233.

[122] M.N. Ahmed, M. Arif, F. Jabeen, H.A Khan, K.A. Yasin, M.N. Tahir, A. Franconetti A Frontera, On the importance of antiparallel π–π interactions in the solid state of isatin-based hydrazides, New J. Chem. 43 (2019) 8122–8131, doi:10.1039/C9NJ00405J.

[123] A. Najafi, M. Mirzaei, A. Bauza, J.T. Mague, A. Frontera, The roles of H-bonding, π-stacking, and antiparallel CO$\cdots$CO interactions in the formation of a new Gd(III) coordination polymer based on pyridine-2,6-dicarboxylic acid, Inorg. Chem. Comm. 83 (2017) 24–26, doi:10.1016/j.inoche.2017.05.029.

[124] D. Debnath, S. Roy, A. Purkayastha, A. Bauza, R. Choudhury, R. Ganguly, A. Frontera, T.K. Misra, Synthesis and structure of 1,3-dimethyl-5-(*p*-sulfonamide-phenylazo)-6-aminouracil and its Ni(II) complex: topological insights and investigation for noncovalent interactions, J. Mol. Struct. 1141 (2017) 225–236, doi:10.1016/j.molstruc.2017.03.121.

[125] H. Andleeb, I. Khan, S. Hameed, A. Bauza, A. Frontera, M.N. Tahir, J. Simpson, A comparative experimental and theoretical investigation of hydrogen-bond, halogen-bond and π–π interactions in the solid-state supramolecular assembly of 2- and 4-formylphenyl arylsulfonates, ActaCryst C74 (2018) 816–829, doi:10.1107/S2053229618008355.

[126] J.D. Woodward, R.V. Backov, K.A. Abboud, D. Dai, H.-J. Koo, M.-H. Whangbo, M.W. Meisel, D.R. Talham, Dramatic variation of magnetic exchange through double end-on azide bridges in a series of ladder-like copper(II) coordination polymers, Inorg. Chem. 44 (2005) 638, doi:10.1021/ic049175q.

[127] J.-Y. Tsao, J.-D. Tsai, C.-I. Yang, Azide-bridged Cu(II), Mn(II) and Co(II) coordination polymers constructed with a bifunctional ligand of 6-(1*H*-tetrazol-5-yl)-2,2′-bipyridine, Dalton Trans. 45 (2016) 3388, doi:10.1039/C5DT04773K.

[128] J.-N. Li, Synthesis, characterization, and antibacterial activity of [Cu$_2$(L^1)$_3$(NCS)]·CH$_3$CN and [Cu$_2$Br$_2$(L^2)$_2$($\mu_{1,1}$-N$_3$)$_2$], Synth. React. Inorg., Met.-Org., Nano-Met. Chem. 43 (2013) 832, doi:10.1080/15533174.2012.750344.

[129] B.-L. Liu, N. Wu, C.-P. Li, J. Chen, Pseudohalide anion directed assemblies of two Cu^{II} complexes based on 3-(2-pyridyl)-4,5-bis(3-pyridyl)-1,2,4-triazole, Transition Met. Chem. 40 (2015) 341 http://dx.doi.org/10.1007%2Fs11243-015-9922-5.

[130] Y.-Y. Zhu, C. Cui, N. Li, B.-W. Wang, Z.-M. Wang, S. Gao, Constructing a series of azide-bridged Cu^{II} magnetic low-dimensional coordination polymers by using pybox ligands, Eur. J. Inorg. Chem. (2013) 3101–3111, doi:10.1002/ejic.201300107.

[131] E. Espinosa, E. Molins, C. Lecomte, Hydrogen bond strengths revealed by topological analyses of experimentally observed electron densities, Chem. Phys. Lett. 285 (1998) 170–173, doi:10.1016/S0009-2614(98)00036-0.

PAPER

Syntheses, crystal structures and supramolecular assemblies of two Cu(ii) complexes based on a new heterocyclic ligand: insights into C–H⋯Cl and π⋯π interactions†

Samit Pramanik,[a] Sudipta Pathak, [ID] *[b]
Antonio Frontera [ID] *[c] and Subrata Mukhopadhyay[a]

A new heterocyclic ligand, N₃L [4-(1-methylimidazole)-2,6-di(pyrazinyl)pyridine] has been synthesized and characterized by several spectroscopic methods. The ligand (N₃L) was then used for the preparation of two complexes, namely, [Cu(N₃L)Cl₂] (complex **1**) and [Cu(N₃L)(Cl)(μ-ONO₂)]ₙ (complex **2**). The crystal structures of these complexes have been established by single-crystal X-ray diffraction analysis. Complex **1** is a mononuclear one whereas complex **2** is a 1D coordination polymer. The structural insights reveal that non-classical hydrogen bonding (C–H⋯Cl, C–H⋯O, C–H⋯N) and π⋯π stacking interactions play a crucial role in stabilizing various supramolecular architectures of the title complexes in the solid state. All the non-classical hydrogen bonding interactions are quantified through the infographic 2D fingerprint plots. Additionally, theoretical calculations (density functional theory) were carried out for both complexes to analyze these non-covalent interactions in the solid state including their characterization using Bader's theory of atoms in molecules and the noncovalent interaction (NCI) plot index.

Introduction

Crystal engineering is the design of molecular solids through an understanding and manipulation of intermolecular interactions.[1] Nowadays, crystal engineering is recognised as a key aspect of supramolecular chemistry which assembles the molecules through intermolecular interactions and such interactions are utilized for controlling molecular architectures in the solid state.[2] Engineering strategies not only rely on hydrogen bonding and coordination bonds, but also use interactions of relatively lower strength such as halogen bonds, π⋯π, cation⋯π, anion⋯π, C–H⋯π, lone pair⋯π and similar ones actively and in conjugation.[3–5] Intermolecular interactions drive the molecular recognition and self-assembly processes in both chemical and biological systems.[6–9] The construction of molecular architecture also depends on the coordination geometry of metal salts for coordination compounds.[10] Hydrogen bonding as a

non-covalent interaction is at the heart of supramolecular chemistry; it is vastly explored and considered as the most imperative noncovalent interaction during self assembly processes.[11] The hydrogen bonds of the types O–H⋯O/Cl/N and N–H⋯O/N/Cl are strong enough compared to the stabilization energy of van der Waals force.[12]

Besides classical hydrogen bonding (Y–H⋯A, Y&A = N, O, F, *etc.*) interactions, non-classical hydrogen bonding interactions have attracted notable attention on a number of fronts.[13,14] Non-classical hydrogen bonding involves less polar C–H donors in the presence of unshared-pair bearing atoms (N, O, X where X = F, Cl, *etc.*).[15] The strength of the H⋯N/O/X interaction is proportional to the polarization of the donor C–H and the charge of the acceptor heteroatom.[16] Such C–H polarization is more effective for heterocyclic rings like pyridine, pyrimidine or the like. In addition, the hydrogen bond acceptor capability of inorganic halides (M–X) is stronger than organic halides (C–X).[17] Among non-classical hydrogen bonding (C–H⋯N/O/X) interactions, the C–H⋯Cl interaction attracts interest in the broad field of materials chemistry,[18] C–H activation,[19] ion transport,[20] and anion recognition,[21] as well as in constricting molecular architectures.[22,23] As anticipated, the C–H⋯Cl distance should be less than the sum of the van der Waals radii (2.95 Å) of the hydrogen atom and the neutral chlorine atom for a superior C–H⋯Cl interaction.[24] In our present work such distances are in the range of 2.49 to 2.83 Å.

[a] Department of Chemistry, Jadavpur University, Kolkata 700032, India
[b] Department of Chemistry, Haldia Government College, Purba Medinipur, 721657, Debhog, West Bengal, India. E-mail: sudiptachemster@gmail.com
[c] Departament de Química, Universitat de les Illes Balears, Crta. de Valldemossa km 7.5, 07122 Palma de Mallorca, Baleares, Spain. E-mail: toni.frontera@uib.es
† Electronic supplementary information (ESI) available: CCDC 2107292 and 2107293. For ESI and crystallographic data in CIF or other electronic format see DOI: 10.1039/d1ce01402a

Experimental section

Materials and apparatus

All the chemical reagents (analytical grade) and solvents (spectroscopic grade) are procured from commercial suppliers and used as received. Freshly prepared doubly distilled water was used throughout the synthetic procedure and all the reactions were carried out under aerobic conditions. Elemental analyses (C, H and N) were performed using a PerkinElmer 2400 Series-II CHN analyzer, USA, elemental analyzer. ^{1}H NMR and ^{13}C NMR spectra were obtained on a Bruker spectrometer (300 MHz) with CDCl$_3$ solvent using trimethylsilane (TMS) as an internal standard. Fourier transform infrared (FTIR) spectra were recorded on a Perkin Elmer LX-1 FT-IR spectrophotometer (4000–400 cm^{-1}) by using a modern diamond attenuated total reflectance (ATR) accessory. ESI-MS (mass spectra) were obtained on a Water HRMS model XEVO-G2QTOF#YCA351 spectrometer.

Synthesis of 4-(1-methylimidazole)-2,6-di(pyrazinyl)pyridine [N$_3$L]

Acetylpyrazine (0.281 g, 2.3 mmol) was added to the ethanolic solution (30 mL) of 1-methyl imidazole-2-carboxaldehyde (0.11 g, 1 mmol) under stirring conditions. 3 mL of 1 M aqueous solution of NaOH followed by 5 mL aqueous NH$_3$ (35%) solution was poured into the reaction mixture at room temperature (Scheme S1, ESI†). The reaction mixture was then refluxed for 3 hours and cooled at room temperature. A light yellow solid was formed which was collected by filtration and washed with cold water several times and dried in air. The desired product was obtained with satisfactory yield and acceptable purity (yield 0.214 g (68%). m.p. >260 °C, Scheme S1 (ESI†)). Anal. calc. for C$_{17}$H$_{13}$N$_7$, C 64.75, H 4.16, N 31.09. Found: C 64.72, H 4.12, N 31.05%. ^{1}H NMR (300 MHz, CDCl$_3$): δ (ppm) = 9.85 (s, 2H), 8.83 (s, 2H), 8.65 (s, 4H), 7.24 (s, 1H), 7.09 (s, 1H), 3.99 (s, 3H) (Fig. S1, ESI†). ^{13}C NMR (75 MHz, CDCl$_3$): δ (ppm) = 154.50, 150.46, 144.93, 143.70, 143.48, 140.37, 129.60, 124.24, 120.55, 35.17 (Fig. S2, ESI†). Main FT-IR absorptions, (KBr, cm^{-1}): 1980(s), 1606(vs), 1570(vs), 1519(s), 1464(s), 1456(s), 1419(s), 1371(vs), 1292(s), 1257(s), 1224(s), 1120(vs) (Fig. S3, ESI†). ESI-MS: m/z 316.12, calcd. for $[C_{17}H_{13}N_7+H]^+$ 316.13 (Fig. S4, ESI†).

Synthesis of [Cu(N$_3$L)Cl$_2$] (complex 1)

An aqueous suspension (15 mL) of the ligand, **N$_3$L** (0.315 g, 1.0 mmol) was added dropwise to an aqueous solution (15 mL) of CuCl$_2$·2H$_2$O (0.170 g, 1.0 mmol) with constant stirring for 3 hours (Scheme S2, ESI†) and a bright green coloured solution was obtained. The solution was then filtered and the filtrate was kept undisturbed for slow evaporation. After one week, light green X-ray quality crystals of **1** were obtained from the mother liquor (yield: 68%). The solubility of the complex was checked in various solvents and found to be insoluble in water but partly soluble in acetonitrile and methanol whereas completely soluble in DMSO and DMF. Anal. calc. for C$_{17}$H$_{13}$N$_7$CuCl$_2$: C, 45.40;

Terpyridines or polypyridines have been widely explored as chelating ligands for d-block metal ions for their strong electron affinity.[25,26] Oligopyridine motifs can be utilized to prepare highly stable metal complexes.[27] Terpyridine based metal complexes have drawn keen interest in contemporary research in the fields of supramolecular chemistry and this knowledge is extended to application of materials science.[28,29] They have interesting magnetic and optoelectronic properties like electrocatalysis, hydrogen evolution, *etc.*[30–34] Terpyridine metal complexes are also employed as the active layer to fabricate resistive switching memory devices,[35] fluorescent probes for pyrophosphate (PPi) detection,[36] and photo-functional nanomaterials.[37] In particular, Cu(II) complexes containing heterocyclic ligands have received increasing attention because of their promising applications in catalysis and energy harvesting devices as well as in medicinal chemistry within the last few decades.[38–41] Being the third most abundant transition metal (after iron and zinc) in the human body, copper plays an important role in hemopoiesis, metabolism, growth and the immune system.[42] In addition, compared to other common metal ions, Cu(II) ions exhibit a high binding constant with various ligands.[43] Inspired by the importance of terpyridine metal complex systems, we here report two Cu(II) complexes using newly synthesized 4-(1-methylimidazole)-2,6-di(pyrazinyl)pyridine [C$_{17}$H$_{13}$N$_7$] as the terpyridine ligand (**N$_3$L**). Complex **1** is formed by reacting with CuCl$_2$·2H$_2$O and **N$_3$L** in aqueous medium. Complex **2** is synthesized by treating Cu(NO$_3$)$_2$·3H$_2$O with **N$_3$L** in the presence of hydrochloric acid in water. Both complexes have been synthesized strategically so that at least one chloride ion should be attached with the metal centers. Single-crystal X-ray structural analysis shows that complex **1** adopts a distorted square pyramidal geometry whereas complex **2** has a distorted octahedral geometry. It is noted that the change in the auxiliary anion exhibits structural variations in the present complexes substantially. In complex **1**, two different 2D arrangements are observed through intermolecular $\pi\cdots\pi$ stacking and C–H$\cdots$Cl hydrogen bonding interactions. Besides, a 2D layer is observed only employing C–H$\cdots$Cl hydrogen bonding interactions. Complex **2** exhibits a 1D polymeric chain (through nitrate bridge) which was extended utilizing $\pi\cdots\pi$ and hydrogen bonding (C–H$\cdots$O, C–H$\cdots$Cl) interactions. The 2D fingerprint plots associated with the Hirshfeld surfaces facilitate a comparison of non-classical hydrogen bonding interactions by quantifying them in an effective visual manner. The present work interlinks experiment and theory (DFT calculations) to explore the noncovalent interactions and their interplay leading the solid state architectures of complexes **1** and **2**. The MEP (molecular electrostatic potential) surface analysis also agrees well with the ability of both compounds to establish the non-classical C–H$\cdots$N/O/Cl hydrogen bonding interactions in the solid state. In particular, the influence of $\pi\cdots\pi$ stacking interactions along with the existence of C–H$\cdots$Cl hydrogen bonds triggered by terminal M–Cl bonds has been well established in the self-assembly of both complexes.

H, 2.91; N, 21.80. Found: C, 45.35; H, 2.88; N, 21.76%. Main FTIR absorptions, (KBr, cm^{-1}): 3345(bs), 3093(s), 3022(s), 1609(vs), 1557(s), 1495(s), 1463(vs), 1438(s), 1410(s), 1316(s), 1296(s), 1278(vs), 1223(s) (Fig. S5, ESI†).

Synthesis of [Cu(N$_3$L)(Cl)(μ-ONO$_2$)]$_n$ (complex 2)

Complex **2** was synthesized by reacting Cu(NO$_3$)$_2$·3H$_2$O (0.241 g, 1.0 mmol) with the title ligand, **N$_3$L**, (0.315 g, 1.0 mmol) in water (30 mL) at 60 °C with constant stirring. After around two hours of constant stirring the reaction mixture became turbid, the turbidity was removed by the addition of a few drops of dilute hydrochloric acid and the reaction mixture was stirred continuously for another one hour (Scheme S2, ESI†). The resultant solution was then filtered and the filtrate was left without any disturbance. Suitable single crystals for X-ray analysis were obtained after three weeks (yield: 62%). Complex **2** was insoluble in water, partly soluble in methanol and completely soluble in DMSO, DMF and acetonitrile. Anal. calc. for C$_{17}$H$_{13}$N$_8$CuClO$_3$: C, 42.87; H, 2.75; N, 23.52. Found: C, 42.83; H, 2.71; N, 23.49%. Main FTIR absorptions, (KBr, cm^{-1}): 3213(w), 3118(s), 3094(s), 3058(s), 3030(s), 1986(s), 1748(s), 1608(vs), 1591(s), 1557(vs), 1469(s), 1446(s), 1434(s), 1402(s), 1372(s), 1318(s) (Fig. S5, ESI†).

X-ray crystallographic analysis

Single crystal X-ray data of both complexes were collected using a Bruker SMART APEX II CCD area detector equipped with a graphite monochromated Mo Kα radiation (λ = 0.71073 Å) source in φ and ω scan mode at 273 K. Cell parameter refinement and data reduction were carried out using a Bruker SMART APEX II instrument and Bruker SMART and Bruker SAINT software[44] for both complexes. The crystal structures of both complexes were solved by SHELXT-2014/5 and refined by full-matrix least squares on F^2 techniques using the SHELXL-2016/6 crystallographic software package.[45] CCDC 2107292 (for **1**) and 2107293 (for **2**) contain the supplementary crystallographic data for this work. Selected crystal data for **1** and **2** are given in Table S1 (ESI†).

Hirshfeld surface analysis

Hirshfeld surfaces[46–48] and the associated two-dimensional (2D) fingerprint[49–51] plots were obtained using Crystal Explorer[52] with bond lengths to hydrogen atoms set to standard values. Two distances, d_e (the distance from the point to the nearest nucleus external to the surface) and d_i (the distance to the nearest nucleus internal to the surface), are defined for each point on the Hirshfeld surface. The normalized contact distance (d_{norm}) based on d_e and d_i is defined as:

$$d_{norm} = \frac{\left(d_i - r_i^{vdw}\right)}{r_i^{vdw}} + \frac{\left(d_e - r_e^{vdw}\right)}{r_e^{vdw}}$$

where r_i^{vdw} and r_e^{vdw} are the van der Waals radii of the atoms. The d_{norm} value is negative or positive depending on intermo-lecular contacts being shorter or longer than the van der Waals separations. The parameter d_{norm} displays a surface with a red-white-blue colour design, where bright red spots highlight shorter contacts, white areas on the same surface correspond to contacts around the van der Waals separation and blue regions are devoid of close contacts. For a given CIF, the Hirshfeld surface is said to be unique.[53]

Theoretical methods

The non-covalent interactions were analysed energetically using Gaussian-16 at the PBE0-D3/def2-TZVP level of theory.[54] The binding energies have been corrected using the Boys and Bernardi counterpoise method.[55] The Grimme D3 dispersion correction has also been used in the calculations.[56] To evaluate the interactions in the solid state, the crystallographic coordinates were used and only the position of the hydrogen bonds has been optimized. This methodology and level of theory has been previously used to analyze non-covalent interactions in the solid state.[57,58] The interaction energies were estimated by calculating the difference between the energies of the isolated monomers and the ones of their assembly. The NCI plot[59] isosurfaces have been used to characterize non-covalent interactions. They correspond to both favourable and unfavourable interactions, as differentiated by the sign of the second density Hessian eigenvalue and defined by the iso-surface color. The color scheme is a red-yellow-green-blue scale with red for ρ_{cut}^+ (repulsive) and blue for ρ_{cut}^- (attractive). Bader's[60] quantum theory of "atoms-in-molecules" (QTAIM) was also used to characterize the interactions. For these calculations, we have used the same level of theory and the program AIMAll.[61]

Results and discussion

Structural description of complex 1

The molecular structure of complex **1** with the atom numbering scheme is shown in Fig. 1. The complex crystallizes in an ortho-rhombic system with the space group $P2_12_12_1$ and its unit cell comprises of four complex units. The selected bond lengths (Å) and bond angles (°) are presented in Tables S2 and S3, respectively (ESI†). Complex **1** shows one mononuclear [Cu(N$_3$L)Cl$_2$] unit where the tridentate ligand N$_3$L is 4-(1-methylimidazole)-2,6-di(pyrazinyl)pyridine. The coordination mode around the metal center can be best described as a distorted square pyramid (the τ value[62] is 0.217, see eqn S1 in the ESI†) where the three pyrazinyl nitrogen atoms (N4, N5 and N6) of our title ligand (N$_3$L) and one chloride ion (Cl1) occupy the basal plane while the axial position is occupied by another chloride ion (Cl2). The average Cu–N bond distance is 2.026 Å [Cu1–N4 = 2.051(2) Å, Cu1–N5 = 1.963(2) Å and Cu1–N6 = 2.064(2) Å]. The axial chloride (Cl2) is positioned somewhere at a longer distance [Cu1–Cl2 = 2.3629(10) Å] than the equatorial one [Cu1–Cl1 = 2.2495(9) Å] likely due to the less 's' character of the orbital engaged in the coordination bond, which makes the axially coordinated chloride anion more electronegative (stronger hydrogen bond acceptor).[23] The Cu(ɪɪ) ion is shifted by a distance of 0.437
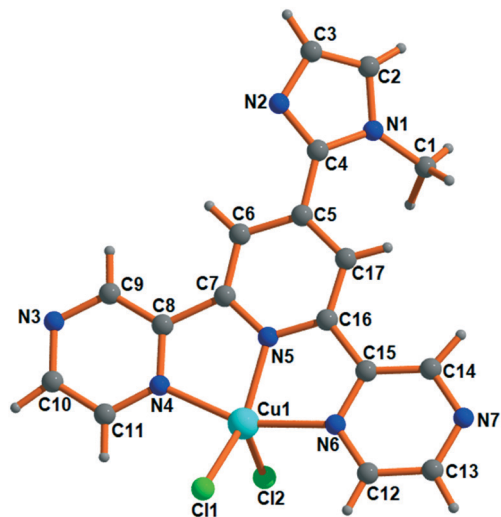
Fig. 1 Molecular structure of complex **1**. Color code: Cu(II), turquiose; Cl, bright green; N, blue; C, grey 50; H, grey 25.

Å towards the axial Cl2 atom from the basal plane (N4, N5, N6 and Cl1). The imidazole ring is twisted by an angle of 34.81° from the plane of the central pyridine ring of the title ligand, **N₃L**. The electrical charge on the Cu(II) ion is compensated by two coordinated chloride ions (Cl1 and Cl2).

The complex units of **1** form a one dimensional polymeric chain (ladder type) through the self-complementary $\pi\cdots\pi$ interactions (Table S5, ESI†) between Cg(3) of one unit with Cg(5) of the other unit and *vice versa*. The interplanar separation distances between consecutive Cg(3) and Cg(5) centroids are 3.5021(18) Å and 3.6867(18). Interestingly, the parallel chains are oriented in such a manner that hydrogen H13 (attached with pyrazine C13) of one unit faces the Cl2 atom at (−1/2 + *x*, 3/2 − *y*, 2 − *z*) of the other unit forming hydrogen bonding interac-

tion (shown by green dotted lines) which generates a 2-D supramolecular framework (wave like) in the *ac*-plane (Fig. 2).

Another 2-D layer is shaped in complex **1** using $\pi\cdots\pi$ and hydrogen bonding interactions (Fig. 3). Firstly, a one dimensional (1-D) zigzag polymeric chain is formed by the $\pi\cdots\pi$ interaction between Cg(4) of one complex unit and Cg(6) of the other unit with a ring centroid separation of 3.958(2) Å (Table S5, ESI†). Now, the intermolecular hydrogen bond [C10–H10···Cl2] connects the parallel chains at (1 − *x*, −1/2 + *y*, 3/2 − *z*) to form a 2-D supramolecular network in the *ab*-plane. The existence of C–H···Cl interactions triggered by charge-assisted terminal M–Cl bonds has been well established in recent times.[23,63]

The formation of a 2-D supramolecular architecture (Fig. 4) is ensured by various C–H···Cl interactions (Table S4, ESI†). Through a closer look it is evident that the mononuclear units are propagated to form a 1-D polymeric chain through two intermolecular hydrogen bonding [C6–H6···Cl1 at an angle of 171° and C9–H9···Cl1 at an angle of 176(3)°] interactions (shown by pink dotted lines) incorporating the terminal chloride ion (Cl1). In association with these intermolecular hydrogen bonding interactions two other intermolecular hydrogen bonding [C14–H14···Cl1 at an angle of 145(4)° and C17–H17···Cl1 at an angle of 157(3)°] interactions (shown by green dotted lines) are involved to extend the dimensionality to 2-D in the *ac*-plane.

In addition, a 1D chain is generated through C1–H1C···Cl2 interactions as depicted in Fig. 5. Here, the methyl C1–H1C acts as a donor to the axial Cl2 atom (stronger H bond acceptor).

Structural description of complex 2

Complex **2** is basically a 1D coordination polymer (Fig. 6) and the perspective view of the molecular structure with the atom
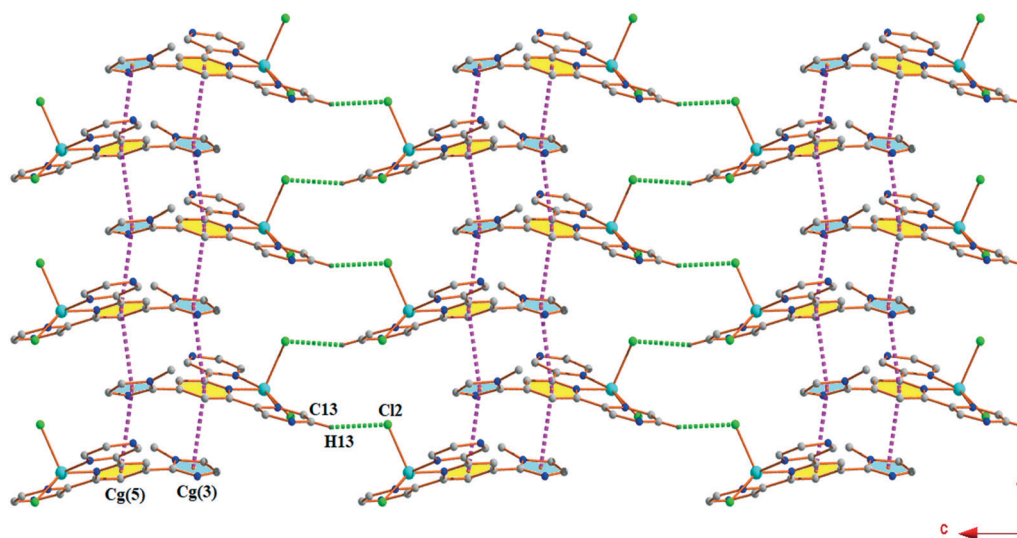

Fig. 2 Perspective view of the 2-D architecture (wave like) incorporating $\pi\cdots\pi$ and C–H···Cl hydrogen bonding interactions in complex **1** (other aromatic hydrogen atoms have been omitted for clarity).
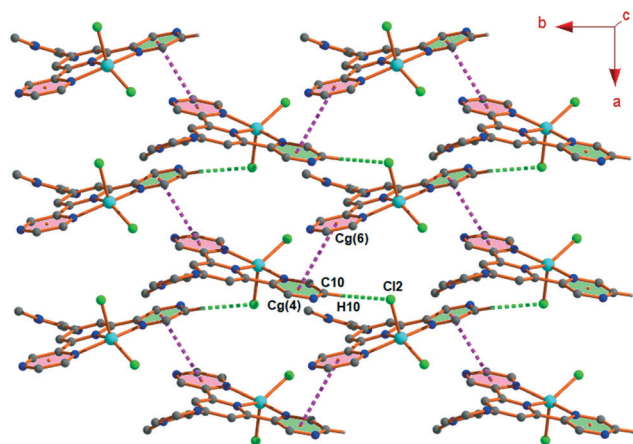
Fig. 3 2-D layer generated through $\pi\cdots\pi$ and C–H$\cdots$Cl hydrogen bonding interactions in complex **1** (other aromatic hydrogen atoms have been omitted for clarity).

numbering scheme is shown in Fig. 7. The single-crystal X-ray diffraction study shows that the complex adopts an orthorhombic system with the space group $P2_12_12_1$ and its unit cell contains four complex units. The important bond lengths (Å) and bond angles (°) are included in Tables S2 and S3, respectively (ESI†). In this complex, the nitrate anion connects the Cu(II) centres along the [100] direction by utilising two different oxygen atoms (O1 and O2) to form a 1D polymeric chain. Here, the 1D chain can be classified within a 2C1 topological type.[64] The central Cu(II) ion is situated in a distorted octahedral geometry where the basal plane is formed by the three pyrazinyl nitrogen atoms (N4, N5 and N6) of the title ligand (**N₃L**) and one chloride ion (Cl1). The *trans* axial positions are occupied by two oxygen atoms (O1 and O2) of the nitrate ion. In the basal plane, the Cu–N bond

lengths vary from 1.938(3) to 2.049(3) Å, whereas the axial Cu–O bond lengths [2.498(5) Å and 2.641(4) Å] are much longer than the equatorial bond lengths, suggesting a pronounced Jahn–Teller effect. The imidazole ring is twisted by an angle of 24.41° from the plane of the central pyridine ring of the title ligand, **N₃L**. The electrical charge on the metal center is stabilised by one coordinated chloride ion and one coordinated nitrate (NO_3^-) ion.

In complex **2**, the parallel chains are interconnected in a zigzag fashion through the $\pi\cdots\pi$ interaction between Cg(4) and Cg(6) of the two units to generate a supramolecular framework in the *ab*-plane (Fig. 8). The ring centroid separation between Cg(4) and Cg(6) is 3.826(3) Å (Table S5, ESI†).

In another architecture (Fig. 9), the parallel chains are interconnected through the C14–H14$\cdots$O3 hydrogen bonding interaction forming a two-dimensional (2-D) supramolecular network which is further strengthened by the C–H$\cdots$Cl hydrogen bond at $(2 − x, 1/2 + y, 1/2 − z)$ between the coordinated chlorine atom (Cl1) and methyl hydrogen atom (H1B) of the adjacent molecule (as depicted in Fig. 9).

This 2D architecture (Fig. 9) is further stabilized through the non-classical C–H$\cdots$O hydrogen bonding and intramolecular anion$\cdots\pi$ interactions synergistically as shown in Fig. S6 (ESI†). Here the π-lobes of pyrazine have been oriented in such a fashion so that it could form the above mentioned intramolecular anion$\cdots\pi$ interaction with the nitrate O3 atom that in turn is reinforced to form the C1–H1B$\cdots$O3 hydrogen bonding interaction and plays a pivotal role from a supramolecular perspective in the solid state architecture of complex **2**.

Due to their self-complementary nature, complex units (extracted from the polymeric chain) are interconnected along the [100] direction through $\pi\cdots\pi$ stacking interactions to form a 1-D zigzag chain. Here, the complex units are
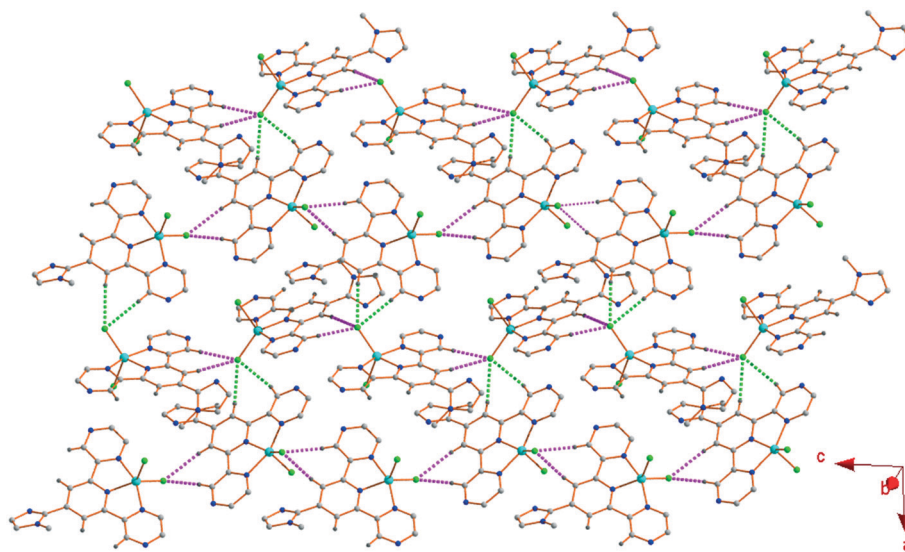

Fig. 4 Formation of a 2-D network comprising C–H$\cdots$Cl hydrogen bonding interactions in complex **1** (other aromatic hydrogen atoms have been omitted for clarity).
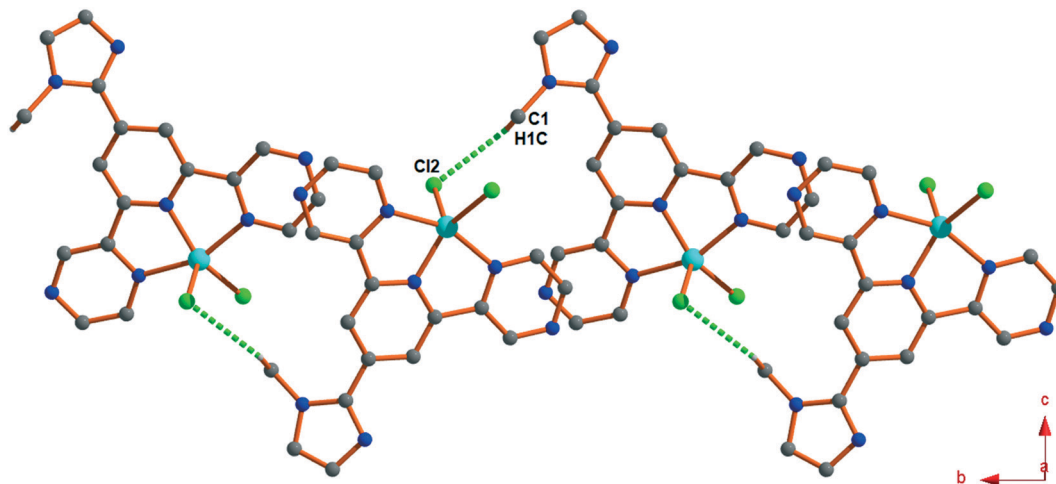
Fig. 5 Propagation of the 1D chain along the [010] direction by C–H···Cl hydrogen bonding interactions in complex **1** (other aromatic hydrogen atoms have been omitted for clarity).
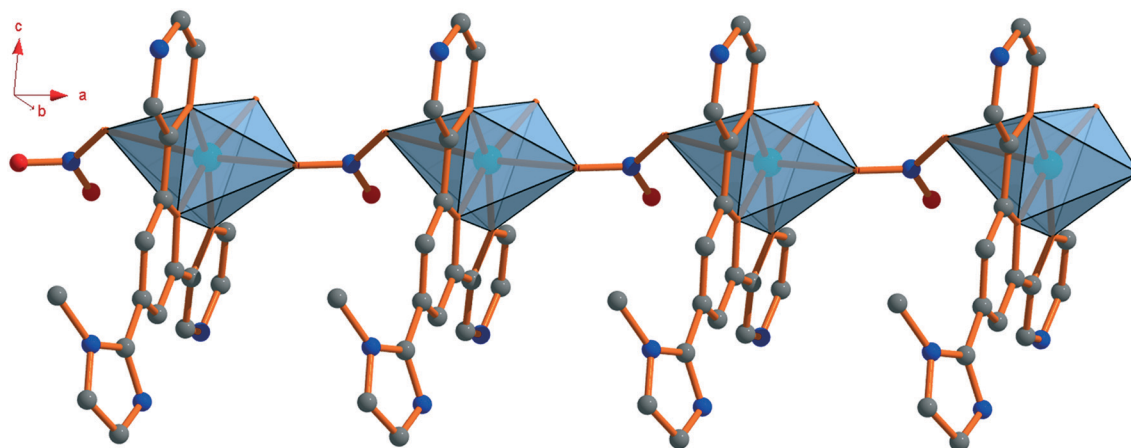

Fig. 6 Formation of a 1-D polymeric chain through nitrate linkage (hydrogen atoms are omitted for clarity).
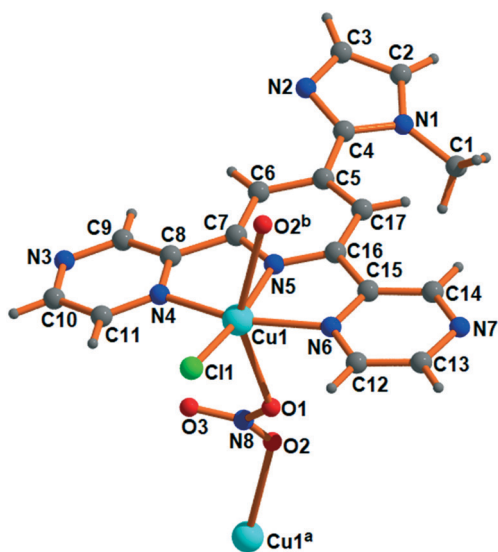

Fig. 7 Molecular structure of complex **2**. Color code: Cu(II), turquoise; Cl, bright green; N, blue; O, red; C, grey 50; H, grey 25.
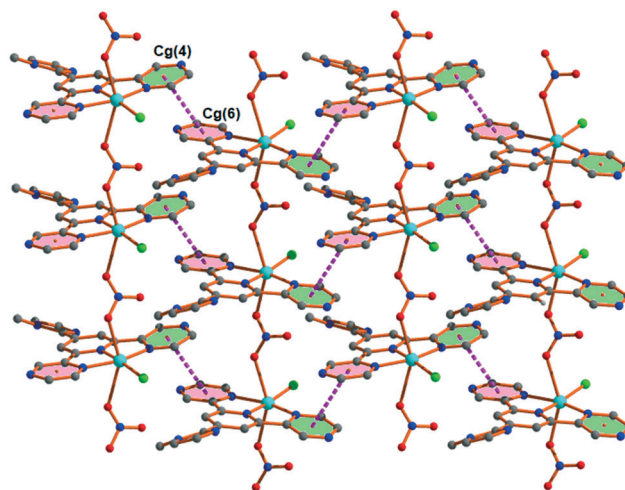

Fig. 8 Perspective view of the 2-D architecture through π···π interactions in complex **2** (other aromatic hydrogen atoms have been omitted for clarity).
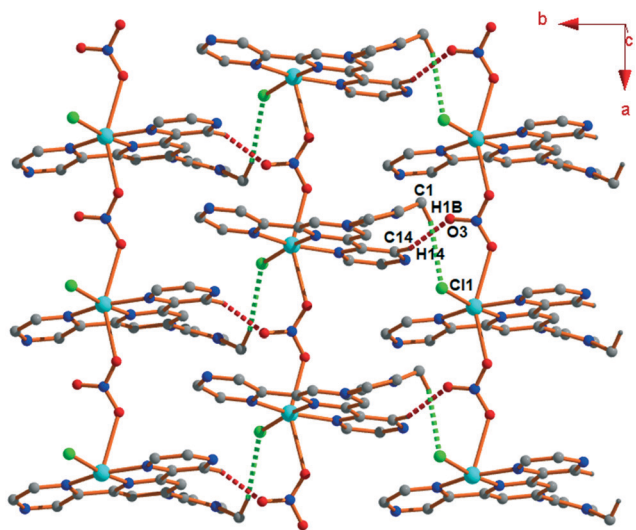
Fig. 9 Perspective view of the 2-D architecture generated through C–H⋯Cl and C–H⋯O hydrogen bonding interactions in complex **2** (other aromatic hydrogen atoms have been omitted for clarity).

arranged in a face-to-face fashion to achieve the π⋯π stacking interaction between Cg(3) and Cg(5) of two units. As the crystal structure of complex **2** departs from the ideal planarity, the Cg(3)–Cg(5) distances are not identical [3.733(3) Å and 3.905(3) Å] (Table S5, ESI†). The parallel chains are interlinked by the C9–H9⋯Cl1 (168°) hydrogen bond at (3/2 − x, 1 − y, 1/2 + z) to build a 2-D (ac-plane) network (Fig. 10) which is further extended in the bc-plane. Now, these two planes are repeating themselves to enhance the dimensionality from 2-D to 3-D (Fig. 11).

Besides, it was observed that the polymeric chains (Fig. 6) are interconnected in a self-complementary manner through C3–H3⋯O2 hydrogen bonding interactions at (1/2 + x, 3/2 − y, 1 − z) to generate a 1D tape along the [100] direction

(Fig. 12). This molecular integrity (1D tape) has been stabilized in collaboration with a comparatively weak C1–H1C⋯N2 hydrogen bonding interaction.

Comparison with structurally related Cu(II) complexes

We have made a brief comparative review on the crystallographic and supramolecular aspects of some related Cu(II) complexes (derived from substituted terpyridine ligands) reported earlier (see Tables S6 and S7 respectively, ESI†). The 4′-substitution on the terpyridine moiety was made by 4-pyridyl (**3**), phenyl (**4**), benzoic acid (**5**), 2-pyridyl (**6**), 3-pyridyl (**7**), quinoline-2-yl (**8**), and quinoline-4-yl (**9**) in comparison to our present 1-methylimidazole analogue (**1** and **2**). Here, it is interesting to note that these substituents do not participate in direct coordination with the metal ions but may impart some electronic inputs so that their ability to participate in supramolecular interactions may vary. Except complex **2**, all other complexes reported in Table S6† have a distorted square pyramidal geometry (as evident from the Addison parameter, τ). Among all square pyramidal complexes except **4** and **5**, the ligands act as a N_3Cl_2 donor chromophore where all the three nitrogen atoms coming from the terpyridine part and one chloride occupy the equatorial positions. Finally, the square pyramidal geometry was completed by coordination with another chloride ion axially. In complex **4**, one of the outer pyrazinyl-N atoms takes part in further complexation and forms a square planar moiety (as N_2Cl_2) around another Cu(II) that in turn forms a discrete trinuclear complex rather than a coordination polymer. In complex **5**, the equatorial positions are occupied by three nitrogen atoms from the terpyridine part and one oxygen atom from the benzoic acid moiety. In comparison to other reported complexes (**3–9**), complex **1** shows a maximum deviation of the central Cu(II) ion from the basal plane (0.437 Å) and results in the shortest
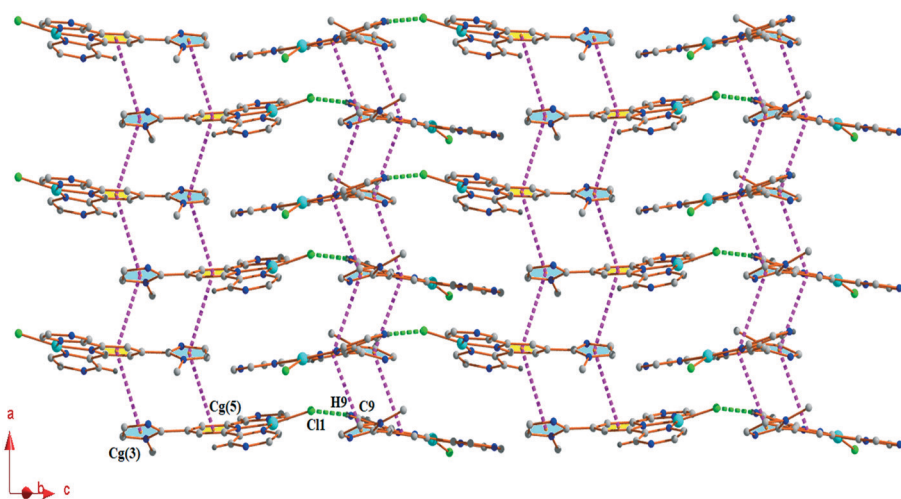

Fig. 10 Perspective view of the 2-D network generated through π⋯π and hydrogen bonding interactions in complex **2** (axial bonds and other aromatic hydrogen atoms have been omitted for clarity).
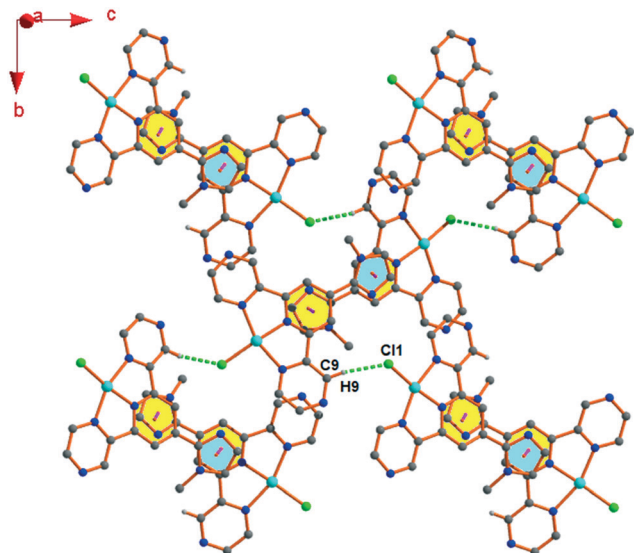
Fig. 11 Formation of an extended network in the *bc*-plane in complex **2** (axial bonds and other aromatic hydrogen atoms have been omitted for clarity).
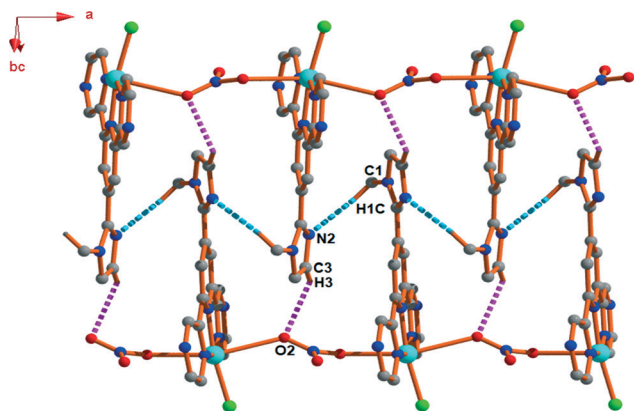

Fig. 12 Formation of a 1D tape through C–H···N and C–H···O hydrogen bonding interactions in complex **2** (other aromatic hydrogen atoms have been omitted for clarity).

axial Cu–Cl bond length (2.363 Å) among **1**–**9.** In all other reported complexes (**3**–**9**), the substituent bears a six membered ring and in the present work we have strategically used a five membered ring (1-methylimidazole). The five membered ring may put some stereo-electronic restriction at the square plane so that the central Cu(ɪɪ) ion is shifted maximum toward axial chloride with respect to that in the analogously substituted six membered ring and consequently results in the shortest axial Cu–Cl distance.

Substitution on the terpyridine moiety not only affects the geometry of the coordination compound but also controls the self-assembly process.[38] From the supramolecular point of view it was evident that in all complexes (details in Table S7†) π···π and C–H···Cl interactions play a crucial role in forming the solid state architectures. The terpyridine moiety with enhanced π electron density acts as an electron rich zone that interacts

with the electron deficient π moiety (caused by coordination of nitrogen atoms of the terpyridine ring) to form a π···π stacking interaction. Generally, the C–H bond becomes silent in hydrogen bonding interactions except when the electron withdrawing group is attached with carbon to make it electron deficient. The coordination of pyridine nitrogen atoms to the central Cu(ɪɪ) ion makes the rings sufficiently electron deficient and introduces some protonic character to the H atom of the C–H bond that in turn exhibits several C–H···Cl hydrogen bonding interactions found in the reported complexes (Table S7†). The H···Cl distance was found to be second shortest in complex **2** (2.49 Å) just next to that in complex **3** (2.44 Å) among other complexes suggesting a strong C–H···Cl interaction. The π···π separation in compounds **1** and **2** ranges 3.5020(18)–3.905(3) Å, comparable to the tabulated complexes (**3**–**9**) (Table S7, ESI†). Some of the authors[38,65–68] reported the existence of π···π and C–H···Cl interactions. However, such contacts were not analyzed using comprehensive DFT calculations like those reported herein.

Hirshfeld surface

The Hirshfeld surfaces of the title complexes were mapped over d_{norm} (range: −0.29 to 1.13 Å), d_i, d_e, shape index and curvedness (Fig. S7 and S8 in the ESI†). The surfaces were made transparent to enable visualization of the molecular moiety around which they are calculated. Furthermore, the 2D fingerprint plots represent all intermolecular interactions that are involved within the structures (Fig. 13 and 14). To quantify each individual contact, we have demonstrated the full-fingerprint plots in unique visual mode for both complexes. The intermolecular interactions appear as distinct spikes in the 2D fingerprint plot which shows the different spikes with their corresponding interactions.

The main non-classical hydrogen bonding interaction is observed for complex **1** between hydrogen and chlorine atoms. In complex **2**, the major interaction is obtained between hydrogen and oxygen atoms. The H···Cl/Cl···H contacts contributed 25.3% in complex **1** whereas that contribution is 10.4% to the total Hirshfeld surface area for complex **2**. Other visible spots in the Hirshfeld surface of complex **1** correspond to the H···N/N···H contacts (17.3%). The proportions of the H···O/O···H and H···N/N···H interactions of the Hirshfeld surface of complex **2** comprise 19.1% and 15.9%, respectively (Fig. 14).

Theoretical DFT study

PBE0-D3/def2-TZVP calculations have been used to analyse and rationalize the H-bonding and the π-stacking interactions described above in Fig. 2–5 and 8–12 that are relevant for the crystal packing of compounds **1** and **2**. The molecular electrostatic potential (MEP) surfaces of compound **1** and compound **2** (monomeric fragment) have been initially obtained to investigate the most electron poor and electron rich parts of the molecules (see Fig. 15). As expected, the most negative MEP values are located at the anionic co-ligands, that is the axial Cl in **1** and nitrate in **2** (−59.6 and −80.3 kcal
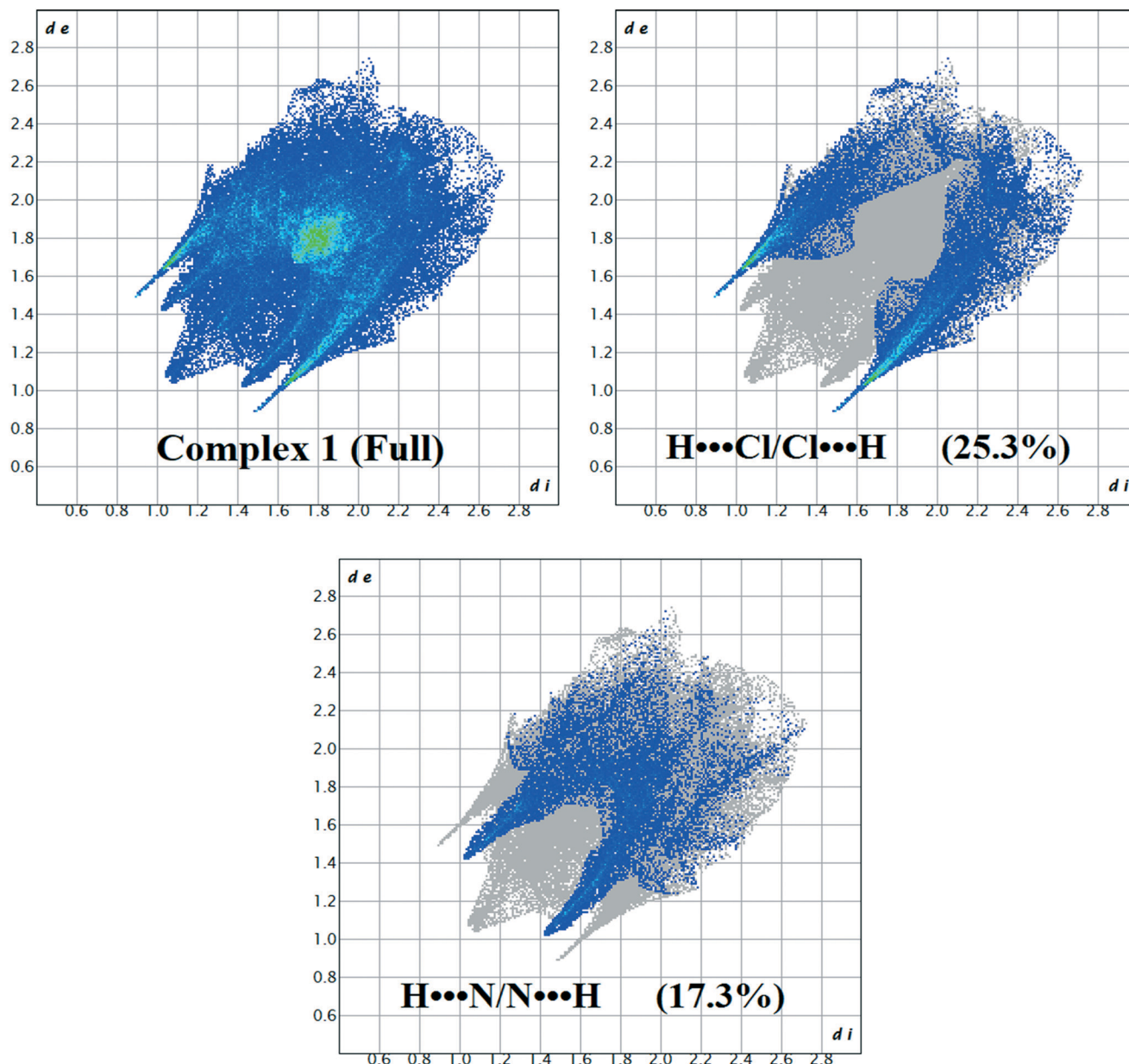
Fig. 13 Fingerprint plots (full) and decomposed plots for each individual interaction in complex **1**.

mol^{-1}). The MEP values at the equatorial Cl atoms in **1** and **2** are −39.5 and −30.1 kcal mol^{-1}, respectively (see Fig. 15b and d), more positive than those at the axial positions. The MEP values at the non-coordinated N-atoms of the organic ligand range from −16.9 to −22.9 kcal mol^{-1} in compounds **1** and **2**. In both complexes, the maximum MEP value (+49.5 kcal mol^{-1} in **1** and 55.0 kcal mol^{-1} in **2**) is located in a cleft that is under the influence of two aromatic H-atoms and one aliphatic H-atom (methyl group of the imidazole ring). The MEP values above and below the aromatic rings of the ligand are positive. Interestingly, they are significantly more positive on the side opposite to the axial ligand (ranging from +15 to +30 kcal mol^{-1}) than on the same side of the axial ligand (ranging from +5 to +15 kcal mol^{-1}. The MEP

values over the accessible chelate rings are also positive and larger in compound **2**. The MEP surface analysis explains the ability of both compounds to establish CH⋯X (X = N, O, and Cl) H-bonding interactions in the solid state (see Fig. 2–4, 9, 10 and 12).

As mentioned in the structural description of **1** (Fig. 1), this compound forms π⋯π interactions where the five membered ring of one complex is stacked over the central six-membered pyridine ring of the adjacent one and *vice versa*. In the present DFT study we have mainly focused on this interaction, where, in good agreement with the MEP surface analysis, the most π-acidic surface of the ligand interacts with the least acidic one to minimize the electrostatic repulsion. Fig. 16a shows a dimer extracted from the solid state of
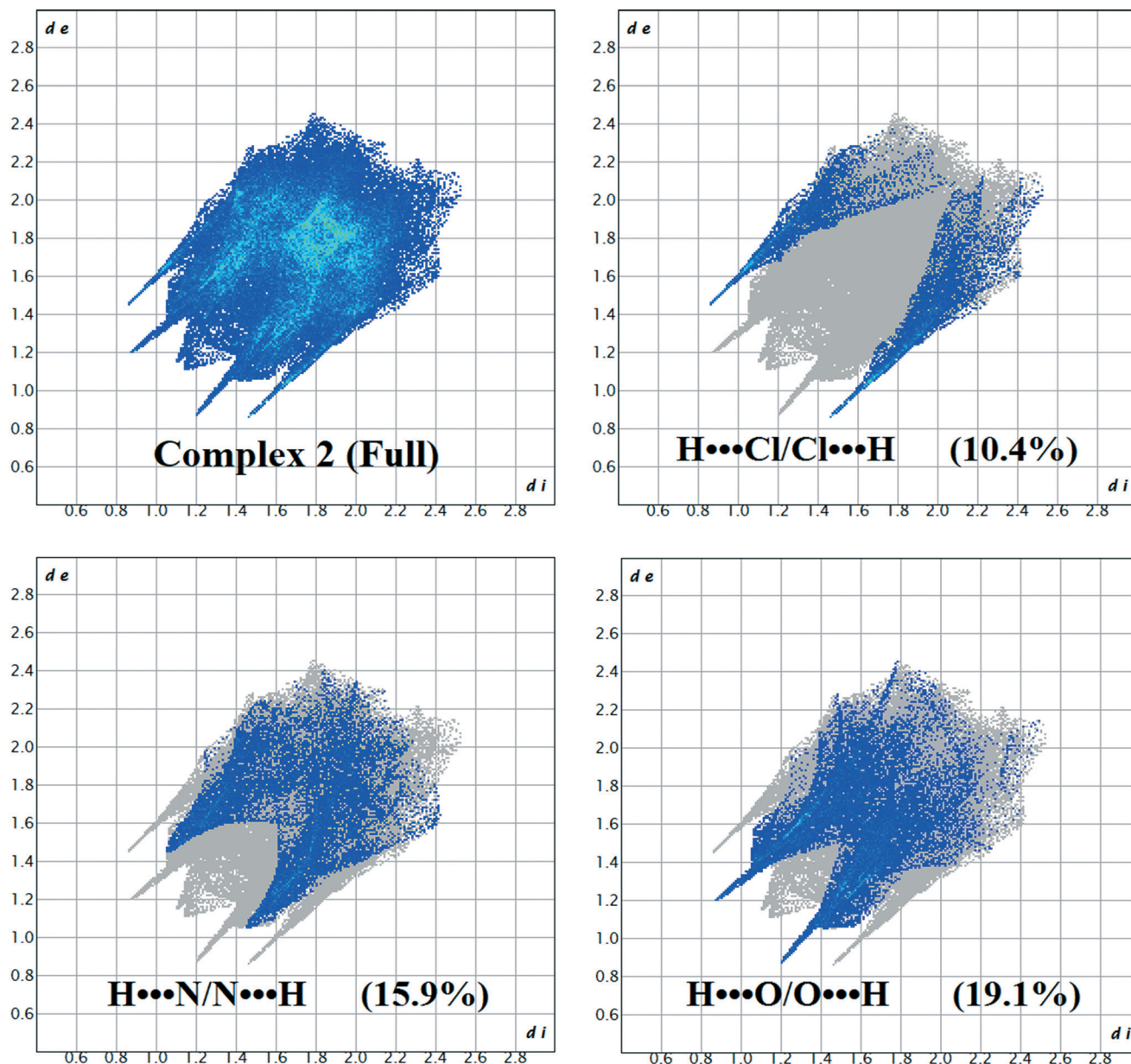
Fig. 14 Fingerprint plots (full) and decomposed plots for each individual interaction in complex **2**.

compound **1** where, in addition to the π···π interactions, two H-bonding interactions (C–H···N and C–H···Cl) are formed. The dimerization energy is very large (ΔE_1 = −17.7 kcal mol^{-1}) due to the contribution of both types of interactions (HB and π···π). We have also analysed this assembly using a combination of QTAIM and NCI plot index computational methods since they are very convenient to reveal non-covalent interactions in real space. The NCI plot index is an intuitive visualization index that facilitates the visualization of non-covalent interactions and shows which molecular regions interact. The colour scheme is a red-yellow-green-blue scale with red (repulsive) and blue (attractive). Yellow and green surfaces correspond to weak repulsive and weak attractive interactions, respectively. The H-bonds are characterized by a bond critical point (represented as a red sphere) and a bond path

connecting the H to the N or Cl atoms. The green NCI plot isosurfaces that characterize the H-bonds are located between the H and N, Cl atoms coincident to the position of the bond CPs. The π···π stacking interactions are characterized by two bond critical points (CPs) and bond paths connecting one N atom and one C-atom of the imidazole ring to two carbon atoms of the pyridine ring. Moreover, green and extended isosurfaces are located between the imidazole and pyridine rings, also confirming the existence of the π···π stacking interactions. Fig. 16b shows a similar QTAIM/NCI plot analysis performed for a different dimer extracted from the solid state. It has been studied to analyse the possibility of the formation of a Cl···CH$_3$ tetrel bonding interaction between the Cl atom and the C-atom of the methyl group. That is, one coordinated chlorine atom (Cl2) and the methyl carbon atom
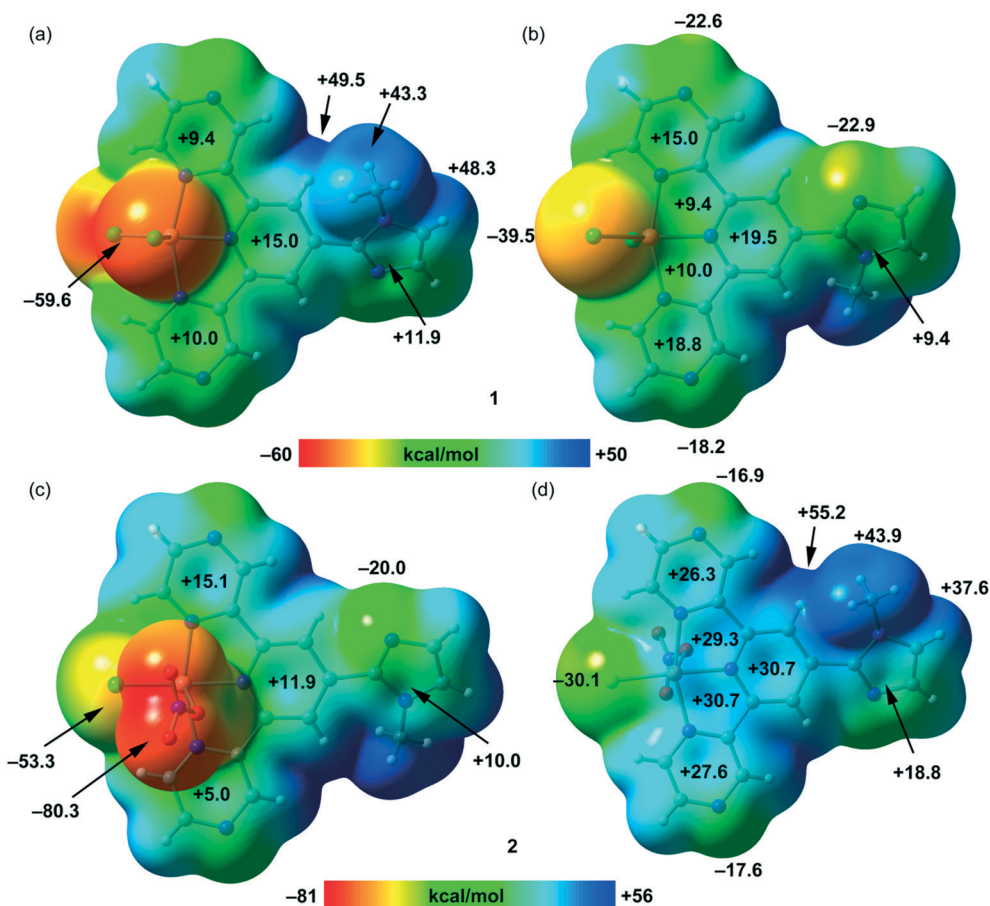
Fig. 15 Two "on-top" views of the MEP surfaces (isosurface 0.001 a.u.) of compounds **1** (a and b) and a monomeric model of compound **2** (c and d) at the PBE0-D3/def2-TZVP level of theory. The MEP values at selected points of the surfaces are given in kcal mol^{-1}.
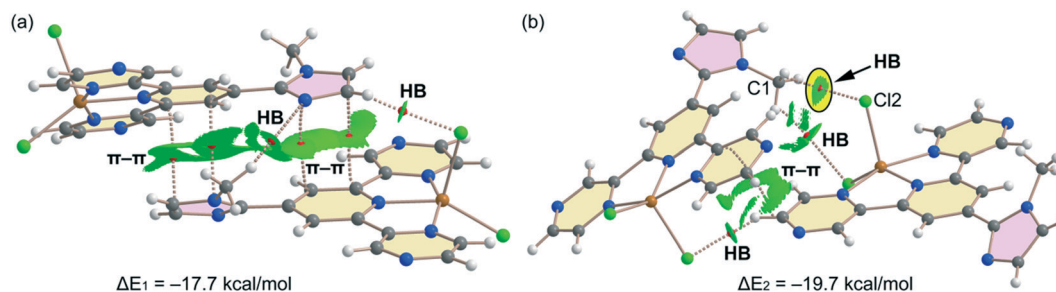

Fig. 16 Combined QTAIM analysis (bond CPs in red) and NCI surfaces of the π-stacked (a) and CH$_3$···Cl (b) assemblies of compound **1**. The gradient cut-off is ρ = 0.04 a.u., isosurface s = 0.5, and the colour scale is −0.04 a.u. < (sign λ_2) ρ < 0.04 a.u. only intermolecular contacts are shown.

(C1) of the imidazole ring have a separation distance of 3.332 Å, that is shorter than their sum of van der Waals radii (3.45 Å), thus suggesting the possibility of a C···Cl tetrel bonding interaction, which has been described in similar systems.[69] However, the combined QTAIM/NCI plot analysis reveals that this interaction is more likely a C–H···Cl hydrogen bond (the interaction is highlighted by a yellow circle in Fig. 16b) characterized by a bond CP, bond path and green isosurface located mostly between one H-atom of the methyl group and the Cl-atom. The NCI plot and QTAIM analyses also disclose

the existence of π···π stacking interactions between two pyrimidine rings and additional C–H···Cl contacts characterized by the corresponding bond CPs and bond paths. The dimerization energy is similar (ΔE_2 = −19.7 kcal mol^{-1}) to that of the other dimer and confirms the energetic significance of the π···π stacking and C–H···Cl interactions in the solid state of compound **1**.

A similar study has been performed in compound **2**. However, since compound **2** is a coordination polymer, we have used dimeric models extracted from the polymeric chain (see
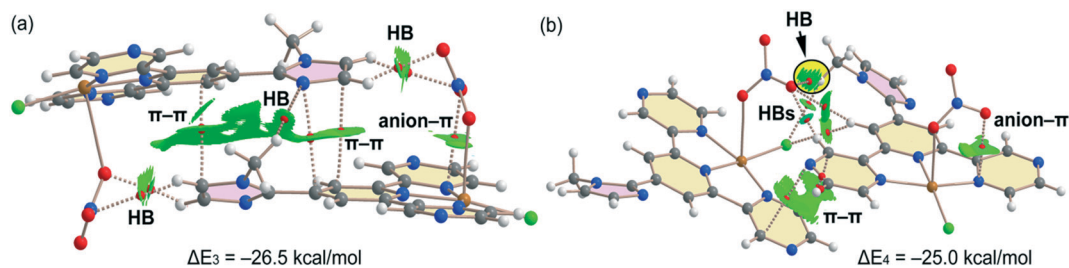
Fig. 17 Combined QTAIM analysis (bond CPs in red) and NCI surfaces of the π-stacked (a) and CH$_3$···O (b) assemblies of compound **2**. The gradient cut-off is ρ = 0.04 a.u., isosurface s = 0.5, and the colour scale is −0.04 a.u. < (sign λ_2) ρ < 0.04 a.u. only intermolecular interactions are shown apart from the anion–π interaction.

Fig. 17). The fact that similar assemblies are observed in the solid state of both compounds in spite of the polymeric nature of compound **2** and monomeric nature of **1** supports the relevance of both assemblies. Fig. 17a shows the model π···π dimer extracted from the solid state of compound **2** where, in addition to the π···π interactions, a C–H···N and four C–H···O H-bonding interactions are formed. This assembly is quite similar to the one discussed above for compound **1** (Fig. 16a). The dimerization energy is larger (ΔE_3 = −26.5 kcal mol^{-1}) due to a large number of HBs. The QTAIM and NCI plot index analyses reveal that the π···π stacking interactions are characterized by three bond critical points (CPs) and bond paths interconnecting the five and six membered rings of both complexes. Moreover, green and extended isosurfaces are located between the imidazole and pyridine rings, also confirming the existence and attractive nature of the π···π stacking interactions. In compound **2**, we have also analysed the possibility of the formation of an O···CH$_3$X tetrel bonding interaction between the nitrate's O3 atom and the C-atom of the methyl group. In this case the O···C distance is 3.313 Å, thus shorter than the sum of O and C van der Waals radii (3.22 Å). But, the combined QTAIM/NCI plot analysis reveals that this interaction is indeed a hydrogen bond (the interaction is highlighted by a yellow circle in Fig. 17b) characterized by a bond CP, bond path and green isosurface connecting the H-atom of the methyl group to the O-atom. The NCI plot and QTAIM analyses also disclose the existence of π···π stacking interactions between two pyrimidine rings and additional C–H···O contacts characterized by the corresponding bond CPs and bond paths. The dimerization energy is similar (ΔE_4 = −25 kcal mol^{-1}) to that of the other dimer (Fig. 17a) and larger than the equivalent dimer of compound **1** Fig. 16b). This agrees well with the larger MEP values observed at the nitrato than at the chlorido anionic ligands in compounds **2** and **1** (see Fig. 15). It should be emphasized that in Fig. 16 and 17 only intermolecular interactions are represented apart from the intramolecular anion–π interaction observed in compound **2** (see Fig. 17). This interaction is characterized by a bond CP connecting an O-atom belonging to nitrate and the N-atom of the pyrazine ring. The anion–π is also revealed by the NCI plot analysis that shows a medium size isosurface between the O-atom and the coordinated N-atom of the pyrazine ring. The isosurface extends toward

two aromatic C-atoms and the Cu atom directly bonded to the N-atom.

Concluding remarks

In conclusion, two Cu(II) complexes (**1** and **2**) are synthesized using a newly synthesized 4-(1-methylimidazole)-2,6-di(pyrazinyl)pyridine (**N$_3$L**) moiety as the backbone ligand and characterized by spectroscopic and single crystal X-ray diffraction methods. The structural insights reveal that π···π stacking and non-classical hydrogen bonding (C–H···O, N, Cl) interactions play a key role in stabilizing the supramolecular architectures of both complexes in the solid state. A thorough analysis of the Hirshfeld surface and associated 2D fingerprint plots has been carried out to explore the nature of all these non-classical hydrogen bonding interactions and their relative contributions in building supramolecular architectures. The energetic features of these interactions have been analyzed by using DFT calculations and the intricate network of non-covalent contacts has been characterized by using a combination of QTAIM and NCI plot computational tools. The MEP values for both complexes also have good agreement to rationalize the π···π stacking and CH···X (X = N, O, and Cl) hydrogen bonding interactions in the solid state. We expect that the findings reported herein will be useful for scientists working in the fields of supramolecular chemistry and crystal engineering, as well as to increase the visibility of non-conventional interactions.

Conflicts of interest

There are no conflicts to declare.

Acknowledgements

References

1 (a) J. J. Novoa, *Intermolecular Interactions in Crystals: Fundamentals of Crystal Engineering*, RSC, Cambridge, 2018;

(b) A. Nangia and G. Desiraju, *Angew. Chem.*, 2019, **58**, 4100–4107.

2 (a) J. T. Hupp, *Nat. Chem.*, 2010, **2**, 432–433; (b) A. S. Mahadevi and G. N. Sastry, *Chem. Rev.*, 2016, **116**, 2775–2825; (c) A. K. Ghosh, A. Hazra, A. Mondal and P. Banerjee, *Inorg. Chim. Acta*, 2019, **488**, 86–119.

3 (a) M. Saccone and L. Catalano, *J. Phys. Chem. B*, 2019, **123**(44), 9281–9290; (b) R. Bu, Y. Xiong, X. Wei, H. Li and C. Zhang, *Cryst. Growth Des.*, 2019, **19**, 5981–5997; (c) R. Thakuria, N. K. Nath and B. K. Saha, *Cryst. Growth Des.*, 2019, **19**, 523–528.

4 (a) A. S. Mahadevi and G. N. Sastry, *Chem. Rev.*, 2013, **113**, 2100–2138; (b) C. Zhao, P. Li, M. D. Smith, P. J. Pelle Chia and K. D. Shimizu, *Org. Lett.*, 2014, **16**, 3520–3523; (c) C. Jia, H. Miao and B. P. Hay, *Cryst. Growth Des.*, 2019, **19**, 6806–6821.

5 S. Pramanik, S. Pathak, S. Jana, M. Mondol, A. Frontera and S. Mukhopadhyay, *New J. Chem.*, 2021, **45**, 12108–12119.

6 (a) D. A. Uhlenheuer, K. Petkau and L. Brunsveld, *Chem. Soc. Rev.*, 2010, **39**, 2817–2826; (b) M. Kolle, P. M. Salgard-Cunha, M. R. J. Scherer, F. Huang, P. Vukusic, S. Mahajan, J. J. Baumberg and U. Steiner, *Nat. Nanotechnol.*, 2010, **5**(7), 511–515.

7 J. Steed and J. L. Atwood, *Supramolecular Chemistry*, John Wiley, New York, 2001.

8 (a) A. J. Neel, M. J. Hilton, M. S. Sigman and F. D. Toste, *Nature*, 2017, **543**, 637–646; (b) A. S. Mahadevi and G. N. Sastry, *Chem. Rev.*, 2016, **116**, 2775–2825; (c) R. R. Knowles and E. N. Jacobsen, *Proc. Natl. Acad. Sci. U. S. A.*, 2010, **107**, 20678–20685.

9 (a) V. K. Pal, R. Jain and S. Roy, *Langmuir*, 2020, **36**, 1003–1013; (b) H. A. Nkabyo, I. Barnard, K. R. Koch and R. C. Luckay, *Coord. Chem. Rev.*, 2021, **427**, 213588–213611.

10 P. Mukherjee, M. G. B. Drew, C. J. Gomez-García and A. Ghosh, *Inorg. Chem.*, 2009, **48**, 5848–5860.

11 (a) X. Zhang, L. Zhou, C. Wang, Y. Li, Y. Wu, M. Zhang and Q. Yin, *Cryst. Growth Des.*, 2017, **17**, 6151–6157; (b) Y. Hirao, S. Seo and T. Kubo, *J. Phys. Chem. C*, 2019, **123**, 20928–20935; (c) Z. Yang, Y. Wang, X. Liu, R. T. Vanderlinden, R. Ni, X. Li and P. J. Stang, *J. Am. Chem. Soc.*, 2020, **142**, 13689–13694.

12 F. Biedermann and H. J. Schneider, *Chem. Rev.*, 2016, **116**, 5216–5300.

13 (a) G. S. Nichol and W. Clegg, *Cryst. Growth Des.*, 2009, **9**, 1844–1850; (b) D. F. Back, M. Hörner, F. Broch and G. M. de Oliveira, *Polyhedron*, 2012, **31**, 558–564.

14 (a) M. J. Ajitha and K.-W. Huang, *Synthesis*, 2016, **48**, 3449–3458; (b) L. M. Eytel, H. A. Fargher, M. M. Haley and D. W. Johnson, *Chem. Commun.*, 2019, **55**, 5195–5206; (c) M. Kumar and J. S. Francisco, *J. Am. Chem. Soc.*, 2020, **142**, 6001–6006.

15 G. R. Desiraju and T. Steiner, *The Weak Hydrogen Bond in Structural Chemistry and Biology*, Oxford Univ. Press, Oxford, 1999, ch. 2 and 3.

16 R. C. Johnston and P. H.-Y. Cheong, *Org. Biomol. Chem.*, 2013, **11**, 5057–5064.

17 (a) L. Brammer, E. A. Bruton and P. Sherwood, *Cryst. Growth Des.*, 2001, **1**, 277–290; (b) F. Zordan, L. Brammer and P. Sherwood, *J. Am. Chem. Soc.*, 2005, **127**, 5979–5989.

18 U. Bentrup, M. Feist and E. Kemnitz, *Prog. Solid State Chem.*, 1999, **27**, 75–129.

19 M. Albrecht, P. Dani, M. Lutz, A. L. Spek and G. van Koten, *J. Am. Chem. Soc.*, 2000, **122**, 11822–11833.

20 S. Chen, S. Zhang, C. Bao, C. Wang, Q. Lin and L. Zhu, *Chem. Commun.*, 2016, **52**, 13132–13135.

21 (a) H. Juwarker, J. M. Lenhardt, D. M. Pham and S. L. Craig, *Angew. Chem., Int. Ed.*, 2008, **47**, 3740–3743; (b) B. W. Tresca, L. N. Zakharov, C. N. Carroll, D. W. Johnson and M. M. Haley, *Chem. Commun.*, 2013, **49**, 7240–7242; (c) J. Cai and J. L. Sessler, *Chem. Soc. Rev.*, 2014, **43**, 6198–6213.

22 (a) A. C. Moro, F. W. Watanabe, S. R. Ananias, A. E. Mauro, A. V. G. Netto, A. P. R. Lima, J. G. Ferreira and R. H. A. Santos, *Inorg. Chem. Commun.*, 2006, **9**, 493–496; (b) W. Jacob and R. Mukherjee, *J. Chem. Sci.*, 2008, **120**, 447–453.

23 P. Pal, K. Das, A. Hossain, A. Frontera and S. Mukhopadhyay, *New J. Chem.*, 2020, **44**, 7310–7318.

24 G. Aullon, D. Bellamy, A. G. Orpen, L. Brammer and E. A. Bruton, *Chem. Commun.*, 1998, 653–654.

25 (a) H. Zhu, J. Fan, B. Wang and X. Peng, *Chem. Soc. Rev.*, 2015, **44**, 4337–4366; (b) L. Zhang, C.-J. Li, J.-E. He, Y.-Y. Chen, S.-R. Zheng, J. Fan and W.-G. Zhang, *J. Solid State Chem.*, 2016, **233**, 444–454.

26 (a) A. Bocian, D. Brykczyńska, M. Kubicki, Z. Hnatejko, M. Wałęsa-Chorab, A. Gorczyński and V. Patroniak, *Polyhedron*, 2019, **157**, 249–261; (b) C. E. Housecroft and E. C. Constable, *Chem. Commun.*, 2020, **56**, 10786–10794.

27 A. Haque, R. Ilmi, I. J. Al-Busaidiand and M. S. Khan, *Coord. Chem. Rev.*, 2017, **350**, 320–339.

28 S. Chakraborty and G. R. Newkome, *Chem. Soc. Rev.*, 2018, **47**, 3991–4016.

29 Y. Wang, D. Astruc and A. S. Abd-El-Aziz, *Chem. Soc. Rev.*, 2019, **48**, 558–636.

30 (a) C.-J. Yao, Y.-W. Zhong, H.-J. Nie, H. D. Abruña and J. Yao, *J. Am. Chem. Soc.*, 2011, **133**, 20720–20723; (b) N. Elgrishi, M. B. Chambers, V. Artero and M. Fontecave, *Phys. Chem. Chem. Phys.*, 2014, **16**, 13635–13644.

31 B. Das, A. Orthaber, S. Ott and A. Thapper, *Chem. Commun.*, 2015, **51**, 13074–13077.

32 K. Takada, R. Sakamoto, S.-T. Yi, S. Katagiri, T. Kambe and H. Nishihara, *J. Am. Chem. Soc.*, 2015, **137**, 4681–4689.

33 (a) S. Elmas, W. Beelders, S. J. Bradley, R. Kroon, G. Laufersky, M. Andersson and T. Nann, *ACS Sustainable Chem. Eng.*, 2017, **5**, 10206–10214; (b) Y. Kuai, W. Li, Y. Dong, W.-Y. Wong, S. Yan, Y. Dai and C. Zhang, *Dalton Trans.*, 2019, **48**, 15121–15126.

34 (a) S. K. Padhi, E. Ahmad, S. Rai and B. Panda, *Polyhedron*, 2020, **187**, 114677–114690; (b) S. Rai and S. K. Padhi, *Electrochim. Acta*, 2020, **364**, 137277–137291.

35 (a) J.-H. Tang, T.-G. Sun, J.-Y. Shao, Z.-L. Gong and Y.-W. Zhong, *Chem. Commun.*, 2017, **53**, 11925–11928; (b) P. Wang, H. L. Wang, Y. Fang, H. Li, J. H. He, J. Y. Ji, Y. Y. Li, Q. F. Xu, J. W. Zheng and J. M. Lu, *ACS Appl. Mater. Interfaces*, 2017, **9**, 32930–32938.

36 (a) S. Y. Jiao, K. Li, W. Zhang, Y. H. Liu, Z. Huang and X. Q. Yu, *Dalton Trans.*, 2015, **44**, 1358–1365; (b) D. Chao and S.

Ni, *Sci. Rep.*, 2016, **6**, 1–8; (*c*) V. D. Singh, R. S. Singh, R. P. Paitandi, B. K. Dwivedi, B. Maiti and D. S. Pandey, *J. Phys. Chem. C*, 2018, **122**, 5178–5187.

37 (*a*) T. Tsukamoto, K. Takada, R. Sakamoto, R. Matsuoka, R. Toyoda, H. Maeda, T. Yagi, M. Nishikawa, N. Shinjo, S. Amano, T. Iokawa, N. Ishibashi, T. Oi, K. Kanayama, R. Kinugawa, Y. Koda, T. Komura, S. Nakajima, R. Fukuyama, N. Fuse, M. Mizui, M. Miyasaki, Y. Yamashita, K. Yamada, W. Zhang, R. Han, W. Liu, T. Tsubomura and H. Nishihara, *J. Am. Chem. Soc.*, 2017, **139**, 5359–5366; (*b*) S. Roy and C. Chakraborty, *ACS Appl. Mater. Interfaces*, 2020, **12**, 35181–35192.

38 K. Choroba, B. Machura, S. Kula, L. R. Raposo, A. R. Fernandes, R. Kruszynski, K. Erfurt, L. S. Shul, Y. N. Kozlov and G. B. Shul, *Dalton Trans.*, 2019, **48**, 12656–12673.

39 (*a*) R. Nasani, M. Saha, S. M. Mobin, L. M. D. R. S. Martins, A. J. L. Pombeiro, A. M. Kirillov and S. Mukhopadhyay, *Dalton Trans.*, 2014, **43**, 9944–9954; (*b*) Z. Ma, L. Wei, E. C. B. A. Alegria, L. M. D. R. S. Martins, M. F. C. G. da Silva and A. J. L. Pombeiro, *Dalton Trans.*, 2014, **43**, 4048–4058; (*c*) J. Z. Gu, M. Wen, Y. Cai, Z. F. Shi, A. S. Arol, M. V. Kirillova and A. M. Kirillov, *Inorg. Chem.*, 2019, **58**, 2403–2412; (*d*) C. Wei, Y. He, X. Shi and Z. Song, *Coord. Chem. Rev.*, 2019, **385**, 1–19.

40 Y. Liu, S. C. Yiu, C. L. Ho and W. Y. Wong, *Coord. Chem. Rev.*, 2018, **375**, 514–557.

41 (*a*) C. Icsel, V. T. Yilmaz, S. Aydinlik and M. Aygun, *Eur. J. Med. Chem.*, 2020, **202**, 112535–112545; (*b*) J. Karges, K. Xiong, O. Blacque, H. Chao and G. Gasser, *Inorg. Chim. Acta*, 2021, **516**, 120137–120142.

42 (*a*) C. Wu, J. Wang, J. Shen, C. Zhang, Z. Wu and H. Zhou, *Tetrahedron*, 2017, **73**, 5715–5719; (*b*) H. Q. Li, X. Q. Sun, T. Zheng, Z. X. Xu, Y. X. Song and X. H. Gu, *Sens. Actuators, B*, 2019, **279**, 400–409.

43 (*a*) F. Cheng, N. Tang, K. Miao and F. Wang, *Z. Anorg. Allg. Chem.*, 2014, **640**, 1816–1821; (*b*) Y. Q. Pan, X. Xu, Y. Zhang, Y. Zhang and W. K. Dong, *Spectrochim. Acta, Part A*, 2020, **229**, 117927–117936.

44 *Bruker, SMART v5.631*, Bruker AXS Inc., Madison, WI, USA, 2001.

45 (*a*) G. M. Sheldrick, *SHELXT-2014*, University of Göttingen, 2014; (*b*) G. M. Sheldrick, *Acta Crystallogr., Sect. C: Struct. Chem.*, 2015, **71**, 3–8.

46 M. A. Spackman and D. Jayatilaka, *CrystEngComm*, 2009, **11**, 19–32.

47 F. L. Hirshfeld, *Theor. Chim. Acta*, 1977, **44**, 129–138.

48 H. F. Clausen, M. S. Chevallier, M. A. Spackman and B. B. Iversen, *New J. Chem.*, 2010, **34**, 193–199.

49 A. L. Rohl, M. Moret, W. Kaminsky, K. Claborn, J. J. Mckinnon and B. Kahr, *Cryst. Growth Des.*, 2008, **8**, 4517–4525.

50 A. Parkin, G. Barr, W. Dong, C. J. Gilmore, D. Jayatilaka, J. J. McKinnon, M. A. Spackman and C. C. Wilson, *CrystEngComm*, 2007, **9**, 648–652.

51 M. A. Spackman and J. J. McKinnon, *CrystEngComm*, 2002, **4**, 378–392.

52 S. K. Wolff, D. J. Grimwood, J. J. McKinnon, D. Jayatilaka and M. A. Spackman, *Crystal Explorer 3.1*, University of Western Australia, Perth, Australia, 2007.

53 J. J. McKinnon, M. A. Spackman and A. S. Mitchell, *Acta Crystallogr., Sect. B: Struct. Sci.*, 2004, **60**, 627–668.

54 M. J. Frisch, G. W. Trucks, H. B. Schlegel, G. E. Scuseria, M. A. Robb, J. R. Cheeseman, G. Scalmani, V. Barone, G. A. Petersson, H. Nakatsuji, X. Li, M. Caricato, A. Marenich, J. Bloino, B. G. Janesko, R. Gomperts, B. Mennucci, H. P. Hratchian, J. V. Ortiz, A. F. Izmaylov, J. L. Sonnenberg, D. Williams-Young, F. Ding, F. Lipparini, F. Egidi, J. Goings, B. Peng, A. Petrone, T. Henderson, D. Ranasinghe, V. G. Zakrzewski, J. Gao, N. Rega, G. Zheng, W. Liang, M. Hada, M. Ehara, K. Toyota, R. Fukuda, J. Hasegawa, M. Ishida, T. Nakajima, Y. Honda, O. Kitao, H. Nakai, T. Vreven, K. Throssell, J. A. Montgomery, Jr., J. E. Peralta, F. Ogliaro, M. Bearpark, J. J. Heyd, E. Brothers, K. N. Kudin, V. N. Staroverov, T. Keith, R. Kobayashi, J. Normand, K. Raghavachari, A. Rendell, J. C. Burant, S. S. Iyengar, J. Tomasi, M. Cossi, J. M. Millam, M. Klene, C. Adamo, R. Cammi, J. W. Ochterski, R. L. Martin, K. Morokuma, O. Farkas, J. B. Foresman and D. J. Fox, *Gaussian 16 (Revision A.03)*, Gaussian Inc., Wallingford, CT, 2016.

55 S. F. Boys and F. Bernardi, *Mol. Phys.*, 1970, **19**, 553–566.

56 S. Grimme, J. Antony, S. Ehrlich and H. Krieg, *J. Chem. Phys.*, 2010, **132**, 154104–154123.

57 P. Manna, S. K. Seth, M. Mitra, S. R. Choudhury, A. Bauzá, A. Frontera and S. Mukhopadhyay, *Cryst. Growth Des.*, 2014, **14**, 5812–5821.

58 M. Mirzaei, H. Eshtiagh-Hosseini, Z. Bolouri, Z. Rahmati, A. Esmaeilzadeh, A. Hassanpoor, A. Bauza, P. Ballester, M. Barceló-Oliver, J. T. Mague, B. Notash and A. Frontera, *Cryst. Growth Des.*, 2015, **15**, 1351–1361.

59 J. Contreras-García, E. R. Johnson, S. Keinan, R. Chaudret, J.-P. Piquemal, D. N. Beratan and W. Yang, *J. Chem. Theory Comput.*, 2011, **7**, 625–632.

60 R. F. W. Bader, *Chem. Rev.*, 1991, **91**, 893–928.

61 T. A. Keith, *AIMAll (Version 19.02.13)*, TK Gristmill Software, Overland Park KS, USA, 2019 (aim.tkgristmill.com).

62 A. W. Addison, T. N. Rao, J. Reedijk, J. Rijn and G. C. Verschoor, *J. Chem. Soc., Dalton Trans.*, 1984, 1349–1356.

63 P. Pal, K. Das, A. Hossain, R. M. Gomila, A. Frontera and S. Mukhopadhyay, *New J. Chem.*, 2021, **45**, 11689–11696.

64 (*a*) J. Z. Gu, X. X. Liang, Y. H. Cui, J. Wu, Z. F. Shi and A. M. Kirillov, *CrystEngComm*, 2017, **19**, 2570–2588; (*b*) J. Z. Gu, Y. Cai, M. Wen, Z. F. Shi and A. M. Kirillov, *Dalton Trans.*, 2018, **47**, 14327–14339.

65 R. G. Miller and S. Brooker, *Inorg. Chem.*, 2015, **54**, 5398–5409.

66 Z. Yin, G. Zhang, T. Phoenix, S. Zheng and J. C. Fettinger, *RSC Adv.*, 2015, **5**, 36156–36166.

67 R. Hao, L. Li, S. Zhu, Z. H. Wang, X. J. Zhao and E. C. Yang, *J. Mol. Struct.*, 2019, **1176**, 376–385.

68 H. R. Khavasi and M. Esmaeili, *Cryst. Growth Des.*, 2019, **19**, 4369–4377.

69 (*a*) A. Frontera, *C*, 2020, **6**, 60–74; (*b*) A. Daolio, P. Scilabra, G. Terraneo and G. Resnati, *Coord. Chem. Rev.*, 2020, **413**, 213265–213284; (*c*) M. M. Ayhan, E. Özcan, B. Dedeoglu, Y. Chumakov, Y. Zorlu and B. Coşut, *CrystEngComm*, 2021, **23**, 268–272.

Check for updates

An experimental and theoretical exploration of supramolecular interactions and photoresponse properties of two Ni(II) complexes†

Samit Pramanik,[a] Sudipta Pathak, [ID][b] Sumanta Jana, [ID][a] Monotosh Mondal,[b] Antonio Frontera [ID] *[c] and Subrata Mukhopadhyay*[a]

Two new nickel(II) complexes, $C_{32}H_2N_8NiClO_9$ (**1**) and $C_{36}H_{28}N_{12}NiOF_{24}P_4$ (**2**), have been synthesized where both 2,4,6-tri(pyridin-2-yl)-1,3,5-s-triazine and dipicolinic acid act as tridentate ligands for complex **1** and only 2,4,6-tri(pyridin-2-yl)-1,3,5-s-triazine is employed as a tridentate ligand for complex **2**. These complexes were characterized by FT-IR spectroscopy and single-crystal X-ray diffraction. The noncovalent interactions occurring in the crystal packing of both the complexes have been well-defined focusing on $\pi \cdots \pi$ (for complex **1**) and anion$\cdots \pi$ (for complex **2**) interactions, which have also been analysed using DFT calculations. Besides, noncovalent interactions such as C–H$\cdots \pi$, lone pair$\cdots \pi$, $\pi \cdots \pi^+$, anion$\cdots \pi^+$, and $\pi^+ \cdots \pi^+$ along with hydrogen bonding interactions play an important role in the stabilization of both the complexes in a solid state. We also observed that the change in auxiliary ligands exhibits significant variations in their structures, band gaps and photoresponse properties. To gain insights into the charge transport mechanism, several Schottky barrier diode (SBD) parameters like carrier mobility, transit time, carrier concentration, diffusion coefficient, diffusion length, and ideality factor were measured in the light of thermionic emission and SCLC (space charge limiting current) theory.

Introduction

Recently, the fields of coordination chemistry and crystal engineering have matured enough and crystal engineering techniques have been extensively developed and assisted to the design and synthesis of materials with precise solid-state intriguing properties.[1,2] Researchers are now focusing on their potential applications as functional materials for use in heterogeneous catalysis, nanotechnology, gas adsorption, gas evolution, optoelectronics, drug delivery, sensors, fuel cell, dye degradation and many more beyond their syntheses.[3–11] In this context, crystal engineers often help to analyze the self-assembly process after a combination of various metals and heterocycle-based organic ligands and guide to find out the relationship between the structure and properties of molecules in a programmed way.[12]

Coordination molecular architectures are the result of mutual interactions to exhibit a broad range of different dimensional frameworks (0D, 1D, 2D or 3D) by a variety of forces.[13] Apart from coordination bonding interactions, forces associated with aromatic–π systems like $\pi \cdots \pi$, lone pair$\cdots \pi$, $\pi \cdots$cation, $\pi \cdots$anion, CH$\cdots \pi$, anion$\cdots \pi^+$, $\pi \cdots \pi^+$, $\pi^+ \cdots \pi^+$, etc. along with relatively strong hydrogen bonding have been vastly scrutinized for the building of various polymeric architectures in the solid state.[14–16] Counter ions, solvent molecules and the electronic nature of ancillary ligands are also responsible for the organised ultimate architectures.[17]

2,4,6-Tri(pyridin-2-yl)-1,3,5-s-triazine and their structural analogues play a pivotal role in metallo-supramolecular chemistry and have drawn much attention in the fields of coordination chemistry and materials science.[18] The chelating aptitude of 2,4,6-tri(pyridin-2-yl)-1,3,5-s-triazine boosts the stability of metal complexes, and the planarity of the ligand with π stacking ability leads to robust intercalative interactions of complexes in biological systems.[19] The binding constant determines the strength of the interaction between the metal and the ligand and controls the formation of coordination molecules thermodynamically,[20] and a competition might arise if more than one ligand is present to bind with a specific metal ion. Thus, there is a smaller number of complexes reported in the literature with two different chelating ligands in one pot.[21] In addition, a majority of coordination

[a] Department of Chemistry, Jadavpur University, Kolkata 700032, India.
E-mail: ju_subrata@yahoo.co.in
[b] Department of Chemistry, Haldia Government College, Debhog, PurbaMedinipur, West Bengal, India
[c] Departament de Química, Universitat de les Illes Balears, Crta. de Valldemossa km 7.5, 07122 Palma de Mallorca, Baleares, Spain. E-mail: toni.frontera@uib.es

compounds are electrical insulators and discrete in nature. However, there are some reports of ordered coordination compounds that show enhanced electron transport and rectifying nature under light illumination.[22–24] It is demonstrated that the structural and electronic properties of coordination compounds can be tuned by changing metal ions and organic linkers. As the conductivities of coordination compounds are generally low, the fabrication of electronic devices becomes a challenge when using these compounds. Beyond structural stability, thermal stability and chemical stability are also considered for the successful implementation of coordination compounds in device making. Considering the above facts, we have synthesised two nickel complexes based on the 2,4,6-tri(pyridin-2-yl)-1,3,5-s-triazine moiety. Initially, nickel(II) reacts with two different ligands (2,4,6-tri(pyridin-2-yl)-1,3,5-s-triazine and pyridine-2,6-dicarboxylic acid) in one pot to obtain an octahedral complex **1** where the triazine moiety and pyridine-2,6-dicarboxylic acid act as tridentate ligands. The unprecedented formation of complex **1** with two different chelating ligands is also established theoretically through the formation of a four-component assembly of complex **1**. When Ni(II) is treated with 2,4,6-tri(pyridin-2-yl)-1,3,5-s-triazine only as a ligand in the molar ratio of 1 : 2, the octahedral complex **2** was obtained. Although a number of complexes built from s-triazine derivatives have been reported in recent years, there still remains much more work to be explored. The structural features and supramolecular aspects of complexes **1** and **2** with the help of a single-crystal X-ray diffraction study along with their electrical conductivities have been investigated. The solid-state structure of complex **1** comprises a combination of C–H···N, C–H···O, C–H···Cl, N–H···O, O–H···O and O–H···Cl hydrogen bonds along with $\pi\cdots\pi$, $\pi\cdots\pi^+$ and lone pair···π interactions. Complex **2** is stabilized by a combination of C–H···F, N–H···O and O–H···F hydrogen bonds along with $\pi\cdots\pi$, C–H···π, anion···π, $\pi^+\cdots\pi^+$ and anion···π^+ interactions. To further understand the charge transportation, a detailed I–V analysis is carried out by making thin films of precursor complexes. Several device parameters like carrier mobility, carrier concentration, transit time, diffusion coefficient, diffusion length, and ideality factor have been measured by considering the SBD characteristics. The change in ancillary ligands alters the structural variations, supramolecular behaviours and electrical properties of both the complexes. An improvement in device performance was observed for complex **2** compared to complex **1**.

Experimental section

Physical measurements

Elemental analyses (C, H and N) were performed using a PerkinElmer 2400 Series-II CHN analyzer. Fourier transform-infrared (FT-IR) spectra of complexes **1** and **2** were recorded using a PerkinElmer LX-1 FTIR spectrophotometer (4000–400 cm^{-1}) by using a modern diamond attenuated total reflectance (ATR) accessory method. UV–vis absorption spectra were obtained using a UV-1700 PharmaSpec UV–vis spectrophotometer (SHIMADZU). The electrical characterization was carried out using a Keithley 4200 I–V instrument in the voltage range of −1 to +1 V.

Single-crystal X-ray data collections of complex **1** (Fig. S1, ESI†) and complex **2** (Fig. S2, ESI†) were completed using a single-crystal X-ray diffractometer (Bruker Smart Apex II).

Materials

All chemicals [2,4,6-tri(pyridin-2-yl)-1,3,5-s-triazine, dipicolinic acid, Ni(II) chloride hexahydrate, and ammonium hexafluorophosphate] were purchased from Sigma-Aldrich Chemical Company, USA and used as received. All reactions were carried out under aerobic environments and doubly distilled water was used throughout (Scheme S1, ESI†).

Synthesis of complex 1

Nickel(II) chloride hexahydrate (0.237 g, 1.0 mmol) was dissolved in 15 mL of water and allowed to react with 2,4,6-tri(pyridin-2-yl)-1,3,5-s-triazine (0.312 g, 1.0 mmol) in the water–ethanol (8 : 2, v/v) medium (20 mL) at 60 °C by continuous stirring. A warm aqueous solution (15 mL) of dipicolinic acid (0.334 g, 2.0 mmol) was added dropwise to the above solution under stirring conditions. After 4 h of constant stirring at 60 °C, the resultant solution was cooled, filtered and left unperturbed for slow evaporation at room temperature. Block-shaped brown-colored single crystals were obtained after one week. The crystals were separated by filtration, washed with cold water, and then dried in air, to obtain a 65% yield (0.495 g). Anal. calcd. for C$_{32}$H$_2$N$_8$NiClO$_9$ (complex **1**): C, 51.96; H, 2.86; and N, 15.15%. Found: C, 51.92; H, 2.81; and N, 15.14%. Main FT-IR absorption (KBr, cm^{-1}): 3364 (w), 3097 (vs), 2781 (s), 2621 (s), 1727 (vs), 1621 (s), 1573 (s), 1557 (vs), 1480 (s), 1453 (s), 1429 (s), 1400 (s), and 1384 (s) (Fig. S3, ESI†).

Synthesis of complex 2

Complex **2** was synthesized by dissolving nickel(II) chloride hexahydrate (0.237 g, 1.0 mmol) in 15 mL of water and allowed to react with 2,4,6-tri(pyridin-2-yl)-1,3,5-s-triazine (0.624 g, 2.0 mmol) in the water–ethanol (8 : 2, v/v) medium (20 mL) at 60 °C by stirring. A few drops of HCl were added into the resultant turbid solution to obtain the clear solution. A warm aqueous solution (15 mL) of ammonium hexafluorophosphate (0.652 g, 4.0 mmol) was added dropwise to the above solution and stirred for another 3 h. The resultant solution was then cooled, filtered, and left for slow evaporation at room temperature without any disturbance. Block shaped, deep brown-colored single crystals were obtained after two weeks. The crystals were separated by filtration, washed with cold water and air dried, to obtain a 62% yield (0.796 g). Anal. calcd. for C$_{36}$H$_{28}$N$_{12}$NiOF$_{24}$P$_4$ (complex **2**): C, 34.17; H, 2.07; and N, 13.28%. Found: C, 34.21; H, 2.04; and N, 13.23%. Main FT-IR absorption (KBr, cm^{-1}): 3454 (w), 3031 (s), 1740 (s), 1635 (s), 1611 (s), 1578 (vs), 1562 (vs), 1530 (vs), 1487 (s), 1473 (s), 1455 (s), 1439 (s), 1399 (s), 1377 (s), and 1313 (s) (Fig. S3, ESI†).

Theoretical methods

The calculations of monomers and dimers (Fig. 7–9) were performed at the DFT level of theory using the PBE0[25]–D3[26] method and the def2-SVP basis set,[27] with the help of the

Gaussian-16 program.[28] The topological analysis of the electron density distribution has been examined using the noncovalent interaction plot (NCI plot)[29–31] using the AIMAll program.[32] The estimation of the individual XB energies was performed using the potential energy density (V_r) predictor as recently proposed in the literature $(E = 0.778V_r)$[33] for the PBE0 functional. MEP surfaces were computed at the same level of theory by means of the Gaussian-16 program.

Results and discussion

X-Ray crystallographic analysis

Single-crystal X-ray data collections for both the complexes were performed using a Bruker SMART APEX II CCD area detector equipped with a graphite-monochromated Mo Kα radiation (λ = 0.71073 A) source in φ and ω scan modes at 273(2) K. The cell parameter refinement and data reduction were carried out using the Bruker SMART APEX II instrument and Bruker SMART and Bruker SAINT Software[34] for both the complexes. The structure of both the complexes was solved by conventional direct methods and refined by full matrix least-squares methods using F^2 data. SHELXL-2014/7[35] was used for the solution and refinement of both the structures. The solvent masking method in the Olex-2 programme was used for complexes **1** and **2** to obtain better fitted models of data. CCDC 2052738 (for complex **1**) and 2052737 (for complex **2**) include additional crystallographic information. Selected crystal data and structure refinement parameters for complexes **1** and **2** are given in Table S1 (ESI†).

Structural description of complex 1

The single-crystal X-ray diffraction study shows that the asymmetric unit of complex **1** comprises one monomeric cationic $[Ni(C_{18}H_{13}N_6)(C_7H_3NO_4)]^+$ unit, one non-coordinated dipicolinic acid, one non-coordinated chloride ion and one non-coordinated water molecule (Fig. S1, ESI†). The complex adopts the triclinic system with the space group $P\bar{1}$ and its unit cell is composed of two asymmetric units. The selected bond lengths and bond angles are tabulated in Tables S2 and S3 (ESI†). In the monomeric cationic $[Ni(C_{18}H_{13}N_6)(C_7H_3NO_4)]^+$ unit, the Ni(II) ion occupies the distorted octahedron structure, where three nitrogen donor atoms (N13, N30 and N36) of triazine-based ligand and another nitrogen atom (N9) of dipicolinate construct the basal plane. Two oxygen atoms O1, at a distance of 2.170(3) Å, and O12, at a distance of 2.109(3) Å, of the same acid ligand are *trans* diaxially coordinated to the metal ion. The lower value of the *trans* axial angle O1–Ni1–O12 [155.94(11)°] induces distortion in the octahedral geometry. The Ni–N bond distances in the basal plane are in the range of 1.960(3) to 2.140(3) Å. The Ni(II) ion is almost placed (deviation, 0.009 Å) in the same mean coordination plane of (N13, N30, N36, and N9). The one N atom (N27) of the monomeric unit is protonated. A non-coordinated chloride anion is present to neutralize the charge of the complex.

The monomeric cationic unit of complex **1** extends to make certain a 1-D polymeric chain through the π···π interaction (Table S5, ESI†) between Cg(6) and Cg(9) of two units along the

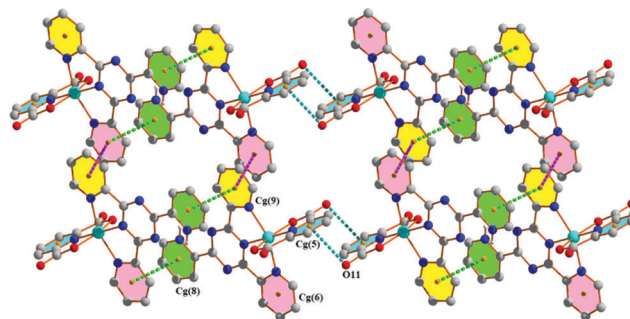Fig. 1 2-D layer of complex **1** incorporating π···π, π···π⁺ and lone pair···π interactions (aromatic hydrogen atoms have been omitted for clarity).

[100] direction (Fig. S4, ESI†). The two parallel chains are then interconnected through the self-complementary π···π⁺ interaction (Table S5, ESI†) between Cg(9) of one unit and Cg(8) of the other unit, thus forming a 1-D tape (Fig. S5, ESI†). The ring centroid separation distances of Cg(6)–Cg(9) and Cg(8)–Cg(9) are 3.715(3) Å and 3.561(3) Å, respectively. This supramolecular architecture is further extended through the self-complementary lone pair···π interactions (Table S7, ESI†) between Cg(5) of one unit and the carboxyl oxygen atom (O11) of the other unit and *vice versa*. Thus, the π···π interaction along with these π···π⁺ and lone pair···π interactions enhances the dimensionality from 1-D to 2-D in the (101) plane (Fig. 1).

A different 2-D layer is fashioned in complex **1** using two different types of hydrogen bonding interactions (Table S4, ESI†). Here, two monomeric cationic units are connected through C5–H5···O48 (154°) and O37–H37···O11 (164°) hydrogen bonds for the propagation of a one-dimensional (1-D) polymeric chain that is further strengthened by the C43–H43···O3 (149°) hydrogen bond, thus forming a $R_2^2(10)$ ring motif. These parallel 1-D chains are interlinked using the C25–H25···O47 (149°) hydrogen bonding interaction to form a 2-D layer (brick wall like) in the (011) plane (Fig. 2).

A comprehensive analysis reveals that four different types of intermolecular hydrogen bonding interactions (C–H···O, C–H···Cl, N–H···O, and O–H···Cl) are involved in the formation
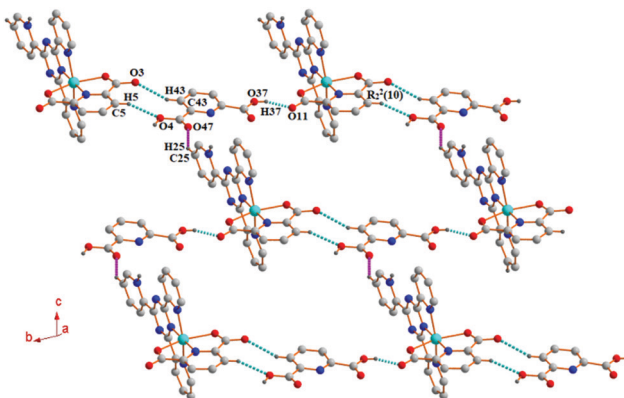

Fig. 2 Perspective view of the 2-D layer of complex **1** incorporating H-bonding interactions (other aromatic hydrogen atoms have been omitted for clarity).
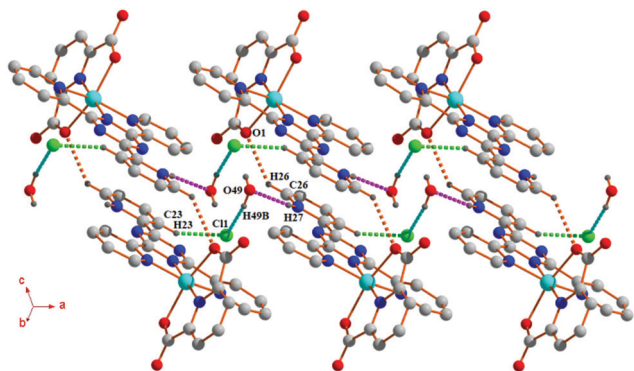
Fig. 3 Formation of 1-D tape through hydrogen bonding interactions in complex **1** (other aromatic hydrogen atoms have been omitted for clarity).

of a 1-D tape (as shown in Fig. 3). The first type of intermolecular hydrogen bonding (shown by green dotted lines) was shaped between the C23–H23 of one monomeric cationic unit and the non-coordinated chlorine atom (Cl1). The second type of intermolecular hydrogen bonding (shown by aqua dotted lines) was formed by the O49–H49B of the non-coordinated water molecule and the non-coordinated chlorine atom (Cl1). The third type of intermolecular hydrogen bonding (shown by pink dotted lines) was formed by the N27–H27 of one unit and O atom (O49) of the non-coordinated water molecule. These three hydrogen bonding interactions played a significant role to form a one-dimensional (1-D) polymeric chain along the [100] direction. The two parallel chains are then interconnected through the self-complementary C26–H26···O1 (type four) bonds (shown by orange dotted lines) for the formation of 1-D tape (Fig. 3).

In complex **1**, a dimeric distribution is observed that is formed by the π···π interaction between Cg(5) of one monomeric cationic unit and Cg(10) of the non-coordinated dipicolinic acid (Fig. S6, ESI†). The dimeric integrity is further stabilized through carbonyl (lp)···π and C35–H35···N45 hydrogen bonding interactions. Here, the carbonyl oxygen atom (O47) approaches the π face of the Cg(1) chelate ring at $(2-x, 1-y, 1-z)$ to form the said (lp)···π interaction. Then, another carbonyl oxygen atom (O39) interacts simultaneously with Cg(1) and Cg(5) of the adjacent dimeric unit to form a 1-D polymeric chain which is further strengthened by the C14–H14···O39 hydrogen bond.

Structural description of complex 2

The asymmetric unit of complex **2** contains one monomeric cationic $[Ni(C_{18}H_{13}N_6)_2]^{4+}$ unit, four non-coordinated hexafluorophosphate anions and one non-coordinated water molecule (Fig. S1, ESI†). The complex crystallizes in the triclinic system having the space group $P\bar{1}$ and its unit cell consists of two asymmetric units. The selected bond lengths and bond angles are summarized in Table S2 and S3 (ESI†), respectively. In this monomeric cationic $[Ni(C_{18}H_{13}N_6)_2]^{4+}$ unit, the Ni(II) ion possesses a distorted octahedron where the six coordination mode around the metal centre is satisfied by six N atoms (N1, N18, N24, N25, N36 and N47) from the two triazine-based ligands. The four N atoms (N1, N18, N24 and N36) are involved

to construct the basal plane and another two N atoms (N25 and N47) are axially coordinated to the metal ion. The Ni–N distances in the basal plane are in the range of 1.990(4) to 2.177(4) Å. The *trans* angle, N25–Ni1–N47, is distorted with a value of 152.86(17)° and the metal ion almost lies (deviation, 0.01 Å) in the mean coordination plane of (N25, N36, N47, and N18). Two nitrogen atoms (N15 and N35) in the monomeric unit of complex **2** are protonated. These two monopositively charged N-centers along with a Ni(II) ion induce the overall tetra-positive charge, which is compensated by four noncoordinated hexafluorophosphate anions.

The monomeric cationic unit of complex **2** propagates to make certain a 1-D polymeric chain through the π···π stacking interaction (Table S5, ESI†) between Cg(9) and Cg(12) of two different units along the [100] direction having a separation distance of 3.957(3) Å (Fig. S7, ESI†). This 1-D array is further extended to 2-D layers through the C–H···π interaction at $(x, -1+y, z)$ (Table S6, ESI†) between C4–H4 of one unit with Cg(9) of the other unit in the (110) plane (Fig. 4).

A different 2-D layer (Fig. 5) is constructed in complex **2** by using hydrogen bonding, π^+···π^+, and anion···π (Table S7, ESI†) interactions. Here, two monomeric cationic units are connected through anion···π interactions *via* two F atoms (F19 and F23) with Cg(5) and Cg(12) of the first unit, respectively, and one F atom (F24) with Cg(10) of the second unit for the propagation of a one-dimensional (1-D) polymeric chain that is again interconnected by the self-complementary C38–H38···F1 and C44–H44···F6 hydrogen bonds (Table S4, ESI†), thus forming a 1-D tape. This 1-D tape is further extended to 2-D layers (011) through the π^+···π^+ interaction between Cg(7) of one unit with

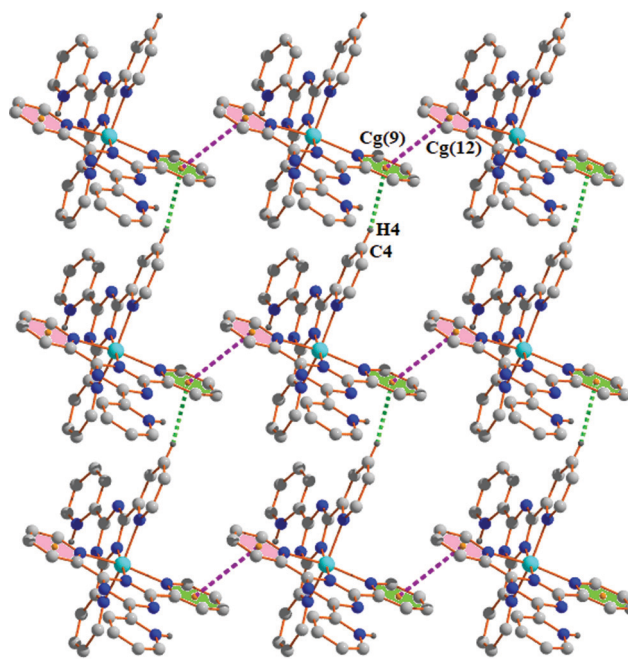**Fig. 4** Perspective view of the 2-D layer generated through π···π and C–H···π interactions in complex **2** (other aromatic hydrogen atoms have been omitted for clarity).
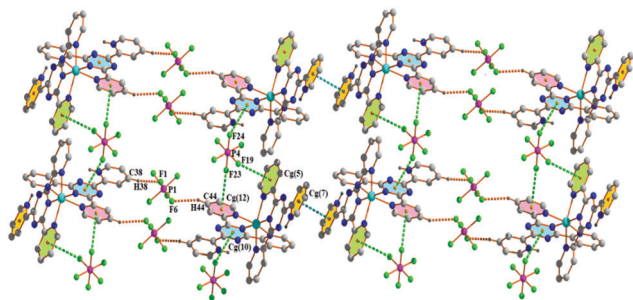
Fig. 5 Perspective view of 2-D architecture incorporating anion···π/π⁺···π⁺/hydrogen bonding interactions in complex **2** (other aromatic hydrogen atoms have been omitted for clarity).

Cg(7) of the other unit having an inter-planar spacing of 3.635(4) Å (Table S5, ESI†).

In addition, one-dimensional (1-D) tape is formed in complex **2** using anion···π (Table S4, ESI†) and hydrogen bonding interactions (Table S4, ESI†). Firstly, monomeric cationic units are connected through anion···π interactions *via* one F atom (F15) with Cg(6) of one unit and one F atom (F17) with Cg(5) of the other unit for the propagation of a one-dimensional (1-D) polymeric chain along the [100] direction. Due to the self-complementary nature, the two parallel chains are interlinked through another anion···π interaction *via* one F atom (F9) with Cg(8) of one monomeric unit and three hydrogen bonding [P2–F10···O2, P2–F12···O2 and N15–H15···H2B] interactions, thus resulting in a 1-D tape (as shown in Fig. 6).

Another two-dimensional (2-D) layer (Fig. S8, ESI†) is formed in complex **2** using anion···π and anion···π⁺ (Table S7, ESI†) interactions. Here, monomeric cationic units are connected through anion···π interactions *via* one F atom (F22) with Cg(5) of the first unit and Cg(10) of the second unit for the propagation of a one-dimensional (1-D) polymeric chain. Now, this 1-D
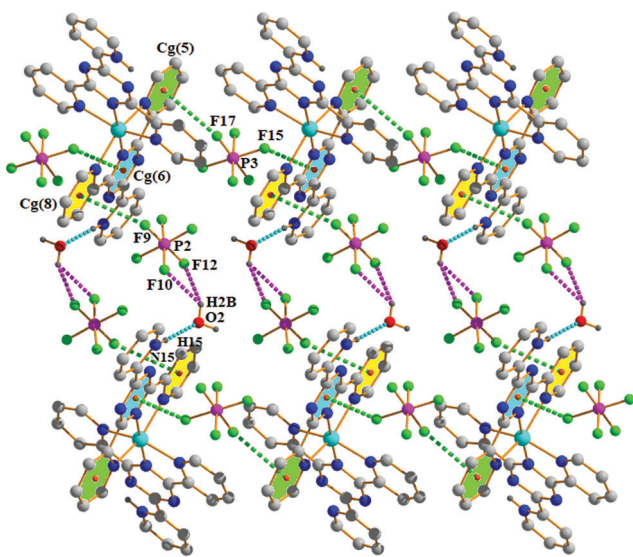
chain is further extended to 2-D layers (110) through another anion···π interaction [*via* one F atom (F17) with Cg(5) of one unit] and anion···π⁺ interaction [*via* one F atom (F18) with Cg(7) of the other unit].

Again, the crystal structure of **2** reveals the existence of various intermolecular hydrogen bonding (Table S4, ESI†) interactions in the solid state leading to the organization of a one-dimensional (1-D) zigzag polymeric chain along the [001] direction (Fig. S9, ESI†). Here, two monomeric cationic units are interconnected through the self-complementary C13–H13···F13, C14–H14···F18, C45–H45···F17 and C46–H46···F15 hydrogen bonds (shown as green dotted lines); thus generating two different $R_2^2(7)$ ring motifs. Now these dimeric units are repeated in a zigzag fashion *via* another two intermolecular hydrogen bonding [C2–H2···F6 and C39–H39···F4] interactions which are self-complementary in nature (shown in pink dotted lines).

DFT calculations

The theoretical study is focused on the analysis of π-stacking assemblies in complex **1** and anion···π interactions in complex **2**. Fig. 7a shows a partial view of the X-ray structure of complex **1** where the π···π/π···π/π···π four-component assembly is highlighted.

Two different types of π-stacking are formed: (i) a non-conventional one, denoted as $(\pi\cdots\pi)_1$, established between two non-coordinated dipicolinic acids, where the exocyclic carboxylic group of one ligand interacts with the π-cloud of the adjacent ligand, and *vice versa* (denoted as homodimer B as shown in Fig. 7c). (ii) A conventional one, denoted as $(\pi\cdots\pi)_2$, where the aromatic rings of the coordinated and non-coordinated dipicolinic acids interact (denoted as heterodimer A as shown in Fig. 7a). The latter is expected to be stronger due to the larger polarization of the π-system as a consequence of the coordination of the ligand to the Ni(II) metal center. The formation energy of this four-component assembly is very large ($\Delta E_{assembly} = -52.4$ kcal mol^{-1}), thus confirming the relevance of cooperative π···π/π···π/π···π interactions in the solid state of complex **1**. In order to compare both types of π-stacking and also the existence of cooperativity effects, we have performed additional calculations, which are summarized in Fig. 7b and c. It can be observed that the interaction energies of heterodimer **A** (Fig. 7b) and homodimer **B** (Fig. 7c) are $\Delta E_{heterodimerA} = -20.6$ kcal mol^{-1} and $\Delta E_{homodimerB} = -10.4$ kcal mol^{-1}, respectively, thus confirming the fact that the $(\pi\cdots\pi)_2$ binding mode is stronger. This larger dimerization energy is also due to the formation of a trifurcated H-bond between one aromatic C–H group and two O-atoms and one N-atom of dipicolinic acid (see dashed lines in Fig. 7b). In order to investigate the existence of cooperativity effects, we have also computed the formation energy of the four-component assembly by using heterodimer **A** as the starting point, which is $\Delta E_1 = -11.0$ kcal mol^{-1}. The comparison of this formation energy with the one of homodimer **B** ($\Delta E_{homodimerB} = -10.4$ kcal mol^{-1}) gives information about the influence of $(\pi\cdots\pi)_2$ on the strength of $(\pi\cdots\pi)_1$. Consequently, $(\pi\cdots\pi)_1$ is reinforced by 0.6 kcal mol^{-1} due to its coexistence with $(\pi\cdots\pi)_2$, thus confirming the existence of cooperativity effects. Similarly, we have also computed the

Fig. 6 Perspective view of 1-D tape generated through incorporating anion···π and hydrogen bonding interactions in complex **2** (aromatic hydrogen atoms have been omitted for clarity).
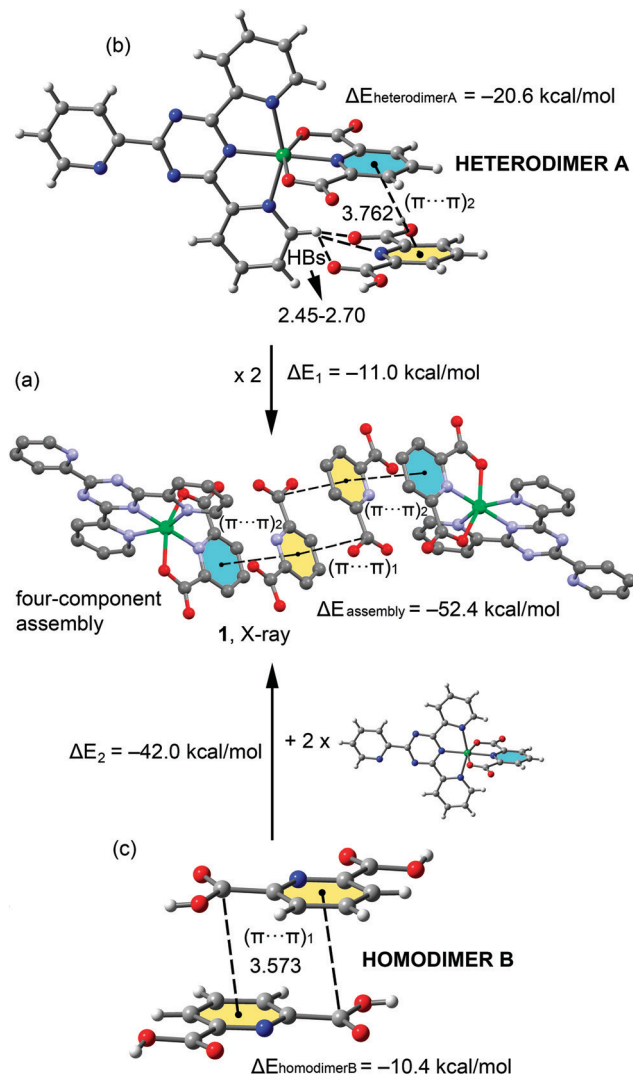
Fig. 7 (a) Partial view of the X-ray structure of complex **1**. H- atoms have been omitted for clarity. (b and c) Theoretical models used to evaluate the interaction energies. Distances are in Å.

Fig. 8 NCI plot of the four-component assembly of complex **1**. Isosurface of 0.4 a.u; density cut-off of 0.04 a.u. Colour scale -0.035 a.u. $\leq$ sign(λ_2)$\rho \leq 0.035$ a.u.

formation energy of the four-component assembly by using homodimer **B** as the starting point. The formation energy is $\Delta E_2 = -42.0$ kcal mol^{-1} which accounts for two symmetrically equivalent $(\pi \cdots \pi)_2$ interactions. The comparison of this inter-action energy with twice the dimerization energy of heterodimer **A** ($2 \times \Delta E_{\text{heterodimerA}} = -41.2$ kcal mol^{-1} reveals that the $(\pi \cdots \pi)_2$ interactions are reinforced by 0.8 kcal mol^{-1} as a consequence of the presence of $(\pi \cdots \pi)_1$.

We have further used the noncovalent interaction plot index (NCI plot) to characterize the $\pi \cdots \pi / \pi \cdots \pi / \pi \cdots \pi$ assembly in complex **1**. The NCI plot is an intuitive method that shows which spatial regions interact between molecules. Consequently, it is very convenient to analyse noncovalent interactions. Moreover, it gives hints regarding the strength of interactions by using a colour code, where green is used for weak interactions and yellow for repulsive ones. Strongly attractive and repulsive interactions are represented by blue and red colours, respectively. The NCI plot of the four-component assembly is given in Fig. 8, which
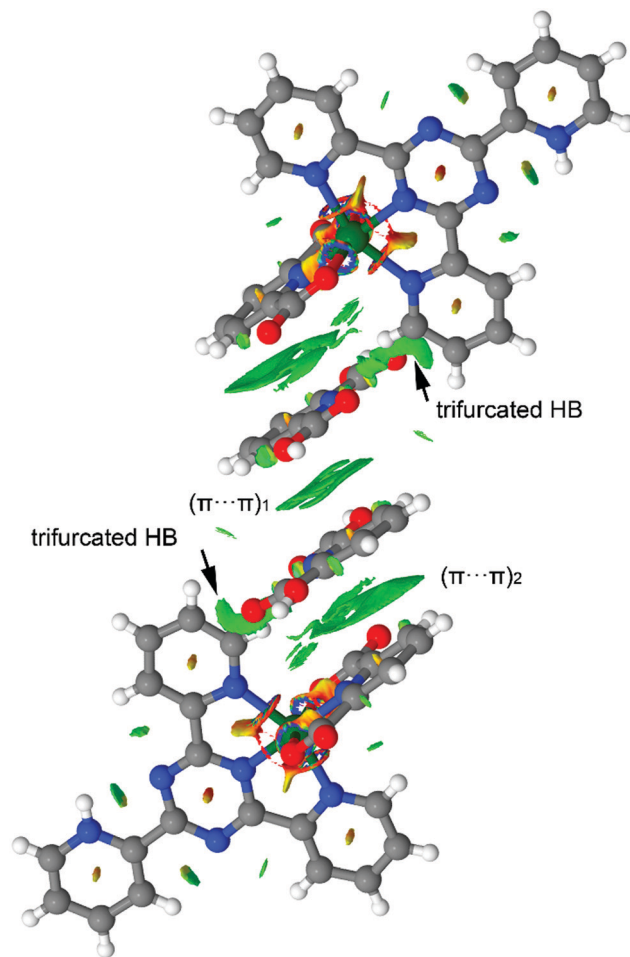
confirms the existence of $\pi \cdots \pi$ stacking interactions that are characterized by large and green isosurfaces. In the case of $(\pi \cdots \pi)_1$, the isosurfaces embrace the carboxylic groups, thus confirming their participation in the π-stacking interaction. In the case of the $(\pi \cdots \pi)_2$ binding mode, the isourface is more extended, confirming a larger overlap of the π-systems. Moreover, the existence of the trifurcated C–H$\cdots$O, N, O interaction is also confirmed by the presence of a green isosurface located between the H-atom and the three electron donor atoms belonging to dipicolinic acid.

Finally, we have also studied anion$\cdots\pi$ interactions observed in the solid state of complex **2** by using the NCI Plot index as shown in Fig. 11. The NCI plot representation shows that up to six PF$_6^-$ anions concurrently form anion–π inter-actions with the extended and π-acidic rings of the Ni(II)-coordinated 2,4,6-tri(pyridin-2-yl)-1,3,5-s-triazine ligands. Due to the protonation of the ligand, the anion$\cdots\pi$ interactions are very strong. We have evaluated two of them as representative contacts (see Fig. 9) and the interaction energies are -98.4 and -89.2 kcal mol^{-1}, which are in the range of previously reported anion–π^+ interactions.[36]
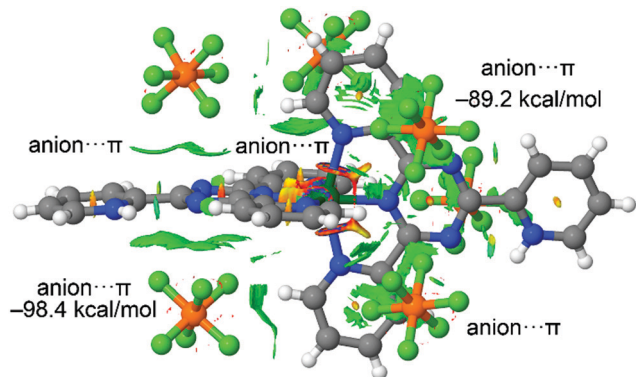
Fig. 9 NCI plot of complex **2** surrounded by six PF_6^- anions establishing anion–π interactions. Isosurface of 0.4 a.u; density cut-off of 0.04 a.u. Colour scale −0.035 a.u. ≤ sign($λ_2$)$ρ$ ≤ 0.035 a.u.

Optical studies

UV–vis absorption spectra were used to calculate the band gap of complexes and to know the type of absorption. Fig. 10(a) and (b) shows UV–vis absorption spectra of complexes **1** and **2**, respectively. Almost similar sharp visible range absorptions are observed for both complexes. To calculate the band gap energy conventional Tauc's relation was used

$$(αhν) \propto (hν - E_g)^n \qquad (1)$$

where $α$ represents the absorption coefficient; $hν$ is the photon energy; E_g represents the band gap of materials and coefficient 'n' is for band-to-band transition having a value of 1/2. Now plotting $(αhν)^2$ *vs.* $hν$ and extrapolating the linear portion of the curve gives the corresponding optical band gap values of the complexes. The band gaps (E_g) were calculated as 3.89 and 3.76 eV for complexes **1** and **2**, respectively and they are shown in the inset of Fig. 10. The wide band gap of both complexes falls under the semiconductor regime and is an indication of their device making properties.

Fabrication of the thin film and FTO/complex/Ag junction

The prime criterion of device making is the small size of the synthesized materials. As the thin film technology bridges in
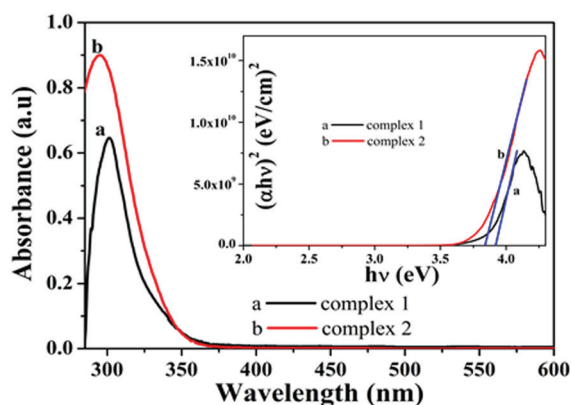

Fig. 10 UV–vis spectrum of (a) complex **1** inset: band gap of complex **1** (b) complex **2** and inset: band gap.

between macro systems and molecular systems where the size of the material is substantially reduced and is welcomed for device fabrication. With this simplification, precursor complexes are turned into thin films. Here, both precursor complexes were taken into account to deposit on FTO substrates (resistance 8–10 Ω cm^{-2} and surface area 1.0×1.0 cm^2) by a spin-coating method. Before the deposition, FTO substrates were properly washed, first with soap-water and then with running distilled water. After this, they were ultrasonicated for an hour and degreased, and thereafter, they were shifted in a hot air oven for proper drying (almost 2 hours). About 4 mg of each complex was then dispersed in DMF in a 1 : 5 ratio and ultrasonicated again for an hour. Now with a micropipette, a few drops of this solution were added onto the centre of FTO and spun at 700 rpm and then 1000 rpm for 2 and 4 minutes, respectively. The resulting films were dried in an inert atmosphere and kept in desiccators. The thicknesses of the films were measured to be 2 μm using a surface profilometer (Bruker Contour G). To fabricate the sandwich device, two contacts were made one from FTO (bottom contact) and the other from the contact metal Ag (FTO/complex/Ag) and a shadow mask was used to maintain an effective area of 7×10^{-2} cm^2.

Electrical measurements

Electrical measurements were performed at room temperature under dark and illumination conditions (sun light) in the voltage range of −1 to +1 V. Fig. 11 represents the characteristics current–voltage (I–V) curves of devices under dark and illumination conditions. The I–V nature of both complexes shows the non-linear rectifying nature which indicates that the materials are of p type and that they form the Schottky junction with the n type FTO substrate. The nature of the I–V curve represents the rectifying behaviour, similar to the Schottky barrier diode (SBD). This indicates that the rectifying nature is highly influenced under illumination of incident radiation. The current rectification values, *i.e.* the on/off ratio of device 1 under dark and photo-illumination conditions, were found to be 2.95 and 31.31 at ±1 V, respectively, whereas for device 2, the rectification values enhanced to 31.32 and 54.93 under dark and illumination conditions, respectively. The conductivity measurement of the devices further indicates the enhanced electron transportation properties of device 2 under light conditions. Room temperature conductivity for device 1 was calculated to be 2.4×10^{-6} S cm^{-1} and 6.0×10^{-6} S cm^{-1} under dark and light conditions, respectively, whereas for device 2 under the same conditions, the conductivity increased to 1.48×10^{-5} S cm^{-1} and 3.24×10^{-5} S cm^{-1}, respectively. The outcome indicates the significant photoresponse of device 2 compared to device 1.

To investigate the predominant charge transportation mechanism, these I–V curves must be carefully analysed. The non-linear I–V nature of the devices arises due to different types of charge transportation mechanisms and can be explained by the established model of Richardson–Schottky or Poole–Frankel.[37] Thermal activation of electrons over the metal-semiconductor interface results in Schottky emission in the presence of an applied field.[38] To obtain a clear understanding of the charge transport mechanism, thermionic emission theory has been
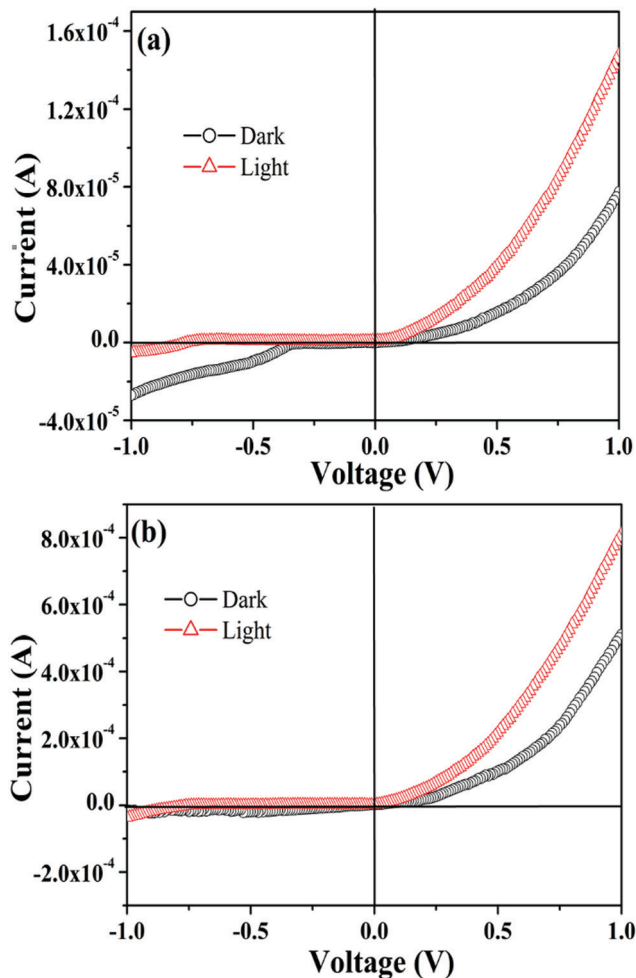
Fig. 11 $I–V$ characteristic curve of (a) device 1 under dark and illumination conditions and (b) device 2 under dark and illumination conditions.

adapted to quantitatively analyse the $I–V$ plots, where device parameters were confirmed by the Cheung's standard equation[39]

$$I = I_0[\exp((qV)/(\eta kT)) - 1] \quad (2)$$

Here, I and I_0 are the forward and reverse saturation currents, V and q are the applied potential and electron charges, k and T are the Boltzmann constant and absolute temperature, and η represents the ideality factor of SBD. The saturation current (I_0) can be expressed as

$$I_0 = AA^{\star}T^2\exp[(-q\,\phi_B)/(KT)] \quad (3)$$

where the term ϕ_B represents barrier height; A and $A^{\star}$ are the diode area and Richardson constant, respectively. For both devices, the diode area was fixed as 7×10^{-2} cm^2, and the effective Richardson constant was taken as 32 A K^{-2} cm^{-2}. Now, $I–V$ characteristics can also be represented as

$$I = I_0[\exp((q(V - IR_S))/(\eta kT))] \quad (4)$$

where the term IR_S stands for the voltage drop across the series resistance and it can be calculated from the following equation:

$$dv/d(\ln I) = \eta KT/q + IR_S \quad (5)$$

Eqn (9) can also be expressed as a function of 'I' by the following form

$$H(I) = IR_S + \eta\Phi_B \quad (6)$$

Hence, the series resistance (R_s) can be measured and calculated by the above two consecutive equations.

$H(I)$ can also be represented by the following equation

$$H(I) = V - (\eta KT/q)\ln(I/(AA^{\star}T^2)) \quad (7)$$

Now using eqn (5), $dV/d(\ln I)$ *versus* I (Fig. 12) is plotted to measure the series resistance (R_S) from the slope and ideality factor (η) from the intercept (under dark and light illumination conditions). The calculated ideality factor (η) values for device 1 are 2.81 and 1.79 under dark and light conditions, respectively, whereas for device 2, the η values become 2.53 and 1.41 under the same conditions, respectively. Hence, with the irradiation of incident radiation, device 2 moves more towards ideality. The deviation of η values from the ideality ($\eta = 1$) is an indication of the improper metal–semiconductor junction which results from trapping states in the interface. The structural disorderliness of the compound plays a significant role; more clutter structures bring more trapping states and thereby easily deviate from the ideal value. There are some reports on the SBD device analysis that impose some other factors, like surface contamination, barrier tunneling, *etc.*, responsible for non-ideality.[40,41]
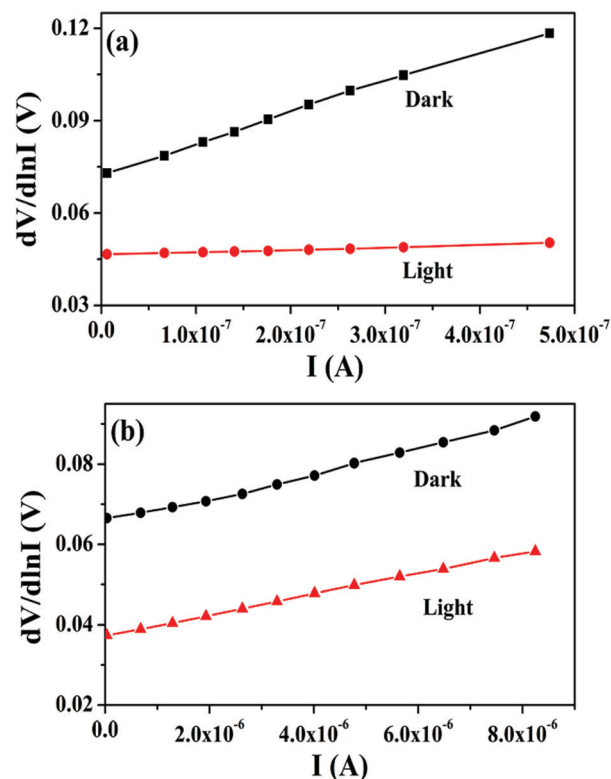

Fig. 12 $dV/d(\ln I)$ *vs.* I plot under dark and illumination conditions for (a) device **1** and (b) device **2**.

Fig. 13 *H* (*V*) *vs.* I plot under dark and illumination conditions for (a) device 1 and (b) device 2.

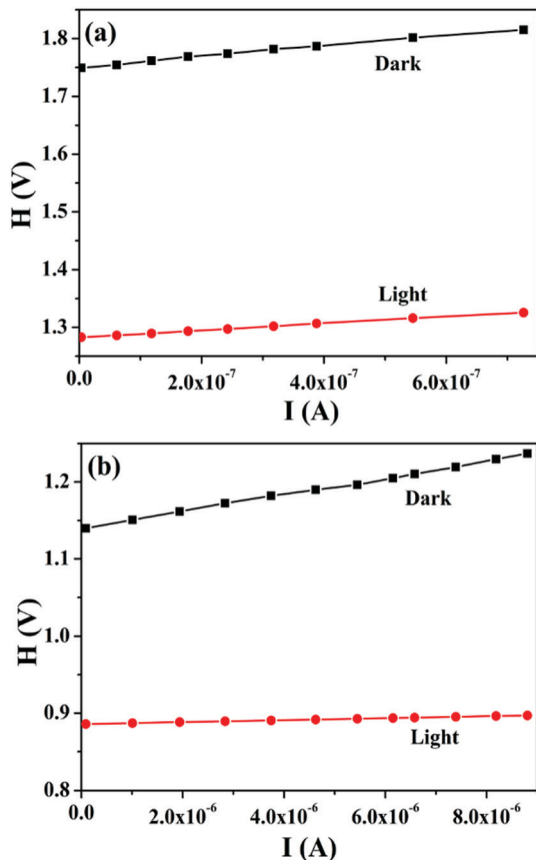Fig. 14 log (*I*) *vs.* log (*V*) plot under dark and illumination conditions for (a) device 1 and (b) device 2.

The potential barrier height (Φ_B) values are calculated from the intercepts of $H(V)$ *vs.* I plot of both devices (Fig. 13) using eqn (6). The 'H' values are calculated by means of η values obtained from Fig. 12 using eqn (5).

To gain insights into the charge transport phenomenon of carrier transport through the interface of the MS junction, the log–log plot, *i.e.*, log(I) *versus* log(V), was analyzed (Fig. 14). The presence of two distinct regions in the log–log plot ensures different conduction mechanisms are operating here. Now applying the power law ($I \propto V^m$) (where m is slope value) on the log–log plot, the governing mechanism prevailing in carrier conduction can be specified. By analyzing the slope value 'm', two distinct zones can be separated, $m \geq 2$ indicates a space-charge-limited-current (SCLC) region whereas a value less than or equal to 1 ($m \leq 1$) indicates the ohmic zone.[42,43] Fig. 14 represents log (I) *vs.* log (V) plot of devices 1 and 2 in the absence and presence of light. The presence of two separate regions indicates that different conduction mechanisms are prevailing here. At region I, *i.e.*, at low bias voltage, the compound exhibits an ohmic nature ($I \propto V$). The I–V characteristic in this region can be imposed to thermionic emission. Just after this, the I–V curve obeys power law behaviour ($I \propto V^m$) and it is assigned as region II.

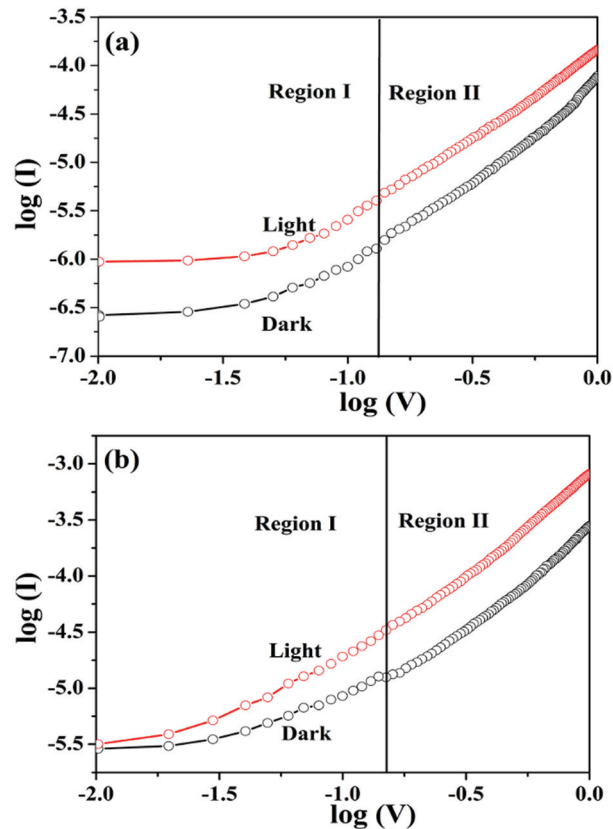In region II, the current is ruled by the space charge limited current (SCLC) which is proportional to the square of the applied voltage ($I \propto V^2$).[44,45] This SCLC region gives several important device performances like carrier concentration (N), carrier mobility (μ_{eff}), diffusion coefficient (D), diffusion length (L_D), transit time (τ), *etc.*

Dielectric constants of the compounds were measured from the saturation capacitance (C) value of capacitance *vs.* frequency plot (Fig. S10, ESI†) by using the following equation.[46]

$$\varepsilon_r = (1/\varepsilon_0)(C \cdot L/A) \tag{8}$$

Here, L is the thickness of the deposited material and A is the diode area. The measured relative dielectric constants of the material were calculated to be 32.26 and 6.45 for complexes **1** and **2**, respectively. A comparatively low dielectric constant of complex **2** suggests its preferential use in power generation to minimize the electric power loss.

The effective carrier mobility (μ_{eff}) of both devices has been calculated from the I *vs.* V^2 (Fig. 15) plot by employing the Mott–Gurney eqn (11)[47]

$$J = (9\mu_{eff}\varepsilon_0\varepsilon_r V^2)/(8d^3) \tag{9}$$

Here J is the current density, ε_0 and ε_r are the permittivity of vacuum and relative dielectric constant of compounds, respectively. The device made of complex **2** has a higher mobility (5.36×10^{-4} cm^2 V^{-1} s^{-1}) than that of complex **1** (3.19×10^{-4} cm^2 V^{-1} s^{-1}).

Other important device performances like carrier concentration (N), carrier mobility (μ_{eff}), diffusion coefficient (D),
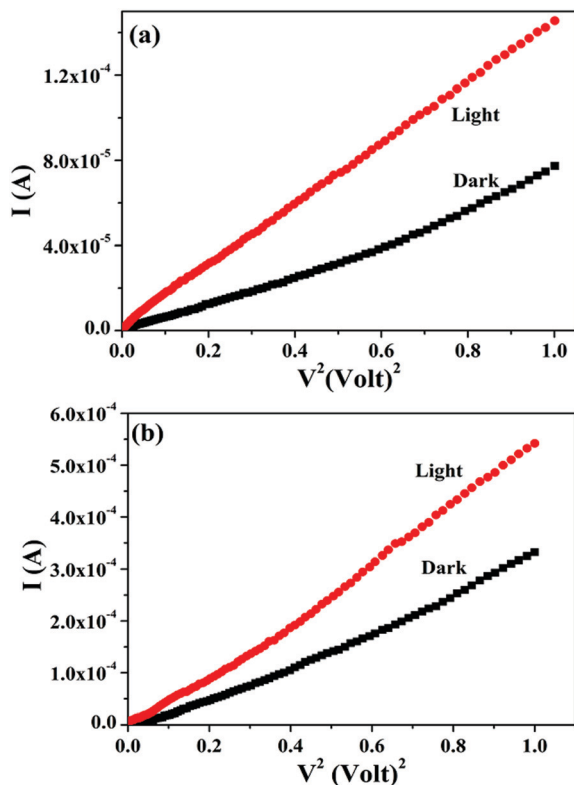
Fig. 15 *I vs. V²* plot under dark and illumination conditions for (a) device 1 and (b) device 2.

diffusion length (L_D), and transit time (τ) *etc.* are calculated using the following set of equations.

$$N = \sigma/(q \cdot \mu_{eff}) \tag{10}$$

$$\tau = (9\varepsilon_0\varepsilon_r V)/(8d \cdot l) \tag{11}$$

$$\mu_{eff} = (q \cdot D)/(k \cdot T) \tag{12}$$

$$L_D = \sqrt{(2D\tau)} \tag{13}$$

The better performance of the SBD device can be categorised by the high values of N, μ_{eff} and L_D. All device parameters for both devices are listed in Table S8 (ESI†) (complex **1**) and Table S9 (ESI†) (complex **2**). From the detailed analysis with respect to device performance, it can be concluded that device 2 made from compound **2** is better than device 1. A comparison of the conductivities of the recently reported Ni(II) based complexes with our synthesized complexes **1** and **2** (Table S10, ESI†) shows that our materials have enough potentiality in optoelectronic applications.

Conclusions

Two new octahedral complexes of nickel(II) have been synthesized and characterized, where both the triazine moiety and pyridine-2,6-dicarboxylic acid act as ligands for complex **1** and only the triazine moiety binds Ni(II) in complex **2**. In the synthesized metal–ligand frameworks, various supramolecular interactions especially $\pi \cdots \pi$ stacking, anion$\cdots\pi$ interactions along with lone pair$\cdots\pi$, C–H$\cdots\pi$, anion$\cdots\pi^+$, $\pi\cdots\pi^+$, $\pi^+\cdots\pi^+$ and H-bonding interactions are present. These imperative interactions are responsible for the construction of extended networks in the solid state architectures of complexes **1** and **2**. DFT calculations evidence the existence of cooperativity effects in the formation of supramolecular $\pi \cdots \pi/\pi \cdots \pi/\pi \cdots \pi$ interactions for complex **1**. Various anion$\cdots\pi$ interactions in complex **2** have been well established by using the NCI plot index.

The realistic applications of both the complexes have been initiated by fabricating the SBD device using silver as the metal contact. The devices made from complexes **1** and **2** exhibit nonlinear rectifying behaviour under dark and light illumination at an applied potential of ±1.0 V. The measured device parameters, *e.g.*, mobility, transit time, carrier diffusion length, and ideality factor, confirm complex **2** as better SBD compared to complex **1**. A likely explanation for this behaviour can be related to the presence of extensive $\pi \cdots \pi$ stacking and a large number of counter-ions in complex **2**. This issue is currently under investigation in our laboratory. Conductivity measurements of the devices further indicated the enhanced charge transportation properties of device 2 compared to that of device 1 under illumination conditions. In fact, both Ni(II) coordination compounds reported herein illustrate reasonably higher electrical conductivities than other Ni-based compounds reported in the literature.

Conflicts of interest

There are no conflicts to declare.

Acknowledgements

References

1 (*a*) M. Du, C.-P. Li, C.-S. Liu and S.-M. Fang, *Coord. Chem. Rev.*, 2013, **257**, 1282–1305; (*b*) K. B. Thapa, Y.-F. Hsu, H.-C. Lin and J.-D. Chen, *CrystEngComm*, 2015, **17**, 7574–7582; (*c*) S. Konar, *Inorg. Chem. Commun.*, 2014, **49**, 76–78; (*d*) S. Konar, A. Dey, S. R. Choudhury, K. Das, S. Chatterjee, P. P. Ray, J. Ortega-Castro, A. Frontera and S. Mukhopadhyay, *J. Phys. Chem. C*, 2018, **122**, 8724–8734.

2 (*a*) L.-P. Xue, Z.-H. Li, L.-F. Ma and L.-Y. Wang, *CrystEngComm*, 2015, **17**, 6441–6449; (*b*) S. Radi, M. El-Massaoudi, H. Benaissa, N. N. Adarsh, M. Ferbinteanu, E. Devlin, Y. Sanakis and Y. Garcia, *New J. Chem.*, 2017, **41**, 8232–8241; (*c*) J. Z. Gu, Y. Cai, X. X. Liang, J. Wu, Z. F. Shi and A. M. Kirillov,

CrystEngComm, 2018, **20**, 906–916; (*d*) S. Jia, Z. Gao, N. Tian, Z. Li, J. Gong, J. Wang and S. Rohani, *Chem. Eng. Res. Des.*, 2021, **166**, 268–280.

3 (*a*) B. Gole, A. K. Bar, A. Mallick, R. Banerjee and P. S. Mukherjee, *Chem. Commun.*, 2013, **49**, 7439–7441; (*b*) X.-Q. Guo, C. Huang, H.-Y. Yang, Z.-C. Shao, K. Gao, N. Qin, G.-X. Li, J. Wu and H.-W. Hou, *Dalton Trans.*, 2018, **47**, 16895–16901; (*c*) J. Z. Gu, M. Wen, Y. Cai, Z. F. Shi, A. S. Arol, M. V. Kirillova and A. M. Kirillov, *Inorg. Chem.*, 2019, **58**, 2403–2412.

4 K. J. Lee, J. H. Lee, S. Jeoung and H. R. Moon, *Acc. Chem. Res.*, 2017, **50**, 2684–2692.

5 (*a*) A. C. Kizzie, A. G. Wong-Foy and A. J. Matzger, *Langmuir*, 2011, **27**, 6368–6373; (*b*) K. S. Song, D. Kim, K. Polychronopoulou and A. Coskun, *ACS Appl. Mater. Interfaces*, 2016, **8**, 26860–26867; (*c*) S. Mondal and P. Dastidar, *Cryst. Growth Des.*, 2019, **19**, 470–478.

6 K. Biradha, A. Goswami and R. Moi, *Chem. Commun.*, 2020, **56**, 10824–10842.

7 (*a*) B. Dutta, R. Jana, A. K. Bhanja, P. P. Ray, C. Sinha and M. H. Mir, *Inorg. Chem.*, 2019, **58**, 2686–2694; (*b*) P. Ghorai, A. Dey, A. Hazra, B. Dutta, P. Brandao, P. P. Ray, P. Banerjee and A. Saha, *Cryst. Growth Des.*, 2019, **11**, 6431–6447.

8 (*a*) B. Deka, T. Sarkar, S. Banerjee, A. Kumar, S. Mukherjee, S. Deka, K. K. Saikia and A. Hussain, *Dalton Trans.*, 2017, **46**, 396–409; (*b*) Q.-P. Qin, Z.-F. Wang, S.-L. Wang, D.-M. Luo, B.-Q. Zou, P.-F. Yao, M.-X. Tan and H. Liang, *Eur. J. Med. Chem.*, 2019, **170**, 195–202.

9 (*a*) D. Das and K. Biradha, *Cryst. Growth Des.*, 2018, **18**, 3683–3692; (*b*) B. Parmar, K. K. Bisht, Y. Rachuri and E. Suresh, *Inorg. Chem. Front.*, 2020, **7**, 1082–1107; (*c*) J. Zhu, P. Zhu, M. Yan, H. Chen and K. Zhang, *CrystEngComm*, 2021, DOI: 10.1039/D0CE01724H.

10 (*a*) G. Xu, P. Nie, H. Dou, B. Ding, L. Li and X. Zhang, *Mater. Today*, 2017, **20**, 191–209; (*b*) M. Inukai, S. Horike, T. Itakura, R. Shinozaki, N. Ogiwara, D. Umeyama, S. Nagarkar, Y. Nishiyama, M. Malon, A. Hayashi, T. Ohhara, R. Kiyanagi and S. Kitagawa, *J. Am. Chem. Soc.*, 2016, **138**, 8505–8511.

11 (*a*) M. Guergueb, S. Nasri, J. Brahmi, F. Loiseau, F. Molton, T. Roisnel, V. Guerineau, I. Turowska-Tyrk, K. Aouadi and H. Nasri, *RSC Adv.*, 2020, **10**, 6900–6918; (*b*) M. Dai, H. X. Li and J. P. Lang, *CrystEngComm*, 2015, **17**, 4741–4753; (*c*) J. Huo, D. Yu, H. Li, B. Luo and N. Arulsamy, *RSC Adv.*, 2019, **9**, 39323–39331; (*d*) J. Liu, D. Xie, W. Shi and P. Cheng, *Chem. Soc. Rev.*, 2020, **49**, 1624–1642; (*e*) J. B. Gilroy and E. Otten, *Chem. Soc. Rev.*, 2020, **49**, 85–113.

12 (*a*) N. Li, R. Feng, J. Zhu, Z. Chang and X.-H. Bu, *Coord. Chem. Rev.*, 2018, **375**, 558–586; (*b*) X. Q. Liang, R. K. Gupta, Y. W. Li, H. Y. Ma, L. N. Gao, C. H. Tung and D. Sun, *Inorg. Chem.*, 2020, **59**, 2680–2688.

13 (*a*) J. Kim, B. L. Chen, T. M. Reineke, H. L. Li, M. Eddaoudi, D. B. Moler, M. O'Keeffe and O. M. Yaghi, *J. Am. Chem. Soc.*, 2001, **123**, 8239–8247; (*b*) Y. N. Gong, C. B. Liu, H. L. Wen, L. S. Yan, Z. Q. Xiong and L. Ding, *New J. Chem.*, 2011, **35**, 865–875; (*c*) G. Mahmoudi, F. A. Afkhami, E. Zangrando, W. Kaminsky, A. Frontera and D. A. Safin, *J. Mol. Struct.*, 2021, **1224**, 129188.

14 (*a*) A. Nijamudheen, D. Jose, A. Shine and A. Datta, *J. Phys. Chem. Lett.*, 2012, **3**, 1493–1496; (*b*) O. Perraud, V. Robert, H. Gornitzka, A. Martinez and J.-P. Dutasta, *Angew. Chem., Int. Ed.*, 2012, **51**, 504–508; (*c*) M. K. Bhattacharyya, D. Dutta, S. M. N. Islam, A. Frontera, P. Sharma, A. K. Verma and A. Das, *Inorg. Chim. Acta*, 2020, **501**, 119233.

15 (*a*) M. Mitra, P. Manna, A. Bauzá, P. Ballester, S. K. Seth, S. R. Choudhury, A. Frontera and S. Mukhopadhyay, *J. Phys. Chem. B*, 2014, **118**, 14713–14726; (*b*) A. Das, S. R. Choudhury, B. Dey, S. K. Yalamanchili, M. Helliwell, P. Gamez, S. Mukhopadhyay, C. Estarellas and A. Frontera, *J. Phys. Chem. B*, 2010, **114**, 4998–5009; (*c*) A. Das, S. R. Choudhury, C. Estarellas, B. Dey, A. Frontera, J. Hemming, M. Helliwell, P. Gamez and S. Mukhopadhyay, *CrystEngComm*, 2011, **13**, 4519–4527; (*d*) L. A. Barrios, G. Aromi, A. Frontera, D. Quiñonero, P. M. Deya, P. Gamez, O. Roubeau, E. J. Shotton and S. J. Teat, *Inorg. Chem.*, 2008, **47**, 5873–5881; (*e*) C. Garau, D. Quiñonero, A. Frontera, P. Ballester, A. Costa and P. M. Deyà, *Org. Lett.*, 2003, **5**, 2227–2229; (*f*) A. Bauzá, T. J. Mooibroek and A. Frontera, *CrystEngComm*, 2016, **18**, 10–23.

16 (*a*) P. Manna, S. K. Seth, M. Mitra, A. Das, N. J. Singh, S. R. Choudhury, T. Kar and S. Mukhopadhyay, *CrystEng-Comm*, 2013, **15**, 7879–7886; (*b*) S. Pramanik, S. Konar, K. Chakraborty, T. Pal, S. Das, S. Chatterjee, M. Dolai and S. Pathak, *J. Mol. Struct.*, 2020, **1206**, 127663.

17 (*a*) J. J. Liu, S. B. Xia, Y. L. Duan, T. Liu, F. X. Cheng and C. K. Sun, *Polymer*, 2018, **10**, 165–176; (*b*) P. Thuéry and J. Harrowfield, *CrystEngComm*, 2015, **17**, 4006–4018; (*c*) Y. Rachuri, B. Parmar, K. K. Bisht and E. Suresh, *Dalton Trans.*, 2017, **46**, 3623–3630.

18 (*a*) S. E. Domínguez, F. E. M. Vieyra and F. Fagalde, *Dalton Trans.*, 2020, **49**, 12742–12755; (*b*) Z. Azarkamanzad, F. Farzaneh, M. Maghami and J. Simpson, *New J. Chem.*, 2019, **43**, 12020–12031; (*c*) A. H. Sun, Q. Wei, A. P. Fu, S. D. Han, J. H. Li and G. M. Wang, *Dalton Trans.*, 2018, **47**, 6965–6972.

19 (*a*) K. Abdi, H. Hadadzadeh, M. Salimi, J. Simpson and A. D. Khalaji, *Polyhedron*, 2012, **44**, 101–112; (*b*) D. A. Safin, J. M. Frost and M. Murugesu, *Dalton Trans.*, 2015, **44**, 20287–20294; (*c*) M. Maghami, F. Farzaneh, J. Simpson, M. Ghiasi and M. Azarkish, *J. Mol. Struct.*, 2015, **1093**, 24–32.

20 (*a*) D. K. Maity, S. Ghosh, K. Otake, H. Kitagawa and D. Ghoshal, *Inorg. Chem.*, 2019, **58**, 12943–12953; (*b*) S. Bala, A. De, A. Adhikary, S. Saha, S. Akhtar, K. S. Das, M.-L. Tong and R. Mondal, *Cryst. Growth Des.*, 2020, **20**, 5698–5708.

21 (*a*) C. W. Machan, M. Adelhardt, A. A. Sarjeant, C. L. Stern, J. Sutter, K. Meyer and C. A. Mirkin, *J. Am. Chem. Soc.*, 2012, **134**, 16921–16924; (*b*) I. Kumar, P. Bhattacharya and K. H. Whitmire, *Organometallics*, 2014, **33**, 2906–2909; (*c*) K. Ghosh, A. Banerjee, A. Bauzá, A. Frontera and S. Chattopadhyay, *RSC Adv.*, 2018, **8**, 28216–28237; (*d*) Q.-P. Qin, Z.-F. Wang, M.-X. Tan, X.-L. Huang, H.-H. Zou, B.-Q. Zou, B.-B. Shi and S.-H. Zhang, *Metallomics*, 2019, **11**, 1005–1015; (*e*) M. D. Olawale, J. O. Obaleyeb and E. O. Oladelec, *New J. Chem.*, 2020, **44**, 18780–18791.

22 (*a*) K. Sinziger, S. Hünig, M. Jopp, D. Bauer, W. Bietsch, J. U. von Schütz, H. C. Wolf, R. K. Kremer, T. Metzenthin,

R. Bau, S. I. Khan, A. Lindbaum, C. L. Lengauer and E. Tillmans, *J. Am. Chem. Soc.*, 1993, **115**, 7696–7705; (*b*) R. Kato, H. Kobayashi, A. Kobayashi, T. Mori and H. Inokuchi, *Chem. Lett.*, 1987, 1579–1582; (*c*) R. Kato, H. Kobayashi and A. Kobayashi, *J. Am. Chem. Soc.*, 1989, **111**, 5224–5232.

23 (*a*) S. Hünig and P. Erk, *Adv. Mater.*, 1991, **3**, 225–236; (*b*) D. Asakura, C. H. Li, Y. Mizuno, M. Okubo, H. Zhou and D. R. Talham, *J. Am. Chem. Soc.*, 2013, **135**, 2793–2799.

24 (*a*) L. Welte, A. Calzolari, R. di Felice, F. Zamora and J. Gómez-Herrero, *Nat. Nanotechnol.*, 2010, **5**, 110–115; (*b*) W. Shi, G. Wu, X. Yong, T. Deng, J. S. Wang, J. C. Zheng, J. Xu, M. B. Sullivan and S. W. Yang, *ACS Appl. Mater. Interfaces*, 2018, **10**, 35306–35315; (*c*) V. Rubio-Giménez, S. Tatay and C. Martí-Gastaldo, *Chem. Soc. Rev.*, 2020, **49**, 5601–5638.

25 C. Adamo and V. Barone, *J. Chem. Phys.*, 1999, **110**, 6158–6170.

26 S. Grimme, J. Antony, S. Ehrlich and H. Krieg, *J. Chem. Phys.*, 2010, **132**, 154104.

27 F. Weigend, *Phys. Chem. Chem. Phys.*, 2006, **8**, 1057–1065.

28 M. J. Frisch, G. W. Trucks, H. B. Schlegel, G. E. Scuseria, M. A. Robb, J. R. Cheeseman, G. Scalmani, V. Barone, B. Mennucci, G. A. Petersson, H. Nakatsuj, M. Caricato, X. Li, H. P. Hratchian, A. F. Iamaylov, J. Bloino, G. Zheng, J. L. Sonnenberg, M. Hada, M. Ehara, K. Toyota, R. Fukuda, J. Hasegawa, M. Ishida, T. Nakajima, Y. Honda, O. Kitao, H. Nakai, T. Vreven, J. A. Montgomery Jr, J. E. Peralta, F. Ogliaro, M. Bearpark, J. J. Heyd, E. Brothers, K. N. Kudin, V. N. Staroverov, R. Kobayashi, J. Normand, K. Raghavachari, A. Rendell, J. C. Burant, S. S. Lyengar, J. Tomasi, M. Cossi, N. Rega, J. M. Millam, M. Klene, J. E. Knox, J. B. Cross, V. Bakken, C. Adamo, J. Jaramillo, R. Gomperts, R. E. Stratmann, O. Yazyev, A. J. Austin, R. Cammi, C. Pomelli, J. W. Ochterski, R. L. Martin, K. Morokuma, V. G. Zakrzewski, G. A. Voth, P. Salvador, J. J. Dannenberg, S. Dapprich, A. D. Daniels, O. Farkas, J. B. Foresman, J. V. Ortiz, J. Cioslowski and D. J. Fox, *Gaussian 09, Revision A.1*, Gaussian Inc., Wallingford CT, 2016.

29 R. F. W. Bader, *Chem. Rev.*, 1991, **91**, 893–928.

30 E. R. Johnson, S. Keinan, P. Mori-Sánchez, J. Contreras-García, A. J. Cohen and W. Yang, *J. Am. Chem. Soc.*, 2010, **132**, 6498–6506.

31 J. Contreras-García, E. R. Johnson, S. Keinan, R. Chaudret, J.-P. Piquemal, D. N. Beratan and W. Yang, *J. Chem. Theory Comput.*, 2011, **7**, 625–632.

32 T. A. Keith, AIMALL (Version 19.02.13), TK Gristmill Software, Overl. Park KS, USA, 2019.

33 L. E. Zelenkov, D. M. Ivanov, K. Sadykov, N. A. Bokach, B. Galmes, A. Frontera, V. Yu. Kukushkin and Yu. Vadim, *Cryst. Growth Des.*, 2020, **20**, 6956–6965.

34 Bruker, SMART *v*5.631, Bruker AXS Inc., Madison, WI, USA, 2001.

35 G. M. Sheldrick, *SHELXL-2014/7: Program for the Solution of Crystal Structures*, University of Gottingen, Gottingen, Germany, 2014.

36 P. Manna, S. K. Seth, M. Mitra, S. R. Choudhury, A. Bauzá, A. Frontera and S. Mukhopadhyay, *Cryst. Growth Des.*, 2014, **14**, 5812–5821.

37 S. M. Sze, *Physics of Semiconductor Devices*, Wiley, New York, 1969, p. 496.

38 J. G. Simmons, *Phys. Rev.*, 1967, **155**, 657–660.

39 S. K. Cheung and N. W. Cheung, *Appl. Phys. Lett.*, 1986, **49**, 85–87.

40 M. W. Allen and S. M. Durbin, *Appl. Phys. Lett.*, 2008, **92**, 12110–12113.

41 D. T. Quan and H. Hbib, *Solid-State Electron.*, 1993, **36**, 339–344.

42 A. Jain, P. Kumar, S. C. Jain, V. Kumar, R. Kaur and R. M. Mehra, *J. Appl. Phys.*, 2007, **102**, 094505.

43 S. Aydogan, M. Saglam and A. Turut, *J. Phys.: Condens. Matter*, 2006, **18**, 2665–2676.

44 Z. Ahmad and M. H. Sayyad, *Phys. E*, 2009, **41**, 631–634.

45 P. Kumar, S. C. Jain, V. Kumar, S. Chand and R. P. Tandon, *J. Appl. Phys.*, 2009, **105**, 104507.

46 S. Suresh, *Int. J. Phys. Sci.*, 2013, **8**, 1121–1127.

47 P. W. M. Blom, M. J. M. D. Jong and M. G. V. Munster, *Phys. Rev. B: Condens. Matter Mater. Phys.*, 1997, **55**, 656–659.

Check for updates

Chromogenic and fluorogenic "off–on–off" chemosensor for selective and sensitive detection of aluminum (Al^{3+}) and bifluoride (HF$_2^-$) ions in solution and in living Hep G2 cells: synthesis, experimental and theoretical studies†

Samit Pramanik,[a] Saikat Kumar Manna,[b] Sudipta Pathak, [iD] *[b] Debasish Mondal,[c] Kunal Pal[d] and Subrata Mukhopadhyay[a]

A simple pyridine-dicarbohydrazide based colorimetric and fluorometric chemosensor **L** was designed and synthesized for Al^{3+} ion sensing in organo aqueous solution. In the presence of Al^{3+} ions, probe **L** exhibited visible color changes and fluorescence enhancement (20-fold) due to Al^{3+} induced chelation-enhanced fluorescence (CHEF) effects. Chemosensor **L** revealed high selectivity toward Al^{3+} ions by "turn-on" fluorescence among the other competitive metal ions examined with a detection limit of 0.8 μM. Probe **L** was found to bind with Al^{3+} ions in a 1 : 2 (probe : metal) stoichiometric fashion, with an association constant (K_a) of 4.26×10^4 M^{-2}. In addition, DFT and TDDFT calculations were carried out to recognize the binding nature and electronic properties of probe **L** and its Al-complex. Furthermore, the *in situ* prepared [**L**–Al] complex was able to detect HF$_2^-$ anions *via* a metal displacement strategy. The bioimaging application of Al^{3+} and HF$_2^-$ was implemented in living human liver cancer cells (Hep G2).

Introduction

Being the third most abundant (8.3% by weight) element (after oxygen and silicon) on the surface of the earth, aluminum is widely associated with our daily contemporary life in the form of food packaging, water purification, cooking utensils, pharmaceuticals, manufacturing of computers, *etc.*[1–3] Aluminium compounds are also extensively used in the paper industry, in dye production, in the textile industry, and as a component of many cosmetic preparations, and are currently utilized in the alimentary industry and in many more.[4,5] Therefore, there is a good chance of accumulation of aluminum ions (Al^{3+}) in the food chain and toxicity towards human health. But, the tolerable daily intake of aluminum is about 3–10 mg and consequently the upper limit of aluminum nutritional intake is about 7 mg per kg of body weight per week according to a WHO report.[6] Excess accumulation of this metal causes some serious diseases like myopathy, Parkinson's disease, Alzheimer's disease, osteoporosis, headaches, anemia, chronic renal failure, dialysis encephalopathy, bone softening, kidney damage and even breast cancer.[7–9] The solubility of aluminium minerals at lower pH increases the amount of available Al^{3+}, which can affect plants' normal growth and development, ultimately hampering agricultural production.[10] Therefore, easy detection of aluminum ions is imperative in various samples connected to the environment, foodstuffs, medicine, *etc.* But detection of aluminium ions is still a major challenge due to their low coordination capability, high hydration aptitude and lack of spectroscopic features.[11] A number of analytical techniques have been used for the detection of aluminum ions, such as atomic absorption spectrometry,[12] inductively coupled plasma atomic emission spectrometry (ICP-AES),[13,14] inductively coupled plasma mass spectrometry (ICP-MS),[15] nanoparticle-based sensors,[16] ion selective membranes,[17] electrochemical methods,[18] and several other methods.[19] But these techniques are restricted to the laboratory because of high equipment cost, time consuming nature and the necessity for trained personnel. However, spectrofluorimetry is superior in terms of quick analysis, high selectivity, sensitivity and ease of operation. As Al^{3+} is a hard acid, it prefers hard base donor sites for coordination,[20] so Schiff base probes with N and O donor centres could be used as good ligands for

[a] *Department of Chemistry, Jadavpur University, Kolkata 700032, India*

[b] *Department of Chemistry, Haldia Government College, Debhog, Purba Medinipur, West Bengal, India. E-mail: sudiptachemster@gmail.com; Tel: +91-8001317336*

[c] *School of Chemistry and Biochemistry, Thapar Institute of Engineering and Technology, Patiala 147004, Punjab, India*

[d] *Department of Life Science and Biotechnology, Jadavpur University, Kolkata 700032, India*

Al^{3+} detection.[21] In several research fields hydrazides have been extensively used as ligands due to their facile syntheses, tunable electronic properties and good chelating capability.[22] In this work, we have designed and synthesized a pyridine-dicarbohydrazide based 'turn-on' chemosensor **L** which shows high selectivity for Al^{3+} with a low detection limit (LOD).

Anions play a vital role in the area of supramolecular chemistry, especially in environmental, chemical, medical and biological systems. Among the different anions, recognition of semi-ionic, three-center, and four-electron bonding bifluoride ions (HF_2^-) is of growing interest because of their extensive applications in various fields including etching of borosilicate glass capillary columns, insecticides, fluorometric detection of ultra-trace levels of beryllium in occupational hygiene samples, and preparation of borane derivatives and molten salts.[23] Until now, very few chemosensors have been reported for bifluoride ions.[24] Therefore, there is an urgent requirement for fluorescent and biocompatible probes that can selectively and sensitively detect bifluoride ions with a rapid response through easy spectral analysis. However, the design and development of fluorescent chemosensors for anions in aqueous solution is still a difficult task due to the strong hydration properties of anions. This problem could be evaded by using the metal displacement strategy. Keeping this in mind, we report here a displacement-based sensing system by using an Al^{3+}-based ensemble (**L**–$2Al^{3+}$) for bifluoride ion recognition. It is noteworthy to mention that chemosensor **L** has interesting analytical features like its easy synthetic route with good yield and reasonably low detection limit for Al^{3+} ions with no interference from a number of cations in comparison to reported methods (Table S1, ESI†). Another notable aspect of the **L**–$2Al^{3+}$ complex is that it displays a good reversible fluorescence response to HF_2^-. Furthermore, probe **L** is effectively applied to image Al^{3+} and HF_2^- ions in cultured Hep G2 cells.

Results and discussion

Scheme 1 outlines the synthetic route of chemosensor **L**. Compound **1** was prepared following a literature procedure.[25] Probe **L** was then synthesized by the condensation reaction between compound **1** and
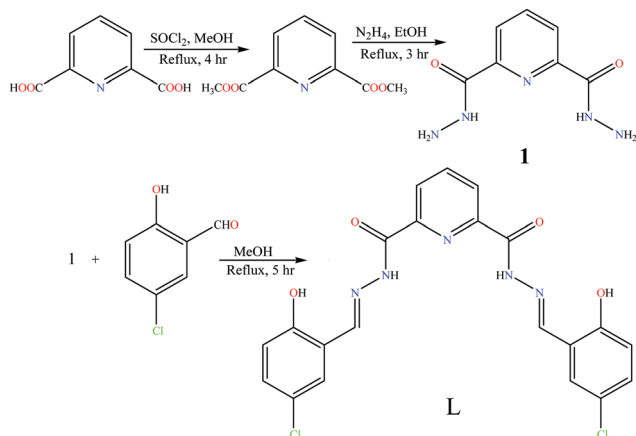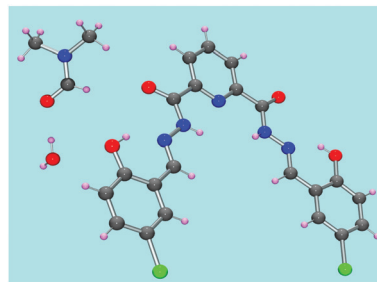

Fig. 1 ORTEP view of molecular probe **L** (with 40% probability).

2-hydroxy-4-chlorobenzaldehyde with 84% yield. The molecular structure of **L** was confirmed by ^1H NMR, ^{13}C NMR, ESI-MS, FT-IR and also by single-crystal X-ray diffraction analysis (Fig. 1 and Table S2, ESI†).

The spectroscopic properties of probe **L** were investigated by monitoring absorption and fluorescence changes in the presence of several metal ions, such as K^+, Na^+, Mg^{2+}, Ca^{2+}, Pb^{2+}, Pd^{2+}, Cd^{2+}, Hg^{2+}, Zn^{2+}, Cu^{2+}, Al^{3+}, Ag^+, Fe^{2+}, Co^{2+}, Ni^{2+} and Mn^{2+} in DMSO : H_2O (8 : 2, v/v, 10 mM HEPES buffer, pH 7.4) solution at room temperature. As illustrated in Fig. 2, free probe **L** displayed a maximal absorption peak at 345 nm, which corresponds to a π–π^* transition from the conjugated moiety of **L**. However, upon gradual addition of Al^{3+} ions to the solution of **L**, the initial absorption band at 345 nm decreased and a simultaneous increase at 402 nm with a red shift of 57 nm was observed, accompanied by a naked eye color change from colorless to light yellow. The clear isosbestic point at 370 nm undoubtedly indicates the formation of an Al^{3+} complex in the binary mixture. Again, chemosensor **L** did not exhibit any noteworthy changes in absorption spectra with the addition of a number of competitive metal ions, signifying the high selectivity of this probe for Al^{3+} ions. To investigate the suitable pH range in which sensor **L** can effectively detect Al^{3+}, a pH titration of **L** was carried out (Fig. S15, ESI†). It is noteworthy to mention that addition of Al^{3+} resulted in a high absorbance in a pH range of 6 to 9. When the pH is greater than 9, the absorbance is decreased due to the formation of colloidal $Al(OH)_3$. These observations indicate that the pH range of 6 to 9 is suitable for monitoring Al^{3+} by chemosensor **L**.

As shown in Fig. 3, in the absence of Al^{3+} ions, probe **L** showed a very weak emission band centred at 483 nm (λ_{ext} = 371 nm) in
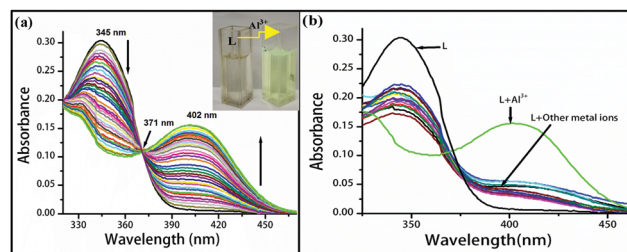

Scheme 1 Chemical structure and synthetic route of **L**.

Fig. 2 (a) The UV-vis absorption spectra of **L** ($c = 2 \times 10^{-4}$ M) in the presence of Al^{3+} ($c = 2 \times 10^{-5}$ M) ions in DMSO–H_2O (8 : 2, v/v, 10 mM HEPES buffer, pH 7.4) solution. Inset: Color change after addition of Al^{3+} to probe **L**. (b) Absorption spectra of **L** in the presence of different metal ions.
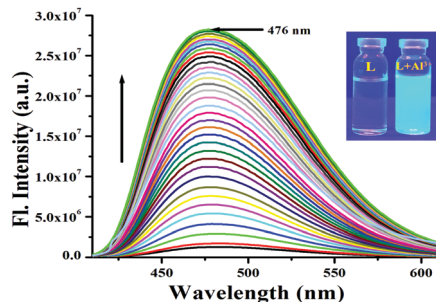
Fig. 3 Changes in the fluorescence spectra of **L** ($c = 2 \times 10^{-4}$ M) in the presence of different amounts of Al^{3+} ($c = 2 \times 10^{-5}$ M) ions in DMSO–H$_2$O (8 : 2, v/v, 10 mM HEPES buffer, pH 7.4) solution. Inset: Fluorescence change after addition of Al^{3+} to probe **L**.

DMSO–H$_2$O (8 : 2, v/v, 10 mM HEPES buffer, pH 7.4). This weak emission of probe **L** is due to the (a) excited state intramolecular proton transfer (ESIPT) from the –OH group to the imine nitrogen; (b) photoinduced electron transfer effect from the lone pair of the imine nitrogen and (c) isomerization of the –HC=N (imine) bond.[26] However, treatment of probe **L** with 3 equivalents of Al^{3+} ions induced a gradual increase in fluorescence (20-fold) along with a blue shift of 7 nm, having the highest emission intensity at 476 nm and a color change from dark to greenish-blue under UV light. This significant fluorescence 'turn-on' in the presence of Al^{3+} ions might be explicated by the formation of a complex between probe **L** and Al^{3+} through the coordination of two "O" and one "N" atom. This inhibits both the ESIPT and PET processes as well as C=N isomerization, resulting in a distinctive chelation enhanced fluorescence (CHEF) effect. In order to explore the practical applicability, the pH effects on the fluorescence response of probe **L** in the absence and presence of Al^{3+} were examined. Fig. S16 (ESI†) shows that **L** is weakly emissive in a wide range of pH (3–13). The low emission intensity of the **L**–Al^{3+} complex at pH < 6 was presumably due to the free **L** that remains uncoordinated to Al^{3+}. At pH > 9, Al^{3+} is converted to $Al(OH)_3$ and $Al(OH)_4^-$, leaving the sensor almost in its free anionic form in the solution. At pH ∼ 7 the sensor is deprotonated and the resulting dianionic ligand forms a chelate with Al^{3+}, leading to fluorescence enhancement *via* the CHEF mechanism (Scheme 2). Therefore, sensor **L** is capable of being used for selective detection of Al^{3+} at physiological pH, and can be a suitable candidate for biological applications.

Additionally, ^{1}H NMR titration was performed by gradual addition of a nitrate salt of Al^{3+} ions to a DMSO-d_6 solution of **L** (Fig. 4).
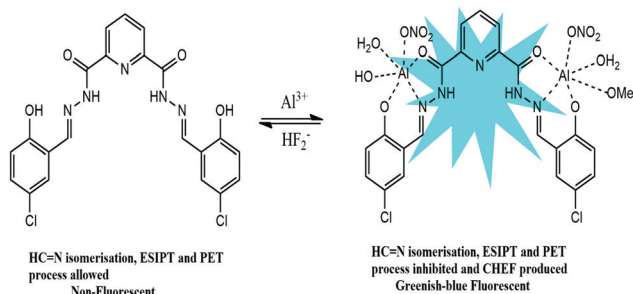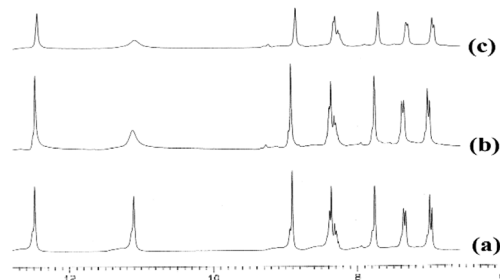

Fig. 4 ^{1}H NMR spectra in DMSO-d_6: (a) **L** only, (b) **L** and 1 equiv. of Al^{3+} and (c) **L** and 2 equiv. of Al^{3+}.

The result shows that the intensity of the proton signal corresponding to the hydroxyl group (–OH) at 11.08 ppm, which is the most probable binding site for Al^{3+} ions, decreases significantly relative to that of other protons upon exposure to Al^{3+} ions.

For chemosensor **L**, the IR spectrum (Fig. S4, ESI†) shows ν(OH), 3472(s); ν(NH), 3248(s); ν(C=O), 1657(s); ν(C=N), 1621 cm^{-1}. On the other hand, the IR spectrum of the **L**–Al^{3+} complex (Fig. S6, ESI†) shows a shifted frequency value and a new signal for NO_3^- at 1349 cm^{-1}. The spectrum shows ν(NH), 3189(s); ν(C=O), 1672(s); ν(C=N), 1617 cm^{-1}, but ν(OH) appears as a broad signal at 3449 cm^{-1}. This result shows that the –OH is the most probable binding site for Al^{3+} ions.

The Job plot revealed that 1 : 2 stoichiometry is the most probable binding mode between **L** and Al^{3+} ions (Fig. S10, ESI†). To attain such a type of stoichiometry, imine nitrogen, carbonyl oxygen and phenolic oxygen atoms are the most likely binding sites for Al^{3+} ions (Scheme 2). The association constant (K_a) of **L** for Al^{3+} was calculated from the Benesi–Hildebrand equation[27] on the basis of fluorometric titration as 4.26×10^4 M^{-2} (Fig. S12, ESI†). The selectivity of chemosensor **L** towards different metal cations was examined under identical working conditions. As shown in Fig. 5, probe **L** demonstrated a strong fluorescence response at 476 nm, while the other cations [K^+, Na^+, Mg^{2+}, Ca^{2+}, Pb^{2+}, Pd^{2+}, Cd^{2+}, Hg^{2+}, Zn^{2+}, Cu^{2+}, Ag^+, Fe^{2+}, Co^{2+}, Ni^{2+} and Mn^{2+}] did not cause any remarkable emission spectral changes. In order to further evaluate the practical capability of probe **L** as an Al^{3+} selective fluorescent chemosensor, we conducted competitive experiments on addition of Al^{3+} ions to a solution of **L** in the presence of excess equivalents of other individual competitive metal ions. The increase in fluorescence intensity induced by
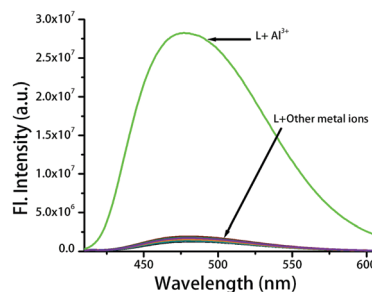

Scheme 2 Proposed sensing mechanism for detection of Al^{3+} by probe **L**.

Fig. 5 Fluorescence response of **L** ($c = 2 \times 10^{-4}$ M) to different metal ions in DMSO–H$_2$O (8 : 2, v/v, 10 mM HEPES buffer, pH 7.4) solution ($\lambda_{ext} = 370$ nm).

mixing Al^{3+} ions with other miscellaneous cations was comparable to that elicited by Al^{3+} alone, indicating stable complexation between **L** and Al^{3+}. The above results indicate high selectivity of probe **L** for Al^{3+} over other commonly coexistent cations in organo-aqueous solution. The fluorescence intensity of **L** at 476 nm exhibited a good linear relationship with the Al^{3+} concentration ranging from 0.99 μM to 20.6 μM, based on which the detection limit[28] for Al^{3+} was calculated to be 0.8 μM (Fig. S11, ESI†).

Reversibility is an essential feature of a probe to be used as a chemosensor to detect particular metal cations. Here, the *in situ* generated **L**–2Al^{3+} complex displayed fluorescence "turn-off" behavior only in the presence of HF$_2^-$ ions. Now, to inspect this, when an excess amount of NaHF$_2$ solution was added to the solution containing the **L**–2Al^{3+} complex system, the emission band at 476 nm gradually decreased, accompanied by emission color changes from deep blue to dark (Fig. 6a). However, various common anions such as Cl$^-$, Br$^-$, AcO$^-$, CO$_3^{2-}$, N$_3^-$, HCO$_3^-$, NO$_2^-$, SO$_4^{2-}$, and H$_2$PO$_4^-$ did not produce any noticeable results under similar conditions except F$^-$. F$^-$ ions decrease the fluorescence intensity but only by a small extent compared to HF$_2^-$ ions (Fig. 6b). The added fluoride source (TBAF) could be hydrolyzed, and a small amount of HF$_2^-$ may be generated *in situ* to assist the quenching of emission of the **L**–2Al^{3+} complex; thus, a quenching response might be observed.[29] Such fluorometric changes were mainly due to the removal of Al^{3+} from the **L**–2Al^{3+} system followed by the regeneration of probe **L** as shown in Scheme 2. These properties indicate that the **L**–2Al^{3+} ensemble can be employed as an "on–off" fluorescent sensor for bifluoride ions. In addition, the reversible and reusable behavior of probe **L** was also verified by performing four alternate cycles of fluorescence titration of **L** with Al^{3+} followed by addition of HF$_2^-$ as shown in Fig. S7 (ESI†). Moreover, from the fluorescence titration experiment, we found a good linear relationship of fluorescence intensity *versus* the HF$_2^-$ concentration over a range of 0.99 to 6.5 μM (Fig. S8, ESI†).

However, incremental addition of HF$_2^-$ ions into a solution of the *in situ* generated **L**–2Al^{3+} complex led to a gradual decrease in the absorption band at 394 nm and a concomitant increase in the intensity of a new absorption band centered at 344 nm (Fig. S9, ESI†).

In order to know the optimized geometry of **L** and **L**–2Al^{3+} and the binding interactions between probe **L** and Al^{3+}, we
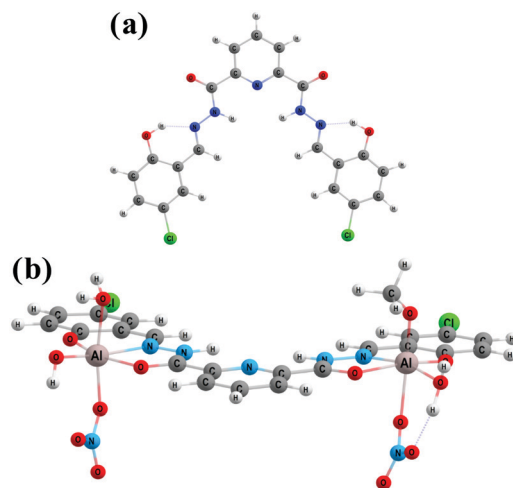

Fig. 7 The calculated energy minimized structures of **L** and the **L**–2Al^{3+} complex.

carried out density functional theory (DFT) calculations with the B3LYP/6-311+G(d,p) basis set using the Gaussian 16 program.[30,31] The energy optimized structures of **L** and its Al-complex are presented in Fig. 7. The highest occupied molecular orbital (HOMO) and lowest unoccupied molecular orbital (LUMO) energies and spatial distribution of **L** and **L**–2Al^{3+} were also calculated (ESI†). As shown in Fig. 8, the HOMO–LUMO energy gap of probe **L** was considerably reduced from 3.83 eV (88.4 kcal mol^{-1}) to 3.16 eV (72.9 kcal mol^{-1}) in the **L**–2Al^{3+} complex, establishing that **L** formed a stable complex with Al^{3+} ions and supporting the red-shift of the absorption band (λ_{max}) in the UV-vis absorption spectra.[32] Moreover, TDDFT calculations were performed on the optimized geometries to explain the electronic properties of probe **L** and its Al-complex. Table S4 (ESI†) shows the details of the vertical excitation energies, oscillator frequencies and wavelengths and from these data it was found that the computed vertical transitions were analogous to the experimentally observed UV-vis bands.

The probe was applied in Hep G2 cells (human liver cancer cell line) for fluorescence imaging of intracellular Al^{3+} ions to investigate its application in biological systems. First, Hep G2
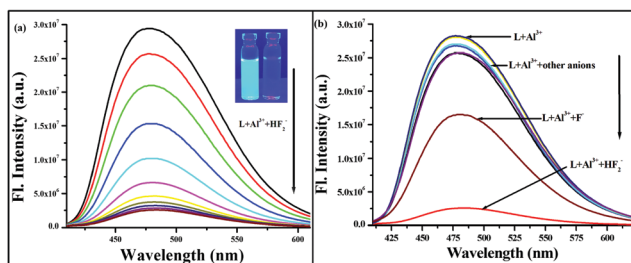

Fig. 6 (a) Fluorescence titrations of the **L**–2Al^{3+} complex with a sodium salt of bifluoride in DMSO−H$_2$O (8 : 2, v/v, 10 mM HEPES buffer, pH 7.4) solution (λ_{ext} = 370 nm). Inset: Fluorescence photographs of **L** + Al^{3+} and **L** + Al^{3+} + HF$_2^-$. (b) Changes in the fluorescence spectra of the **L**–2Al^{3+} complex in the presence of different anions.
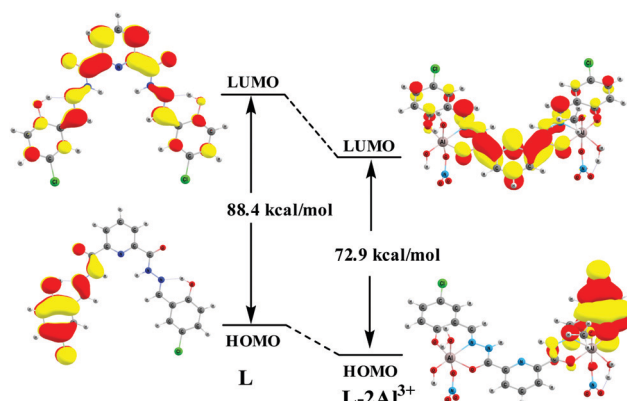

Fig. 8 HOMO and LUMO distributions of **L** and the **L**–2Al^{3+} complex.
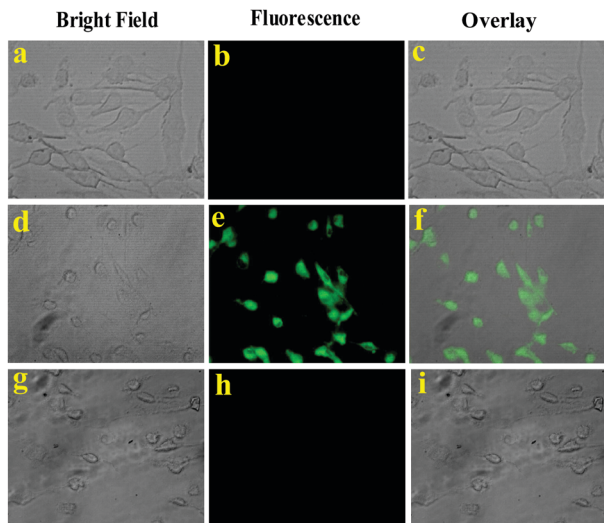
Fig. 9 Bright field, fluorescence and overlay images of Hep G2 cells. (a–c) The cells were incubated with 10 μM probe **L** for 30 min, (d–f) followed by addition and incubation with 10 μM Al³⁺ for another 30 min and (g–i) then with NaHF₂ for 30 min.

cells were treated with probe **L** (10 μM) for 30 min at 37 °C and then washed with PBS buffer to remove excess probe. After that, the treated cells were incubated with Al³⁺ ions (10 μM) for another 30 min at 37 °C. Then, these incubated cells were washed again with PBS buffer and images were recorded using a fluorescence microscope. Hep G2 cells treated with only probe **L** displayed no fluorescence signal, whereas an intense green fluorescence signal was detected in the intracellular area when stained with **L** followed by Al(NO₃)₃. Again, this bright fluorescence signal disappeared when the cells were treated with NaHF₂ (10 μM) solution (Fig. 9). Furthermore, there were no gross morphological changes in the bright-field images of the cells, suggesting that the cells remained viable throughout the imaging studies. The above results established the good cell-membrane permeability of **L** and that it could be employed in living cells for *in vitro* imaging of Al³⁺ and HF₂⁻ ions. Additionally, an MTT assay determined that probe **L** displayed very low cytotoxicity toward living cells (Fig. S14, ESI†).

Conclusions

In conclusion, we have successfully designed and synthesized a colorimetric and fluorometric probe, **L**, based on pyridine-dicarbohydrazide. Probe **L** shows both color and switch-on emission responses to Al³⁺ ions in organo aqueous solution as a result of the metal enhanced chelation effect (CHEF) inhibiting the PET, ESIPT and C=N isomerization processes. With a detection limit of 0.8 μM, this chemosensor displays high selectivity for Al³⁺ ions over 18 other commonly coexistent metal ions. The stoichiometry of **L**–Al³⁺ is determined to be 1 : 2 (**L** : Al³⁺) and is confirmed by Job plot analysis. The association constant for **L** with Al³⁺ is found to be 4.26×10^4 M⁻² on the basis of fluorescence studies, proposing a strong binding affinity for Al³⁺. Besides, the *in situ* prepared **L**–2Al³⁺ complex can be utilized for

the detection of HF₂⁻ ions *via* the displacement approach and it exhibits a "turn-off" type of fluorescence response. Moreover, the detection of Al³⁺ and HF₂⁻ ions was also carried out in Hep G2 cells to demonstrate the "off–on–off" fluorescence cellular image. It proves that the molecule penetrates into cells and thus it is applicable to biological systems. We anticipate that such cell imaging studies will be useful for Al³⁺ and HF₂⁻ ion related biological studies.

Experimental section

Materials and apparatus

All the chemical reagents and solvents (analytical and spectroscopic grades) were procured from commercial suppliers and used without additional purification. Millipore water was used throughout the experiment. Nitrate salts of Al³⁺ and Ag⁺, chloride salts of metal ions (Na⁺, K⁺, Cr³⁺, Cd²⁺, Fe²⁺, Zn²⁺, Hg²⁺, and Pb²⁺) and perchlorate salts of metal ions (Ni²⁺, Mn²⁺, Cu²⁺, Fe²⁺, and Co²⁺), terabutyl ammonium salts of F⁻, Br⁻, AcO⁻, and HSO₄⁻ and sodium salts of HF₂⁻, PPi, Pi, and NO₃⁻ were used for the experiments. Elemental analyses (C, H and N) were performed using a PerkinElmer 2400 Series-II CHNS, USA, elemental analyzer. ESI mass spectra were obtained using a Waters HRMS model XEVO-G2QTOF#YCA351 spectrometer. ¹H NMR and ¹³C NMR spectra were obtained using a Bruker spectrometer (400 MHz) and ¹H NMR titration spectra were obtained using a Bruker spectrometer (300 MHz) with DMSO-d_6 solvent using trimethylsilane (TMS) as an internal standard. Fourier transform infrared (FT-IR) spectra were recorded on a PerkinElmer LX-1 FT-IR spectrophotometer (4000–400 cm⁻¹) by using a modern diamond attenuated total reflectance (ATR) accessory. UV-vis absorption spectra were obtained using a UV-1700 PharmaSpec UV-vis spectrophotometer (SHIMADZU). Fluorescence emission spectra were measured using a Horiba Jobin Yvon Fluoromax-4P spectrofluorometer. Single crystal structures (Fig. 1) were obtained using a single-crystal X-ray diffractometer (Bruker Smart Apex II). The cells were imaged by using a Zetasizer fluorescence microscope (Leica).

Calculations for the detection limit

The detection limit of **L** for Al³⁺ was calculated using the following equation:[28]

$$\text{Detection limit} = 3Sb1/S \qquad (1)$$

where Sb1 is the standard deviation of the blank solution and S is the slope of the calibration curve.

Theoretical calculations

All the geometries for **L** and **L**–2Al³⁺ were optimized by density functional theory (DFT) calculations using the Gaussian 16 software package (basis set: B3LYP/6-31+G(d,p)). TDDFT calculations were also performed at the same level of theory.

Cell imaging studies

Cell line culture. Human liver cancer cell line Hep G2 cells and human lung fibroblast cells WI-38 were collected from the

National Center for Cell Science (NCCS) Pune, India. The cells were grown in DMEM (Dulbecco's Modified Eagle Medium) with 10% FBS (Fetal Bovine Serum) and penicillin/streptomycin (100 units per ml) at 37 °C and 5% CO_2. All the treatments were performed at 37 °C and at a cell density allowing exponential growth.

Cell survivability assay. The cell survivability of the ligand was studied for human lung fibroblast cells WI38 following a reported procedure.[33] In brief, the viability of WI-38 cells after exposure to various concentrations of probe **L** was assessed by MTT assay. The cells were seeded in 96-well plates at 1×10^4 cells per well and exposed to probe **L** at concentrations of 0 μM, 20 μM, 40 μM, 60 μM, 80 μM, and 100 μM for 24 h. After incubation the cells were washed with $1 \times$ PBS twice and incubated with MTT solution (450 μg ml^{-1}) for 3–4 h at 37 °C. The resulting formazan crystals were dissolved in an MTT solubilization buffer and the absorbance was measured at 570 nm by using a spectrophotometer (BioTek) and the value was compared with control cells.

Cellular imaging. According to a reported procedure, the Hep G2 cells were grown on a coverslip for more than 24 h. Then, the Hep G2 cells were treated with 10 μM of probe **L** for 30 min followed by addition and incubation with 10 μM Al(NO$_3$)$_3$ solution and then with NaHF$_2$ solution. The cells were washed with $1\times$ PBS. Lastly, they were then mounted on a glass slide and fluorescence images were taken using a Leica fluorescence microscope.

Synthesis of bis(2-hydroxy-4-chlorobenzaldehyde)-2,6-pyridinedicarbohydrazone (L)

2,6-Pyridinedicarbohydrazide was synthesized following a reported method (Scheme 1).[25] A mixture of 2,6-pyridinedicarbohydrazide (0.19 g, 1.0 mmol) and 2-hydroxy-4-chlorobenzaldehyde (0.36 g, 2.3 mmol) was refluxed in methanol for 5 h. The light yellow solid formed was filtered off and dried in a vacuum (yield 0.39 g (84%), m.p. > 200 °C. Anal. calc. for $C_{21}H_{15}Cl_2N_5O_4$, C 53.41, H 3.20, N 14.83. Found: C 54.12, H 4.01, N 15.23%. ^1H NMR (400 MHz, DMSO-d_6): δ = 12.47 (s, 2H), 11.09 (s, 2H), 8.88 (s, 2H), 8.35 (d, J = 7.2 Hz, 2H), 8.28 (m, 1H), 7.92 (s, 3H), 7.75 (d, J = 2.4 Hz, 2H), 7.34 (m, 6.8 Hz, 2H), 6.97 (d, J = 8.8 Hz, 2H). ^{13}C NMR (100 MHz, DMSO-d_6): δ = 207.02 (for C=O of DMF), 162.79, 160.01, 156.46, 148.43, 147.17, 140.52, 131.64, 127.39, 126.22, 123.67, 121.48, 118.76, 31.17. IR (KBr, cm^{-1}): 3472, 3248, 1657, 1621, 1538, 1481, 1353, 1264, 1187, 1089, 1000, 950, 824, 716, 608, 560. ESI-MS: m/z 472.11, calcd for $[C_{21}H_{15}Cl_2N_5O_4 + H]^+$ 472.06. Crystals suitable for X-ray structural determination were obtained by slow evaporation of DMF solution.

Conflicts of interest

There are no conflicts to declare.

Acknowledgements

References

1 (a) S. Sen, T. Mukherjee, B. Chattopadhyay, A. Moirangthem, A. Basu, J. Marek and P. Chattopadhyay, *Analyst*, 2012, **137**, 3975–3981; (b) R. J. Lakowicz, *Principles of Fluorescence Spectroscopy*, Springer, New York, 3rd edn, 2006, p. xxvi; (c) A. P. de Silva, H. Q. N. Gunaratne, T. Gunnlaugsson, A. J. M. Huxley, C. P. McCoy, J. T. Rademacher and T. E. Rice, *Chem. Rev.*, 1997, **97**, 1515–1566; (d) B. Valeur and I. Leray, *Coord. Chem. Rev.*, 2000, **205**, 3–40.

2 R. A. Yokel, *Food Chem. Toxicol.*, 2008, **46**, 2261–2266.

3 S. H. Kim, H. S. Choi, J. Kim, S. J. Lee, D. T. Quang and J. S. Kim, *Org. Lett.*, 2010, **12**, 560–563.

4 D. Krewski, R. A. Yokel, E. Nieboer, D. Borchelt, J. Cohen, J. Harry, S. Kacew, J. Lindsay, A. M. Mahfouz and V. Rondeau, *J. Toxicol. Environ. Health, Part B*, 2007, **10**, 1–269.

5 M. J. Cullen, M. J. Allwood and D. M. Ambach, *Environ. Sci. Technol.*, 2012, **46**, 13048–13055.

6 (a) A. K. Mahapatra, S. S. Ali, K. Maiti, A. K. Manna, R. Maji, S. Mondal, M. R. Uddin, S. Mandal and P. A. Sahoo, *RSC Adv.*, 2015, **5**, 81203–81211; (b) T. Khan, S. Vaidya, D. S. Mhatre and A. Datta, *J. Phys. Chem. B*, 2016, **120**, 10319–10326.

7 (a) M. R. Wills and J. Savory, *Lancet*, 1983, **2**, 29–34; (b) C. A. Shaw and L. Tomljenovic, *Immunol. Res.*, 2013, **56**, 304–316; (c) G. Berthon, *Coord. Chem. Rev.*, 2002, **228**, 319–341.

8 (a) A. C. Alfrey, *Adv. Clin. Chem.*, 1983, **23**, 69–91; (b) A. M. Pierides, W. G. Edwards Jr, U. X. Cullum Jr, J. T. McCall and H. A. Ellis, *Kidney Int.*, 1980, **18**, 115–124; (c) T. P. Flaten, *Brain Res. Bull.*, 2001, **55**, 187–196; (d) M. Yasui, T. Kihira and K. Ota, *Neurotoxicology*, 1992, **13**, 593–600; (e) P. Nayak, *Environ. Res.*, 2002, **89**, 101–115.

9 (a) B. Wang, W. Xing, Y. Zhao and X. Deng, *Environ. Toxicol. Pharmacol.*, 2010, **29**, 308–313; (b) P. D. Darbre, *J. Inorg. Biochem.*, 2005, **99**, 1912–1919.

10 (a) C. S. Cronan, W. J. Walker and P. R. Bloom, *Nature*, 1986, **324**, 140–143; (b) J. Barcelo and C. Poschenrieder, *Environ. Exp. Bot.*, 2002, **48**, 75–92.

11 V. Kumar, A. Kumar, U. Diwan, R. Shweta and S. K. Srivastava, *Sens. Actuators, B*, 2015, **207**, 650–657.

12 M. Frankowski, A. Zioła-Frankowska and J. Siepak, *Talanta*, 2010, **80**, 2120–2126.

13 G. Tangen, T. Wickstrom, S. Lierhagen, R. Vogt and W. Lund, *Environ. Sci. Technol.*, 2002, **36**, 5421–5425.

14 M. Rezaee, Y. Yamini, A. Khanchi, M. Faraji and A. Saleh, *J. Hazard. Mater.*, 2010, **178**, 766–770.

15 A. Sanz-Medel, A. B. Soldado Caabezuelo, R. Milačič and T. Bantan Polak, *Coord. Chem. Rev.*, 2002, **228**, 373–383.

16 Y. C. Chen, I. L. Lee, Y. M. Sung and S. P. Wu, *Talanta*, 2013, **117**, 70–74.

17 (*a*) V. K. Gupta, A. K. Jain and P. Kumar, *Sens. Actuators, B*, 2006, **120**, 259–265; (*b*) V. K. Gupta, B. Sethi, N. Upadhyay, S. Kumar, R. Singh and L. P. Singh, *Int. J. Electrochem. Sci.*, 2011, **6**, 650–663; (*c*) V. K. Gupta, R. Jain and K. M. Pal, *Int. J. Electrochem. Sci.*, 2010, **5**, 1164–1178.

18 H. Wang, Z. Yu, Z. Wang, H. Hao, Y. Chen and P. Wan, *Electroanalysis*, 2011, **23**, 1095–1099.

19 (*a*) S. Samanta, B. Nath and J. B. Baruah, *Inorg. Chem. Commun.*, 2012, **22**, 98–100; (*b*) J. F. G. Reyes, P. O. Barrales and A. M. Diaz, *Talanta*, 2005, **65**, 1203–1208.

20 (*a*) J. C. Qin, L. Fan, T. R. Li and Z. Y. Yang, *Synth. Met.*, 2015, **199**, 179–186; (*b*) S. Sinha, B. Chowdhury and P. Ghosh, *Inorg. Chem.*, 2016, **55**, 9212–9220.

21 (*a*) A. Sahana, A. Banerjee, S. Lohar, B. Sarkar, S. K. Mukhopadhyay and D. Das, *Inorg. Chem.*, 2013, **52**, 3627–3633; (*b*) S. Kim, J. Y. Noh, K. Y. Kim, J. H. Kim, H. K. Kang, S.-W. Nam, S. H. Kim, S. Park, C. Kim and J. Kim, *Inorg. Chem.*, 2012, **51**, 3597–3602; (*c*) V. Saini, R. Krishnan and B. Khungar, *Photochem. Photobiol. Sci.*, 2020, **19**, 931–942; (*d*) P. Ghorai, K. Pal, P. Karmakar and A. Saha, *Dalton Trans.*, 2020, **49**, 4758–4773.

22 M. Wang, C. Cheng, C. Li, D. Wu, J. Song, J. Wang, X. Zhou, H. Xiang and J. Liu, *J. Mater. Chem. C*, 2019, **7**, 6767–6778.

23 (*a*) K. Ashley, A. Agrawal, J. Cronin, J. Tonazzi, T. M. McCleskey, A. K. Burrell and D. S. Ehler, *Anal. Chim. Acta*, 2007, **584**, 281–286; (*b*) T. L. Peters, T. J. Nestrlck, L. L. Lamparski and R. H. Sthel, *Anal. Chem.*, 1982, **51**, 2397–2398; (*c*) C. R. Wade, A. E. J. Broomsgrove, S. Aldridge and F. O. P. Gabbaï, *Chem. Rev.*, 2010, **110**, 3958–3984.

24 (*a*) K. Murugesan, V. Jeyasingh, S. Lakshminarayanan, S. Narayanan, S. Ramasamy, I. V. M. V. Enoch and L. Piramuthu, *Spectrochim. Acta, Part A*, 2019, **209**, 165–169; (*b*) A. Ghorai, S. S. Thakur and G. K. Patra, *RSC Adv.*, 2016, **6**, 108717–108725; (*c*) K. Dutta, R. C. Deka and D. K. Das, *J. Fluoresc.*, 2013, **23**, 823–828.

25 N. Yadav and A. K. Singh, *New J. Chem.*, 2018, **42**, 6023–6033.

26 (*a*) N. Xiao, L. Xie, X. Zhi and C. Fang, *Inorg. Chem. Commun.*, 2018, **89**, 13–17; (*b*) J. Wang and Y. Pang, *RSC Adv.*, 2014, **4**, 5845–5848; (*c*) S. K. Asthana, A. Kumar, Neeraj, Shweta, S. K. Hira, P. P. Manna and K. K. Upadhyay, *Inorg. Chem.*, 2017, **56**, 3315–3323.

27 (*a*) C. Yang, L. Liu, T. W. Mu and Q.-X. Guo, *Anal. Sci.*, 2000, **16**, 537–539; (*b*) H. A. Benesi and J. H. Hildebrand, *J. Am. Chem. Soc.*, 1949, **71**, 2703–2707; (*c*) Y. Shiraishi, S. Sumiya, Y. Kohono and T. Hirai, *J. Org. Chem.*, 2008, **73**, 8571–8574.

28 (*a*) L. L. Long, D. D. Zhang, X. F. Li, J. F. Zhang, C. Zhang and L. P. Zhou, *Anal. Chim. Acta*, 2013, **775**, 100–105; (*b*) T. Mandal, A. Hossain, A. Dhara, A. A. Masum, S. Konar, S. K. Manna, S. K. Seth, S. Pathak and S. Mukhopadhyay, *Photochem. Photobiol. Sci.*, 2018, **17**, 1068–1074.

29 R. Purkait and C. Sinha, *New J. Chem.*, 2019, **43**, 9815–9823.

30 (*a*) B. Miehlich, A. Savin, H. Stoll and H. Preuss, *Chem. Phys. Lett.*, 1989, **157**, 200–206; (*b*) A. D. Becke, *J. Chem. Phys.*, 1993, **98**, 5648–5662; (*c*) C. Lee, W. Yang and R. G. Parr, *Phys. Rev. B: Condens. Matter Mater. Phys.*, 1988, **B37**, 785–799.

31 M. J. Frisch, G. W. Trucks, H. B. Schlegel, G. E. Scuseria, M. A. Robb, J. R. Cheeseman, G. Scalmani, V. Barone, G. A. Petersson, H. Nakatsuji, X. Li, M. Caricato, A. V. Marenich, J. Bloino, B. G. Janesko, R. Gomperts, B. Mennucci, H. P. Hratchian, J. V. Ortiz, A. F. Izmaylov, J. L. Sonnenberg, Y. D. Williams, F. Ding, F. Lipparini, F. Egidi, J. Goings, B. Peng, A. Petrone, T. Henderson, D. Ranasinghe, V. G. Zakrzewski, J. Gao, N. Rega, G. Zheng, W. Liang, M. Hada, M. Ehara, K. Toyota, R. Fukuda, J. Hasegawa, M. Ishida, T. Nakajima, Y. Honda, O. Kitao, H. Nakai, T. Vreven, K. Throssell, J. A. Montgomery Jr, J. E. Peralta, F. Ogliaro, M. J. Bearpark, J. J. Heyd, E. N. Brothers, K. N. Kudin, V. N. Staroverov, T. A. Keith, R. Kobayashi, J. Normand, K. Raghavachari, A. P. Rendell, J. C. Burant, S. S. Iyengar, J. Tomasi, M. Cossi, J. M. Millam, M. Klene, C. Adamo, R. Cammi, J. W. Ochterski, R. L. Martin, K. Morokuma, O. Farkas, J. B. Foresman and D. J. Fox, *Gaussian 16, Revision C.01*, Gaussian, Inc., Wallingford CT, 2016.

32 (*a*) R. Purkait, A. Dey, S. Dey, P. P. Ray and C. Sinha, *New J. Chem.*, 2019, **43**, 14979–14990; (*b*) P. B. Thale, P. N. Borase and G. S. Shankarling, *Inorg. Chem. Front.*, 2016, **3**, 977–984.

33 (*a*) A. Samui, K. Pal, P. Karmakar and S. K. Sahu, *Mater. Sci. Eng., C*, 2019, **98**, 772–781; (*b*) K. Pal, S. Roy, P. K. Parida, A. Dutta, S. Bardhan, S. Das, K. Jana and P. Karmakar, *Mater. Sci. Eng., C*, 2019, **95**, 204–216.

Check for updates

Revealing the supramolecular features of two Zn(II) complexes derived from a new hydrazone ligand: a combined crystallographic, theoretical and antibacterial study†

Samit Pramanik,[a] Anowar Hossain,[a] Sudipta Pathak, [iD] *[b]
Sougata Ghosh Chowdhury,[c] Parimal Karmakar, [iD] [c]
Antonio Frontera [iD] *[d] and Subrata Mukhopadhyay[a]

A new hydrazone ligand, HL [(1-methylimidazol-2-yl)methylene]isonicotinohydrazide, has been synthesized and characterized by several spectroscopic methods. The ligand (HL) was then utilized for the preparation of two new complexes, namely, [Zn(L)$_2$]·2H$_2$O (complex **1**) and [Zn(H$_2$L)Cl$_3$]·H$_2$O (complex **2**). The crystal structures of these complexes have been established by single-crystal X-ray analysis. The non-covalent interactions and supramolecular assemblies observed in the crystal packing of both complexes have been described focusing on π···π (for **1**) and O···π–hole (for **2**) interactions along with various hydrogen bonding interactions. A DFT study has been carried out to analyse their non-covalent interactions with rationalization using molecular electrostatic potential (MEP) surfaces and the combined QTAIM/NCI plot computational tools. In addition, the *in vitro* biological activities of the synthesized ligand (HL) and the water-soluble complex **2** were evaluated against *Escherichia coli* and *Staphylococcus aureus*.

Introduction

The field of non-covalent interactions (NCIs) is extensive and covers the whole of science. The NCIs involving hydrogen bonding, halogen bonding, π···π stacking, lone pair···π, cation···π, anion···π, C–H···π, N–H···π, and O–H···π interactions have attracted recent interest to elucidate the outstanding importance of these weak forces in controlling the structure and function of macromolecules.[1–7] A deep understanding of these weak interactions is essential to go forward in many fields, especially in crystal growth and crystal engineering.[8] Recently, much attention has also been given to π–hole interactions owing to their cooperative participation in chemical reactions and crystal engineering, as well as in biological applications. Theoreticians have established that the electron density distribution around covalently bonded atoms is not isotropic, *i.e.*, the atoms develop some regions of higher and lower electron density.[9] A π–hole can be defined as positive electrostatic potential on unoccupied π* orbitals, which have the capability to interact with some electron-dense region (anion, Lewis base, π-system, *etc.*).[10,11] It is typically located above and below to the molecular framework of π-systems, such as carbonyls or conjugated π–acidic systems, such as hexafluorobenzene.[12] One of the promising but comparatively less studied systems is the imidic C=N group, acting as a Lewis acid (π–hole donor).[13–15]

Schiff base ligands with nitrogen or oxygen donor atoms are a good class of organic compounds that play an important role by serving as chelating ligands in the main groups and transition metal coordination chemistry.[16,17] The diverse role of the transition metal complexes of Schiff base ligands in inorganic and metal–organic compounds and biochemistry has received considerable attention owing to their stability in different oxidative and reductive conditions.[18,19] Hydrazone ligands are a special type of Schiff base which can accommodate with different coordination modes according to the demand of variable geometries and valences of metal ions in coordination complexes.[20] Due to the presence of the N–H functionality adjacent to the azomethine (C=N) chromophore, they can form interesting hydrogen bonded self-assembly in metal complexes.[21]

[a] *Department of Chemistry, Jadavpur University, Kolkata 700032, India*
[b] *Department of Chemistry, Haldia Government College, Debhog, Purba Medinipur, 721657, West Bengal, India. E-mail: sudiptachemster@gmail.com*
[c] *Department of Life Science and Biotechnology, Jadavpur University, Kolkata 700032, India*
[d] *Departament de Química, Universitat de les Illes Balears, Crta. de Valldemossa km 7.5, 07122 Palma de Mallorca, Baleares, Spain. E-mail: toni.frontera@uib.es*
† Electronic supplementary information (ESI) available: Experimental details. CCDC 2209945 and 2209946. For ESI and crystallographic data in CIF or other electronic format see DOI: https://doi.org/10.1039/d2ce01445a

However, in the metal-coordinated hydrazone ligand, the electron withdrawing N–H group induces acidity to the imidic C=N bond which can interact with electron rich atoms and develop distinct supramolecular interaction.[22] The interaction of these donor ligands and metal ions gives complexes of different geometries, and a literature survey reveals that these complexes have biologically active properties such as anticancer, antifungal, antibacterial, anti-malarial, anti-inflammatory, antiviral, and antipyretic properties.[23–25] It should be noted that metal chelation can tremendously influence the antimicrobial/bioactive behavior of the organic ligands.[26] Thus, various transition metal complexes have been synthesized in this field.

After iron, zinc (Zn) is the second most abundant trace element in the human body and is one of the most important micro-elements for human physiology.[27] Zn^{2+} (d^{10} configuration) has zero ligand field stabilization energy that can support a variable coordination geometry around the metal centre (zinc) and assist the fast exchange of ligands.[28,29] Besides, due to the lack of redox activity of divalent zinc ions, this eliminates any chances of free radical reactions and makes it crucial for the body's antioxidant protection system.[27] However, a random mix of transition metal components such as Co–M (M = Zn, Cu, Fe) was reported in several studies to enhance the catalyst efficiency.[30] The importance of zinc in biological systems is related to its unique chemical properties. It plays an important role in the catalytic activity of various enzymes, protein synthesis, DNA synthesis, and immune functions and determines the conformations of many proteins through binding in the active sites. This makes zinc an essential element for all cellular functions and the development of all forms of life. Compared to other metal-based drugs, Zn(ɪɪ) complexes generally exert lower toxicity and have fewer side effects.[31] In the last few years different classes of zinc coordination complexes have shown good potential in diverse applications, in nonlinear optics, in photo-catalysis and in several diseases, and as anti-inflammatory, anti-diabetic, antimicrobial, antioxidant, and antitumor agents.[32–40]

As a part of our efforts to explore the non-covalent interactions in coordination compounds, herein, we have designed and prepared two Zn(ɪɪ) complexes (**1** and **2**) using a newly synthesized [[(1-methylimidazol-2-yl)methylene] isonicotinohydrazide [**HL**] ligand in aqueous medium. Single crystal X-ray analysis shows that complex **1** is a distorted octahedron whereas complex **2** is a distorted tetrahedron in nature. Complex **1** shows π⋯π, O–H⋯π and hydrogen bonding interactions that are responsible for forming various supramolecular architectures. Interestingly, the non-coordinated water molecules are interconnected through hydrogen bonds to form a tetrameric water cluster which has a significant role in stabilizing the molecular structure of complex **1**. The solid-state structure of complex **2** is stabilized through π⋯π⁺ stacking, lone pair⋯π/π⁺ and various types of hydrogen bonding interactions which are responsible for

forming various supramolecular architectures. More importantly, the imidic C=N bond of the Zn(ɪɪ)-coordinated hydrazone ligand is able to interact favorably with the electron-rich oxygen atom of a non-coordinated water molecule (O⋯π–hole interaction) in complex **2**, which is a rare example. Another interesting phenomenon is that the π-system of the –NNHCO– group takes part in the stacking interaction to give additional stability in complex **2**. These NCIs have been confirmed using combined QTAIM/NCI plot analysis and supported by MEP surface analysis. Moreover, the cooperative and energetic features of both conventional and unconventional interactions have also been evaluated by means of DFT calculations. In addition, the antibacterial activities of **HL** and its complex (**2**) were tested against Gram-negative (*Escherichia coli*) and Gram-positive (*Staphylococcus aureus*) bacteria.

Experimental

Materials and apparatus

All the chemicals (analytical grade) and solvents (spectroscopic grade) were purchased from commercial suppliers and used without any further purification. Freshly prepared double distilled water was used throughout the synthetic procedure, and all the reactions were carried out under aerobic conditions. Elemental analyses (C, H and N) were performed using a PerkinElmer 2400 Series-II CHN analyzer, a USA elemental analyzer. ESI mass spectra were obtained using a Water HRMS model XEVO-G2QTOF#YCA351 spectrometer. The ^{1}H NMR spectrum was obtained using a Bruker spectrometer (400 MHz) with DMSO-d_6 solvent using trimethylsilane (TMS) as an internal standard. Fourier transform infrared (FT-IR) spectra were recorded on a Perkin Elmer LX-1 FT-IR spectrophotometer (4000–400 cm^{-1}) by using a modern diamond attenuated total reflectance (ATR) accessory method. The single crystal structures were characterized using a single-crystal X-ray diffractometer (Bruker Smart Apex II).

Synthesis of [[(1-methylimidazol-2-yl)methylene]isonicotino-hydrazide [HL]

Isonicotinic hydrazide (0.137 g, 1 mmol) was added into 30 mL ethanolic solution of 1-methyl imidazole-2-carboxaldehyde (0.11 g, 1 mmol). The reaction mixture was then refluxed for 3 hours
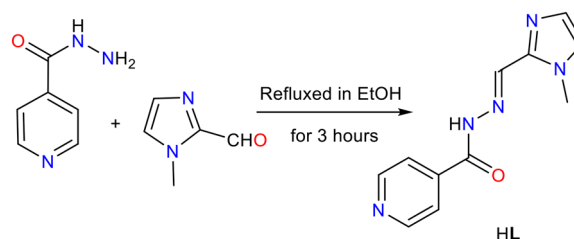
Scheme 1　Synthetic route for the ligand, HL.

(Scheme 1). After completion of the reaction, the solution was cooled at room temperature. A light yellow solid formed, which was collected by filtration, washed repeatedly with cold water and dried in air. The desired product was obtained with good yield and acceptable purity. Yield 0.174 g (76%). The ligand (**HL**) is soluble in water ($S_{25°C} \approx 3.3$ mg mL^{-1}), methanol ($S_{25°C} \approx 4.2$ mg mL^{-1}), acetonitrile ($S_{25°C} \approx 3.8$ mg mL^{-1}) as well as in DMSO ($S_{25°C} \approx 5.1$ mg mL^{-1}). Anal. calc. for $C_{11}H_{12}N_5O$, C 57.63, H 4.84, N 30.55. Found: C 57.61, H 4.83, N 30.52%. ^{1}H NMR (400 MHz, CDCl$_3$): δ (ppm) = 12.11 (s, 1H), 8.78 (d, J = 6 Hz 2H), 8.42 (s, 1H), 7.81 (d, J = 6 Hz, 2H), 7.35 (d, J = 6 Hz, 2H), 7.08 (d, J = 7 Hz, 2H), 3.97 (s, 3H) (Fig. S1, ESI†). Main FT-IR absorptions, (KBr, cm^{-1}): 3210(bs), 3118(s), 3101(vs), 3054(s), 1683(s), 1456(vs), 1625(s), 1613(vs), 1602(s), 1556(s), 1525(s), 1499(s), 1471(s), 1437(s), 1412(s) (Fig. S2, ESI†). ESI-MS: m/z 252.150, 230.181; calcd. for $[C_{11}H_{12}N_5O + Na^+]$ = 252.089, $[C_{11}H_{12}N_5O + H^+]$ = 230.10 (Fig. S3, ESI†).

Synthesis of [Zn(L)$_2$]·2H$_2$O (complex 1)

An aqueous suspension (20 mL) of the ligand, **HL** (0.229 g, 1 mmol), was added to 20 mL of aqueous Zn(NO$_3$)$_2$·6H$_2$O (0.297 g, 1 mmol) solution with constant stirring (Scheme 2). A clear bright yellow solution was appeared after 3 hours of constant stirring. Then the solution was filtered, and the filtrate was left for slow evaporation without any disturbance. After one week, yellow coloured X-ray quality crystals of **1** were isolated (yield: 65%). Complex **1** is sparingly soluble in water ($S_{25°C} \approx 0.5$ mg mL^{-1}), slightly soluble in methanol ($S_{25°C} \approx 1.3$ mg mL^{-1}) and acetonitrile ($S_{25°C} \approx 0.9$ mg mL^{-1}), and completely soluble in DMSO ($S_{25°C} \approx 5.3$ mg mL^{-1}). Anal. calc. for $C_{11}H_{14}N_5O_3Zn$: C, 40.08; H, 4.28; N, 21.25. Found: C, 40.05; H, 4.26; N, 21.21%. Main FT-IR absorptions, (KBr, cm^{-1}): 3564(w), 3359(w), 3118(vs), 3098(vs), 3045(s), 2955(s), 1946(s), 1791(s), 1704(s), 1634(vs), 1604(s), 1595(s), 1565(vs), 1500(s), 1489(s), 1469(s), 1456(s), 1415(vs) (Fig. S4, ESI†).

Synthesis of [Zn(H$_2$L)Cl$_3$]·H$_2$O (complex 2)

Complex **2** was synthesised by reacting an aqueous suspension (20 mL) of the ligand, **HL** (0.229 g, 1 mmol) with

20 mL aqueous ZnCl$_2$ (0.136 g, 1 mmol) solution under stirring. The solution became turbid after one hour of constant stirring (Scheme 2). Two drops of 1 (M) HCl were added into the resultant turbid solution to obtain a clear pale yellow solution. Then the solution was filtered, and the filtrate was left undisturbed for slow evaporation. Two weeks later, deep yellow X-ray quality crystals of **2** were obtained (yield: 68%). Complex **2** is soluble in water ($S_{25°C} \approx 5.7$ mg mL^{-1}), methanol ($S_{25°C} \approx 3.7$ mg mL^{-1}), and acetonitrile ($S_{25°C} \approx 3.4$ mg mL^{-1}), as well as in DMSO ($S_{25°C} \approx 6.5$ mg mL^{-1}). Anal. calc. for $C_{11}H_{14}Cl_3N_5O_2Zn$: C, 31.46; H, 3.36; N, 16.67. Found: C, 31.44; H, 3.35; N, 16.64%. Main FT-IR absorptions, (KBr, cm^{-1}): 3507(s), 3402(s), 3200(s), 3144(vs), 3102(s), 3059(vs), 1979(s), 1673(vs), 1620(vs), 1544(vs), 1498(s), 1475(vs), 1422(vs) (Fig. S5, ESI†).

X-ray crystallographic analysis

Single crystal X-ray data collections were made using a Bruker SMART APEX II CCD area detector equipped with a graphite monochromated Mo Kα radiation (λ = 0.71073 Å) source in the φ and ω scan modes at 296 K for both the complexes. Cell parameter refinement and data reduction for both complexes were carried out using a Bruker SMART APEX II instrument, Bruker SMART and Bruker SAINT software.[41] The crystal structures of the title compounds were solved by an intrinsic phasing method using SHELXT-2014/5 and refined by full-matrix least squares on F^2 techniques using the SHELXL-2016/6 crystallographic software package.[42] The CIFs have been deposited with CCDC no. 2209945 (complex **1**) and CCDC no. 2209946 (complex **2**). The selected crystal data for **1** and **2** are given in Table S1 (ESI†).

Theoretical methods

The calculations of the non-covalent interactions were carried out using Gaussian-16 (ref. 43) and the PBE0-D3/def2-TZVP level of theory[44,45] and the crystallographic coordinates. The interaction energies have been computed by calculating the difference between the energies of isolated monomers and their assembly. The interaction energies are corrected for the basis set superposition error (BSSE) employing the methodology proposed by Boys–Bernardi.[46] The Bader's "Atoms in molecules" theory (QTAIM)[47] has been used to study the interactions by means of the AIMAll calculation package.[48] The molecular electrostatic potential surfaces have been computed using the Gaussian-16 software and the 0.001 a.u. isovalue. To reveal the interactions in real space, we have used the NCIPLOT index[49] based on the reduced density gradient (RDG) isosurfaces that are derived from the electronic density and its first derivative. The sign of the second Hessian eigenvalue times the electron density [*i.e.* sign(λ_2)ρ in atomic units] enables the identification of attractive/stabilizing (blue-green coloured isosurfaces) or repulsive (yellow-red coloured isosurfaces) interactions using 3D-plots.[50]
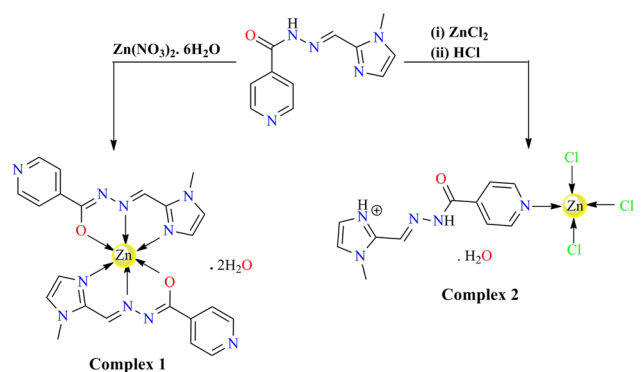
Scheme 2 Schematic representation of the synthesis of the title complexes.

Bacterial strains and culture conditions

Properly distinguished cells of *E. coli DH5α* (K12) and *S. aureus* (ATCC 29737) were obtained from the National Institute of Cholera and Enteric Diseases (NICED), Kolkata, India. Cultures were nourished on Luria broth (LB). The bacteria were cultured overnight in 3 ml of LB in a shaker at 37 °C prior to incubation with complex **2**, ligand H**L**, and positive control $ZnCl_2$ until the absorbance of the culture reached 1.0 at 600 nm, indicating the colony formation of 10^9 CFU (colony-forming unit) ml^{-1}. Sterile broth was used to dilute the overnight cultures to 10^7 CFU ml^{-1}.

Antibacterial activity study

Complex **1** was sparingly soluble in water, whereas the ligand (H**L**) and complex **2** were completely soluble in water. Thus, we did not perform the antibacterial study for complex **1**. The antibacterial activity of $ZnCl_2$ and complex **2** was confirmed through the determination of minimum inhibitory concentration (MIC). The lowest concentration of the antimicrobial agent at which no growth is observed in medium is termed as MIC. 3 ml of LB was taken in test tubes, and each of them was inoculated with overnight cultures of the bacteria, and thereafter various concentrations of complex **2** (0–5 mM), ligand H**L** (0–5 mM) and $ZnCl_2$ (0–5 mM) were added in every test tube. The tubes were shaken at 37 °C for 24 h, and the absorbances were measured at 600 nm to determine bacterial growth.

Results and discussion

Synthesis

The facile condensation of isonicotinic hydrazide with 1-methyl imidazole-2-carboxaldehyde (1 : 1 molar ratio) in ethanol furnished a neutral *ONN* donor Schiff base ligand (H**L**), [[(1-methylimidazol-2-yl)methylene]isonicotinohydrazide]. After isolation and characterization by several spectroscopic techniques, the ligand (H**L**) was utilized to prepare two zinc(II) complexes, namely, $[Zn(L)_2] \cdot 2H_2O$ (**1**) and $[Zn(H_2L)Cl_3] \cdot H_2O$ (**2**). Complex **1** was produced by reacting the ligand (H**L**) with $Zn(NO_3)_2 \cdot 6H_2O$ in an aqueous medium, whereas complex **2** was synthesized by treating $ZnCl_2$ with the ligand (H**L**) in the presence of dilute hydrochloric acid in water. In complex **1**, the ligand (H**L**) acts as an *ONN* tridentate chelating ligand, but in complex **2**, due to the protonation of the imidazole nitrogen atom, the chelating ability of the ligand (H**L**) was diminished, and it behaved as a simple monodentate ligand. Thus, a small variation in the reaction condition leads to the formation of zinc(II) complexes with two different geometries (distorted octahedra for **1** and distorted tetrahedra for **2**). The complexes were separated as block-shaped yellow single crystals from their mother solutions. The synthetic route for the complexes is shown in Scheme 2.
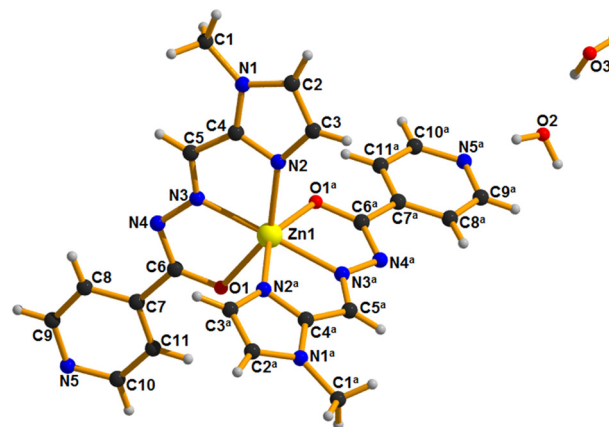

Fig. 1 Perspective view of complex **1**.

Structural description of complex 1

The perspective view of complex **1** with atom numbering scheme is displayed in Fig. 1. The single crystal X-ray diffraction study shows that the asymmetric unit of complex **1** consists of one-half of $[Zn(L)_2]$ unit (the other half being generated by an inversion center) and two non-coordinated water molecules.

Complex **1** crystallizes in a monoclinic system with the space group $C2/c$. The metal centric bond lengths and bond angles are summarized in Tables S2 and S3, respectively (ESI†). During complex formation, the ligand undergoes lactam–lactim tautomerism, and the deprotonation of the mono-negative ligand (L^-) results in the formation of first order inner metallic complex. Here, the ligand acts as the *ONN* tridentate chelating ligand through O1, N3 and N2 atoms that occupy the respective meridional planes resulting in a distorted octahedral geometry around the Zn(II) ion. The great distortion from the regular octahedral geometry is mainly due to the formation of four planar 5-membered chelate rings having bite angles in the range from 72.42(6)° to 76.76(6)°. The average Zn–N and Zn–O bond distances are 2.1388 Å and 2.1877 Å, respectively, which are in the range found for similar kinds of octahedral Zn(II) complexes. The electrical charge on the metal centre is stabilized by the two deprotonated Schiff base ligands (L^-).

Complex **1** is stabilized through π⋯π stacking, O–H⋯π and hydrogen bonding (C–H⋯O, O–H⋯N and O–H⋯O) interactions (Tables S4–S6†) that are responsible to form various supramolecular architectures. In complex **1**, the non-coordinated water molecules interact among themselves through two different self-complementary hydrogen bonding interactions (O3–H3A⋯O2 and O3–H3B⋯O2) to form a tetrameric water cluster having a $R_4^2(8)$ ring motif (Fig. 2). These water clusters connect the monomeric units of complex **1** by O2–H2A⋯N5 (169°) hydrogen bonding interactions to produce a 1D zigzag polymeric chain as depicted in Fig. 2.

Bulk water is assumed to be a combination of various small water clusters like dimers, trimers, tetramers,
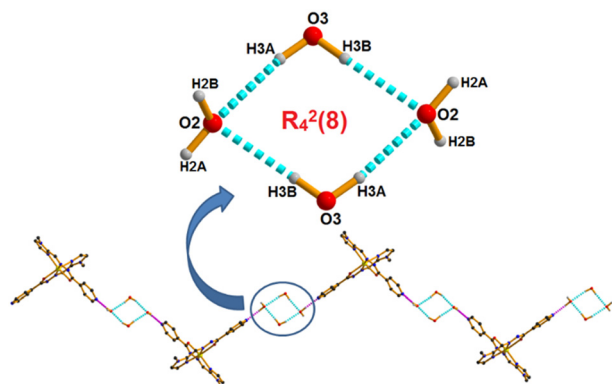
Fig. 2 Formation of 1D zigzag polymeric chain and the perspective view of water cluster through hydrogen bonding interactions in complex **1**.

pentamers, hexamers, *etc.*[51] Water clusters are smaller assemblies of a limited number of water molecules, and they are very interesting for analysis as they can reveal the nature of host–guest interactions at the molecular level.[52] Among the water clusters, the cyclic water tetramer is particularly interesting as it plays a vital role in understanding the two-structure model of liquid water and ice.[53] The study of the possible structures of water clusters in different surroundings is important to understand the nature of water–water interactions in the ice or bulk water, as well as in many biological and chemical processes.[54] Water tetramers encapsulated within different metal complex hosts have been reported by several researchers.[51,52,55–57] In our work, the water tetramer may be assigned to have a D_{2h} symmetry.

In another structure metallic moieties are connected through $\pi\cdots\pi$ interactions [Cg(5)⋯Cg(6)] and form dimeric structures, which are further connected through chelate ring⋯π interactions [Cg(1)⋯Cg(6) and Cg(3)⋯Cg(6)] and generate a 2D layered structure in *bc* plane as shown in Fig. 3. The interplanar spacing of Cg(5)⋯Cg(6), Cg(1)⋯Cg(6) and Cg(3)⋯Cg(6) is 3.8699(14) Å, 3.8699(14) Å and 3.8699(14) Å respectively.

Interestingly, the water cluster helps in the growth of the molecular crystal by filling the void spaces present in
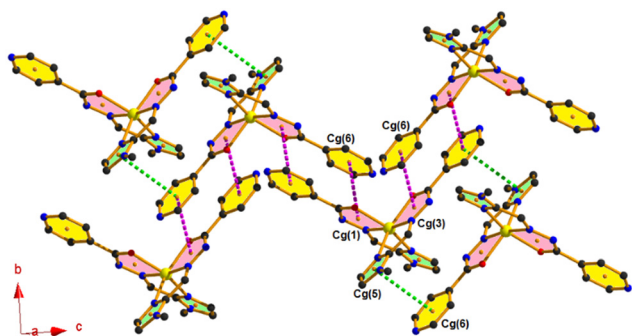
complex **1** through O2–H2B⋯O1 and O2–H2B⋯Cg(2) [O–H⋯π] hydrogen bonding interactions. Here, the hydrogen atom (H2B) of the water molecule interacts simultaneously with carbonyl oxygen (O1) and Cg(2) of the same monomeric unit in a bifurcated manner to produce a 1D chain.

Such parallel chains are further connected through weak C2–H2⋯O3 interactions symbiotically to generate a 2D architecture, as shown in Fig. 4. The space-filling model (Fig. S6†) reveals how the tetrameric water cluster helps in the growth of the molecular crystal by filling the void spaces present in complex **1**.

Structural description of complex 2

The perspective view of complex **2** with the atom numbering scheme is shown in Fig. 5. The asymmetric unit of complex **2** shows one [Zn(H₂L)Cl₃] unit and one non-coordinated water molecule. Structural investigation shows that the complex adopts a monoclinic crystal system with the $P2_1/c$ space group, and its unit cell comprises four asymmetric units. The metal centric bond lengths and bond angles are tabulated in Tables S2 and S3, respectively (ESI†). Protonation of the imidazole nitrogen atom (N2) inhibits the chelating ability of the Schiff base ligand (**HL**), and thus it behaves as a simple monodentate ligand instead of an *ONN* tridentate chelating ligand towards a Zn(II) ion. The Zn(II) ion is in a distorted tetrahedral environment completed by one pyridine nitrogen
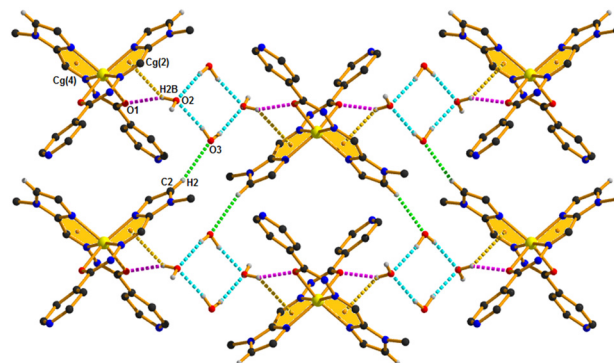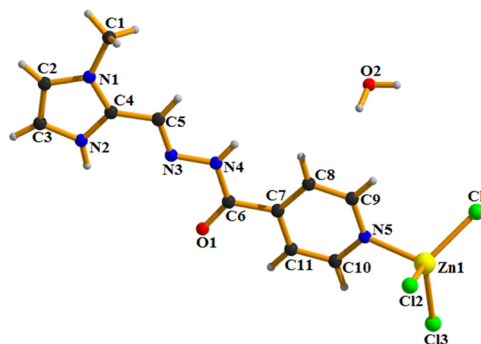

Fig. 4 Perspective view of the formation of a 2D architecture through O–H⋯π and hydrogen bonding interactions in complex **1**.

Fig. 3 Formation of supramolecular assembly through $\pi\cdots\pi$ interactions in complex **1**.

Fig. 5 Perspective view of complex **2**.

atom (N5) of the protonated Schiff base ligand (H_2L^+) and three chloride anions (Cl1, Cl2 and Cl3). The degree of distortion of the Zn(II) ion can be expressed using the parameter τ_4 (τ_4 = 0.88; τ_4 = 0 for a square planar geometry and τ_4 = 1 for a tetrahedral geometry).[58]

The bond angles around the metal center are ranging from 101.88(6)° to 119.21(3)° indicating the deviation from the ideal tetrahedral geometry. The overall tripositive charge of the complex is satisfied by the three chloride ions.

The solid-state structure of complex **2** is stabilized through $\pi\cdots\pi$ stacking, lone pair$\cdots\pi$ and various types of hydrogen bonding (C–H$\cdots$Cl, N–H$\cdots$O, N–H$\cdots$Cl, O–H$\cdots$N, O–H$\cdots$O and O–H$\cdots$Cl) interactions (Tables S4–S6†). The self-complementary nature of complex **2** results in a 2D architecture involving $\pi\cdots\pi^+$ and lone pair$\cdots\pi^+$ interactions (Fig. 6). Here, the oxygen atom (O1) of the carbonyl group (attached with one complex unit) interacts with Cg(1) of the adjacent protonated imidazole ring (π^+), which in turn interacts with Cg(2) of another unit having an interplanar spacing of 3.710(2) Å. Hence the combined effect of the lone pair$\cdots\pi^+$ and $\pi\cdots\pi^+$ interactions mutually strengthens each other.

A different 2D supramolecular network is generated incorporating lone pair$\cdots\pi$ and hydrogen bonding interactions (Fig. 7). Here, the coordinated chlorine atom (Cl2) interacts with the complex unit through two different intermolecular hydrogen bonding (C5–H5$\cdots$Cl2 and N4–H4C$\cdots$Cl2) interactions that lead to the formation of an $R_2^2(6)$ ring motif. Now, these ring motifs are further connected through the self-complementary lone pair$\cdots\pi$ interactions where the lone pair of coordinated chlorine atom (Cl3) faces towards the Cg(2) ring of the adjacent unit at ($1 - x$, $2 - y$, $1 - z$) with an angle of 101.49(3)°. Thus the lone pair$\cdots\pi$ interactions along with these two types of intermolecular hydrogen bonding interactions enhance the dimensionality from 1D to 2D as shown in Fig. 7.

In complex **2**, the non-coordinated water molecule interacts with the complex unit by the three different

Fig. 7 Perspective view of the 2D supramolecular network through lone pair$\cdots\pi$ and hydrogen bonding interactions in complex **2**.

intermolecular hydrogen bonding (N2–H2C$\cdots$O2, O2–H2A$\cdots$N3, and O2–H2A$\cdots$O1) interactions that lead to the formation of two different types of synthons, namely, $R_2^2(7)$ [A] and $R_1^2(5)$ [B]. These two synthons (A and B) are further connected by another type of intermolecular hydrogen bonding (O2–H2B$\cdots$Cl3) interaction to form a 1D zigzag polymeric chain (Fig. 8). Now, the adjacent chains interact themselves through unconventional O2$\cdots$C5 contact (tetrel bond) in a self-complementary manner resulting in a 2D layered assembly in the *bc*-plane (Fig. 8). Here, the oxygen atom (O2) of water molecule is also close to the carbon atom (C5) of the C=N bond, *i.e.*, 3.132 Å (shorter than the sum of their van der Waals radii 3.22 Å),[59] which indicates a significant O$\cdots\pi$–hole interaction.

Protonation of the nitrogen atom (N2) of the imidazole ring enhances the positive potential over the C=N bond favoring the π–hole interaction with an electron rich oxygen atom (O2), which is strongly supported by the MEP surface analysis, as well as by the QTAIM/NCI plot in the theoretical part.

DFT calculations

The theoretical study is devoted to the analysis of the hydrogen bonds involving the co-crystallized water molecules, both in the water cluster and between the water and the ligands.
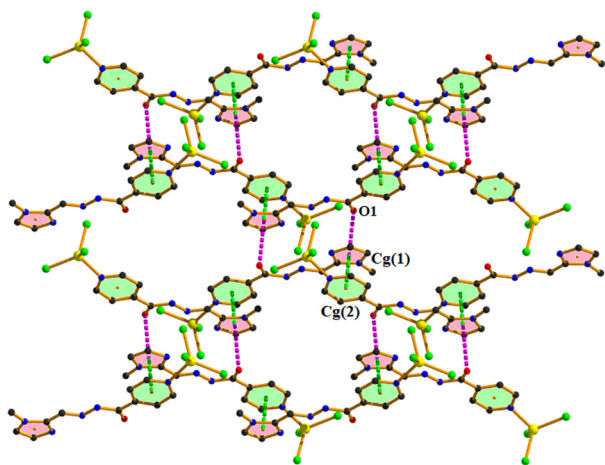

Fig. 6 Perspective view of the formation of a 2D architecture through $\pi\cdots\pi^+$ stacking and lone pair$\cdots\pi^+$ interactions in complex **2**.
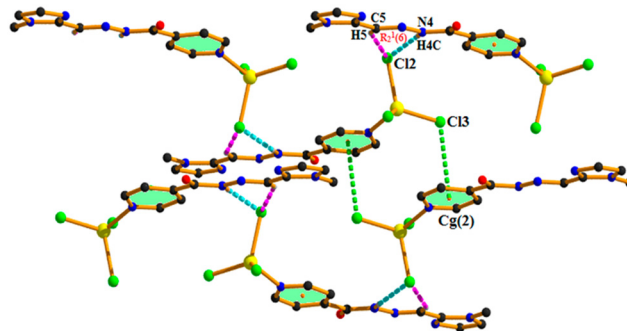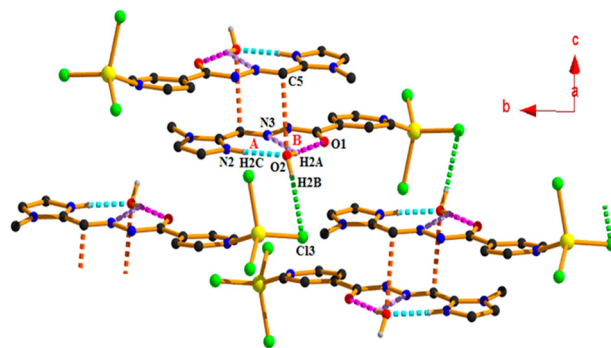

Fig. 8 2D layered assembly through O$\cdots\pi$–hole and hydrogen bonding interactions in complex **2**.

Fig. 9 MEP surface of complexes **1**·H_2O (a) and **1** (b). Isovalue 0.001 a.u. The energies at the selected points of the surfaces are given in kcal mol^{-1}. Level of theory: PBE0–D3/def2-TZVP.
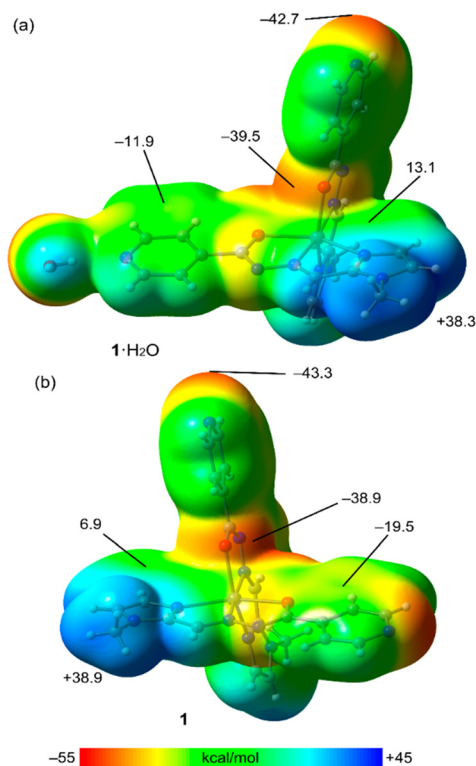

Fig. 10 MEP surface of complexes **2**·H_2O (a) and **2** (b). Isovalue 0.001 a.u. The energies at the selected points of the surfaces are given in kcal mol^{-1}. Level of theory: PBE0–D3/def2-TZVP.

Moreover, we have also analysed the influence of the water molecules on the electronic structure of the ligands and their ability to form π-stacking interactions.

We have first computed the MEP surfaces of the complexes **1** and **2** with and without the hydrogen-bonded water molecules. The MEP surfaces of **1**·H_2O and **1** are represented in Fig. 9, evidencing that the MEP minimum is located at the pyridine N-atom followed by the coordinated O-atom of the hydrazide ligand. The hydrogen-bonded water molecule slightly affects the MEP values over the aromatic rings, making the MEP values more positive. That is, the MEP value over the pyridine ring changes from −19.5 kcal mol^{-1} in **1** to −11.9 kcal mol^{-1} in **1**·H_2O, and that over the imidazole ring increases from 6.9 kcal mol^{-1} in **1** (Fig. 9b) to 13.1 kcal mol^{-1} in **1**·H_2O. The different electronic natures of both rings support the formation of the π-stacking assemblies described in Fig. 3, where the pyridine ring is stacked over the imidazole ring, which is electrostatically favoured.

The MEP surfaces of **2**·H_2O and **2** are represented in Fig. 10, showing that the MEP minimum is located at the chlorido ligands of Zn^{2+}, as expected. The MEP maximum is located at the NH of the hydrazide group in **2**·H_2O and in the imidazole group in **2**. In this complex, the MEP over the imidazole ring is very large and positive due to its protonation. The MEP over this ring is only slightly reduced by the formation of the hydrogen bond with the water molecule.
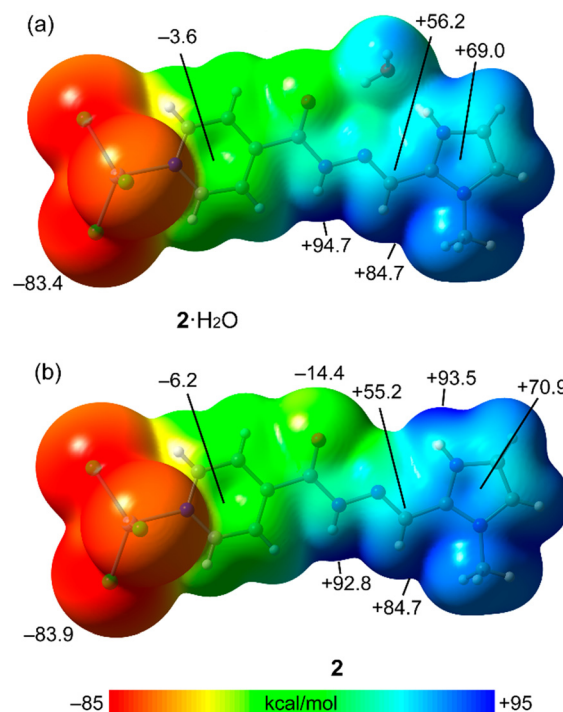
The effect of the hydrogen-bonded water on the pyridine ring is also small, slightly changing the MEP value from −6.2 kcal mol^{-1} in **2** to −3.6 kcal mol^{-1} in **2**·H_2O. Finally, it is worth mentioning that the MEP value over the C-atom of the C=N bond is large and positive (+56.2 kcal mol^{-1} in **2**·H_2O), which is thus adequate for interaction with electron rich atoms, as further analysed below.

The strength of the different hydrogen bonds involving the water molecules has been studied using the QTAIM method for the water cluster in **1** and also for the **1**·H_2O and **2**·H_2O dimers. Each hydrogen-bond is characterized by a bond critical point CP (represented as a small red sphere) and a bond path (dashed bond) connecting the H-atoms to the O/N-atoms (see Fig. 11).

The energetic results are also indicated in Fig. 11, disclosing the strong nature of the O–H⋯N and N–H⋯O H-bonds in **1**·H_2O and **2**·H_2O dimers, respectively (−6.1 kcal mol^{-1} in **1** and −6.0 kcal mol^{-1} in **2**). The QTAIM analysis confirms the existence of the three hydrogen-bonds in the **2**·H_2O dimer connecting the water molecule to the ligand. Due to the worse directionality and longer distance, the O–H⋯N is the weakest one (Fig. 11c). The total interaction energy is very large (−12.2 kcal mol^{-1}) due to the contribution of the three hydrogen-bonds, fixing the position of the water molecule and explaining the co-crystallization. Regarding the water cluster of **1**, the individual O–H⋯O hydrogen-bonds are generally weaker than those observed between water and the ligands; however the binding energy is significant (−12.6 kcal mol^{-1}) and similar to those previously reported for this type of cluster.[60]
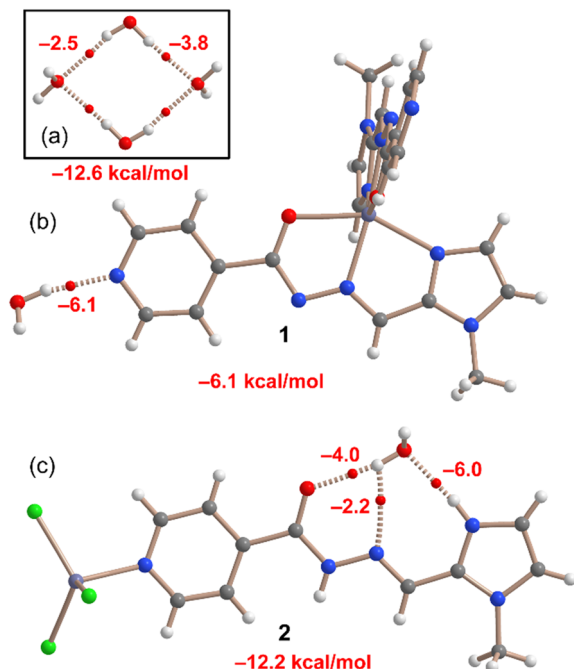
Fig. 11 QTAIM analysis (bond CPs in red) of the water cluster (a), **1**·H$_2$O dimer (b) and **2**·H$_2$O (c). The individual and total hydrogen-bond energies are indicated next to the bond CPs. Only intermolecular bond CPs and bond paths are presented.

We have also studied the influence of the water molecule on the π-stacked dimers observed in the solid state of **1**, which is described in Fig. 3. To do so, we have computed the binding energies of the dimers with and without the presence of the hydrogen-bonded water molecule, as indicated in Fig. 12. Moreover, the combined QTAIM/NCI plot analysis of the dimer is also included in Fig. 12. The NCI plot, *via* the representation of the reduced density gradient (RDG) isosurfaces, is very convenient to represent noncovalent interactions in real space. The QTAIM/NCI plot analysis confirms the existence of the pyridine⋯imidazole π-stacking
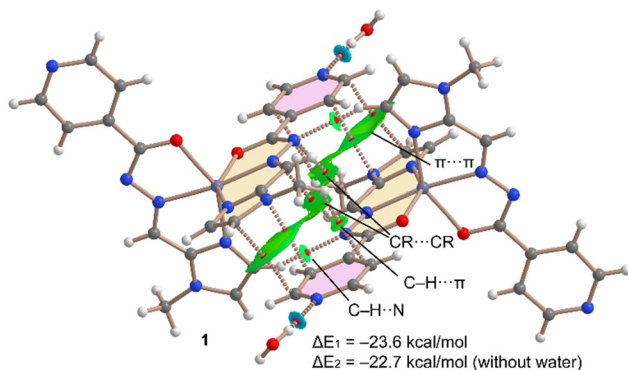
interactions, characterized by two bond CPs, bond paths and extended green RDG isosurfaces. Moreover, the analysis also shows the participation of the chelate ring (CR) interactions, since two atoms of the five membered CRs are connected *via* two bond CPs, bond paths and green RDG isosurfaces. Other ancillary interactions are also observed like the C–H⋯π and C–H⋯N contacts, both characterized by the corresponding bond CPs, bond paths and green isosurfaces. This intricate combination of interactions explains the large interaction energy of this assembly ($\Delta E_1 = -23.6$ kcal mol^{-1}) and confirms its relevance in the solid state of complex **1**. The binding energy without the presence of the hydrogen-bonded water molecules is only reduced to $\Delta E_2 = -22.7$ kcal mol^{-1}, thus suggesting that the water molecule slightly reinforces the stacking, in line with the small differences observed in the MEP values over the aromatic rings (see Fig. 9).

A similar analysis has been performed for complex **2** (see Fig. 13), showing a different behaviour. That is, the binding energy of the π-stacked dimer is strongly influenced by the presence of the water molecule. This is due to the formation of an extra interaction (O⋯C) where the O-atom of the water molecule is located over the imidic C-atom, thus forming a O⋯π–hole contact. This is strongly supported by the QTAIM/ NCI plot analysis, which shows a bond CP, bond path and green isosurface connecting the O and C-atoms. The difference between the dimerization energies (with and without water) is −6 kcal mol^{-1}, thus disclosing that such contacts are energetically significant and further contributes to the stabilization of the assembly. Moreover, the extended RDG isosurface located between the imidazole ring and the hydrazido group suggests that the π-system of the –NNHCO– groups participate in the stacking interaction.

Antibacterial effects of complex 2

Minimum inhibitory concentration affirms the antibacterial activity of complex **2** and positive control ZnCl$_2$ on both Gram-positive and Gram-negative bacteria as shown in Fig. 14. A lower concentration of complex **2** (1.89 mM) completely inhibits the growth of Gram-positive bacteria whereas a higher

Fig. 12 QTAIM analysis of intermolecular bond CPs (red spheres) and bond paths (dashed lines) of **1**·H$_2$O. Only intermolecular interactions are shown. The settings for the NCIplot are as follows: RDG = 0.5, ρ cut-off = 0.04 a.u., color scale −0.04 a.u. ≤ sign(λ_2)ρ ≤ 0.04 a.u.
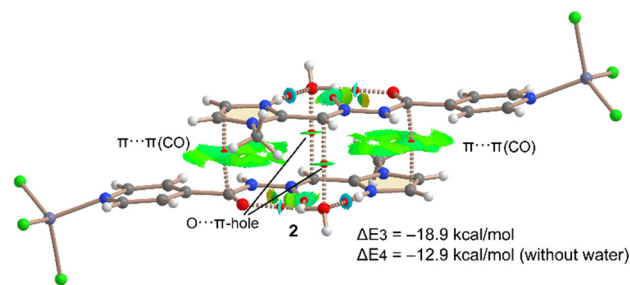

Fig. 13 QTAIM analysis of the intermolecular bond CPs (red spheres) and bond paths (dashed lines) of **2**·H$_2$O. Only intermolecular interactions are shown. The settings for the NCIplot are the following: RDG = 0.5, ρ cut-off = 0.04 a.u., color scale −0.04 a.u. ≤ sign(λ_2)ρ ≤ 0.04 a.u.
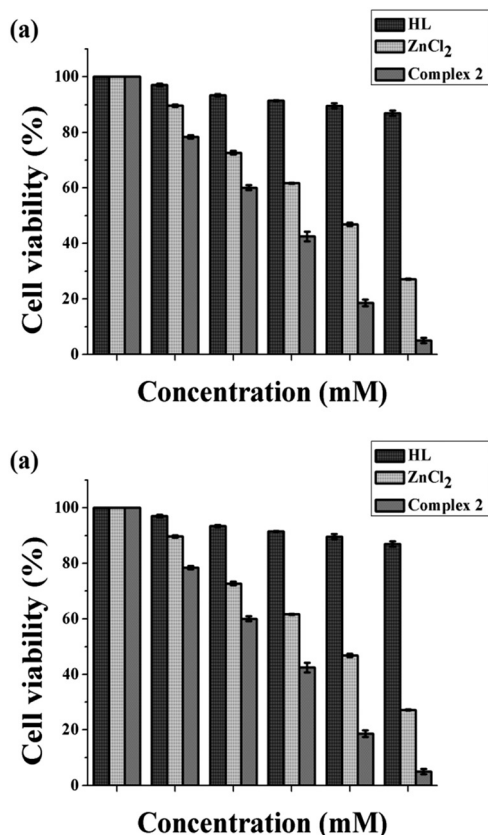
Fig. 14 Determination of minimum inhibitory concentration of ligand HL and complex **2** toward the (a) *E. coli DH5α* strain and (b) *S. aureus* strain. The results are the mean ± SD of two independent experiments.

concentration (2.64 mM) of the same was needed to inhibit the growth of Gram-negative bacteria. The MIC of $ZnCl_2$ required to inhibit the growth of *S. aureus* and *E. coli* was found to be 2.93 mM and 3.34 mM, respectively, indicating that complex **2** has higher antibacterial activity than $ZnCl_2$. However, ligand HL did not show any cytotoxic activity. The findings suggest that complex **2** has more antibacterial effect on the Gram-positive *S. aureus* strain than the Gram-negative *E. coli* strain due to the different natures of their cell walls. The cell walls of Gram-positive bacteria are composed of a thick peptidoglycan layer and teichoic acid, allowing various molecules including complex **2** to penetrate, unlike Gram-negative bacteria which inhibits the penetration of any external molecule due to presence of a unique protective outer membrane and a thin peptidoglycan layer in their cell wall.

The higher percentage in the bar graph indicates biocompatibility, whereas the lower percentage shows enhanced cell mortality. The decrease in the number of active bacterial cells on the treatment with complex **2** can be ascribed to lipophilicity and cell permeability.[61] The interaction between the Zn(II) ion and cell membrane through electrostatic forces destroys the plasma membrane and cause leakage of intracellular materials.[62]

Moreover, the protonation of the hydrazone ligand (HL) diminishes its chelation properties and makes complex **2**

more polar, preferring stronger interactions with the amino acids/proteins in bacteria. Another concept is that the metal complex can hampers the process of respiration of cells, which lead to the blockage in the synthesis of proteins causing the death of bacteria.[63]

Conclusions

In conclusion, we have successfully synthesized two Zn(II) complexes (complexes **1** and **2**) using [(1-methylimidazol-2-yl) methylene]isonicotinohydrazide [HL] as the backbone ligand with two different metal salts and crystallographically characterized and explored the non-covalent interactions related with their crystal structures. The DFT study discloses the importance of the water lattice molecules in the solid state of complexes **1** and **2**. The energetic features of the hydrogen-bonds have been studied, either interacting with the hydrogen-bond donor and acceptor groups of the ligands or forming a tetrameric water cluster.

Moreover, the influence on the stacking assemblies of complexes **1** and **2** has been studied both energetically and using MEP surface analysis, showing a strong influence in **2** due to the formation of additional π–hole O···C tetrel bonds. The QTAIM analysis further confirms that the π-system of the −NNHCO− groups participate in the stacking interaction to give additional stability to complex **2**. Besides, complex **2** shows better antibacterial activity against the Gram-positive *S. aureus* (1.89 mM) over the Gram-negative *E. coli DH5α* (2.64 mM) bacteria, whereas the ligand (HL) exhibits no such activity.

Author contributions

Samit Pramanik, Anowar Hossain, and Sudipta Pathak: investigation, methodology, data analysis and general discussion. Antonio Frontera: DFT calculation and silico studies. Subrata Mukhopadhyay: conceptualization, supervision, and validation. Sougata Ghosh Chowdhury and Parimal Karmakar: biological application. All the authors have given approval to the final version of the manuscript.

Conflicts of interest

There are no conflicts to declare.

Acknowledgements

References

1 K. T. Mahmudov, M. N. Kopylovich, M. F. C. Guedes da Silva and A. J. L. Pombeiro, *Coord. Chem. Rev.*, 2017, **354**, 54–72.

2 I. A. Rather, S. A. Wagay and R. Ali, *Coord. Chem. Rev.*, 2020, **415**, 213327–213387.

3 (*a*) M. Mitra, P. Manna, A. Bauzá, P. Ballester, S. K. Seth, S. R. Choudhury, A. Frontera and S. Mukhopadhyay, *J. Phys. Chem. B*, 2014, **118**, 14713–14726; (*b*) A. Das, S. R. Choudhury, C. Estarellas, B. Dey, A. Frontera, J. Hemming, P. Gamez and S. Mukhopadhyay, *CrystEngComm*, 2011, **13**, 4519–4527; (*c*) A. Il'ya, D. Escudero, A. Frontera, P. V. Solntsev, E. B. Rusanov, A. N. Chernega, H. Krautscheid and K. V. Domasevitch, *Dalton Trans.*, 2009, 2856–2864.

4 K. T. Mahmudov, A. V. Gurbanov, F. I. Guseinov and M. F. C. Guedes da Silva, *Coord. Chem. Rev.*, 2019, **387**, 32–46.

5 S. Jena, J. Dutta, K. D. Tulsiyan, A. K. Sahu, S. S. Choudhury and H. S. Biswal, *Chem. Soc. Rev.*, 2022, **51**, 4261–4286.

6 (*a*) S. Pramanik, S. Pathak, S. Jana, M. Mondol, A. Frontera and S. Mukhopadhyay, *New J. Chem.*, 2021, **45**, 12108–12119; (*b*) L. A. Barrios, G. Aromi, A. Frontera, D. Quinonero, P. M. Deya, P. Gamez, O. Roubeau, E. J. Shotton and S. J. Teat, *Inorg. Chem.*, 2008, **47**, 5873–5881; (*c*) C. Garau, D. Quiñonero, A. Frontera, P. Ballester, A. Costa and P. M. Deyà, *Org. Lett.*, 2003, **5**, 2227–2229.

7 N. Mohan, K. P. Vijayalakshmi, N. Koga and C. H. Suresh, *J. Comput. Chem.*, 2010, **31**, 2874–2882.

8 G. R. Desiraju, *J. Am. Chem. Soc.*, 2013, **135**, 9952–9967.

9 P. Politzer, J. S. Murray and T. Clark, *Phys. Chem. Chem. Phys.*, 2013, **15**, 11178–11189.

10 D. Dutta, P. Sharma, A. Frontera, A. Gogoi, A. K. Verma, D. Dutta, B. Sarma and M. K. Bhattacharyya, *New J. Chem.*, 2020, **44**, 20021–20038.

11 P. Politzer, J. S. Murray and T. Clark, *J. Phys. Chem. A*, 2019, **123**, 10123–10130.

12 A. Bauzá, A. V. Sharko, G. A. Senchyk, E. B. Rusanov, A. Frontera and K. V. Domasevitch, *CrystEngComm*, 2017, **19**, 1933–1937.

13 T. Basak, A. Bhattacharyya, M. Das, K. Harms, A. Bauzá, A. Frontera and S. Chattopadhyay, *ChemistrySelect*, 2017, **2**, 6286–6295.

14 A. Bhattacharyya, M. Das, A. Bauzá, S. Herrero, R. González-Prieto, A. Frontera and S. Chattopadhyay, *New J. Chem.*, 2017, **41**, 13585–13592.

15 D. Sadhukhan, M. Maiti, A. Bauzá, A. Frontera, E. Garribba and C. J. Gomez-García, *Inorg. Chim. Acta*, 2019, **484**, 95–103.

16 S. Shaygan, H. Pasdar, N. Foroughifar, M. Davallo and F. Motiee, *Appl. Sci.*, 2018, **8**, 385–397.

17 C. Verma and M. A. Quraishi, *Coord. Chem. Rev.*, 2021, **446**, 214105–214127.

18 W. Al Zoubi and Y. G. Ko, *Appl. Organomet. Chem.*, 2017, **31**, 3574–3586.

19 K. Ghosh, A. Banerjee, A. Bauzá, A. Frontera and S. Chattopadhyay, *RSC Adv.*, 2018, **8**, 28216–28237.

20 D. K. Kölmel and E. T. Kool, *Chem. Rev.*, 2017, **117**, 10358–10376.

21 D. Sadhukhan, A. Ray, G. Pilet, G. M. Rosair, E. Garribba, A. Nonat, L. J. Charbonnière and S. Mitra, *Bull. Chem. Soc. Jpn.*, 2011, **84**, 764–777.

22 D. Sadhukhan, M. Maiti, A. Bauzá, A. Frontera, E. Garribba and C. J. Gomez-García, *Inorg. Chim. Acta*, 2019, **484**, 95–103.

23 B. D. Nath, M. M. Islam, M. R. Karim, S. Rahman, M. A. A. Shaikh, P. E. Georghiou and M. Menelaou, *ChemistrySelect*, 2022, **7**, 202104290.

24 Y. Gou, J. Li, B. Fan, B. Xu, M. Zhou and F. Yang, *Eur. J. Med. Chem.*, 2017, **134**, 207–217.

25 M. A. Malik, O. A. Dar, P. Gull, M. Y. Wani and A. A. Hashmi, *MedChemComm*, 2018, **9**, 409–436.

26 M. Streater, P. D. Taylor, R. C. Hider and J. Porter, *J. Med. Chem.*, 1990, **33**, 1749–1755.

27 M. Porchia, M. Pellei, F. Del Bello and C. Santini, *Molecules*, 2020, **25**, 5814.

28 S. Adhikari, T. Bhattacharjee, R. J. Butcher, M. Porchia, M. De Franco, C. Marzano, V. Gandin and F. Tisato, *Inorg. Chim. Acta*, 2019, **498**, 119098.

29 M. V. Kirillova, A. M. Kirillov, M. F. C. G. da Silva, M. N. Kopylovich, J. J. F. da Silva and A. J. Pombeiro, *Inorg. Chim. Acta*, 2008, **361**, 1728–1737.

30 X. Luo, R. Abazari, M. Tahir, W. K. Fan, A. Kumar, T. Kalhorizadeh, A. M. Kirillov, A. R. Amani-Ghadim, J. Chen and Y. Zhou, *Coord. Chem. Rev.*, 2022, **461**, 214505.

31 J. B. Araškov, A. Višnjevac, J. Popović, V. Blagojević, H. S. Fernandes, S. F. Sousa, I. Novaković, J. M. Padrón, B. B. Holló, M. Monge and M. Rodríguez-Castillo, *CrystEngComm*, 2022, **24**, 5194–5214.

32 R. Abazari, E. Yazdani, M. Nadafan, A. M. Kirillov, J. Gao, A. M. Slawin and C. L. Carpenter-Warren, *Inorg. Chem.*, 2021, **60**, 9700–9708.

33 J. Z. Gu, Y. Cai, X. X. Liang, J. Wu, Z. F. Shi and A. M. Kirillov, *CrystEngComm*, 2018, **20**(7), 906–916.

34 G. Psomas, *Coord. Chem. Rev.*, 2020, **412**, 213259.

35 Y. Deswal, S. Asija, A. Dubey, L. Deswal, D. Kumar, D. K. Jindal and J. Devi, *J. Mol. Struct.*, 2022, **1253**, 132266.

36 K. Chkirate, K. Karrouchi, N. Dege, N. K. Sebbar, A. Ejjoummany, S. Radi, N. N. Adarsh, A. Talbaoui, M. Ferbinteanu, E. M. Essassi and Y. Garcia, *New J. Chem.*, 2020, **44**, 2210–2221.

37 A. Gaber, M. S. Refat, A. A. Belal, I. M. El-Deen, N. Hassan, R. Zakaria, M. Alhomrani, A. S. Alamri, W. F. Alsanie and E. M. Saied, *Molecules*, 2021, **26**, 2288.

38 A. Tarushi, X. Totta, A. Papadopoulos, J. Kljun, I. Turel, D. P. Kessissoglou and G. Psomas, *Eur. J. Med. Chem.*, 2014, **74**, 187–198.

39 M. Pellei, F. Del Bello, M. Porchia and C. Santini, *Coord. Chem. Rev.*, 2021, **445**, 214088.

40 B. Kaya, Z. K. Yılmaz, O. Şahin, B. Aslim and B. Ülküseven, *New J. Chem.*, 2020, **44**, 9313–9320.

41 *Bruker, SMART v5.631*, Bruker AXS Inc., Madison, WI, USA, 2001.

42 G. M. Sheldrick, *SHELXT-2014*, University of Göttingen, 2014.

43 M. J. Frisch, G. W. Trucks, H. B. Schlegel, G. E. Scuseria, M. A. Robb, J. R. Cheeseman, G. Scalmani, V. Barone, G. A. Petersson, H. Nakatsuji, X. Li, M. Caricato, A. V. Marenich, J. Bloino, B. G. Janesko, R. Gomperts, B. Mennucci, H. P.

Hratchian, J. V. Ortiz, A. F. Izmaylov, J. L. Sonnenberg, D. Williams-Young, F. Ding, F. Lipparini, F. Egidi, J. Goings, B. Peng, A. Petrone, T. Henderson, D. Ranasinghe, V. G. Zakrzewski, J. Gao, N. Rega, G. Zheng, W. Liang, M. Hada, M. Ehara, K. Toyota, R. Fukuda, J. Hasegawa, M. Ishida, T. Nakajima, Y. Honda, O. Kitao, H. Nakai, T. Vreven, K. Throssell, J. A. Montgomery, Jr., J. E. Peralta, F. Ogliaro, M. J. Bearpark, J. J. Heyd, E. N. Brothers, K. N. Kudin, V. N. Staroverov, T. A. Keith, R. Kobayashi, J. Normand, K. Raghavachari, A. P. Rendell, J. C. Burant, S. S. Iyengar, J. Tomasi, M. Cossi, J. M. Millam, M. Klene, C. Adamo, R. Cammi, J. W. Ochterski, R. L. Martin, K. Morokuma, O. Farkas, J. B. Foresman and D. J. Fox, *Gaussian 16, Revision C.01*, Gaussian, Inc., Wallingford CT, 2016.

44   S. Grimme, J. Antony, S. Ehrlich and H. Krieg, *J. Chem. Phys.*, 2010, **132**, 154104.

45   F. Weigend, *Phys. Chem. Chem. Phys.*, 2006, **8**, 1057–1065.

46   S. F. Boys and F. Bernardi, *Mol. Phys.*, 1970, **19**, 553–566.

47   R. F. W. Bader, *J. Phys. Chem. A*, 1998, **102**, 7314–7323.

48   T. A. Keith, *AIMAll (Version 13.05.06)*, TK Gristmill Software, Overland Park, KS, 2013.

49   J. Contreras-García, E. R. Johnson, S. Keinan, R. Chaudret, J.-P. Piquemal, D. N. Beratan and W. Yang, *J. Chem. Theory Comput.*, 2011, **7**, 625–632.

50   E. R. Johnson, S. Keinan, P. Mori-Sánchez, J. Contreras-García, A. J. Cohen and W. Yang, *J. Am. Chem. Soc.*, 2010, **132**, 6498–6506.

51   E. A. Cobar, P. R. Horn, R. G. Bergman and M. Head-Gordon, *Phys. Chem. Chem. Phys.*, 2012, **14**, 15328–15339.

52   S. Thakur, A. Frontera and S. Chattopadhyay, *Inorg. Chim. Acta*, 2021, **515**, 120057.

53   B. Dutta, S. R. Ghosh, A. Ray, S. Jana, C. Sinha, S. Das, A. D. Jana and M. H. Mir, *New J. Chem.*, 2020, **44**(, 15857–15870.

54   B. Bagchi, *Water in Biological and Chemical Processes: From Structure and Dynamics to Function*, Cambridge University Press, Cambridge, 2013.

55   O. Fabelo, J. Pasán, L. Cañadillas-Delgado, F. S. Delgado, A. Labrador, F. Lloret, M. Julve and C. Ruiz-Pérez, *CrystEngComm*, 2008, **10**, 1743–1746.

56   D. Sun, M. Z. Xu, S. S. Liu, S. Yuan, H. F. Lu, S. Y. Feng and D. F. Sun, *Dalton Trans.*, 2013, **42**, 12324–12333.

57   S. Roy, T. Basak, S. Khan, M. G. Drew, A. Bauzá, A. Frontera and S. Chattopadhyay, *ChemistrySelect*, 2017, **2**, 9336–9343.

58   L. Yang, D. R. Powell and R. P. Houser, *Dalton Trans.*, 2007, 955–964.

59   H. Kruse, K. Mrazikova, L. d'Ascenzo, J. Sponer and P. Auffinger, *Angew. Chem.*, 2020, **132**, 16696–16703.

60   S. Li, A. Azizi, S. R. Kirk and S. Jenkins, *Int. J. Quantum Chem.*, 2020, **120**, 26361.

61   R. S. Joseyphus and M. S. Nair, *Mycobiology*, 2008, **36**, 93–98.

62   S. Mahato, N. Meheta, M. Kotakonda, M. Joshi, M. Shit, A. R. Choudhury and B. Biswas, *Polyhedron*, 2021, **194**, 114933.

63   H. Kargar, A. A. Ardakani, M. N. Tahir, M. Ashfaq and K. S. Munawar, *J. Mol. Struct.*, 2021, **1233**, 130112.